Digitized by the Internet Archive
in 2024

https://archive.org/details/physica-scripta_1954_8

QC
1
S923

634

ARKIV FÖR FYSIK

UTGIVET AV

K. SVENSKA VETENSKAPSAKADEMIEN

Band 8

Med 54 avhandlingar

STOCKHOLM
ALMQVIST & WIKSELLS BOKTRYCKERI AB

LONDON
H. K. LEWIS & CO., LTD
136, GOWER STREET

1954

PARIS
LIBRAIRIE C. KLINCKSIECK
11 RUE DE LILLE

Häfte	1	innehållande	Nr	1—6	utkom	den	15	maj	1954
»	2	»	Nr	7—17	»	»	13	okt.	1954
»	3	»	Nr	18—28	»	»	27	okt.	1954
»	4	»	Nr	29—39	»	»	20	nov.	1954
»	5	»	Nr	40—48	»	»	14	dec.	1954
»	6	»	Nr	49—54	»	»	30	»	1954

ÅTTONDE BANDETS INNEHÅLL

Sid.

1. Borelius, G. and Rudberg, E., Reports from the Conference of the Swedish National Committee for Physics in 1953 . . . . 1—20
2. Bergström, I. and Hill, R. D., Auger electrons from the L-shell in mercury 21—26
3. Mladjenović, M., Natural widths of the internal conversion lines of RaB 27—48
4. Mladjenović, M. and Hedgran, A., An investigation of the Compton secondaries from RaC gamma-rays . . . . 49—64
5. Mladjenović, M. and Slätis, H., Internal conversion spectrum of the active deposit of radon . . . . 65—82
6. Lagerqvist, A., Ultra-violet and blue bands of calcium oxide . . . . . 83—95
7. Brogren, G. and Adell, Ö., The anomalous X-ray transmission in calcite 97—112
8. Adell, Ö., The transmission and reflection of X-rays in a thin calcite crystal . . . . 113—119
9. v. Friesen, S. and Stigmark, L., Photo-electric mass determinations in nuclear emulsions. Part III. Description of the new experimental arrangements . . . . 121—127
10. Sandström, A. E., The resolving power of a large bent crystal spectrograph 129—146
11. Sandström, A. E. and Nordfors, B., The transparency of cellulose acetate, cellophane, nylon, mylar, and teflon in the region 3 to 10 Å . . 147—149
12. Giansoldati, A., Paramagnetic susceptibility of Au Cr alloys . . . . . 151—154
13. Norlind, N., A note on mass estimation by the range-scattering method 155—160
14. Ahnlund, K. and Mileikowsky, C., Proton groups from the reaction $O^{18}(d, p)O^{19}$ . . . . 161—163
15. Holte, G., On the spatial distribution of neutrons slowed down in carbon and water . . . . 165—171
16. Fröman, P. O., A simple derivation of a general equilibrium equation, with two astrophysical applications . . . . 173—175
17. Lundqvist, S. O., A quantum mechanical investigation of the binding energy of the LiH-crystal . . . . 177—196
18. Minnhagen, L. and Nordberg, U.-B., Relative intensities of Stark effect components in the arc spectrum of helium . . . . 197—200
19. Taylor, C., A peak height comparison method for mass spectrometry . 201—210
20. Avellén, S., The vacuum-ultraviolet spectrum of Cl I . . . . 211—212
21. Pauli, R., Ahnlund, K. and Mileikowsky, C., The reaction energy of $O^{17}(d, \alpha)N^{15}$ . . . . 213—217
22. Thulin, S., Moreau, J. and Atterling, H., The decay of As^{71} . . . . 219—228
23. Thulin, S., Moreau, J. and Atterling, H., The decay of Kr^{79} . . . . 229—238
24. Coulson, C. A. and Danielsson, U., Ionic and covalent contributions to the hydrogen bond. Part I . . . . 239—244
25. Coulson, C. A. and Danielsson, U., Ionic and covalent contributions to the hydrogen bond. Part II . . . . 245—255
26. Lindholm, E., Ionization and fragmentation of N_2 by bombardment with atomic ions. Dissociation energy of N_2 . . . . 257—264
27. Uhler, U., The blue band-system of niobium oxide . . . . 265—279

Sid.

28. Lagerqvist, A., Uhler, U., and Barrow, R. F., The rotational analysis of the α and γ systems of zirconium oxide . . . . 281—293
29. Uhler, U., The rotational analysis of the β-system of zirconium oxide . 295—304
30. von Friesen, S., Photo-electric mass determinations in nuclear emulsions. Part II. A new correction for local variations in the emulsion with a report on the photo-electric identificaton of K-particles . . . . 305—310
31. Kristiansson, K., Photo-electric mass determinations in nuclear emulsions, Part I. An investigation of the accuracy of mass determinations 311—331
32. Kleman, B. and Lindkvist, S., The band-spectrum of the Cu$_2$-molecule 333—339
33. Erlandsson, G., Microwave spectrum of chlorobenzene . . . . 341—342
34. Hulthén, E. and Neuhaus, H., Diffraction gratings in immersion . . . 343—353
35. Norinder, H. and Salka, O., The determination of electric discharge fields with a special klydonograph . . . . 355—368
36. Waldeskog, B., A delayed disintegration of a heavy nucleus . . . . . 369—370
37. Brogren, G., The reflection and transmisson of X-rays in quartz near the Bragg angle . . . . 371—382
38. Djurle, E., On the origin of unsymmetrical Rowland ghosts in optical gratings . . . . 383—389
39. Brogren, G., A note on the widths of X-ray emission lines . . . . . . 391—400
40. Brogren, G. and Adell, Ö., The anomalous X-ray transmission in calcite. II. Investigations in the wavelength range 558 X.U.–1932 X.U. . . . . 401—426
41. Lagerqvist, A. und Huldt, L., Über die Höhe der angeregten Elektronenzustände von CaO, SrO und BaO . . . . 427—432
42. Lindholm, E., Ionization and fragmentation of CO by bombardment with atomic ions. Dissociation energy of CO. Heat of sublimation of carbon 433—440
43. Slätis, H., On the determination of the relative intensities of conversion lines recorded photographically in a semicircular beta-ray spectrograph 441—450
44. Beckman, L., Experiments with an ion source having magnetic analysis of the ion beam . . . . 451—456
45. Bergstrand, E., The group velocity of light in glass and calcite . . . . 457—469
46. Minnhagen, L. and Stigmark, L., Equipment for excitation of spectra by high frequency pulses . . . . 471—479
47. Lagerqvist, A. und Almkvist, G., Das ultraviolette Bandensystem des Strontiumoxydes . . . . 481—488
48. Ahnlund, K., Thulin, S. and Pauli, R., The reaction energies of $O^{17}(d,p)O^{18}$ and $C^{13}(d,p)C^{14}$ . . . . 489—494
49. Åström, H. U., The solubility of nitrogen in α-iron . . . . 495—503
50. Kleman, B., Lindkvist, S. and Selin, L-E., The band spectrum of the Au$_2$-molecule . . . . 505—510
51. Linde, J. O. and Edwardsson, S., Investigation of the critical shear stress for single crystals of metallic solid solutions. II. . . . . 511—519
52. Sjölander, A. and Köhler, S., Polarization of nucleons by scattering with spin-orbit coupling . . . . 521—525
53. Dinger, H., A quantum mechanical study of the fluorine molecule . . . 527—550
54. Lennander, S., Measurements of electron diffraction intensities by means of Geiger counters. Experimental determination of relative values of the atomic factor for gold, silver, and aluminium . . . . 551—613

ARKIV FÖR FYSIK Band 8 nr 1

Read 13 January 1954

Reports from the Conference of the Swedish National Committee for Physics in 1953

By GUDMUND BORELIUS and ERIK RUDBERG

The seventh general physics conference arranged by the Swedish National Committee for Physics was held on September 28–30, 1953. This was the first time such a gathering convened in Gothenburg. Chalmers Institute of Technology had most generously assumed the task to serve as host to the meeting, which assembled in the lecture halls of the Department of Physics. The buildings, the facilities for research and teaching and the research work now in progress were shown to the conference members by the Director, Prof. NILS RYDE. The organisation of teaching and research in the Department of Electrical Engineering was the subject of a lecture by Prof. S. EKELÖF, after which the assembly was invited by Prof. EKELÖF, Prof. RYDBECK and Prof. WALLMAN to visit their new laboratories for Electrical Measurements, for Electronics and for Telecommunication. The Gothenburg physics conference had the pleasure of welcoming to its sessions several distinguished visitors from other countries. Dr. M. EDLUND of Oak Ridge gave a survey of recent reactor developments in the United States. Prof. T. W. BONNER, just arrived from the Rice Institute, Houston, lectured on excited states of light nuclei. Contributions to nuclear theory were presented by the two guests from Copenhagen: Dr. A. BOHR spoke about rotational states of the atomic nuclei, and Dr. T. HUUS discussed Coulomb excitation of heavier atomic nuclei. The other papers presented at the Gothenburg physics conference are included as short summaries in the remainder of this report.

As the Secretary of the conference, Dr. SVEN BENNER, of the Radiophysics Laboratory at the King Gustaf V Jubilee Clinic in Gothenburg, shared with the Director and the staff of the Physics Department the responsibility for the success of this meeting.

KATARINA AHNLUND, Nobel Institute of Physics, Stockholm

Reaction energies of $Ne^{20}(d,p)Ne^{21}$ and $Ne^{22}(d,p)Ne^{23}$ and the atomic mass of Ne^{23}

At the High Voltage Laboratory of the Nobel Institute thin electromagnetically separated gas-targets of Ne^{20} and Ne^{22} were bombarded with 0.87 MeV deuterons and the proton groups were analyzed in a heavy particle spectrometer. The values obtained are:

$Ne^{20}(d,p)Ne^{21}$ $\quad Q_0 = 4.526 \pm 0.009$ MeV
$Q_1 = 4.177 \pm 0.009$ MeV
$Q_0 - Q_1 = 0.349 \pm 0.006$ MeV

$Ne^{22}(d,p)Ne^{23}$ $\quad Q_0 = 2.968 \pm 0.008$ MeV

From the last value we calculate the atomic mass of Ne^{23} and get $Ne^{23} = 23.001763 \pm 0.000027$ a.m.u.

O. Almén and A. Lundén, Department of Physics, Chalmers Institute of Technology, Gothenburg

An electromagnetic isotope separator

An electromagnetic isotope separator has been built at the Department of Physics, Chalmers University of Technology. An ion source of magnet type is used. The ions are accelerated to 45 keV in a lens system which produces a parallel beam. A magnet with the radius 100 cm deflects the ions 90° before they are collected on the target. The magnetic field is stabilized directly by means of a rotating coil. The output voltage from this coil through an electronic device controls the machine that produces the direct current fed to the magnet. The rotating coil is driven by a synchronous machine run on 50 c/sec. from a frequency standard. The stability of the magnetic field is better than 0.05 %.

Hugo Atterling, Nobel Institute of Physics, Stockholm

Cyclotron acceleration of heavy ions

The 225-cm fixed-frequency cyclotron at the Nobel Institute of Physics,[1] Stockholm, has been used for acceleration of heavy ions (in particular $^{12}C^{6+}$, $^{14}N^{6+}$ and $^{16}O^{6+}$). With the present oscillator frequency the ions can be accelerated to about $12.5 \times A$ MeV, A being the atomic mass number of the ion. The maximum attainable energy therefore is for ^{12}C ions 150 MeV, and for ^{16}O ions 200 MeV. The magnetic field used for deuteron acceleration is 11,500 oersteds. As, however, the maximum obtainable field is approximately 18,000 oersteds, ions with as high mass-to-charge ratio as 3 can be accelerated. The current of ions is increased by increasing the pressure of gas in the cyclotron chamber. The best beam current so far obtained of $^{14}N^{6+}$ ions reaching the maximum radius with energies > 60 MeV is about 10^{10} ions/sec. For $^{16}O^{6+}$ ions with energies > 60 MeV the current is about 10^9 ions/sec. When producing nitrogen ions, the ion source is fed with nitrous oxide (N_2O) or nitrogen. Nitrous oxide is also used for the production of oxygen ions. A more detailed description of the experiments will be published in *Arkiv för Fysik*.

Allan Bergstedt, Department of Physics, Atomic Energy Laboratory, Stockholm

Electrostatic precipitation apparatus for air monitoring

Two types of instruments are described, both utilizing electrostatic precipitation for the collection of the dust. In the first (portable) type the dust is precipitated on a plate, and the alpha, beta or gamma activity is then measured by means of scintillation counters. The second type is a continuous air monitor in which the dust is collected on a moving aluminium tape. The tape speed and the positions of the detectors along the tape can be varied for different applications. For monitoring of atmospheric dust activity the positions of the detectors are usually chosen to give a delay of about six hours between collection and measurement in order to allow the short-lived activity (mainly from radon products) to decay. The activity is recorded on a triple-channel chart recorder.

---

[1] H. Atterling and G. Lindström, Nature, *169*, 432 (1952).

LARS BLOCK, Department of Electronics, Royal Institute of Technology, Stockholm

Electric discharges in magnetic dipole fields

STÖRMER has calculated orbits of charged particles in magnetic dipole fields. Particularly with regard to the theory of aurora and magnetic storms, it is valuable to study electric discharges in such fields. An experiment on this subject is now in progress at the Department of Electronics, Royal Institute of Technology, Stockholm. Comparisons are made between the current orbits observed in the discharge, the orbits calculated by STÖRMER and those required to explain the magnetic disturbances on the earth during a magnetic storm. Particular interest is devoted to the energies and temperatures of the ions and electrons in the discharge for making comparisons with the energies of the impinging particles of the aurora.

E. BLOMSJÖ, Department of Physics, Atomic Energy Laboratory, Stockholm

A 150 kV neutron generator

A transportable accelerator has been built. The acceleration tube and vacuum system can be moved in a vertical direction. The acceleration tube can also be turned to any angle about a horizontal axis, so that the ion beam can be directed in the most convenient direction for any particular experiment. High voltage is obtained from a Philips X-ray set, type MG 150. Neutrons are produced by the D-D-reaction. The equipment has been used as a pulsed neutron source.

E.-Å. BRUNBERG, Department of Electronics, Royal Institute of Technology, Stockholm

On the anisotropy of cosmic radiation and the determination of its direction by measurements of the diurnal variation

During the last decades the intensity of cosmic radiation has been measured by means of counter telescopes and ionization chambers. As a result of detailed measurements a diurnal variation in the primary radiation has been definitely proved. The problem is now to determine the direction of this anisotropy, which is of great importance for the understanding of the origin of cosmic rays and other cosmical phenomena.

As the deflection of cosmic particles in the magnetic field of the earth is known by experiments using models,[1] this determination is now possible.

Preliminary results show that the anisotropy has a direction approximately tangential to the earth's orbit and that the excess radiation comes in from the evening side of the orbit. It seems probable that this direction depends on the solar activity.

G. F. VON DARDEL, Department of Physics, Atomic Energy Laboratory, Stockholm

The slowing down of neutrons

The time scale for the slowing down process for neutrons in a moderator has been studied by measuring, with a BF_3-detector connected to a time-analyzer, the transmission through various absorbers and the rate of decay of the neutron flux, produced by a pulsed neutron source, in a moderator. In water of room temperature the slowing down process occurs very nearly as if the moderator were a monatomic gas of free nuclei, having the mass of the water molecules, a case which has been studied theoretically. In ice of 98° K the bonds between the molecules give rise to a discrepancy between the experimental results and this simple theory. Measurements on neutrons slowed down in heavy water indicate a much slower process than in ordinary water. Good agreement is obtained between experimental results and the calculated curve, assuming the moderator to consist of free deuterons, for the transmission through a cadmium absorber. The logarithmic slope of the measured decay curves which is determined by the geometric buckling of the moderating geometry, and by the diffusion coefficient and mean life for absorption of the neutrons in the moderator, can be used for the determination of these quantities.

G. F. VON DARDEL, Department of Physics, Atomic Energy Laboratory, Stockholm

The mean life of neutrons in water and the neutron-proton capture cross-section

The mean life of neutrons in distilled water of 20° C has been determined by measuring the decay of the integrated neutron intensity produced by a pulsed neutron source in a sufficiently large tank, so that leakage can be neglected. The integration in the axial direction was carried out automatically by cylindrical boron trifluoride counters which extended through the entire depth of the tank, whereas the integration in the radial direction was performed numerically. After applying corrections for background, for counting losses, and for the depression caused by the counters, a neutron mean life of 212 ± 3 μsec. is obtained, which corresponds to a neutron-proton capture cross-section of 0.321 ± 0.06 barns, in satisfactory agreement with the recent determination by a quite different method of HAMERMESH, RINGO and WEXLER.

---

[1] Å. BRUNBERG and DATTNER, Tellus, *5*, 135, 269 (1953).

ERIK DJURLE, ERIK INGELSTAM, LARS JOHANSSON, Optics Laboratory, Royal Institute of Technology, Stockholm

Comparison of performance between a photoelectric and a visual intensity ratio meter (receivers for the phase contrast refractometer)

Two new receivers have been constructed for use with the phase contrast refractometer,[1] one visual (E.I. and L.J.) and one photoelectric (E.D.). The principle is that the luminance ratio of two rectangular areas in the image is measured, and used to find the optical path differences. In the visual photometer the light from each area is polarized in a fixed direction, and a prism and lens system brings the images of the slits close together in the viewing microscope. Equal luminance for the slits is achieved by a turnable polaroid placed in the exit light beam. According to measurements of eye discrimination factors, the ratio measurements should be accurate to within 2.5 per cent, which corresponds to a phase change of $0.003\,\lambda$. This agrees with our experience.

The photoelectric ratio meter uses one photomultiplier tube and a modulation of the light beams from the two areas, which are alternately switched onto the photocathode. The resulting a.c. voltage from the photomultiplier is amplified and fed to an oscilloscope synchronized with the modulation. A grey wedge in one of the beams from the double slit is adjusted till the signal on the oscilloscope is zero, i.e., the electronic circuit serves as a null indicator. The intensity ratio can be measured with an accuracy of 0.3 per cent, corresponding to $0.0004\,\lambda$.

GUNNAR ERLANDSSON, Department of Physics, University of Stockholm

Microwave spectroscopic determination of the molecular structure of fluorobenzene

The pure rotational spectrum of monofluorobenzene in the region 17.7–27.7 kMc/s has been analysed. 50 absorption lines have been observed. 21 of these have been identified as arising from transitions $J = 3$–4, 4–5, 5–6 and 6–7. 16 lines have been identified as transitions having $\Delta J = 0$ and J-values up to 57. The rotational constants have been calculated from the theory of the rigid asymmetric rotator. For J-values below 30 the agreement between observed and calculated frequency values is complete within the limits of error in the measurements, i.e. ± 5 Mc/s $= 0.02\,\%$. Assuming the molecular structure to be plane and regularly hexagonal (except for the fluorine atom), and the C–H distance to be $d_{\mathrm{CH}} = 1.05 + \Delta d_{\mathrm{CH}}$ Å, the C–C and C–F distances have been calculated. The results are

$$d_{\mathrm{CC}} = 1.4043 \pm 0.0003 - 0.13\,\Delta d_{\mathrm{CH}}\ \text{Å}$$
$$d_{\mathrm{CF}} = 1.294 \pm 0.010 - 0.47\,\Delta d_{\mathrm{CH}}\ \text{Å},$$

in good agreement with FINBAK's and HASSEL's results from electron diffraction measurements, which are

$$d_{\mathrm{CH}} = 1.04 \pm 0.05\ \text{Å},\ d_{\mathrm{CC}} = 1.40 \pm 0.01\ \text{Å},\ d_{\mathrm{CF}} = 1.31 \pm 0.03\ \text{Å}.$$

---

[1] E. INGELSTAM, Arkiv för Fysik, *6*, No. 29 (1953).

G. EKSPONG, Department of Physics, University of Uppsala

Inelastic scattering of π-mesons

In a nuclear research emulsion, which had been exposed to cosmic radiation, an event was found which has been interpreted as an example of inelastic scattering of a π^+-meson. As very little is known up to now about this process at the low energy in question, the interest devoted to this study would seem to be justified.

The track of the primary π-meson enters the emulsion from its surface and suffers a deviation of 66° after a track length of 1200 μ. The ionization of the track is quite different before and after the deflection, being much greater afterwards. This fact indicates a large loss of energy in the collision. After the deflection the track ends in the emulsion, the π-meson decaying to a μ-meson of usual energy (μ-meson track length being 606 μ).

From scattering and ionization measurements on the primary track its nature is definitely shown to be a π- or a μ-meson. As it seems to be out of question to assume the corresponding particle to be a μ-meson, the only alternative is to regard it as a π-meson. From the measurements its energy at the point of deflection is calculated to be 7.9 ± 0.4 MeV.

After the deflection the energy of the π-meson is found from its range to be 2.92 ± 0.08 MeV. The errors are standard deviations. The energy loss is thus 5.0 ± 0.5 MeV.

One interesting feature of the event is the low energy of the outgoing positive meson. It is assumed that the meson must have been in close contact with the struck nucleus in order to be able to transfer the energy of 5 MeV. The low energy of the outgoing meson is compatible with a collision with a carbon, nitrogen or oxygen nucleus only.

The energy loss of the π-meson is about 60 per cent.

INGA FISCHER-HJALMARS, Department of Theoretical Physics, University of Stockholm

On hybridization of atomic valence orbitals

The condition of maximum penetration, previously suggested by the present author (Ark. Fys. 5 (1952) 349; 6 (1953), in press), gives a method for the estimation of the hybridization of atomic valence orbitals. According to this condition the bond-forming power of a valence orbital φ_A at the atom A should be roughly proportional to its penetration terms P_A. P_A is the sum of the orbital energy at the isolated atom A and the energy of interaction between the valence electron at A and the other atom B. The potential of this interaction is assumed to be $-e^2/r_B$, where r_B is the distance from the nucleus B to the electron in the orbital φ_A. Thus, B is treated as a singly charged nucleus with one valence electron. The orbital of this electron can be studied separately in the same way as φ_A. The interaction of the two valence electrons is neglected in the present approximation. The value of P_A is a function of those parameters in φ_A which give the degree of hybridization. By variation of these parameters an extreme value of P_A can be obtained.

The computation of the hybridization for the extreme value of P_A can be carried out in slightly different ways. The results of the different computations agree satisfactorily, provided that the differences in orbital energies between ns, np, nd . . . orbitals are properly accounted for. The essential advantage of the condition of maximum penetration, when compared to the condition of maximum overlapping, is that it is possible to make allowance for the promotional energy which is necessary for the transfer of the atom from the ground state to the valence state. As the promotional energy is the difference between the mean values of the atomic hamiltonian computed with the electronic wave functions corresponding to the two different states, its computation is somewhat laborious. However, this computation can be avoided when the promotional energy can be obtained from the term values of atomic spectra.

One of the results of the present calculations is that the promotional energy seems to be an important factor in the determination of the valence angles in the molecules NH_3 and H_2O. Details will be published later.

J. Flinta and R. Pauli, Department of Physics, Atomic Energy Laboratory, Stockholm

A high intensity ion source for pulse operation

A cold-cathode ion source intended for pulse operation has been developed at the Atomic Energy Laboratory. It makes use of the "Penning discharge" and is similar to that described by Keller.[1] The longitudinal magnetic field is slightly inhomogeneous along the axis, being 1200 gauss at the upper cathode and 800 gauss at the lower cathode. Several different cathode materials have been tested with pulse operation (2–10 A pulse amplitude). Uranium was found to be suitable, giving a stable discharge down to pressures as low as 0.005 Torr of D_2 when the working voltage is 500 V and the starting voltage 2000 V. With magnesium (electron alloy) there was no stable discharge at low pressures.

The ion source may run in three different ways, depending on the pressure range. The ratio (ion current)/(discharge current) = (I_i/I_d) is best in the medium pressure range (0.006–0.012 Torr of D_2), being about 1.0 % for a 3 mm diameter outlet hole.

The proportion of atomic ions increases with the current amplitude and is 50 % at 2 A and 70 % at 10 A.

The ion source has been tested on a small accelerator tube with an electrostatic lens consisting of three electrodes (0–70 kV, 0–10 kV, 0–70 kV). Output currents of 20 mA pulse peak have been focused to a 30 mm diameter spot 500 mm from the outlet. The gas consumption is about 30 cc NPT/hour.

S. Floberg, Department of Physics, Chalmers Institute of Technology, Gothenburg

Silver isotope enrichment by ionic migration in molten AgCl

In molten AgCl, the difference in the ionic velocities of the silver isotopes in relation to the chlorine ions, as determined by the moving boundary method, has been found to be 0.0012. The mass effect calculated from this value, $u = -0.064 \pm 0.006$, confirms a previously formulated rule.[2]

A detailed report will be published in *Zeitschrift für Naturforschung.*

---

[1] Keller, Helv. Phys. Acta, *21*, 170 (1948); *23*, 627 (1950).

[2] A. Klemm *et. al.* Z. Naturforschg. *7 a*, 560 (1952).

S. v. **Friesen**, Department of Physics, University of Lund

Heavy mesons and V-particles

Our present views (summer 1953) are summarized in the following

Table

Type of particle	Name		Decay scheme, Q in MeV	Mass/m_e	Charge	Mean life seconds
	new	old				
Hyperons	Ω°	V_1°	$\Omega^\circ \to P + \pi^- + 37$	2 190	0	$3 \cdot 10^{-10}$
H	Ω^+	V_1^+	$\Omega^+ \to N + \pi^+ + 130$	2 360	+	$4 \cdot 10^{-11}$
			$\Omega^+ \to P + \pi^\circ + 115$		+	
			$\Omega^+ \to P + \pi^\circ + 26\text{–}38$		+	
		V_x°	$V_x^\circ \to D + \pi^-$	$\sim 4\,000$	0	
		V_-^*	$V_-^* \to \Omega^\circ + \pi^-$	2 700	–	
Mesons	$\tau^\pm$		$\tau^\pm \to \pi^\pm + \pi^\pm + \pi^\mp + 72$	970 ± 5	±	$10^{-8} - 10^{-10}$
K	Θ°		$\Theta^\circ \to \pi^+ + \pi^- + 214$	971 ± 10	0	$\sim 1.5 \cdot 10^{-10}$
	$T^\circ ?$	V_2°	$V_2^\circ \to \pi^+ + \pi^- + \pi^\circ + < 75$	~ 970	0	
	$\varkappa^\pm$		$\varkappa^\pm \to \mu^\pm + ?^\circ + ?^\circ$	920 1 200 990 1 300	±	
	$\chi^\pm$		$\chi^\pm \to \pi^\pm + ?^\circ\ (+ ?^\circ)$	990	±	
		V_3°	$V_3^\circ \to \mathrm{K} + \mathrm{L}$		0	
		$V_y^\pm$	$V_y^\pm \to \Theta^\circ + \pi^\pm$	$1\,600 \pm 90$	±	
Mesons	$\pi^\pm$		$\pi^\pm \to \mu^\pm + \nu$	274 ± 2	±	$2.6 \cdot 10^{-8}$
L	π°		$\pi^\circ \to 2\,\gamma$	265 ± 4	0	$\sim 10^{-14}$
	$\mu^\pm$		$\mu^+ \to e^\pm + \nu + \nu$	207 ± 1	±	$2.15 \cdot 10^{-6}$

${}^{x}_{y}\mathrm{A}^* \to {}^{x}_{z}\mathrm{B} + \pi^\pm$.

T. R. **Gerholm**, Department of Physics, Royal Institute of Technology, Stockholm

A new type of a high transmission coincidence β-spectrometer

For the analysis of complicated radioactive decays it is necessary to utilize the coincidence technique. In order to resolve closely spaced lines one is obliged to use a two-channel β-spectrometer.

A double lens coincidence β-spectrometer has been developed, consisting of an ordinary magnetic spectrometer, with iron, which is divided into two magnetically independent halves by means of iron shielding in the middle of the spectrometer. In this way each of the two spectrometer halves can be used as a β-spectrometer, and thus the whole equipment can focus two different energies in the spectrum. Scintillation detectors with anthracene crystals are used, and from these the signals are led to a fast coincidence unit.

By delayed coincidences it is possible to measure lifetimes of excited states of nuclei. A variable delay is introduced in the coincidence equipment.

The two spectrometers are designed to give an optimum relation between transmission and resolution.

The whole apparatus can easily be changed into an ordinary β-spectrometer or into a β-γ-coincidence equipment with a single channel NaJ(Tl)-scintillation spectrometer.

Curves showing the shape of the magnetic field and the independence of the two magnetic fields were presented at the meeting.

T. GRÁF, Meitner Laboratory, Department of Physics, Royal Institute of Technology Stockholm

Construction and alignment of a double-lens beta-ray spectrometer

An iron-free spectrometer has been constructed giving exact proportionality between magnetic field and focusing current. The field is produced by two pairs of symmetrically placed coils. The distribution of the field on the axis may be varied by changing the distance between the two coil-groups. A higher transmission is obtained with the coil-groups near the ends of the instrument, while electrons of higher energy can be focused with the coils grouped in the middle. The presently adopted coil-configuration is a compromise, which enables the spectrometer to focus electrons emitted within a solid angle of 1 per cent of a sphere, up to a maximum energy of 4 MeV, with less than 4 kw electric power. The resolution is then about 2 per cent.

The spectrometer is provided with (1) a closed water-cooling system comprising a heat-exchanger, (2) a ring-focus baffle, which is adjustable in its own plane, and (3) a new type of gate-valve for the introduction of the source.

The coils were lined up individually, by means of an improved ballistic method, with an accuracy of a few hundredths of a millimeter with respect to the common magnetic axis. Thanks to the new gate-valve the source could be rapidly and accurately centered by means of a photographic method. Also the dimensions of the ring-baffle and its distance from the counter-window were determined photographically. The centering of this baffle with respect to the magnetic axis was done in one single operation with the aid of an accurately centered Cs^{137}-source. The accuracy of the final alignment of the spectrometer may be judged by the fact that the focused image shows source-structure details finer than 0.1 mm.

ERIC HELLSTRAND, Department of Physics, Atomic Energy Laboratory, Stockholm

Resonance absorption of neutrons in a uranium rod

The resonance absorption of neutrons in a uranium rod has been studied by measuring the induced Np^{239} activity. A chemical separation of neptunium from thin layers of uranium at different depths of an irradiated rod was made and the β-activity measured with an end-window G.M. counter. The thinnest uranium layer had a thickness of 6×10^{-3} mm. The rod was cylindrical, 200 mm long and 24 mm in diameter. It was shielded during irradiation with 1.5 mm Cd. Two Ra-Be sources of about 280 mC each served as the neutron source. A curve showing the induced activity as a function of the distance from the surface of the rod was presented at the meeting.

C. H. HERTZ, Department of Physics, University of Lund

Point corona against lacquer-coated metal surface

If in a point-plane corona arrangement the plane is covered by a thin lacquer layer, the corona current in air has been found to be much higher than without such a coating. Further the breakdown voltage of the gap is found to be much lower than without such a lacquer coating. This somewhat unexpected effect is caused by minute holes in the lacquer layer in which high electric field intensities are created. As a result of this the gas atoms are exited and ionized in the holes. These small glow discharges can be seen in each hole in darkness. This effect should provide a simple tool for the investigation of lacquer layers and should be of interest in high-voltage engineering.

LENNART HULDT, Department of Physics, University of Stockholm

Absorption experiments on atomic and molecular spectra

A peak absorption method for the determination of f-values for atomic and molecular lines is discussed. This method, combined with measurement of the total absorption, may also permit the determination of the line shape.

ERIK HULTHÉN and W. MULD, Department of Physics, University of Stockholm

Interferometric studies of the lead isotopes

A preliminary report is given concerning the hyperfine-structure of Pb II, λ 5372. A helium-filled hollow cathode was used as light source and the hyperfine-structure of the spectral line was recorded electrically by a photomultiplier, RCA type IP 21. The observations were performed on the central spot of the interference fringes from a Fabry-Perot interferometer, which was enclosed in an airtight chamber in which the air pressure could be varied.

The main object of our investigations was to determine the isotopic abundances of lead from geologically interesting lead-ores.

ERIK INGELSTAM, Optics Laboratory, Royal Institute of Technology, Stockholm

Optical uncertainty relations concerning the information on phase obtainable from interference and phase contrast methods

Extending the ideas developed in a recent paper,[1] uncertainty relations are also outlined for phase contrast under general assumptions. Analogous formulae are the following, u being the diffraction angle, z the optical path, Δx the area in which this path difference (counted from the surrounding field) is present, and X the total width of the wave front:

---

[1] E. INGELSTAM, Arkiv för fysik, 7, No. 24 (1953).

for ordinary imagery	$\Delta x\cdot\Delta u\approx\lambda$
for interference of a field not intersected by reflecting surfaces	$\Delta x\cdot\Delta z\approx\lambda^2$
for phase contrast	$\Delta z\cdot\dfrac{X^2}{\Delta x}\approx\lambda^2.$

This means that we cannot obtain accurate information from a wave field by means of interferences unless the region investigated is sufficiently large: the condition is that $|k_x|\cdot|k_z|\approx 1$, where $|k_x|$ and $|k_z|$ are the lengths of the sides of the region, expressed in numbers of wavelengths. If the z information is to be obtained very accurately, some other information has to be given up, and it is the aim of the experimenter to construct and dimension his apparatus to obtain the information wanted for his particular purpose. The same relation is valid and of practical importance for Fourier synthesis of crystal structures from X-ray diffractions and for locating objects by means of radio waves.

KARL-ERIK JOHANSSON, Department of Physics, Chalmers Institute of Technology, Gothenburg

Measurements of gamma-ray intensities with a scintillation spectrometer

A scintillation spectrometer has been built and used for investigations about the possibility of determining intensities of gamma-rays with satisfactory accuracy. A NaJ(Tl)-crystal has been used as a phosphor. This is located directly on the glass envelope of an EMI 5311 photomultiplier. The pulses are analyzed in a single channel pulse analyzer, as described by C. W. JOHNSTONE. The pulse height distribution is determined, and the sizes of the photo-electric peaks are measured. Investigations have mostly been made on the isotopes Sc^{46} and In^{114}, both of which have two gamma-energies in cascade. By measuring the ratio of the areas of the photoelectric peaks it is possible to get a conception of the photoelectric absorption in the crystal within the considered energy region. A few different sizes of crystals have been used to find out how this factor affects the result. If too large crystals are used one must pay attention to multiple absorption processes.

The measurements performed show that reproducible values of the intensities may be obtained with satisfactory accuracy.

A. KELEN, Department of Physics, Royal Institute of Technology, Stockholm

An electrically controlled precision thermostat for elevated temperatures

An electrically heated and controlled thermostat for temperatures between 100° and about 550° C with a very low error differential was designed and constructed for calorimetrical purposes. The on-off control of the heating power gives rise to small temperature oscillations in a thickwalled Al-tube, on the outer periphery of which the heating elements are mounted. These oscillations are transmitted to a central Al-slab which lies coaxially with the outer cylinder, but they are considerably damped as a result of the design of the thermostat. The inner slab, therefore, has a very high degree of temperature constancy. The quantities which are used for the input of the controlling system are the time derivative of the tube temperature and the temperature of the inner slab, represented by changes in resistance of platinum coils. Care is taken to prevent heat losses in the axial direction from the inner slab, such losses being covered from outer parts of the thermostat.

In connexion with the thermostat a measuring cell was constructed for determination of the heat evolved in metal samples during phase transformations. The cell has a great sensitivity and a small time constant.

O. KLEIN, Department of Theoretical Physics, University of Stockholm

Some cosmological considerations in connexion with the problem of the origin of the elements

In trying to develop the program sketched in last year's lecture, a tentative derivation of the Eddington relations between the dimensions and average density of the supergalatic system is given on the assumption that the system was once a very thin and large cloud of cold hydrogen gas contracting under the influence of its proper gravitation until sufficient ionization and radiation is produced to bring the contraction to a preliminary standstill. These considerations entail the condition that the average density ϱ of the supergalactic system at present and the reciprocal (T) of the Hubble constant fulfill the following inequality

$$\varrho > \frac{3}{8\pi\gamma T^2}$$

where γ is the gravitational constant, an inequality, which seems to be consistent with present estimates of ϱ and T.

In order to connect the assumptions mentioned with the question of the origin of elements, the possibility of local condensations of sufficienty high temperature and density for the formation of neutrons from protons and electrons has been considered and has led to the following estimate of the upper limit of the mass of such a condensation

$$M \approx \frac{1}{20}\left(\frac{\hbar c}{e^2}\right)^{3/2}\left(\frac{m_p}{m_e}\right)^{1/2}\left(\frac{e^2}{\gamma m_e m_p}\right)^{3/} m_p \approx 3\cdot 10^5 M_\odot,$$

where $\hbar$ is Plancks quantum of action divided by 2π, e the elementary quantum of electricity, m_p and m_e the masses of the proton and the electron, respectively, and $M_\odot$ the mass of the sun. This upper limit of the mass is comparable with the masses of the largest star clusters and may perhaps be connected with certain ideas of AMBARTZUMIAN on the formation of stars from a kind of protoclusters.[1]

---

[1] See the report of the "Colloque internationale d'Astrophysique 1953 à Liège" (soon to appear).

BENGT KLEMAN, Department of Physics, University of Stockholm

The spectra of the diatomic hydrides

The knowledge of the spectra of the diatomic hydrides is reviewed. The features of molecules belonging to the same group in the periodic system are compared. The transitions between electronic terms of different multiplicity are discussed.

Among the molecules which are at present the object of experimental investigations may be mentioned SiH, GeH, GaH and InH.

KRISTER KRISTIANSSON, Department of Physics, University of Lund

Accuracy of mass determinations in nuclear emulsions by photoelectric measurements

The resolving power of a mass determination in an Ilford G-5 emulsion has been determined by photoelectric measurements of about 100 tracks of singly charged particles ending in the emulsion. The standard deviation of such a measurement has been calculated at 10 % from the distribution of masses in the proton and the μ-meson groups in the mass-spectrum. The standard deviation depends on the length of the tracks, and the above-mentioned deviation applies to proton tracks with a residual range of about 4000 μ, and to μ-meson tracks with a residual range of 700–800 μ. The ratios of the masses are correct in the whole of the spectrum investigated.

ALBIN LAGERQVIST, Department of Physics, University of Stockholm

About the ground states of the alkaline earth oxides

The analyses of the band spectra of the alkaline earth oxides show that the lowest states hitherto found of all these molecules are $^1\Sigma$ states. All these states are unperturbed and usually considered as the normal states. Determining the dissociation energies of the molecules under this assumption, and using the current spectroscopic method, one obtains, however, values for the dissociation energies which, except for BeO and BaO, do not agree with those obtained by other methods. This can be explained by assuming the existence of lower states (triplets ?) than the $^1\Sigma$ states found so far, or by assuming an ionic binding, or by assuming that the vibrational constants of the $^1\Sigma$ states are not known with sufficient accuracy.

KURT LIDÉN, Laboratory for Radiophysics, Lund

Gamma-rays, X-rays and bremsstrahlung from Tm^{170} sources

The spectral distribution of the electromagnetic radiation from a thin Tm^{170} source, placed between Tm radiators of various thicknesses, has been investigated using a scintillation spectrometer. The experimental results have been used in a calculation of the relative intensities of the γ-rays, the X-rays and the bremsstrahlung from homogeneously activated Tm^{170} sources. The calculated distribution of the radiation from a Tm^{170} source, 1.0 g/cm^2, shows good agreement with experiments. With a Tm^{170} source, 150 mg/cm^2, the intensity of the continuous external bremsstrahlung excited by the β-particles in the source, amounts to 29 % of the total intensity. With 1.0 g/cm^2 the spectral composition is 10 % 84 keV γ-rays, 47 % Tm + Yb K X-rays, and 43 % bremsstrahlung.

PER LINDBERG, Optics Laboratory, Royal Institute of Technology, Stockholm

Routine apparatus for obtaining contrast transmission curves of optical imaging systems

The resolving power of non-coherent image formation in optical systems, such as a photographic lens, should not be given as the number of lines per millimeter which can be separated by the human eye aided in a particular way, but should be specified in terms of contrast transmission curves. These curves give the percentage "transmitted contrast" from the object to the image at different line frequencies. They are the Fourier transform of the light distribution in the image of a luminous line.

As a further development of an earlier apparatus,[1] a photoelectric device is under construction in which a point source is imaged by the system under test upon a rotating sector wheel with 72 transparent sectors. From a photocell behind the sector wheel an a.c. is thus obtained. The fundamental frequency in the output from the photocell is separated from the overtones by a band pass filter, amplified, rectified, and recorded as a function of the distance between the point image and the centre of the sector wheel. This wheel moves towards the point image, thereby increasing the line frequency without changing the electrical frequency. Thus a contrast transmission curve on a reciprocal line frequency scale is obtained on the recorder.

EINAR LINDHOLM, Department of Physics, Chalmers Institute of Technology, Gothenburg

Collisions between ions and molecules

Two mass spectrometers are placed in a big vacuum container. In the first mass spectrometer the ions are produced, and in the second mass spectrometer the charged fragments obtained from the molecules in the collisions are analysed. Two semicircular permanent magnets with ion radius 75 mm are used. The ion current from the first mass spectrometer is measured with an electrometer tube amplifier. This current amounts to about 10^{-10} A. The ion currents from the second mass spectrometer amount to 10^{-12} or 10^{-13} A. The energy of the ion is about 500 eV.

The measurements have shown that the condition for a high intensity of a certain fragment is that the energy obtained when the ion is neutralized equals the energy which is necessary for dissociation of the molecule so that the fragment in question is obtained. This means that the mass spectra obtained in this manner are often simpler than the mass spectra obtained in an ordinary mass spectrometer with electrons as the colliding particles.

---

[1] LINDBERG, P., Optica Acta (in print).

A. LUNDÉN, Department of Physics, Chalmers Institute of Technology, Gothenburg

Concentration of copper 65 by countercurrent electromigration in molten cuprous chloride

The chain of molten salts, $-$LiCl, KCl/CuCl/$PbCl_2+$, was electrolysed 70 hours at a temperature of 530° C. The heavy copper isotope was enriched in a separation tube containing the sharp boundary between the cuprous and the lead chlorides. After the electrolysis the isotope concentration in the different samples was determined by measuring the activities produced when the copper was irradiated with thermal neutrons at the Norwegian reactor. Preliminary results give a mass effect (the relative difference in velocity divided by the relative difference in mass) of -0.087, which is in good agreement with a rule given by KLEMM. The definite results will be published in *Zeitschrift für Naturforschung.*

Work is in progress to achieve the enrichment of isotopes of lead and of other elements by the same method.

CURT MILEIKOWSKY, Nobel Institute of Physics, Stockholm

Astigmatic double directional focusing for the study of particle groups from nuclear reactions

In the study of energies of particle groups from nuclear reactions relatively large solid angles are often desirable. The energy spread caused by the motion of the center of mass can be considerable. If one has a magnetic system which gives a point-shaped image of a point-shaped source, for instance a double focusing spectrometer, the energy spread from reactions on light nuclei generally determines the line width, which often becomes large for this reason.

One can, however, avoid this, still keeping the large solid angle for a given gap and a given mean radius of a double directional focusing system, by choosing an n-value that differs somewhat from $n = 0.50$ (for instance, $n - 0.57$). Thus one introduces on purpose an astigmatism so that a point-shaped source gives a line image of definite length in the radial focus. The line slopes to the axis direction of the magnetic field due to the energy spread caused by the motion of the center of mass. The line width is not now determined by the energy spread; two close particle groups from the same nuclear reaction give lines with the same slope, which can simply be detected on the photographic plate or be separated by means of a sloping slit, if electric detection is used. The slope of the lines can help, to a certain degree, to identify the nuclear reaction. Also, the energy measurement becomes independent of corrections for the angular distribution of the intensity of the reaction.

CURT MILEIKOWSKY, Nobel Institute of Physics, Stockholm

Reaction energies and atomic masses

Magnetic analysis of particle energies in nuclear reactions, performed at a number of laboratories during the last years, has given us a considerable knowledge of energy levels and ground states of the light nuclei. In the region from hydrogen up to sulphur we now know a network of accurately measured reaction energies corresponding to transitions to the ground states. Among these are also reactions having O^{16} as a target or residual nucleus. Thus the atomic masses are known of all nuclei in the network, i.e. all stable and many unstable isotopes in the region hydrogen-sulphur. The accuracy, about 1 part in a million, is the same as that claimed in mass spectroscopy.

In general, there is agreement between reaction data and mass spectroscopic data for the atomic masses of the light nuclei which, conversely, can be regarded as an experimental check on a large scale of the momentum laws and the relation $E=mc^2$, with an accuracy of 0.1 %. In certain cases, however, there are differences between reaction data and mass spectroscopic data up to five times the given probable error, and in some cases there are differences between mass spectroscopic values from different laboratories which amount to several times the probable error.

When reaction cycles and reaction results from different laboratories are compared, it is found that reaction data show a better internal consistency than mass spectroscopic data. Therefore, it is now recommended to use reaction masses for the atoms up to sulphur.

The large amount of reaction data now available has been produced by a number of laboratories in the United States and Europe, among these the Nobel Institute, where we have concentrated on some key reactions for which a combination of an isotope separator, a high voltage accelerator and a precision spectrometer for heavy particles was necessary. The gap between the fluorine and neon isotopes was long open, because it was difficult to make thin targets of the noble gas neon. The problem was solved with a suitable separation technique; the Q-values were measured of the reactions $Ne^{20}(d,\alpha)F^{18}$, $Ne^{21}(d,\alpha)F^{19}$ and $O^{18}(p,\alpha)N^{15}$ and the gap was closed via a complete nuclear cycle. This showed that the particle groups in question corresponded to transitions to the ground states. The reaction net above neon was in this way connected to the standard O^{16}, and the masses in the region neon-sulphur could be expressed in abs. mass units.

ROLF PAULI, Nobel Institute of Physics, Stockholm

Low levels in N^{16}

Low levels in N^{16} have been investigated by means of the reaction $O^{18}(d,\alpha)N^{16}$. Thin targets of O^{18}, prepared in the isotope separator of the Nobel Institute, were bombarded with deuterons of 850 keV and the energy of the produced α-particles was determined with a double-focusing magnetic spectrometer.[1]

We found four different α-groups with Q-values of 4.23 ± 0.02, 4.11 ± 0.02, 3.93 ± 0.02, 3.83 ± 0.02 MeV corresponding to levels in N^{16} with energy 10.40 ± 0.03

---

[1] C. MILEIKOWSKY, Ark. f. Fys., *4*, 337 (1952); *ibid.*, *7*, 33 (1953).

MeV, 10.52 ± 0.03 MeV, 10.70 ± 0.03 MeV and 10.80 ± 0.03 MeV over the ground state in O^{16}. The first level, 10.40, is probably the ground level of N^{16}. The second and fourth of these levels have not been observed earlier. The first and third levels were observed by WYLY[1] by means of the reaction $N^{15}(d,p)N^{16}$ and ionisation chamber technique. From his measurements one calculates 10.44 ± 0.15 and 10.74 ± 0.15 MeV for these levels. MALM and BUECHNER[2] using the same reaction found only the third level with a Q-value corresponding to a level energy of 10.70 ± ± 0.01 MeV above the ground state of O^{16}. In order to make certain that the four α-groups came from the reaction $O^{18}(d,\alpha)N^{16}$ we measured the α-s in different angles to the deuteron beam (45°, 105°, 120°, 135°). The α-group pertaining to the second level (10.52 MeV) showed a strong angular anisotropy, being most intense in the backward direction (135°).

On the basis of a nuclear model with charge independent nuclear forces the levels in N^{16} would correspond to levels in O^{16} about 12.5 MeV over the O^{16} ground state.[3] One possible matching is that the first $T = 1$ level in O^{16} of 12.51 MeV corresponds to the (presumed) ground state in N^{16}, 10.40 MeV above the ground level of O^{16}. In this case the second $T = 1$ level in O^{16} (12.95 MeV) only differs by 40 keV from the fourth level in N^{16}. The other two levels in N^{16} have no known counterparts in O^{16}. Measurements are now in progress with the object of finding out whether there are some still lower levels in N^{16}.

ROLF PERSSON, Department of Physics, Atomic Energy Laboratory, Stockholm

Neutron multiplication in a heterogeneous system of uranium and ordinary water

To determine the multiplication constant of the subcritical system of uranium rods and ordinary water, two different kinds of measurements have been performed.

(1) The neutron distribution from a Ra-Be-source has been measured, and the "buckling" and the multiplication constant of an infinite medium, k_∞, have been calculated. The maximum value of k_∞ seems to be close to unity.

(2) Using the D-D reaction from a pulsed accelerator and a 40 channel time analyser, the time dependence of the neutron flux has also been measured. In this case the effective multiplication constant, k_{eff}, is determined.

The uranium rods have been placed in a hexagonal lattice and it has been possible to change the lattice dimensions continuously.

The results are only preliminary.

J. O. RASMUSSEN and H. SLÄTIS, Nobel Institute of Physics, Stockholm

On the decay of Np^{238}

The β-spectrum of Np^{238} has earlier been investigated by FREEDMAN, JAFFEY and WAGNER (1950). They found two β-components of allowed shape and with the energies 1272 and 258 keV, respectively, and a number of conversion lines, which were considered as belonging to transitions with the energies 1030, 983, 103, 47, and 43 keV, respectively. We have confirmed most of these radiations, but found the low energy conversion lines to be L_{II}, L_{III} and M-lines of only one soft transition of energy 44 keV, corresponding to the first excited state of Pu^{238}. The energy 44 keV agrees with the difference between the high energy transitions 1030 and 986 keV. A new K-line corresponding to a gamma-ray of 939 keV was found. The conversion coefficients for these lines and also the $L_I:L_{II}$-ratio for the 44 keV radiation show that all transitions have an E2 character. A new decay scheme is proposed. The lower levels in this scheme for the residual nucleus are in agreement with the levels observed in the α-decay of Cm^{242}.

---

[1] L. D. WYLY, Phys. Rev. *76*, 316 (1949).

[2] R. MALM and W. W. BUECHNER, Phys Rev. *80*, 771 (1950).

[3] D. R. INGLIS, Rev. Mod. Phys. *25*, 396 (1953).

Carl Reuterswärd, Department of Physics, University of Uppsala

A new method for isotopic ratio measurements in mass spectrometry

Precision determinations of isotopic electrical null methods are known previously. The set-up hitherto employed comprises a double beam mass spectrometer and two d.c. amplifiers with separate high-ohmic resistors. Drift in the resistor characteristics and differences in the ion path geometry make the method unsuitable for absolute ratio determination. The present communication deals with a null method of measurement in which these drawbacks are eliminated.

Two isotopic ions are alternatingly brought to the collector slit of a single beam spectrometer by an automatic switching device, and the alternating output from the d.c. amplifier is fed through a synchronously switched precision attenuator into a capacitor of some microfarads. The periodic charging and discharging current gives the indication of "bridge unbalance" and is read on a galvanometer after rectification. Balance is achieved by adjusting the attenuator tap, which yields the isotopic ratio figure. Additional features of the system developed are automatic compensation for amplifier zero shifts and elimination of the switching transients in the galvanometer circuit. The switching frequency is limited chiefly by the response time of the magnet; it amounted to 0.35 c/s in these experiments. The requirements regarding the quality of the mass spectrum and the stability of the power supplies are discussed, and figures on the accuracy attained are presented.

The method is valuable when an accuracy of 0.1 per cent is required, or when measurements are made on very weak, decaying, or fluctuating ion currents. The same principle of measurement is thought to be applicable to cases of photometry, where phototubes and amplifiers are used, thus eliminating the effects of fluctuations in the behaviour of the detecting and amplifying system.

P. Risberg, Department of Physics, University of Lund

Wavelength measurements of some simple atomic spectra in the photographic infrared

The spectrum of Ca II has been observed with a conventional hollow cathode and a grating spectrograph in the region from 3347 A to 11950 A. The infrared measurements have made possible the identification of several strong lines in the solar spectrum.

The work is now carried on with Mg II and the arc spectra of the alkali metals. This work has also led to new identifications of solar lines.

ARNE ELD SANDSTRÖM, Department of Physics, University of Uppsala

A critical survey of the excitation potentials as measured in the course of h/e-determinations

For a long time there have been discussions as regards the effect of the cathode work-function on the accelerating voltage in an X-ray tube. However, it is quite possible to determine any correction to the measured voltages by combining the results from measurements corresponding to two high-frequency limits sufficiently separated. When calculating this correction for a tungsten cathode from measurements by OHLIN, by PANOFFSKY, GREEN and DUMOND, and by BEARDEN, JOHNSON and WATTS, the resulting values are distributed in such a way as to suggest that there exists a systematical error in the voltage measurements. The result will be the same if one also takes into account the measurements by NILSSON who applied a slightly different method.

The curve describing the excitation potential as a function of the high-frequency limit should be a straight line. When a line is drawn so as to fit all the values given by the authors cited, the deviations of the measured points lead to the same conclusion as above.

KAI SIEGBAHN, Department of Physics, Royal Institute of Technology, Stockholm

Precision apparatus for studying β-rays in the low energy region

In order to increase the reliability and precision in β-ray spectroscopy in the low energy region (<300 keV) an ironfree double focusing spectrometer has been built. The radius of curvature is 30 cm. The correct field form has been obtained by means of a semiempirical procedure which has resulted in an accurate and simple solution of the problem. The current through the spectrometer coils and thus the magnetic field can be continuously changed and measured with a precision of $1:10^5$. The earth's field has been compensated by means of big Helmholtz coils to less than $1:10^3$ and the behaviour of the residual field has been studied. In order to enable the study of binding energies in atomic shells, the spectrometer is provided with an X-ray tube of special design and a well stabilized, oil-insulated high voltage supply for max. 100 kV. A new method to measure h/e accurately is discussed.

N. G. SJÖSTRAND, Departments of Physics, Atomic Energy Laboratory, Stockholm

Neutron resonances in iodine

Measurements have been made, with the Brookhaven fast chopper, of the total neutron cross section of iodine in the energy region 10–1000 eV. Ten resonances have been resolved between 10 and 200 eV, and the measurements indicate moreover a group of resonances around 400 eV. If the results for the six first resonances are analyzed assuming a Γ_γ of 0.1 eV, Γ_n° (the neutron width reduced to 1 eV) for four of them is found to be close to the value 0.004 eV expected from the level density. The two other resonances, including the first, give however a value smaller than this by a factor of about 10.

C. TAYLOR, Department of Physics, Atomic Energy Laboratory, Stockholm

A peak switching device for mass spectrometers, using recorder

A method is described for facilitating isotope abundance measurements. Instead of using a Nier double collector, the maxima of the two ion beams are swept in turn across a single slit. A relay device selects the gain of the mass-spectrometer, so that both the mass peaks are brought to the same height, and they are then traced in the usual way by a Speedomax recorder. By shifting the zero and increasing the gain, a change of 1 per cent in isotope ratio can easily be made to appear as a difference of 30 mm in the level of the peaks on the recorder.

The equipment, which contains two double-triodes and two relays, includes provision for automatically disconnecting the recorder during the change-over periods. Its main advantages over the double-collector method are that peaks not adjacent to each other can be compared directly, and that no changes need be made to the spectrometer when working in different parts of the mass spectrum.

BERNDT WALDESKOG, Department of Physics, University of Lund

Identification of particles in the primary cosmic radiation

The photoelectric method has been used to determine the charge of "heavy" primaries ($Z \geq 2$) ending in the emulsion.

The end of such a track has a characteristic appearance owing to the capture of electrons. About 50 tracks have been measured up to now. It has been proved that one need only measure about 300 μ (10 slit-lengths) to get a good resolution, and if 600 μ or more are measured the resolution is such that it is possible with certainty to discriminate between different Z. The material that has been investigated has contained particles with $Z \leq 14$. Particles with $Z = 3, 4, 5$ have not yet been found among the "primaries". The particles with those charges are with certainty secondaries. They are all tracks emanating from stars in the emulsion.

HANS ÅSTRÖM, Department of Physics, Royal Institute of Technology, Stockholm

Physical methods to determine equilibriums in metallic solutions with small solubility

Some methods for measuring small quantities of solute atoms are described, an isothermal calorimetric method, which for some years has been used at this institution, and mechanical relaxation methods. The magnitude of the relaxation effect can be determined by a vibration method (KÊ 1948) or in a "static" way.

The solubility of nitrogen in α-Fe has been studied by the calorimetric method and the "static" relaxation method. It has been found that the ratio between relaxation and amount of nitrogen in solution is not constant as has been assumed (DIJKSTRA 1949), but changes with the concentration. By correcting earlier vibration measurements good agreement has been obtained between values from all three methods for the solubility of nitrogen in α-Fe.

Tryckt den 20 april 1954

Uppsala 1954. Almqvist & Wiksells Boktryckeri AB

ARKIV FÖR FYSIK Band 8 nr 2

Communicated 28 October 1953 by MANNE SIEGBAHN

Auger electrons from the L-shell in mercury*

By I. BERGSTRÖM** and R. D. HILL

Introduction

In an Auger process involving emission of L-sub-shell electrons, an atom, initially ionized in the K-shell, undergoes a transition to an atom, doubly ionized in the L-shell, and an electron in a free positive energy state. The energy $E_{KL_pL_q}$ of the ejected electron, no matter what the mechanism of the Auger transition, has a definite quantum value which can be approximately determined by considering the process as an internal x-ray photo-effect[1], i.e. $E_{KL_pL_q}$ is given by:

$$E_{KL_pL_q}=E_K-E_{L_p}-E_{L_q} \tag{1}$$

where $(E_K-E_{L_p})$ is the energy an emitted photon would have had, and E_{L_q} is the L_q-sub-shell electron binding energy. (L_p and L_q denote any two sub-shells of the L shell. p and q may have any value; I, II or III, and may even be identical. p and q have been used in preference to i and j so as to involve no implication of initial and final states.)†

In actual fact, the energy of an Auger electron is more accurately given by:

$$E_{KL_pL_q}=E_K-E_{L_p}-E'_{L_q} \tag{2}$$

where E'_{L_q} is the binding energy of an L_q-sub-shell electron in an atom already once-ionized in one of its L sub-shells.†† Experimentally it is found, and it is clearly theoretically consistent with the picture of the Bohr atom, that $E'_{L_q} > E_{L_q}$. The numerical evaluation of E'_{L_q}, although theoretically straightforward, is tedious on account of having to use empirically-obtained electronic wave-functions, and except for a number of light atoms[2] has not been carried out. In the present paper we give the results of accurate energy measurements of the *L*-Auger lines of mercury and show that the values of E'_{L_q} so determined are consistent with the energy values of doubly-ionized states.

---

* This work was performed at Physics Department, University of Illinois, Urbana. Assisted by the joint program of AEC and ORNL.

** On leave of absence from the Nobel Institute for Physics, Stockholm. Assistance in part from Svenska Atomkommittén greatly acknowledged.

[1] E. H. S. BURHOP, "The Auger Effect and Other Radiationless Transitions" (Cambridge University Press, London, 1952).

† The calculation of the energy $E_{KL_pL_q}$ is of course independent of any detailed model of the ejection of the Auger electron. Since the total energy of the system (nucleus + a certain number of electrons) has to be conserved, the energy difference between the initial and final states of the atom has to be transferred to the Auger electron. Let E_K, E_{L_p} and E_{L_q} be the energies of the atom ionized in the K, L_p and L_q shells and the energy of the neutral atom zero. It is then evident that $E_K=E_{L_p}+E_{L_q}+E_{KL_pL_q}$, which gives the same Auger electron energy as (1).

†† In E'_{L_q} the prime denotes a primary ionization. L_{I}, L_{II}, L_{III} etc. will be used when detailed information of the primary ionization is wanted.

Experiment

During an investigation of the electron spectrum of a number of *K*-capturing isotopes of thallium[3] we observed Auger electrons from the *L* shells of mercury quite free from the interference of either continuous or conversion electrons. Further, on account of the comparatively high energies of the mercury Auger lines, the individual lines were well separated under a resolving power of the order of 0.2 %.

An accurate experimental determination of the electron line energies depended upon a number of factors associated with the photographic 180° magnetic spectrometer used in our experiments. The actual measured quantitities involved in the determination were the following: (a) The distance of the line from either a reference line or mark on the photographic film, (b) the distance of either the reference line or mark from the edge of the slit, (c) the slit width, (d) the distance of the plane of the slit from the plane of the source, (e) the width of the source, (f) the shrinkage of the film. Apart from these quantitities there are certain setting-up adjustments, the accuracy of which may affect the accuracy of the measurements. These factors include: (g) the 90° angle between the line of the film and the line joining the centers of the source and slit, (h) the parallelism of the planes of the slit and of the source, (i) the known uniformity of the permanent magnetic field relating the unknown line to the reference line.

The resultant error of measurement may indeed be quite large but can be reduced somewhat by a large number of independent observations on different sources with different setting adjustments. In mass, optical and x-ray spectroscopy, however, it is well known that systematic errors can be much reduced by measuring an unknown line as a close doublet against a second line which is known absolutely with small error. For our measurements it was convenient to use the *K*- and *L*-conversion electron lines of the 80.164 kev gamma-ray from a small amount of I^{131} which was placed on the source backing simultaneously with the thallium activity*. Other secondary calibration lines in the same energy region showed that within our accuracy of measurement it was also reliable to apply a small linear correction for the magnetic field variation in the region between the *K*- and *L*-lines.

---

[2] H. C. Wolfe, Phys. Rev. *43*, 221 (1953); E. H. Kennard and E. Ramberg, Phys. Rev. *46*, 1040 (1934).

[3] I. Bergström, R. D. Hill, and G. De Pasquali Phys. Rev. *92*, 918, (1953).

* The *K* and *L* conversion lines of a 177 kev γ-ray were also observed in I^{131} spectrum. These lines, which have been sporadically reported by other observers (J. M. Cork, Nucleonics, Nov 1950) are not included in the decay scheme I^{131} now accepted. Since the lines are weak and superimposed on a decaying β-spectrum, it is very hard to measure their half lives with the photographic method. They seem, however, to be of the same order of magnitude as the other lines.

Measurements were made in two instruments, one of approximately 100 gauss magnetic field, the other of approximately 50 gauss. In the latter instrument, although the separation between the lines was larger and the length measurements therefore relatively better than in the former, the magnetic field variation was larger than in the former instrument on account of the larger separation of trajectories. The change in the magnitude of the field between the K- and L-lines of the calibrating 80 kev gamma ray was 6 parts in 1 000 in the 50 gauss instrument as compared with 5 parts in 10 000 in the 100 gauss magnet. The separation between the K-line and the Auger line A_6 $(KL_{\mathrm{III}}L_{\mathrm{III}})$ of highest energy corresponded in the 50 gauss magnet to 2.5 parts in 1 000 and only 2 parts per 10 000 in the 100 gauss magnet. This indicates that the accuracy of the Auger line measurements is probably of the order of 1 part per 1 000. The positions of the lines were measured with a recording micro-photometer. The scale amplification of about 7 of the micro-photometer allowed small separations of a few mm on the film to be made with a precision of a few per cent. Measurements were made between the extrapolated edges of the lines.

Results and analysis

The mean energy values of four independent measurements are given in column E Table 1. The mean values of four completely independent measurements which were not doublet measurements are listed in column F. The errors indicated are such as to bracket all the measured values. It is clear that the energy values of the doublet method are superior to the straight-out measurements of the energies.

From Eq. 2 it is clear that there are nine different ways of permuting L_{I}, L_{II} and L_{III} in $E_{KL_pL_q}$ $(KL_{\mathrm{I}}L_{\mathrm{I}},\ KL_{\mathrm{I}}L_{\mathrm{II}},\ KL_{\mathrm{I}}L_{\mathrm{III}},\ KL_{\mathrm{II}}L_{\mathrm{I}},\ KL_{\mathrm{II}}L_{\mathrm{II}},\ KL_{\mathrm{II}}L_{\mathrm{III}},\ KL_{\mathrm{III}}L_{\mathrm{I}},$ $KL_{\mathrm{III}}L_{\mathrm{II}}$ and $KL_{\mathrm{III}}L_{\mathrm{III}})$. However, $E_{KL_{\mathrm{I}}L_{\mathrm{II}}} = E_{KL_{\mathrm{II}}L_{\mathrm{I}}}$, since in both cases the initial and final states of the atom are identical. For the same reason, $E_{KL_{\mathrm{II}}L_{\mathrm{III}}} = E_{KL_{\mathrm{III}}L_{\mathrm{II}}}$ and $E_{KL_{\mathrm{I}}L_{\mathrm{III}}} = E_{KL_{\mathrm{III}}L_{\mathrm{I}}}$. Therefore only six electron lines will be observed in the KL_pL_q group. In Table II the value of E'_{L_q} is given using the binding energies E_K and E_{L_p} of the normal atom* and the experimental values of $E_{KL_pL_q}$. It can be seen from the table that within the experimental errors ($\pm$1:1000 the L binding energy of an atom ionized a second time in a particular L-sub-shell is independent on which L shell is primarily ionized.

In columns B and C of Table 2 the binding energies in the L-sub-shells are listed for the normal atoms of mercury and thallium respectively, and it is apparent that the experimental values of E'_{L_q} lie intermediate between those of these two Z-values. An effective incremental charge, ΔZ, can be obtained by considering a linear increase of binding energy with atomic number. The calculated values of ΔZ from our experimental data and using the expression:

$$\Delta Z = \frac{E'_{L_q} - E^{z}_{L_q}}{E^{z+1}_{L_q} - E^{z}_{L_q}} \qquad (3)$$

are given in column E of Table 2.

---

* It would have been more accurate to use energies of emission lines ($E_K - E_{L_{\mathrm{III}}} = E_{K_{\alpha_1}}$, $E_K - E_{L_{\mathrm{II}}} = E_{K_{\alpha_2}}$, $E_K - E_{L_{\mathrm{I}}} = E_{K_{\beta_1}} - E_{L_{\beta_3}}$). However, in the case of mercury these lines have not been measured.

Table 1. Experimental Energies and Intensities of Auger Electrons from the L-shell.

Auger line defined by Eq. (2)	A	B	C	D	E	F	G
$E_{A_1}=E_K-E_{L_I}-E_{L_I}^{L_I}$ . . .	53.19	53.19	53.14	53.21	53.18±.04	53.14±.11	1.0
$E_{A_2}=E_K-E_{L_I}-E_{L_{II}}^{L_I}$ $E_{A_2}-E_K-E_{L_{II}}-E_{L_I}^{L_{II}}$ . .	53.79	53.83	53.78	53.76	53.79±.04	53.83±.12	1.2
$E_{A_3}=E_K-E_{L_{II}}-E_{L_{II}}^{L_{II}}$ . .	—	—	—	54.32	(54.32)	—	~ 0.2
$E_{A_4}=E_K-E_{L_I}-E_{L_{III}}^{L_I}$ $E_{A_4}=E_K-E_{L_{III}}-E_{L_I}^{L_{III}}$.	55.71	55.71	55.67	55.73	55.71±.04	55.77±.16	0.7
$E_{A_5}=E_K-E_{L_{II}}-E_{L_{III}}^{L_{II}}$ $E_{A_5}=E_K-E_{L_{III}}-E_{L_{II}}^{L_{III}}$.	56.36	56.40	56.32	56.31	56.35±.05	56.90±.20	1.4
$E_{A_6}=E_K-E_{L_{III}}-E_{L_{III}}^{L_{III}}$. .	58.27	58.31	58.21	58.29	58.27±0.5	58.30±.07	0.6

Cols. A and B refer to measurements in the 100 gauss instrument.
C and D refer to measurements in the 50 gauss instrument.
Col. E. gives the mean values of cols. A, B, C and D; all doublet measurements.
Col. F, mean value of four separate and independent measurements in the 50 gauss instrument, not using doublet method.
Col. G, relative intensities of the L Auger lines, estimated errors about 30 %.

In view of the accuracy claimed in our measurements, it seems clear that the observed values of ΔZ are significantly less than the value of unity which has been frequently recommended as an approximate figure.* Similar conclusions have been drawn earlier by Ellis[5], Mihelich[6], and Robinson and Cassie[7]. In particular, Robinson and Cassie measured the L-Auger electrons from copper by the somewhat different method of first ionizing the K-shell by the x-ray photo-electric effect. They observed E'_{L_I} to be 1.175 kev as compared with $E_{L_I}=1.100$ kev for copper. Their value of ΔZ for the L_I shell is therefore equal to 0.75 which is in reasonable agreement with ours of 0.55. However, our values also show that ΔZ may be different for the different L-sub-shells. From the fact that $\Delta Z=0.55$ for the L_I ($s_{1/2}$-electrons) and L_{II} ($p_{1/2}$-electrons), and $\Delta Z=$ $=0.76$ for the L_{III} ($p_{3/2}$-electrons) it may be that ΔZ, calculated according to equation (3), is correlated in some way with the azimuthal dependence of the electronic wave function.

The energy of any KL_pL_q Auger line is probably to be given, within an accuracy of the order of 2 parts per 1 000, by the following relationship:

$$E_{KL_pL_q}=(E_K-E_{L_p})_Z-(E_{L_q})_{Z+\Delta Z} \qquad (4)$$

where ΔZ is 0.7. For higher accuracy of the order of 1 part per 1 000, ΔZ is better approximated as (i) 0.6 when L_p is L_I, L_{II}, L_{III} and L_q is either L_I

---

* See reference (1), pp. 60 and 75.

[5] C. D. Ellis, Proc. Roy. Soc. A *139*, 336 (1933).

[6] J. W. Mihelich, Phys. Rev. 88, *415* (1952).

[7] Robinson and Cassie, Proc. Roy. Soc. *A 113*, 282 (1926).

Table 2. Values of the effective L-sub-shell binding energies for doubly ionized mercury.

Transition involved in evaluation of energy	A	B	C	D	E
$E_{L_{\mathrm{I}}}^{L_{\mathrm{I}}} = E_K - E_{L_{\mathrm{I}}} - E_{A_1}$	15.09	15.11	14.84	15.34	0.54
$E_{L_{\mathrm{I}}}^{L_{\mathrm{II}}} = E_K - E_{L_{\mathrm{II}}} - E_{A_2}$	15.11				
$E_{L_{\mathrm{I}}}^{L_{\mathrm{III}}} = E_K - E_{L_{\mathrm{III}}} - E_{A_4}$	15.12				
$E_{L_{\mathrm{II}}}^{L_{\mathrm{I}}} = E_K - E_{L_{\mathrm{I}}} - E_{A_2}$	14.48	14.48	14.21	14.70	0.55
$E_{L_{\mathrm{II}}}^{L_{\mathrm{II}}} = E_K - E_{L_{\mathrm{II}}} - E_{A_3}$	(14.58)				
$E_{L_{\mathrm{II}}}^{L_{\mathrm{III}}} = E_K - E_{L_{\mathrm{III}}} - E_{A_5}$	14.48				
$E_{L_{\mathrm{III}}}^{L_{\mathrm{I}}} = E_K - E_{L_{\mathrm{I}}} - E_{A_4}$	12.56	12.56	12.28	12.65	0.76
$E_{L_{\mathrm{III}}}^{L_{\mathrm{II}}} = E_K - E_{L_{\mathrm{II}}} - E_{A_5}$	12.55				
$E_{L_{\mathrm{III}}}^{L_{\mathrm{III}}} = E_K - E_{L_{\mathrm{III}}} - E_{A_6}$	12.56				

A, values obtained using E_K and E_{L_p} binding energies of mercury (Hill, Church and Mihelich, Rev. Sci. Inst. *23*, 523 (1952)).

B, weighted mean values E'_{L_p}.

C, values of binding energies, E_{L_p}, of mercury (HCM).

D, values of binding energies, E_{L_p}, of thallium (HCM).

E, values of the effective incremental charge, ΔZ, equation (3).

or L_{II}, and (ii) 0.8 when L_p is L_{I}, L_{II}, L_{III} and L_q is L_{III}. $(E_L)_{Z+\Delta Z}$ is obtained by linear interpolation in the binding energy tables. The use of this information would seem to be of some importance for the calibration of β-ray spectroscopes in the low energy region.

As already mentioned, Wolfe has calculated the energies of several light elements doubly ionized in the K and L shells. He was thus able to account quantitatively for a number of K x-ray satellites on the basis of single electron transitions between doubly ionized atomic states. A large number of K x-ray satellites have been observed[8] in a large number of elements, also including mercury, but accurate calculations on the energies of the doubly ionized states are generally lacking. It might be pointed out, too, that where identification of the initial and final states has been carried out without accurate evaluation, the energy differences derived from x-ray satellites may not give directly the energy differences involved in Auger transitions. This is illustrated in the following example.

A tentative assignment of the α_s'' satellite has been given by Groven and Morlet[8]. The quantum energy, $h\nu_{\alpha_s''}$, probably arises from a single electron transition between an initially K- and L_{I}-ionized state and a doubly ionized L_{I} final state. Thus the conservation of energy requires:

---

[8] Cauchois and Hulubei, "Longeurs d'onde des émissions X et des discontinuités d'absorption X", Paris, Hermann (1947); Hulubei, C. R. Acad. Sci. Paris *224*, 773 (1947); Cauchois, J. Phys. Radium *5*, 1 (1944); Groven and Morlet, Bull. Acad. Roy. Belg. *37*, 630 (1951).

$$E_K + E^K_{L_I} = E_{L_I} + E^{L_I}_{L_I} + h\nu''_{\alpha_s}$$

or

$$E_{L_I} + E^{L_I}_K = E_{L_I} + E^{L_I}_{L_I} + h\nu''_{\alpha_s} \tag{5}$$

Introduce:

$$\left.\begin{aligned} E^{L_I}_K - E_K &= \Delta E_1' \\ E^K_{L_I} - E_{L_I} &= \Delta E_1'' \end{aligned}\right\} = \Delta E_1 \tag{6}$$

$$E^{L_I}_{L_I} - E_{L_I} = \Delta E_2$$

Combination of (5) and (6) shows that $\Delta E_1' = \Delta E_1''$ and the x-ray energy will be:

$$h\nu''_{\alpha_s} = E_K - E_{L_I} + \Delta E_1 - \Delta E_2$$

The experimental value[8] of 8.57084 kev for $h\nu''_{\alpha_s}$ for zinc yields a value of 0.109 kev for $(\Delta E_1 - \Delta E_2)$. Extrapolating the curves of GROVEN and MORLET, we obtain a value of 0.103 kev for $(\Delta E_1 - \Delta E_2)$ in copper.

The energy, E_{A_1}, of the $KL_I L_I$ Auger line from copper has been determined by ROBINSON and CASSIE.[7] As considered previously, this energy is given by:

$$E_{A_1} = E_K - 2E_{L_I} - \Delta E_2.$$

For an energy of E_{A_1} equal to 6.856 kev, the value of ΔE_2 is therefore 0.075 kev for copper. Combining both $(\Delta E_1 - \Delta E_2)$ and ΔE_2 values, we obtain $\Delta E_1 = 0.178$ kev, a figure which does not seem unreasonable since ΔE_1 involves the effects of K-shell ionization. For mercury, the value of ΔE_2 from our experiments for all cases of $L_p L_I$, $L_p L_{II}$, $L_p L_{III}$ ionizations is 0.290 kev.

In conclusion, attention should be drawn to the intensity measurements of the Auger components listed in Table 2. It has been pointed out[6, 9] that the experimental values are at variance with the theoretical predictions.

The present experiments support strongly the method used by ROBINSON[10] and others to obtain the binding energies of electrons within atoms. Gamma-ray spectroscopy in the future will require improved binding energy values in order to achieve the highest accuracy which would appear to be technically attainable.[4, 11] The use of still higher resolution in beta ray spectroscopy will also make the interesting study of natural line widths possible.[12]

---

[9] R. D. HILL, Phys. Rev. *91*, 770 (1953). F. A. JOHNSON and J. S. FOSTER, Can. J. of Physics *31*, 469, (1953).

[10] ROBINSON and RAWLINSON, Phil. Mag. *28*, 227 (1914); see also COMPTON and ALLISON "X-rays in Theory and Practice", pp. 500–510.

[11] K. SIEGBAHN, Physica *18*, 1043 (1952).

[12] H. SLÄTIS and G. LINDSTRÖM, Phys. Rev. *88*, 1429 (1952).

Tryckt den 20 april 1954

Uppsala 1954. Almqvist & Wiksells Boktryckeri AB

ARKIV FÖR FYSIK Band 8 nr 3

Communicated 10 March 1954 by MANNE SIEGBAHN and ERIC HULTHÉN

Natural widths of the internal conversion lines of RaB

By MILORAD MLADJENOVIĆ[1]

With 6 figures in the text

Contents

Page
Introduction 27

I. Experimental

A) Spectrometer adjustment 29
B) Monitoring 30
C) Experimental and theoretical resolution 31
D) Accuracy of measurements 33
    1. Variation of continuous background 33
    2. Statistics of measurements 34
    3. Field measuring system 34
    4. Variation of the field gradient 35
E) Experimental results 36

II. Theoretical

A) Width of nuclear excited state 40
B) Width of atomic levels 41
C) Recoil of the nucleus 44
D) Effect of change of Z to Z + 1 44
E) Ionisation of atom by beta particles 45
F) Multiple ionisation of atoms after internal conversion 46
G) Line width of multiply ionised atoms 46
H) Energy change of the outgoing conversion electron 47

Conclusions 47
Aknowledgements 48

Introduction

High resolution measurements of the internal conversion lines of ThB, made by LINDSTRÖM and SLÄTIS (1) revealed a difference in the widths of the K and L lines. LINDSTRÖM found in the semicircular spectrometer, that the F line is 4 parts in 10,000 wider than the I line. Similar results were obtained by SLÄTIS, who investigated the widths of several conversion lines of ThB in his permanent magnet spectrometer with photographic detection (2). Their results are summarized in the Table 1.

---

[1] On leave from the Institute for Nuclear Sciences "Boris Kidrič", Beograd.

Table 1. Slätis' and Lindström's values of the widths of the internal conversion lines of ThB.

Author	Type of spectrometer	Name of line	Origin of line	Energy kev	Full width at half maximum, %	Difference of widths
Lindström	Semicircular	F	K	147.8	0.14	4/10,000
		I	L_I	221.8	0.10	
Slätis	Perm. magnet	F	K	147.8	0.050	3/10,000
		I	L_I	221.8	0.020	
		G	K	188.8	0.039	2.7/10,000 2.9/10,000
		I a	L_{II}	222.4	0.012	
		H	K	209.7	0.041	

K. Siegbahn suggested (1) that the broadening of the K lines is due to the width of K X-rays which follow the internal conversion in the K shell. By extrapolation from the widths of K_α lines for the elements of lower Z, he obtained 70 ± 5 ev for the width of the K_α X-ray line of bismuth. The broadening of the K conversion line was evaluated to be 80 ev, in good agreement with the width of the K_α X-ray line. The widths of the L conversion lines were expected to be about 10 ev, a value too small to be observed at present.

The study of internal conversion line widths and their comparison with the widths of atomic levels, derived from X-ray measurements, may be of interest because some essential differences exist between these two phenomena. We shall mention some of them:

(*a*) X-ray emission is a purely atomic phenomenon in which a photon is created in a transition between two atomic levels. On the other hand, in internal conversion an electromagnetic interaction between the nucleus and the orbital electron takes place, and thus the transition involves the nucleus also.

(*b*) The initial atomic state in X-ray transitions is a relatively simple one, namely, an electron is missing in one of the inner shells. The initial atomic state in the internal conversion might be more complicated, since the conversion is preceded by a beta decay, or another conversion, and the phenomena accompanying these processes may influence the state of atom, causing excitations and ionisations in the atomic shells.

(*c*) The fact that in one case we observe the photons and in another the electrons should also be taken into consideration, because of their different interactions with atoms.

If these differences were reflected in the respective line widths, then a detailed comparison of conversion and X-ray line widths could give us some information on the second order phenomena accompanying beta decay and internal conversion.

The resolution which is necessary for an efficient study of conversion line broadening is at least of the order of 0.1 %, but a still higher resolution is to be preferred, as it can reveal finer details. This need for very high resolution introduces important restrictions in the choice of nuclides and instruments for the line width investigations. The choice of nuclides is mainly limited by the following requirements:

(*a*) The source has to be infinitesimally thin.

(*b*) The specific activity should be high, because high resolution seriously reduces the transmission, and very good statistics are needed.

(*c*) It should have strong, highly converted gamma transitions with an energy not greater than a few hundreds of keV.

(*d*) It would be desirable that the half-life be not too short, in order to facilitate the accumulation of statistics.

We have investigated the widths of conversion lines of RaB, which satisfies all the above requirements except the last. Infinitesimally thin recoil sources with high specific activity can be easily prepared. It has four prominent gamma-rays in the range from 50–350 keV. The only inconvenience is that RaB has a short half-life of 26.8 minutes and is a member of a radioactive series in which it is preceded and followed also by short half-life nuclides. This presents serious experimental difficulties.

The measurements were made with the 50 cm radius double focusing spectrometer (3).

The double focusing spectrometers are, generally, more convenient for the line width investigation than the semicircular types, since they have a better transmission for the same resolution. Iron-free double focusing spectrometers are, however, much more suitable than the double focusing spectrometers with iron, because the difficulties inherent in the measurement when iron is present become very critical with very high resolution. We shall later return to this point more in detail.

I. Experimental

A. Spectrometer adjustment

The double focusing spectrometer at the Nobel Institute was described in detail by HEDGRAN *et al.* (3). We shall only indicate the particular arrangements which we have used.

The source holder was made from the wolfram wire, 0.21 mm in diameter. It had an extended Π-shape and was fastened to an aluminium frame. The first diaphragm, which was previously adjustable only in the radial direction, was recently modified by Hedgran by the addition of an axial adjustment. While the first diaphragm, by fixing the aperture angles, determines the transmission and the aberrations, the second diaphragm merely serves as the anti-scattering diaphragm, and was always set to be 1 cm larger than the first diaphragm. Two values of counter slit width were used, namely 0.5 and 1 mm. As there was always some radon adsorbed on the source, which is released into the spectrometer and increases the background, a double GM counter in coin-

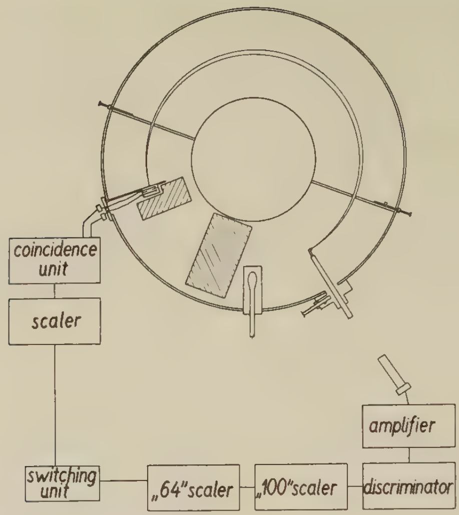

Fig. 1. Double focusing spectrometer and the electronic apparatus shown schematically.

cidences had to be used. The counter window was prepared from formvar, and was about 90 $\mu g/cm^2$ thick.

The irradiations were made in the radon chamber described by SLÄTIS and MLADJENOVIĆ (26). The Π-shaped wolfram wire source holder was mounted in a lucite frame which fitted the cover of the radon chamber. The samples were irradiated for 1–1.5 hours. Two identical samples were alternatively used, one being in the irradiation chamber while the second was in the spectrometer. The strength of the samples was from 1–10 mC.

B. **Monitoring**

The gamma-rays of RaB were monitored by a NaI(Tl) scintillation counter, which was placed outside the spectrometer chamber close to the source. 6400 counts from the monitor were taken as unit of measurements. The corresponding time intervals were from about 1 min. in the beginning of the measurements with a fresh source to about 10 min. at the end. Preliminary measurements had shown that, for the high counting rate obtained with a new source, non-negligible fluctuations are introduced by the inability of the operator to break the GM circuit exactly when the monitor is showing the 6400th count. A simple switching arrangement was then devised by which after 6400 counts the monitor itself breaks the GM circuit. The set-up of the apparatus is shown schematically in Fig. 1. The monitor has two scalers in series. After each 100 counts in the first scaler, the pulse is sent to the second scaler. When it has counted 64 counts a pulse energizes the relay in the switching unit which breaks the circuits of the GM counter and the monitor. Both circuits start to count simultaneously again when the relay is deenergized. Fig. 2 shows the low energy scintillation spectrum of RaB + C. The prominent photo-peak on the high energy side is due to 609 keV gamma-ray of RaC. The three main gamma-rays of RaB

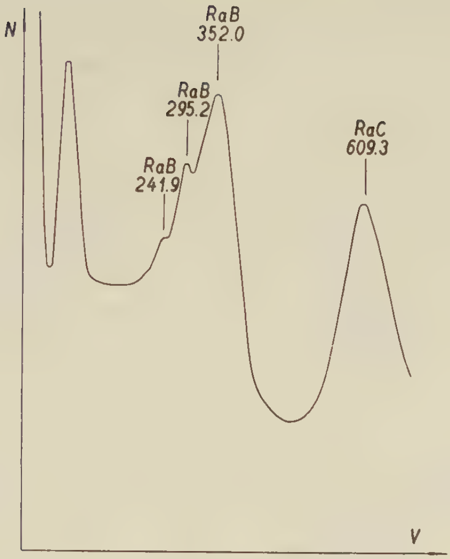

Fig. 2. Scintillation spectrum of RaB + C.

could not be separated. Their common photo peak is superposed on the Compton distribution from RaC gamma-rays. The discriminator was set on this photopeak. The ratio of detected RaB to RaC gamma-rays changes slowly in favour of RaC, because of the RaB decay. The error thus introduced will be dealt with more in detail in the section on the sources of error.

C. **Experimental and theoretical resolution**

The measurements were made with the resolutions of 0.043 % and 0.063 %. The geometry for these two settings is given in Table 2.

Table 2. Source and diaphragm dimensions for the resolutions used.

Resolution	0.063 %	0.043 %
Source dimensions	0.21 × 6 mm	0.21 × 6 mm
First diaphragm	8 × 40 mm	4 × 20 mm
Aperture angles radial	0° 46′	0° 23′
Aperture angles axial	3° 48′	1° 55′
Solid angle	0.028 % of 4 π	0.007 of 4 π
Counter slit width	1 mm	0.5 mm

The table shows that an increase in resolution from 0.063 % to 0.043 % was obtained at the expense of a fourfold reduction in the transmission. Further reduction of aperture angles does not result in any significant change of resolution. The probable cause of this limitation is a slight asymmetry of the field, which was noticed earlier by HEDGRAN.[1] This asymmetry has no effect at the resolutions ordinarily used, but its importance increases with the increase of resolution.

It is of interest to compare the resolution experimentally obtained with the theoretical predictions. The resolution of the double focusing spectrometer depends on four main factors: sample width, spherical aberrations, astigmatism and the counter slit width. Each of the first three factors contribute a certain width, which we shall denote δ_0, δ_s and δ_{as} respectively to the width δ of a distribution $f(x)$ which by sweeping over the window slit gives the observed distribution $F(x)$. If the width of the counter slit s were negligible compared to δ, the observed distribution $F(x)$ would be nearly equal to $f(x)$, and the relation between the total width δ and the observed resolution would be given by

$$\frac{\Delta H\varrho}{H\varrho} = \frac{\delta}{4r_0} \tag{1}$$

where r_0 is the radius of the central ray in the spectrometer. When s is not much smaller than δ we have

$$F(x) = \int_{x-s/2}^{x+s/2} f(\xi)\,d\xi. \tag{2}$$

The observed width W_0 depends therefore on δ and s, and the shape of $f(x)$.

In order to find the separate contributions to the total line width we should compute δ_s and δ_{as} from the expressions:

$$\delta_s = \frac{4}{3}\gamma_1^2 r_0 \tag{3}$$

$$\delta_{as} = r_0 \gamma_1 \varepsilon \pi \sqrt{2} \tag{4}$$

where γ_1 is the radial aperture and ε is an unknown coefficient which measures the relative deviation of the field gradient from the prescribed values. It would be difficult to get a precise value for ε by the mapping of the field and it is probably easier to derive δ_{as} from the value of δ by supposing that δ is approximately equal to the sum of δ_0, δ_s and δ_{as}.

δ_0 and δ_s are easily computed while δ can be approximately found by assuming a simple distribution for $f(\xi)$ and performing the integrations of the equation (2) for different values of δ until we find the one which yields the right value for W_0. We have found an approximate value for δ by assuming that $f(\xi)$ has the shape of an isosceles triangle. All the data relating to the theoretical analysis of the resolution are given in Table 3.

It can be seen from the table that the most important single contribution to the width comes from the astigmatism.

---

[1] Private communication.

Table 3. Data on the theoretical contributions to the resolutions used.

Magnitude	Expression	Width in units of 10^{-4} Higher res.	Width in units of 10^{-4} Lower res.
Relative sample width	$\delta_0/4\,r_0$	1	1
Rel. aberration width	$\gamma_1^2/3$	0.15	0.57
Rel. astigmatism width (approximately)	$\sqrt{2\pi\varepsilon\gamma_1}/4$	2.35	3.63
Rel. width of $f(x)$ (approximately)	$\delta/4\,r_0$	3.50	5.7
Rel. width of counter slit	$s/4\,r_0$	2.5	5
Observed width	W_0	4.3	6.3

D. Accuracy of measurements

The sources of error in the determination of the width of RaB conversion lines can be divided into four classes: background variation, statistics, field measuring system, and variation of the field gradient.

1. **Variation of continuous background.**—The width of a line is uncertain if the background varies from one end of the line to the other. In that case the usual procedure is to extend the measurements in both directions from the line in order to obtain sufficient information on the variation of the background, so that it can easily be substracted. This was impractical in our case, for two reasons. Firstly, the short half-life requires the greatest possible economy of time, and secondly, the background is changing with time, making it more difficult to establish exactly its variation over the line. Fortunately, different contributions to the background variations are complementary and the mean error in the determination of the background is not greater than 3 % of the height of the line.

The change of the background over the line is caused by three factors: the slope of the continuous beta distribution, the contribution of radon to the background, and the contribution of the RaC to the monitoring.

(*a*) The continuous beta distribution is shown in Fig. 3. The arrows indicate the positions of the lines. The relative difference in the background over the lines is 10 % for the A line, 2 % for the F line, 1 % for the G and Ga lines, and less than 1 % for the other RaB lines. The A and F lines, which have the highest background differences, are more than ten times higher than the continuous beta background, so that the error is less than 1 %.

(*b*) The steady rise of background, which was always observed in the first few minutes after the introduction of the source into the spectrometer, indicates that a considerable amount of radon is adsorbed on the source during the irradiation and is released into the spectrometer chamber. The background rise is probably due to RaB, which is rapidly formed, since the half-life of RaA is only 3 min. After the first 10 minutes the background rise becomes less pronounced, and it is only then that the proper measurements can start.

(*c*) While the continuous beta distribution and the adsorbed radon increase the background on the high energy side of the line, the contribution of RaC

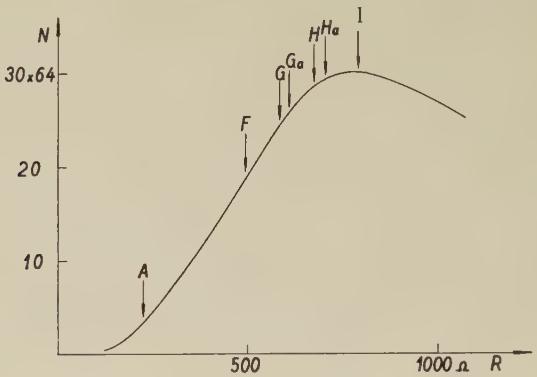

Fig. 3. Continuous beta distribution of RaB + C.

to the monitoring has the opposite effect. From the decay curves of the RaB and C it is known that 20 minutes after the saturated activation, the number of RaC atoms disintegrating per second is 36 % greater than the number of disintegrating RaB atoms, and this proportion is rising steadily, changing the ratio of RaB to RaC gamma rays detected by the monitor, and thus making the time intervals set by the monitor smaller than they would be if the monitor were detecting only RaB gamma-rays. For instance, the same line measured after a delay of one hour, was found to be 14 % lower in the second measurement. The time taken to run over one line was always less than 20 minutes, so that the distortion due to the reduction of background was not greater than 4 %. Actually, an inspection of the curves shows that the mean error in the determination of the line widths introduced by the variation of the background due to all three causes is about 3 %.

2. **Statistics of measurement.**—The short half-life of RaB does not allow a long accumulation of statistics, as would be desirable in this kind of measurement. Furthermore, the effective time of measurement is reduced by the presence of the iron in the spectrometer, because the remanent field displaces the line by an unknown amount and the search for the line takes on the average more time than it takes to run over the line itself. One source cannot be used for more than 1.5 hour, which is just enough to measure 2–4 lines. The standard errors in counting at the peaks of the lines are 1.5–2 % for K lines and 2.5–3 % for L lines. Dead-time corrections are low, being only 1–2 % for K lines and negligible for L lines. Finally, the unit of measurement set by 6400 counts from the monitor has a statistical standard error of 1.25 %. The total error in the determination of the line widths arising from statistics is not greater than 3 %.

3. **Field measuring system.**—A detailed discussion of the field measuring system and the accuracy of the 50 cm radius double focusing spectrometer was given by HEDGRAN (3). In the line width measurement we are not so much interested in the absolute accuracy of the energy determination, as we are interested in the relative accuracy of the points on the line. Our main con-

cern is that the interval between the two points which we read on the potentiometer corresponds accurately to the change of the spectrometer field. As the time of measurement of a line is short and the energy range over which the line is stretched is very small, several problems associated with changes of circuit components with time, and with changes of the current in the coils, are less important than in the case of energy calibration measurements. The main sources of error in our case are: (*a*) the inaccuracy of balancing between the field in the spectrometer and in the standard coil, and (*b*) the error in the galvanometer reading. The balancing was always carefully adjusted before the measurement of a line starts, and no appreciable readjustment was needed over the line. Inaccuracy in the location of the galvanometer light spot becomes non-negligible for the small separations between points in high resolution work. It is difficult to evaluate the error arising from the field measuring system, as it depends to a great extent on the carefulness of the operator. From some checks made during the measurement, we conclude that the mean error in the line width determination arising from inaccuracies in the field measurement are not greater than 5 %.

The estimated total error in the line width determination due to background variation, statistics, and field measuring system is probably not greater than 7 %. This is only valid for a single set of measurements in which all the experimental conditions are kept strictly constant. Otherwise, from one set of measurements to another, small changes of parameters cause changes in the line width. For that reason it is not possible to accumulate statistics by the addition of several measurements of the same line.

4. **Variation of the field gradient.**—HEDGRAN has discussed (3) the variation of the field gradient in this spectrometer with the prehistory of iron and the field strength. He has found that the dependence on the prehistory of iron may be considerably reduced by a careful demagnetization before the measurement start, and by varying the current, during the measurement, only in one direction. The variation of the field gradient with the strength of the field could be expected because of the presence of a large quantity of iron. This variation should show up in the variation of the instrumental width with the energy. It is quite difficult, at present, to evaluate, by measurements, the dependence of the instrumental width on the energy. Hedgran found that the half-width changes from 0.35 % to 0.30 % when the momentum of electrons changes from 1400 gauss-cm to 10,000 gauss-cm respectively. The difference of 0.05 % is of the order of K-conversion line broadening, which for 1400 gauss-cm should be about 3–4 parts in 10,000, while at 10,000 gauss-cm it should be negligible. It will be possible to find exactly the energy dependence of the instrumental line width of this spectrometer, only when the precise absolute values of the natural widths of internal conversion lines become available. The variation of the instrumental line width caused by the field-dependence of the gradient can be reasonably expected to be represented by a smooth curve. Because of the possible unknown variation of the instrumental width with the energy, we have to restrict our measurements to the evaluation of relative differences of the widths of K and L conversion lines of comparable energies, while the absolute values of the widths cannot be at present established by this spectrometer.

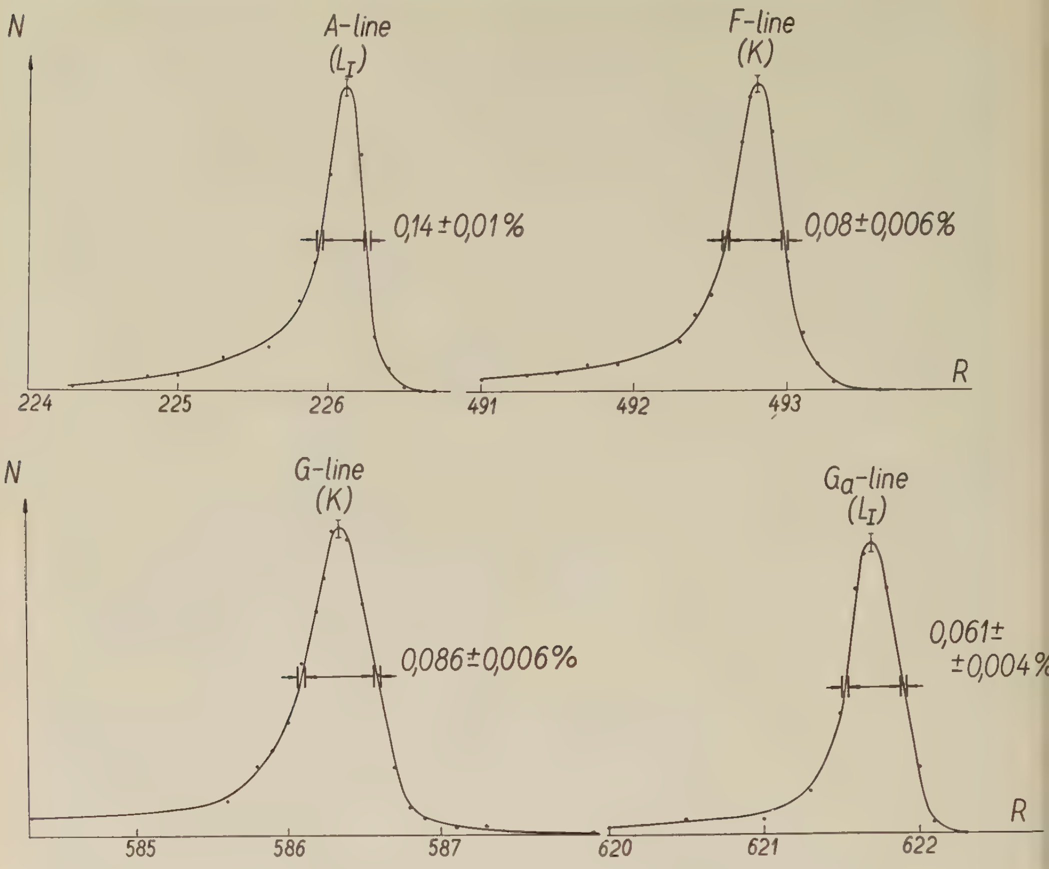

E. Experimental results

In Fig. 4 we give the curves of one set of measurements made with higher resolution. In order to show the variation of relative line width with the resolution, we give below the line widths obtained in another set of measurements with lower resolution. Table 4 summarizes the data on the observed line widths in both sets of measurements.

Table 4. The data on the observed line widths.

Name of line	A	F	G	Ga	H	Ha	I
Origin of line	L	K	K	L	K	L	L
Electron energy	36.9	151.5	204.7	225.5	261.3	278.7	335.7
Width at high res., %	0.14	0.08	0.086	0.061	0.077	0.053	0.043
Width at low res., %	0.21	0.105	0.113	0.08	0.091	0.07	0.063

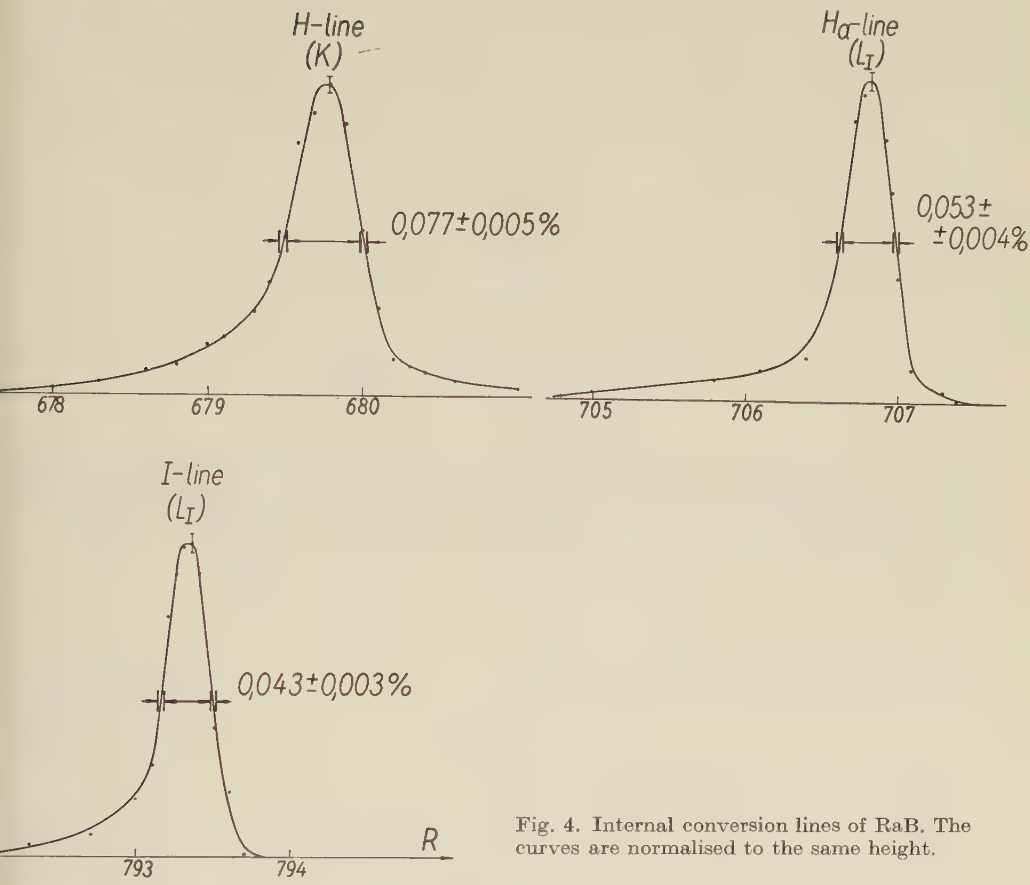

Fig. 4. Internal conversion lines of RaB. The curves are normalised to the same height.

An important qualitative conclusion can be drawn from the results given in the above tables:

All K lines are broader than L lines of comparable energy, confirming the results obtained by SLÄTIS and LINDSTRÖM with ThB.

In order to proceed to a quantitative analysis of the above results we must first derive the true line distribution from the observed line shape. If the true distribution is $f(x)$, and if the spectrometer for various reasons gives $g(x)$ as the shape of a strictly monochromatic line, then the observed distribution $X(x)$ is given by the relation:

$$X(x) = \int_{-\infty}^{+\infty} f(\xi)\, g(x-\xi)\, d\xi. \tag{5}$$

In this analysis we shall suppose that the width of a monochromatic line is constant and that its shape is approximately given by the I line distribution. If the width of the I line were slightly greater than the width of a monochromatic line, then the true widths which we shall obtain by assuming that the

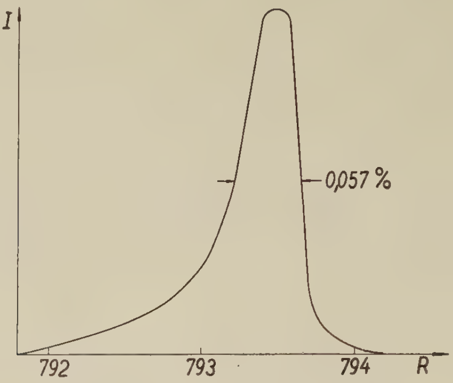

Fig. 5. True distribution of F line.

I line corresponds to a monochromatic line will be somewhat reduced, and we can consider that in any case they represent a lower limit of the true widths.

The equation (5) is easily solved if the distributions can be approximated by Gauss or dispersion curves. In the case of the Gauss distribution given by

$$g(x) = \exp\left[-x^2 \log 2 \Big/ \left(\frac{W_g}{2}\right)^2\right]$$

the relation between the widths is

$$W_X^2 = W_f^2 + W_g^2. \tag{6}$$

On the other hand, the dispersion curve

$$g(x) = 1 \Big/ \left(1 + \frac{x^2}{(W_g/2)^2}\right)$$

gives for the relation between the widths

$$W_x = W_f + W_g. \tag{7}$$

This shows that the relation between the line widths is very sensitive to the shape of curves, and only in the case of dispersion curves we have $W_f = W_X - W_g$, while the Gauss curve gives $W_f > W_X - W_g$.

The shapes of our curves do not correspond to either one of these two simple distributions. We have solved the equation (5) numerically for the F line. The F line and I line were devided into a number of equidistant elements, and a system of 27 equations of the form

$$X_i = \sum_{k=1}^{n} f_k \, g_{k-i} \tag{8}$$

was set up. The determinant of the system had the strongest terms in the diagonal, falling off gradually on both sides. This type of equation is readily solved by analogue computer machines. The solution is shown in Fig. 5. It is interesting to note that the curve is not symmetrical, but has a low energy tail. This tail must be due to an effect occurring inside the atoms where the conversion takes place, since external effects are included in the tail of the monochromatic line $g(x)$.

The width of the true distribution W_f, numerically computed for the F line satisfies the relation

$$W_X^{1,5} = W_f^{1,5} + W_g^{1.5}. \tag{9}$$

The width of the other lines may be approximately computed by assuming that the relation (9) is valid for the whole set of curves. From the widths expressed in $H\varrho$ units we get the widths in ev by the formula:

$$\frac{\Delta V}{V} = \left(1 + \frac{\mu}{\mu + V}\right) \frac{\Delta H\varrho}{H\varrho} \tag{10}$$

where μ is the rest mass of the electron.

The true widths so obtained are given in the Table 5.

Table 5. True widths of RaB conversion lines.

Name of line	A	F	G	Ga	H	Ha
Origin of line	$\mathrm{L_I}$	K	K	$\mathrm{L_I}$	K	$\mathrm{L_I}$
W_f in $\Delta H\varrho/H\varrho$, %	0.126	0.057	0.064	0.033	0.053	0.022
W_f in ev	90	153	227	126	230	109

The relation (9) applied to the set of lower resolution widths would yield greater true widths than those given in the above table. That means that either the relation (9) is not valid for the lower resolutions, or that the exponential should be lower than 1.5 for both sets of curves. The lower limit should in any case be given by the relation $W_X = W_f + W_g$. The corresponding values of the true widths are given in the table below.

Table 6. Lower limit of true widths given by $W_f = W_X - W_g$.

Name of line	A	F	G	Ga	H	Ha
Origin of line	$\mathrm{L_I}$	K	K	$\mathrm{L_I}$	K	$\mathrm{L_I}$
W_f in $\Delta H\varrho/H\varrho$, %	0.097	0.037	0.043	0.018	0.033	0.01
W_f in ev	69	100	151	69	143	46

The true widths of L lines obtained with the assumption that the instrumental width does not vary with the energy, and that it is equal to the width of I line, are larger than those found by SLÄTIS (1). As the energy variation of the instrumental width is not known, the values for L widths cannot be accepted, and the only quantitative conclusion which we can draw from our experimental results is that the relative difference in line width between the K and L conversion lines is of the order of 80–100 ev.

These conclusion are in agreement with the results of LINDSTRÖM and SLÄTIS. If as a first approximation we take that the difference of true widths of K and L lines is equal to the difference of the observed widths of these lines, we obtain the following values from Lindström and Slätis data:

Table 7. Difference between the widths of K and L lines measured by LINDSTRÖM and SLÄTIS.

Author	Difference	$\Delta H\varrho / H\varrho$, %	ev
LINDSTRÖM . .	$W_F - W_I$	0.04	105
SLÄTIS	$W_F - W_I$	0.03	79
	$W_G - W_{Ia}$	0.027	88
	$W_H - W_{Ia}$	0.029	104

These differences between the K and L lines agree with those which we have found.

II. Theoretical

We shall now proceed to a brief discussion of several phenomena which may be responsible for the broadening of the internal conversion lines. We must first examine the contribution of the width of the initial nuclear excited state. Next, we have to consider the widths of K and L levels from the X-ray analysis, and how they can be affected by the phenomena accompanying the beta decay.

A. Width of excited nuclear state

The contribution of the width of the excited nuclear state to the width of the internal conversion lines should be same for the K and L lines. The considerable difference between the widths of the K and L lines makes it obvious that the width of the excited nuclear state cannot represent the major part of the broadening of the conversion lines. More information on the width of the nuclear excited states can be obtained from the half-life of the excited state, using Heisenberg's uncertainty principle

$$\Delta E \cdot \Delta \tau \sim \hbar$$

where ΔE is the width of the level, and $\Delta \tau$ the half-life. For the M 1 and E 2 transitions the half-lives are mostly between 10^{-4}–10^{-9} seconds, corresponding to level widths of 6.10^{-12}–6.10^{-7} ev (4). For the transitions of higher multipole orders the level widths are still smaller. The only transition which could theoretically give observable widths is the electric dipole, which should have the half-life of 10^{-17} sec. (5), corresponding to the level width of 60 ev. It appears from the L_{I}/L_{II} ratios (26) that all four main RaB gamma-rays are magnetic dipoles, so that the contribution of the nuclear excited state to the line widths of RaB conversion lines is probably negligible.

B. **Widths of the atomic levels**

The main information which exists on the widths of the K, L and M levels of the atom originates from the analysis of the widths of X-ray lines. The first theoretical interpretation of the line widths, based on Dirac's radiation theory, was given by WEISSKOPF and WIGNER (6). PRINS and MARGENAU have given somewhat simplified treatments (7), and, quite recently, the line width phenomena were studied from the point of view of quantum electro-dynamics by ARNOUS and HEITLER (8).

Classical theory of line width starts from the assumption that the radiating atom can be treated as a linear oscillator, and the line width then results from the damping of the oscillations caused by the reaction force. The displacement of the damped harmonic oscillator is given by

$$A(t) = A_0 e^{-\pi \Gamma t} \cos (2\pi \nu_0 t - \varphi) \tag{11}$$

where A_0 is the initial amplitude of the oscillator, ν_0 is undamped frequency, and φ a phase constant. $2\pi\Gamma$ is the damping coeffecient and is given by

$$\Gamma = \frac{4\pi}{3} \frac{e^2 \nu_0^2}{m c^3}. \tag{12}$$

It is connected with mean life τ of the atom in its excited state by the expression

$$\Gamma = \frac{1}{2\pi\tau}. \tag{13}$$

The intensity distribution of the radiation from such an ascillator is obtained by the development of (11) in a Fourier series and is given by:

$$J(\nu)\, d\nu = \frac{\Gamma}{2\pi} \frac{d\nu}{2\pi(\nu_0 - \nu)^2 + \left(\frac{\Gamma}{2}\right)^2} \tag{14}$$

from which we see that Γ is the full width at half maximum of the line. If the line width is expressed in wave-length units, one finds that the line width is independent of frequency and equal to 0.116 XU, which is contrary to the experimental results. The observed line widths depend on the wave-lengths and may be several times greater than 0.116 XU.

In the quantum theory the intensity distribution has a similar expression to that given in equation (14). A transition between the initial state A and the final state B has the spectral distribution given by

$$J_{AB}(\nu)\, d\nu = \frac{\Gamma_A + \Gamma_B}{2\pi} \cdot \frac{d\nu}{(\nu_{AB} - \nu)^2 + [(\Gamma_A + \Gamma_B)/2]^2} \tag{15}$$

where

$$\nu_{AB} = \nu_A - \nu_B = (E_A - E_B)/h.$$

Γ_A and Γ_B are related to the mean lives of the excited state A and B by the formula:

$$\Gamma_A = \frac{1}{2\pi\tau_a} \qquad \Gamma_B = \frac{1}{2\pi\tau_B}. \tag{16}$$

The meaning of Γ is changed in the quantum mechanical formula. Now $2\pi\Gamma$ is the sum of the probabilities $2\pi\gamma_{AC}$ that in unit time a transition will take place spontaneously from the state A to another state C of the same or lower energy:

$$\Gamma_A = \Sigma'(C)\,\gamma_{AC} \qquad \Gamma_B = \Sigma'(D)\,\gamma_{AD} \tag{17}$$

$$E_C \leq E_A \qquad E_D \leq E_A.$$

The main points of the quantum theory of line widths are therefore the following:

(*a*) The width of a line is equal to the sum of the widths of the initial and the final states.

(*b*) The width of an energy state is proportional to the probability that in unit time the atom leaves that state, changing to any other of the same or lower energy.

In the theoretical calculations of the width of a given state it is necessary to compute the probability for transitions with the emission of radiation, and for the Auger transitions to all the states of the same or lower energy. Such a calculation was performed by RAMBERG and RICHTMYER (9) for the level widths of Au (79). Their results are reproduced in the following table:

Table 8. RAMBERG and RICHMYER's values for the level widths of Au (79), in ev.

Level	K	L_I	M_I	M_{II}	M_{III}	N_I
Calculated width	67.15	13.69	10.31	11.58	4.50	13.60
Observed width	54	8.7	15.5	10.7	12.1	11.7

The only measurements of K X-ray lines of Bi 83 known to the author are those made by INGELSTAM (10). He found that K_{β_1} and K_{β_3} should be about 80 ev, the possible error being not greater than 15 %. The uncertainty was caused by the fact that the experimental curve did not fit to either the Gauss or the dispersion curve so that the author took the mean of results obtained with the two curves. We obtain the width of the K level W_K from the width of the K_{β_1} radiation line from the relation

$$W_{K_{\beta_1}} = W_K + W_{M_{III}}. \tag{18}$$

The width of the M_{III} level for Bi was not measured. If we take the width of the M_{III} level from gold as measured by RICHTMYER (9), which is 12.1 ev, and

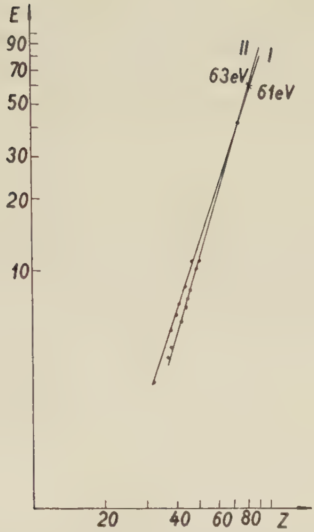

Fig. 6. The widths of K lines. I represents the data given in COMPTON and ALLISON's book; II represents the data given by GOKHALE.

extrapolate to Bi with the law Z^4, we get 14.7 ev. We thus find for the width of the K level of RaB the value 65.3 ev. This value can be checked by extrapolating from the lower Z values of the widths of $K_{\alpha 1}$ lines. In Fig. 6 we give two extrapolation curves, one based on the data given in the book by COMPTON and ALLISON (11), and the other based on recent measurements of GOKHALE (12). By substracting 5.4 ev, the width of the L_{III} level from RICHTMYER's data, from 61–63 ev which we obtain from extrapolation from the values of $K_{\alpha 1}$ lines for lower Z, we obtain 55.6–57.6 ev for the width of K level of Bi. We shall take 60 ± 5 ev as the most probable value for the width of the K level.

L X-ray lines of Bi were measured by WILLIAMS (13). His values agree with the values for the levels extrapolated, using the law of Z^4, from RICHTMYER's values for gold. We shall take the values extrapolated from RICHTMYER for the values of the L and M levels. They are:

Table 9. Widths of L and M levels extrapolated from the values for gold, in ev.

Level	L_I	L_{II}	L_{III}	M_I	M_{II}	M_{III}	N_I
Widths	10.6	4.5	5.4	18.9	13	14.7	14.3

The difference between the widths of K and L_I atomic levels for Bi 83 as derived from X-ray data is of the order of 50 ev. The difference between the widths of K and L_I conversion lines is almost twice as great, being of the order of 80–100 ev. It appears, therefore from the present data on the line widths of internal conversion lines, which should by all means be considered as very preliminary, that the secondary phenomena connected with the beta decay and the internal conversion might give observable effects, and that a careful study of the witdhs of internal conversion lines may yield quantitative information on these phenomena.

C. Recoil of the nucleus

There are two possible ways in which the recoiling nucleus can influence the widths of internal conversion lines. First is the contribution of the velocity of the recoiling atom to the velocity of the emitted electron, and second is the perturbing effect of the sudden change of nuclear velocity on the orbital electrons. In the case of RaB decay, both these effects are negligible.

The energy of the recoiling nucleus can be calculated from the approximate formula

$$\mathrm{E_R} \sim \frac{536.10^{-6}}{\mathrm{M}} (\mathrm{W}^2 - 0.26)\ \mathrm{Mev} \tag{19}$$

where M is the mass of the nucleus in atomic mass units and W the maximum energy of beta disintegration. The high energy end of the RaB beta spectrum is at 0.72 Mev, giving for the energy of the recoiling nucleus 0.65 ev, and for the velocity roughly $7 \cdot 10^4$ cm/sec. This effect is negligible.

The probability for the excitation of the atom was computed by LEVINGER (14). Treating the sudden change of the nuclear velocity as a sudden perturbation, he finds that the probability for the excitation is of the order of $\mathrm{K}^2/\mathrm{Z}^2$, where K is numerically equal to the nuclear recoil velocity, devided be the characteristic electron velocity $e^2/\hbar$ and Z is the effective charge of the atom. In the case of RaB, K^2 is of the order of 10^{-7}, so that the probability of the excitation of the atom by the nuclear recoil is also negligible.

D. Effect of the change from Z to Z+1

Internal conversion is preceded by beta decay in which the atomic charge changes from Z to Z+1. This change is accompanied be a readjustment of the orbital electrons to the new charge. The total binding energy of the heavy atoms is given according to FOLDY (15) by the relation

$$E_{\mathrm{B}}(\mathrm{Z}) = -\mathrm{R}\,\mathrm{Z}^{12/5} \quad (\mathrm{R} = 13.6\ \mathrm{ev}). \tag{19}$$

The difference in binding energies for the beta decay of RaB is equal to 15.8 keV. Only a small part of this energy is on the average retained by the atom, the main part being given to the outgoing particles. This small part which is not given to the outgoing particles causes the excitations and the ionisations of the atom. The average value of the energy expended in the excitation and ionisation of the atom was calculated by SERBER and SNYDER (16). The mean energy of the excitation depends essentially on the velocity of the outgoing particle. If the velocity is low compared to the velocity of the orbital electrons, as it is the case in alpha decay, the electron cloud will have time to reajust itself and the process is adiabatic, while if the velocity of the outgoing particle is high compared to the orbital velocities, as it is in the case of beta decay, the electron cloud will not have time for the readjustment and a part of the difference in binding energies is left in the atom and serves for the excitation of orbital electrons. SERBER and SNYDER find that this energy is equal to

$$\Delta E = 22.85 \cdot Z^{2/5}\ \text{ev}. \tag{19}$$

For the beta decay of RaB, this amounts to 133 ev. They also find that the average excitation of each closed shell should be about 27 ev. There is a definite probability for the excitation or the ionisation of each shell in the atom, and the energy of excitation or ionisation averaged over the probabilities should give 27 ev for each shell.

The probabilities for the ionisation of K, L, and M electrons were calculated by a number of authors (17) by essentially similar theoretical approaches. When the velocity of beta particles is higher than 150 keV, for the heavy atoms, the sudden change of the Z to Z + 1 can be treated theoretically as a sudden perturbation. The approximate solutions obtained by using the hydrogen-like one-electron wave functions, and neglecting the relativity corrections, are given in Table 10 for the probabilities of ionisation of K, L and M levels (18).

Table 10. Probabilities of the ionisation of the orbital electrons by the change of Z to Z + 1.

Shell	K	L	M
Probability of ionisation . .	$0.66/Z_{\text{eff}}^2$	$2.26/Z_{\text{eff}}^2$	$4.28/Z_{\text{eff}}^2$

We see that the probabilities are inversely proportional to the square of the effective charge and are slowly increasing with the main quantum number n. For RaB, $1/Z_{\text{eff}}^2$ is of the order of 10^{-4} for the K, L, and M shells. The probability of ionisation of the inner shells is therefore very small, and one could expect that only outer shells will be appreciably ionised.

Assuming that the proportionality of ionisation to $1/Z_{\text{eff}}^2$ is valid for the outer shells also, one finds that the probability for ionisation of the outer shells is of the order of a few times 10 %.

In a recent measurement of the average charge of recoil atoms VEXLER (19) finds that in the beta decay of A^{41} and C^{14} in the compound $C^{14}O_2$, the average positive charge is 1 ± 0.1 e and 1 ± 0.2 e respectively.

E. Ionisation of atom by beta particles

The excitation or the ionisation of the atom may result also from the direct collision between the beta particle and an electron in the cloud through which it passes after leaving the nucleus. According to FEINBERG (17) the ratio of the probability of ionisation by direct collision, P_{dc}, to the probability of ionisation by the change of Z to Z + 1, P_s, for relativistic electrons is given by

$$\frac{P_{\mathrm{dc}}}{P_{\mathrm{s}}} \sim \frac{I}{m\,c^2} \tag{20}$$

where I is the ionisation energy.

Assuming the proportionality of P_s to $1/Z^2_{\mathrm{eff}}$ we find that the probability of ionisation by direct collision with the beta particle is of the order of 10^{-5} per beta decay, for any shell. This effect is therefore much smaller than the effect of change of Z to Z + 1.

F. Multiple ionisation of atoms after internal conversion

There is one case where we have more evidence that the atom is multiply ionised before the internal conversion, and that is when two internally converted gamma-rays are in cascade. Then the Auger transitions which follow the first conversion will cause a multiple ionisation of the atoms. PERLMAN and MISKEL (20) have recently measured the average charge of daughter atoms produced in the beta decay of A^{37} and $Xe^{131\,m}$. They found that the average charges on the Cl^{37} and Xe^{131} atoms are 3.41 e and 8.5 e respectively, the main cause of ionisation being the Auger cascade which follows the K capture in A^{37} and the internal conversion in $Xe^{131\,m}$. It is also known from neutrino experiments (21) that the recoil atom is multiply ionised. In those cases of nuclear isomer separations where the recoil energy is insufficient to rupture the molecular bond, it is found that the multiple ionisation of the atom after the internal conversion may cause the dissociation of the molecule. COOPER (22) has calculated the accumulation of charge by the Auger process for the Br atom and found that within 10^{-9} sec. after the K conversion the charge of the atom is equal to 4.7 e.

G. Line widths of multiply ionised atoms

We have seen that in beta decay about 10–20 % of the daughter atom can be doubly ionised in the outermost shells, while the internal conversion may leave the atom more than doubly ionised. The deexcitation of these ionised atoms depends on the material used for source backing. We have used the wolfram and it is known from relatively large widths of soft X-ray emission lines from metals (23) that the deexcitation of ionised atom by the electron from the continuum represent a fast process. The deexcitation would also depend on the state of the surface of wolfram wire and its cleanness. In the case of beta decay of RaB it is quite possible that a large number of the ionised atoms has returned to the neutral state before the internal conversion start, and since the initial number of doubly ionised atoms may be of the order of 10 %, one can conclude that the effect of doubly ionised atoms should be very small. The effect may be greater in the case when the internal conversion is preceded by another internal conversion. The mechanism by which the multiply ionised atoms can influence the width of the internal conversion lines is the following. The absence of some of the electrons reduces the screening, and increases the binding energy of the rest of the electrons in the atom. Since the energies of the internal conversion electrons depend on the binding energies, we should have as many discrete energies of the conversion electrons from the same shell as we have possible ionisation states of the atom. If the differences between the binding energies are smaller than the line widths caused by other phenomena, then all the discrete lines will merge into one broad line, while greater differences should give separate lines. This is well known from X-ray work, where the so-called satellite lines and the broadening of lines in chemical compounds is explained by the multiple ionisation.

Satellite lines correspond to transitions between the doubly ionised atoms. As an example, we can mention that the separations of L satellites for gold may be of the order of 27 to 130 ev (24). The broadening of K X-ray lines in chemical compounds may be seen from the example of cobalt, which in the metallic form has the K line width 57.4 ev, while in the form of $CoCl_3 \cdot 6\,H_2O$ the width is 84 ev (25). The cause of the broadening is that the cobalt atom looses three electrons to the other atoms in the molecule.

From these examples we see that the magnitude of the broadening of levels due to multiple ionisation is of the same order as the internal conversion line broadening.

In our case, the data on the amount of ionization after beta decay are not sufficiently well known, so that no definite conclusion can be reached regarding the possible contribution of the multiple ionisation to the natural line widths of conversion lines, although it seems likely that it is not great.

H. The energy change of the outgoing conversion electron

The conversion electron has to pass through the electron cloud, before leaving the atom. Two effects could then influence its energy. Firstly, a collision may take place between the outgoing conversion electron and an electron from the cloud. The FEINBERG's results given by the relation (20) should be valid for this case also. According to FEINBERG this effect should be negligible.

Second effect similar to the effect of change of Z to Z + 1 in the case of beta decay.[1] When a K electron has left its shell, the other orbital electrons find themselves in a changed field, and the resulting reajustment may influence the outgoing conversion electron. The magnitude of the effect would depend on the velocity of conversion electron, being greater for faster electrons. No theoretical calculation exists for this effect, but one could expect it to be smaller than similar effect for beta decay calculated by SNYDER and SERBER.

Conclusions

1. The difference in widths of K and L internal conversion line of RaB was experimentally found to be 80–100 ev.

2. The difference in width of K and L atomic levels was found from the published data on the X-ray lines to be about 50 ev. It appears from present measurements that there might be some other causes of the broadening besides the normal widths of K and L levels as found by X-ray analysis.

3. Some of the possible causes may be left out without doubt, as for instance the influence of the nuclear recoil on the line width. The contribution of other possibilities such as multiple ionisation after a preceding internal con-

---

[1] This possibility was suggested by Dr. Koffoed-Hansen.

version are not clear yet. More theoretical work should be done on these effects, since up to now they were usually neglected in the theoretical calculations, as they were not measurable.

ACKNOWLEDGEMENTS

My sincere thanks are due to Professor MANNE SIEGBAHN for the hospitality and the interest shown for this work. I am grateful to Profs. K. SIEGBAHN and H. SLÄTIS and to Drs. R. WALLEN, K. KOFFOED-HANSEN and A. WINTHER for the discussions on the line widths. My appreciations are due to Civ.ing. B. ÅSTRÖM for the loan of scintillation counter equipment and for the construction of the switching unit. Finally I wish to thank Ing. P. MADIĆ for the computations done with the analogue computer machine in the Institute for Nuclear Sciences "B. Kidrić", Belgrade.

Nobel Institute for Physics, Stockholm, March, 1954.

REFERENCES

1. SLÄTIS, H., and LINDSTRÖM, G., Phys. Rev. *88*, 1429 (L), (1952).
2. SLÄTIS, H., Arkiv f. Fysik *6*, No. 41 (1953).
3. HEDGRAN, A., SIEGBAHN, K., and SVARTHOLM, N., Proc. Phys. Soc. *63*, 960 (1950).
4. GOLDHABER, M., and SUNYAR, A. W., Phys. Rev. *83*, 906 (1951).
5. BLATT and WEISSKOPF, Theoretical Nuclear Physics, Willey, 1952.
   BETHE, Elementary Nuclear Theory, Willey, 1947.
6. WEISSKOPF, V., and WIGNER, E., Zeit. f. Physik *63*, 54 (1930).
7. PRINS, J. A., Physica *2*, 231 (1935).
   MARGENAU, H., Phys. Rev. *47*, 89 (1935).
8. ARNOUS and HEITLER, Proc. Roy. Soc. A 220, 290 (1953).
9. RAMBERG, E. G., and RICHTMYER, F. K., Phys. Rev. *51*, 913 (1937).
10. INGELSTAM, K., Nova Acta Regiae Soc. S. C. Upsaliensis, Ser. IV, *Vol. 10*, No. 5.
11. COMPTON, A. H., and ALLISON, S. K., X-rays in Theory and Experiment, Van Nostrand, 1935.
12. GOKHALE, B. G., Ann. Phys. *7*, 852 (1952).
13. WILLIAMS, J. H., Phys. Rev. *45*, 71 (1934).
14. LEVINGER, L. S., Phys. Rev. *90*, 11 (1953).
15. FOLDY, Phys. Rev. *83*, 397 (1951).
16. SERBER, R., and SNYDER, H. S., Phys. Rev. *87*, 152 (1952).
17. MIGDAL, A., J. Phys. (USSR) *4*, 449 (1941).
    FEINBERG, E. L., J. Phys. *4*, 423 (1941).
    WINTHER, A., Kgl. Danske Videnskab. Mat.-Fys. Med. *27*, No. 2 (1952).
    BENOIST-GUEUTAL, P., Ann. Phys. *8*, 593 (1953).
    SCHWARTZ, H., J. Chem. Phys. *21*, 45 (1953).
    LEVINGER, L. S., Phys. Rev. *90*, 11 (1953).
18. SCHWARTZ, H., J. Chem. Phys. *21*, 45 (1953).
19. VEXLER, S., Phys. Rev. *93*, 182 (1954).
20. PERLMAN, M. S., and MISKEL, J. A., Phys. Rev. *91*, 899 (1953).
21. KOFFOED-HANSEN, Physica, *18*, 1287 (1952).
22. COOPER, E. P., Phys. Rev. *61*, 1 (1942).
23. SKINNER, H. W. B., Rep. Progr. Phys. *5*, 257 (1939).
24. RICHTMYER, F. K., and RAMBERG, E. G., Phys. Rev. *51*, 925 (1937).
25. SNYDER, T. M., Phys. Rev. *59*, 168 (1941).
26. MLADJENOVIĆ, M., and SLÄTIS, H., Arkiv f. Fysik *8*, No. 5 (1954).

Tryckt den 20 april 1954

Uppsala 1954. Almqvist & Wiksells Boktryckeri AB

ARKIV FÖR FYSIK Band 8 nr 4

Communicated 10 March 1954 by MANNE SIEGBAHN and ERIK HULTHÉN

An investigation of the Compton secondaries from RaC gamma-rays[1]

By MILORAD MLADJENOVIĆ[2] and ARNE HEDGRAN

With 9 figures in the text

Contents

Page
1. Introduction 49
2. Choice of the instrument 51
3. Experimental arrangements 52
4. Choice of the parameters 53
   A. Area of the radiator. 53
   B. Gamma-ray beam aperture 53
   C. Thickness of the radiator and the spectrometer aperture angle . . . 54
5. Intensity determination 57
6. Experimental results 62

1. Introduction

The beta spectrometric analysis of gamma rays from radioactive substances has been mostly made by means of the photo-electric effect. The other two principal modes of interaction of gamma-rays with matter, i.e. the Compton effect and pair production, have been much less used in gamma spectroscopy, the main reason being the broadness of the electron energy distribution in the latter processes, in contrast to the more convenient monoenergetic spectrum of the photo-electrons.

The energy of Compton electrons for a given gamma-ray energy $h\nu$, depends on the electron recoil angle φ, the dependence being given by the equation:

$$E_{\text{electron}} = h\nu \left(\frac{2\alpha}{1 + 2\alpha + (1+\alpha)^2 \tan^2 \varphi} \right) \tag{1}$$

where $\alpha = h\nu/mc^2$. Hence, the width of the energy distribution of the Compton electrons will depend on the angular spread of recoil angles of the Compton electrons accepted by the spectrometer entrance diaphragm. In external photo-conversion experiments, the source is placed close to the radiator, so that the Compton electrons ejected at angles φ from 0° to nearly 90° can be accepted by the diaphragm, giving a very broad continuous distribution. This angular spread is reduced when the source is moved away from the radiator, and at a sufficient distance, where the divergence of the gamma-ray beam hitting the radiator is very small, the width of the Compton distribution becomes comparable to the width ordinarily obtained with external photo-conversion, provided the radiator is sufficiently thin. If the entrance diaphragm of the spectrometer accepts only those Compton electrons ejected within a cone of a few degrees, the width of the Compton lines[1] may be of the order of 3–5 %. These lines can be used for energy and intensity measurements of the gamma-rays. The obvious shortcoming of this method is the very poor efficiency, the source strengths needed being of the order of a hundred times greater than those used in external photo-conversion. By pile irradiation it is, however, now possible to produce the desired strengths in many cases. On the other hand, the Compton method possesses the following advantages:

---

[1] A brief preliminary report of this investigation was given at the Beta and Gamma Radioactivity Conference in Amsterdam, September 1952.

[2] On leave from the Institute for Nuclear Sciences "Boris Kidrič", Beograd.

(*a*) In the Compton process the ejection of electrons in the forward direction becomes more and more prominent with the increase of gamma-ray energy, so that, although the total cross section for the ejection of Compton electrons decreases with the increase of energy, the cross section for the ejection of Compton electrons into a small solid angle in the forward direction increases with the energy increase. The intensity of Compton lines therefore increases with the energy increase, while the intensity of photo-lines decreases, and the two methods are in this respect complementary, the Compton method being more favorable for high energies.

(*b*) In the external photo-conversion method, the broad Compton distributions are inconvenient, and may mask the low intensity photo-peaks. The use of higher source intensities is then of limited help, since the ratio of Compton to photo-electrons remains the same. On the other hand, in the Compton method, if low Z materials are used as radiators, no photo-peaks will appear, so that one has a pure Compton spectrum. This is convenient in complex spectra with many gamma-rays of different intensity.

(*c*) The interpretation of the intensity measurements is more reliable for the Compton process, because the Klein-Nishina theoretical treatment of the Compton effect is in good agreement with many experimental results, while there is no completely satisfactory general theory of the photo-electric process.

Latyshev *et al.* (1) were the first to use the Compton line method, which they applied to the investigation of RaC gamma-rays, using a semicircular spectrometer. They measured the gamma-rays in the energy range from 1.12 to 2.4 Mev. The lower energy gamma-rays could not be observed because of the high background. In addition to the previously known high energy gamma-rays of RaC, they detected a number of lower intensity gamma-rays. These low intensity gamma-rays were not found in the subsequent investigations of

---

[1] In the following we shall use the term "Compton line" for those energy distributions of Compton electrons which have the width under 5 %.

MANN and OZEROFF (2) who used external conversion, and CORK *et al.* (3) who used both external and internal conversion.

No attempt seems to have been made to confirm the results of LATYSHEV using a similar method, nor has it been applied to the study of the gamma-rays from other radioactive substances. The present work was started in order to investigate further the potentialities of the method of Compton lines, and to get more information about the disintegration scheme of RaC, which is still imperfectly known. After this investigation was started, MARTIN and PARRY (4) reported their measurements of ThC″ gamma-ray of 2.6 Mev by the Compton method, and quite recently a spectrometer for the analysis of Compton electrons was described by MOTZ *et al.* (5).

2. Choice of the instrument

The disadvantage of the method being the health harzard and the high cost of very strong sources, the most convenient type of the spectrometer for the study of Compton lines would be one which needs the weakest source for a given resolution and intensity of lines.

The flat types are, for the present purpose, preferable to the lens types of spectrometers—for two reasons. Firstly, because they use the central rays, accepting the Compton electrons ejected in the forward direction, for which the cross section increases with the energy. Secondly, because it is easier to shield a detector in the flat type than in the lens type, where it is in line with the source, resulting in a high background. The importance of low background may best be appreciated if we note that in the case of narrow Compton lines, a 500 mC source of Co 60 gives a counting rate of the order of 100 Compton electrons per minute, at the peak of the line. Such a source in an ordinary lens spectrometer would produce a background much higher than the counting rate of Compton electrons from the radiator.

When choosing between the different types of flat spectrometers one must consider the radiator dimensions, the transmission and the background. One obtains a greater peak and a smaller width of the line by using an extended and thin radiator than by using a thicker radiator of smaller area and the same weight. In this respect, the double focusing spectrometer is superior to the other flat types, since sources of larger area can be used for a given resolution. Another advantage of the double focusing over the other types of flat spectrometers is its higher transmission. Finally, we should mention that in order to obtain a low background, it is important to use large instruments, since the scattering in the chamber is reduced and the detector may be very well shielded.

We have used a 50 cm radius double focusing spectrometer (6) which was quite convenient for work with Compton secondaries, except perhaps for the fact that the source had to be placed inside the spectrometer, which made it necessary to lift off the heavy upper pole piece each time the new source is to be mounted. In instruments especially adopted for Compton line measurement, this could of course be avoided.

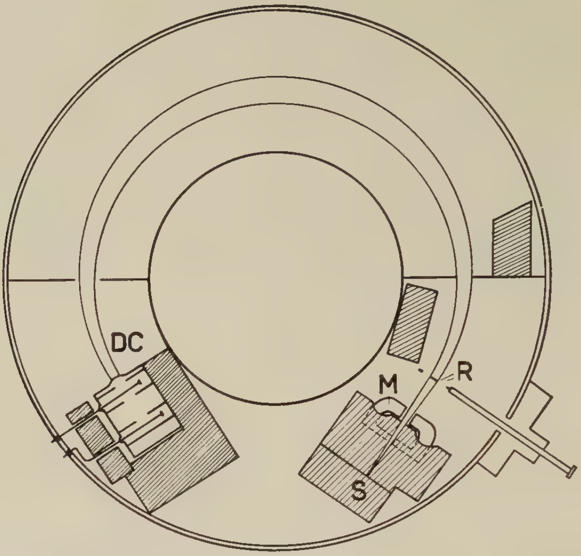

Fig. 1. Schematic cross section of the double focusing spectrometer adjusted for the Compton line measurements. *S*–radioactive source. *M*–sweeping magnet. *R*–radiator. *DC*–double counter.

3. Experimental arrangements

A schematic cross section of the spectrometer arrangements is shown in Fig. 1. An aluminium radiator is placed at the normal source position in the spectrometer. The area of the radiator was 2×2 cm^2, and the thickness was 16 mg/cm^2. It was suspended by narrow strips of Scotch tape from a larger frame, which was fixed to the source holder rod. This rod could be pulled out whenever the background without radiator had to be checked. The source was placed normally to the radiator and at a distance of 30 cm from it. As source for the RaC investigation, radon enclosed in a glass tube was used. The source strength was 350–500 mC and the tube had a length of 10 mm and a diameter of 1 mm. A brass tube slipped over the glass tube served as a beta-ray absorber. The whole fitted into one end of the lead collimator. The half-aperture of the lead collimator was 2.3°, corresponding to a solid angle of 0.04 % of 4π. The collimator was 16 cm long, and a number of lead bricks were piled up all round the source. A permanent magnet with a strong, localised field was placed between the collimator and the radiator so as to deflect all the secondary electrons coming out of the collimator. The entrance diaphragm of the spectrometer had an opening of 4×4 cm^2 subtending a solid angle of 0.1 % at the source. As the counting rates to be expected in the experiment were only of the order of 100 counts per minute on the line peaks, it was necessary to reduce the background to the lowest possible level. This was achieved by the use of a double counter working in coincidence. It consisted of a large brass box of dimensions $16 \times 11 \times 7.5$ cm with a mica window of diameter 4 cm and thickness 2 mg/cm^2. In the box two brass cylinders with lateral holes, of the same size as the window served as cathodes and were fixed at a distance of 10 cm from each other. The counter was evacuated together with the spectrometer and filled when a good vacuum was obtained. Lead shielding for the counter was also provided. The background was 6 counts/min. with a source of 500 mC.

4. Choice of parameters

The width and the relative intensity of Compton lines depend principally on four parameters: the area and thickness of the radiator, the angle subtended at the source by the radiator, and the aperture angle of the spectrometer. Various combinations of these parameters may yield different intensities for the same resolution. The choice of parameters is dictated mainly by the available strength of the source and the minimum resolution which is estimated to be necessary for the problem at hand. In order to make the best choice of parameters in a given case, the most efficient procedure is probably to make a rough evaluation of the resolution and the intensity from the theoretical data on Compton distribution, the multiple scattering of the electrons, and the spectrometer characteristics, and then to make a set of preliminary measurements in which the different parameters are varied.

We have taken the value of 3–4 % as the average resolution which can reasonably be obtained with the strength of sources at our disposal. In the rest of this section we shall give a short discussion of the parameters and the results of our preliminary investigations on the experimental relations between the different parameters.

A. Area of the radiator.—The dimensions of the radiator, the aperture angle and the counter slit width together determine the instrumental contribution to the width of the line. We can assume to a first approximation, which is quite sufficient for our rough evaluation, that the observed width is equal to the sum of the true width of the line and the instrumental width. If we do not want to reduce the intensity too much, we should then leave at least 2–3 % for the true width so that the instrumental width should be around 1 %. This means that in the expression for the resolution of this spectrometer, given by

$$\Delta H\varrho / H\varrho = \frac{\delta}{4\,r_0} = \frac{\delta}{200} \tag{1}$$

the value of δ should be equal to 2. Now, δ is composed of contributions from the radiator width δ_0, spherical abberation width δ_s, and the astigmatism width δ_{as}. The latter two are of the order of 0.2 for the angles used, so that if we take $\delta_0 = 2$ cm, the instrumental resolution should be about 1 %. The dimensions of the radiator which we have used are 2×2 cm^2.

B. Gamma-ray beam aperture angle.—This angle determines the percentage of the radiation falling on the radiator, and contributes also to the energy spread. Since we were interested to see how narrow Compton lines could be obtained with the source strengths available, we have chosen a collimator with

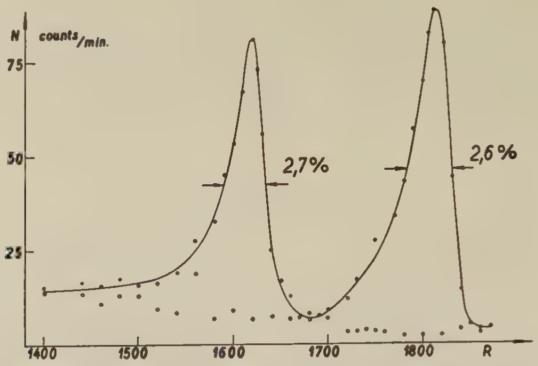

Fig. 2. Compton spectrum of the two Co 60 gamma-rays of 1.17 and 1.33 Mev. The thickness of Al radiator was 5.4 mg/cm^2. Each point was obtained with 4 minutes' measurement. The circles represent the background taken without the radiator.

a small solid angle, so that it should not limit the resolution. The half-aperture angle of 2.3° which we have used gives an energy spread lower than 1 % for the energies which we have measured. Another reason for choosing such a small angle was that the corresponding distance of 30 cm between the source and the radiator gives us enough space for a safe shielding, and allows the sweeping magnet to be sufficiently far away from the radiator, not to influence the ejected electrons.

C. Thickness of the radiator and the spectrometer aperture angle.—An increase in the intensity of a line can be obtained either by using a thicker radiator or a larger spectrometer aperture. In both cases this is accompanied by a loss of resolution, because a thicker foil increases the scattering and the energy loss, while a larger aperture angle increases the energy spread of Compton electrons. Obviously, same resolution can be obtained with different combinations of thicknesses and angles, and it is interesting to know which combination gives the highest intensity for a given resolution. We know that the scattering and the relative energy loss diminish at higher energies, while the energy spread of Compton electrons within a given small solid angle in the forward direction increases with the energy. Hence, one can conclude that for the lower energies it is better to have thinner foils and larger aperture angles, while for higher energies it is more suitable to use thicker foils and a smaller aperture.

In order to obtain a closer view of these relationships, a set of measurements with a 500 mC Co 60 source was made. Fig. 2 shows the Compton spectrum of the two Co 60 gamma-rays of 1.17 and 1.33 MeV. The lines are almost completely separated and the resolution is about 2.7 %. The thickness of the Al radiator used was 5.4 mg/cm^2.

Fig. 3 shows the results from measurement of the higher energy line of Co 60 for Al foil thicknesses of 2.7, 5.4, 8.1 and 16 mg/cm^2 for the entrance diaphragm settings of 3×3, 4×4, 5×5, 6×6, and 7×7 cm^2. The distance from radiator to the diaphragm was 30 cm.

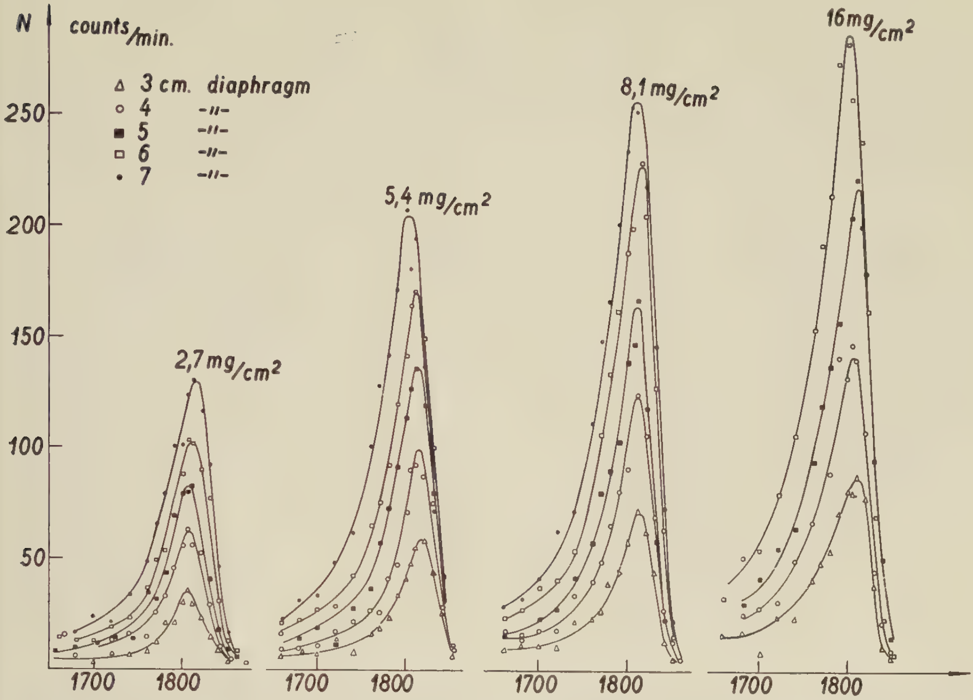

Fig. 3. Compton lines of 1.33 Mev gamma-ray of Co 60 obtained with the radiator thicknesses of 2.7, 5.4, 8.1 and 16 mg/cm², and with entrance diaphragm of 3 × 3, 4 × 4, 5 × 5, 6 × 6, and 7 × 7 cm². The curve for 16 mg/cm² and 7 × 7 cm² is not shown. Each point was obtained with 2 minutes' measurements.

From these lines we can get the relationships between the intensity and the resolution for different thicknesses and apertures. They are shown in Fig. 4. In Fig. 4 A we can see the influence of the scattering on the peak intensity. If there were no scattering or energy loss, these curves would have been the straight lines. They have instead the shape of saturation curves. Fig. 4 B shows that the resolutions are between 2.2–4 %. The most useful set of curves for the choice of parameters is the one shown in Fig. 4 C. There we can see that for the energy considered the optimum thickness for resolutions below 2.4 % is 2.7 mg/cm^2, between 2.4 and 2,9 % it is 5.4 mg/cm^2, and so on. This kind of curves permits the choice of optimum parameters to be made for a given problem. In our case the energy range from 0.6 to 2.4 Mev is so large that one set of parameters obviously cannot be optimal for the whole range, but nevertheless we preferred to use the same set throughout in order to facilitate the comparison of intensities. Since it is in the high energy region that the Compton method is superior to the external conversion method and also the majority of new lines found by LATYSHEV are in the high energy region, we have chosen the parameters which are favorable to the measurement of the energies higher than 1.5 Mev. A radiator thickness of 16 mg/cm^2 and a diaphragm of size 4 × 4 cm^2 were therefore used.

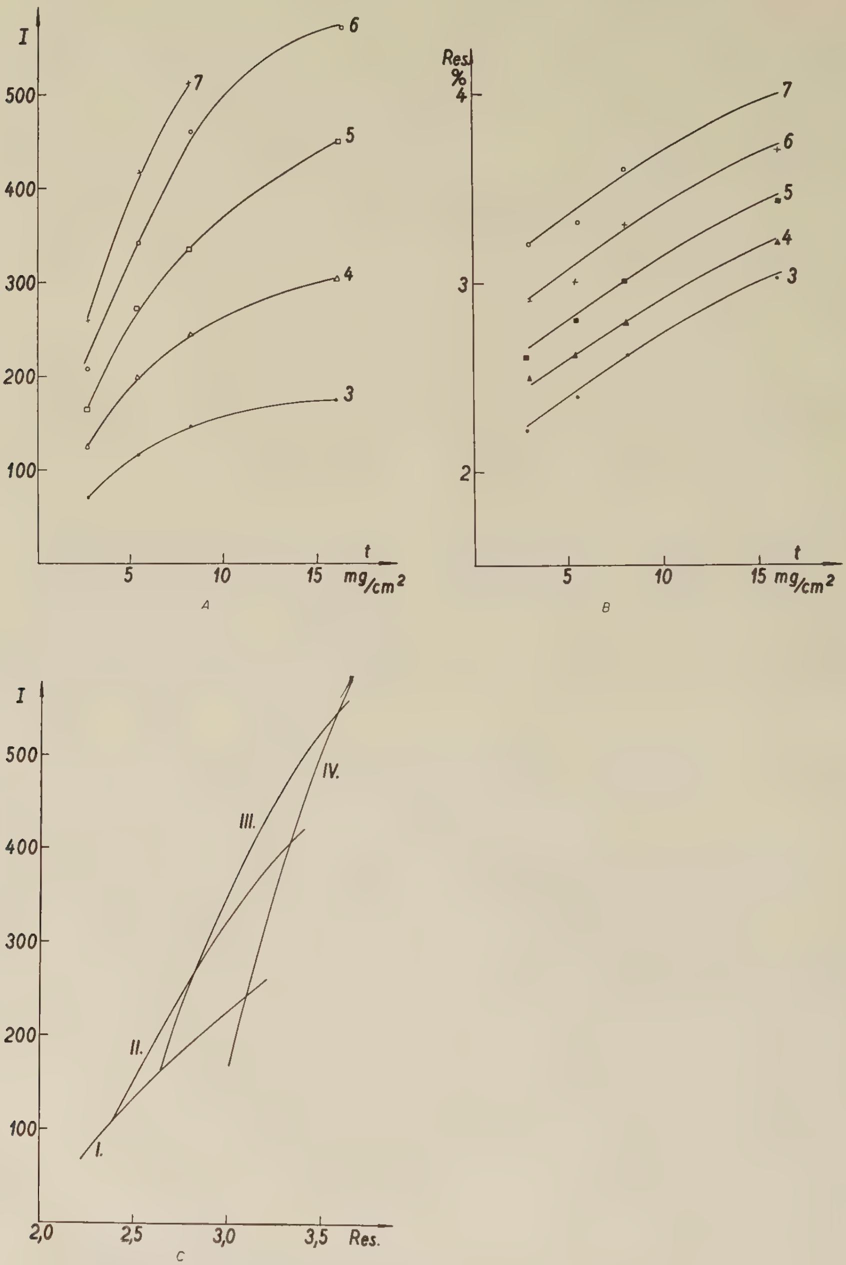

Fig. 4 A–C. Relationships between the intensity and resolution for different thicknesses and apertures. 4 A shows the intensity as a function of the thickness for different apertures. 4 B shows the resolution as a function of the thickness for different apertures. 4 C shows the intensity as a function of the resolution for different thicknesses. Curve I corresponds to 2.7 mg/cm², curve II to 5.4 mg/cm², curve III to 8.1 mg/cm², curve IV to 16 mg/cm².

5. Intensity determination

In the Compton spectra the lines are often not well resolved and it is therefore more convenient to base the intensity estimations on the peak height rather than on the area under the curves. The peak height of a Compton line depends chiefly on three factors:

(*a*) Klein-Nishina differential cross section for the ejection of the Compton electrons into the solid angle defined by the spectrometer entrance diaphragm.

(*b*) Multiple scattering of the electrons in the radiator has the effect that the electrons ejected at large recoil angles which normally could not enter the spectrometer, may be scattered into the direction of entrance diaphragm. This results in a broadening of the line. But a still more important effect of the multiple scattering is the reduction of the peak height due to the scattering out of the electrons which would normally enter the spectrometer entrance diaphragm. Since the concentration of the electrons ejected in forward direction is greater than the concentration of the electrons ejected into greater angles the scattering out is greater than the scattering in, and in the calculation of the intensities we can, in the first approximation, take into account only the scattering out.

(*c*) Energy loss in the radiator has also the effect of broadening the line and reducing the peak height.

A convenient method for computing the peak intensities of the Compton lines has been given by Motz *et al.* (5). According to them the peak counting rate $R(k)$ is given by the expression

$$R(k) = P(k) \cdot n \cdot T(t, k) \cdot A \cdot \int_0^{\pi/2} f(\theta) \frac{d\sigma(k)}{d\theta} d\theta \tag{2}$$

where $P(k)$ = photon flux/cm^2/sec.
n = number of electrons/cm^2 in the foil
$T(t, k)$ = correction for the scattering of the electrons and the energy loss in the foil
A = area of the foil in the beam
$\frac{d\sigma}{d\theta}$ = Klein-Nishina differential cross section in cm^2/electron
$f(\theta)$ = fraction of the electrons leaving foil at the angle which can be focused at the detector
t = foil thickness in cm
k = gamma energy in Mev.

The quantity $T(t, k)$ includes the correction for the Coulomb scattering $T_{\text{cs}}(t, k)$ and the energy loss in the foil $T_{\text{el}}(t, k)$, so that we can write

$$T(t, k) = T_{\text{cs}}(t, k) \cdot T_{\text{el}}(t, k). \tag{3}$$

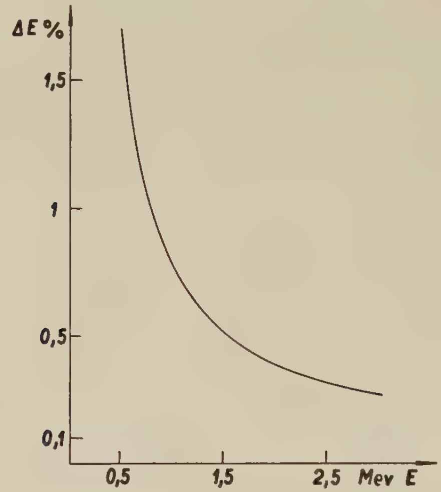

Fig. 5. The percentage of energy loss as computed from the formula given by LANDAU, for the foil thickness of 8 mg/cm², which is a mean value of thickness for the electrons ejected uniformly in the foil of 16 mg/cm².

$T_{cs}(t, k)$ is given by the relation

$$T_{cs}(t, k) = \frac{\psi^2}{[1 - \exp(-\psi^2/\theta_0^2)]\, C(E_0)\, t} \cdot \left\{ \ln(1+x) - \frac{1}{2}\frac{\psi^2}{\theta_0^2}\left(1 - \frac{1}{1+x}\right) + \cdots \right\} \tag{4}$$

where ψ = aperture angle, which is in our case $3^\circ 51'$

θ_0 = characterises the width of the distribution $\left(\frac{1}{\sin\theta}\frac{d\sigma}{d\theta}\right)_{t=0}$ and is obtained by fitting the Gauss curve $\exp\left[-\frac{\theta^2}{\theta_0^2(k)}\right]$ to that distribution. Numerical values for θ_0 are given in paper by MOTZ *et al.*

$$C(E_0) = 6.76 \cdot \frac{E_0^2}{(E_0^2 - \mu^2)^2}\,[\ln 6.1 \cdot 10^4 (E_0^2 - \mu^2) - 1]$$

$$x = \frac{C t}{\theta_0^2}$$

E = total energy of the electron

μ = rest energy of the electron.

In our case $f(\theta)$ is approximately equal to a rectangular function such that

$$f(\theta) = 1 \text{ for } \theta \leq \psi = 3^\circ 51' \text{ and } f(\theta) = 0 \text{ for } \theta > \psi.$$

The calculation of the integral and T_{cs} is straightforward.

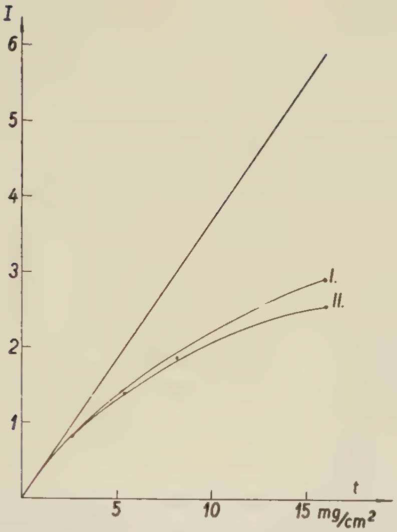

Fig. 6. Derivation of T_{cs} for 1.33 Mev. Straight line represents the number of Compton electrons as the function of the foil thickness if there is no reduction. Curve I is obtained by multiplying the values given by the straight line with T_{cs} computed from the formula (4). Line II is obtained from the experimental measurements shown in Fig. 3.

In the calculation of T_{el} we have taken as a base the work of WHITE and MILLINGTON (7) who have studied the change of the shape of monochromatic lines due to the energy loss in thin foils. The energy loss of monokinetic electrons passing through a foil causes a shift of the line towards lower energies, reduction of the peak height and a broadening of the line. The true line shapes which WHITE and MILLINGTON compute with the assumption that the line broadening as well as the peak reduction are directly proportional to the peak shift, when folded with the spectrometer window curve, were found to be in agreement with the observed line shapes. WARSHAW and CHEN (8) have shown that the peak shift is proportional to the most probable energy loss of electrons in the foil. Hence, we can obtain an aproximate value for the variation of T_{el} with the energy by assuming that the peak height reduction is proportional to the most probable energy loss. The expression for the most probable energy loss as given by LANDAU (9) is

$$\Delta E_{\text{prob}} = \xi\,[\ln(\xi/\varepsilon) + 0.37] \qquad (5)$$

where

$$\xi = n\,z\,(2\,\pi\,e^4/mc^2\,\beta^2) \quad \text{and} \quad \varepsilon = [I^2\,(1-\beta^2)/2\,mc^2\,\beta^2)\ \exp\ (\beta^2).$$

n = number of atoms in cm² of the foil
m = mass of the electron
I = mean excitation potential.

The percentage energy loss computed from (5) is given in Fig. 5.

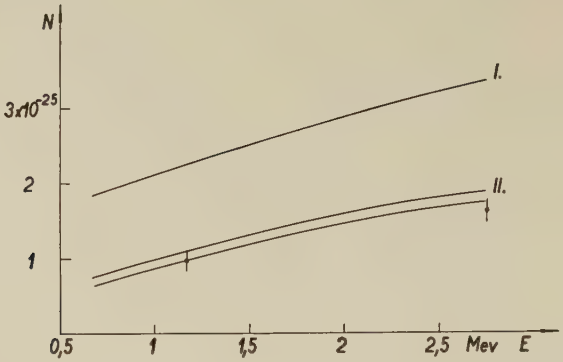

Fig. 7. The relative peak height values of Compton lines. Line I gives the values of $\int_0^{\pi/2} f(\theta)\frac{d\sigma}{d\theta}\,d\theta$. Curve II is obtained by multiplying curve I with T_{cs}. The curve below is the final theoretical curve obtained by multiplying curve II with T_{el} and gives the relative peak as function of energy for our experimental set-up. The points shown are the experimentally found peak heights of the Na 24 gamma-rays, with the lower one normalized to the curve.

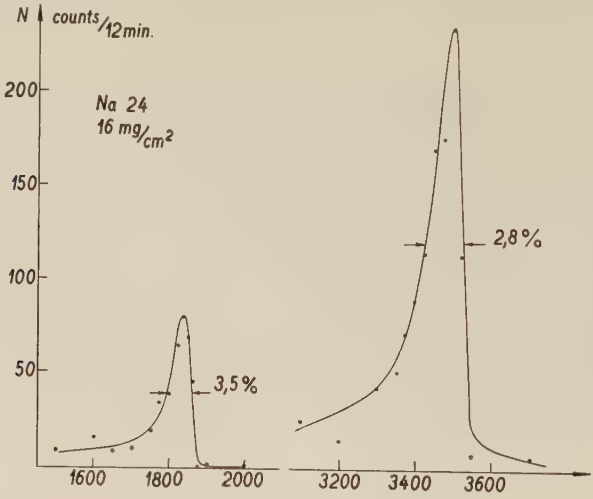

Fig. 8. Compton spectrum of Na^{24}.

The value of T_{el} for the energy of 1.33 Mev was found from our measurements of the high energy gamma-ray of Co 60. The values of T_{el} for the other energies were then derived using LANDAU's values of the most probable energy loss.

Fig. 6 shows how the value of T_{el} for 1.33 Mev was obtained. The straight line represents the peak height which one would obtain if there were no reduction of any kind. The reduction of the peak height due to the scattering is

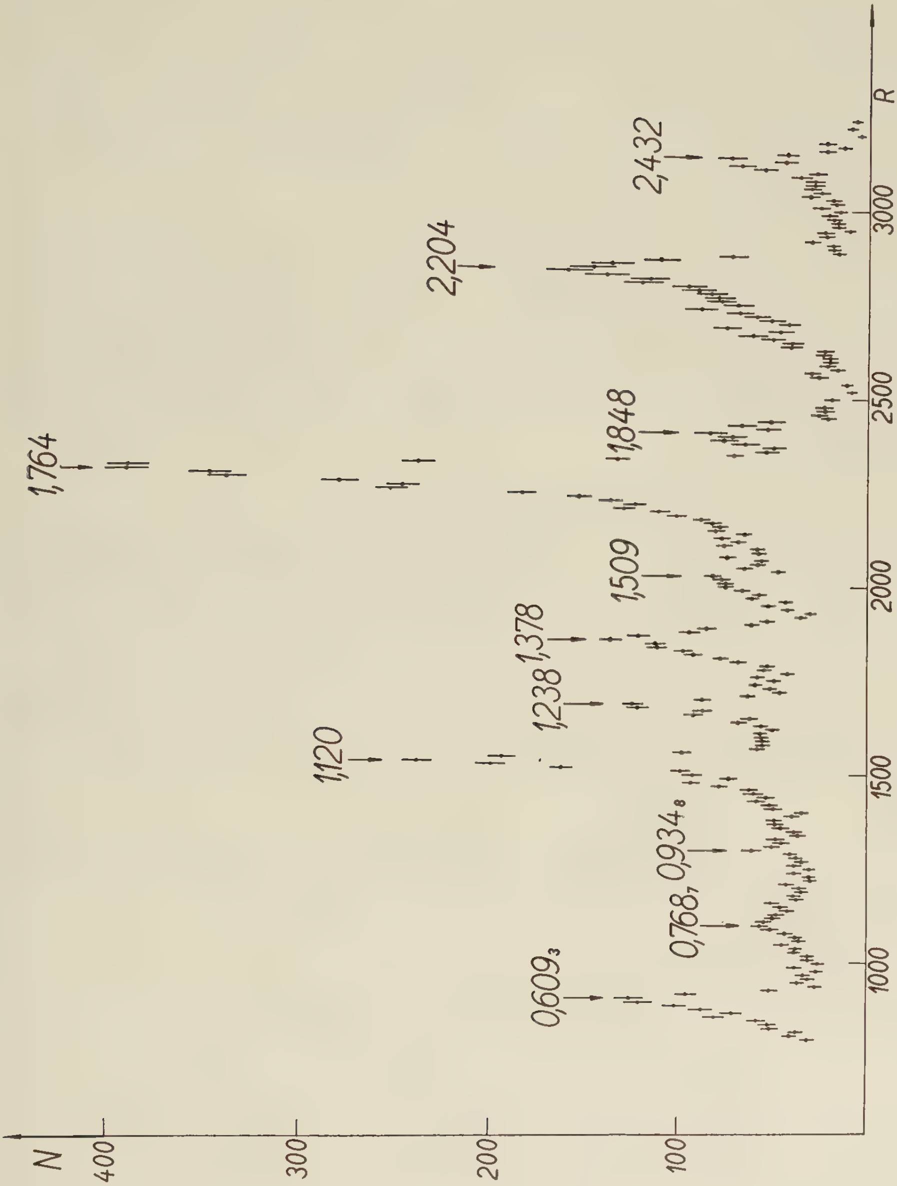

Fig. 9. Compton spectrum of RaC gamma-rays.

shown by the line I. It represents peak height as the function of the foil thickness, when the scattering correction T_{cs} is taken into account. Curve II is the experimental curve, obtained from the measurements of 1.33 Mev Co 60 line. The difference between curve I and curve II should approximately give the correction factor T_{el}. For 16 mg/cm^2 it amounts to about 8 %. The values for the other energies derived from the assumption that the reduction of peak heights is proportional to the most probable energy loss are only approximately exact, because this assumption is valid for the peak heights of true distributions, while we use it for the observed peak heights. The error due to this should, however, not be significant in our case.

The results of the intensity calculations are shown in Fig. 7 An experimental check of the theoretical curve was made by measurement of the Compton spectrum of Na 24, which has two gamma-rays of 1.37 and 2.75 Mev in cascade. Fig. 8 shows the Compton spectrum of Na 24. The source strength was 70 mC. It is interesting to note how much higher is the high energy peak. The agreement between the experimental and theoretical peak ratios is good, considering the aproximations used in the theoretical computation, and gives good reason for accepting as reliable the evaluation of intensities of the much more complicated RaC spectrum.

6. Experimental results

The Compton line spectrum of RaC gamma radiations is shown in Fig. 9. The spectrum is the average of three separate measurements. It agrees in general with LATYSHEV's results. A number of low intensity lines with insufficient statistics may be seen in the spectrum. Most of these lines were confirmed by internal conversion measurements (11). For instance, two small peaks can be noticed on the low energy side of the 2.204 Mev line, corresponding to the gamma-rays of 2.016 and 2.116 Mev found in the internal conversion spectrum. For the present purpose we are however interested in the intensities of prominent lines. These are given in Table 1, where the energy values are those

Table 1. The relative intensities of RaC gamma-rays. The intensity of 2.204 Mev was taken as equal to unity. The values obtained by LATYSHEV *et al.* and by ELLIS and ASTON (10) are given for comparison.

Energy	Intensity		
	M.-H.	Latyshev	Ellis
0.609	5.13	–	8.9
0.769	1.11	–	0.88
0.934	0.54	–	0.9
1.120	3.9	1.76	2.8
1.238	1.42	0.41	0.85
1.378	1.66	1.32	0.86
1.509	0.56	0.56	
1.764	3.14	2.51	0.35
1.848	0.33	0.32	
2.204	1	1	1
2.432	0.36	0.34	

derived from more precise internal conversion measurements (11). The intensities were computed according to the procedure described above. The relative intensities are considered to be correct within 10 %. Larger errors are possible only in the value given for the 1.378 Mev line, which has a somewhat greater width, and is probably composed of two lines. The contribution to the main peak height made by the small peaks superposed on the lines 1.764 and 2.204 Mev is certainly less than 10 %.

Nobel Institute for Physics, Stockholm, March 16, 1954.

REFERENCES

1. Latyshev, G. D., Kompaneetz, A. F., Borisov, N. P., and Gusak, I. M., J. Phys. (USSR) *3*, 251 (1940).
2. Mann, K. C., and Ozeroff, M. J., Can. J. Phys. *27*, 164 (1949).
3. Cork, J. M., Branyan, C. E., Stoddard, A. E., Keller, H. B., LeBlanc, J. M., and Childs, W. J., Phys. Rev. *83*, 681 (L) (1951).
4. Martin, D. G., and Parry, G., Physica *18*, 1157 (1952).
5. Motz, J. W., Miller, W., Wyckoff, H. O., Gibson, H. F., and Kirn, F. S., Rev. Sci. Instr. *24*, 929 (1953).
6. Hedgran, A., Arkiv Fysik *5*, No. 1 (1952).
7. White, P., Millington, G., Proc. Roy. Soc. *A 120*, 701 (1928).
8. Warshaw, S. D., and Chen, J., Phys. Rev. *80*, 97 (L) (1950).
9. Landau, L., J. Phys. (USSR) *8*, 201 (1944).
10. Ellis, C. D., and Aston, G. H., Proc. Roy. Soc. *A 129*, 180 (1930).
11. Mladjenović, M., and Slätis, H., Arkiv f. Fysik *8*, No. 5 (1954).

Tryckt den 21 april 1954

Uppsala 1954. Almqvist & Wiksells Boktryckeri AB

ARKIV FÖR FYSIK Band 8 nr 5

Communicated 10 March 1954 by MANNE SIEGBAHN and ERIK HULTHÉN

Internal conversion spectrum of the active deposit of radon

By MILORAD MLADJENOVIĆ and HILDING SLÄTIS[1]

With 6 figures in the text

Contents

Introduction 65
I. Experimental arrangements 66
  1. Source holder 66
  2. Activation chamber 67
II. Determination of energy values 68
III. Determination of relative intensities of conversion lines recorded photographically 69
IV. Experimental results 73
  Discussion 73
V. Multipole order of gamma-rays of RaB 80
  Summary 81

Introduction

The investigation of the radiations from RaB + C was started at the early stage of radioactivity, and they were some of the first spectra which were measured when the new technique of magnetic analysis of beta-rays was initiated by O. v. BAEYER and O. HAHN [1], J. DANYSZ [2], and E. RUTHERFORD and H. ROBINSON [3].The first magnetic spectrum of the internal conversion lines from RaB + C was reported by O. v. BAEYER, O. HAHN and L. MEITNER [4], who found four lines in RaB and five lines in RaC spectrum. Soon afterwards, E. RUTHERFORD and H. ROBINSON [3] found 16 lines in the RaB spectrum and 48 lines in the RaC spectrum, using a semicircular magnetic spectrometer with photographic detection. A very thorough study of RaB + C was made by C. D. ELLIS, who, with different collaborators, published a number of papers between 1921 and 1934 [5]. He found 30 internal conversion lines in the spectrum of RaB and 67 internal conversion lines in RaC [6]

---

[1] On leave from the Institute for Nuclear Sciences "Boris Kidric", Beograd.

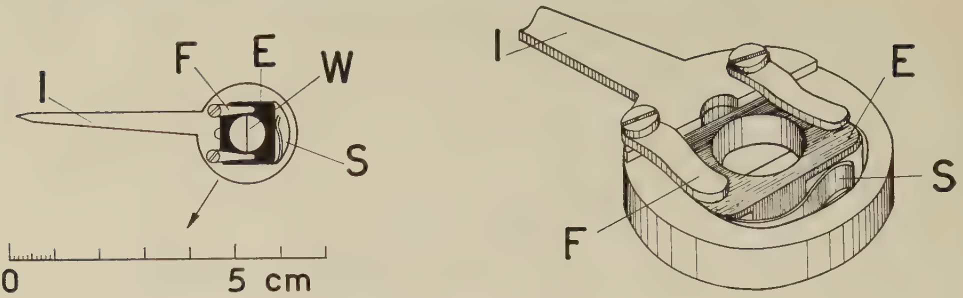

Fig. 1. The source holder.

and also made an attempt to establish the disintegration schemes [7]. A number of lines were relatively very weak and the assignment uncertain while in the disintegration schemes different combinations were possible. The part of the internal conversion spectrum of RaC above 150 keV was measured by K. Siegbahn [8], who essentially confirmed the results of Ellis and found some new low intensity lines. An investigation of the gamma radiation associated with radium and daughter products has recently been made by Cork *et al.* [9]. There is a considerable divergence between the results of Ellis and those reported by Cork *et al.*, especially in regard to the relative intensities, and while Cork *et al.* find some new lines, the total number of lines they reported is just over one half the number found by Ellis. A number of measurements with other methods were made [10], including the measurement of Compton electrons ejected by RaC gamma-rays [11], and also of the positron spectrum [12], but our knowledge of the disintegration schemes of RaB, and especially of RaC, is still unsatisfactory. In view of this we have undertaken a remeasurement of the internal conversion spectrum of RaB + C, using a permanent magnet beta-ray spectrometer, with photographic detection and thermostatically regulated temperature, which assures a constancy of the field, and permits of obtaining resolutions of the order of 0.01 %.

I. Experimental arrangements

A detailed description of the spectrometer has been given earlier [13].[1] Three different values of the magnetic field were used. Almost the whole spectrum of RaB, from the A line to the Ia1 line was obtained on the same film with the field of 147 gauss. The spectrum from the H line of RaB to the Vb line of RaC was obtained with the field of 463 gauss, and finally the whole spectrum of RaC was measured with the field of 847 gauss.

1. Source holder

The source holder described in paper I was adapted for the work with RaB + C, and is shown in Fig. 1. The wire was stretched over a rectangular ebonite frame by a spring. This frame fitted the cover of the radon irradiation chamber. After the irradiation the frame can be quickly and accurately placed into the brass holder

---

[1] We shall hereinafter refer to that paper as paper I.

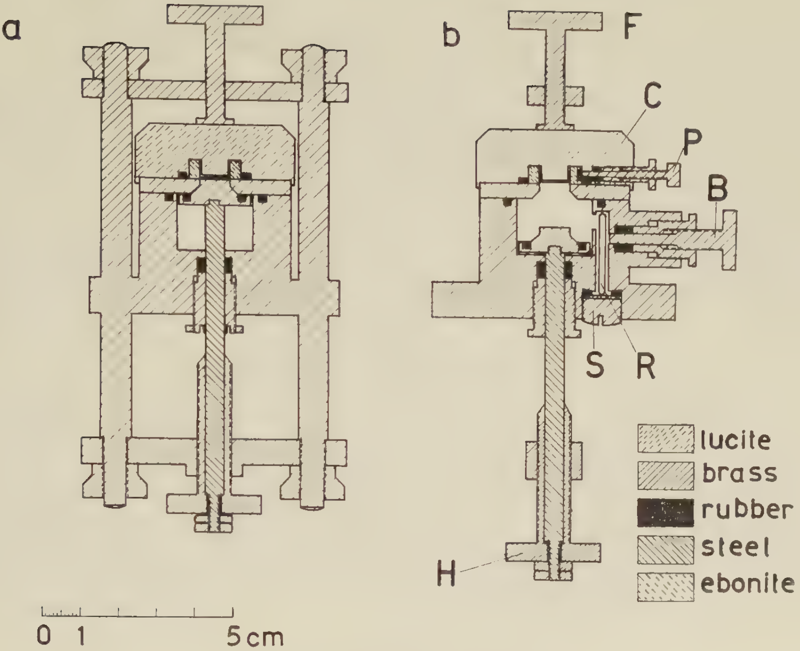

Fig. 2. The activation chamber.

I, which is then introduced into the spectrometer as described in paper I. The wires used were 12 μ wolfram, 25 μ platinum, and 150 μ wolfram wire. The two thin diameter wires were used for high resolution measurements, whereas the thick diameter wire was used for the measurement of the very weak lines in the high energy region of RaC, where we considered a good intensity to be more important than a high resolution. The reason for the use of the thicker wire was that a considerable amount of radon and its products is adsorbed on the ebonite frame during the irradiation, and when introduced into the spectrometer it increases seriously the background. Separate measurements of the activity of the frame have shown that it is equal to 30 % of the activity on the wire. Hence, it was desirable not to introduce the exposed frame into the spectrometer. A change of the frame would have been difficult in the case of very thin wires, since they are not easy to handle, and the time left for the operation is short considering that the half-life of RaB is only 20 min., while the change of frame in the case of 150 μ diameter wolfram wire was found to be relatively easy.

2. Activation chamber

Fig. 2 shows the radon chamber constructed for the activation of the wires. The operation of the chamber is as follows. The chamber is first closed by the handle *H*. The radon glass tube is introduced into *R*, and the chamber made tight with the screw *S*. Then the glass tube is broken by turning the screw *B*, so that radon enters the chamber. The ebonite frame is placed in the cover *C* and the cover is fastened to the chamber by the screw *F*. Then the chamber is opened by moving the handle

H downwards, and a high potential is brought on the pin *P*. After the irradiation the ebonite frame is taken out by a reverse operation. New rubber seals were mounted each time before a new radon tube was broken.

The radon tubes contained 300–500 mC of radon.[1] The strength of the sources obtained in the radon chamber was 10–180 mC. The first source taken from the chamber had the activity of 60–180 mC, the next was about 50–70 % of the first one, and so on. The first three to four sources were used for the permanent magnet spectrometer measurement, and the next five sources for the measurement with the double focusing spectrometer.

The time of the irradiation was 1.5–2.5 hours, and several sources were alternatively used, one being in the spectrometer while another one was on the irradiation.

II. Determination of energy values

The $H\varrho$ values of the internal conversion lines were determined by multiplication of a measured ϱ value with a value of *H* derived from standard lines.

The values of ϱ were measured by the method described in paper I. In Fig. 3 we see that we can compute the value 2ϱ of a line of *L*, if we measure (*a*) the distance *d* from the calibration edge to the source, (*b*) the distance *x* from the calibration edge to the line, and (*c*) the distance *a* from the calibration edge to the center of the slit. Then 2ϱ is given by the relation:

$$2\varrho = d + a\cdot\frac{x}{d} + \frac{h^2}{2d}\cdot\frac{x^2}{d^2}. \tag{1}$$

The possible errors in the measurement of the distances *d*, *x*, and *a* are the following.

(1) *Error in the measurement of d.*—An error in the measurement of *d* may arise if the source and the edge between which we measure the distance are not in the same plane, perpendicular to the axis of the microscope, and also if the calibration edge is not well defined. The coplanarity of the source and the edge could be adjusted very accurately, so that the probable error is less than 0.01 %. On the other hand, in those cases where the calibration edges were not well defined, we measured the distance *d* to a definite part of the edge and then we measured the distance *x*, also from the same part, so that the error was minimized.

(2) *Error in the measurement of x.*—The distance *x* is measured on the film and consequently depends on the variation of the film length due to the development and other causes, such as humidity and temperature. By comparing the distances between the edges in the spectrometer and on the film it was found that the probable error due to the variation of the film length is about 0.02 %. Another cause of the error in the measurement of *x* is that the calibrating edge is not sharply defined on the film, the uncertainty being of the order of 0.01 %. Finally, the precision of the measurements of *x* depends on the width of the line, and on the intensity of the line. The distance was measured from the high energy edge of the line. The broad high intensity K lines may have a somewhat greater error than the rest of

---

[1] We are indebted to Mag. Phil. A. EGMARK and Mag. Phil. B. HELLSTRÖM at the *Radiofysiska Institutionen, Radonlaboratoriet*, for the kind delivery of the radon samples.

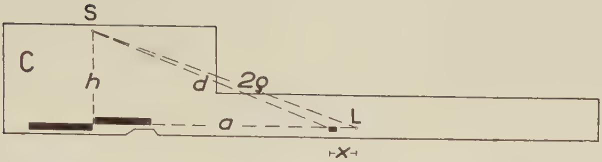

Fig. 3. Principle for measuring the diameter 2ϱ of the electron paths.

lines, and it is therefore preferable to base the computation of the energy of gamma-rays on the energies of L lines rather than K lines.

(3) *Error in the measurement of a.*—It was shown in paper I that the probable error in the determination of a is about 0.02 %.

We estimate that the probable error in the determination of ϱ is 0.03 %, most of the well-defined lines having an error smaller than 0.03 %, while the very weak lines and some of the broad lines may have errors greater than 0.03 %.

As already mentioned in paper I, the spectrometer was not designed for high precision *absolute* measurement of energies, the accuracy of the magnetic field measuring apparatus being only of some parts in 1000. For that reason we have used the energy values of the ThB F line given by LINDSTRÖM [14], and that of the RaC T line determined by LINDSTRÖM, HEDGRAN and ALBURGER [15], as standard energy values, for the low and for the high energy region respectively. The $H\varrho$ values of these lines are:

$$H\varrho\,(\mathrm{F})_{\mathrm{ThB}} = 1388.56 \pm 0.15 \text{ gauss cm}$$

$$H\varrho\,(\mathrm{T})_{\mathrm{RaC}} = 5874.4 \pm 0.6 \text{ gauss cm.}$$

The energy values obtained in this way are in good agreement with the values for RaB given by MULLER *et al.* [16], as will be shown later.

The use of a constant value of the magnetic field for all the lines introduces another error in the determination of H values, since the mean values of the magnetic field over different electron paths may be different. It was found that the difference is of the order of 0.02 %, and therefore no corrections were made for the variation of the mean field over the paths.

The $H\varrho$ values which we give should have a relative accuracy of 0.01–0.05 %.

III. Determination of the relative intensities of conversion lines recorded photographically

The problem of the determination of the intensities of conversion lines was treated already by ELLIS and WOOSTER in 1927 [17]. They point out the importance of studying:

(1) the relation between photographic density and exposure,

(2) the photographic density as a function of the energy of the electrons,

(3) the intensity of the conversion lines as a function of the position of the line (value of 2ϱ).

The photographic density D is defined by

$$D = {}^{10}\mathrm{Log}\,\frac{I_0}{I} \qquad (2)$$

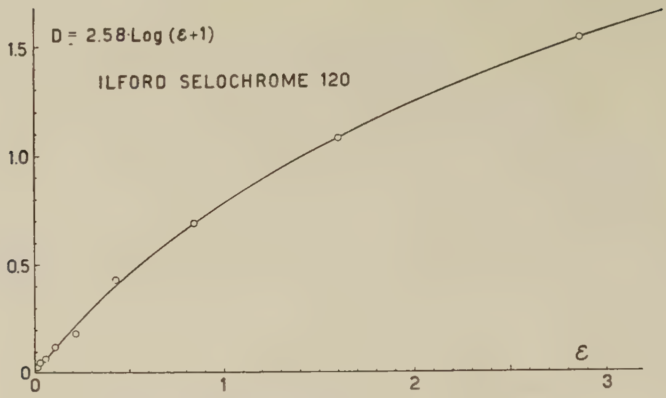

Fig. 4. Test of the density-exposure relation.

where I_0/I is the ratio of the incident to the transmitted light passing through the darkened patch. The relation between the density D and the exposure E, expressed for instance in millicuries times the number of hours exposure is given by the SILBERSTEIN [18] formula

$$D = C\,{}^{10}\mathrm{Log}\,(\alpha E + 1) \tag{3}$$

where C and α are constants. We have tested this formula for an "Ilford Selochrome 120" film, which was exposed to electrons from a ThB sample. The electrons passed through a channel of 7 mm width between lead blocks and hit the film, which was moved in steps of 19 mm length between each exposure. Fig. 4 shows the experimental points and the theoretical curve

$$D = 2.58\ {}^{10}\mathrm{Log}\,(\varepsilon + 1), \tag{3'}$$

where $\varepsilon = \alpha E$ and $\alpha = 0.034$. For ε we shall use hereinafter the denomination "electron density". Fig. 4 shows that the validity of the formula (3′) is very good, in any case for higher densities. The deviations for lower values are due to the difficulty in determining the height of the photometer peaks over the background "noise" originating in the grains in the emulsion.

In order to study the photographic density as a function of the energy of the electrons a special device was made for a lens spectrometer. In the circular focus of the lens spectrometer a baffle was placed with a circular hole of 6 mm diameter. Behind this a Geiger-Müller counter was placed, and alternatively a film could be inserted between the baffle and the GM-counter. ThB was used for these calibration experiments. Fig. 5 shows the result. The maximum sensibility at about 80 keV or 1000 gauss cm corresponds to a range of electrons equal to the thickness of the emulsion.

A similar curve has earlier been given by ARNOULT [19] who studied the relative photographic sensitivity of Ilford X-ray plates for electrons of different energies.

The line intensity as a function of the position of the line depends on the geometrical arrangement of the baffles in the spectrograph. A beam of monoenergetic electrons emitted from a sample gives a higher density for small ϱ-values than for large ones, because the beam for the higher ϱ-value is spread over a larger area of

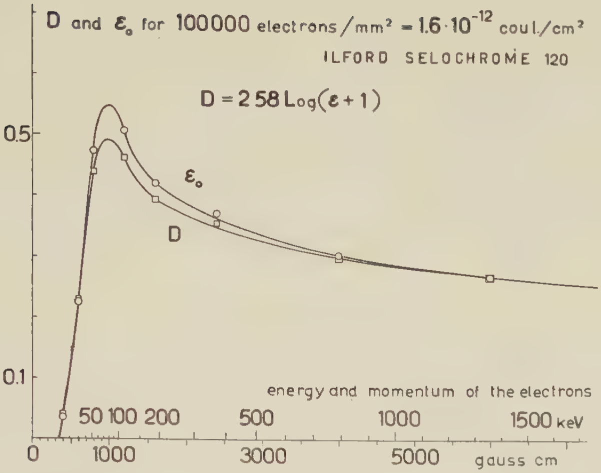

Fig. 5. Density D and efficiency ε as a function of the energy and the momentum of the exposing 100,000 electrons per mm².

the focal plane. The baffles can be constructed in such a way that the measured line intensity is proportional to $1/\varrho$.

In order to measure the relative intensities of conversion lines from photometer records of photographic films we have first to change the densities for the different points on the photometer curves to the corresponding electron densities ε according to the formula (3′) and then to integrate the areas under the ε-curves. If these areas be A, then the relative intensities I of the conversion lines are given by

$$I = A \cdot \varrho \cdot \frac{1}{\varepsilon_0} \tag{4}$$

where ε_0 is obtained from the energy-sensitivity calibration curve in Fig. 5.

The correction for the density and the integrating process for the areas A is, however, a very laborious work. In addition, the integrating process for the weak lines is almost impossible because of the difficulty to decide the background on the low energy tail of the lines.

In order to overcome these difficulties the following approximate method [20] was used.

The line shape, different for different sources and baffle sizes, does not vary appreciably for different values of ϱ. Instead of the area under the electron density distribution curve for a conversion line a rectangle is taken, the height of which is equal to the height of the line in the electron density distribution and the width of which is equal to the true half width w of the conversion line. It is found that the relative intensities of the conversion lines are within about ± 10 % equal to the relative areas of the corresponding rectangles.

The true *half-width* w is found in the following manner. The conversion lines are recorded by means of a photometer with photocell and galvanometer.[1] Fig. 6 shows

---

[1] We wish to thank Phil. kand. Mrs. MUUSA PUNNIS for the laborious photometer work in recording the conversion lines.

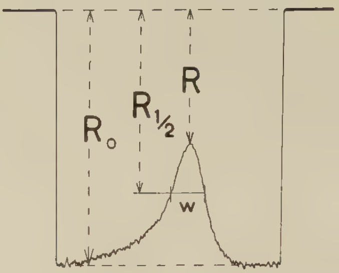

Fig. 6. Determination of the true half-width of a conversion line.

diagrammatically such a photometer record of a line. R_0 is the galvanometer deviation for light through the background or the continuous spectrum in the neighbourhood of the line, R the deviation for the top of the line (maximum density) and $R_{1/2}$ the deviation obtained for an electron density half-way between the electron densities corresponding to R_0 and R.

If R_u be the deviation corresponding to an unexposed part of the film, E and $E+\varepsilon$ the electron densities corresponding to the deviations R_0 and R, respectively, we have according to (3′)

$$\operatorname{Log} \frac{R_u}{R_0} = 2.58 \operatorname{Log} (E+1)$$

$$\operatorname{Log} \frac{R_u}{R} = 2.58 \operatorname{Log} (E+\varepsilon+1) \tag{5}$$

$$\operatorname{Log} \frac{R_u}{R_{1/2}} = 2.58 \operatorname{Log} \left(E+\frac{\varepsilon}{2}+1\right) \cdot$$

Hence,

$$\operatorname{Log} \frac{R_0}{R} = 2.58 \operatorname{Log} \left(\frac{\varepsilon}{E+1}+1\right)$$

$$\operatorname{Log} \frac{R_0}{R_{1/2}} = 2.58 \operatorname{Log} \left(\frac{\varepsilon/2}{E+1}+1\right) \cdot$$

Curves were constructed for E as a function of $\frac{R_u}{R_0}$. These curves were also used for the calculation of $R_{1/2}$. For a given $\frac{R_0}{R}$ the curves give the corresponding value of $\frac{\varepsilon}{E+1}\cdot$ This quantity was divided by 2 and the curves again used for the determination of $R_0/R_{1/2}$. When R_0 was divided by this ratio, $R_{1/2}$ was obtained, and then w was found diagrammatically (Fig. 5). Instead of the formula (4) the following expression was now used for the intensity of a conversion line:

$$I = w \cdot \varepsilon \cdot \frac{\varrho}{\varepsilon_0} \cdot \tag{7}$$

It was found that the mean differences between the line intensities computed in this way for two different films were 25 %. This value is a mean for 13 lines in the internal conversion spectrum of RaC. It should be pointed out, however, that this large error was caused mainly by the very low intensity of the lines measured. The mean error for the 7 strongest lines out of those 13 lines was 16 % and for the weaker ones 40 %. The accuracy of the intensity measurement depends highly on the background density. While for low background densities and strong lines the accuracy in the intensity measurements is high (error some %), it will be almost impossible to measure the intensity of weak lines on a high background.

IV. Experimental results

The results of our measurement of the energies and the intensities of the internal conversion lines and the Auger lines from the active deposit of radon are given in Table 1. The energies and the intensities reported by ELLIS [6] and by CORK *et al.* [9] are included in the table. ELLIS' notation was used for the spectrum given by ELLIS, while numbers were given to the lines in the spectrum given by us. Our intensities are normalized to the value of 425 for the F line in order to facilitate the comparison with ELLIS' values.

Table 2 shows the assignment of lines and the energies of gamma-rays. We have considered as established only those gamma-rays for which at least K and one L line were found, and those gamma-rays for which only a well-defined K line exists, but a corresponding Compton line was found in the Compton spectrum measured by MLADJENOVIĆ and HEDGRAN [21].

Table 3 lists the energies, intensities and tentative assignments of the Auger lines found in the spectrum of the active deposite of radon. The error in the energy determination of the Auger lines is of the order of a few pro mille, and is due to the fact that the lines are generally weak, and are superposed on a very high background, so that the distances from the edges could only be indirectly measured.

Discussion

Our results are in general agreement with ELLIS' results. We have confirmed most of the lines reported by ELLIS, and in addition we have found a number of new lines. Most of the new lines which we have found are weak lines, which were not detected by ELLIS, while some of them are resolved from previously known lines. We have thus resolved L_{II} lines from L_I lines for the gamma-rays of 241.9, 295.2, 352, and 609.3 keV, which is of importance for the assignment of the multipole order of transitions. ELLIS has also resolved the L_{II} from the L_I line for the gamma-ray of 352 keV, but he assigned it to RaC. The energy values of strong lines generally agree with ELLIS' values, the difference being considerable only for some very weak lines. This difference may be explained by the fact that a great number of hardly visible lines appear on the film and that one estimates, somewhat arbitrarily, which of those lines can be considered as established, so that some lines accepted by us were not accepted by ELLIS and vice versa.

Most of the energy values given by CORK *et al.* agree with our values, the difference being greater for weaker lines. It should be mentioned, however, that we did not find three lines of 30, 30.6, and 33 keV respectively which should be L_I, L_{II}, and

Table 1. The internal conversion and Auger spectrum of the active deposit of radon.

Number of line	Ellis' notation	Energy				Intensity		
		Ellis $H\varrho$	Mlad.–Slätis $H\varrho$	Mlad.–Slätis kev	Cork *et al.* kev	Ellis	Ml.–Sl.	Cork *et al.*
					30.0			10
					30.6			4
					33.0			1
1	A	657.66	659.26	36.892	36.6	240	650	9
2	Aa	663.45	665.17	37.532	37.2	40	124	3
3	Aa1	683.99	685.50	39.778	39.5	8	10.1	1
4		—	690.14	40.299	—		2.6	
5		—	695.64	40.919	—		6.1	
6	Aa2	698.7	699.78	41.390	42.4	0.2	10.2	8
	Aa3	725.47	—	—	45.5	20		7
	Aa4	746.78	—	—	46.2	8		3
		—	—	—	47.2			1
7	B	762.66	766.38	49.277	49.2	80	201	8
8	Ba	764.66	768.66	49.559	—	24	63	
9	Ba1	769.25	772.74	50.062	—	4	7.5	
10	C	787.25	790.68	52.304	52.2	40	76	5
11	Ca	793.13	796.62	53.056	52.9	10	16.5	3
12		827.9	830.96	57.490	—	1.2	26.3	
13		832.3	835.95	58.15	58	2.2	32.3	2
14		838.3	841.81	58.92	—	0.9	3.5	
15		844.0	849.28	59.92	—	0.9	6.8	
16		849.5	853.95	60.55	60.9	1.6	14.8	2
17		854.5	858.49	61.16	—	2.8	32.4	
18		861.7	866.02	62.17	—	0.3	5.6	
19		867.2	870.40	62.77	—	0.3	3.1	
20		871.5	875.60	63.48	63.3	1.5	6	1
21		885.4	889.02	65.33	—	0.2	2	
22	Cg	890.8	896.42	66.36	66	6	20	1
23		—	913.27	68.73	—		3.1	
24		920.8	923.53	70.19	70.2	0.7	21.2	2
25		923.7	925.11	70.41	—	0.7	4.1	
26		—	927.82	70.80	—		7.1	
27		929.5	934.31	71.74	—	0.6	2.2	
28		941.7	941.81	72.82	—	1	4.9	
29		946.0	947.17	73.60	73.4	0.7	6.7	2
30		—	949.45	73.93	76.2		4.2	1
31	Cj	983.85	987.42	79.55	79.3	3	2.6	1
32		—	1061.39	90.96	87.5		7.3	6
33	D	1146.9	1151.77	105.73	105.9	11	15.6	4
34		—	1198.84	113.74	—		2.4	
35	Da	1200.6	1208.33	115.38	—	5	5.6	
36		—	1222.23	117.80	—		4.4	
37		—	1240.79	121.06	—		4.7	
38		—	1270.30	126.30	—		5.1	
39		—	1280.88	128.20	—		3.1	
40	Da1	1269.6	1377.15	145.95	—	0.5	4	
41	F	1400.4	1406.36	151.49	151	425	425	10
	F1	1428.3	—	—	—	0.5		
42	Fa	1485.9	1493.3	168.37	168.2	21	31	6
43	Fa1	1546.6	1550.96	179.89	171.3	5.3	14	4
44		—	1555.2	180.74	176.2		16.8	1
45	Fb	1565.5	1573.26	184.40	181.4	11	19.2	5
46	Fb1	1583.4	1592.67	188.36	184.6	1	6.3	4
47	G	1665.9	1671.7	204.75	204.7	480	510	10
48		—	1700.74	210.87	—		5.8	
49		—	1760.45	223.63	—		4.3	
50	Ga	1762.4	1769.17	225.51	225.5	53	78	5

Table 1 (cont.).

Number of line	ELLIS' notation	Energy				Intensity		
		ELLIS H_ϱ	MLAD.–SLÄTIS		CORK *et al.* kev	ELLIS	ML.–SL.	CORK *et al.*
			H_ϱ	kev				
51		—	1772.20	226.16	228.1		17.1	1
52	Ga1	1820.1	1826.25	237.92	237.3	13	16.4	4
53	Ga2	1822.1	1827.57	238.21	—	1	6.3	
54		—	1836.33	240.14	—		6.2	
55	Ga3	1838.0	1839.96	240.93	240.8	3	5.8	3
56		—	1843.60	241.73	—		2.8	
57		—	1846.70	242.42	—		5.4	
58	Ga4	1899.7	1905.02	255.36	—	0.5	1.8	
59		—	1909.27	256.31	—		6.8	
60		—	1913.54	257.26	—		1.7	
61		—	1920.60	258.84	—		3	
62		—	1922.82	259.34	—		2.6	
63	H	1925.5	1931.44	261.28	260.8	530	550	10
64	Ha	2002.2	2008.3	278.70	278.1	64	79	8
65		—	2011.78	279.50	281.2		13	1
66	Ha1	2050.9	2062.78	291.22	290.2	11	18	4
67		—	2063.80	291.46	—		6.4	
68		—	2073.46	293.69	293.4		9.9	2
69	Ha2	2071.8	2075.96	294.27	—	2.6	8.5	
70	Ha3	2096.6	2082.41	295.77	—	8	5.2	
	Ha4	2142.4	—	—	—	0.5		
71	I	2241.9	2252.00	335.73	334.8	85	94	7
72	I1	2241.9	2254.70	336.37	337.5	1.6	16.8	1
73	Ia	2292.6	2303.8	348.16	346.9	42	21	4
74	Ia1	2306.6	2305.1	348.47	—	8	6.6	
75		—	2316.6	351.25	350		10.6	3
76		—	2320.1	352.09	—		5.9	
	Ia2	2375.2	—	—	—	0.5		
77	Ia3	2418.0	2408.36	373.56	369.6	8	4	3
78		—	2426.75	378.06	—		5	
	Ia4	2464.7	—	—	—	8		
79		—	2481.26	391.49	390.4		0.6	2
	Nb	2534.4	—	—	—	0.5		
	Nc	2703.6	—	—	442	1		1
	Nc1	2823.0	—	—	—	0.5		
	Nc2	2872.8	—	—	—	0.5		
80	O	2962.3	2973.65	516.56	516.3	40	30	8
81	O1	3126.5	3136.79	559.26	—	2.6	2	
82	O2	3184.3	3167.80	567.74	572.7	2.6	2	1
83	P	3251.9	3261.79	592.34	592.8	9	6	5
84		—	3264.40	593.04	—		4	
85	P1	3287.8	3273.22	595.38	—	1.6	2	
86	P2	3306.7	3311.04	605.45	605	1.6	2.7	1
87		—	3321.05	608.11	—		2.2	
88		—	3328.15	610.01	651		1.6	1
89	Pa	3563.4	3572.41	675.65	676	3.2	5.1	4
90		—	3613.51	686.79	—		0.9	
91		—	3639.90	693.95	696		1	1
92		—	3710.37	713.11	—		2.3	
93		—	3765.4	728.13	—		1.3	
94	Pa1	3802.3	3853.58	752.26	752	2.1	1.3	1
95		—	3898.96	764.71	—		0.7	
96	Q	4172.7	4177.65	841.67	842	5	4.5	5
97	Qa	4379.9	4450.80	917.83	918	2.6	1.4	1
98		—	4497.07	930.80	—		0.8	
99	R	4839.7	4840.55	1027.52	1029	13	12.6	8
100	R1	4964.3	4963.50	1062.33	—	1	2.6	

Table 1 (cont.).

Number of line	Ellis' notation	Energy				Intensity		
		Ellis H_ϱ	Mlad.–Slätis H_ϱ	Mlad.–Slätis kev	Cork *et al.* kev	Ellis	Ml.–Sl.	Cork *et al.*
101	Ra	5108.7	5108.27	1103.43	1105	2.1	3	3
102		—	5145.16	1113.94	—		1	
103	Ra1	5150.5	5152.61	1116.07	1117	1	1.4	1
104		—	5233.04	1138.97	—		0.5	
105	S	5253.0	5254.93	1145.20	1148	3.6	5	3
106		—	5368.27	1177.56	—		0.7	
107	S1	5399.3	5404.74	1187.99	—	0.86	1.4	
108	Sa	5522.9	5521.10	1221.28	—	0.85	1.5	
109	Sa1	5585.6	5570.74	1235.52	—	0.2	0.6	
110		—	5674.45	1265.20	—		0.4	
111	Sb	5744.9	5741.70	1284.58	—	0.9	1.3	
112		—	5768.12	1292.18	—		0.8	
113		—	5788.07	1297.91	—		0.8	
114		—	5805.79	1303.38	—		1.4	
115		—	5824.95	1308.52	—		1.4	
116		—	5846.98	1314.86	—		1.1	
117	T	5873.3	5874.4	1322.75	1326	25	25	9
118	T1	5917.0	5951.10	1344.85	—	1	1	
119	T2	5998.2	6012.51	1362.55	—	0.4	0.5	
120	U	6127.9	6138.4	1398.89	1402	3.7	4.9	3
121	Ua	6178.0	6181.12	1411.34	—	1.4	1.4	
122		—	6198.31	1416.20	—		1.5	
	Ua1	6286.5	—	—	—	0.2		
	Ua2	6348.3	—	—	—	0.2		
123	Ua3	6441.8	6452.42	1489.76	—	0.4	0.5	
124	Ua4	6484.4	6530.36	1512.36	—	0.25	0.8	
125	Ua5	6615.3	6667.84	1552.27	—	0.25	0.6	
126	Ua6	6703.3	6721.28	1567.79	—	0.2	0.8	
127	Ua7	6757.4	6746.77	1575.20	—	0.25	0.8	
128		—	6790.35	1587.87	—		0.7	
	Ua8	6887.8	—	—	—	0.2		
129	Ub	6952.8	6952.64	1635.09	—	0.7	0.9	
130		—	7001.75	1649.40	—		0.5	
131	V	7062.7	7076.75	1671.24	1673	4.2	4.6	3
132	Va	7106.9	7143.18	1690.61	—	0.85	0.5	
133	Va1	7192.0	7184.50	1697.55	—	0.3	0.4	
134	Vb	7330.8	7338.63	1747.65	—	0.95	1.1	
135		—	7365.05	1755.36	—		0.6	
136		—	7381.65	1760.21	—		0.5	
137		—	7412.22	1769.15	—		0.5	
	Vb1	7479.3	—	—	—	0.2		
	Vb2	7637.5	—	—	—	0.2		
	Vb3	7768.7	—	—	—	0.2		
138	Vc	7918.3	7940.15	1923.65	—	0.4	0.4	
	Vc1	8033.0	—	—	—	0.2		
139	Vd	8253.7	8281.90	2023.91	—	0.4	0.4	
	Ve	8396.0	—	—	—	0.4		
140	W	8554.2	8580.12	2111.54	—	0.95	1.1	
141	Wa	8610.5	8837.90	2187.39	—	0.4	0.14	
142	Wa1	8819.2	8879.56	2199.65	—	0.2	0.1	
	Wa2	8999.9	—	—	—	0.2		
	Wa3	9095.8	—	—	—	0.2		
	Wa4	9352.5	—	—	—	0.2		
	Wa5	9580.1	—	—	—	0.2		
	Wa6	9941.0	—	—	—	0.2		

Table 2. Analysis of the internal conversion spectrum.

Number of the line	Energy of the line		Assignment of the line	Intensity	Gamma-ray energy, kev
	kev	H_ϱ			
1	36.892	659.26	L_{I}	650	53.277
2	37.532	665.17	L_{II}	124	53.241
3	39.778	685.50	L_{III}	10.1	53.195
7	49.277	766.38	M_{I}	201	53.277
8	49.559	768.66	M_{II}	63	53.253
9	50.062	772.74	M_{III}	7.5	53.239
10	52.304	790.68	N_{I}	76	53.242
11	53.056	795.62	O_{I}	16.5	53.213
				Mean energy	53.23 RaB
41	151.49	1406.36	K	425	242.03
50	225.51	1769.17	L_{I}	78	241.89
51	226.16	1772.20	L_{II}	17.1	241.87
52	237.92	1826.25	M_{I}	16.4	241.92
53	238.21	1827.57	M_{II}	6.3	241.91
55	240.93	1839.96	N_{I}	5.8	241.87
56	241.73	1843.60	O_{I}	2.8	241.89
				Mean energy	241.9 RaB
42	168.37	1493.3	K	31	258.91
57	242.42	1846.7	L_{I}	5.4	258.80
				Mean energy	258.85 RaB
47	204.75	1671.7	K	510	295.29
64	278.70	2008.3	L_{I}	79	295.09
65	279.50	2011.78	L_{II}	13	295.21
66	291.22	2063.78	M_{I}	18	295.22
67	291.46	2063.80	M_{II}	6.4	295.15
69	294.27	2075.96	N_{I}	8.5	295.21
				Mean energy	295.2 RaB
63	261.28	1931.44	K	550	351.82
71	335.73	2252.0	L_{I}	94	352.11
72	336.37	2254.70	L_{II}	16.8	352.08
73	348.16	2303.80	M_{I}	21	352.16
74	348.72	2305.10	M_{II}	6.6	352.17
75	351.25	2316.60	N_{I}	10.6	351.99
76	352.09	2320.10	O_{I}	5.9	353.25
				Mean energy	352.0 RaB
80	516.56	2973.65	K	30	609.72
83	592.34	3261.79	L_{I}	6	609.27
84	593.04	3262.40	L_{II}	4	609.27
85	595.38	3273.22	L_{III}	2	609.19
86	605.45	3311.04	$M_{I,\,II}$	2.7	609.29
87	608.11	3321.05	N_{I}	2.2	609.29
				Mean energy	609.3 RaC

Table 2 (cont.).

Number of the line	Energy of the line		Assignment of the line	Intensity	Gamma-ray energy, kev
	kev	H_ϱ			
89	675.65	3572.41	K	5.1	768.81
94	752.26	3853.58	$L_{I,\,II}$	1.3	768.49
95	764.71	3898.96	M_I	0.7	768.85
				Mean energy	768.7 RaC
96	841.67	4177.65	K	4.5	934.83
97	917.83	4450.80	L_I	1.4	934.76
98	930.80	4497.07	M_I	0.8	934.95
				Mean energy	934.8 RaC
99	1027.52	4840.55	K	12.6	1120.68
101	1103.43	5108.27	L_I	3	1120.36
103	1116.07	5152.61	M_I	1.4	1120.22
				Mean energy	1120.42 RaC
100	1062.33	4963.50	K	2.6	1155.49
104	1138.97	5233.04	$L_{I,\,II}$	0.5	1155.20
				Mean energy	1155.35 RaC
105	1145.20	5254.93	K	5	1238.36
108	1221.28	5521.10	L_I	1.5	1238.21
109	1235.52	5570.74	M	0.6	1238.31
				Mean energy	1238.3 RaC
107	1187.99	5404.74	K	1.4	1281.09
110	1265.20	5674.45	L	0.4	1281.43
				Mean energy	1281.26 RaC
111	1284.58	5741.7	K	1.3	1377.7
119	1362.55	6012.5	L	0.4	1378.78
				Mean energy	1378.24 RaC
117	1322.75	5874.4	K	25	1415.9
120	1398.89	6138.40	L	4.9	1415.8
121	1411.24	6181.12	M	1.4	1415.4
				Mean energy	1415.9 RaC
122	1416.2	6198.31	K	1.5	1509.3 RaC
129	1635.09	6952.64	K	0.9	1728.3 RaC
131	1671.24	7076.75	K	4.6	1764.40
134	1747.65	7338.63	L	1.1	1764.58
136	1760.21	7381.65	M	0.5	1764.36
				Mean energy	1764.4 RaC
135	1755.36	7365.05	K	0.6	1848.5 RaC
138	1923.65	7940.15	K	0.4	2016.7 RaC
139	2023.91	8281.9	K	0.4	2117.0 RaC
140	2111.54	8580.12	K	1	2204.64
141	2187.39	8837.90	L	0.14	2204.32
142	2199.65	8839.56	M	0.1	2203.80
				Mean energy	2204.25 RaC

Table 3. Auger spectrum of the active deposite of radon.

Number of line	Energy		Intensity	Assignment
	$H\varrho$	kev		
12	830.96	57.49	26	KL_IL_I (83)
13	835.95	58.15	32.3	KL_IL_{II} (83)
14	841.81	58.92	3.5	KL_IL_I (84)
15	849.28	59.92	6.8	$KL_{II}L_{II}$ (84)
16	853.95	60.55	14.8	KL_IL_{III} (83)
17	859.49	61.16	32.4	$KL_{II}L_{III}$ (83)
18	866.02	62.17	5.6	KL_IL_{III} (84)
19	870.40	62.77	3.1	$KL_{II}L_{III}$ (84)
20	875.60	63.48	6	$KL_{III}L_{III}$ (83)
21	889.02	65.33	2	$KL_{III}L_{III}$ (84)
24	923.53	70.19	21.2	KL_IM_I (83)
25	925.11	70.41	4.1	KL_IM_{II} (83)
26	927.82	70.80	7.1	$KL_{II}M_I$ (83)
27	934.31	71.74	2.2	KL_IM_I (84)
28	941.81	72.82	4.9	$KL_{II}M_I$ (84)
29	947.17	73.60	6.7	$KL_{II}M_{III}$ (84)
30	949.45	73.93	4.2	$KL_{III}L_{II}$ (83)

L_{III} lines of a 46 keV gamma-ray belonging to RaB. The first of these lines was reported by CORK *et al.* to have an intensity of the same order as F, G, and H line, and should have been easily detected in our measurements. These lines were not reported by ELLIS either.

It is of interest to compare our energy values and the values given by MÜLLER *et al.* [16] for five strong gamma-rays of RaB + C, which they have measured using a high precision curved crystal spectrometer. The values are given in Table 4.

Table 4. The energies of five RaB + C lines as determined by MULLER *et al.* and by MLADJENOVIĆ and SLÄTIS.

MULLER *et al.*	MLADJENOVIĆ-SLÄTIS	Difference, %
53.226 ± 0.00014	53.23	0.008
241.924 ± 0.030	241.9	0.009
295.217 ± 0.039	295.2	0.006
351.992 ± 0.062	352.0	0.002
609.37 ± 0.16	609.30	0.01

The agreement is very good, showing a fine consistency of results obtained by different methods.

Our intensity values mainly agree in the order of magnitude with the values given by ELLIS, and disagree in the order of magnitude with most of the values given by CORK *et al.* The most important difference between the intensity values given by ELLIS and our values exists in the low energy lines of RaB, where our values are several times higher than the values visually estimated by ELLIS.

V. Multipole order of gamma-rays of RaB

ELLIS has given the multipole orders of RaB and RaC gamma-rays based on the measurements of the internal conversion coefficients. Since there are no published theoretical calculations of the internal coefficients in L shells for the energies above 300 keV nor reliable empirical curves of the K/L ratios for high energies, we shall restrict our discussion of multipole orders to the gamma-rays of RaB. ELLIS has found that the four prominent gamma-rays of RaB correspond to the electric quadrupoles with a strong admixture of magnetic dipoles [17]. In order to obtain as complete an information as possible on the multipole orders, we shall examine the $L_{\mathrm{I}}/L_{\mathrm{II}}/L_{\mathrm{III}}$ ratios, K/L ratios and the internal conversion coefficients.

The experimentally found $L_{\mathrm{I}}/L_{\mathrm{II}}/L_{\mathrm{III}}$ ratios for the four prominent RaB gamma-rays, together with the theoretical ratios calculated from GELLMAN *et al.* [22], are given in Table 5. L_{III} lines were not found for the gamma energies of 241.9, 295.2, and 352 keV, and we have indicated that they are $< 1\,\%$.

Table 5. $L_{\mathrm{I}}/L_{\mathrm{II}}/L_{\mathrm{III}}$ ratios calculated from GELLMAN, and experimental values.

Gamma-ray energy	E1	E2	M1	Exp.
53.23	1 : 0.74 : 0.94	1 : 30 : 30	1 : 0.085 : 0.0012	1 : 0.19 : 0.01
241.9	1 : 0.26 : 0.2	1 : 4 : 2	1 : 0.081 : 0.0025	1 : 0.22 : < 0.01
295.2	1 : 0.24 : 0.18	1 : 2.5 : 1.2	1 : 0.081 : 0.0026	1 : 0.16 : < 0.01
352	1 : 0.22 : 0.16	1 : 1.5 : 0.6	1 : 0.08 : 0.003	1 : 0.18 : < 0.01

It is clear from this table that E2 transitions are ruled out because of the $L_{\mathrm{I}}/L_{\mathrm{II}}$ ratios. Nor are E1 probable because of the $L_{\mathrm{I}}/L_{\mathrm{III}}$ ratios. The most probable assignment is M1, possibly with an admixture of E2 to account for somewhat lower experimental ratios than those theoretically predicted for pure M1 transitions.

We shall compare our experimental values of K/L ratios with the theoretical values calculated from the values of REITZ for K coefficients [23], and the values of GELLMAN *et al.* for L coefficients [22]. Table 6 contains the theoretical and our experimental values for the K/L ratios.

Table 6. Theoretical and experimental K/L ratios.

Gamma-ray energies	E1	E2	M1	Experimental
241.9	5.3	0.7	5.3	4.5
295.2	5.7	1.2	5.6	5.5
352	6	1.6	5.7	5.0

Our experimental values agree within the experimental error with M1 and E1 transitions, but, as E1 do not come into consideration because of $L_{\mathrm{I}}/L_{\mathrm{III}}$ ratios, this also indicates that the transitions in question are M1 transitions. The average value of about 5 for the K/L ratio of M1 transitions is in agreement with the value of 5.5 for the 209 keV transition in Au^{199} as found by P. M. Sherk and R. D. Hill [24]. Our results support the conclusion of J. B. Swan and R. D. Hill [25] that the single empirical curve for K/L ratios in M1 transitions given by Goldhaber and Sunyar [26] represents the ratios for lower Z elements, and that the ratios for higher Z may have lower values, as it also follows from theoretical computations.

An indication of the multipole order may also be obtained by comparing our intensity values for F, G, and H line with the intensities of corresponding gamma-rays reported by Muller *et al.* [16], using the internal conversion coefficient given by Rose [27]. In Table 7 we give the values obtained by dividing our intensity values with the corresponding internal conversion coefficient for K shell and normalizing to the value of 1 for 352 keV.

Table 7. The relative intensities of three prominent RaB gamma-rays.

Gamma-ray energies	Relative intensity from internal conversion			Measured relative intensity
	E1	E2	M1	
241.9	0.32	0.31	0.28	0.2
295.2	0.64	0.63	0.6	0.55
352	1	1	1	1

It will be seen from the Table 7 that although the differences are small between various multipole orders, M1 still gives the best fit to the data of Muller *et al.* It should also be noted that our intensity values are in good agreement with the values given by Muller.

In conclusion, the four prominent gamma-rays of RaB are most probably M1 transitions, possibly with an admixture of E2.

Summary

1. The energy and the intensity of Auger and internal conversion lines of the active deposit of radon were measured by means of a high resolution permanent magnet beta-ray spectrometer with photographic recording.

2. Ellis' results were generally confirmed. In addition, a number of new lines were found.

3. For four prominent low energy gamma rays, the L_{II} lines were resolved from L_I lines and their ratio measured.

4. The multipole order of 53.23, 241.9, 295.2, and 352.0 keV gamma-rays was established to be magnetic dipole with a possible mixture of electric quadrupole.

Nobel Institute of Physics, Stockholm 50, Sweden.

REFERENCES

1. Baeyer, O. von, and Hahn, O., Phys. Zs. *11*, 488 (1910).
2. Danysz, J., C. R. 153, 339, 1066 (1911); Le Radium *9*, 1 (1911).
3. Rutherford, E., and Robinson, H., Phil. Mgg. (6), *26*, 717 (1913).
4. Baeyer, O. von, Hahn, O., and Meitner, L., Phys. Zs. *12*, 1099 (1911).
5. Ellis, C. D., Proc. Roy. Soc. A *99*, 261 (1921).
   Ellis, C. D., and Skinner, H. W., Proc. Roy. Soc. A *105*, 165 (1923).
   Ellis, C. D., and Aston, G. H., Proc. Roy. Soc. A *129*, 180 (1930).
   Ellis, C. D., and Wooster, W. A., Proc. Roy. Soc. A *114*, 276 (1927).
   Ellis, C. D., Proc. Roy. Soc. A *139*, 336 (1933).
   Ellis, C. D., Proc. Roy. Soc. A *143*, 350 (1934).
6. Ellis, C. D., Proc. Roy. Soc. A *143*, 350 (1934).
7. Ellis, C. D., Intern. Conf. Phys. London 1934, 43.
8. Siegbahn, K., Arkiv f. Mat. Astr. och Fysik *30*, No. 20 (1944).
9. Cork, J. M., Branyan, C. E., Stoddard, A. E., Keller, H. B., LeBlanc, J. M., and Childs, W. J., Phys. Rev. *83*, 681 (L), (1951).
10. Mann, K. C., and Ozeroff, M. J., Can. J. Phys. *27*, 164 (1949).
    Wapstra, A. H., Physica *18*, 1247 (1952).
    Constantinov, A. A., and Latyshev, G. D., J. Phys. (USSR) *5*, 249 (1941).
    Kageyama, S., J. Phys. Soc. Japan *6*, 285 (1951).
    Kageyama, S., J. Phys. Soc. Japan *6*, 285 (1951).
    Kageyama, S., J. Phys. Soc. Japan *8*, 689 (1953).
11. Latyshev, G. D., Kompaneetz, A. F., Borisov, N. P., and Gusak, I. M., J. Phys. (USSR) *3*, 251 (1940).
12. Alichanow, A. I., and Latyshev, G. D., J. Phys. (USSR) *3*, 263 (1940).
13. Slätis, H., Arkiv f. Fysik *6*, No. 41 (1953).
14. Lindström, G., Arkiv f. Fysik *4*, No. 1 (1952).
15. Lindström, G., Hedgran, A., and Alburger, D., Phys. Rev. *89*, 1303 (1) (1953).
16. Muller, D. E., Hoyt, H. C., Klein, D. J., and DuMond, J. W. M., Phys. Rev. *88*, 775 (1952).
17. Ellis, C. D., and Wooster, Proc. Roy. Soc. A *114*, 266, 727 (1927).
18. Silberstein, L., Phil. Mag. *44*, 257, 956 (1932); *45*, 1069 (1933).
19. Arnoult, R., Ann. de Phys. *12*, 241 (1939).
20. Slätis, H., Arkiv f. Fysik, in print.
21. Mladjenović, M., and Hedgran, A., Arkiv f. Fysik *8*, No. 4 (1954).
22. Gellman, H., Griffith, and Stanley, J. P., Phys. Rev. *85*, 944 (2) (1952).
23. Reitz, J. R., Phys. Rev. *77*, 10 (1950).
24. Sherk, P. M., and Hill, R. D., Phys. Rev. *83*, 1097 (1951).
25. Swan, J. B., and Hill, R. D., Austr. J. Phys. *6*, 371 (1953).
26. Goldhaber, M., and Sunyar, A. W., Phys. Rev. *83*, 906 (1951).
27. Rose, M. E., Goertzel, G. H., and Perry, C. L., ORNL 1023.

Tryckt den 24 april 1954

Uppsala 1954. Almqvist & Wiksells Boktryckeri AB

ARKIV FÖR FYSIK Band 8 nr 6

Communicated 13 January 1954 by ERIK HULTHÉN and ARNE WESTGREN

Ultra-violet and blue bands of calcium oxide

By ALBIN LAGERQVIST

With 3 figures in the text

Abstract

Two band systems of CaO, consisting of a $^1\Pi-^1\Sigma$ system in the blue and violet part of the spectrum and a $^1\Sigma-^1\Sigma$ system in the ultra-violet, here designated $B\rightarrow X$ and $C\rightarrow X$ respectively, have been made the object of a rotational analysis. The following bands have been examined: in $B\ ^1\Pi-X\ ^1\Sigma$: 0,2, 0,1, 1,0 and 1,3; in $C\ ^1\Sigma-X\ ^1\Sigma$: 0,3, 0,2, 1,0, 1,4, 2,0 and 3,0. The common lower state is already known. The constants derived for the states B and C are:

$B\,^1\Pi$	$C\,^1\Sigma$
$B_v^c = 0.388_2 - 0.005_5\ (v+\frac{1}{2})$ cm^{-1}	$B_v = 0.3731 - 0.0032\ (v+\frac{1}{2})$
$D \sim 0.7\times 10^{-6}$	$D \sim 0.7\times 10^{-6}$
$r_e = 1.950\times 10^{-8}$ cm	$r_c = 1.989\times 10^{-8}$ cm
$\omega_e - \omega_e x_e = 574._4$	$\omega_e = 560.9$
$\nu_{0,0} = 25913.0$	$\omega_e x_e = 4._0$
	$\nu_{0,0} = 28772.3_6.$

In the upper states several perturbations have been found. It is difficult to predict anything about the nature of the perturbing states. From the appearance of some perturbations in the $B^1\Pi$ state it is not out of the question that the interacting state is a $^3\Sigma$ state. Supposing $X\ ^1\Sigma$ to be a $^1\Sigma^+$ state, then this perturbing state is a $^3\Sigma^+$.

§ 1. Introduction

The band spectrum of the calcium oxide is very complicated. Bands belonging to this molecule have been found from the ultra-violet part of the spectrum up to the photographically extreme infra-red region. Several attempts have been made to arrange the bands in vibrational equations. The agreement between the analyses performed is very poor. In the short-wave region MAHANTI (1932) reported two systems:

a blue one,

$$\nu = 23817.62 + 726.53\ (v'+\tfrac{1}{2}) - 11.66\ (v'+\tfrac{1}{2})^2 - 811.28\ (v''+\tfrac{1}{2}) + 6.60\ (v''+\tfrac{1}{2})^2,$$

and an ultra-violet one,

$$\nu = 28849.81 + 565.06\ (v' + \tfrac{1}{2}) - 4.48\ (v' + \tfrac{1}{2})^2 - 725.37\ (v'' + \tfrac{1}{2}) + 3.56\ (v'' + \tfrac{1}{2})^2.$$

In 1936 BRODERSEN considered that the band-heads from the ultraviolet up to the infra-red could be arranged as ten band systems corresponding to transitions between seven different electron levels. In this paper BRODERSEN also made a rotational analysis of some bands in the blue region and altered an earlier published rotational analysis of some infra-red bands. The term-scheme suggested by BRODERSEN seems to be very little reliable. LEJEUNE (1945) tried to give vibrational equations for the orange and green bands, and LEJEUNE and ROSEN contributed head equations for the blue and ultra-violet bands. They also made an attempt to collect into a term-scheme all systems known until then. LEJEUNE and ROSEN arranged some violet bands in a system ε, which is the same system as the blue system of BRODERSEN if we increase the v''-numbering by one unit. An ultra-violet system named ξ agrees with that given by MAHANTI if, also in this case, the v''-numbering is increased by one unit.

A rotational analysis of an infra-red band system was performed by HULTIN and myself in 1950. The transition was of the type $^1\Sigma$–$^1\Sigma$, where the upper vibrational levels are strongly perturbed and the lower levels unperturbed. The analyses of these bands by BRODERSEN proved to be incorrect. The vibrational equation for the origins is

$$\nu^0_{v',\,v''} = 11548.84 + 716\,(v' + \tfrac{1}{2}) - 1.6\ (v' + \tfrac{1}{2})^2 - 732.1_1\ (v'' + \tfrac{1}{2}) + 4.8_1\ (v'' + \tfrac{1}{2})^2.$$

The three lowest differences $\Delta G''_v$ of the lower level are 722.5, 712.9 and 703.3, in that order. If we consider the corresponding differences in the lower state of MAHANTI's ultra-violet system we get 718, 711 and 704; in the blue system of BRODERSEN we find 721, 711 and 704. The agreement between these vibrational differences from the three systems is striking, especially as the differences from MAHANTI's and BRODERSEN's systems are determined from the heads. In MAHANTI's blue system the ω-value of the upper level agrees very well with the ω-value discussed, but the ωx-value seems to be very high. The lowest differences $\Delta G'_v$ are 703, 680 and 657, and they do not agree with the other differences. Several of the heads in MAHANTI's ultra-violet system are also used in BRODERSEN's blue system and in the system ε of LEJEUNE and ROSEN. It seems therefore very likely that the analysis of the blue bands by MAHANTI is incorrect. In order to decide whether MAHANTI's or BRODERSEN's analysis is the right one, we have to make a rotational analysis of the blue bands. If we wish to show that the ultra-violet bands have the same lower level as the infra-red system, also these bands must be rotationally analysed.

In this paper and in a preliminary report (LAGERQVIST, 1953) it is shown that the vibrational analysis of the ultra-violet system of MAHANTI and the blue (or violet) system of BRODERSEN are correct, and that they have the same lower level as the infra-red system. This has been established through rotational analyses of the ultra-violet and violet systems. The ultra-violet system corresponds to a $^1\Sigma$–$^1\Sigma$ transition, the violet system to a $^1\Pi$–$^1\Sigma$ transition. In this paper the lowest state $^1\Sigma$ is called X, though we do not know whether it is the ground state. The upper state $^1\Sigma$ in the infra-red system is called A, the upper state in the violet system B, and that in the ultra-violet system C. BRODERSEN showed that the B–X system was a $^1\Pi-^1\Sigma$ transition, and made rotational analyses of the 0,1, 0,2 and 0,3 bands. His analysis is right except for the J-numbering, which must be increased by one unit.

§ 2. Experimental

Spectrograms were taken in a first order of a 21-ft. Wood concave grating (165,000 lines) having a dispersion in the region in question of about 1.25 Å/mm. The source of light was an arc burning in air between pure calcium electrodes. The current was about 4 amp. from a 440-volt D.C. output. For comparison, iron lines were used. The wave-lengths for the atom lines were taken from M.I.T. tables (1939).

§ 3. Structure of the bands

As regards the plates showing the region between λ 3000–λ 4500 Å, one is at first strongly inclined to refrain from any attempt to put these thousands of lines in order, so entangled in each other are the blue and the ultra-violet systems. After a closer investigation, however, one finds some regions which may be suitable for a rotational analysis. This is especially the case with the 3,0 band of the ultra violet system (see Fig. 1).

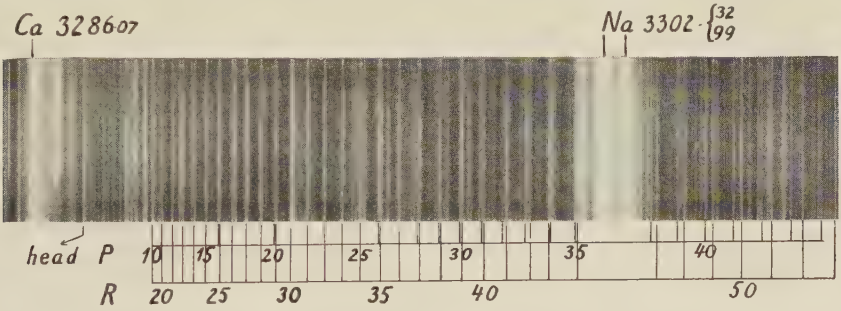

Fig. 1. Reproduction of the 3,0 band of the ultra-violet system. The magnification is 6.

Some selected bands between λ 3280 and λ 4130 Å have been measured. The analyses were possible as the lower state had been accurately analysed in an earlier investigation. The origins of the analysed bands are given in Tables 1 and 2. The heads of the ultra-violet bands are given in Table 3.

Table 1. Band-origins of the analysed $C^1\Sigma-X^1\Sigma$ bands in cm^{-1}.

v' \ v''	0	1	2	3	4
3	$30407._{26}$ $537._{45}$				
2	$29869._{81}$ $544._{12}$				
1	$29325._{69}$				$26493._{44}$
0			$27337._{00}$ $703._{25}$	$26633._{75}$	

Table 2. Band-origins of the analysed $B\,^1\Pi - X\,^1\Sigma$ bands in cm^{-1}.

1	$26487._{43}$			$24348._{89}$
0		$25190._{54}$ $712._{91}$	$24477._{63}$	
v' / v''	0	1	2	3

Table 3. Band-heads of the analysed $C\,^1\Sigma - X\,^1\Sigma$ bands in Å.

3	$3287._{54}$				
2	$3346._{69}$				
1	$3408._{7}$				$3773._{0}$
0			$3656._{63}$	$3753._{20}$	
v' / v''	0	1	2	3	4

In the ultra-violet system, corresponding to a $^1\Sigma - {}^1\Sigma$ transition, the 3,0, 2,0, 1,0, 1,4, 0,2 and 0,3 bands have been analysed. The combination differences for the lower state agree completely with those for the lower state in the earlier investigated infra-red system $A\,^1\Sigma - X\,^1\Sigma$. This proves that the ultra-violet and the infra-red systems have the same lower level. The ultra-violet system is called $C\,^1\Sigma - X\,^1\Sigma$. The level $v'' = 4$ has not previously been investigated, but the combination differences now obtained for this level agree well with those calculated with the rotational constants given in the expressions in the paper on $A\,^1\Sigma - X\,^1\Sigma$. More than ten perturbations were found in the upper vibrational levels. The level $v' = 1$ was followed up only to $J \sim 50$, owing to the richness of lines in the region in question. The wave-numbers for the lines are given in Tables 4 and 5. Overlapped lines are indicated with an asterisk. The accuracy in the line measurements for not overlapped lines is estimated as 0.05 cm^{-1}. To distinguish the perturbations, two types of printing are used in the wave-number tables.

The violet system is a $^1\Pi - {}^1\Sigma$ transition. The 0,1 and 0,2 bands and parts of the 1,0 and 1,3 bands have been analysed. The combination differences for the lower state are the same as those for $X\,^1\Sigma$, and we can therefore call the system $B\,^1\Pi - X\,^1\Sigma$. Both the upper Λ split levels in $^1\Pi$ are strongly perturbed. I have not been able to continue the R and P branches after the culmination of the perturbation. In the Q-branches it was possible to follow the rotational levels over two perturbations. A proof that the right lines have been chosen was carried out in the following way. The differences, $Q(J)_{0,1} - Q(J)_{0,2}$, between the Q-lines with the same J-values from the two bands were calculated. These differences were now compared with those between the rotational levels and the same J-values from the vibrational level $v = 1$ and 2 in $X\,^1\Sigma$. The agreement is very good. In the 1,0 and 1,3 bands only the Q-branches were found, owing to overlappings with other bands. The wave-numbers for the lines of the $B\,^1\Pi - X\,^1\Sigma$ system are given in Table 6.

Table 4. Wave-numbers for the 0,2, 0,3, 2,0 and 3,0 bands of the system CX.

J	0,2		0,3		2,0		3,0	
	$R(J)$	$P(J)$	$R(J)$	$P(J)$	$R(J)$	$P(J)$	$R(J)$	$P(J)$
4					29871.74*	29865.17		
5					71.74*	63.59	30409.17*	
6					71.74*	61.99	09.17*	
7					70.84*	60.16	08.60	30397.55*
8	27338.85				70.84*	58.21	07.99	95.86
9	38.32				69.98	56.24	07.32	93.44*
10	37.70	27322.26*			69.21	53.81	06.38	91.03*
11	37.10	19.97*	26634.35		68.20	51.44	05.32	88.59*
12	36.26	17.85	33.52	26614.97	67.20	48.76	04.14	85.89*
13	35.24	15.43	32.66	12.59	65.80	46.34	02.75	83.09*
14	34.14	12.77	31.52	10.09	64.42	atom line	01.18	80.09*
15	32.87	09.99	30.45	07.50	62.78	atom line	399.50	76.98*
16	31.59	07.17	29.02	04.82	61.12	37.07	97.55*	73.89
17	29.93	04.11	27.61	01.92	59.16	33.60	95.50	70.18*
18	28.31	01.10	26.28	598.86	57.09	30.17	93.44*	66.53*
19	26.38	297.79	24.43	95.73	54.90	26.42	91.03*	62.64*
20	24.41	94.40	22.52	92.43	52.45	22.63	88.59*	58.92
21	22.26*	90.76	20.59	89.03	49.89	18.58	85.89*	54.81
22	19.97*	87.07	18.45*	85.49	47.29	14.42	83.09*	50.44*
23	17.40* _19.97*_	83.11	15.87 _18.45*_	81.61	44.37	10.19	80.09*	45.97*
24	_17.40*_	79.04	_16.23_	77.81	atom line	05.73	76.98*	41.38*
25	_14.78_	74.69 _77.32_	_13.71_	73.47 _76.30_	38.13	01.14	73.54	36.69
26	_12.06_	_73.08_	_11.16_	_72.07_	34.82	796.32	_70.18*_	31.87
27	_09.18_	_68.67_	_08.45_	_67.91_	_31.69_	91.41	_66.53*_	26.42*
28	_06.24_	_64.24_	_05.66_	_63.60_	_28.06_	86.15	_62.64*_	_21.57_
29	_03.20_	_59.66_	_02.76_	_59.07*_	_24.22_	_81.45_	_58.40_	_16.09_
30	_299.96_	_54.88_	_599.71_	_54.78_	_20.26_	_75.86_	54.81	_10.45_
31	_96.70_	_50.16_	_96.98_	_49.90_	_16.13_	_70.32_	50.44	_04.62_
32	_93.26_	_45.16_	_93.44_	_45.28_	_11.94_	_64.63_	45.97	299.21
33	_89.66_	_40.07_	_90.02_	_40.54_	_07.44_	_58.75_	41.38	93.15
34	_85.94_	_35.02_	_86.66_	_35.58_	_02.84_	_52.64_	36.53	86.61
35	_82.09_	_29.64_	_83.03_	_30.54_	_798.22_	_46.50_	31.42	80.26
36	_78.18_	_24.27_	_79.29_	_25.31_	_93.31_	atom line	26.42	Na line
37	_74.08_	_18.64_	_75.49_	_20.02_	_88.22_	,, ,,	20.96	,, ,,
38	_69.94_	_12.99_	_71.40_	_14.63_	_83.10_	_27.10_	15.49	60.21
39	_65.45_	_07.21_	_67.49_	_09.12_	_77.64_	_20.37_	09.81	53.17
40	_61.06_	_01.30_	_63.32_	_03.46_	_72.16_	_13.43_	04.03	45.99
41	_56.52_	_195.29_	_59.07_	_497.66_	_66.52_	_06.26_	298.08	38.57
42	_51.77_	_89.08_	_54.63_	_91.72_	_60.62_	_698.89_	91.98	31.01
43	_46.89_	_82.82_	_49.90_	_85.70_	55.12	_91.55_	_86.61_	23.32
44	_41.92_	_76.27_	_45.28_	_79.54_	48.64	_83.91_	_79.46_	15.46
45	_36.83_	_69.76_	_40.54_	_73.35_	42.22	76.74	Na line	_08.41_
46	_31.61_	_63.04_	_35.58_	_66.89_	atom line	68.40	,, ,,	_199.43_
47	_26.13_	_56.10_	_30.54_	_60.37_	28.97	60.46	_58.76_	_91.05_
48	_20.66_	_49.20_	_25.31_	_53.79_	_21.98_	52.24	_51.53_	_82.20_
49	_15.02_	_42.07_	_20.02_	_47.02_	_14.42_	43.50	_44.06_	_73.42_

Table 4 (cont.)

J	0,2		0,3		2,0		3,0	
	$R(J)$	$P(J)$	$R(J)$	$P(J)$	$R(J)$	$P(J)$	$R(J)$	$P(J)$
50	*27209.30*	*27134.96*	*26514.63*	*26440.32*	*29707.19*	*29634.81*	*30236.40*	*30164.50*
51	*03.38*	*27.64*	*09.12*	*33.28*	*00.06*	*25.59*	*28.49*	*55.30*
52	*197.34*	*20.13*	*03.46*	*26.18*	*692.82*	*16.74*	*20.29*	*45.90*
53	*91.26*	*12.50*	*497.66*	*18.99*	*85.30*	*07.84*	*11.69*	*36.30*
54	*84.94*	*04.84*	*91.72*	*11.66*	*77.09*	*598.83*	*02.79*	*26.31*
55	*78.56*	*096.98*	*85.70*	*04.23*	70.09	*89.62*	*193.21*	*16.05*
56	*72.05*	*89.06*	*79.54*	*96.56*	61.95	*79.74*	*82.82* 96.38	*05.28*
57	*65.32*	*80.92*	*73.35*	*88.88*	53.81	71.08	85.74	*093.95*
58	*58.55*	*72.62*	*66.89*	*80.99*	45.37	61.04	76.00	*81.95* 95.52
59	*51.60*	*64.31*	*60.37*	*73.06*	36.95	51.25	66.31	83.26
60	*44.53*	*55.88*	*53.79*	*65.08*	28.05	41.11	56.42	71.69
61	*37.32*	*47.28*	*46.86*	*56.81*	19.08	30.78	*47.14*	60.32
62	*29.99*	*38.52*	*40.04*	*48.53*	09.86	20.30	*37.20*	48.82
63	*22.58*	*29.62*	*33.09*	*40.09*	00.25	09.60	*27.08*	*37.77*
64	*14.99*	*20.62*	*25.93*	*31.62*	590.40	498.68	*16.79*	*26.08*
65	*07.27*	*11.55*	*18.56*	*22.92*	80.45	87.47	*06.27*	*14.23*
66	*099.32*	*02.24*	*11.10*	*14.11*	69.49	75.82		*02.25*
67	*91.33*	*26992.84*	*03.53*	*05.10*		64.08		*29990.06*
68	*83.28*	*83.26*	*395.96*	*296.08*	*62.33*	51.43		
69	*74.98*	*73.59*	*88.19*	*86.82*	*49.20*			
70	*66.58*	*63.83*	*80.17*	*77.50*	*36.79*	*40.81*		
71	*58.09*	*54.01*	*72.23*	*68.01*	*25.36*	*26.08*		
72	*49.38*	*43.88*	*64.18*	*58.56*	*14.27*	*12.22*		
73	*40.68*	*33.63*	*55.81*		*03.04*	*399.10*		
74	*31.78*	*23.39*	*47.39*		*491.64*	*86.20*		
75	*22.74*		*38.93*		*79.98*	*73.35*		
76	*13.49*		*30.22*		*68.06*	*60.27*		
77	*04.18*		*21.50*		*55.78*	*47.00*		
78	*26994.64*		*12.41*		*42.87*	*33.38*		
79	*85.02*		*03.42*		*29.25*	*19.37*		
80	*75.44*		*294.13*		*14.68*	*04.81*		
81	*65.65*		*84.83*			*289.53*		
82	*perturbed*		*perturbed*			*73.11*		
83					393.19			
84					79.39			
85					66.11	246.73		
86					52.89	31.28		
87					39.51	16.46		
88					25.72	01.47		
89					11.98	186.38		
90					297.82	71.18		

§ 4. Determination of rotational constants

As the constants for the lower unperturbed v''-levels are alreday known with great accuracy from the infra-red system, I have here refrained from any redetermination.

Table 5. Wave-numbers for the 1,0 and 1,4 bands of the system $C X$.

J	1,0		1,4		J	1,0		1,4	
	$R(J)$	$P(J)$	$R(J)$	$P(J)$		$R(J)$	$P(J)$	$R(J)$	$P(J)$
5	29328.32				30	29278.91	29234.06	26459.12	26414.25*
6	28.20				31	75.03	28.76	56.12*	09.85
7	27.71	29316.70			32	70.88	23.19	52.91*	05.01*
8	27.04	14.80	26495.97		33	66.73	17.72	49.57*	00.02*
9	26.36	12.67	95.26	26481.75	34	62.41	11.71	45.84*	395.25*
					35	57.85	05.84	42.34*	90.48
10	25.72*	09.99	94.59	79.05	36	53.17	199.72	38.81*	85.15*
11	24.63	07.64	93.98	77.15	37	48.36	93.52	35.20*	80.17*
12	23.53	05.12	93.37	75.00*	38	43.47	87.05	31.14	74.67
13	22.44	02.51	92.65	72.77*	39	38.38	80.60	27.05*	69.21
14	20.89	299.78	91.72*	70.18*					
15	19.37*	96.84	90.55	67.58*	40	33.02	73.85	22.92*	63.57
16	18.00	93.65	89.64	64.92*	41	27.71	66.93	18.56*	57.95
17	16.13	90.36	87.80	62.10*	42	22.18	52.92	14.25*	52.00
18	14.06	87.12	86.43	59.30	43	16.46	52.82	09.63	46.02
19	11.98*	83.46	84.64	56.12*	44	10.55		05.01*	40.09*
					45	04.52		00.02	33.82
20	09.78	79.71	83.20	52.91*	46	198.40		395.25*	27.43
21	07.31	75.69	81.17	49.57*	47	92.16		90.24	20.93
22	04.81*	71.71	79.54*	45.84*	48	85.59		85.15*	14.24
23	02.29	67.56	77.65	42.75	49	79.06		79.53	07.59
24	299.21	63.16	75.00*	38.81*					
25	96.24	58.97	72.77*	35.20*	50	72.39		74.42	
26	92.98	54.20	70.18*	31.41*	51	65.41		68.91	
27	89.65*	49.34	67.58*	27.05*	52	58.29		62.91	
28	86.24	44.47	64.92*	22.92*	53	51.14		57.37	
29	82.61	39.29	62.10*	18.56*					

I have used three different methods for determining the rotational constants of the states B and C. The first method is the well-known graphical one — plotting $\Delta_2 F'(J)/(J+\frac{1}{2})$ against $(J+\frac{1}{2})^2$. As the levels are perturbed, this method gives only rough B-values, but for some levels a rather good estimation is obtained for the D-values.

The second method is that introduced by GERÖ (1935) for detecting perturbations in the upper state. The following expressions are formed:

$$\frac{\Delta R P}{4J} = \frac{R(J-2) - R(J-1) + P(J) - P(J+1)}{4J} = B'' - B'_d + 6D' - 2J^2(D'' - D'),$$

$$\frac{\Delta Q}{2J} = \frac{Q(J-1) - Q(J)}{2J} = B'' - B'_c - 8J^2(D'' - D').$$

If we plot the left-hand-side espressions against J^2, ΔB is obtained as the intercept at $J = O$. ΔD is obtained from the slope. As we know B'' and D'', this method gives B' and D'. The values for B' are rather accurate.

To test the B'-values obtained we can use a third method, which at the same time gives accurate ν_0-values. The following expressions are formed

Table 6. Wave-numbers for the 0,1, 0,2, 1,0 and 1,3 bands of the system BX.

J	0,1			0,2			1,0	1,3
	$Q(J)$	$R(J)$	$P(J)$	$Q(J)$	$R(J)$	$P(J)$	$Q(J)$	$Q(J)$
6				24475.47				
7				74.67				
8				73.98				24344.97
9				72.99		24466.19	26481.75	43.89
10				72.12		64.35	80.51	43.09
11				70.88		62.53	79.05*	41.95
12				69.71		60.38	77.63	40.50
13				68.42*	24479.59	58.43*	75.94	39.37
14				67.06	78.66	56.35*	74.15	37.65
15				65.53	77.92	54.43*	72.28	36.02
16				63.88	77.05	52.05*	70.18*	34.42
16				62.16	76.14	49.60*	68.22	32.63
18	25172.09			60.38	75.12	46.62*	65.86	30.78
19	70.11			58.43*	73.98	43.91*	63.41	28.52
20	67.85		25152.55*	56.35*	72.70	41.06*	60.68	26.56
21	65.43		49.61*	54.24	71.43	38.24	58.18	24.10
22	63.24		46.46*	52.05*	69.93	35.15	55.26	21.81
23	60.65		43.24*	49.60*	68.42*	32.28	52.26	19.21
24	atom line		40.01*	47.29	66.79	29.02	49.08	16.56
25	» »		36.48*	44.70	64.97	25.69	45.84*	13.47
26	52.55*	25173.48	32.80*	41.94	63.04	22.41	42.34	10.76
27	49.61*	71.39	29.03*	39.17	61.13	18.88	38.68	07.66
28	46.46*	69.24	25.20*	36.17	59.05	15.10	34.46	04.27
29	43.24*	66.94	20.92	33.31	56.83	11.61	30.51	00.67
30	40.01*	64.24	17.38*	30.13	54.43*	07.69	26.18*	96.85*
31	36.48*	61.62	13.14	26.93	52.05*	03.71	21.37	92.91
32	32.80*	atom line	08.91	23.46	49.60*	399.39		
33	29.03*	» »	04.52	19.88*	46.62*	95.18		
34	25.20*	52.55*	00.14	16.28	43.91*	atom line		
35	20.92	49.61*	095.37	12.51	41.06*	86.81		
36	16.93	46.46*	90.64	08.54	37.90	82.28		
37	12.43*	42.78	85.67	04.42	34.60	77.60		
38	07.98	39.14	80.62	00.10	31.19	72.63		
39	03.14	35.38	75.36	395.62*	atom line	67.77		
40	098.14	31.21	69.96	atom line	23.85	62.57		
41	92.85	26.99	64.41	85.91	19.88*	57.28		
42	87.32 _125.20_	22.42	58.47	80.42* _418.28_	15.56	51.78		
43	81.33 _16.93_	17.38*	52.61	74.95 _10.51_	11.14	46.07		
44	75.36* _08.91_	12.43	46.47	69.02 _02.83_	06.40	40.17		
45	68.42 _01.01_	06.99	39.97	62.57 _395.18_	01.27	33.84		
46	61.18 _093.26_	01.01	33.06	55.68 _87.67_	395.62*	27.46		
47	53.48 _85.67_*	094.70	25.98	48.31 _80.42_*	89.78	20.54		
48	45.44 _78.21_	88.23	18.48	40.54 _73.27_	83.33	13.47		
49	36.92 _070.64_		10.30	32.26 _66.02_	76.45	05.73		

Table 6 (cont.)

J	0,1			0.2		
	$Q(J)$	$R(J)$	$P(J)$	$Q(J)$	$R(J)$	$P(J)$
50	25027.37 *63.12*			24323.42 *58.85*		24297.73
51	*55.70*			13.70 *51.77*		89.15
52	*48.17**			*44.41*		
53	*40.18**			*36.99*		
54	*31.91**			*29.13*		
55	*23.63* 65.92			*21.17* 63.46		
56	*14.83* 56.90			*12.71* 54.74		
57	*05.50* 48.17*			*03.71* 46.42		
58	40.02			38.58		
59	31.91*			30.78		
60	23.81			23.42		
61	16.09			16.08		
62	08.50			08.82		
63	00.96			01.75		
64	24993.35			294.55		
65	85.75			87.41		
66	78.17			80.19		
67	70.38			72.97		
68	62.33			65.40		
69	53.70			57.32		
70	44.56			48.39		

$$R(J-1)+P(J)-2(B'-B'')J^2=2\nu_0+2\Delta B'J^2$$

$$Q(J)-(B'-B'')J(J+1) \qquad =\nu_0+\Delta B'J(J+1).$$

The left-hand-side expressions, with approximate B' and accurate B''-values, are plotted against J^2 or $J(J+1)$. Unless a perturbation is present, a straight line ought to be the result. The method gives ν_0 and the correction $\Delta B'$ to the B'-value used.

The B-values B_c and B_d from the two Λ-type doubled terms of the $B^1\Pi$ state do not differ so very much. The difference from the above methods agrees well with that obtained from the combination defect

$$R(J)-Q(J)-Q(J+1)+P(J+1)\sim 2(B_d-B_c)(J+1)^2.$$

The combination-defect expression gives $B_d - B_c = 0.0005$. The notations c and d for the Λ-type doubled levels are those of Mulliken (1931). In using them here I have assumed the transition to be a ${}^1\Pi - {}^1\Sigma^+$.

The B-values are given in Table 7.

Table 7. B-values for the $B\,^1\Pi$ and $C\,^1\Sigma$ states

v	B_c in $B\,^1\Pi$	B_d in $B\,^1\Pi$	B in $C\,^1\Sigma$
0	0.3855 cm^{-1}	0.3859 cm^{-1}	0.3715 cm^{-1}
1	0.380		0.3682
2			0.3651
3			0.3619

The B-values can be collected in the expressions

$$B'_{c,v}(B\,^1\Pi) = 0.388_2 - 0.005_5(v+\tfrac{1}{2})$$

$$B'_v\ \ (C\,^1\Sigma)\ = 0.3731 - 0.0032(v+\tfrac{1}{2}).$$

The great difference between the two values $B_{c,0}$ and $B_{c,1}$ is probably due to a perturbation in the level $v' = 1$. For both the upper states we have

$$D' \sim 0.7 \times 10^{-6}\ \text{cm}^{-1}.$$

The internuclear distances are

$$r'_e(B\,^1\Pi) = 1.950 \times 10^{-8}\ \text{cm and } r'_e(C\,^1\Sigma) = 1.989 \times 10^{-8}\ \text{cm}.$$

§ 5. Determination of vibrational constants

The origins of the bands are given in Tables 1 and 2. They are calculated with the method mentioned in § 4, but also according to the method by KOVÁCS (1952). He determines the origins from the expressions

$$\nu_0 = B'' + \tfrac{1}{4}\{[P(J)+R(J-2)](J+1) - [P(J+1)+R(J-1)](J-1)\},$$

$$\nu_0 = \tfrac{1}{2}[Q(J-1)\times(J+1) - Q(J)\times(J-1)].$$

The two methods give the same result.

Owing to perturbations the v'-levels in $B\,^1\Pi$ as well as in $C\,^1\Sigma$ lie irregularly, and the calculated vibrational constants cannot be given with any higher degree of accuracy.

The constants derived are:

$B\,^1\Pi$	$C\,^1\Sigma$
$\omega_e - 2\,\omega_e x_e = 574.4$;	$\omega_e = 560.9$
	$\omega_e x_e \sim 4.$

§ 6. Perturbations

Perturbations have been found in both the upper states $B\,^1\Pi$ and $C\,^1\Sigma$. They are treated with GERÖ's method mentioned in § 4. The perturbations are not so great in C as in B. The perturbation at about $J \sim 24$ in $v = 0$ in $C\,^1\Sigma$ is, however, rather

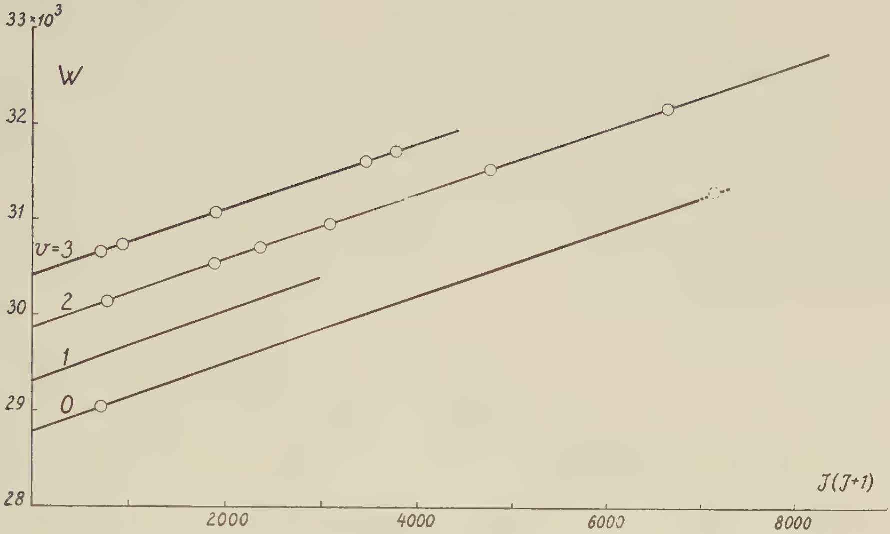

Fig. 2. Perturbations in term values of $C\,^1\Sigma$ plotted against $J\,(J+1)$.

strong. In Fig. 2 the vibrational term-levels of the state C are plotted against $J\,(J+1)$, and the places where the perturbations culminate are indicated by circles. The perturbations in the level C are given in Table 8.

Table 8. Perturbations in the level $C\,^1\Sigma$.

v	J_0	v	J_0	v	J_0
0	24	2	55.5	3	44
0	~83	2	69	3	57
2	27.5	2	81.5	3	61.5
2	43.5	3	26.5		
2	48.5	3	30.5		

The state $B\,^1\Pi$ is more strongly influenced by perturbing states. The expressions $\frac{\Delta\,RP}{4\,J}$ and $\frac{\Delta\,Q}{2\,J}$ (given in § 4) plotted against J are for the state $B\,^1\Pi$ drawn in Fig. 3. In the Q-branches of the 0,1 and 0,2 bands I have found two strong perturbations at about $J \sim 47$ (culmination at $J_0 = 46.7$) and $J \sim 56$ ($J_0 = 55.8$). Another perturbation seems to arise at the last-analysed lines of the branch. The R and P branches have a perturbation which seems to culminate at about $J \sim 51$. I have not been successful in my attempts to find the branch after the perturbation. The appearance of the two perturbations in the Q-branch and the one in the R and P branches — the latter culminating at a J-value lying between the J-values where the perturbations culminate in the Q-branch — reminds one of a $^1\Pi\,^3\Sigma$ interaction. Assuming the state X to be a $^1\Sigma^+$ state, the perturbing state must be a $^3\Sigma^+$ state. The $^3\Sigma_j$-component

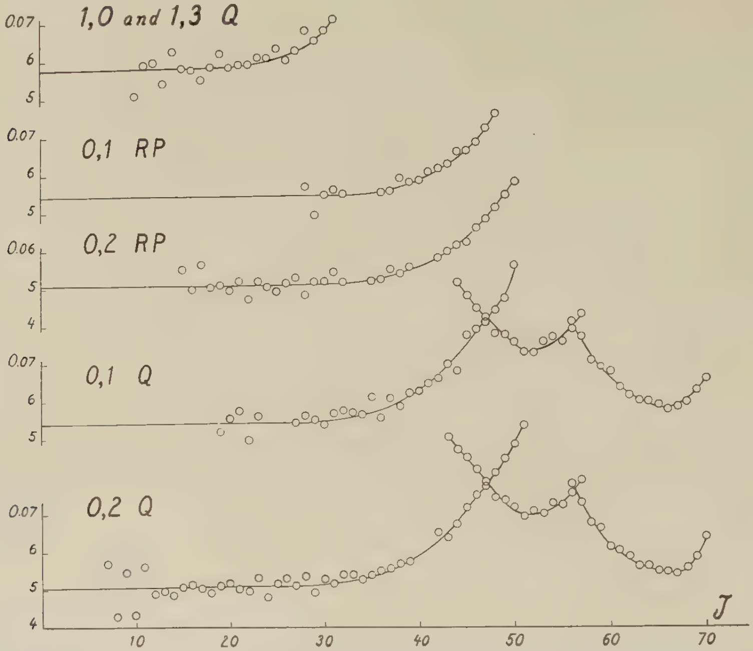

Fig. 3. $\Delta RP/4J$ and $\Delta Q/2J$ plotted against J for the blue bands.

interacts with the *c*-levels of $^1\Pi$, and the $^3\Sigma^+_{J-1}$ and $^3\Sigma^+_{J+1}$-components interact with the *d*-levels of $^1\Pi$. As several extra lines have been found in the *c*-levels, a value of the rotational constant B of the perturbing state may be determined with the method by Kovács (1951). One obtains $B_{^3\Sigma^+} \sim 0.33$.

In the level $v = 1$ of $B\,^1\Pi$ only the Q-branch up to $J = 31$ is followed. Fig. 3 shows that a perturbation causes the lines at higher J-values to deviate more and more.

Results and comparison of CaO with SrO

The data obtained about the electronic states in CaO are given in Table 9, which also gives the data about corresponding states in SrO. The same singlet states, $X\,^1\Sigma$, $A\,^1\Sigma$, $B\,^1\Pi$ and $C\,^1\Sigma$ are known in SrO. The transitions AX and CX have been analysed by Almkvist and myself (1949 and 1952) and the system BX by Kovács and Budó (1953). The agreement between the two molecules is striking.

No perturbing states have been entered in the table. The state A in CaO is perturbed by six electronic states or substates, the corresponding state in SrO by four. The B-state of CaO is probably perturbed by a $^3\Sigma^+$ state, while no perturbations have been found in the B-state of SrO. The C-states of CaO and SrO both show a lot of interactions with perturbing states.

For all the alkaline earth-oxides the lowest known state is a $^1\Sigma$ state, but only for BaO can we say with certainty that this state is the ground state. For all the oxides the state $X\,^1\Sigma$ must dissociate into excited states of the atoms. The normal states $^1S_g + {}^3P_g$ of the metal and oxygen are correlated to the states $^3\Sigma^-$ and $^3\Pi$ of the

Table 9. States of CaO and SrO.

State	CaO					SrO				
	T_0	ω	ω/ω_x	B	B/B_x	T_0	ω	ω/ω_x	B	B/B_x
$C\ ^1\Sigma$	28772	561	0.766	0.3731	0.839	28531	498	0.762	0.273	0.808
$B\ ^1\Pi$	25913	~580	0.792	0.3882	0.873	23989	520	0.796	0.2936	0.869
$A\ ^1\Sigma$	11549	716	0.978	0.4063	0.914	10872	619.6	0,948	0.3047	0.902
$X\ ^1\Sigma$	0	732.1	1.000	0.4444_7	1.000	0	653.5	1.000	0.3377_9	1.000

molecule. By a slip KOVÁCS and BUDÓ stated in their paper (1953) that according to Wigner-Witmer's rules the state X in SrO is a $^1\Sigma^-$ state dissociating into $^1S_0$(Sr) + $^3P_2$(O). They have remarked this to me and are sorry for the unnecessary lapse.

The green and orange systems in CaO and SrO are still unanalysed. In a future investigation I hope to return to these systems and to the second infra-red system in CaO, earlier investigated by MEGGERS (1953).

For valuable help during the experimental work I am indebted to Fil. lic. MATS HULTIN.

Physics Department, University of Stockholm, January 1954.

REFERENCES

ALMKVIST, G. and LAGERQVIST, A., 1949, Arkiv Fysik *1*, 477.
—— 1952, Nature *170*, 885.
BRODERSEN, P. H., 1932, Z. Physik *79*, 613.
—— 1936, Z. Physik *104*, 135.
GERÖ, L., 1935, Z. Physik *93*, 669.
HULTIN, M. and LAGERQVIST, A., 1950, Arkiv Fysik *2*, 471.
KOVÁCS, I., 1951, Acta Phys. Hung. *1*, 97.
—— 1952, Acta Phys. Hung. *2*, 141.
KOVÁCS, I. and BUDÓ, A., 1953, Ann. Physik *12*, 17.
LAGERQVIST, A., 1953, Naturwissenschaften *40*, 268.
LEJEUNE, J. M., 1945, Bull. Soc. roy. Sci. Liège *14*, 318.
LEJEUNE, J. M. and ROSEN, B., 1945, Bull. Soc. roy. Sci. Liège *14*, 322.
MAHANTI, P. C., 1932, Phys. Rev. *42*, 609.
MEGGERS, W. F., 1953, Bur. Stand. Journ. Res. *10*, 669.
M.I.T. Wavelength Tables, 1939 (Chapman and Hall, London).
MULLIKEN, R. S., 1931, Rev. Mod. Phys. *3*, 89.

Tryckt den 24 april 1954

Uppsala 1954. Almqvist & Wiksells Boktryckeri AB

ARKIV FÖR FYSIK Band 8 nr 7

Communicated 14 October 1953 by AXEL E. LINDH and G. HÄGG

The anomalous X-ray transmission in calcite

By GÖSTA BROGREN and ÖVED ADELL

With 6 figures in the text

If an X-ray beam of intensity I is incident upon a non-absorbing crystal, it will be divided in two parts after the passage through the crystal; viz., a transmitted beam of intensity T, which has passed the crystal without change of direction, and a beam of intensity R, which has been reflected in the crystal. As the crystal is non-absorbing, the sum of the energies of the transmitted and the reflected beams must be equal to that of the incident beam. Hence

$$I = R + T.$$

If the crystal is absorbing, an intensity A will be absorbed and we have

$$I = R + T + A \quad \text{or} \quad R + T = I - A.$$

If the crystal consists of a plane-parallel plate where the reflecting atomic planes are perpendicular to the crystal surface, and if we consider a small angular region around the Bragg angle, the absorption may be considered constant and we should obtain

$$R + T = I - A = T_0.$$

However, this discussion is based on the assumption that absorption and reflection are two independent processes. If this is not the case, and the absorption is influenced by the presence of interference maxima, the conditions are changed. If the effective absorption coefficient diminishes when the glancing angle of the incident radiation is near the Bragg angle, the intensity of the transmitted radiation may in consequence increase near the Bragg angle. This is the case in perfect crystals like calcite and quartz, where it has been experimentally demonstrated [1–2]. We have investigated the problem experimentally for both calcite and quartz, and a report on some of the calcite measurements is given below. These were carried out with a double crystal spectrometer in the (1–1) position, and comprise determinations of the intensities of the transmitted and reflected beams in the symmetric Laue case, for plane-parallel calcite plates (cut with the reflecting atomic planes perpendicular to the surface of the crystal plate). The monochromators used were also calcite plates, either cut as above so that Laue diffraction took place, or with the reflecting planes parallel to the surface (the normal Bragg case). Simultaneously, the shapes of the transmission and reflection curves in the region around the Bragg angle were calculated.

Theoretical discussion

In order to carry out a theoretical calculation of the shapes of the curves for the transmitted and reflected intensities in the double crystal spectrometer, it is necessary to compute the shapes of the transmission and reflection patterns in the Laue case and that of the reflection pattern in the Bragg case. (In this publication the Bragg case is taken to be the case where the diffracted beam emerges from the same side of the plane-parallel crystal plate as the incident beam, and the Laue case that where the diffracted beam emerges from the opposite side as the incident.) These two cases have been studied by means of the dynamical theory of X-ray diffraction in perfect, absorbing crystals, and a short survey of the application to our problem is given below. It is based on ZACHARIASEN's account of the dynamical theory, and his notations are generally used [3–4].

The fundamental equation of the dynamical theory represents the conditions for the self-consistency of the wave-fields in the crystal. If this is combined with the boundary conditions of the crystal plate and, if the intensity of the incident parallel and monochromatic beam is I, we obtain for the intensities R and T of the reflected and transmitted beams
in the Laue case

$$\frac{R_L}{I} = \left| \frac{x_1 x_2 (c_1 - c_2)}{x_2 - x_1} \right|^2 \tag{1}$$

$$\frac{T_L}{I} = \left| \frac{x_2 c_1 - x_1 c_2}{x_2 - x_1} \right|^2 \tag{2}$$

in the Bragg case

$$\frac{R_B}{I} = \left| \frac{x_1 x_2 (c_1 - c_2)}{c_2 x_2 - c_1 x_1} \right|^2 \tag{3}$$

$$\frac{T_B}{I} = \left| \frac{c_1 c_2 (x_2 - x_1)}{c_2 x_2 - c_1 x_1} \right|^2 \tag{4}$$

where

$$c_1 = e^{-i\varphi_1 t_0}, \qquad c_2 = e^{-i\varphi_2 t_0} \tag{5 a, b}$$

$$\varphi_1 = 2\pi \frac{k_0 \delta_0'}{\gamma_0}; \qquad \varphi_2 = 2\pi \frac{k_0 \delta_0''}{\gamma_0} \tag{6 a, b}$$

$$x_{1,2} = \frac{-z \pm \sqrt{q + z^2}}{\psi_{\bar{H}}} \tag{7}$$

$$\left.\begin{matrix} \delta_0' \\ \delta_0'' \end{matrix}\right\} = \frac{1}{2}\{\psi_0 - z \pm \sqrt{q + z^2}\} \tag{7 a}$$

$$z = \frac{1-b}{2}\psi_0 + \frac{b}{2}\alpha \tag{8}$$

$$q=\psi_H\psi_{\bar{H}}\cdot b \tag{9}$$

$$\alpha=2\,(\vartheta_B-\vartheta)\sin 2\,\vartheta_B \tag{10}$$

where

$k_0=\frac{1}{\lambda_0}$ (= the wave vector),
t_0 is the thickness of the crystal plate,
ϑ is the glancing angle,
ϑ_B is the Bragg angle,
b is the ratio of the direction cosines (γ_0, γ_H) of the incident and reflected beams relative to the normal to the surface, ψ_0', ψ_0'', ψ_H', ψ_H'' are the real and imaginary parts of the Fourier components of order 0 and H of 4π times the polarizability. For these, if n is the index of refraction, we have

$$n=1+\frac{1}{2}\psi_0. \tag{11}$$

ψ_0' is thus twice the amount by which the real part of the refractive index exceeds unity, and ψ_0'' twice the imaginary part. If μ is the linear absorption coefficient and λ the wavelength, we have

$$\psi_0''=-\frac{\mu\,\lambda}{2\,\pi}. \tag{12}$$

ψ_H is given by

$$\psi_H=-\frac{4\,\pi\,e^2\,F_H}{m\,\omega_0^2\,V}=-\frac{e^2\cdot\lambda^2\,F_H}{\pi\,m\,c^2\,V} \tag{13}$$

where F_H is the structure factor of plane H, V the volume of the unit cell, m the mass of the electron, e its electric charge, and c the velocity of light.

The Laue case is studied first. By introducing

$$v+i\,w=\sqrt{q+z^2} \tag{14}$$

$$a=\pi\,k_0\frac{t_0}{\gamma_0} \tag{15}$$

$$t=\frac{1}{2}\left(\frac{1}{\gamma_0}+\frac{1}{\gamma_H}\right)t_0 \tag{16}$$

the expression for the intensity of the reflected radiation can be simplified to

$$\frac{R_L}{I}=b^2\,|\psi_H|^2\,e^{-\mu_0 t}\,\frac{\sin^2(a\,v)+\sinh^2(a\,w)}{|q+z^2|}. \tag{17}$$

Calcite is a rhombohedral crystal and has an inversion centre, so that $\psi_H=\psi_{\bar{H}}$. If we further assume that the ratio ψ_H''/ψ_H' is small, and that the reflections from the actual atomic plane are strong, the expression can be simplified.

Introducing

$$\frac{\psi''_H}{\psi'_H} = \varkappa \qquad (\varkappa \ll 1) \tag{18}$$

we obtain approximately,

$$\psi_H \cdot \psi_{\bar{H}} \approx |\psi'_H|^2 \, (1 + 2 i \varkappa). \tag{19}$$

Substitute

$$y = \frac{z_r}{K\,|\psi'_H|\,\sqrt{|b|}} = \frac{\frac{1-b}{2}\,\psi'_0 + \frac{b}{2}\,\alpha}{K\,|\psi'_H|\,\sqrt{|b|}} \tag{20}$$

$$g = \frac{z_i}{K\,|\psi'_H|\,\sqrt{|b|}} = \frac{\frac{1-b}{2}\,\psi''_0}{K\,|\psi'_H|\,\sqrt{|b|}} \tag{21}$$

$$A = a K\,|\psi'_H|\,\sqrt{|b|} = \pi\,k_0\,K\,|\psi'_H|\,\frac{t_0}{\sqrt{|\gamma_0\,\gamma_H|}} \tag{22}$$

where z_r and z_i are the real and imaginary parts of z, and K the polarization factor.

Equation (14) now gives

$$\sqrt{q + z^2} = v + i w = K\,|\psi'_H|\,\sqrt{|b|}\;\sqrt{1 + 2 i \varkappa + (y + i g)^2}. \tag{23}$$

In the Laue case $b = 1$, so that $g = 0$. As $|\varkappa| \ll 1$, we get from equations (15), (22) and (23)

$$a v \approx A \sqrt{1 + y^2} \tag{24}$$

$$a w \approx \frac{\varkappa A}{\sqrt{1 + y^2}}. \tag{25}$$

Equation (17) now gives when the polarization is taken in consideration

$$\frac{R_L(y)}{I} = e^{-\frac{\mu_0 t_0}{\gamma_0}} \left[\frac{\sin^2\left(A\sqrt{1 + y^2}\right)}{1 + y^2} + \frac{\sinh^2 \left[\frac{\varkappa A}{\sqrt{1 + y^2}}\right]}{1 + y^2} \right]. \tag{26}$$

As the thickness of the crystal plate is always large in relation to the wavelength of the X-rays used in transmission experiments, $A \gg 1$. Furthermore, the thickness is not exactly the same all over the surface, so that it is not sharply defined. Hence, the term $\sin^2 (A\sqrt{1 + y^2})$ may be replaced by its mean value $1/2$, and we get

$$\frac{R_L(y)}{I} = \frac{e^{-\frac{\mu_0 t_0}{\gamma_0}}}{2\,(1 + y^2)} \left[1 + 2 \sinh^2 \frac{\varkappa A}{\sqrt{1 + y^2}} \right] \tag{27}$$

$$\frac{R_L(y)}{I} = \frac{e^{-\frac{\mu_0 t_0}{\gamma_0}}}{2(1+y^2)} \cosh \frac{2\varkappa A}{\sqrt{1+y^2}}. \tag{27 a}$$

In the same way we obtain from equation (2)

$$\frac{T_L(y)}{I} = \frac{e^{-\frac{\mu_0 t_0}{\gamma_0}}}{2(1+y^2)} \Bigg[(1+2y^2) \cosh \frac{2\varkappa A}{\sqrt{1+y^2}} + \\ + 2y\sqrt{1+y^2} \sinh \frac{2\varkappa A}{\sqrt{1+y^2}} + \cos(2A\sqrt{1+y^2}) \Bigg]. \tag{28}$$

In this expression the cosine term may be replaced by its mean value 0 for the above reasons.

From equations (3) and (4), the corresponding expressions for the reflected and transmitted intensities may be derived for the *Bragg* case. The same substitutions can be used. As the Bragg case was involved only in the production of a monochromatic X-ray beam by reflection, we only need the expression for the reflected intensity. After substituting (14–16) and introducing the polarization factor, equation (3) gives

$$\frac{R_B}{I} = \frac{b^2 K^2 |\psi_H|^2 (\sin^2 av + \sinh^2 aw)}{|q+z^2| + (|q+z^2| + |z|^2)\sinh^2 aw - (|q+z^2| - |z|^2)\sin^2 av + 0.5\left|(|q+z^2| + |z|^2)^2 - |q|^2\right|^{\frac{1}{2}} \sinh|2aw| + 0.5\left|(|q+z^2| - |z|^2)^2 - |q|^2\right|^{\frac{1}{2}} \sin|2av|}. \tag{29 a}$$

The effective thickness of the crystal plates used in the Bragg case is so large, that the hyperbolic terms become very large. Terms which do not contain hyperbolic expressions can then be neglected. Then

$$\frac{R_B}{I} = \frac{b^2 K^2 |\psi_H|^2}{|q+z^2| + |z|^2 + \sqrt{(|q+z^2| + |z|^2)^2 - |q|^2}}. \tag{29 b}$$

Substituting (18–23) we get

$$\frac{R_B(y)}{I} = L - \sqrt{L^2 - (1+4\varkappa^2)} \tag{30}$$

where

$$L = \sqrt{(-1+y^2-g^2)^2 + 4(gy-\varkappa)^2} + y^2 + g^2. \tag{31}$$

The angular coordinate y is obtained from equation (20) by substituting (10), which gives

$$y = \frac{\frac{1-b}{2}\psi_0' + b(\vartheta_B - \vartheta)\sin 2\vartheta_B}{K|\psi_H'|\sqrt{|b|}}. \tag{32}$$

In the Laue case we have $b = +1$ and in the Bragg case $b = -1$. The polarization factor K is $= 1$ for the radiation whose electric vector is perpendicular to the plane of incidence (the normal component), and $K = |\cos 2\vartheta_B|$ for the radiation where the electric vector lies in the plane of incidence (the parallel component). In order to obtain the same angular coordinate for all curves, the normal and parallel y-coordinates were replaced by the same angular coordinate ϑ in all cases.

The intensity distributions obtainable from equations (27), (28), and (30), are based upon the assumption that the incident radiation is monochromatic and parallel. Experimentally, such a supposition cannot be even approximately realized, as the angular width of a beam from a pair of slits is always great in relation to the half width of the diffraction pattern; moreover this beam must contain "white" X-radiation. After reflection by a crystal, it is possible to attain a good approximation of a monochromatic beam, which can then be examined with another crystal parallel to the first.[1] If both reflections take place in identical positions, as, for instance, when both crystals are in the Bragg position, the equation $R(k)$ of the rocking curve, the per cent reflection P and the double-crystal coefficient of reflection R_D are given by

$$R(k) = \frac{1}{2}\int_{-\infty}^{+\infty} R^n(\vartheta)\, R^n(\vartheta - k)\, d\vartheta + \frac{1}{2}\int_{-\infty}^{+\infty} R^p(\vartheta)\, R^p(\vartheta - k)\, d\vartheta. \tag{33}$$

$$P = \frac{\int_{-\infty}^{+\infty} [R^n(\vartheta)]^2\, d\vartheta + \int_{-\infty}^{+\infty} [R^p(\vartheta)]^2\, d\vartheta}{\int_{-\infty}^{+\infty} R^n(\vartheta)\, d\vartheta + \int_{-\infty}^{+\infty} R^p(\vartheta)\, d\vartheta}. \tag{34}$$

$$R_D = \frac{\left[\int_{-\infty}^{+\infty} R^n(\vartheta)\, d\vartheta\right]^2 + \left[\int_{-\infty}^{+\infty} R^p(\vartheta)\, d\vartheta\right]^2}{\int_{-\infty}^{+\infty} R^n(\vartheta)\, d\vartheta + \int_{-\infty}^{+\infty} R^p(\vartheta)\, d\vartheta}. \tag{35}$$

R^n and R^p are obtained from equation (27) or (30), depending on the case which is treated. Indices n and p refer to normal and parallel polarization. The intensity I of the incident beam is taken as unity. The calculations must be carried out by tedious graphic integrations.

If the monochromator crystal is in the Bragg position, and the analyser crystal in the Laue position, the above quantities are obtained from

---

[1] In reality, we obtain a small spectral window, whose spectral width depends on the geometry of the slit system. After reflection, every wavelength present is represented by a divergent beam, the angular width of which depends only on the diffraction pattern. If a crystal is investigated with a double crystal spectrometer in (1–1) position, the spectral window will have the same properties as a monochromatic beam, as the dispersion of the double crystal spectrometer is zero in this position, and the spectral extension of the beam is so small that the properties which depend on the wavelength may be considered constant.

$$R(k)=\frac{1}{2}\int_{-\infty}^{+\infty} R_B^n(\vartheta)\,R_L^n(\vartheta-k)\,d\vartheta+\frac{1}{2}\int_{-\infty}^{+\infty} R_B^p(\vartheta)\,R_L^p(\vartheta-k)\,d\vartheta \tag{36}$$

$$P=\frac{2\,R(k)_{\max}}{\int_{-\infty}^{+\infty} R_B^n(\vartheta)\,d\vartheta+\int_{-\infty}^{+\infty} R_B^p(\vartheta)\,d\vartheta} \tag{37}$$

$$R_D=\frac{2\int_{-\infty}^{+\infty} R(k)\,dk}{\int_{-\infty}^{+\infty} R_B^n(\vartheta)\,d\vartheta+\int_{-\infty}^{+\infty} R_B^p(\vartheta)\,d\vartheta} \tag{38}$$

where the indices B and L refer to the functions for the Bragg and Laue cases respectively.

In order to obtain the intensity distribution of the transmitted radiation, equation (28) must be modified to take into account the diffraction pattern of the monochromator.

This gives

$$T(k)=\frac{1}{2}\int_{-\infty}^{+\infty} A^n(\vartheta)\,T_L^n(\vartheta-k)\,d\vartheta+\frac{1}{2}\int_{-\infty}^{+\infty} A^p(\vartheta)\,T_L^p(\vartheta-k)\,d\vartheta \tag{39}$$

where the function A is identical with R_B, R_L or T_L, depending on the position of the monochromator. These functions are given by equations (27), (28), and (30), in which the intensity I of the incident radiation is put equal to one.

The per cent transmission and the integrated transmission can be calculated analogously, from equations (37) and (38).

Experimental part

Earlier experimental investigations of the anomalous transparency of thick crystals to X-rays have been carried out in such a way that the experimental results cannot be used for a quantitative comparison with the theory [1–2, 5–9]. We have therefore investigated the effect in the wavelength range 558–1932 X.U. with a double spectrometer. The experimental arrangement is shown in Fig. 1. The monochromator crystal A, which in the figure is a calcite crystal in the Bragg position with the surface parallel to the (211) plane, could be replaced by another crystal A' (dotted in the figure) in which the (211) plane was perpendicular to the surface, giving reflection in the Laue position. The analyser crystal was in all cases a calcite crystal in the Laue position, cut in the same way as A', so that both the transmitted and the Laue-reflected radiation had the same length of path in this crystal.

The spectrometer was first adjusted optically, after which two calcite plates with the surfaces parallel to the (211) plane were inserted and adjusted until minimum width of the rocking curve was attained. (For Mo $K\alpha_1$ we got the

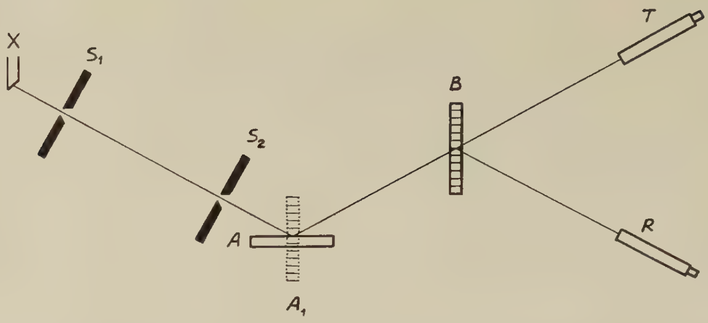

Fig. 1. The experimental arrangement. A is a monochromator crystal, cut for Bragg reflection, that could be replaced by A_1 (dotted in the figure), cut for symmetric Laue reflection. The analyser crystal B in which the anomalous transmission and reflection was studied was cut for symmetric Laue reflection.

value 5.2″ and for Cu $K\alpha_1$ 10.2″.) The analyser crystal was replaced with a crystal cut for symmetric Laue reflection, and this was also adjusted to give the minimum width of the "rocking curve". In the Laue-Laue-arrangement the monochromator crystal had to be exchanged and adjusted as above.

The spectrometer was provided with two Geiger-Müller counters with their accessory circuits, so that the intensities of the transmitted and the reflected radiation could be registered simultaneously. The counters were calibrated against each other very carefully for every wavelength used. Their relative sensitivity was checked over the whole range of intensity within which measurements were carried out, and was found to be independent of the incident intensity. The latter, i.e. the intensity of the beam reflected from the monochromator, was measured with both counters.

As analyser crystals we used calcite plates with the approximate thicknesses 1.0, 0.5 and 0.3 mm. They were etched with 0.7 normal hydrochloric acid for at least ten seconds before insertion in the holder, so that possible surface defects were eliminated. The thickness was measured with a micrometer gauge before etching, but was checked after being inserted by means of careful absorption determinations with copper and molybdenum K-radiation. The 0.34 mm crystals were obtained by etching two thick crystals, the thickness being repeatedly checked by absorption measurements. These showed that the thickness varied somewhat over the surface. Measurements with these crystals in the Laue-Laue position were made where the thickness was about the same for both crystals. The value, 0.34 mm, which is given for them both, is a mean value.

Calculations

The purpose of the investigation was to see whether the experimental results agreed with what could be calculated from the dynamical theory for X-ray diffraction in perfect absorbing crystals. As has been pointed out, the numerical calculations are very tedious. For this reason we have been obliged to limit them to only one wavelength, 1537 X.U. (the Cu $K\alpha_1$ line). This wavelength is shorter than the K-absorption wavelength of all the elements in calcite. The atomic scattering factors must then be corrected for the anomalous contribution to the scattering power due to the K-electrons, which can be calculated from the formulas given by HÖNL [10–11]. We get

$$\begin{aligned} f_{\mathrm{Ca}} &= f^0_{\mathrm{Ca}} + f'_{\mathrm{Ca}} + i\, f''_{\mathrm{Ca}} \\ f_{\mathrm{C}} &= f^0_{\mathrm{C}} + f'_{\mathrm{C}} + i\, f''_{\mathrm{C}} \\ f_{\mathrm{O}} &= f^0_{\mathrm{O}} + f'_{\mathrm{O}} + i\, f''_{\mathrm{O}}. \end{aligned}$$

The structure factor F_{211} is

$$F_{211} = 2\,(f_{\mathrm{Ca}} + f_{\mathrm{C}} + f_{\mathrm{O}}).$$

The (211) plane has $\sin\vartheta/\lambda = 0.165$. The normal values of the atomic scattering factors can then be calculated from JAMES and BRINDLEY's tables [12].

The K-absorption wavelength of calcium is 3064 X.U., that of carbon 43 500 X.U., and that of oxygen 23 500 X.U. These enable us to compute the anomalous contributions to the scattering factors, and we get

$$\begin{aligned} f_{\mathrm{Ca}} &= 15.3 + 0.2 + 1.21i \\ f_{\mathrm{C}} &= 3.4 \\ f_{\mathrm{O}} &= 6.0 + 0.04i \\ F_{211} &= 49.8 + 2.50i. \end{aligned}$$

The unit cell of calcite is a rhombohedron with the side $a = 6\,361$ X.U. and the rhombohedron angle $\alpha = 46^\circ\ 7'$. It contains two molecules $\mathrm{CaCO_3}$. The refractive index is less than unity by $8.8 \cdot 10^{-6}$ and the linear absorption coefficient is 193 $\mathrm{cm^{-1}}$. From the relations given earlier, we obtain

$$\begin{aligned} \psi'_0 &= -17.6 \cdot 10^{-6} \\ \psi''_0 &= -0.473 \cdot 10^{-6} \\ \psi'_{211} &= -8.65 \cdot 10^{-6} \\ \varkappa &= 0.050. \end{aligned}$$

The polarization factor for the normal polarization is $K = 1$, and for the parallel polarization $K = \cos 2\vartheta_B = 0.871$. When the angular coordinates y are converted into seconds of arc, y^n has to be multiplied by 3.62 and y^p by 3.15.

The parameter g in equation (21) is for the normal polarization $= -0.055$, and for the parallel polarization $= -0.063$.

The thicknesses of the analyser crystals were 0.47 mm and 0.34 mm. $\varkappa A$ can be calculated from equation (22), which gives 4.30 and 3.10 respectively for the normal polarized components of the beam, and 3.74 and 2.70 resp. for the parallel polarized components.

The diffraction pattern for the Bragg case calculated from equation (30) is given in Fig. 2, which also gives the diffraction and transmission patterns for the Laue case, for a crystal 0.47 mm thick.

For this thickness there is only a maximum in the transmission curve, but when $|\varkappa A| < 1$ there appears a minimum too.

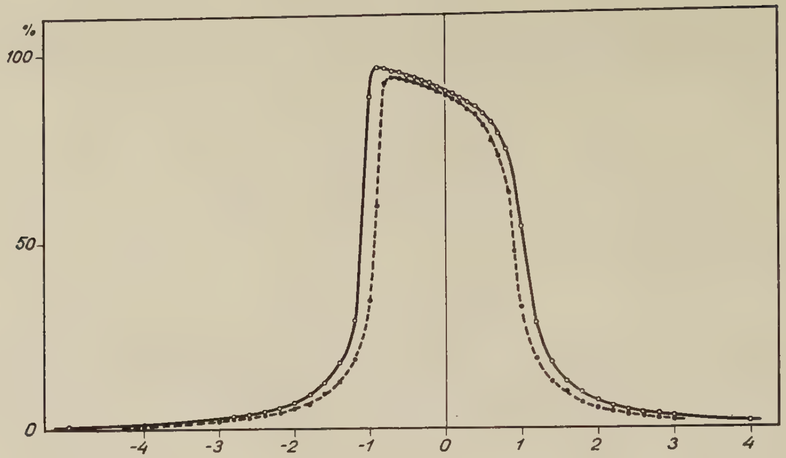

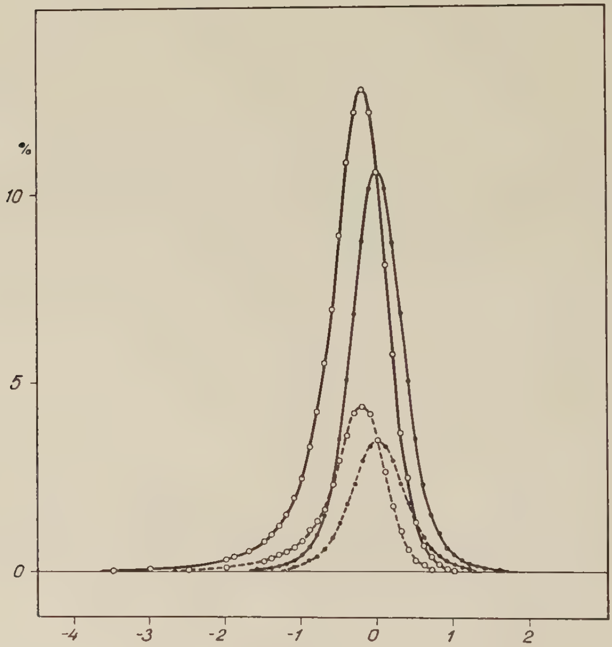

Fig. 2. The upper figure shows the diffraction pattern for the (211) reflection of a thick calcite crystal in the Bragg case, calculated from eq. (30). The unbroken curve refers to the normal polarized component, the dotted to the parallel. The lower figure gives the shapes of the intensity curves of the reflected and transmitted radiation for the (211) reflection of calcite in the symmetric Laue case. The thickness of the crystal was 0.47 mm. In this and the following figures the open circles refer to the transmitted radiation, the filled ones to the reflected. The unbroken curve gives the normal component, the dotted the parallel. The calculations were carried out for the Cu $K\alpha_1$ line (wavelength 1537 X.U.). The angular unit is 3.6″. The intensities are given in per cent of the incident radiation.

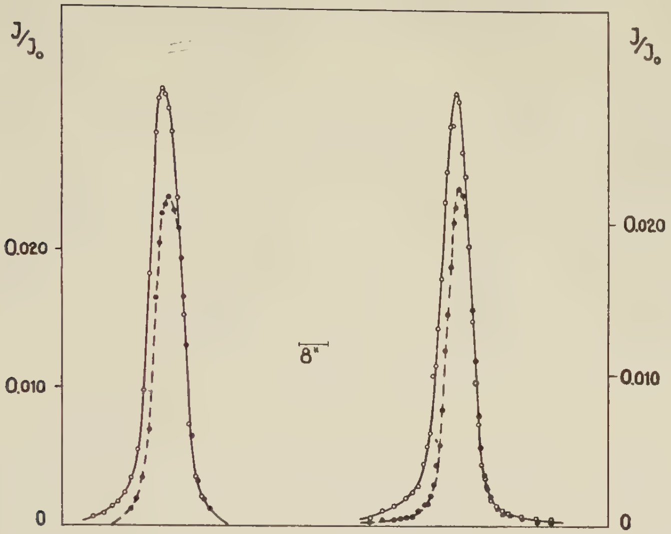

Fig. 3. Transmitted and reflected intensities of Cu $K\alpha_1$ radiation through a 0.47 mm thick calcite crystal. Monochromator in Bragg position. The left-hand curve gives the calculated values, the right-hand one those obtained experimentally. The following data were obtained from the curves (the calculated values are given first). The full width w_R of the reflection curve at half maximum intensity: 8.0″ and 8.2″. The per cent reflection: 2.4 % and 2.0 %. The full width w_T of the transmission curve at half maximum intensity: 8.3″ and 8.4″. The per cent transmission (the maximum transmitted intensity in per cent of the incident intensity): 3.2 % and 2.6 %. The ratio between the per cent reflection and the per cent transmission: 0.76 and 0.78. The distance Δ between the maxima of the two curves: 1.6″ and 1.4″.

Results and discussions

As has been mentioned above, up to the present calculations have been carried out for only one wavelength. In the Bragg-Laue arrangement the transmission through two crystals of thicknesses 0.47 mm and 0.34 mm was studied, and in the Laue-Laue case two crystals 0.34 mm thick were used. With respect to the rather soft X-rays that were used all transmission crystals must be considered thick, so that no minimum appears in the transmission curve. The results appear best from the figures. For each experimental arrangement we have given the calculated and the experimental curves for the transmitted intensity T and the reflected intensity R. The ordinate scales for the calculated and the experimental intensities are not the same, having been adjusted so that the two maxima in the reflection curves have about the same height. This simplifies the qualitative comparison.

The theoretical diffraction and transmission patterns for the 0.47 mm thick calcite crystal, given in Fig. 2, were obtained on the assumption that the incident beam was monochromatic and parallel, and that the crystal specimen had a completely perfect structure. In such a case the width of the intensity curve at half maximum intensity is about 2.9″ for both the transmitted and reflected beams. The two curves cut each other in the maximum point of the R curve,

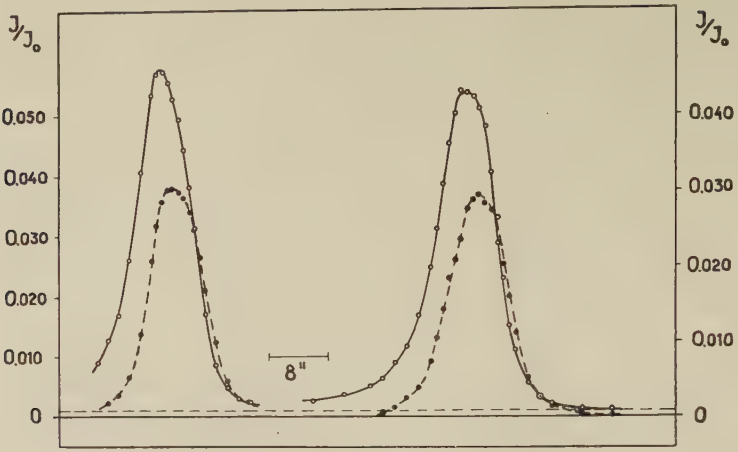

Fig. 4. Transmitted and reflected intensities of Cu $K\alpha_1$ radiation through a 0.34 mm thick calcite crystal. Monochromator in Bragg position. Notation as in the preceding figure. The following characteristic data were obtained (calculated values are given first). The full width w_R of the reflection curve at half maximum intensity: 8.8″ and 9.0″. The per cent reflection: 3.8 % and 2.9 %. The full width w_T of the transmission curve at half maximum intensity: 9.0″ and 9.0″. The per cent transmission: 5.7 % and 4.3 %. The ratio between per cent reflection and per cent transmission: 0.67 and 0.69. The distance Δ between the peaks of the curves: 1.4″ and 1.6″.

at which point the angular coordinate y is 0 (at the Bragg angle). $R < T$ for $y < 0$, but $R > T$ for $y > 0$ in a small region where the two curves lie very near each other.

Experimentally, an approximately monochromatic beam was obtained by reflections at the monochromator crystal A. When this crystal was in the Bragg position the reflected beam had an angular half width of 7.3″. (See Fig. 2.) This causes a broadening of the R and T curves, and at the same time a decrease in the maximum intensities. For this reason the distance between the two intensity curves must be diminished in the region $y > 0$, so that the two curves nearly coincide. The R values are still somewhat higher than the T values (see Fig. 3).

It is also clear that the agreement between the calculated and the experimental curves is very good as regards their shape and form, their full widths at half maximum intensity and the relation between the transmitted and reflected intensities. On the other hand, the measured intensities are always less than the calculated values. The experimental values of the full widths w_R and w_T at half maximum intensity are somewhat greater than the corresponding theoretical values. The experimental values of the integrated transmission and reflection power (the area between the T curve and the ordinate for the normal transmission and the area under the R curve, respectively) are less than the calculated values.

When the monochromator crystal was that cut for Laue reflection, 0.34 mm thick, the monochromatic beam had an angular width of only 3″. The broadening effects are then much smaller, and discrepancies in the structural details are less marked. Furthermore, the intensity curves are well separated (see Fig. 5).

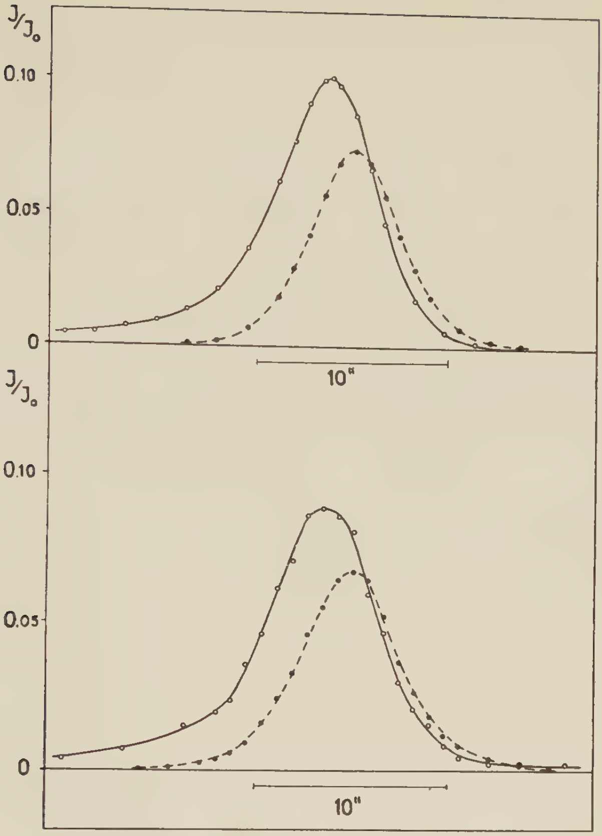

Fig. 5. Transmitted and reflected intensities of Cu $K\alpha_1$ radiation in the Laue-Laue case. Both calcite crystals 0.34 mm thick. Notation as before. The upper curves give the calculated intensities, the lower ones those experimentally determined. The following characteristic data were obtained (calculations first). The full width w_R of the reflection curve at half maximum intensity: 5.2″ and 5.5″. The per cent reflection: 7.3 and 6.7 %. The integrated reflection power: $2.1 \cdot 10^{-7}$ radians in both cases. The full width w_T of the transmission curve at half maximum intensity: 5.6″ and 5.9″. The per cent transmission: 10.1 % and 8.8 %. The ratio between the per cent reflection and the per cent transmission: 0.73 and 0.75. The distance Δ between the peaks of the two curves: 1.3″ and 1.5″.

Here too, the experimental values of the widths at half maximum intensity are greater and those of the intensities smaller than the theoretical values. The integrated transmission and reflection powers are about the same as the theoretical ones. The general agreement between experimental and theoretical results is extremely good. A comparison between the Bragg-Laue and the Laue-Laue arrangements with the same thickness of the analyser crystal indicates that the Laue-Laue arrangement gives definitely superior results. This is due to the much narrower angular width of the beam from the monochromator, and to the fact that a much smaller part of the monochromator crystal is involved in the reflection. (The Bragg angle is 14° 42′, so that a rather large crystal area is

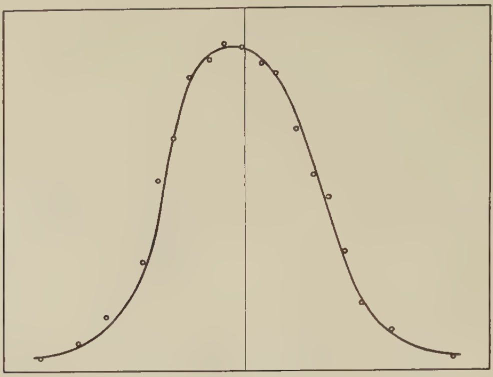

Fig. 6. A comparison between the calculated and the experimental reflection curves ("rocking curves") in the Bragg-Laue case for a 0.47 mm thick calcite crystal and Cu $K\alpha_1$ radiation. The unbroken curve is the calculated curve, the open circles are experimental points, which are adjusted to the curve so that the same maximum point is obtained. The asymmetrical shape of the curve appears clearly.

irradiated in the Bragg position, compared with that in the Laue case. Hence the probability of imperfections in the irradiated part of the crystal increases.)

An investigation of the reflection curve (= the rocking curve) shows that this is symmetrical in the Laue-Laue case. As both crystals had the same thickness, the diffraction patterns were identical for the two crystals. In such a case the resultant reflection curve must be symmetric, regardless of whether the diffraction pattern is symmetric or not. The rocking curve thus gives no information about the shape of the diffraction pattern. (In this case there is strong evidence for its theoretically predicted symmetric form: the agreement between the theoretical and the experimental transmission curves is very good.) In the Bragg-Laue case the "rocking curve" is asymmetric. The theoretical diffraction pattern from a single crystal cannot be investigated experimentally direct, but as appears from Fig. 2, the dynamical theory predicts an asymmetric form in the Bragg case and a symmetric in the Laue case. The resultant rocking curve (the reflection curve) in the Bragg-Laue case should then be asymmetric, on account of the Bragg diffraction pattern. It will be seen from Figs. 3–4 that both the theoretical and the experimental reflection curves are asymmetric, and that there is a very good agreement between them. As far as we known, this is the first experimental verification of the asymmetry of the Bragg diffraction pattern for a perfect absorbing crystal. (Previously, an indirect verification of the asymmetric form has been obtained by experimental investigations of the reflecting properties of calcite, diamond and quartz with double crystal spectrometers, followed by comparisons with theoretical calculations based on the dynamical theory. Very good agreement between theory and experiments has been achieved.) A comparison between the experimental and the theoretical rocking curves is given in Fig. 6, where the calculated curve is drawn and the experimental points given as open circles. The agreement is very good and the asymmetry quite distinct.

A further proof that the asymmetry arises from the Bragg diffraction pattern is obtained from a comparison between the transmission curves in the Bragg-Laue and the Laue-Laue cases for a transmission crystal of thickness 0.34 mm (Figs. 4 and 5). In the former case there is an asymmetrical flattening at the top, similar to that in the reflection curve. No such flattening is discernible in the latter case.

It may be mentioned that experimental results with other wavelengths show the same kind of asymmetry.

In all experimental intensity curves, the full widths at half maximum intensity are greater and the maximum intensities smaller than the corresponding theoretical values. The latter have been calculated on the assumption that calcite is a perfect crystal, which means that every crystal plate should contain only one crystallite. In a real crystal the individual crystallites have relatively small dimensions and they have not exactly the same orientation. These circumstances must give rise to a broadening of the theoretical reflection and transmission curves, which is also in accordance with our results. At the same time the maximum intensities must decrease. When an X-ray beam is incident on a crystallite from such a direction that maximum intensity would be obtained for the R curve, and if the beam later passes through other crystallites, this passage will take place under less favourable conditions, so that the absorption will be greater than in the first crystallite. The result is that the intensity of the outgoing beam will be less than if the crystal plate had consisted of only one crystallite. This interpretation of the deviations from the theoretical curves due to slight imperfections of crystal structure is in conformity with our earlier calcite investigations with a double crystal spectrometer, where both crystals were in the Bragg position [13].

As the qualitative agreement between theory and experiments is very good and the deviations are completely explained by slight imperfections in the crystal structure, the above investigations indicate that the conditions for anomalous transmission of X-rays near the Bragg angle in perfect absorbing crystals can be predicted both qualitatively and quantitatively by the dynamical theory for X-ray diffraction in centrosymmetrical crystals. This investigation verifies the dynamical theory in all respects. Previously, good agreement between theory and experiment had been attained in double crystal spectrometer experiments with calcite and quartz crystals in the Bragg-Bragg arrangement; now it has been verified by investigations of the transmitted and reflected intensities in both the Bragg-Laue and the Laue-Laue arrangements. The present results also give the first direct quantitative verification of the theoretical predictions of asymmetrical Bragg diffraction patterns with perfect absorbing crystals.

Comparison with earlier investigations

No comparison between theoretical and experimental curves for transmission and reflection in the Laue case has been made previously. Qualitative investigations with double crystal spectrometers have been made by CAMPBELL [5–6], by ROGOSA and SCHWARZ [7–8], and by the present authors [9]. CAMPBELL made his measurements with the Bragg-Laue arrangement and Cu $K\alpha_1$ radiation, but used cleft calcite crystals 0.40 mm thick. The experimental arrangement was otherwise the same as here. The distance between the maxima in the R and T curves was in his case 6″, which can be compared with our value 1.6″ for a thickness of 0.47 mm (theoretical value 1.4″). His large value is probably due to some defects in the crystals. ROGOSA and SCHWARZ used the double crystal spectrometer in the $(1+1)$ position as monochromator, and investigated transmission and reflection in a third crystal. The intensities were registered with a single Geiger-Müller counter, connected with a counting-rate meter followed by a graphic recorder. Transmission and reflection intensities had to be measured by separate recordings. The experimental arrangement and the method used make it impossible to use the results for a quantitative comparison with theoretical calculations. Their type of monochromator gives a smaller spectral window than the Bragg monochromator, but the angular width of the beam is $\sqrt{2}$ times greater than in the Bragg case, and the broadening effect is therefore much greater. For the purpose on question their method is inferior to both our Bragg and our Laue monochromators, of which the latter gives the smallest angular width of the beam. For transmission measurements the Laue-Laue arrangement gives the best resolving power. When the monochromator crystal is relatively thick and the analyser crystal thin, the angular width of the diffraction pattern of the monochromator is smaller than the widths of the reflection and transmission patterns of the analyser, which provides the most favourable experimental conditions for a study of the anomalous transparency. It also seems necessary to use two counters in order to obtain simultaneous registration of transmitted and reflected radiation, otherwise it is impossible to ensure reliable registrations in the regions where the intensity curves adjoin each other.

Institute of Physics, University of Uppsala, Uppsala, Sweden, Aug. 1953.

REFERENCES

1. G. BORRMANN, Phys. Zs. *43*, 157, 1941.
2. —— Zs. f. Phys. *127*, 297, 1950.
3. W. H. ZACHARIASEN, Theory of X-Ray Diffraction in Crystals. New York 1945.
4. —— Proc. Nat. Acad. Sci. *38*, 378, 1952.
5. H. N. CAMPBELL, Acta Cryst. *4*, 180, 1951.
6. —— J. Appl. Phys. *22*, 1139, 1951.
7. G. L. ROGOSA and G. SCHWARZ, Phys. Rev. *86*, 421, 1952.
8. —— Ibid. *87*, 995, 1952.
9. G. BROGREN and Ö. ADELL, Ark. f. Fys. *7*, 1, 1953.
10. R. W. JAMES and G. W. BRINDLEY, Phil. Mag. *12*, 81, 1931.
11. H. HÖNL, Zs. f. Phys. *84*, 1, 1933.
12. —— Ann. der Phys. *18*, 625, 1933.
13. G. BROGREN, Ark. f. Fys. *6*, 479, 1953.

Tryckt den 9 augusti 1954

Uppsala 1954. Almqvist & Wiksells Boktryckeri AB

ARKIV FÖR FYSIK Band 8 nr 8

Communicated 14 October 1953 by AXEL E. LINDH and G. HÄGG

The transmission and reflection of X-rays in a thin calcite crystal

By ÖVED ADELL

With 6 figures in the text

Experimental part

The author has investigated the transmission and the Laue reflection of X-rays in the region near the Bragg angle in a calcite crystal with the reflecting planes parallel to the (655) planes. The investigation was carried out with a double crystal spectrometer (1). The reflecting planes of the monochromator A and the analyser B were parallel, (1–1) position, Fig. 1. In this position the double spectrometer gives zero dispersion, and the reflected wavelengths provide a good approximation to a monochromatic beam. During each series of measurements the X-ray tube and the monochromator were fixed, and the analyser was turned through an interval of 30′ around the Bragg angle ϑ_B. The transmitted and reflected intensities, T and R, were measured for a series of values of the glancing angle ϑ, simultaneously by means of two GM counters. The incident intensity I_0, i.e. the total intensity reflected from the monochromator, was determined before and after each series. The experimental method has been described in detail by BROGREN and ADELL (2, 3).

The monochromator A was an etched crystal plate with the faces parallel to the (655) planes. The analyser B was an etched crystal about 0.04 cm thick and cut for symmetrical Laue reflection, so that the reflecting planes were perpendicular to the faces. The thickness t_0 of the analyser varied over the surface and was calculated for each series from the incident intensity and the normal transmitted intensity, i.e. the intensity transmitted for glancing angles differing considerably from the Bragg angle.

The investigation was carried out with wavelengths corresponding to the X-ray lines Au $L\alpha_1$, Au $L\beta_1$ and Mo $K\alpha_1$. The results are shown in Figs. 2, 3 and 6, and Table 1.

The results confirm the finding from a previously published investigation (3), that if the transmitted and reflected intensities are added, there is an angular interval where this sum is less than the normal transmitted intensity, i.e. where the absorption is higher than normal. This effect can occur only in thin crystals. For thick ones we have lower absorption over the whole range around the Bragg angle. Furthermore, we find that for decreasing wavelength the angular distance Δ between the maxima of the reflection curve R and the transmission curve T increases, and the distance Δ' between the reflection maximum and the transmission minimum decreases.

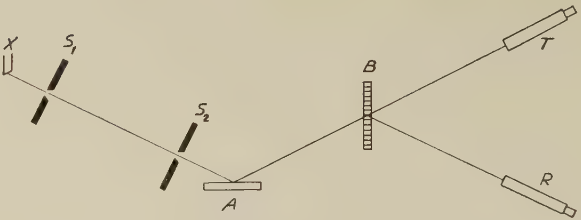

Fig. 1. The experimental arrangement.

Theoretical reflection and transmission curves

The theoretical shapes of the reflection and transmission curves were calculated for Mo $K\alpha_1$ radiation. The diffraction patterns in the symmetrical Bragg case have earlier been calculated by BROGREN (4) according to the DARWIN-EWALD-PRINS dynamical theory for a perfect absorbing crystal. This calculation was used here for the theoretical angular intensity distribution from the monochromator crystal. The full width of this curve at half maximum intensity is 0.57″.

The calculations for the curves, R_L and T_L, of the reflected and transmitted intensities from the analyser crystal for the symmetrical Laue case and a parallel monochromatic incident beam were carried out as described by BROGREN and ADELL (2).[1]

---

[1] Formulas (27) and (28) were used. They are applicable, as the crystal can be expected to be strongly reflecting.

Table 1. The characteristic data for the reflection and transmission curves, R and T. As regards the experimental curves, the mean results from all determinations are given.

Line	Wavelength X.U.	t_0 cm	w''	Δ''	$\Delta'\,''$	$\int_{-\infty}^{+\infty} R\,d\vartheta\cdot 10^7$ radians	$\frac{T_{\text{max}}}{T_{\text{normal}}}$
Au $L\alpha_1$ exp.	1274	0.036	2.0	0.4	3	1.8	7
Au $L\beta_1$ exp.	1079	0.037	1.8	0.7	1.4	3.0	2.3
Mo $K\alpha_1$ exp.	708	0.041	1.3	1.4	0.5	7.8	1.10
Mo $K\alpha_1$ theor.	708	0.041	0.8	0.6	0.3	7.5	1.18

t_0 = the thickness of the crystal plate, w – the full width of R at half maximum intensity, Δ = the angular distance between R_{max} and T_{max}, Δ' = the distance between R_{max} and T_{min}, $\int_{-\infty}^{+\infty} R\,d\vartheta$ – the integrated reflection power, T_{normal} = the intensity transmitted for a glancing angle differing widely from the Bragg angle.

It will be seen from the experimental values that the characteristics of the curves depend on the wavelength. The discrepancy between experimental and theoretical data for Mo $K\alpha_1$ radiation may be explained by crystal defects. The agreement is good for the integrated reflection power.

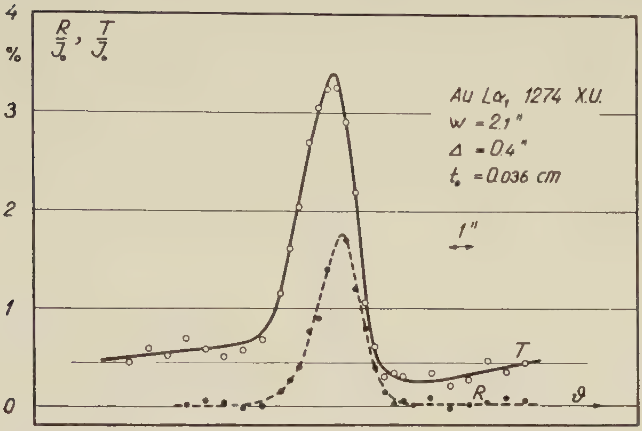

Fig. 2. Experimental reflection and transmission curves, R and T. The intensity distributions are given in per cent of the total incident intensity I_0 and plotted against the glancing angle ϑ. w = the full width of R at half maximum intensity, Δ = the angular distance between $R_{\max}$ and $T_{\max}$, Δ' = the distance between $R_{\max}$ and $T_{\min}$, t_0 = the thickness of the crystal plate B.

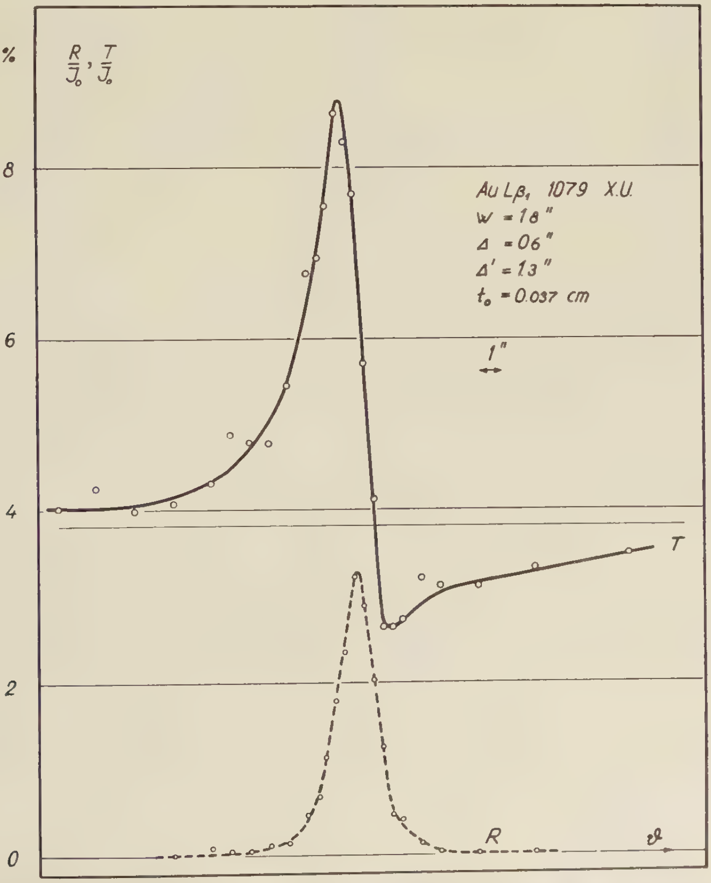

Fig. 3. Experimental curves. Compare with Figs. 2 and 6. When the wavelength decreases the transmission maximum decreases and the minimum becomes more apparent, Δ increases and Δ' decreases.

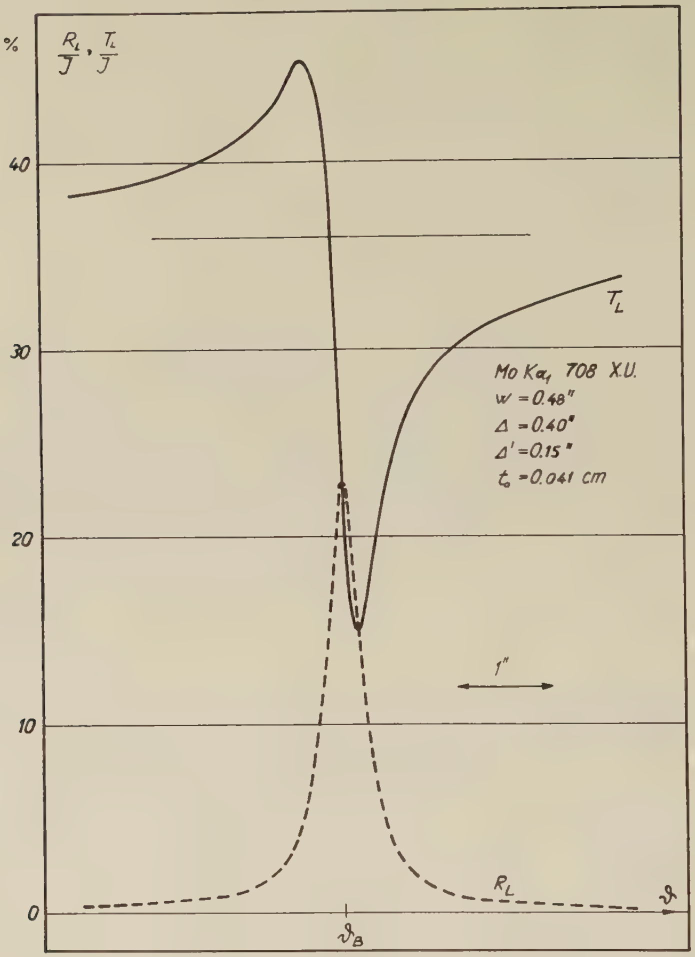

Fig. 4. The theoretical reflection and transmission curves, R_L and T_L, for the analyser crystal in the symmetrical Laue case, when the incident beam I is parallel and monochromatic. ϑ_B = the Bragg angle. T_L intersects R_L where $\vartheta = \vartheta_B$, at the maximum of R_L.

The following data were used in the calculations:

The wavelength of Mo $K\alpha_1$ is 707.8 X.U.

The spacing of the (655) planes in calcite is 1032 X.U.

The normal values of the atomic scattering factors were taken from JAMES and BRINDLEY's tables (5). The imaginary parts of the anomalous contributions to the scattering factors were calculated by HÖNL's formulas (6, 7).

For the structure factor F_{655} we have (4):

$$F_{655} = 2 \cdot (f_{Ca} + f_C + f_O).$$

The numerical form here is

$$F_{655} = 24.6 + i \cdot 0.57.$$

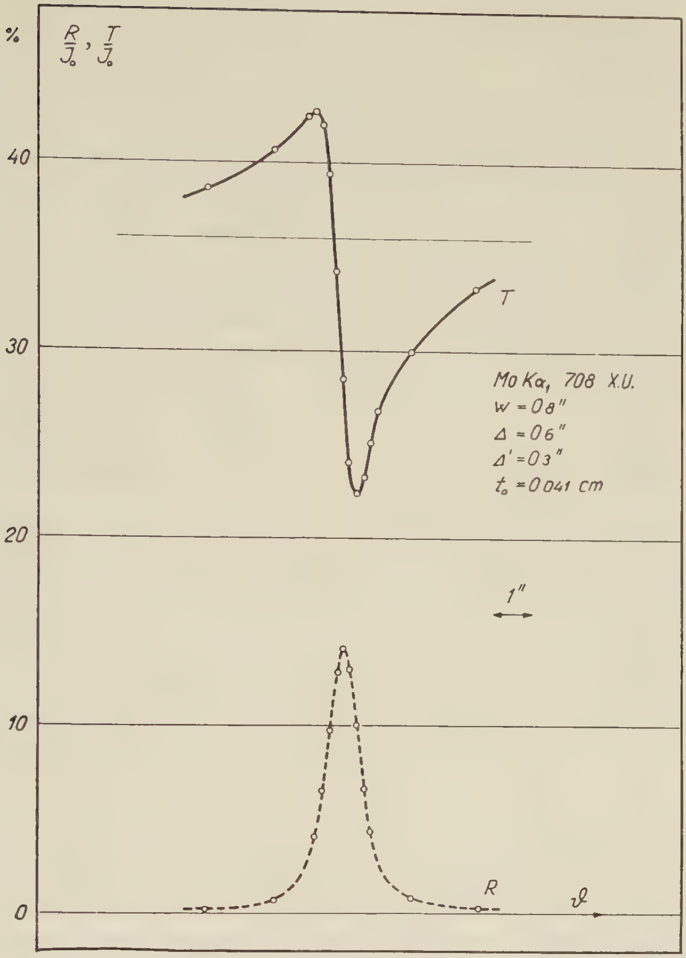

Fig. 5. The theoretical shapes of R and T when the incident beam is obtained by Bragg reflection of a parallel monochromatic beam. A comparison with Fig. 4 shows how the curves R_L and T_L are affected by the angular width of the incident beam.

From the relation between the imaginary and real parts of the structure factor we get $\varkappa = 0.023$.

We also have

$$\psi'_{655} = -8.95 \cdot 10^{-7} \qquad \psi'_0 = -3.70 \cdot 10^{-6}.$$

The value of the linear absorption coefficient is 23.4 cm^{-1}. The polarization factor is for the normal polarization $K = 1$ and for the parallel polarization $K = \cos 2\vartheta_B = 0.765$.

With a crystal thickness t_0 of 0.041 cm we get:

$$(\varkappa A)_n = 0.402, \ (\varkappa A)_p = 0.308, \text{ and } e^{-\frac{\mu_l t_0}{\gamma_0}} = 0.360.$$

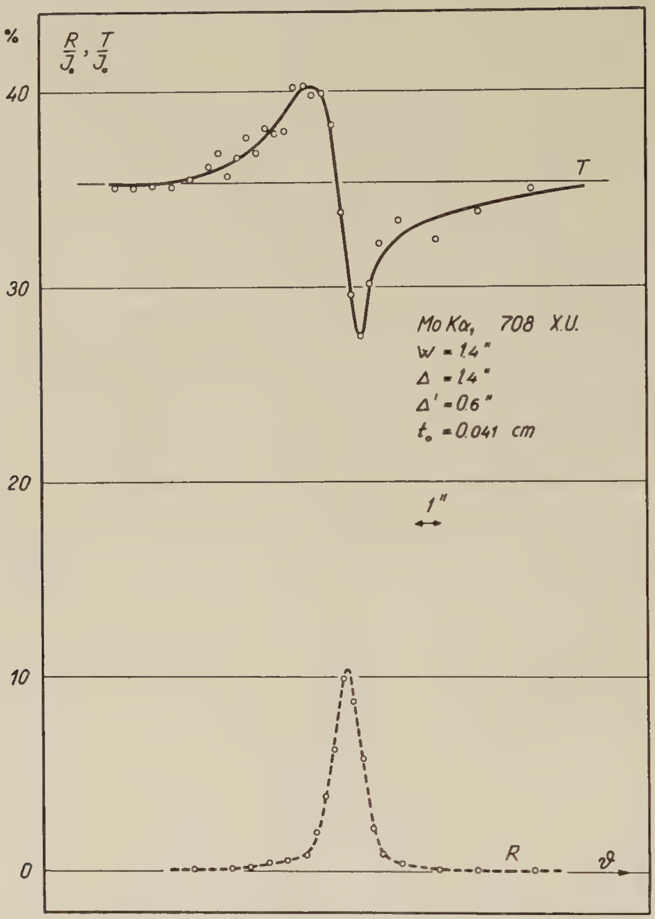

Fig. 6. Experimental curves. A comparison with Fig. 5 shows how the curves are affected by crystal defects.

When the angular coordinates y and l are converted into seconds of arc, the following relation is applied:

$$\vartheta - \vartheta_B = 0.286'' \cdot y_n = 0.219'' \cdot y_p = 1.18'' \cdot (l+1).$$

The calculated intensity curves, R_L and T_L, are shown in Fig. 4.

The theoretical reflection and transmission curves, R and T, were obtained from the curves R_L and T_L, combined with the intensity distribution from the monochromator crystal by graphical integration. The curves are shown in Fig. 5.

A comparison between Figs. 4 and 5 shows how the reflection and transmission curves, R_L and T_L, are affected by the angular width of the incident beam. The curve structures are broadened and flattened. The full width of the reflection curve R_L is 0.48″, whereas that of R is 0.8″. The curves R_L and T_L intersect, whereas R and T do not.

Comparison between theory and experiment

If we compare the theoretical reflection and transmission curves and the experimental ones for Mo $K\alpha_1$ (Figs. 5 and 6), we find that the latter have been broadened to a greater extent than is accounted for by the theoretical angular distribution of the incident intensity. This discrepancy may be explained by slight imperfections in the crystals used. If the orientation of the crystallites in the monochromator crystal varies slightly, this must cause an angular widening of the beam incident on the analyser. As the theoretical width of this beam is very small, this widening must be of relatively large significance [much larger than for Cu $K\alpha_1$ radiation and the (211) planes of calcite (2)]. This will lead to additional broadening of the curves. The monochromator crystal used had also been used earlier in an investigation of the rocking curve for the (655) planes of calcite. On that occasion the smallest experimental value for the full width of the rocking curve at half maximum intensity was 1.0″, and the calculated value 0.7″ (4).

Defects in the analyser crystal would affect the curve structures in a similar way.

The integrated reflection power will only be affected by imperfections of the analyser. These will cause an increase of the effective absorption and consequently a decrease of the integrated reflection power. But since the radiation is hard and the crystal thin, it can be expected that small imperfections will be of only slight significance here. The good agreement obtained confirms this.

Because of the general similarity of the curve structures and the good agreement for the integrated reflection power, it seems justified to say that qualitative agreement between theory and experiment has been obtained.

Acknowledgements

I thank my teachers, Professor AXEL E. LINDH and Professor PER OHLIN, very warmly for their interest and encouragement in this work. I also wish to thank Docent GÖSTA BROGREN, who introduced me into this part of X-ray physics.

Institute of Physics, University of Uppsala, Sweden, September 1953.

REFERENCES

1. G. BROGREN, Arkiv för fysik *3*, 507, 1951.
2. G. BROGREN and Ö. ADELL, Arkiv för fysik *8*, 97, 1954.
3. —— Arkiv för fysik *7*, 1, 1953.
4. G. BROGREN, Arkiv för fysik *6*, 479, 1953.
5. R. W. JAMES and G. W. BRINDLEY, Phil. Mag. *12*, 104, 1931.
6. H. HÖNL, Zeitschr. f. Phys. *84*, 1, 1933.
7. —— Ann. der Phys. *18*, 625, 1933.

Tryckt den 7 augusti 1954

Uppsala 1954. Almqvist & Wiksells Boktryckeri AB

ARKIV FÖR FYSIK Band 8 nr 9

Communicated 14 April 1954 by Manne Siegbahn and Bengt Edlén

Photo-electric mass determinations in nuclear emulsions

Part III. Description of the new experimental arrangements

By S. v. Friesen and L. Stigmark

With 5 figures in the text

Technical improvements

The value of a new method of making accurate physical measurements does not depend solely upon the precision attainable. It is quite often of importance that the amount of work involved in reaching the accuracy should be kept within reasonable limits. Parts I and II of this paper deal with questions of accuracy in photo-electric mass determinations. The present part will be devoted to means of reducing the time and work required in order to attain the desired precision.

With our original experimental arrangements[1] tracks of slow charged particles could be measured at a rate of about 1,400 microns per hour. In order to increase this rate and to make the measurements less tiring, several improvements have been introduced. They are mainly as follows:

1. A Leeds and Northrup Speedomax Recorder, Type G, has been substituted for the Spot galvanometer as a means of registering the current from the photo-multiplier tube.
2. The x- and y-motions of the stage of the Leitz BS 48 microscope have been provided with micrometric adjustments to facilitate the alignment of the image of the track in the slit.
3. A plane-parallel glass plate has been placed in the beam of light inside the microscope tube in order to make it possible to switch easily from the track to the background, as described by Kristiansson (Part I p. 311).
4. A green glass filter has been mounted between the microscope lamp and the condenser in such a way that it can be swung out of the beam of light by pressing a lever. This filter reduces the intensity to a comfortable level for the visual observation of the track.

The improvements have made it possible to proceed at a rate of 3,800 microns per hour without undue fatigue.

Fig. 1 shows the modified Leitz microscope and the recorder. To the left of the microscope the synchronous motor can be seen, which was used in the investigation

---

[1] S. v. Friesen and K. Kristiansson, Ark. f. Fysik *4*, nr 35 (1952).

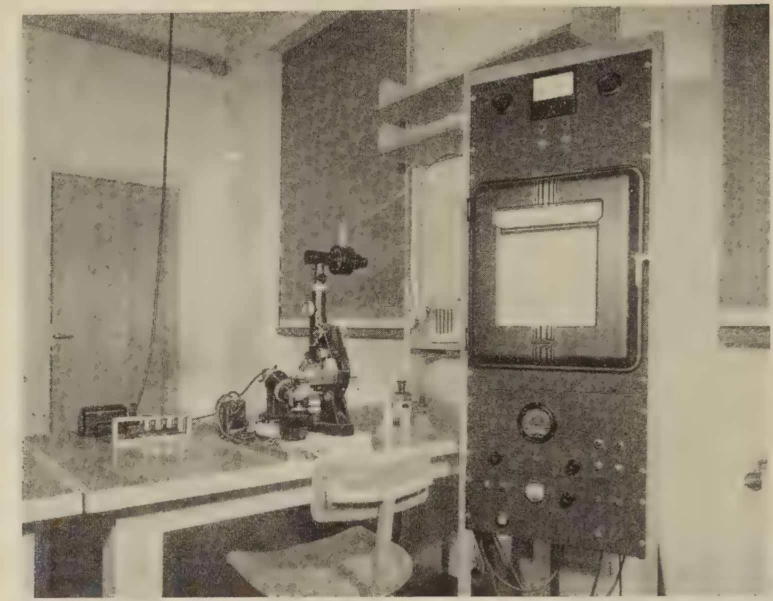

Fig. 1. Experimental arrangement for photo-electric mass-determinations.

of the background (Part II p. 305). Fig. 2 is a recording of the measurement of 1,400 microns of a proton track, 4,000 microns from the end of its range.

In Fig. 3a a schematic representation is given of the recording of a single 30 micron section of a track in order to illustrate the course of the measurements. With the plate on the microscope stage the image of the track is focussed and brought to fall on the middle of the slit. When the mirror, by means of which the slit has been watched, is turned aside, the pen of the recorder moves from its resting position A_1 to the new position B_1. When the green glass filter is removed by pressing the lever the pen moves to C_1 which corresponds to the amount of light passing through the slit with the track in place. The filter is then returned to its original position, and the background to one side of the track is moved into the slit by turning the plane parallel glass plate one notch. When the lever is pressed again the reading D_1 is obtained. The same procedure is repeated with the background from the other side of the track. The pen moves to D_2. Finally, a new reading is taken with the track back in the slit. This results in a recording C_2. With the green glass filter we get B_2 and, finally, when the mirror is allowed to cut the beam of light again we get the zero-value A_2.

We obtain values for the mean track width by measuring the diagram and forming the expressions

$$\frac{A_1 D_1 - A_1 C_1}{A_1 D_1} \quad \text{and} \quad \frac{A_2 D_2 - A_2 C_2}{A_2 D_2}.$$

A_1 and A_2 are practically always identical, and the same applies to C_1 and C_2. For this reason it is convenient to mark the mean of D_1 and D_2 directly on the diagrams. A special tool, ruled on a sheet of Perspex, enables the direct reading of the ratio, thus resulting in a considerable gain of time.

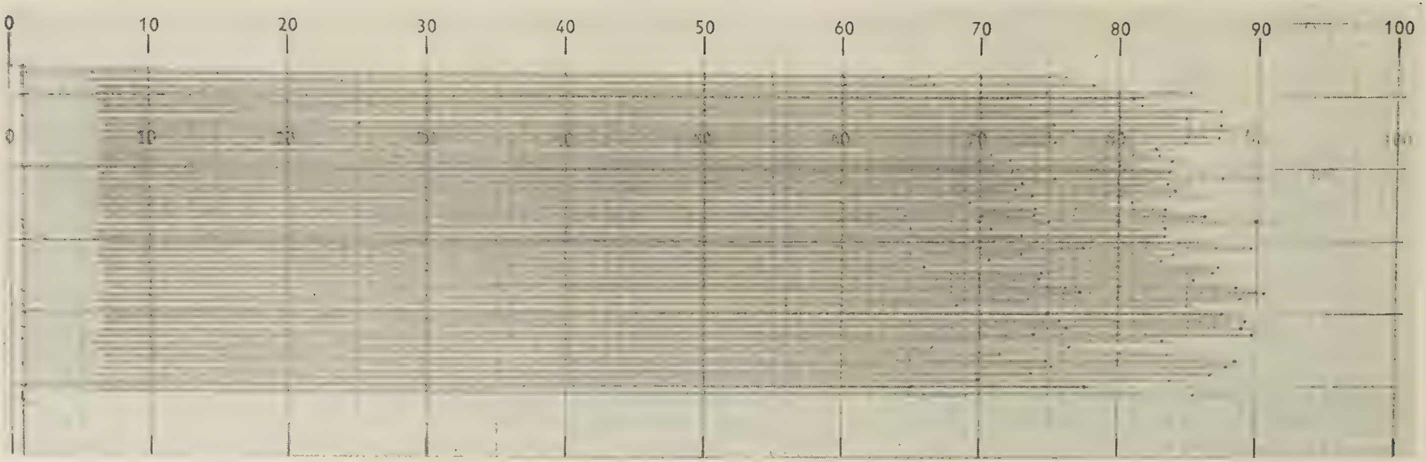

Fig. 2. A recording of 1,400 microns of a proton track 4,000 microns from the end of its range.

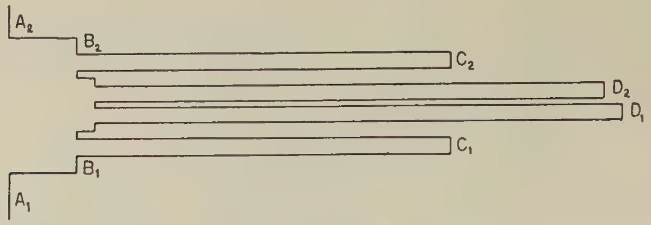

Fig. 3. Schematic representation of the measurement of a single 30 micron section of a track.

The electronic equipment[1]

The electronic equipment for the measurement of mean track widths in photographic emulsions consists of a multiplier unit directly attached to the microscope, a stabilized high voltage supply for the different electrodes of the multiplier tube, and a balanced DC-amplifier connected to the Leeds and Northrup Speedomax recorder. The above equipment is supplemented by a calibration unit, the purpose of which is to ensure that no overloading of the DC-amplifier occurs and also to serve as a check of linearity, which will be described later on.

The multiplier unit

As already mentioned the multiplier tube RCA 1P21 is directly attached to the microscope in a box containing all necessary resistors for a voltage divider from which the dynode voltages are obtained. All resistors in the voltage divider are equal (47 kohm) except the last one, controlling the voltage between the last dynode and the collector anode of the multiplier tube. This resistor can be changed, and the resistance value might be adjusted for minimum dark current, the linearity between the light flux and the output current of the multiplier tube being thus preserved. The value, however, is not very critical. Owing to the fact that the available light flux is relatively high the multiplier tube can be operated with fairly low dynode voltages. The total voltage across the voltage divider is normally of the order of 500 volts. The gain of the multiplier has thus a moderate value, and consequently the shot-noise component of the output current will be of no importance. The output current from the collector-anode passes a suitable resistor at the input end of the DC-amplifier.

The stabilized high-voltage supply

To maintain a constant gain of the multiplier tube a well stabilized power supply is necessary. A power supply fulfilling high demands of stability has been constructed, the diagram of which will be seen in Fig. 4. The high voltage from one of the secondary windings of transformer T_1 is rectified in a single diode 2 X 2 followed by a resistance-capacitance filter. The positive side of the rectified voltage is grounded through a series valve 6J7G. The negative side is directly connected to the output terminal of the power supply. The available voltage drop between this output terminal and

---

[1] Designed by L. S.

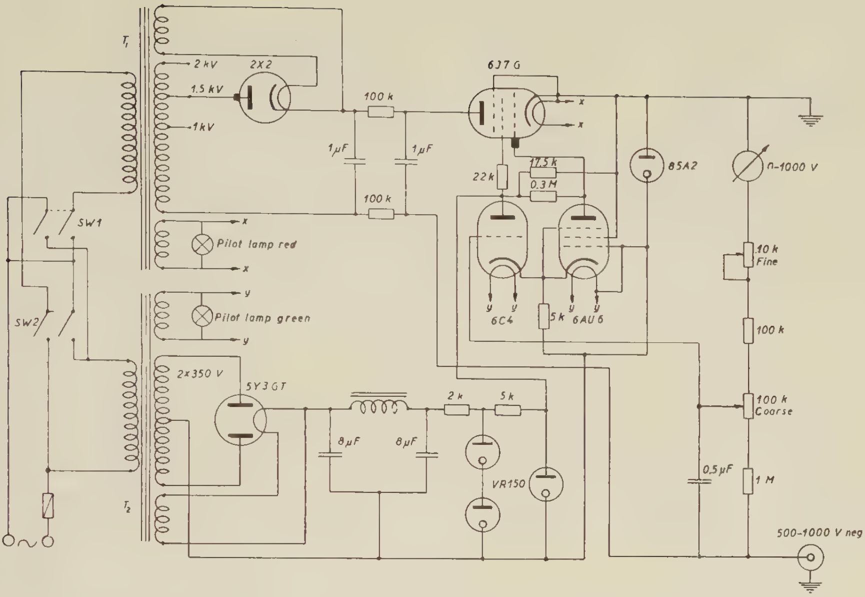

Fig. 4. Diagram of the stabilized power supply for the photo-multiplier tube.

ground will be determined by the voltage drop in the series valve. The amount of this voltage drop is controlled by part of the output voltage, taken between the 100 kohm potentiometer and ground. Any changes in the output voltage will be amplified in a direct-coupled amplifier, using one 6C4 and one 6AU6, and finally fed to the control grid of the series valve. The triode 6C4 acts as a cathode-follower, and the pentode 6AU6 works as a grounded grid amplifier. All necessary voltages for the amplifier section and also the screen-grid voltage of the series valve 6J7G are obtained from a low voltage rectifier, containing the transformer T_2, the full-wave rectifier 5Y3G and its associated π-filter section. The ripple filter is followed by a double voltage stabilizer using three valves VR150. The output from this low voltage section will be a constant voltage of about 150 volts. The 85A2 valve maintains the lower end of the DC-amplifier at a constant voltage with respect to ground, thereby acting as a voltage reference valve. The negative high voltage available at the output terminal of the power supply can be adjusted by setting the 100 kohm potentiometer (coarse control) and a 10 kohm variable resistor (fine control). The voltage range is about 500–1,000 volts, covering the normal working conditions of the multiplier tube. A microammeter (0–100 μA) is connected in series with the resistor chain between the terminals of the output voltage. A suitable shunting resistor of the instrument gives full scale reading at 1,000 volts. All resistors except those in the filter section of the high voltage rectifier are wire-wound in order to ensure stable operation. To prevent a possible flash-over in the series valve 6J7G, it is of importance that the tubes of the control section are functioning before the high voltage is applied to the series valve. The main switches SW_1 and SW_2 are therefore arranged in such a manner that the low voltage rectifier always starts first, independent of the sequence in which the switches are being manipulated. The

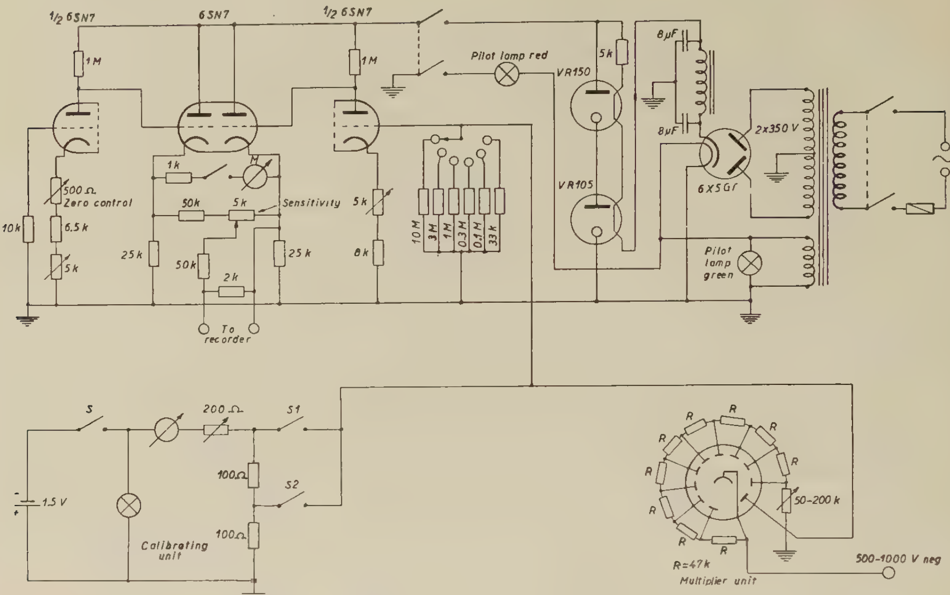

Fig. 5. Diagram of the balanced DC-amplifier.

power supply may be loaded with a current of about 2 mA. The constancy of the output voltage will be about ± 0.2 volts at a variation of ± 10 per cent of the main voltage. The ripple content of the output voltage is negligible.

The DC-amplifier

The DC-amplifier consists of two double-triodes 6SN7, connected in a balanced circuit in order to provide low zero-drift. The grid of one of the input triodes is maintained at a constant potential while the other input grid is connected via a switch to a suitable resistor giving a negative voltage drop with respect to ground, controlled by the output current from the multiplier tube, as will be seen in the diagram Fig. 5. The value of the grid resistor should be chosen with regard to the available current from the multiplier tube, in such a way that maximum photo-current will not cause a voltage drop exceeding about 1 volt, this being a safe limit of perfect linearity between photo-current and output voltage from the amplifier. The input triodes employing negative feedback are directly coupled to the control grids of the output triodes, which are working as cathode-followers. With no input voltage applied to the amplifier the potentials at the cathodes of the output tubes will be equal when the amplifier is properly balanced. This balancing is achieved by a variable resistor (zero control) in one of the cathode leads of the input valves and indicated by zero-reading of the meter M. The Speedomax recorder is coupled to the cathodes of the output valves via a variable voltage dividing network, which may be adjusted (sensitivity control) until a suitable reading is obtained at the recorder. Because of the high sensitivity of the recorder (5 mV full scale deflection) the final voltage applied to the recorder will be much less than the input voltage of the amplifier, which might therefore be more adequately described as an impedance transforming device. The power supply of the amplifier consists of a full-wave rectifier. The filter section is followed by two series connected voltage stabilizers giving a constant voltage of about 250 volts to the amplifier valves. Working with input voltages to the amplifier of the order of 1 volt no stabilization of the heater currents has been found necessary in order to avoid zero-drift. After a heating period of about half an hour this drift will have become negligible. Only if the voltage-sensitivity of the amplifier has to be increased 10 or 20 times, will it be advantageous to introduce a constant-voltage transformer for the heaters. Known voltages can be applied to the input terminals in order to check the working conditions of the amplifier. These voltages are obtained from a calibrating unit consisting of a battery from which a constant current of 5 mA passes through two resistors of 100 ohms each. With the contact S_1 depressed (input 1 volt) the sensitivity control of the amplifier is adjusted just below full scale reading of the recorder, thus indicating the minimum allowable setting of the sensitivity of the amplifier. This ensures that the limit of linear operation of the amplifier cannot be exceeded. At the same time the linearity can be checked by depressing contact S_2, which gives an input voltage of 0.5 volt. After the above adjustment the grid resistor at the input of the amplifier is given such a value that the maximum voltage drop caused by the photo-current will give a suitable reading at the recorder.

All units of the electronic equipment are mounted in a standard rack, as shown in the photograph, Fig. 1. From top downwards: high voltage supply, Speedomax recorder, DC-amplifier and calibrating unit.

Summary

A description is given of the apparatus used for photo-electric mass determination at Lund.

Department of Physics, University of Lund, February 1954.

Tryckt den 23 september 1954

Uppsala 1954. Almqvist & Wiksells Boktryckeri AB

ARKIV FÖR FYSIK Band 8 nr 10

Communicated 10 February 1954 by AXEL E. LINDH and GUNNAR HÄGG.

The resolving power of a large bent crystal spectrograph

By ARNE ELD SANDSTRÖM

With 10 figures in the text

Abstract.—Some line groups have been recorded with a large bent crystal instrument and a Geiger counter. The X-ray tube is described as well as devices for its adjustment relative to the crystal. To study how the diffraction pattern of the crystal and other broadening effects combine with the natural line width, a special apparatus was built for scale model experiments. The results confirm the validity of the equation

$$W_m^2 = W_\lambda^2 + W_c^2,$$

W_m, W_λ, and W_c being the full widths at half maximum of the recorded line, the natural line, and the diffraction pattern, respectively. By means of this equation and comparison with two-crystal measurements the resolving power of the bent crystal instrument has been estimated as regards ideal conditions as well as in practice. The widths of some L- and M-series lines are given.

The spectrograph has already been described in a former paper [1]. In the first instance it was built for the purpose of studying the details of X-ray absorption spectra. As it is often essential to decide whether a very close structure really can be resolved, it was considered necessary to gather at least some knowledge as to the resolving power of the instrument. Before discussing this, some experimental details which were omitted in the first paper will be described.

The X-ray tube

The X-ray tube has to be mounted inside the vacuum-tank of the spectrograph which to a certain degree complicates the cooling system. Cross-sections of the tube are reproduced in Fig. 1. It has a brass body, *1*, with a flange, *2*, for clamping it to the tube carrier, which was described and illustrated in our first paper [1]. The target is mounted on a heavy water-cooled copper cylinder, *3*, clamped to the body of the tube by means of three screws, *4*. The cathode is fixed to a porcelain insulator, *5*, rigidly kept in position by means of a slit ring, *6*. It consists of a brass tube, *7*, attached to the inside of the porcelain insulator, *5*, by means of a flange in its lower end and a ring-nut in its upper end. A flat spring between this nut and the flange of the insulator allows for the thermal changes. In the upper end of the tube, *7*, a threaded brass cylinder, *8*, can be set so as to give the desired distance between filament and target. The cylinder, *8*, carries one of two nickel-silver rods, *9*, while the second rod passing through a hole in the same cylinder is attached to a small

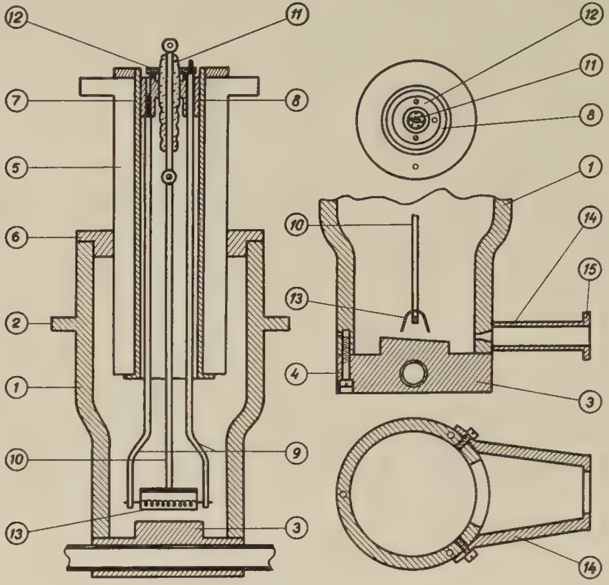

Fig. 1. The X-ray tube. Scale 1 : 3.

ring, *12*. This ring is insulated from the rest of the cathode by a sheet of mica. The two rods *9* serve as supports for the filament and as conductors for the filament current. A third rod, *10*, is fixed to a glass-sealed conductor, *11*. It carries a reflector, *13*, in the form of a parabolic cylinder and kept in position relative to the rods, *9*, by means of a sheet of mica joined to the end of the brass tube *7*. The filament consists of a cylindrical platinum spiral with oxide coating. It is placed 9 mm from the centre of the target and 6 mm below the bottom of the reflector. The purpose of the latter is to concentrate the cathode rays to a narrow linear focus-spot.

The filament voltage is applied between the cylinder, *8*, and the ring, *12*. These two points as well as the top of the glass-sealed connection *11* are connected with the insulated conductors in the end-wall of the spectrograph-tank by means of three rubber-coated cables for 30 kV.

The X-ray beam emerges through a window in the lower part of the tube. On the inside this window has a height of 2 mm. As seen from the target, its angular width is 60°. To prevent the X-ray beam from spreading in undesired directions this window opens on a small flat box, *14*. At the end facing the crystal this box has a flange, *15*, for the mounting of diaphragms limiting the height of the X-ray beam.[1]

Since for large glancing angles the reflected beam passes close to the X-ray tube, the dimensions of the latter put an upper limit of 84° to the glancing angle.

The dimensions of the spectrograph combined with the mounting of the tube inside the vacuum-tank complicate an experimental determination *in situ* of the most favourable working conditions. Accordingly a special sealed X-ray tube was made with the same target-cathode arrangements and directly connected to the pumping system. With this tube the height of the focus-spot was determined as a function of the distance between the electrodes and as a function of the quotient between the reflector voltage, V_{refl}, and the accelerating voltage, V_{acc}. The most favourable distances were found to be those quoted above.

---

[1] Compare Fig. 10.

For accelerating voltages exceeding 10 kV the focusing is comparatively good even when the potential of the reflector is the same as that of the cathode. For voltages below 10 kV it appears necessary, in the first instance, to apply a lower voltage to the reflector than to the cathode. The focusing effect is small for $V_{\text{refl}}/V_{\text{acc}} < 1.15$. For increasing $V_{\text{refl}}/V_{\text{acc}}$ the width of the linear focus decreases until the emission disappears. Regardless of the accelerating voltage this happens for $V_{\text{refl}}/V_{\text{acc}} \approx 1.55$. However, running the original X-ray tube in the vacuum spectrograph we found that, contrary to what was expected, the intensity did not increase with decreasing width of the linear focus, while the filament current had to be increased to prevent the emission from falling below its former level. Evidently the sharp focus in one direction is accompanied by a fan-like spread of the cathod rays along the plane of symmetry of the reflector. Mapping of the electric field by means of an electrolytical phantom confirmed the above results. The application of end-pieces to the reflector did not improve these conditions. In practice, therefore, the tube was always run with the reflector on the same potential as the cathode.

The high voltage set

When recording spectrograms by means of counters a very stable X-ray intensity becomes a necessity. Accordingly the tube voltage has to be maintained at a constant level. This was ensured by equipping the high voltage set with a stabilizing circuit as developed by OHLIN [2]. The maintenance of a constant emission was also found to be troublesome, although a set of accumulators was used for feeding the filament. The fact that the cathode has to be insulated for 25 kV complicates matters. The difficulties were met by utilizing a modified form of the stabilizing circuit described by LE MIEUX and BEEMAN [3]. Both circuits have been found to work satisfactorily.

Naturally the alternating voltage across the filament terminals will increase the amplitude of the low frequency superimposed on the accelerating voltage. The filament voltage is 1.5 to 2.0 volts. The A.C. component of the accelerating voltage is at least twice as large. It increases with the load, but does not exceed 0.1 per cent of the accelerating voltage.

The positive terminal of the high voltage set was earthed. When not the same as that of the cathode, the reflector voltage was taken from a small high tension set built for television purposes.

The counter

The spectrograms were recorded by means of an alcohol quenched argon counter of a type which during the last few years has been put to extensive use in this laboratory [4]. It was made from a brass rod with a square cross-section having a cylindrical central bore of 20 mm. The anode consisted of a 0.15 mm stainless steel thread stretched between two small springs inside the pyrex cones in both ends of the counter. The dimensions are given by the scale in Fig. 2. The X-rays entered through a window on one of the plane sides. In most instances this window had a circular aperture of only 2 mm. When recording details of low intensity, such as absorption spectra, apertures were used 5 to 20 mm long and 2 mm wide. Mostly thin cellulose

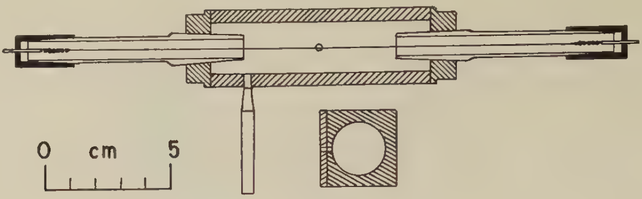

Fig. 2. The counter.

acetate foils ("Zapon-lack") were used as covers, but a new plastic, mylar, was found to be still better [5]. With very thin window covers it becomes necessary to fill the counter *in situ* inside the vacuum-tank. When of the oblong type the window was always parallel to the anode. The counter was mounted with its anode parallel to the spectrograph slit on the small bracket provided for this purpose [1]. A Neher-Pickering quenching circuit was placed immediately on the outside of the vaccum-tank. Screened cables were used for all electrical connections.

Position and adjustment of the X-ray tube

In the present case the geometry of the spectrograph necessitates a short distance between the X-ray tube and the crystal. This position has also been used by the author [6] and others [7] while employing photographic recording. In that case a long linear focus-spot not too distant from the crystal centre ensures that a sufficiently wide wave-length can be exposed with approximately constant intensity while the crystal and the X-ray tube are in fixed positions.

The conditions will be quite different, if the spectrograms are recorded through intensity measurements point by point. In this case a point source on the Rowland circle would be preferable. As this was impracticable because of the geometry of the instrument, a linear focus-spot of up to 20 mm was used. The distance between the focus-spot and the centre of the crystal was 142 mm. The length of the focus-spot should be sufficient for irradiating the whole crystal surface. During some test runs the intensity appeared to increase when the focus-spot was shortened. However, a short focus-spot necessitates a far sharper adjustment of the X-ray tube to the desired Bragg angle.

As mentioned in the detailed description of the spectrograph [1] the angular setting of the X-ray tube can be done from the outside. To determine the right position, the intensity was recorded with the tube on a series of points to both sides of the true Bragg angle. Fig. 3 reproduces the recorded intensities as a function of the angle. The curves cover most of the angular region of the spectrograph. Evidently, the region of constant intensity is rather narrow, 15 minutes being the limit of the allowable deviation from the true Bragg angle. In practice, when registering a spectrogram, the tube has to be reset at least once for every whole turn of the precision screw.

The height of the crystal being 2 mm and the X-ray beam being limited by diaphragms of the same height, the tube has to be comparatively accurately set in a plane through the middle of the crystal surface and the counter window, if the beam is to strike the crystal with full intensity. It turned out that the mechanical rigidity of the movable tube stand was insufficient for making this adjustment once and for all. To meet this difficulty the arrangement for moving the X-ray tube along with the crystal holder (compare the detailed description of the spectrograph [1]) was

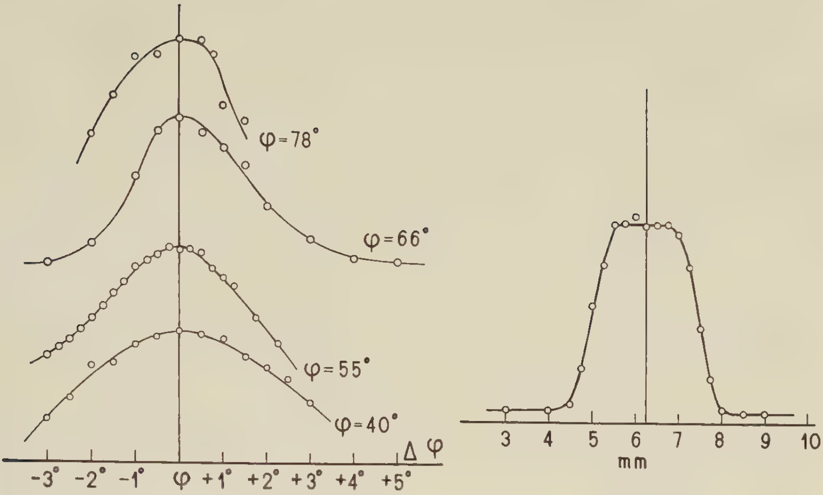

Fig. 3. Diagram I describes how the intensity of the reflected radiation varies with the position of the X-ray tube relative to the true Bragg angle. Diagram II describes how the intensity varies with the position of the tube relative to the direction of spectral distribution. The vertical lines indicate the positions which have been considered most suitable.

slightly changed so as to allow a certain degree of adjustment in a direction parallel to the axis of rotation of the crystal. The track carrying the tube stand was made to turn around a vertical axle in the end away from the X-ray tube, the other end resting on a couple of roller-bearing balls. By means of a small screw working on the end near the X-ray tube the track can be turned through a small angle. A spring keeps the end of the track in close contact with the screw. The latter is turned from the outside by means of a flexible axle and one of the vacuum-tank manipulators already described [1].

The intensity was recorded point by point, the position of the X-ray tube being changed sideways in small steps. A curve corresponding to such a set of positions is reproduced in Fig. 3. This curve has a region indicating constant intensity. Besides, it offers the possibility of estimating how far off from the ideal position the tube can be moved without seriously affecting the intensity of the reflected beam. With the present instrument the evaluation of wave-lengths has to be based on relative measurements, and consequently the readings from the scale and the drum of the precision screw moving the slit and counter have to be evaluated by means of accurately determined X-ray lines. Both for this reason and for studying the properties of the instrument several line groups were recorded in the first to the fourth order. Some examples are reproduced in Figs. 4 and 5.

The resolving power

It is most interesting to note that the two lines in the curve of the molybdenum $L\alpha_1\,\alpha_2$ group in Fig. 5 appear on the verge of being resolved. If we compare this line group to corresponding groups recorded by means of a double crystal spectrometer, for instance the rhodium $L\alpha_1\,\alpha_2$ group reproduced by RANDALL and PARRATT [8], we recognize clearly that in the angular region above 35° the resolution of the

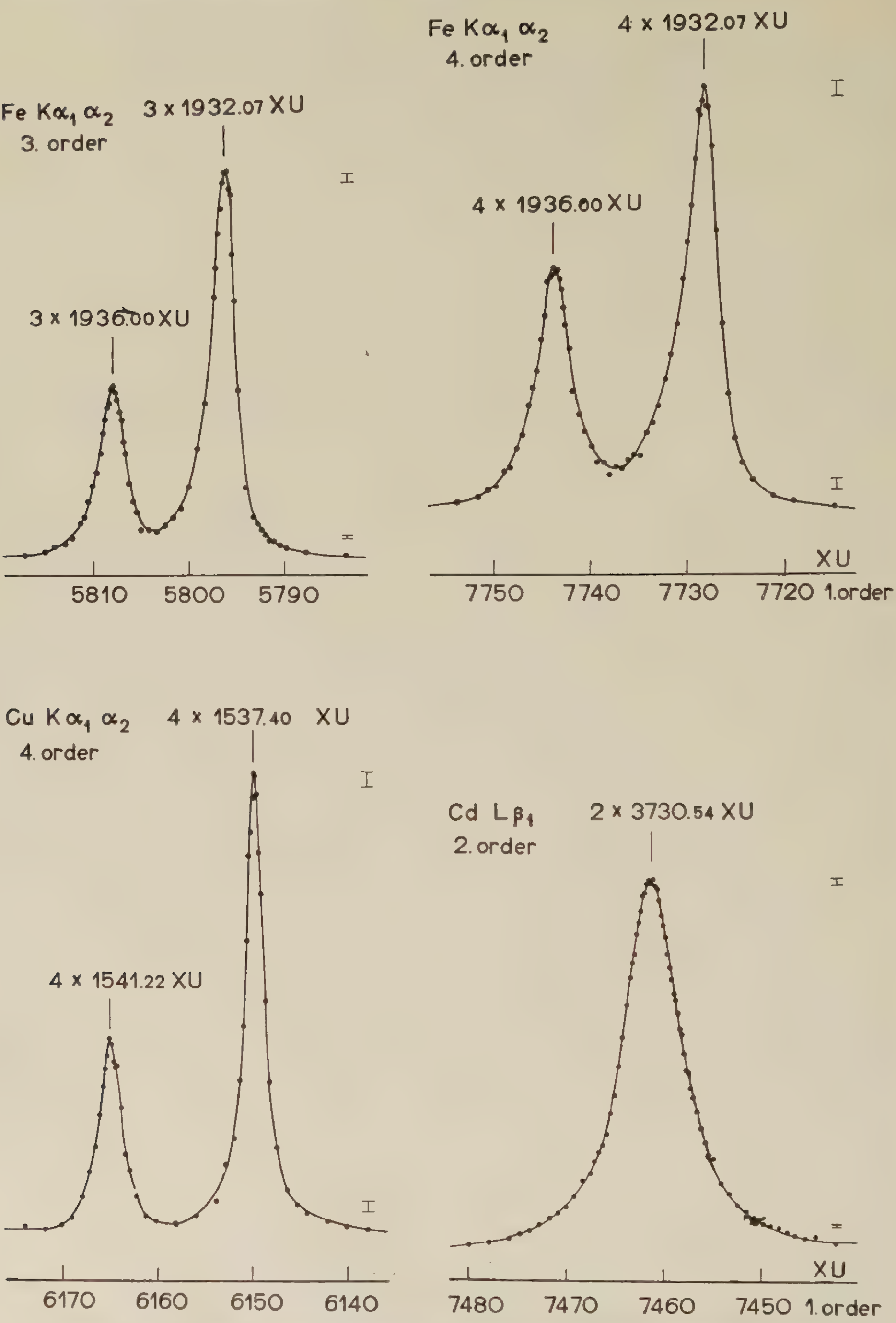

Fig. 4. Some $K\alpha$ and $L\alpha$ lines as recorded with the large bent crystal spectrograph.

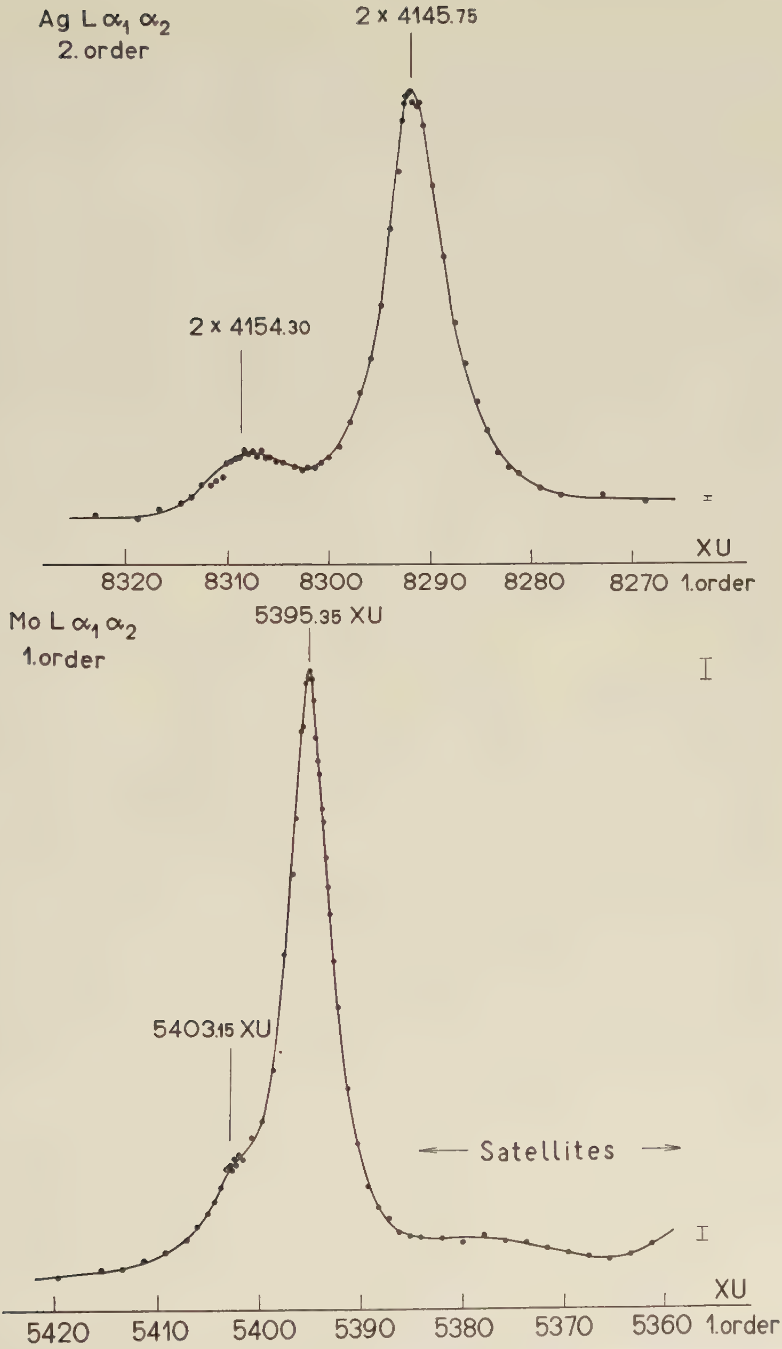

Fig. 5. The $L\alpha$-groups of silver and molybdenum as recorded with the large bent crystal spectrograph.

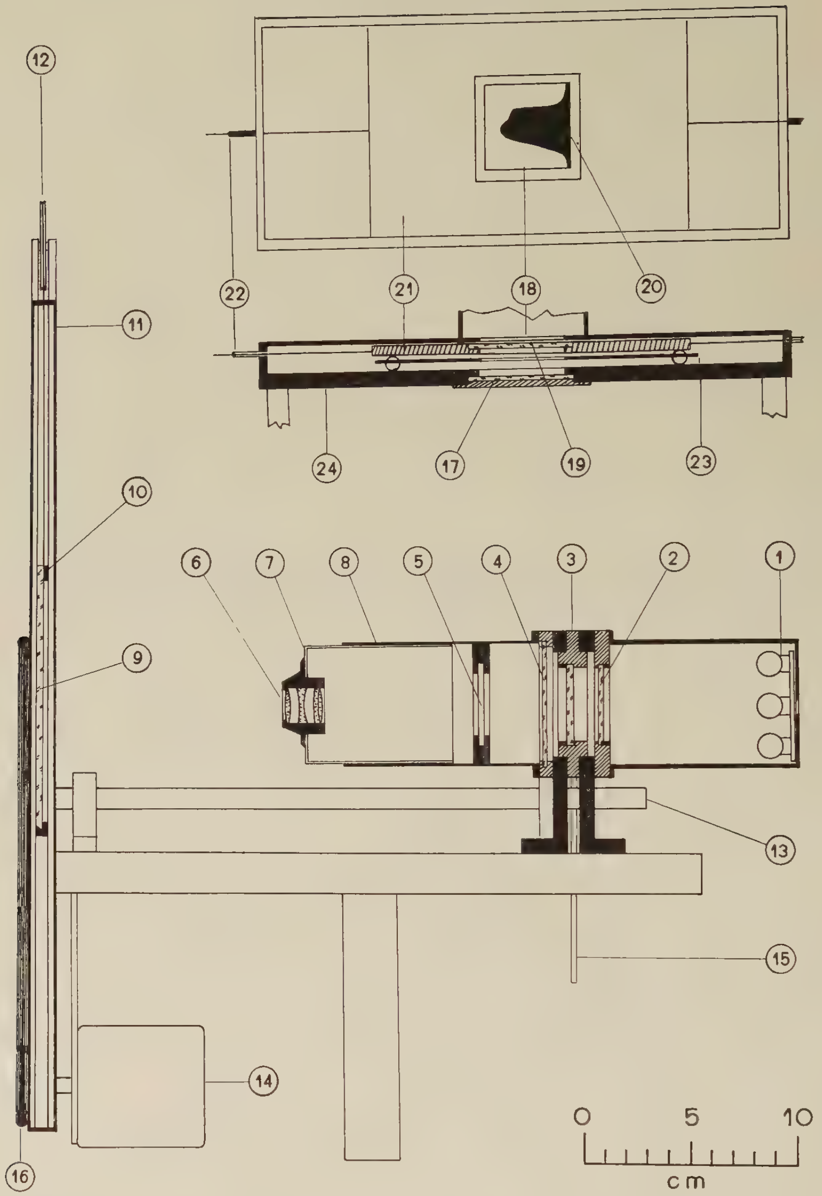

Fig. 6. The principal elements of the apparatus for scale model experiments on line shape and resolution. Numbers 1–16 belong to the main instrument, numbers 17–24 to the auxiliary machine for making the diaphragms.

large bent crystal spectrograph appears to be quite as good as that of a two-crystal instrument. It should be observed that the α_1 and α_2 lines of rhodium are far easier to resolve than those of molybdenum.

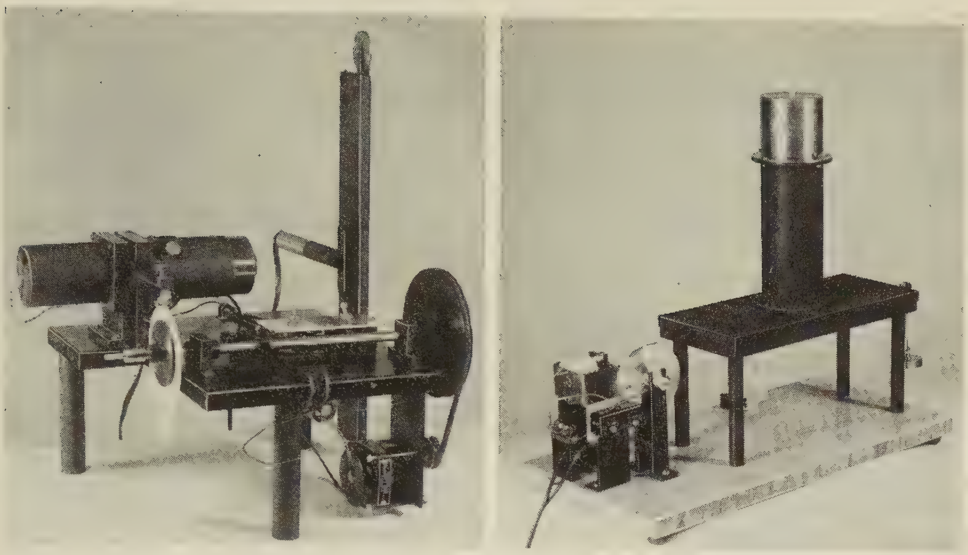

Fig. 7. The apparatus for scale model experiments on line shape and resolution. The picture to the left shows the main instrument, that to the right the auxiliary machine for making the diaphragms.

Apart from the geometrical conditions, the resolution of an X-ray crystal spectrograph is limited by the finite resolving power of the crystal. The latter is determined not only by the diffraction pattern but also by the number and size of irregularities in the crystal, presumably in its surface. Given good samples of crystals these irregularities can be diminished considerably by etching [9].

At present no means of studying experimentally the diffraction pattern of a single crystal exists although the two-crystal spectrograph enables us to determine at least the width of this pattern for pairs of crystals. Theoretically the diffraction pattern of a single crystal can be calculated for every wave-length and order of reflection. The general methods of these calculations are to be found in text books [10]. PARRATT [11] has published diffraction patterns for calcite at various Bragg angles.

In order to understand how all plausible factors affect the resolving power, it becomes necessary to study how the diffraction pattern combines with the geometrical power of the instrument and with the function describing the intensity variations across a spectral line. It would be far more valuable if we could investigate this interaction not only for an ideal case but also with due regard for the influence of crystal irregularities. Even the complicated shape of the diffraction pattern by itself makes direct calculations difficult. It ought to be possible, however, to gather some information by means of an instrument reproducing under control the intensity curve resulting from the addition of successive overlapping diffraction patterns.

An experimental study of the effect of overlapping

An instrument was built for the purpose outlined above. Its construction is shown in Fig. 6. The light source, *1*, consists of a ring of four small electric bulbs. A polaroid film, *2*, is clamped in front of the light source. A second polaroid, *3*, is mounted in a ring, which can be turned around the optical axis of a lens, *6*, by means of a lever (easily recognized on the left picture in Fig. 7). In this way the intensity of the transmitted light is controlled by the position of the lever. A ground glass plate, *4*, serves to diffuse the light before it passes through a diaphragm, *5*. With a good camera lens, *6*, an image of the diaphragm, *5*, is projected on to a photographic plate, *9*. For focusing purposes the lens, *6*, is mounted on the frontal end of a cylinder, *7*, which can be moved back and forth in another cylinder, *8*.

The photographic plate is placed in a frame, *10*, sliding in a vertical direction inside a closed box, *11*. The latter has a window 40 × 16 mm facing the lens. The height of this window is just sufficient to allow the image of the diaphragm to fall on the photographic plate. The frame, *10*, is hung on a cord running over a small wheel, *12*, down to a drum on a shaft, *13*, driven by a small motor, *14*. These latter details are easily recognized on the left picture in Fig. 7. *16* is the belt between the motor and the shaft.

The diaphragm, *5*, consists of a photographic plate exposed in such a way as to have a density variation in one direction corresponding to the pattern to be employed. The luminosity of its image, projected on the photographic plate, *9*, varies in the direction of movement of the plate. The diaphragms can be made in the following way. A photographic plate, *17*, is placed facing an illuminated window, *18*. A glass plate, *19*, can be drawn across this window in the direction of the arrow. It is partly covered by a patch of black paper, *20*, limited by a curve roughly resembling that of the desired diffraction pattern. The device for moving the plate, *19*, consists of a frame, *21*, drawn by a wire, *22*, running over a drum on the axis of a small synchronous motor counteracted by a weight. The frame, *21*, rests on four guided steel balls, *23*. The whole arrangement is enclosed in a light-tight box, *24*. In Fig. 6 the light source illuminating the window, *18*, is indicated by its lower part only. A photograph of the complete arrangement is reproduced to the right in Fig. 7. At right angles to the direction of movement the density of the plate, *17*, will vary as determined by the shape of the black paper, *20*. By exposing a series of plates under varying conditions of illumination diaphragms were made transmitting light beams approximately representing the diffraction patterns for calcite as calculated by PARRATT [11]. To these were added one diaphragm representing an ideal symmetrical pattern and another shaped as a very narrow slit. The intensity distribution in the transmitted beam was determined by means of a Moll micro-photometer. Some of these records are reproduced in Fig. 8.

In the instrument for scale model experiments (Figs. 6 and 7) the spectral line is represented by an eccentric, *15*, acting upon the lever turning one of the polaroids, *3*. This eccentric is mounted on the same axle as the drum for the string carrying the frame, *10*. An infinitely narrow "line width" can be produced by running an exposure with the polaroid lever in a fixed position. The widths and shapes of the "spectral lines" were recorded by exchanging the frame and photographic plate for a photovoltaic cell in a fixed position. Then each eccentric was run without any diaphragm across the beam. One of these records is reproduced in Fig. 8 (curve 7).

For the evaluation of the photographic plates density marks were made by means of a small electric bulb placed on one side of the box, *11*. Through a rectangular diaphragm light from this bulb is thrown by a prism on to the photographic plate. This part of the apparatus is easily recognized in Fig. 7. A set of marks was made by successive exposures of increasing length, the reciprocity in this instance between

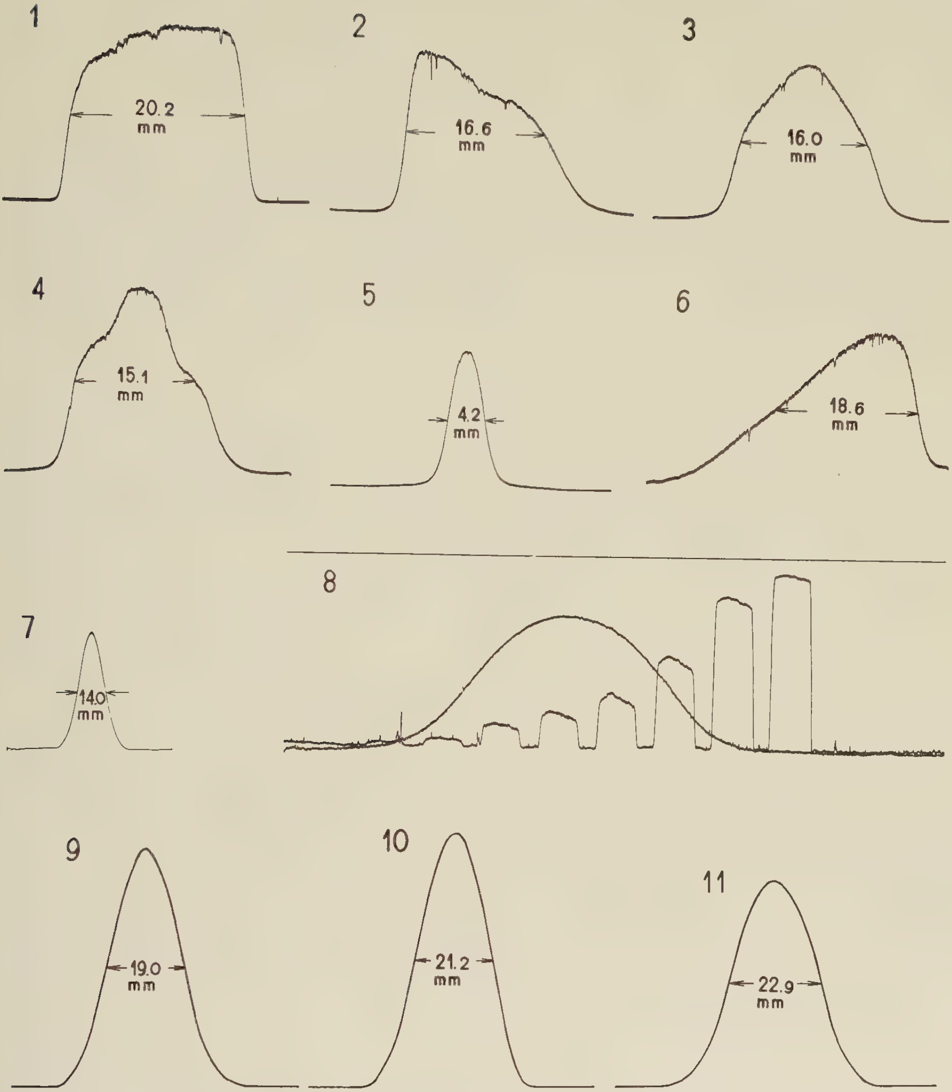

Fig. 8. *1–6* are photometer records showing the intensity distribution in the beam transmitted by the diaphragms in the apparatus of Figs. 6 and 7. Curves *1-4* correspond roughly to diffraction patterns as calculated by PARRATT for calcite. Curve *5* represents a narrow slit and curve *6* an extremely asymmetrical pattern. Curve *7* is the intensity distribution of the "emission line" as produced by the relative positions of the polaroids. *8* is an example of the records of the resulting lines. The curve representing the intensity marks is easily distinguishable from the "line". Curves *9–11* show the intensity distribution, when the "patterns" 2,4 and 6 are combined with the "emission line" 7.

intensity and exposure time having been checked previously by a separate series of tests.

The densities of the resulting photographic plates were determined by means of a Moll micro-photometer. An example is given in Fig. 8. From the curves 9–11 in

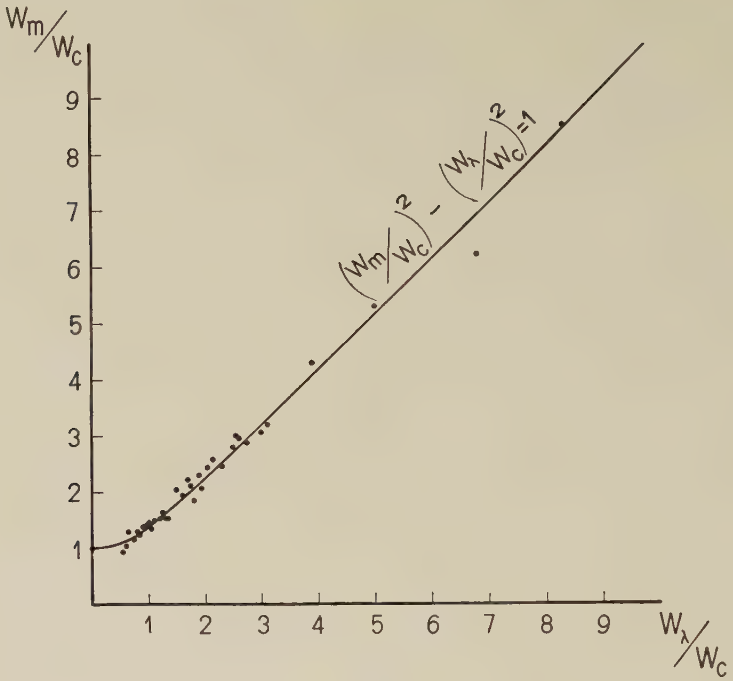

Fig. 9. W_m/W_c as a function of W_λ/W_c.

Fig. 8 we find that, given a finite "natural line width", none of the details of the "diffraction pattern" is reproduced in the "measured line". The same happens in the two-crystal spectrograph, where the rocking curve does not show any trace of the structure of the diffraction pattern. However, in both cases a small asymmetry is apparent [10]. When the "natural line width" is infinitely small the "measured line" appears to be a fairly good reproduction of the "diffraction pattern", the small differences being most probably due to photographic effects. The results can be considered as representing in general the broadening of any line by the diffraction pattern or by geometrical conditions or crystal irregularities.

We shall denote the width at half maximum of the resulting intensity curve by W_m, the width at half maximum of the natural spectral line by W_λ and the corresponding width of the diffraction pattern by W_c. To find a function satisfying all our measurements we plot W_m/W_c as a function of W_λ/W_c in Fig. 9. The points of measurements appear to have a random distribution along an arc of the hyperbola

$$(W_m/W_c)^2-(W_\lambda/W_c)^2=1.$$

The curve in Fig. 9 represents this hyperbola, not the most probable locus of the points of measurements. For practical purposes we have the relation

$$W_m^2=W_\lambda^2+W_c^2. \tag{1}$$

This equation is a well-known formula first derived for combining the diffraction patterns of the crystals in a two-crystal spectrometer [10]. Other formulas have also been applied for that purpose. Many of these can be considered as approximations of eq. (1), valid in certain regions, for instance

$$W_m = W_\lambda + \tfrac{1}{2} W_c, \text{ for } W_\lambda \gg W_c. \tag{2}$$

Parratt [11] has published an empirical equation of unusual form. For small values of W_c his equation gives corrections which do not differ very much from those derived from eq. (2). However, it is impossible to overlook that our results from the scale model experiments are at variance with Parratt's formula. The only possible explanation is that his line widths in the (n, + n) position include some broadening effect which does not appear in his rocking curves.

The ideal resolving power

The resolving power is not limited solely by the diffraction pattern combined with the geometrical properties of the instrument. The effective "combined" diffraction pattern is an uncalculable intensity distribution, where the ideal conditions are influenced by flaws in the crystal, irregularities in the cylindrical surface etc. Nevertheless, it is of considerable interest to know the theoretical resolving power of the instrument. Four factors have to be considered:

1) The diffraction pattern, which can be computed [10], although the numerical calculations are laborious.

2) The focusing defect calculated by Johann [12] to a first approximation.

3) The height of the focus-spot combined with the effective height of the crystal. Both these finite heights cause an overlapping of slightly displaced arcs each one corresponding to a radiation cone having its point somewhere in the focus-spot.

4) The width and height of the detector slit.

All these effects combine according to eq. (1) except, perhaps, the last one. There might be some doubt as to the half width of the focusing defect. In this case the intensity distribution curve is extremely asymmetrical [12]. An asymmetrical pattern was therefore included in the experiments described above. Eq. (1) was found to be valid in this case, too. As the full width at half maximum we will use half the maximum width as calculated by Johann [12]. The uncertainty caused by this approximation will scarcely introduce any error, as for glancing angles larger than 35° the focusing defect is small as compared to the diffraction pattern and other effects.

The third factor mentioned above ought to be made negligible by following the general rule that the geometrical resolving power has to be far higher than the physical resolution. This can be achieved by a convenient arrangement of diaphragms such as that presented in Fig. 10. From the point of view of a good resolution the focus-spot ought to be on the Rowland circle. However, this is impossible from geometrical reasons and the diaphragm system becomes a necessity.

No differences in line widths were observed when the width of the detector slit was changed from 10 to 50 microns. In the latter case the resolution ranged from 18,000 at a glancing angle of 36° to 230,000 at 80°. The counter window limiting the height of the slit was 2 mm in most cases, although an aperture of 5 mm was used occasionally. Thus the curvature of the spectral lines did not diminish the resolution in any observable way.

As regards the $10\bar{1}0$ planes of quartz, the calculated width of the two-crystal

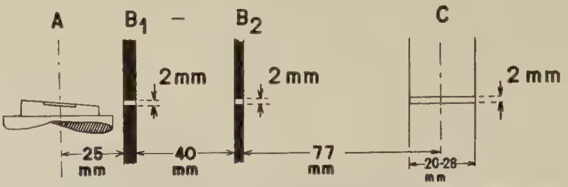

Fig. 10. The diaphragms limiting the X-ray beam in a direction perpendicular to that of the spectral distribution. A is the anticathode, B_1 is the window of the X-ray tube. B_2 a diaphragm at the end of the radiation protection attached to the tube. C consists of the crystal holder.

rocking curve at the wave-length of Cu $K\alpha_1$ is 4.9″ [13]. The corresponding single crystal diffraction pattern should have a width of 3.5″. The width of the diffraction pattern of calcite for the Mo $K\alpha_1$ radiation is 3.6″ [10]. The focusing defect of crystals with a radius of 200 cm and an aperture of 20 mm has little influence in the angular region above 35°. Accordingly we find the resolutions listed in Table 1. The $11\bar{2}0$ plane system in quartz recently studied by Brogren [13], has been included.

Table 1

Crystal	Atomic planes	Resolving power
Calcite	100	9,800
Quartz	$10\bar{1}0$	10,600
Quartz	$11\bar{2}0$	16,000

The resolving power in practice

When being bent, every crystal shows a tendency to saddle form. Regions with faulty bending are also common. It is therefore reasonable to expect a focusing defect larger than that computed from the geometry of the instrument. In practice calculations become impossible, as W_c of eq. (1) will include all the combined effects, known and unknown. However, W_c can be determined by comparison with the line-widths measured by means of the two-crystal spectrometer. Unfortunately, the widths reported by various authors differ considerably. Amongst the lines recorded with the present bent crystal instrument the widths of the $K\alpha_1$ line of copper and the $L\alpha_1$ line of silver have been accurately measured by Parratt [11]. His values together with the bent crystal values are listed in Table 2. As already stated, Parratt corrects his widths for the influence of the diffraction pattern by means of a rather unusual formula. As in his case its validity is experimentally verified there is no reason why the line-widths reported by him should not be accepted. However, when combining Parratt's W_λ values with the W_m values of the present investigation, eq. (1) has been used. In Table 2 as in the following text W_c' is the width of the "combined pattern" in the second to the fourth orders W_c being reserved for first order spectra.

The $K\alpha_1$ line of iron was recorded in the third and fourth orders. Unfortunately the width of this line has not been measured by anyone with an accuracy approaching that claimed by Parratt for the other two lines. However, as the third order of Fe $K\alpha_1$ is comparatively near Cu $K\alpha_1$ in the fourth order, it seems reasonable to use

Table 2

Line	W_m in XU Present bent crystal values	W_λ in XU from two-crystal values by PARRATT	W_c' in XU
Cu $K\alpha_1$ 4th order . . .	2.40	1.82	1.57
Ag $L\alpha_1$ 2nd order . . .	6.89	6.52	2.21
Fe $K\alpha_1$ 3rd order . . .	3.30		1.57 (1st approx.) 1.71 (2nd approx.)
Fe $K\alpha_1$ 4th order . . .	4.00		1.01 (1st approx.) 1.36 (2nd approx.)

the same value of W_c' in both cases. Then the width of Fe $K\alpha_1$ calculated from its third order gives the value of W_c' for the same line in the fourth order. We will assume that in the first approximation W_c' varies linearly with the wave-length as illustrated in the upper diagram of Fig. 11. If instead we select W_c' values from a straight line drawn through the two points corresponding to Cu $K\alpha_1$ and Ag $L\alpha_1$ we get quite absurdly differing widths from the two orders of Fe $K\alpha_1$. Likewise, if we assume W_c' to be constant, the two orders of Fe $K\alpha_1$ give a W_c' value of 2.08, which is improbable as compared to the value derived by means of the very accurately known width of Cu $K\alpha_1$. Accordingly, our first assumption appears to be the most probable. The considerable width of Ag $L\alpha_1$ makes it difficult to determine the corresponding W_c' value with any accuracy, which probably explains the divergence (compare Table 3).

By combining the W_c' value determined by means of Cu $K\alpha_1$ with that corresponding to the fourth order of Fe $K\alpha_1$ a more accurate value of W_c' can be read for the third order of the latter line. Then by successive approximation we arrive at the values represented by the crosses in the upper diagram of Fig. 11.

In all orders but the first the width of the true diffraction pattern is negligible as compared to other effects. Therefore, in the present case the limiting of the resolving power must be due to these other causes. As regards the copper $K\alpha_1$ line in the fourth order, the full width at half maximum of the focusing defect ought to be 0.05 XU, only. The height of the focus-spot and the height of the counter window are, as already stated, too small to add appreciably to the broadening effect. The detector slit allows a wave-length region of 0.21 XU to pass. This is of small significance as compared to the total broadening effect. Accordingly, it is reasonable to suppose that, in the present case, most of the latter is due to flaws in the crystal and deviations of its reflecting surface from the true cylindrical form.

Some time after the start of recording, the crystal had to be removed from the bending block for cleaning. On being bent again, it gave somewhat lower resolution than before. This fact appears to support the assumption that the resolving power is seriously affected by flaws in the crystal surface caused by uneven bending. The values cited above refer to the rebent crystal. The first set of records did not include a sufficient number of lines suitable for comparisons. The Cu $K\alpha_1$ line had a width indicating a W_c' value of 1.32.

As already remarked the W_c' values listed in Table 2 do not include the true diffraction pattern. Therefore, when determining the resolution in the first order, we combine the W_c' values from the curve in the upper diagram of Fig. 11 with the

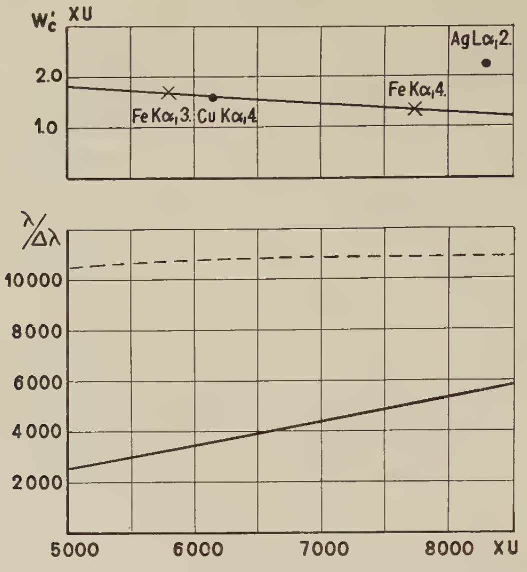

Fig. 11. Upper diagram: W_c' as a function of the wave-length. Lower diagram: the corresponding resolution as a function of wave-length. The dotted curve indicates the ideal resolution. Quartz crystal (10$\bar{1}$0).

diffraction pattern. As a result we find the resolving power increasing with increasing wave-length as shown by the lower diagram in Fig. 11.

It is still an open question whether the influence of flaws in the crystal surface is in all cases covered by the value of W_c' as derived above. If not, the diffraction pattern ought to be given a value other than that for an ideal crystal. The above determination of the resolving power ought to be regarded as a first approximation only.

There has been much discussion as regards the most convenient type of instrument to meet the demand for high resolution in X-ray spectroscopy. Due to the fact that, usually, the resolving power can be increased only by a small factor, the advantage of one instrument as compared to another is quite superficial. Although theoretically the resolution of a two-crystal spectrometer should be $\sqrt{2}$ times that of a tube spectrometer with the same kind of crystal, it is nevertheless difficult to distinguish between the two instruments. In several instances the tube spectrometer has been reported to show a resolution slightly higher than that of the average two-crystal instrument. Evidently the small increase in resolving power is insufficient to obviate the effects of flaws in the crystal surface or in the lattice. In addition, all types of spectrographs are subject to the effect of the divergence of the X-ray beam. As a result the increased resolution scarcely materializes, even should the employed crystals be good specimens. In the present case an inferior crystal limits the resolution. At 5000 XU it is only 1/4, and at 8000 XU $\frac{1}{2}$ of that of the ideal case. Far better results are to be expected with really good specimens.

The widths of some lines of the L and M series

In general the two-crystal spectrograph is the most convenient instrument for measuring line widths. However, as regards broad and diffuse lines, the correction for the finite resolving power of the bent crystal spectrograph is of the same order of magnitude as the random errors. It is justifiable, therefore, to quote in Table 3 the widths of some L lines which have been registered with the large bent crystal instrument, in some cases for the first time. For comparison, values have been included from measurements by PARRATT [14] and by MUNIER, BEARDEN, and SHAW [15].

Table 3. The widths of some L and M lines

Line	Bent crystal measurements in X U		Two-crystal measurements corrected for finite resolving power	
	Uncorrected	Corrected according to eq. (1)	PARRATT	BEARDEN, MUNIER, and SHAW
51 Sb $L\beta_1$	3.39	3.30		
50 Sn $L\alpha_1$	3.22	3.14		
$L\beta_1$	3.20	3.11		
48 Cd $L\alpha_1$	3.49	3.43		
$L\beta_1$	3.41	3.34		
47 Ag $L\alpha_1$	3.45	3.39	3.26	
$L\beta_1$	3.38	3.3	3.0	
$L\beta_2$	4.46	4.40	4.11	
$L\beta_3$	7.14	7.1	7.8	
42 Mo $L\alpha_1$	5.52	5.20		
$L\beta_1$	5.39	5.04		
74 W $M\alpha$	7.83	7.67		6.6
$M\beta$	7.41	7.23		7.85

The work with the bent crystal vaccum spectrograph is being sponsored by *Statens Naturvetenskapliga Forskningsråd.* While expressing his gratitude to this board, the author also wishes to thank Mr. BERTIL NORDFORS and Mr. GÖRAN WASSBERG for their valuable assistance.

Department of Physics, University of Uppsala, Januari 1954.

REFERENCES

1. SANDSTRÖM, ARNE E., Arkiv f. Fysik *4*, 517 (1952).
2. OHLIN, P., Dissertation, Uppsala Univ. Årsskrift, Uppsala 1941.
3. LE MIEUX, A. F., and BEEMAN, W. W., Rev. Sci. Instr. *17*, 130 (1946).
4. BROGREN, G., Dissertation, Nova Acta Reg. Soc. Scient. Ups. IV, *14*, No. 4, 1949.
5. SANDSTRÖM, A. E., and NORDFORS, BERTIL, Ark. f. Fysik *8*, 147 (1954).
6. SANDSTRÖM, ARNE, ZS. f. Physik *84*, 541 (1933); *92*, 622 (1934); Dissertation, Nova Reg. Soc. Scient. Ups., IV, *9*, No. 11, 1935.
7. HAGLUND, PH., Dissertation, Ark. f. Mat., Astr. o. Fys. *28* A, No. 8 (1941). V. H. SANNER, Dissertation, Uppsala Univ. Årsskrift, Uppsala 1941.
8. RANDALL, C. A., and PARRATT, L. G., Phys. Rev. *57*, 786 (1940).
9. RICHTMYER, F. K., BARNES, S. W., and MANNING, K. V., Phys. Rev. *44*, 311 (1933).

10. Compton, A. H., and Allison, S. K., X-rays in Theory and Experiment, London and New York 1935.
11. Parratt, L. G., Rev. Sci. Instr. *6*, 387 (1935).
12. Johann, H., ZS. f. Physik *69*, 185 (1931).
13. Brogren, G., Ark. f. Fysik *6*, 321 (1953).
14. Parratt, L. G., Phys. Rev. *54*, 99 (1938).
15. Munier, J. H., Bearden, J. A., and Shaw, C. H., Phys. Rev. *58*, 537 (1940).

Tryckt den 10 augusti 1954

Uppsala 1954. Almqvist & Wiksells Boktryckeri AB

ARKIV FÖR FYSIK Band 8 nr 11

Communicated 10 February 1954 by Axel E. Lindh and Gunnar Hägg

The transparency of cellulose acetate, cellophane, nylon, mylar, and teflon in the region 3 to 10 Å

By Arne Eld Sandström and Bertil Nordfors

With 4 figures in the text

In the region 5 Å and upwards it is always difficult to get sufficiently thin foils for counter windows or as substrates for absorbers. The organic compounds usually display a high and increasing absorption until the nitrogen, oxygen, and carbon K-edges have been traversed.

Once goldbeater's skin, alone or combined with very thin aluminium foils, was the only resource. Transmission data for such combinations have been available for a long time [1]. Nowadays goldbeater's skin has been supplanted by several kinds of plastics. For work now planned or in progress we found it necessary to study the relative qualities of some of these.

The absorption coefficients were measured with a large vacuum spectrograph already described by one of us [2]. The foils were mounted on a revolving disk in such a position as to be easily brought across the X-ray beam. The revolving disk was turned from the outside by means of one of the manipulators mentioned in the paper already cited [2].

The X-ray intensities were registered with a Geiger counter consisting of a brass block having a cylindrical bore of 20 mm and a length of 80 mm. The wire was of stainless steel 0.15 mm thick. The counter was filled with a mixture of 80 mm argon and 15 mm ethyl alcohol. The radiation entered the side of the counter through a small window covered by a thin foil of cellulose acetate (zapon lacquer). The counter was filled *in situ* inside the vacuum tank.

The X-ray tube will be described elsewhere [3]. The accelerating voltage and the emission were both kept constant by means of electronic devices [4]. Silver, molybdenum, tungsten, and aluminium were used as targets. To ensure the highest possible intensity, thus diminishing the time of observation, the absorption coefficient was determined by using the $L\beta_1$- and $L\alpha_1$-lines of silver and molybdenum, the $M\beta$- and $M\alpha$-lines of tungsten, and the $K\alpha_1$-line of aluminium. The first four lines were observed in the second order, the last three in the first order. The peak of the desired line was projected on the slit in front of the counter. The intensity was registered first without and then with the foil across the beam. This procedure was repeated a second time to ensure that changes in the focus spot did not seriously interfere with the registrations. The influence of the continuous background was eliminated by measuring the intensity to both sides of the line with and without the absorption foil. The average of each pair of values was then subtracted from the corresponding intensity registered for the peak of the line.

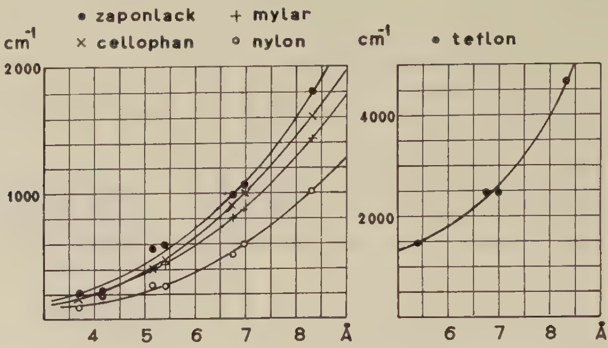

Fig. 1. The absorption coefficients of cellulose acetate, cellophane, nylon, mylar, and teflon in the region 3–9 Å.

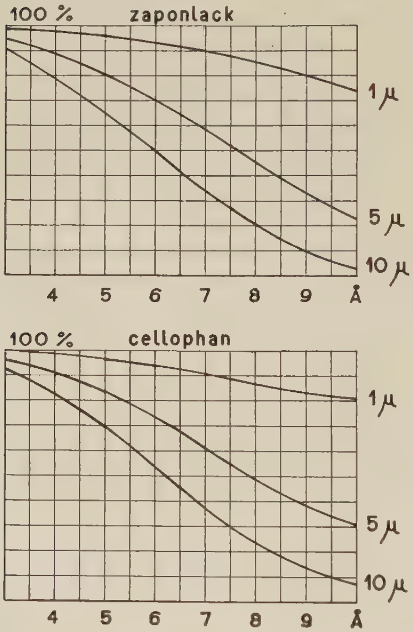

Fig. 2. The transparency of cellulose acetate and cellophane.

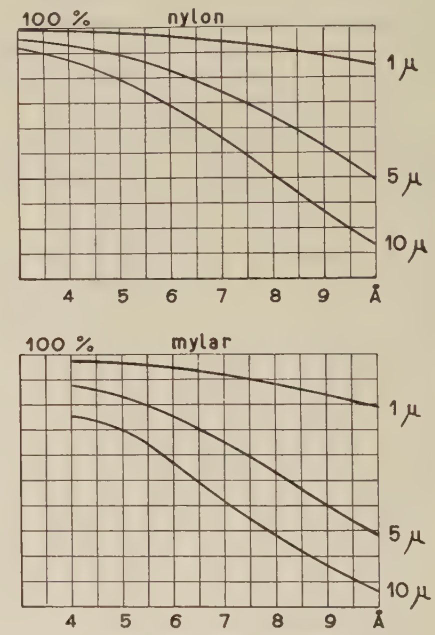

Fig. 3. The transparency of nylon and mylar.

The measurements were made successively for all the foils on each line, mylar and teflon excepted, which were added later. For these two compounds, therefore, only four points determine the curves illustrating the variation of the absorption coefficient with wave-length.

The thickness of the foils was measured by means of an indicator arrangement (microcator from C. E. Johansson, Eskilstuna), which could be read to $^{1}/_{10}$ of a micron. In cases, where foils of two different thicknesses were applied, the values of the absorption coefficient indicated that the accuracy was sufficiently good. The degree of

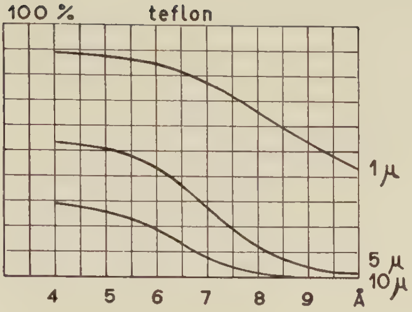

Fig. 4. The transparency of teflon.

accuracy can also be estimated from the curves in Fig. 1. Owing to the fact that the foils in general were very thin, their absorption was low for the wave-lengths of the silver lines, resulting in a correspondingly low accuracy, especially in the case of nylon. However, the most interesting region is above 5 Å. The results are given by the transmission curves in Figs. 2–4, which speak for themselves. These curves have been extrapolated from 8.3 up to 10 Å. With regard to the general trend of the curves this extrapolation does not seem too hazardous.

It is quite apparent from Fig. 1 that cellulose acetate, cellophane, and mylar have much the same qualities. In nylon the absorption is much lower. Teflon absorbs too much to be really useful in this wave-length region. This material contains fluor, which probably explains its high absorption coefficient.

Evidently as regards counter windows and absorber substrates in the wave-length region above 5 Å, foils from the materials listed here have to be very thin. Nylon, 5 microns thick, is quite acceptable up to 9 Å. The new plastic mylar is not quite as good but it is reported to be resistent to ethyl alcohol, which nylon is not. This makes it rather suitable for counter windows. The nylon and cellophane foils were ordinary commercial qualities, the mylar and teflon foils from E. I. Du Pond de Nemours & Co. Inc.

The measurements reported here as well as all work done with our vacuum spectrograph have been supported by grants from Statens Naturvetenskapliga Forskningsråd.

Fysiska Institutionen, Uppsala, June 1953.

REFERENCES

1. SIEGBAHN, MANNE, Spektroskopie der Röntgenstrahlen, 2. Aufl., p. 121, Berlin 1931.
2. SANDSTRÖM, ARNE ELD, Ark. f. Fysik *4*, 517 (1952).
3. —— Ark. f. Fysik, *8*, 129 (1954).
4. OHLIN, P., Dissertation 1941; LE MIEUX, A. F., and BEEMAN, W. W., Rev. Sci. Instr. *17*, 130 (1946).

Tryckt den 10 augusti 1954

Uppsala 1954. Almqvist & Wiksells Boktryckeri AB

ARKIV FÖR FYSIK Band 8 nr 12

Communicated 10 March 1954 by G. Borelius

Paramagnetic susceptibility of Au Cr alloys

By Aldo Giansoldati

With 3 figures in the text

The present investigation on alloys of gold with small amounts of chromium is one of a series of investigations (1–6) being conducted in this laboratory on the paramagnetic susceptibility of transition metals dissolved in Cu, Ag, or Au. Although the magnetic properties of the system Au Cr have already been studied by Neel [7], Vogt [8], and Kronqvist [4], there is still a need for further information about the quantum state of the Cr-atoms when dissolved in Au.

The present work comprises measurements on six alloys from about 2 to 20 atomic percent of Cr in the range from room temperature to about 800 °C. Weight control of the moulded samples show the uncertainty of the concentrations to be of the order of 0.05 atomic percent of Cr. The samples were given the form of wires of about 12 cm length and 0.9 mm diameter. Before the measurements they were homogenized at about 950 °C. The apparatus used was the magnetic balance described by Gustafsson [3] which had, however, been improved in certain details. The calibration of the apparatus for the present measurements was made by wires of Pd and Pt of the same dimensions as the measuring wires, using the consistent values for the atomic susceptibility at 18 °C, 200.5 for Pt obtained by Gustafsson [3], and 569.0 for Pd obtained by Wucher [9]. The paramagnetic susceptibility χ_P per gram mol of the alloy was obtained from the measured mol susceptibility χ_A by deducting the diamagnetic contribution of the gold atoms only, that is by means of the formula

$$\chi_P = \chi_A - \chi_D (1 - \alpha) \tag{1}$$

where χ_D is the diamagnetic mol susceptibility of gold and α the atomic fraction of Cr in the alloy.

The results concerning the atomic susceptibility at room temperature agree fairly well with those of the earlier investigators as is shown by the diagram of Fig. 1.

The temperature dependence of χ_P/α is shown in Fig. 2 where α/χ_P is plotted against the absolute temperature T. The figure contains one set of measurements for each alloy. For the sake of plainness the curve for the 6.75 percent alloy is displaced somewhat upwards as marked in the figure.

If the law of Curie-Weiss is fulfilled, the diagram should give a straight line described by the formula

$$\frac{\alpha}{\chi_P} = \frac{\alpha T}{C} - \frac{\alpha \theta}{C} \tag{2}$$

where C and θ are constants. The constant C/α then allows the calculation of the magnetic moment μ of the Cr atoms by the formula

$$\mu = \sqrt{\frac{2kC}{N\alpha}} \tag{3}$$

where k is the Boltzmann constant, and N the Avogadro number.

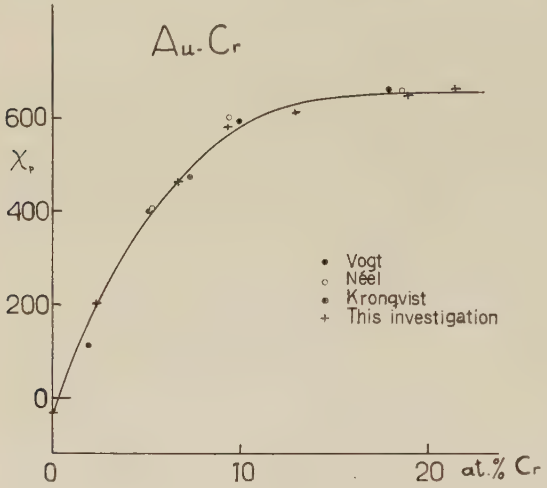

Fig. 1. Paramagnetic atom susceptibility of Au Cr alloys at 20 °C versus concentration.

In the most dilute alloys with 2.35 and 6.75 atomic percent of Cr, the Curie-Weiss law is fulfilled, within the limits of error, over the whole range of temperature covered by the measurements, giving only one set of the constants C, μ, and θ. At higher concentrations there is at about 500–600 °K a transition in the diagrams from one straight line to another. A break in curves of this kind has been observed earlier for Au Cr alloys by NEEL [7], and also by various observers in other similar systems. The present measurements seem to show that there is not only a simple break, but, at least in the less dilute alloys, a more complicated structure of transition. The author will not here enter upon a discussion of this transition but confines himself to a description of the phenomena by comparing the different sets of C, μ and θ for the ranges of temperature above and below the transition, that is the ranges of about 500–900 °K and 300–500 °K, respectively. The results are given in Table 1. Five series of measurements on the alloy with 13.00 % Cu are in rather good agreement with each other.

The results concerning the number of Bohr magnetons per atom μ/μ_B given in this table are shown in Fig. 3 in their dependence of the concentration of Cr. With increasing dilution the magneton numbers μ/μ_B for both ranges of temperature converge to a value which, within the limits of error, coincides with the value 4.90 obtained from the "spin-only" formula

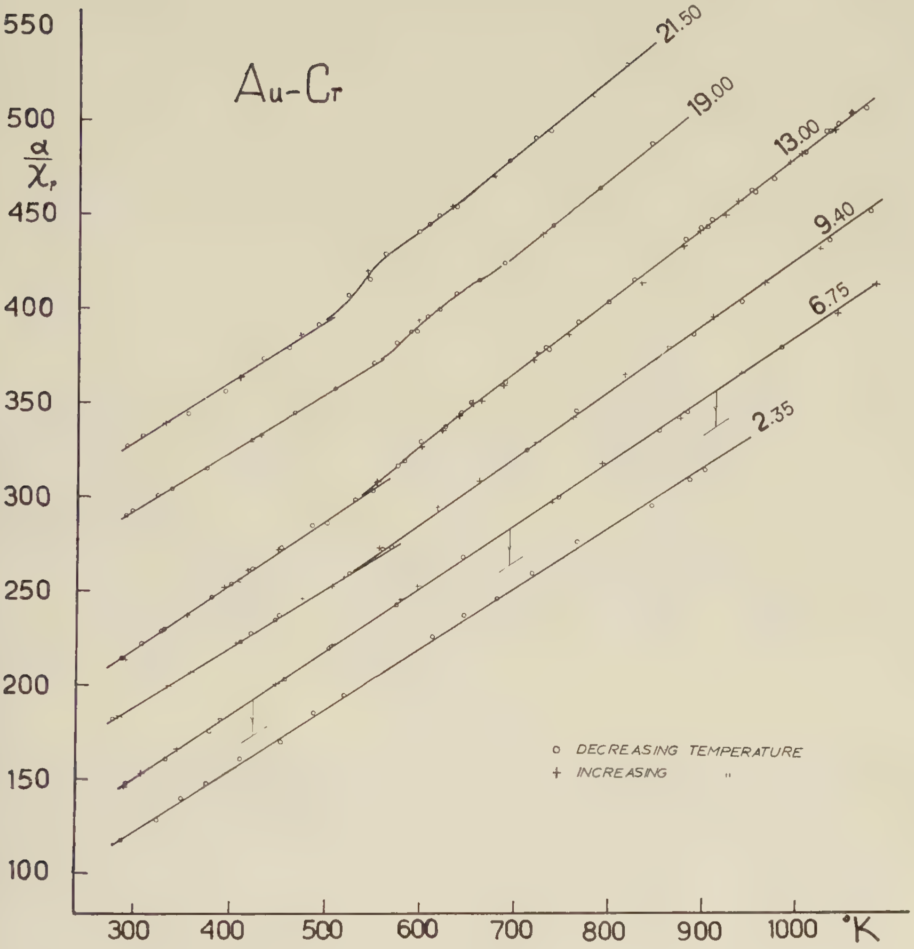

Fig. 2. The reciprocals of atomic susceptibility per mol Cr versus temperature.

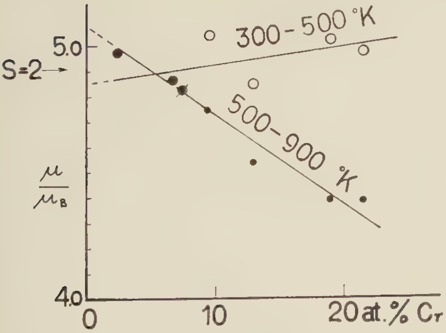

Fig. 3. Atomic moments of Cr in Bohr magnetons. The dashed point is from the measurements of KRONQVIST [4].

Table 1.

Atom % Cr	Range of temperature °K	C	$\frac{\mu}{\mu_B}$	θ
2.35	300–900	0.074	4.97	− 86
6.75	300–900	0.199	4.86	− 80
9.40	300–500	0.293	5.04	−288
	500–1050	0.274	4.74	−239
13.00	300–500	0.380	4.83	−340
	600–1050	0.345	4.53	−277
	300–500	0.385	4.87	−336
	600–1050	0.334	4.52	−230
	300–500	0.389	4.86	−342
	300–500	0.377	4.82	−315
	600–1050	0.336	4.56	−238
	300–500	0.377	4.82	−327
	600–1050	0.329	4.51	−223
19.00	300–500	0.603	5.04	−625
	600–820	0.457	4.38	−345
21.50	300–500	0.650	4.97	−695
	600–820	0.518	4.38	−457

$$\mu = \mu_B \sqrt{4\,s\,(s+1)} \tag{4}$$

with $s = 2$, the value observed for the Cr^{++} ion in aqueous solutions and in salts. With increasing concentration the magneton number decreases. A possible reason for this decrease, which appears in a similar way in the Au Mn and Ag Mn alloys, is discussed to some extent in a paper by KRONQVIST and GIANSOLDATI [6].

The author wishes to express his gratitude to Professor G. BORELIUS and Dr. J. O. LINDE for valuable discussions, and to the Swedish Council for Scientific Research for financial support.

Stockholm, Royal Institute of Technology, Department of Physics.

REFERENCES

1. B. SVENSSON, Ann. d. Physik *14* (1932) 669.
2. G. GUSTAFSSON, Ann. d. Physik *25* (1936) 545.
3. ——, Ann. d. Physik *28* (1937) 122.
4. E. KRONQVIST, Arkiv. mat. astr. fysik *34 B* (1947) nr 7.
5. ——, Arkiv för Fysik *5* (1952) 453.
6. E. KRONQVIST and A. GIANSOLDATI, Arkiv för Fysik *7* (1953) 343.
7. L. NEEL, Ann. de Physique *3* (1932) 160.
8. E. VOGT, Zeitschr. f. Metallkunde *27* (1935) 40.
9. J. WUCHER, Ann. de Physique *7* (1952) 317.

Tryckt den 10 augusti 1954

Uppsala 1954. Almqvist & Wiksells Boktryckeri AB

ARKIV FÖR FYSIK Band 8 nr 13

Communicated 14 April 1954 by Bengt Edlén

A note on mass estimation by the range-scattering method

By Nils Norlind

With 3 figures in the text

In research on nuclear photographic emulsions the range-scattering method is used to estimate the mass of a particle, which stops in the emulsion (ref. a). The following is a calculation of the best estimate which can be expected from these measurements.

The method of Fowler is used (ref. b). The track is adjusted parallel to the x-axis of motion of the microscope stage. We measure a set of ranges R_i and the corresponding y_i-coordinates and get the second differences $\Delta_2 y_i$. $R_1, R_2 \ldots R_n$ are arranged in ascending order. $\Delta_2 y_i$ may be written

$$\Delta_2 y_i = u_i + \theta_i, \tag{1}$$

where u_i is the genuine scattering effect and θ_i the spurious scattering effect (ref. d). All the u_i and θ_i are considered as normal independent variables (ref. d and ref. a).

The expected values are denoted by $E(\ )$ and the standard deviations by s.d. or $\sigma(\ )$. We have

$$E(u_i) = E(\theta_i) = 0. \tag{2 a}$$

For a normal variable x with $E(x) = 0$ we have the following relations

$$E(|x|) = \sqrt{\frac{2}{\pi}}\,\sigma(x) \tag{2 b}$$

$$E(x^2) = \sigma^2(x) \tag{2 c}$$

$$\sigma^2(x^2) = E[(x^2 - \sigma^2(x))^2] = 2\,\sigma^4(x). \tag{2 d}$$

The theory of scattering gives (ref. c)

$$E(|u_i|) = \frac{K\,a\,Z\,s^{3/2}}{2\,T_i\,\dfrac{1+j/2}{1+j}}. \tag{3}$$

K = scattering constant $\left(\frac{\text{MeV x degrees}}{(100\,\mu)^{1/2}}\right)$

a = numerical factor

T_i = kinetic energy of the particle (MeV)

j = kinetic energy/rest energy

Z = the charge number of the particle

s = the cell-length in μ.

In these calculations $Z = 1$ and $j \approx 0$. The range-energy relation (ref. e) gives for $Z = 1$

$$T_i = A\, M^p\, R_i^{1-p}. \tag{4}$$

A = constant

p = constant

M = the mass of the particle.

(3) and (4) give the usual relation

$$E\,(|\,u_i\,|) = \frac{\text{const} \cdot s^{3/2}}{M^p\, R_i^{1-p}}. \tag{5}$$

An estimate of the mass is based on the second differences $\Delta_2\, y_i$. According to relation (1) $\Delta\, y_i$ is composed of two parts. The genuine scattering effect u_i is a normal variable. $E\,(|\,u_i\,|)$ and consequently $\sigma\,(u_i)$ are dependent on the mass of the particle and the corresponding range R_i (5). It is convenient to introduce here a new variable z with a $\sigma\,(z)$, which only depends on the mass. We substitute

$$u_i = c_i\, z_i$$

$$c_i \sim \frac{1}{R_i^{1-p}}, \tag{6}$$

and (1) is rewritten

$$\Delta_2\, y_i = c_i\, z_i + \theta_i\,. \tag{7}$$

z_i may now be considered as a normal variable, and from (5) we obtain

$$\sigma\,(z_i) \sim E\,(|\,z_i\,|) \sim \frac{s^{3/2}}{M^p}, \tag{8}$$

i.e. $\sigma\,(z)$ depends only on the mass. An estimate of $\sigma^2\,(z)$ or $\sigma\,(z)$ may be made in many different ways. However, the method of maximum likelihood does not give any convenient expression. Here the following estimate φ of $\sigma_2\,(z)$ is used

$$\varphi = \frac{1}{n}\sum\left(\frac{\Delta_2 y_i}{c_i}\right)^2 - \sigma^2(\theta)\frac{1}{n}\sum\frac{1}{c_i^2}. \tag{9}$$

When the spurious scattering effect is small compared to the genuine effect, φ corresponds to the estimate with minimum s.d. All the $\Delta_2 y_i$ are considered as normal, independent variables, and from (1), (2 c) and (7) follows

$$E(\varphi) = \frac{1}{n}\sum\frac{E[(\Delta_2 y_i)^2]}{c_i^2} - \sigma^2(\theta)\frac{1}{n}\sum\frac{1}{c_i^2}$$

$$E[(\Delta_2 y_i)^2] = \sigma^2(\Delta_2 y_i) = c_i^2\sigma^2(z) + \sigma^2(\theta) \tag{10}$$

$$\therefore E(\varphi) = \sigma^2(z).$$

The s.d. of φ is computed with the aid of the relation (2 d).

$$\sigma^2(\varphi) = \frac{1}{n^2}\sum\frac{1}{c_i^4}\sigma^2[(\Delta_2 y_i)^2] = \frac{2}{n^2}\sum\frac{1}{c_i^4}\sigma^4(\Delta_2 y_i)$$

$$\sigma^2(\varphi) = \frac{2\sigma^4(z)}{n^2}\sum\left[1+\left(\frac{\sigma(\theta)}{c_i\sigma(z)}\right)^2\right]^2. \tag{11}$$

Putting

$$k_i = \frac{c_i\sigma(z)}{\sigma(\theta)} = \frac{E(|u_i|)}{E(|\theta|)} \tag{12}$$

we have

$$\sigma^2(\varphi) = \frac{2\sigma^4(z)}{n}\cdot\frac{1}{n}\sum\left(1+\frac{1}{k_i^2}\right)^2. \tag{13}$$

$E(|\theta|)$ is called the noise level (ref. d) and k_i, the genuine scattering effect divided by the noise level, is called the noise-factor. If the measurements are made with a constant cell-length s, then

$$k_1 > k_2 > \ldots > k_n,$$

because the genuine scattering effect decreases with increasing ranges. From relation (3) the cell-length which corresponds to a given value of k_n may be computed, when we know the noise level of the measurements. We ask for the optimum value of the noise-factor k_n, i.e. the value which minimizes $\sigma^2(\varphi)$. This optimum value is dependent of R_1/R_n. It may be shown that

$$1.6 < k_n\,(\text{opt}) < 2.3.$$

The upper limit is valid for $R_1/R_n \approx 1$; the lower for $R_1/R_n \approx 0$. Fig. 1 shows the graph of $\frac{\sigma(\varphi)}{E(\varphi)}$ for a proton track with $R_n = 10{,}000\ \mu$ for different values of k_n and R_1/R_n. Relation (13) gives

$$\left(\frac{\sigma(\varphi)}{E(\varphi)}\right)^2 = \frac{\sigma^2(\varphi)}{\sigma^4(z)} = \frac{2}{n}\cdot\frac{1}{n}\sum\left(1+\frac{1}{k_i^2}\right)^2. \qquad (14)$$

The graph was based on (14) where the sums were replaced by definite integrals using the relations (5) and (12). The following numerical constants were used:

$$K = 27.0 \text{ (see (3))}, \quad 1-p = 0.57 \text{ (4)}, \quad E(|\theta|) = 0.10\ \mu.$$

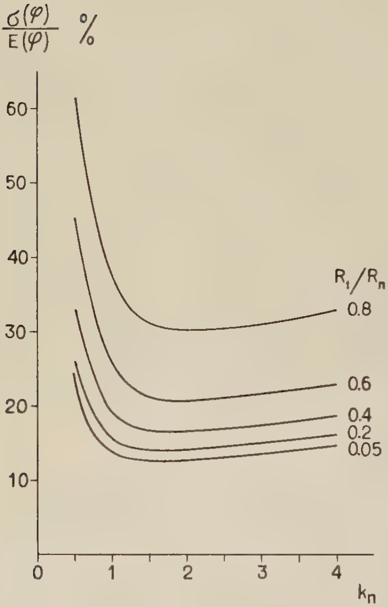

Fig. 1. The relative standard error of the scattering parameter φ for a proton track $R_n = 10{,}000\ \mu$ plotted against the noise-factor k_n for different values of the smallest range R_1.

It is clear that $k_n\,(\text{opt}) = 2$ may be used with sufficient accuracy. Fig. 2, curve (1), shows the minimum values of $\frac{\sigma(\varphi)}{E(\varphi)}$ for different ranges R_n. R_1 was chosen $= 500\ \mu$ because the relation (4) is not valid for ranges, which are too short. The value of $\frac{\sigma(\varphi)}{E(\varphi)}$ for different noise level values is easily derived

$$\left[\frac{\sigma(\varphi)}{E(\varphi)}\right]_1 = \left[\frac{\sigma(\varphi)}{E(\varphi)}\right]_2 \cdot \left(\frac{E(|\theta|)_1}{E(|\theta|)_2}\right)^{1/3}. \qquad (15)$$

Here $\left[\frac{\sigma(\varphi)}{E(\varphi)}\right]_1$ corresponds to the noise level $E(|\theta|)_1$ and $\left[\frac{\sigma(\varphi)}{E(\varphi)}\right]_2$ to a second noise level $E(|\theta|)_2$.

Fig. 2, curve (2), shows the minimum values when the measurements are made with a variable cell-length s in the following way. First $s = 30\ \mu$ is used up to R_2' corresponding to $k_n = 2$, $s = 30\ \mu$, then $40\ \mu$ is used up to R_3' ($k_n = 2$, $s = 40$) and so on. In this case the following formula was derived

$$\frac{\sigma(\varphi)}{E(\varphi)} = \frac{1.68}{\sqrt{n}}. \tag{16}$$

$n =$ the total number of observations. Fig. 2 also gives the relative mass error $\frac{\Delta M}{M}$ derived from (8)

$$\frac{\sigma(\varphi)}{E(\varphi)} = \frac{\Delta E(\varphi)}{E(\varphi)} = 0.86\,\frac{\Delta M}{M}. \tag{17}$$

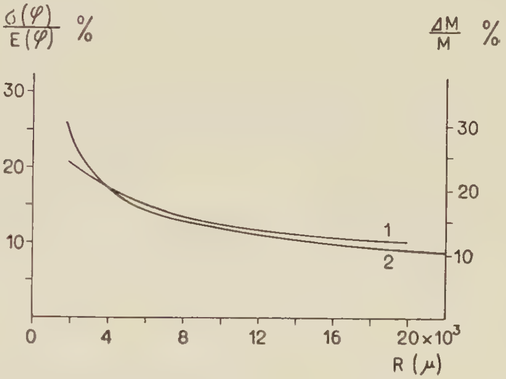

Fig. 2. The minimum standard error of the scattering parameter φ and of the mass M for protons plotted against the range R_n. The first $500\ \mu$ of the track are excluded; the noise-factor ≥ 2. Curve 1: the same cell-length is used over the whole track. Curve 2: variable cell-lengths are used ($30\ \mu$, $40\ \mu$ . . .).

Fig. 3 shows the expected resolution of the mass spectrum of different single-charged particles: tritons (T), deuterons (D), protons (P), K- and τ-mesons. (The mass of the K-meson is put equal to 1450 electron masses.) The arrows mark an interval ΔM around M taken from Fig. 2, curve 2. However, we may expect deviations as great as $3\,\Delta M$. Using a cell-length corresponding to $k_n = 2$ for protons, the noise-factors of the other particles are given:

Particle	k_n
τ	2.7
K	2.2
P	2.0
D	1.5
T	1.3

According to Fig. 1 the minimum errors may be used even in these cases.

From these calculations we deduce the smallest errors, defined by (17), that we may expect in the mass determination, when we use the range-scattering method in the usual way. According to Fig. 3 the mass errors corresponding to $R = 5{,}000\ \mu$ and $10{,}000\ \mu$ are 20 % and 14 % respectively. In these cases the different mass-distributions overlap each other. A single particle can hardly be identified by such a determination only. Theoretically the errors can be reduced to a certain extent by reducing the noise level (15) or by making use of the last 500 μ of the track. This seems to be difficult in practice. Even if we are able to reduce the noise level to 0.05 μ, which hardly seems possible, the mass errors for $R = 5{,}000$ and $10{,}000\ \mu$ according to (15) only reduce to 16 % and 11 % respectively. There are however still other factors which complicate the mass estimation. An exhaustive discussion of these factors is given in reference (e).

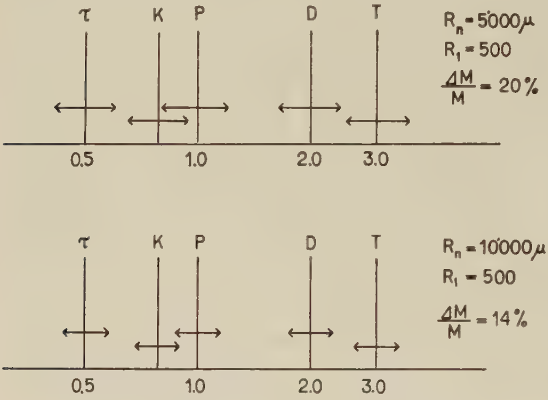

Fig. 3. The expected resolution of the mass spectrum of different single-charged particles: tritons (T), deuterons (D), protons (P), K- and τ-mesons ($K = 1450\ m_e$) for $R = 5{,}000\ \mu$ and $10{,}000\ \mu$. The arrows mark the error ΔM of the mass M taken from Fig. 2, curve 2.

Summary

The smallest errors to be expected in the mass determination by the range-scattering method are derived. With a noise level of 0.10 μ these errors are for the ranges $R = 5{,}000\ \mu$ and $10{,}000\ \mu$ 20 % and 14 % respectively. The effect of using a variable cell-length is found to be small.

ACKNOWLEDGEMENT

The author is very grateful to Professor von Friesen for suggesting the present problem and for his continual interest and encouragement.

Department of Physics, University of Lund, February 1954.

REFERENCES

(a) Menon, Rochat, 1951, Phil. mag. Ser. 7, *42*, 1232.
(b) Fowler, 1950, Phil. mag. Ser. 7, *41*, 169.
(c) Gottstein, *et al.*, 1951, Phil. mag. Ser. 7, *42*, 708.
(d) Menon, O'Ceallaigh, Rochat, 1951, Phil. mag. Ser. 7, *42*, 932.
(e) Menon, O'Ceallaigh, 1953, Phil. mag. Ser. 7, *44*, 1291.

Tryckt den 10 augusti 1954

Uppsala 1954. Almqvist & Wiksells Boktryckeri AB

ARKIV FÖR FYSIK Band 8 nr 14

Communicated 27 January 1954 by MANNE SIEGBAHN

Proton groups from the reaction $O^{18}(d,p)O^{19}$

By KATARINA AHNLUND and CURT MILEIKOWSKY

With 2 figures in the text

Introduction

The reaction $O^{18}(d,p)O^{19}$, which has not been reported earlier, is interesting because it leads to O^{19} as the residual nucleus. Not much is known about O^{19}. Its mass, obtained from the maximum energy of the β^- spectrum from O^{19}, is uncertain to ± 0.3 MeV (ref. 1, absorption measurement). No excited states have hitherto been found.

In this paper two proton groups from the reaction $O^{18}(d,p)O^{19}$ are reported. Both of them, it seems, lead to excited states in O^{19}. The work was done with the Cockcroft-Walton accelerator and the heavy particle spectrometer at the Nobel Institute (refs. 2, 3).

Identification of the reaction $O^{18}(d,p)O^{19}$

For our first study of $O^{18}(d,p)O^{19}$ we had available only a comparatively weak thin target of O^{18}, produced by electromagnetic separation of ordinary water vapor at mass number 20, the products being collected on a thick silver plate. In the investigated energy interval one proton group was found, which should be due to $O^{18}(d,p)O^{19}$. If this was true the O^{19} nuclei formed at the same time should give a β activity of predictable minimum intensity. The target activity was therefore studied with a scintillation counter (ref. 4). Without absorber most of the activity was due to N^{13} formed by the reaction $C^{12}(d,n)N^{13}$ because of C^{12} build-up on the target. This 11 min β^+ activity from N^{13} has however a low energy, $E_{\max} = 1.24$ MeV, compared to the O^{19} β^- activity, 4.5 MeV, and could be kept away from the counter by means of an Al absorber. The remaining activity measured immediately after bombardment with 0.9 MeV deuterons had a half life of 31 ± 4 sec. One decay curve is shown in Fig. 1.

Stronger targets were desired, however, and they were produced by electromagnetic separation of water supplied by A.E.R.E., Harwell, where the O^{18} is enriched by a factor 25. Mass number 20 was again used for the separation and stainless steel was the backing. Steel was found to hold much more of the sample than silver.

Two proton groups were found from $O^{18}(d,p)O^{19}$ and they could now also be identified by measuring the proton energies in backward and forward directions (135° and 60°).

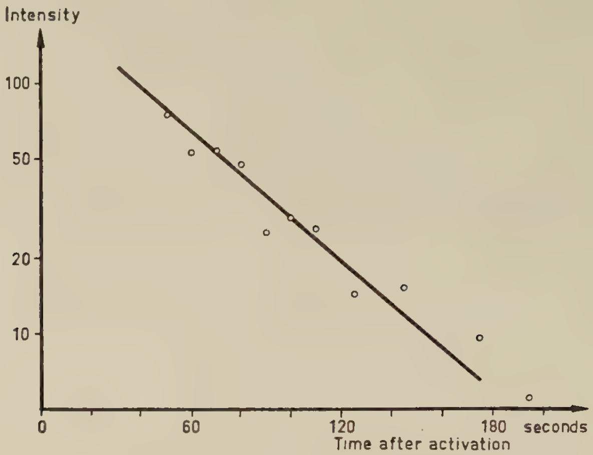

Fig. 1. Decay of β^- activity produced on a separated O^{18}-target by 0.9 MeV deuterons. At $t = 0$ the bombardment was stopped and the target plate placed in front of a scintillation detector screened by a 3 mm Al-absorber. The half-life 31 ± 4 sec. was obtained as a mean of six runs. O^{19} is known to have $T_{1/2} = 29$ sec. (ref. 7).

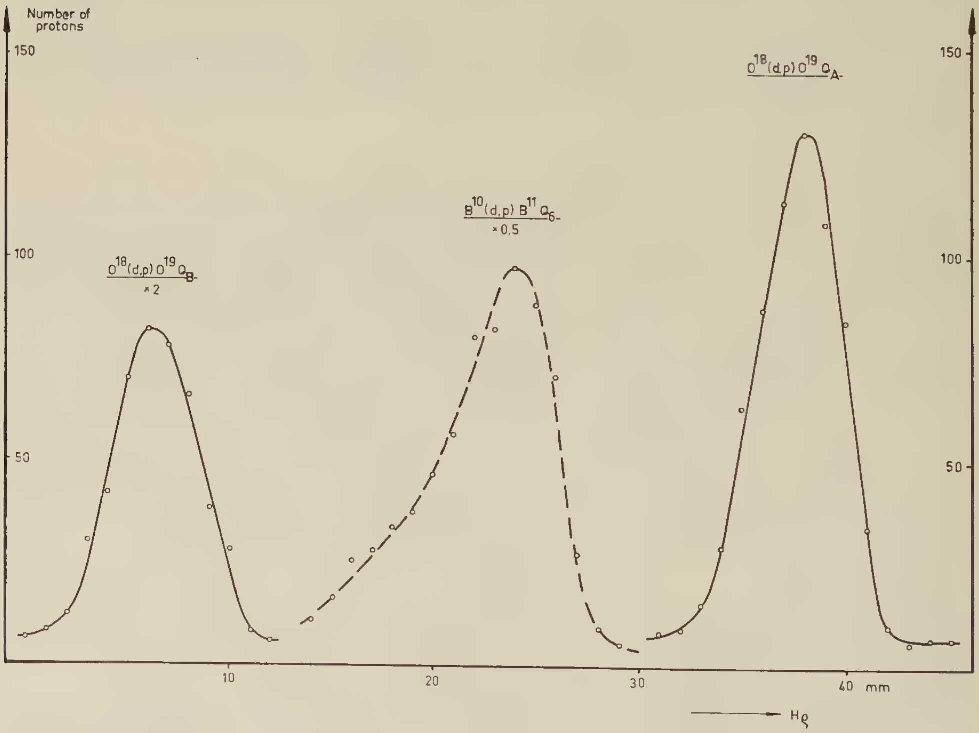

Fig. 2. Proton spectra from (d,p)-reactions on O^{18} and B^{10}. The figure is a combination of two different photographic plates. For each plate the deuteron exposure was 2400 μC at $E_D = 836.0$ keV, $\Theta = 134.4°$ and $2\Delta\Theta = 3.2°$. 10 mm plate corresponds to 27.2 keV proton energy.

Experimental results

The measurements of angles, target layers, and deuteron bombarding energy were similar to earlier measurements made in this laboratory (ref. 5). The calibration of the spectrometer was done with the proton group from $B^{10}(d,p)B^{11}$, $Q_6 = 1937$ keV. This group, which has been measured to ± 6 keV (ref. 6) falls conveniently between the two $O^{18}(d,p)O^{19}$ groups. An evaporated natural boron target was used. The result is shown in Fig. 2. 10 mm in Fig. 2 correspond to 27.2 keV. Whether the proton groups in Fig. 2 are read at the high energy edges, using min. angle and no layer correction, or if they are read at peak values, using mean angle and layer correction, they give the same result within 2 keV. We obtain

$$Q_A = 1730 \pm 8 \text{ keV}$$
$$Q_B = 1636 \pm 8 \text{ keV}$$

The total probable error is calculated from the following partial probable errors, referred to Q:

Q of $B^{10}(d,p)B^{11}$	± 5.6 keV
Bombarding deuteron energy	± 1.8 keV
Angle measurement	± 0.5 keV
Reading of proton peaks	± 3.6 keV
Dispersion in plate	± 3.2 keV
Total probable error	± 7.6 keV

At present we do not know whether Q_A corresponds to the ground state transition. In the region of somewhat higher proton energies there is strong proton background from other reactions, e.g. the D − D reaction, which have hitherto complicated the search for higher proton groups. This background should be eliminated for a major part of spectrum by the use of targets on thin backing. Such targets have now been produced by electromagnetic separation in this laboratory. In the direction of lower proton energies we have investigated a region down to $Q = 1100$ keV at an angle of 135° without finding any further line due to $O^{18}(d,p)O^{19}$.

ACKNOWLEDGEMENTS

The authors want to thank Professor MANNE SIEGBAHN for his interest in this work and Tekn. lic. S. THULIN for preparing the separated targets.

Nobel Institute of Physics, Stockholm 50.

REFERENCES

1. BLEULER, E., and ZÜNTI, W., Helv. Phys. Acta *20*, 195 (1947).
2. MILEIKOWSKY, C., and PAULI, R. T., Ark. f. Fys. *4*, nr 12, 287 (1952).
3. MILEIKOWSKY, C., Ark. f. Fys. *4*, nr 16, 337 (1952).
4. BERGSTRÖM, I., NYBÖ, K., THULIN, S., WAPSTRA, A. H., and ÅSTRÖM, B., Ark. f. Fys. *7*, 22, 239 (1953).
5. MILEIKOWSKY, C., Ark. f. Fys. *7*, nr 8, 89 (1953).
6. v. PATTER, D. M., BUECHNER, W. W., and SPERDUTO, A., Phys. Rev. *82*, 248 (1951).
7. HOLLANDER, J. M., PERLMAN, I., and SEABORG, G. T., Table of Isotopes, 4 (1952).

Tryckt den 10 augusti 1954

Uppsala 1954. Almqvist & Wiksells Boktryckeri AB

ARKIV FÖR FYSIK Band 8 nr 15

Communicated 25 November 1953 by IVAR WALLER

On the spatial distribution of neutrons slowed down in carbon and water

By GUNNAR HOLTE

With 4 figures in the text

In two previous papers [1] general analytic expressions are calculated for the stationary density of slow, epithermal neutrons in a moderator at all distances from the source. Fast neutrons are supposed to be emitted isotropically from a point source of constant strength in a homogeneous and infinite moderator. The neutrons are slowed down by elastic collisions with the atomic nuclei of the moderator. The atoms are assumed to be at rest before a collision with a neutron occurs and their chemical binding is neglected. Further, the scattering is supposed to be isotropic in the center-of-mass system of the neutron and the nucleus.

The basis of the investigation is the transport equation, which is solved by means of a Fourier-Laplace transformation, a method introduced in this problem by WALLER [2], MARSHAK [3] and others [3]. Then the case of constant mean free path λ of the neutrons in the moderator is treated, using a method of developments and analytic continuation in the variables of the transform, combined with the method of steepest descent for the final integration. The result is formula I (40) for the collision density $F_0(r, E)$, i.e. the number of collisions per unit time, per unit volume at the distance r from the source and per unit of energy range at the neutron energy E. For small E this expression is valid for all r, which completes earlier important results by WALLER [2] for small and intermediate distances and by WICK [4] for very large r.

The more realistic case of variable λ is treated in II, taking for $\lambda(E)$ a form II (1), used earlier by MARSHAK [2]. The case of variable λ, in general, is mathematically much more complicated than that of constant λ. However, in II this case is also solved to practically the same extent as the constant λ case. An essential difficulty is the solution of the system of difference equations in two variables II (2), resulting from the transformation of the transport equation. These equations being solved, the general methods of calculation used in I are also applied in II. An important theorem by WICK [4] is also of great use in these calculations. For the case of practical importance when $\lambda(E)$ decreases with decreasing E we then obtain analytic expressions for $F_0(r, E)$ valid for all r when E is small. The main formula is II (37), completed for large r by II (48) and (49), the latter of which is the complete asymptotic formula.

Of course, the knowledge of $F_0(r, E)$ for slow neutrons at all distances r requires numerical calculations for each kind of moderator. These are more complicated for variable λ than for constant λ, although for a moderate variation of λ and for r not too large the numerical computation is rather rapidly done. In I and II all the constants required for the use of the various expressions for $F_0(r, E)$, for all r, are calculated for moderators of carbon and water. Unfortunately, the formulae for $F_0(r, E)$ are not very simple, so that they are best illustrated by computation of numerical values for F_0 corresponding to different values of r, E and of E_0, the energy of the neutron source, supposed to be monoenergetic. It is the purpose of this paper to complete the previous papers I and II in this respect in giving tables and diagrams for $F_0(r, E)$ for carbon and water. In this way we obtain a concentration of the physical results of I and II meant for experimental physicists not interested in the mathematical side of the problem. In order to make clear in detail the limitations of the simple and widely used age-theory we have computed throughout also the values $F_{0_{\text{age}}}(r, E)$ so that a direct comparison with the exact values can be made.

We have limited ourselves to values of E of the order 1 ev, and thus the tables are useful for resonance neutrons. Their space distribution for some values of E_0 may be obtained from the tables. Explicit values of F_0 are given only for $E = 1$ ev. Now, except for the factor $1/E$ in F_0, this function depends on E (for a given value of E_0) only in the combination $x = \log(E_0/E)$, and varies very slowly with E. Thus the values for $E = 1$ ev are representative for resonance neutrons in general, at least qualitatively. But in order to make the tables even quantitatively useful for other values of E near $E = 1$ ev we have also computed the first derivative term in a Taylor development in the variable x of $E F_0(r, E)$ around $E = 1$ ev, $x = \log E_0$ (thus 1 ev is taken as the unit of energy). To write down the explicit formula, we have, taking $\Delta x = -\log E$,

$$F_0(r, E) = \frac{Q}{E} \cdot 10^{-4}\, G(r) \cdot (1 + \varkappa \cdot \Delta x + \cdots). \tag{1}$$

Here $G(r) = \frac{10^4}{Q} \cdot F_0(r, 1)$ and $\varkappa$ are the values given in the tables, and Q is the number of neutrons emitted by the source per unit of time. The tables also contain, for comparison with age-theory, the values $G_a(r) = \frac{10^4}{Q} \cdot F_{0_{\text{age}}}(r, 1)$. For the calculation of $\varkappa$ we only have to differentiate formulae I (17) and II (31) partially with respect to x which introduces factors θ and $\theta_0(k)$ respectively into the integrands of the formulae. They are slowly variable functions of the same kind as $A(\theta)$ and $A(k)\theta_0(k)$, respectively, and formula I (40), for example, is applicable after the obvious redefinition of the quantities m_i $(A(\theta) \to \theta A(\theta))$. An analogous change has to be made in II (37) and in other expressions for F_0. Finally, the values thus obtained are divided by the corresponding value of F_0 in order to give $\varkappa$. It must be stressed, however, that in this calculation for small r the fourth approximation of I (40) and II (37) has always to be used (the zeroth approximation obviously should give $\varkappa$ zero for r zero). The values of $\varkappa$ are therefore not as accurate as those of $G(r)$, but sufficiently good for using (1) for energies near 1 ev.

Carbon. Here we have taken four different values of E_0: 0.1, 0.5, 1.0 and 2.0 Mev. For 0.1 Mev the treatment in I for constant λ is applicable, taking $\lambda = 2.65$ cm (supposing the carbon density to be 1.60 g/cm^3). As the highest value of r considered is 150 cm, it should be pointed out that only the first few coefficients in I, Table 3 (β_n and α_n) are necessary for this computation. Table 4 is not used at all for these small r. For the other values of E_0, II must be used, supposing λ to be linearly increasing with the neutron energy according to II (56) (in this formula 1 Mev is the unit of energy). This is a very good approximation up to 2.5 Mev. Formula II (37) is then applicable for all values of r in question with good accuracy. This was also tested in some cases by numerical integration of II (31). The following values are obtained.

Table 1. Carbon

r (cm)	0	10	20	30	50	80	150
$E_0 = 0.1$ Mev:							
$G(r)$	0.623	0.534	0.339	0.163	0.0183	$1.74 \cdot 10^{-4}$	$7.24 \cdot 10^{-11}$
$G_a(r)$.	0.587	0.511	0.336	0.168	0.0181	$0.79 \cdot 10^{-4}$	$1.47 \cdot 10^{-14}$
$\varkappa$.	−0.13	−0.12	−0.08	−0.01	0.15	0.44	1.05
$E_0 = 0.5$ Mev:							
$G(r)$	0.450	0.398	0.276	0.152	0.0250	$4.85 \cdot 10^{-4}$	$1.32 \cdot 10^{-9}$
$G_a(r)$.	0.433	0.386	0.275	0.156	0.0253	$3.01 \cdot 10^{-4}$	$3.44 \cdot 10^{-12}$
$\varkappa$.	−0.11	−0.10	−0.07	−0.03	0.09	0.29	0.75
$E_0 = 1.0$ Mev:							
$G(r)$	0.370	0.331	0.241	0.142	0.0288	$8.58 \cdot 10^{-4}$	
$G_a(r)$.	0.359	0.324	0.240	0.145	0.0292	$5.86 \cdot 10^{-4}$	
$\varkappa$.	−0.10	−0.09	−0.07	−0.03	0.06	0.22	
$E_0 = 2.0$ Mev:							
$G(r)$	0.269	0.246	0.189	0.123	0.0330	$1.88 \cdot 10^{-3}$	$2.33 \cdot 10^{-7}$
$G_a(r)$.	0.264	0.243	0.190	0.126	0.0342	$1.42 \cdot 10^{-3}$	$2.77 \cdot 10^{-9}$
$\varkappa$.	−0.08	−0.08	−0.06	−0.04	0.03	0.13	0.24

Here three figures are always given for $G(r)$, but the last one is uncertain in most cases, the best accuracy being for $E_0 = 0.1$ Mev. On account of its use in (1), where no higher terms of the development are calculated, $\varkappa$ is only written with two decimals, supposed to be correct.

Because of the large mass of the carbon nucleus and the moderate variation of λ, age-theory is a rather good approximation for carbon. Its deviations from the exact values appear in detail in the table. The general behaviour is here as in all other cases of practical interest[1] the following. For small values of r up to a value r_1 age-theory gives too small values of the slow neutron density. In an intermediate range between r_1 and some value r_2 it gives too large values. At distances beyond r_2 age-theory gives too small values of F_0 and very rapidly breaks down. This is because of the well-known fact that for large r the real dependence on r tends towards an exponential decay. For carbon, the value of r_1 varies a few cm around 20 cm, decreasing with increasing E_0, whereas r_2 increases with increasing E_0, varying around 50–55 cm. The largest errors of age-theory for $r < r_2$ occur for $r = 0$ (varying roughly from 6 % for $E_0 = 0.1$ Mev to 2 % for $E_0 = 2$ Mev) and, of course, for a value of r between r_1 and r_2, varying around 40–45 cm (the error is 3–4 %, increasing with increasing E_0). Figure 1 shows the functions $r^2 G(r)$ and $r^2 G_a(r)$ for $E_0 = 2$ Mev. Their characteristically different behaviours for large r is well illustrated. The curves for the other values of E_0 are quite similar. The figure can also be used as a further check on the values of E_0 are quite similar. The figure can also be used as a further check on the

---

[1] Cf. Holte, Ark. Fys., *6*, 243, 1953, where the case of heavy water is treated.

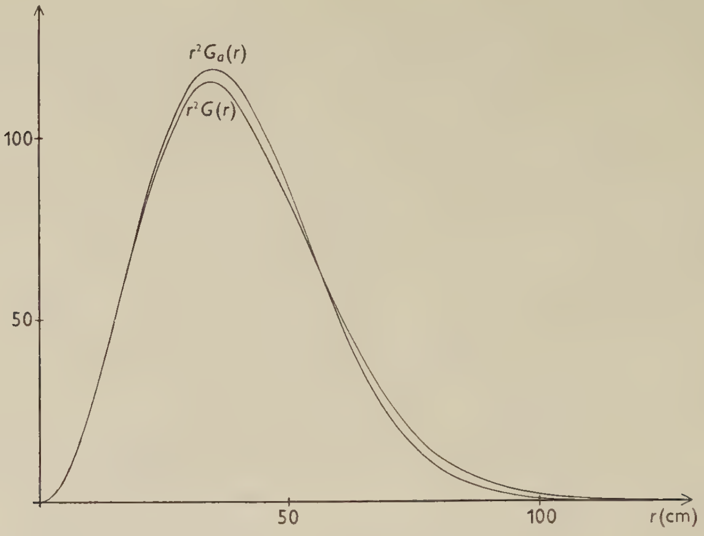

Fig. 1. Carbon, $E_0 = 2$ Mev.

calculation of $G(r)$. The areas between the curves and the r-axis must be equal because when multiplied with a certain constant they are both identical with the neutron energy distribution function (for $E = 1$ ev), which is correctly given by age-theory for slow neutrons. This fact is of great importance for the use of age-theory because it always puts a certain limit to its errors for small and intermediate distances.

Water. This is a case of extremely rapid variation of λ with E. The formula II (58) for $\lambda(E)$ gives a good approximation and is used here. The fundamental constants for water are then given by II (59), (60), (61) and Table 3. A simple treatment according to I, assuming constant λ, requires so low values of E_0 that it is hardly of practical interest. Thus II is used throughout and the values chosen for E_0 are 0.2, 0.5, 1.0 and 2.0 Mev. These are also the values taken in II for the calculation of those constants which depend on E_0. They are given in II Table 4. As for carbon, II (37) is the main formula for the calculation of F_0, always used for small r. But in this case II (48) is also useful, because the very large distances normally required for its applicability are here in the range of practical interest. However, its accuracy is, of course, the better the larger r is, and there is an intermediate range of r-values where II (37) as well as II (48) could be used but where they had to be checked by numerical integration of II (31). In Table 2 below we reproduce the values obtained for $G(r)$, $G_a(r)$ and $\varkappa$. $F_0(r, E)$ is then calculated from (1) for slow neutrons with energy near 1 ev.

As for carbon, the last figure of the values of $G(r)$ (when they are given with three figures) is uncertain. The error of $G(r)$ may amount to 1 % in the worst cases. This is the purely mathematical error obtained in the evaluation of the integral, but then there is also the error coming from the approximations made in the basic assumptions of the theory. The formula for $\lambda(E)$ is not exact, for example, and we have further assumed the ratio of the total mean free path and the mean free path in hydrogen to be constant for all E. These approximations, however, are not serious

Table 2. Water

r (cm)	0	3	6	12	20	30	50	80
$E_0 = 0.2$ Mev:								
$G(r)$	19.1	11.7	3.40	0.098	$3.2 \cdot 10^{-4}$	$1.7 \cdot 10^{-7}$	$2.5 \cdot 10^{-14}$	
$G_a(r)$	17.7	12.1	3.85	0.040	$7.8 \cdot 10^{-7}$	$4.9 \cdot 10^{-16}$	$1.8 \cdot 10^{-45}$	
$\varkappa$	-0.09	-0.06	0.01	0.13	0.22	0.27	0.29	
$E_0 = 0.5$ Mev:								
$G(r)$	12.3	8.29	3.17	0.198	$2.72 \cdot 10^{-3}$	$1.17 \cdot 10^{-5}$	$2.2 \cdot 10^{-10}$	
$G_a(r)$	11.4	8.56	3.65	0.121	$3.8 \cdot 10^{-5}$	$5.3 \cdot 10^{-12}$	$6.3 \cdot 10^{-34}$	
$\varkappa$	-0.08	-0.05	-0.01	0.07	0.10	0.11	0.12	
$E_0 = 1.0$ Mev:								
$G(r)$	7.59	5.78	2.70	0.312	$1.20 \cdot 10^{-2}$	$2.46 \cdot 10^{-4}$	$1.1 \cdot 10^{-7}$	$1.2 \cdot 10^{-12}$
$G_a(r)$	6.74	5.51	3.02	0.273	$9.2 \cdot 10^{-4}$	$1.3 \cdot 10^{-8}$	$4.6 \cdot 10^{-24}$	$9 \cdot 10^{-62}$
$\varkappa$	-0.06	-0.04	-0.01	0.04	0.05	0.05	0.05	0.05
$E_0 = 2.0$ Mev:								
$G(r)$	4.54	3.54	1.91	0.364	0.0384	$2.48 \cdot 10^{-3}$	$1.3 \cdot 10^{-5}$	$5.9 \cdot 10^{-9}$
$G_a(r)$	3.17	2.81	1.95	0.456	0.0145	$1.7 \cdot 10^{-5}$	$8 \cdot 10^{-15}$	$1.2 \cdot 10^{-37}$
$\varkappa$	-0.04	-0.03	-0.01	0.01	0.02	0.02	0.02	0.02

at moderate distances where the maximum error can be estimated to be of the same order of magnitude as the mathematical error.

Age-theory is a very poor approximation for water. This well-known fact appears in detail from Table 2. Of course, it predicts the right order of magnitude for the neutron density for small r, since an integration over all space gives the correct value for the low energy distribution. But the relative variation with r of $G_a(r)$ is of quite another form than for $G(r)$ even for small r. And for large r, $G_a(r)$ becomes increasingly wrong. A detailed comparison of $G_a(r)$ with $G(r)$ gives the following result. For the first intersection point r_1 we have an increase from roughly 2.5 cm for $E_0 = 0.2$ Mev to 5.5 cm for $E_0 = 2.0$ Mev. For the same values of E_0 we have for r_2 an increase from 8 cm to 15.5 cm, roughly. The error of age-theory at $r = 0$, where it gives too small values, varies from 8 % for $E_0 = 0.2$ Mev to 30 %, roughly, for $E_0 = 2$ Mev. The maximum error in the interval $r_1 < r < r_2$, where age-theory gives too large values, is about 13 % for $r = 5.5$ cm and $E_0 = 0.2$ Mev, increasing to about 32 % around $r = 10$ cm and $E_0 = 2.0$ Mev. Finally, for $r > r_2$ age-theory very rapidly becomes useless. For these values of r $F_0(r, E)$ tends for increasing r towards the asymptotic expression II (49). For water, this formula begins to be approximately valid at distances of practical interest. This does not occur for carbon or heavy water, for example. But even for water this requires a high value of E_0. Thus for $E_0 = 2$ Mev the asymptotic formula II (49) ($\lambda_m = 4.2$ cm, $\mu = 1.65$, $\varrho = 1.00$) gives for $G(r)$: 0.49 for $r = 12$ cm, 0.043 for $r = 20$ cm, $2.54 \cdot 10^{-3}$ for $r = 30$ cm, and so on with increasing accuracy, and is therefore a useful approximation for these values of r. On the other hand, for $E_0 = 0.2$ Mev, II (49) gives $7.8 \cdot 10^{-4}$ for $G(r)$ at the distance 20 cm, and a distance of roughly 50 cm is required for the asymptotic formula to be as good as for $E_0 = 2$ Mev, $r = 12$ cm. Finally, $r^2 G(r)$ and $r^2 G_a(r)$ are shown in figures 2, 3 and 4.

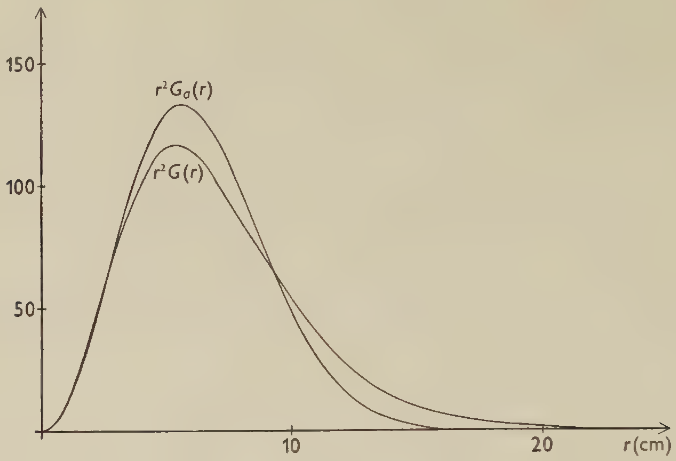

Fig. 2. Water, $E_0 = 0.5$ Mev.

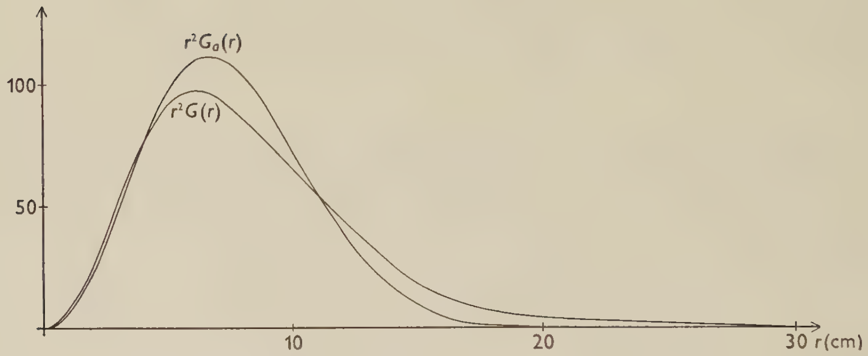

Fig. 3. Water, $E_0 = 1$ Mev.

In this paper we want to point out also that similar calculations have been made for heavy water [5], too. Here as in ordinary water the errors of age-theory are serious and show the same general behaviour. A marked difference between these two moderators is, however (apart from the different "scales of length"), that for heavy water the error of $G_a(r)$ for fixed values of r depends only very little on E_0. This is because the mean free path is (almost) constant for heavy water. In this connection we wish to correct a minor slip in the paper mentioned [5]. If Table 3 in that paper is used $G(r)$ and $G_a(r)$ cannot be defined as for carbon and water but we must divide by a factor 0.1035 in the definition formula for $G(r)$ and $G_a(r)$. Or, defining $G(r)$ and $G_a(r)$ as for carbon and water we have to multiply all the values given in the table for heavy water with the constant 0.1035.

Summary. The stationary density of slow, epi-thermal neutrons around a point source of fast neutrons has been studied. The calculations are made using methods developed in previous papers. Numerical values for the neutron density in homo-

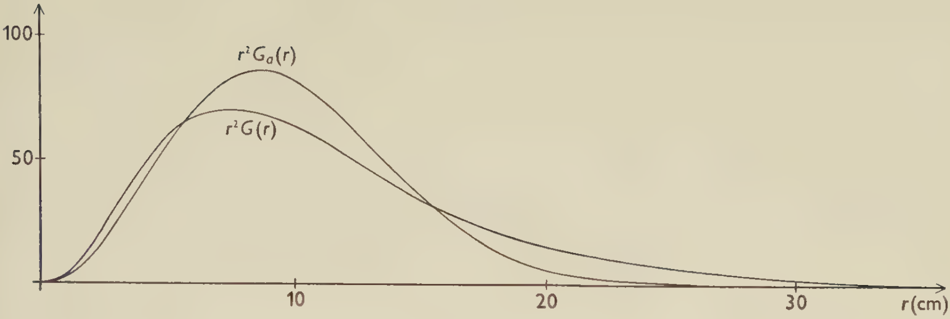

Fig. 4. Water, $E_0 = 2$ Mev.

geneous moderators of carbon and water, respectively, are given in tables and diagrams for different values of the source energy. The validity of the much-used age-theory for these moderators has been studied in detail. For water this theory is practically useless, at least for high energy of the neutron source.

I wish to express my gratitude to the *Swedish Atomic Committee* for a grant for performing the numerical calculations, and to Fil. mag. TURE ERIKSSON, Mr. STIG HOLMQUIST and Mr. CLAES TENGDAHL for assisting me in carrying out this numerical work.

Uppsala, Institute for Mechanics and Mathematical Physics.

REFERENCES

[1] HOLTE, Ark. Fys., *2*, 523, 1951, in the paper referred to as I, Ark. Fys., *3*, 209, 1951, referred to as II.
[2] WALLER, Ark. Mat. Astr. Fys., *34 A*, Nr 3 and 5, 1946.
[3] MARSHAK, Rev. Mod. Phys., *19*, 185, 1947.
[4] WICK, Phys. Rev., *75*, 738, 1949.
[5] HOLTE, Ark. Fys., *6*, 243, 1953.

Tryckt den 10 augusti 1954

Uppsala 1954. Almqvist & Wiksells Boktryckeri AB

ARKIV FÖR FYSIK Band 8 nr 16

Read 10 February 1954 by Oskar Klein

A simple derivation of a general equilibrium equation, with two astrophysical applications

By Per Olof Fröman

Summary. — If the statistical mechanical formula (1), which has been derived by O. Klein, is combined with the well-known thermodynamical equilibrium condition (2) containing the chemical potentials μ_r, one immediately obtains the general equilibrium equation (3), which contains as special cases Saha's formula (4) and another well-known formula (5) of great astrophysical importance.

Using the powerful concept of a Gibbs' grand canonical ensemble, O. Klein has derived the following formula[1]:

$$N_{r,s} = \left(\frac{2\pi m_r k T}{h^2}\right)^{\frac{3}{2}} g_{r,s}\, e^{\frac{\mu_r - E_{r,s}}{kT}}, \tag{1}$$

from which it follows that

$$N_r = \sum_s N_{r,s} = \left(\frac{2\pi m_r k T}{h^2}\right)^{\frac{3}{2}} e^{\frac{\mu_r}{kT}} \sum_s g_{r,s}\, e^{-\frac{E_{r,s}}{kT}}, \tag{1a}$$

where

$N_{r,s}$ is the mean number of particles (per unit volume) of kind r which are in the internal quantum state s, regardless of the translatory motion of the particle
$g_{r,s}$ is the statistical weight of the internal quantum state s of the particles of kind r
$E_{r,s}$ is the energy of the internal quantum state s of the particles of kind r
μ_r is the chemical potential of the particles of kind r
m_r is the mass of a particle of kind r
T is the absolute temperature
k is Boltzmann's constant
h is Planck's constant.

We now consider a possible reaction

$$\sum_r \varkappa_r A_r = 0,$$

---

[1] O. Klein, G. Beskow and L. Treffenberg, Arkiv för mat., astr. o. fys., Band 33 B, No. 1 (1946–47); O. Klein, Supplemento al volume VI, Serie IX del Nuovo Cimento, N. 2 (1949). For one kind of particle the formula was also given in Professor Klein's lectures on statistical mechanics in 1951–52.

between the different kinds of particles. Here, A_r is the symbol for a particle of kind r, and $\varkappa_r$ are coefficients (of which some are positive and some negative). For the above reaction we have the well-known thermodynamic equilibrium condition[1]

$$\sum_r \varkappa_r \mu_r = 0. \tag{2}$$

Combining (1) and (2), we immediately obtain the following general equilibrium equation[2]

$$\prod_r (N_{r,s})^{\varkappa_r} = \prod_r \left\{ \left(\frac{2\pi m_r k T}{h^2} \right)^{\frac{3}{2}} g_{r,s}\, e^{-\frac{E_{r,s}}{kT}} \right\}^{\varkappa_r}. \tag{3}$$

We obtain

$$\prod_r (N_r)^{\varkappa_r} = \prod_r \left\{ \left(\frac{2\pi m_r k T}{h^2} \right)^{\frac{3}{2}} \sum_s g_{r,s}\, e^{-\frac{E_{r,s}}{kT}} \right\}^{\varkappa_r} \tag{3 a}$$

from (1 a) and (2), and

$$\frac{N_{r,s}}{N_r} = \frac{g_{r,s}\, e^{-\frac{E_{r,s}}{kT}}}{\sum_s g_{r,s}\, e^{-\frac{E_{r,s}}{kT}}} \tag{3 b}$$

from (1) and (1 a). The formulae (3 a) and (3 b) together constitute an equilibrium equation which is as general as (3).

We shall now use (3) to obtain two well-known equilibrium equations of considerable astrophysical importance.

I. Let r denote those atoms of a certain kind which have lost r electrons. If (3) is applied to the special reaction in which such an ion loses a further electron, one immediately obtains SAHA's formula in the form

$$N_e \frac{N_{r+1,s'}}{N_{r,s}} = \left(\frac{2\pi m_e k T}{h^2} \right)^{\frac{3}{2}} \cdot \frac{2 g_{r+1,s'}}{g_{r,s}}\, e^{-\frac{E_{r+1,s'} - E_{r,s}}{kT}} \tag{4}$$

if the electron mass is neglected in comparison with the atomic mass. N_e denotes the mean number of free electrons per unit volume, and m_e denotes the electron mass.

II. Let $N(n_K, n_L, \ldots)$ denote the mean number of atoms or ions of a certain kind (per unit volume) with n_K electrons bound in the K-shell, n_L electrons bound in the L-shell, etc. If (3) is applied to the special reaction in which such an atom or ion loses all its electrons, one immediately obtains

$$\frac{N(n_K, n_L, n_M, \ldots)}{N(0,0,0,\ldots)} = \left(\frac{N_e}{2\left(\frac{2\pi m_e k T}{h^2} \right)^{\frac{3}{2}}} \right)^{n_K + n_L + n_M + \cdots} \cdot \binom{2\cdot 1^2}{n_K} \cdot \binom{2\cdot 2^2}{n_L} \cdot \binom{2\cdot 3^2}{n_M} \cdots e^{\frac{n_K \chi_K + n_L \chi_L + n_M \chi_M + \cdots}{kT}} \tag{5}$$

---

[1] This equilibrium condition can be derived by the use of Gibbs' grand canonical ensemble. See O. KLEIN, Supplemento al volume VI, serie IX del Nuovo Cimento, N. 2 (1949).

[2] For the sake of simplicity we have suppressed the subscript r on the index s.

if the mass of the electrons is neglected in comparison with the atomic mass. Here $\chi_K, \chi_L, \chi_M, \ldots$ denote the (mean) ionization potentials for the K-, L-, M-, ... shells. The formula (5) is very important for calculations of the ionization (and the opacity) of stellar matter.

This note was initiated by Professor O. KLEIN's lectures on statistical mechanics given in 1951–52 at Stockholms Högskola. I am indebted to Professor KLEIN for valuable discussions and for his kind criticism of my manuscript.

CERN (European Council for Nuclear Research),
Theoretical Study Group at the Institute for Theoretical Physics,
University of Copenhagen.

Tryckt den 10 augusti 1954

Uppsala 1954. Almqvist & Wiksells Boktryckeri AB

ARKIV FÖR FYSIK Band 8 nr 17

Communicated 3 June 1953 by Oskar Klein and Ivar Waller

A quantum mechanical investigation of the binding energy of the LiH-crystal

By Stig O. Lundqvist

With 1 figure in the text

Summary

The binding energy of the lithium hydride crystal has been computed, using a wave function constructed from the one-electron wave functions of the free ions. The approximations in the earlier treatments of ionic crystals have been investigated, and we found, that some neglections in the earlier papers seem to be justified but a certain approximation used in a number of theoretical investigations of molecules and crystals must be considered inadmissible unless only a rough estimate of the binding energy is desired. The free ion orbital approach cannot be justified to the same extent here as in certain other crystals e.g. NaCl, as the deformation of the diffuse hydrogen ions in the field of the crystal must be expected to be considerable. The total energy was minimized with respect to the effective nuclear charge of the hydrogen ion. The effective nuclear charge for hydrogen ions in the lattice was nearly the same as for free ions and the corresponding value of the cohesive energy was -205 kcal/mol to be compared with the experimental value -217 ± 7 kcal/mol.

I. Introduction

The Heitler-London theory applied to ionic crystals has been rather successful in predicting correctly the binding energy and lattice constant of some of the simplest ionic crystals. In the earlier investigations by Hylleraas [1], Landshoff [2], and Löwdin [3] the one-electron wave functions used in the calculations have been those of the free ions. From a closer examination it is clear, however, that even for some of the simplest ionic crystals this approach must be insufficient and that a good agreement between theory and experiment may be somewhat fortuitous. This can be understood from the following qualitative argument. An electron moving close to a positive ion is acted upon mainly by the field due to that ion. So, in general it cannot be considered as a fair approximation to describe the electrons in this region by the free ion wave functions associated with the neighbouring negative. In some crystals like NaCl and KCl, however, the probability of an electron in a free negative ion in an arbitrary orbital to be found at a distance from the nucleus comparable to the interionic distance in the lattice is very small and we can therefore at least hope, that the effect of the deformation in the field of the crystal will not be large. In other cases we find that the probability of an electron associated with a free negative ion in certain orbitals to be at a distance from the nucleus comparable to the interionic distance is rather large; this will be the case e.g. in crystals, where the one-electron functions associated with the outer shells of the negative ion are falling off very slowly and the positive ion is small. In such crystals it is clear, that we must explicitly account for the deformations of the negative ions in the field of the crystal.[1]

An excellent example of a crystal of the latter kind is the LiH-crystal, formerly investigated by Hylleraas. Here the negative ions are extremely diffuse and it seems to be rather little justification to consider the electrons as well localized around the hydrogen nuclei in the lattice. The electrons associated with the lithium ions are very strongly bound and it seems therefore to be a good approximation to neglect the deformation of the lithium ions. The problem then consists in treating the motion of the two remaining electrons per unit cell in the field of the hydrogen nuclei and the lithium ions, and it is obvious that the ground state of the crystal may not be adequately described in terms of ionic- and covalent binding in the conventional sense. A satisfactory way to treat this problem would be to solve the Hartree-Fock equations for the crystal, neglecting the deformation of the lithium ions. An attempt to calculate a self-consistent field for LiH has been made by EWING and SEITZ [4], using the cellular idea. Unfortunately, so many approximations had to be introduced, that the method may be used only for qualitative purposes. As yet, no accurate methods for solving the Hartree-Fock equations for a crystal have been developed.

Because of the difficulties in solving the Hartree-Fock equations we have tried a molecular orbital approach, where in the first approximation we have constructed the molecular orbitals from the orbitals of the free hydrogen ions, thus neglecting the effect of the crystal field. This approximation is of course identical to the Heitler-London approach, because of the invariance of the energy against linear transformations of the one-electron wave functions. Due to the slow decrease of the free hydrogen ion wave functions we had to consider the overlapping between neighbouring negative ions up to the sixth order neighbours. As expected the results showed, that the change in the wave functions due to the crystal field must be of rather large importance. We have tried to estimate the order of magnitude of this change by regarding the effective nuclear charge of the hydrogen ions as a variable parameter and minimized the total energy of the crystal with respect to this parameter. We found that about $\frac{1}{3}$ of the discrepancy between the theoretical values of the binding energy was removed, but that the corresponding change in the effective nuclear charge was very small. This result suggests, that the wave functions may not deviate much from the free ion wave functions in the neighbourhood of the hydrogen nuclei, but the remaining discrepancy indicates that the deformations at larger distance from the hydrogen nucleus cannot be described in this simple fashion but that a more general approach is necessary.

In the earlier investigations terms of third and higher orders in the overlap integrals have been neglected in the expression for the cohesive energy. The condition for using this approximation has been discussed in an earlier paper [5]. In the case of LiH this approximation consists in taking the first term in a divergent expansion of the expression for the cohesive energy. Nevertheless there are some indications in the earlier investigations, that this approximation might give reasonable results even in cases, where, from a strict point of view, it must be considered inadmissible. We have investigated this approximation and found that, if the overlapping up to the fourth order neighbours is considered, the lattice constant agrees well with the experimental value, and that the value of the binding energy is about the same as that obtained in the complete calculation already in the most naïve approximation, where only the overlapping between nearest neighbours is considered.

---

[1] The arguments above will still be true, even if we include the effect of the exchange interaction between electrons associated with different ions into account, because this interaction will be small, the overlap between the wave functions being small, but may be of importance in crystals, where the overlap is considerable.

We should also like to make a remark about an approximation extensively used in the theory of molecules. When deriving the expression for the binding energy, it has often been assumed, that the wave functions are solutions of the atomic problem in the one-electron approximation. Certain simplifications of the energy expression are then possible. However, in most calculations approximate wave functions of a simple analytical form, e.g. derived from the variational principle, have been used. Hereby an error is introduced, which may be of a rather large magnitude. In our case we have estimated the error due to this approximation to be about 10 % of the binding energy (or more correctly 30 % of the repulsive energy, the electrostatic energy of the lattice not depending on the wave functions). Therefore approximations of this kind must be considered as inadmissible, unless only a rough estimate of the molecular energies is desired.

II. The energy formula

For the numerical calculations it is convenient to express the energy of the system in terms of the non-orthogonal atomic orbitals. Because of the invariance of the energy against linear transformations of our original set of one-electron wave functions, it is possible to express the energy in terms of the atomic wave functions in such a way, that the coefficients in the crystal orbitals will not appear. As the basis of the present investigation we will take the formula for the total energy of the crystal, derived by Löwdin [3], which can be written in the following form:

$$E = E_{\mathrm{I}} + E_{\mathrm{II}} + E_{\mathrm{III}} \tag{1}$$

$$E_{\mathrm{I}} = \sum_{\mu} (\mu \,|\, H^{\mu} \,|\, \mu) + \sum_{\mu} \sum_{\nu}{}^{\mu} \{ (\mu\,\nu \,|\, G \,|\, \mu\,\nu) - (\mu\,\nu \,|\, G \,|\, \nu\,\mu) \} \tag{2}$$

$$E_{\mathrm{II}} = -\sum_{\mu} \sum_{\nu} P_{\mu\nu} \{ (\nu \,|\, H^{\mu} \,|\, \mu) + 2 \sum_{\varkappa}{}^{\mu} \{ (\nu\,\varkappa \,|\, G \,|\, \mu\,\varkappa) - (\nu\,\varkappa \,|\, G \,|\, \varkappa\,\mu) \} \tag{3}$$

$$E_{\mathrm{III}} = E_1 + E_2 + E_3 + E_4 \tag{4}$$

$$E_1 = W + \sum_{\mu} \{ (\mu \,|\, H^{(\mu)} \,|\, \mu) + \sum_{\nu}{}^{(\mu)} (\mu\,\nu \,|\, G \,|\, \mu\,\nu) \} \tag{4 a}$$

$$E_2 = -\sum_{\mu} \sum_{\nu}{}^{(\mu)} (\mu\,\nu \,|\, G \,|\, \nu\,\mu) \tag{4 b}$$

$$E_3 = -\sum_{\mu} \sum_{\nu} P_{\mu\nu} \{ (\nu \,|\, H^{(\mu)} \,|\, \mu) + 2 \sum_{\varkappa}{}^{(\mu)} \{ (\nu\,\varkappa \,|\, G \,|\, \mu\,\varkappa) - (\nu\,\varkappa \,|\, G \,|\, \varkappa\,\mu) \} \} \tag{4 c}$$

$$E_4 = \sum_{\mu} \sum_{\nu} \sum_{\varkappa} \sum_{\lambda} P_{\mu\varkappa} P_{\nu\lambda} \{ (\varkappa\,\lambda \,|\, G \,|\, \mu\,\nu) - (\varkappa\,\lambda \,|\, G \,|\, \nu\,\mu) \} \tag{4 d}$$

The symbols used here have the following meaning:

$$(\mu \,|\, H \,|\, \nu) = \int \psi_{\mu}^{*}(1)\, H_1\, \psi\ (1)\, d\,\tau_1$$

$$(\mu\nu|G|\varkappa\lambda)=\iint \psi_\mu^*(1)\,\psi_\nu^*(2)\,\frac{e^2}{2|\boldsymbol{r}_1-\boldsymbol{r}_2|}\,\psi_\varkappa(1)\,\psi_\lambda(2)\,d\tau_1\,d\tau_2$$

$$W=\frac{e^2}{2}\sum_g\sum_{g'}{}^{(g)}\frac{Z_g\,Z_{g'}}{|\boldsymbol{r}_g-\boldsymbol{r}_{g'}|}$$

$$H_i^\mu=\frac{1}{2\,m}\boldsymbol{p}_i^2-e^2\frac{Z_{g_\mu}}{|\boldsymbol{r}_i-\boldsymbol{r}_{g_\mu}|}$$

$$H_i^{(\mu)}=-e^2\sum_{g'}{}^{(g_\mu)}\frac{Z_{g'}}{|\boldsymbol{r}_i-\boldsymbol{r}_{g'}|}$$

Here $\Psi_\mu(1)$ are the normalized one-electron wave functions including spin, $(1)=(r_1,\xi_1)$. The index μ refers to an electron with the quantum number n, l, m, j associated with an ion at a certain lattice point g. The sign $\int d\tau_i$ implies a summation over the spin coordinate ξ_i and an integration over the space coordinates $\boldsymbol{r}_i$. Z_g is the atomic number of the nucleus at a certain lattice point g, e is the electron charge and $\boldsymbol{p}_i$ denotes the momentum of the electron i. $\sum_\nu^{(\mu)}$ means a summation over all indices ν except those associated with the same ion as μ. The quantities $P_{\mu\nu}$ are the elements of a matrix $\boldsymbol{P}$ defined by

$$\boldsymbol{P}(\boldsymbol{1}+\boldsymbol{S})=\boldsymbol{S} \tag{5}$$

where $\boldsymbol{S}$ is the Hermitian matrix

$$S_{\mu\nu}=\int\psi_\mu^*(1)\,\psi_\nu(1)\,d\tau_1-\delta_{\mu\nu} \tag{6}$$

If ψ_μ are wave functions for the free ions then E_{I} is the expectation value of the total energy of the free ions. E_{II} equals zero if ψ_μ satisfy the Hartree-Fock equations for free ions; in this case therefore E_{III} represents the cohesive energy of the system. If, however, ψ_μ are only approximate wave functions for the free ions, then E_{II} is no longer equal to zero, tending however towards zero, when the lattice constant goes to infinity. The cohesive energy is then equal to $E_{\text{II}}+E_{\text{III}}$. The expression for the energy given above is not written in a form suitable for numerical calculations, as each term in it is not proportional to the crystal volume (the lattice constant being fixed) and the spin has not been eliminated. The corresponding transformed expression for the cohesive energy specialized to LiH can be found in ref. [5].

Provided that the condition

$$\sum_\nu|S_{\mu\nu}|<1 \tag{7}$$

is fulfilled for all μ, the matrix P can be expanded in the power series.[1]

$$\boldsymbol{P}=\boldsymbol{S}-\boldsymbol{S}^2+\boldsymbol{S}^3-+\cdots \tag{8}$$

Introducing this expansion into (4 c) and (4 d) and regarding integrals whose integrand is a product of $\psi_\mu^*(1)\psi_\nu(1)$ and a slowly varying function as a quantity small of the first order, then if neglecting terms small of the third order and higher we obtain the following approximate expressions.[1]

---

[1] Cf. ref. [5] p. 434.

$$E_3 = -\sum_{\mu}\sum_{\nu}^{(\mu)} S_{\mu\nu}\left\{(\nu\,|\,H^{(\mu)}\,|\,\mu) + 2\sum_{\varkappa}^{(\mu)}(\nu\,\varkappa\,|\,G\,|\,\mu\,\varkappa) - 2\,(\nu\,\nu\,|\,G\,|\,\nu\,\mu)\right\} -$$

$$+\sum_{\mu}(S^2)_{\mu\mu}\left\{(\mu\,|\,H^{(\mu)}\,|\,\mu) + 2\sum_{\nu}^{(\mu)}(\mu\,\nu\,|\,G\,|\,\mu\,\nu)\right\} \qquad (4\,\mathrm{c}')$$

$$E_4 = -\sum_{\mu}\sum_{\nu}^{(\mu)} S_{\mu\nu}\,S_{\nu\mu}\,(\mu\,\nu\,|\,G\,|\,\mu\,\nu) \qquad (4\,\mathrm{d}')$$

A detailed discussion of these formulae has been given by LÖWDIN, ref. [3] (Cf. also ref. [6] pp. 28 and 29). Equations (4 a), (4 b), (4 c′), and (4 d′) form the essential basis of the calculations performed by HYLLERAAS, LANDSHOFF, and LÖWDIN.[2]

We will now introduce the following definition. Two ions associated with two lattice points g and g' are said to be neighbours of the k:th order if the distance between the lattice points, $|\boldsymbol{r}_g - \boldsymbol{r}_{g'}|$ is equal to $a\,k^{\frac{1}{2}}$ where a is the interionic distance. It is immediately seen that in a lattice of the NaCl-type odd values of k always represent a pair of unequal ions, whereas even values of k correspond to a pair of ions of the same kind. As in our case the overlap between neighbouring positive ions is negligible, the interaction between two neighbours of even order will always mean an interaction between a pair of negative ions. As both ions have only two electrons, each in a 1s-state a quantity dependent only on an index pair (μ, ν) will then be completely determined by the order k together with an information as to which kind of ion one of the indices μ, ν is associated with (in the case of odd k). We wish to point out that we make use of these terms to describe mathematical quantities appearing in the energy expression and that only the complete expression for the cohesive energy has a clear physical meaning.

The condition (7) can be written

$$\sum_{k} |\,n_k\,S_k^{\mu}\,| < 1,$$

where μ can be associated with either a positive or a negative ion and n_k is the number of neighbours of the k:th order. In the following table we have given $n_k S_k^{H^-}$ and a quantity $\sigma_k^{H^-}$ defined by

$$\sigma_k^{H} = \sum_{k\;1}^{k} |\,n_k\,S_k^{H^-}\,|$$

for the first few values of k.

Table of $n_k\,S_k^{H^-}$ and $\sigma_k^{H^-}$.

k	1	2	3	4	5	6
$n_k\,S_k^{H^-}$	0.443	2.633	0.088	0.460	0.070	0.766
$\sigma_k^{H^-}$	0.443	3.076	3.164	3.624	3.694	4.460

---

[1] Cf. ref. [3] p. 38.

[2] We wish to point out that Hylleraas has only given the formulae specialized to LiH, and in the corresponding expression given by LANDHOFF, the term (4 d′) is missing.

The table exhibits clearly the slow decrease in the overlap between the negative ions with increasing k and shows the necessity of investigating the interaction terms between a negative ion and a large number of its neighbours. It is also seen that the (sufficient) condition for the convergence of the series expansion is not satisfied for LiH. Unfortunately a comparison with the alkali chlorides and -fluorides could not be made, as the overlap integrals between neighbours of order higher than the first have not been computed. From tables, which Löwdin has kindly placed at our disposal, we have estimated σ_1'' for NaCl, KCl, NaF, and KF at the observed interionic distances and have found the largest value of σ_1'' to be considerably less than unity for NaCl and NaF but not far from the critical value for KCl and KF. Because of the large interionic distance in the latter crystals, however, the contributions from neighbours of higher orders will probably be rather small.

The good agreement between the theoretical and experimental values of the binding energy obtained by previous investigators, especially HYLLERAAS, in cases, where contributions from terms of third and higher orders in the overlap integrals may be expected to be important, motivates a detailed numerical investigation of the S^2-approximation, despite the fact that, in the case of LiH, it represents the first term in a divergent series expansion of the energy of the crystal. In the first stage of approximation (A) we will only consider the overlapping between nearest neighbours, which is the approximation considered by LANDSHOFF and LÖWDIN. In the next approximation (B) we include the interaction between neighbours of the second order. From the table on p. 10 it is seen that the overlapping between neighbours of the fourth order is of the same order of magnitude as that between nearest neighbours. In (C) therefore the overlap between neighbours of the first, the second, and the fourth order is considered, the interaction between third order neighbours is neglected because of the small overlap integrals. The results in A, B, and C will be compared with the results obtained when using the complete expression for the cohesive energy. In this approximation (D) we have considered the overlap between neighbours up to the sixth order. Because of the large number of integrals involved in this case we have carried through the computations only at the observed interionic distance, whereas in A, B, and C the calculations have been performed in four equidistant points.

The atomic wave functions used in our calculation are the hydrogen-like 1s-wave functions

$$\psi(|\boldsymbol{r}-\boldsymbol{r}_g|)=\sqrt{\frac{Z_g'^3}{\pi}}\,e^{-Z_g'|\boldsymbol{r}-\boldsymbol{r}_g|} \tag{9}$$

with an effective nuclear charge

$$Z_g'=Z_g-{}^5/_{16}$$

Here the atomic units are used. For the lithium ion this function will be sufficiently close to the Hartree-Fock function for our purpose. For the hydrogen ion we have compared the radial charge density calculated from (9) with that obtained from the two-electron wave function including correlation given by BETHE [7]. The agreement is not so good, the charge density calculated from (9) falls off more rapidly at large distances from the nucleus, and the maximum value is somewhat higher. A better wave function given analytically as a sum of two exponential functions has been calculated by LÖWDIN.[1]

---

[1] P. O. LÖWDIN, private communication.

It was, however, our intention to carry through the whole calculation analytically and even the use of a wave function with two exponential functions would have meant a tremendous increase of the numerical work. At the time, when our calculations were nearly finished, Löwdin derived a general approximate formula for the energy of a molecule or crystal which essentially contains only overlap and coulomb integrals.[1] Using this expression the calculations can be carried through in a rather simple manner even when using more complicated wave functions. For LiH, however, which is a rather exceptional case, it does not yet seem quite certain that all types of integrals occurring can be expressed in terms of coulomb and overlap integrals with sufficient accuracy.

Before presenting the numerical results we should like to make a remark about an approximation which has been extensively used in molecular calculations based upon the use of atomic orbitals.[2] Let H' denote the Hartree-Fock operator of an electron in a free atom and Ψ_μ a set of approximate wave functions for the same atom, e.g. obtained from the variational principle. The diagonal elements of H' with respect to Ψ_μ are

$$(\mu|H'|\mu)=\varepsilon_\mu \tag{10}$$

where ε_μ is an approximate value of the parameter occurring in the Hartree-Fock equation. The approximation consists in putting the nondiagonal elements equal to

$$(\nu|H'|\mu)=\varepsilon_\mu S_{\nu\mu} \tag{11}$$

Introducing (10) and (11) into (3) we get

$$E_{\text{II}}=-\sum_\mu\sum_\nu P_{\mu\nu}(\nu|H'|\mu)=-\sum_\mu \varepsilon_\mu \sum_\nu P_{\mu\nu}(1+S)_{\nu\mu}=$$
$$=-\sum_\mu \varepsilon_\mu\{\boldsymbol{P}(\boldsymbol{1}+\boldsymbol{S})\}_{\mu\mu}=-\sum_\mu \varepsilon_\mu S_{\mu\mu}=0$$

However, the relation (11) holds only if ψ_μ are the solutions of the Hartree-Fock equations for a free atom, and an improper use of (11) will lead to incorrect results. In our case E_{II} will be different from zero and will exhibit a variation with the interionic distance, tending to zero when the interionic distance tends to infinity; it must therefore be included in the cohesive energy. A similar approximation was introduced by HYLLERAAS, who, when deriving his eq. 11 p. 776 [1], assumed the wave functions to be the solutions of the atomic eigen-value problem but later introduced approximate wave functions. In view of the fact that approximations of the kind mentioned above have been used in a large number of theoretical investigations of molecules, we will first give the results of our calculation of E_{III} separately and then add the contributions from E_{II}, in order to show clearly how these approximations affect the results. For details of the calculations we refer to the appendix.

III. The numerical results

A comparison term by term between the first and the second columns shows clearly the necessity of including the overlapping between the negative ions, but it also shows that these interaction terms cancel to a large degree. Most surprising is the

---

[1] P. O. LÖWDIN, to appear in Journal of Chemical Physics.

[2] When this work was already finished, Dr. LÖWDIN kindly pointed out that a similar discussion has been given by H. MARGENAU, ref. 16, pp. 88–90, in the case of two atoms having closed shells.

Table of E_{III} (in kcal/mol). $a = 3.875$ a.u.

A. Overlap between neighbours of the first order.
S^2-approximation: *B.* ,, ,, ,, ,, ,, ,, and second order.
C. ,, ,, ,, ,, ,, ,, , second, and fourth orders.
Complete expression: *D.* ,, ,, ,, up to the sixth order.

	A	*B*	*C*	*D*
E_1	− 255.3	− 285.4	− 286.0	− 286.0
E_2	− 36.4	− 147.4	− 153.7	− 158.7
E_3	+ 107.9	+ 282.2	+ 279.1	+ 284.1
E_4	− 10.7	− 75.9	− 78.4	− 62.1
E_{III}	− 194.7	− 226.5	− 239.0	− 222.7

agreement between *B*, *C*, and *D* with regard to the non-orthogonality term E_3. As to E_4 the agreement is not very close, but in fact one could hardly expect any agreement at all. The interionic distance to which the table refers is very close to the observed interionic distance, $a_0 = 3.860$ a. u. We note that in the last column the value of E_{III} is fairly close to the experimental value of the cohesive energy which is -217 ± 7 kcal mol.

In the next table we have given the values of E_{III} for the interionic distances $a = 3.5$, 3.75, 4.0, and 4.25 a.u. Here, in the last column (*E*) we have used Hylleraas formula for the repulsive potential eq. 24 p. 782 [1] and considered the overlap between neighbours of the first and the second orders.

Table of E_{III}.

a	*A*	*B*	*C*	*E*
3.50	− 164.1	− 213.9	− 245.5	− 196.2
3.75	− 186.3	− 225.1	− 242.5	− 212.4
4.00	− 200.9	− 226.6	− 236.2	− 223.1
4.25	− 204.7	− 220.0	− 225.6	− 220.0

We find that in (*A*) E_{III} has a minimum value ≈ -205 kcal mol at $a \approx 4.2$ a.u. in (*B*) the minimum of E_{III} is about -227 kcal mol at $a \approx 3.95$, rather near the observed interionic distance, but in (*C*) E_{III} has no minimum in the interval. In (*D*) the minimum agrees rather well with Hylleraas own results $E_{\mathrm{III}} \approx -225$ kcal/mol, $a_0 \approx 4.1$ a.u. to be compared with his own results: -219 kcal/mol and 4.18 a.u. respectively. This shows that the approximations introduced by him when computing the integrals do not appreciably affect the results. A comparison with (*B*) shows, however, that the terms in the energy which HYLLERAAS neglected correspond to an attractive potential which is rather small, but which tends to displace the minimum in the direction of the observed interionic distance.

The term E_{III} alone represents the cohesive energy of the crystal if the atomic wave functions satisfy the Hartree-Fock equations for free ions or if the contributions from E_{III} can be neglected. It has generally been believed that the use of (11) or similar approximations will only introduce a minor error. That this is not the case, at least not in our case, is clear from the following table.

Table of E_{II} *(in kcal/mol).*

a	A	B	C
3.50	12.1	43.2	47.7
3.75	9.3	37.0	40.1
4.00	7.1	30.6	32.6
4.25	5.4	25.8	27.1

It is immediately seen, that this quantity can by no means be neglected. It corresponds to a repulsive potential which varies rapidly with the interionic distance. Adding this term to E_{III} we obtain the results appearing in the following table.

Table of $E_{\mathrm{coh}} = E_{\mathrm{II}} + E_{\mathrm{III}}$ *(in kcal/mol).*

a	A	B	C
3.50	− 152.0	− 170.7	− 197.8
3.75	− 177.0	− 188.1	− 202.4
4.00	− 193.8	− 196.0	− 203.6
4.25	− 199.3	− 194.2	− 198.1

From these results we have estimated the minimum values of E_{coh} which are given in the following table together with the observed values, and the results for $a = 3.875$ a.u. calculated from the complete expression (D). In this approximation we found $E_{\mathrm{II}} = 22.9$ kcal mol.

Cohesive energy (in kcal/mol) and lattice constant (in Ångströms).

	A	B	C	D	Observed
Cohesive energy	− 199.3	− 196.4	− 203.9	− 199.1	− 217 ± 7
Lattice constant	4.50	4.34	4.16	4.10	4.085

The results show that the good agreement with the observed value of the binding energy when E_{II} is neglected is purely fortuitous. The discrepancy between the calculated and the observed values is in reality considerable. Rather astonishing, however, is the close agreement between the minimum values of E_{coh} in the different stages of approximation. The results indicate that the terms of third and higher orders in the overlap integrals cancel to a large degree and that even the most naïve approximation (A), where only the overlap between neighbours of the first order has been taken into account, gives about the same value of E_{coh} as (D), where the overlap up to the sixth order neighbours is considered. As regards the lattice constant, however, the situation is different. The interaction between the second and the fourth order neighbours has an attractive character and tend to displace the minimum in the direction of the observed lattice constant. It seems that it is not sufficient to include only the interaction between the first and the second order neighbours, but that also the interaction between neighbours of higher order must be considered.

In a large number of theoretical investigations of molecules approximate atomic wave functions have been used, e.g. hydrogen-like wave functions with an effective nuclear charge for the electrons in the first two shells, and a relation like (11) or some similar approximation has been used in order to simplify the calculations. In many cases the results have been in good agreement with the experimental values and it has generally been considered that the best atomic orbitals can be replaced equally well by a set of approximate wave functions, e.g. analytical wave functions of a simple form which in many problems are easier to work with than the numerically given Hartree-Fock functions. Our results show clearly the danger in using approximations of this kind, and that the conclusions drawn from the results can be incorrect. The good agreement in our case when E_{II} is neglected would in fact indicate that the choice of atomic wave functions would have been a good one, but the final results show that better wave functions must be used in order to get a closer agreement with the experimental binding energy.

IV. Variation of the effective nuclear charge of the hydrogen ion

Our results show that a better choice of wave functions is necessary in order to improve the energy value. In the first step one could either solve the Hartree-Fock equations for a free hydrogen ion and repeat the calculations in order to see whether the discrepancy is due to the rather poor wave functions used here — or one could choose wave functions of a certain analytical form containing a number of parameters and minimize the total energy with respect to these parameters. In the latter way the deformations in the field of the crystal can be accounted for. Such a minimization has recently been performed by YAMASHITA [8] and YAMASHITA and KOJIMA [9] treating LiF and MgO. They minimized the total energy with respect to parameters introduced in the wave functions of the 2 p-orbitals of F^- and O^{--} and found in the case of LiF a slight contraction of the F^--ion. However, their investigation is based upon Landshoff's expression for the cohesive energy, which is not quite correct to the second order in the overlap integrals as the term corresponding to E_4 in our notation is missing. This term corresponds to an attractive potential and is of the order of magnitude -10 kcal mol. It seems also doubtful whether the term corresponding to E_{II} is taken into account in their calculation since these writers do not mention it. Even if this term is negligible for the free atom values of the parameters, the variation in E_{II} must necessarily be considered, when determining the minimum. Finally we wish to point out an error in their table for LiF (p. 285 [8]). As the binding energy must be numerically larger for the varied functions than for the corresponding atomic functions, the results given in the table cannot be correct. A comparison with the tables on p. 286 suggests that the figures in the second and the third rows should change their places.

We should like to make some remarks here about the method of minimizing the total energy with respect to parameters in the atomic wave functions. The expression for the total energy can often be written in the form $E = E_0 + E_1$ where, if atomic wave functions are used, E_0 represents the energy of the atoms and E_1 the interaction between them, i.e. the binding energy. We note that $|E_1| \ll |E_0|$ and that a small change in the wave functions will produce a change in E_1 which is small compared with E_1 itself. We further know that the large term E_0 has its minimum value for the free atom values of the parameter and that δE_0 therefore always is positive.

Considering all variations which are possible in our system of interest we can exclude from the very beginning all variations, which, for a small change in the wave functions, will make δE_0 of the same order of magnitude as E_1, as the minimum of the total energy must then be very close to the minimum of E_0. This will be the case e.g., if the wave functions of a large number of electrons of each atom are varied simultaneously and especially if the inner shell wave functions are varied. Therefore, we have only to consider variations that will produce a small δE_0 for a small change in the wave functions.

We further know that, when distorting the wave function of an electron in a free atom in the region where its radial probability density is large, the energy of the atom will rise more rapidly than if we distort the wave functions at large distances from the nucleus. However, in molecular problems the behaviour at distances from the nucleus comparable to the interatomic distance is often very important, and a change in the wave functions in this region may produce considerable changes in the values of the molecular integrals and therefore in E_1, whereas δE_0 will be comparatively small.

When investigating the deformation of the atoms in a molecule or a crystal, the symmetry of the system must be taken into consideration. In systems with strong overlap and bonding effects the charge distribution differs appreciably from the sum of the charge densities of the constituents. In LiH, where the free ions are spherically symmetrical, the charge density around a nucleus will not be spherically symmetrical but will have the cubical symmetry of the lattice. When changing the radial dependence of the wave functions, the overlap densities $\psi_g^*(\boldsymbol{r})\psi_{g'}(\boldsymbol{r})$, which have axial symmetry with respect to the axis $\boldsymbol{r}_{gg'}$, will also change, thus producing a non-spherical deformation of the charge distribution. Therefore, part of the angle-dependent deformations is in fact taken into account by only changing the radial part of the atomic wave functions.

In our calculation we have used the hydrogen-like wave functions with a variable effective nuclear charge. Of course it would have been most desirable to represent the wave functions of the hydrogen ions by a sum of at least two exponential functions, permitting an independent variation of the inner and outer parts of the wave function. This would, however, necessitate a calculation of a tremendous number of integrals and therefore we have chosen the simpler functions in order to make use of the integral tables already computed.

The electrons of a free lithium ion are very strongly bound, and the wave functions fall off very rapidly from the nucleus. The electrons of a free hydrogen ion, on the other hand, are very loosely bound and their wave functions decrease rather slowly. The energy of a free lithium ion amounts to about -7.2 a.u. whereas the energy of a free hydrogen ion is only about -0.5 a.u. Disregarding the electrostatic energy of the lattice, which does not depend on the wave functions, the remaining part of the cohesive energy is of the order of magnitude 0.1 a.u. per pair of ions. When varying the effective nuclear charge of the lithium ion, the large term representing the energy of the free lithium ions rises so rapidly, that it seems out of question that the minimum value could appreciably deviate from that for free ions. Therefore this parameter has been kept fixed, and only the effective nuclear charge of the hydrogen ion has been varied.

When undertaking this part of the investigation the aim was not only to get a better agreement with the experimental binding energy but still more to find out how much the wave functions would change. For a value of the effective nuclear charge fairly close to 11/16 the wave functions will still have the characteristics of a free hydrogen-ion wave function. If, however, the minimum would occur for a value of the effective nuclear charge far from the free ion value, this would have clearly indicated that the whole approach of constructing a wave function by using the orbitals of free hydrogen ions had been insufficient. In order to get the most reliable result, we did not dare to use the approximate expressions, but the calculations have been based upon the complete expression and the overlap up to the neighbours of the sixth order has been taken into account. The variable effective nuclear charge is expressed in terms of a parameter f by

$$Z_{\text{eff}} = 11/16\, f$$

In the following table we have given the results in terms of a new parameter λ defined by

$$f = 1 + 0.03226\,\lambda$$

Table of δE (in kcal/mol). $a_0 = 3.875$ a.u.

λ	-3	-2	-1	$+1$	$+2$	$+3$
δE_{I}	$+5.1$	$+2.3$	$+0.6$	$+0.6$	$+2.3$	$+5.2$
δE_{II}	-13.5	-7.0	-3.1	$+3.1$	$+5.6$	$+8.7$
δE_{III}	$+28.2$	$+18.4$	$+9.5$	-8.5	-12.5	-15.0
δE	$+19.9$	$+13.7$	$+7.0$	-4.8	-4.7	-1.1

We note the very slow variation in the large term E_{I}. The second part E_{II}, however, varies rather rapidly and it is obvious, that this term must be taken into consideration even in cases, where the contribution for the free ion values of the parameters may be neglected. We find at the minimum point $\delta E = -5.5$ kcal mol at $\lambda = 1.50$. The effective nuclear charge is increased by a factor 1.048, or from 0.6875 to 0.7208. The improvement in the energy value is rather small, giving the final result $E_{\text{coh}} = -204.6$ kcal mol. However, the wave functions used here are probably rather poor approximations to the best one electron wave functions for free hydrogen ions and by introducing only one parameter one cannot expect to remove more than part of the discrepancy between the theoretical and experimental binding energy. In order to account properly for the deformations in the field of the crystal more parameters must be used. The rather small change in the effective nuclear charge is interesting, suggesting that it seems possible to use the free ion orbital approach in a first approximation. If it had been possible to use wave functions of a more complicated analytical form, we had been able to give a more definite answer to that question. However, in this problem already a minimization of the total energy with respect to only three or four parameters would be so prohibitively complicated that it would perhaps be easier to try another approach, e.g. to include configuration interaction or to solve the Hartree-Fock equations for the crystal.

V. The charge distribution in LiH

The charge distribution in the crystal is given by the expression

$$\varrho(\boldsymbol{r}) = \sum_{\xi}\sum_{\mu}\sum_{\nu} T_{\mu\nu}\, \psi_\nu(x)\, \psi_\mu^*(x) = 2 \sum_{g}\sum_{g'} t_{gg'}\, \psi_{g'}(\boldsymbol{r})\, \psi_g^*(\boldsymbol{r})$$

where T is the matrix

$$\boldsymbol{T} = (\mathbf{1} + \boldsymbol{S})^{-1}$$

and t is a matrix related to T by

$$T_{\mu\nu} = t_{g g'}\, \delta_{j j'}$$

Here j and j' are the spin quantum numbers associated with μ and ν and g and g' refer to the lattice points. For a system of non-overlapping ions $\boldsymbol{T}$ reduces to the unit matrix and accordingly the charge density is the sum of the densities of the individual ions. When constructing a wave function with the correct symmetry properties we take into account the repulsion between electrons with parallell spins; this implicates that, when the charge clouds associated with different ions overlap, a deformation will occur and the magnitude of this deformation depends on the overlap integrals and the overlap densities $\Psi_{g'}(r)\,\Psi_{g}^{*}(r)$. In LiH this deformation is considerable as is seen from a few values of the matrix elements $t_{gg'}$.

$t_{gg} = 1.419$ g associated with a hydrogen ion
$t_{gg} = 1.021$ g associated with a lithium ion
$t_{gg'} = -0.052$ g and g' nearest neighbours
$t_{gg'} = -0.165$ g and g' next nearest negative neighbours.

The overlap densities where g and g' refer to unlike neighbours are different from zero only in a small region around the lattice point of the positive ion. When g and g' refer to nearest negative neighbours, the density is rather diffuse and has axial symmetry with respect to the axis $r_{gg'}$, the surfaces of constant density being rotational ellipsoids. One can get an approximate picture of the charge distribution by attributing to each positive ion a charge cloud of a rather small extension with the total charge $2e$, to each negative ion a very extended spherical charge cloud with the total charge $2.84e$, and to each pair of nearest negative ions an axial symmetric charge of $-0.14e$. This picture differs most appreciably from that of free ions in the lattice and shows clearly that, when speaking about the separate interaction terms in the energy expression, one must be careful not to attribute any physical interpretation.

A more fundamental approach to treat this problem would consist in solving the Hartree-Fock equations for the crystal. An attempt to calculate a self-consistent field for LiH has been made by EWING and SEITZ [4] using the cellular idea. They divided the lattice in space-filling cubes each having half the volume of the unit cell and its centre in a lattice point and derived the boundary equations for prominent directions of the pseudo-momentum $\boldsymbol{k}$. When calculating the self-consistent field, however, they replace the cubes by spheres of the same volume and assume the field to be spherically symmetrical within each sphere. Furthermore, the exchange term in the Hartree-Fock equation was neglected and, when calculating the charge distribution, they have taken the spherically symmetrical part of $|\psi_0|^2$ summed over the band, thus neglecting the variation of $|\psi_{\boldsymbol{k}}|^2$ with the pseudo-momentum k. These approximations have recently been investigated by BELL, HUM, PINCHERLE, SCIAMA, and WOODWARD [10] treating PbS. They found that the approximation of treating only the electrons with $k = 0$ was not representative in their case. In view of all these approximations it is quite clear that the results of EWING and SEITZ may be only qualitatively correct and therefore conclusions drawn from a comparison with their results cannot be decisive. In one respect, however, a comparison is interesting. When computing the self-consistent field the initial field was taken as

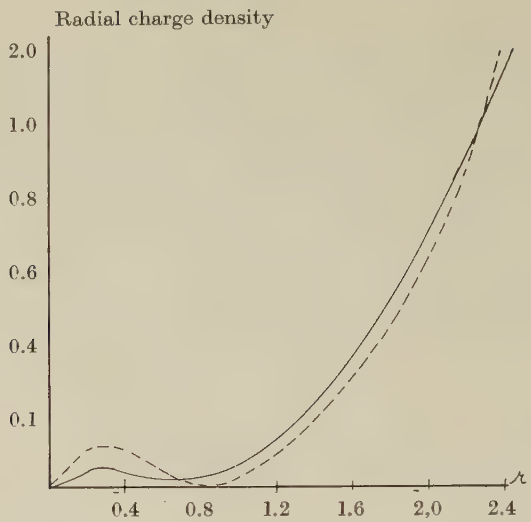

Fig. 1. The radial charge density in the Li-cell. ——— Calculated using the wave functions free ions. - - - - - Self-consistent distribution according to Ewing and Seitz.

that of neutral lithium and hydrogen atoms, where the wave functions of the valence electrons, that is the 2*s*-electron of Li and the 1*s*-electron of *H*, were squeezed so as to fit into the lattice. The final distribution was not far from the initial one. We have calculated the contribution from the valence electrons[1] to the radial charge density in a Li-sphere and found a rather good agreement with the self-consistent distribution. From fig. 1 we can make an approximate comparison between the results. The comparison cannot be made accurately because we had to take Ewing and Seitz curve from a figure in their paper.

The agreement is in fact remarkable in view of the entirely different starting points. In their case the distribution is essentially due to the squeezed valence electron of the lithium atom, in our case it is due to the overlap effects together with the contributions from the surrounding hydrogen ions, but nevertheless the distribution is essentially the same in both cases. From this comparison it would seem as if the repulsion between electrons with parallel spins would tend to deform the charge distribution in such a direction as to approach the self-consistent distribution. In the hydrogen sphere the agreement is not very good, which is not surprising, regarding for instance the fact that the continuity conditions are not the same in the two cases. Calculating the total negative charge in the lithium sphere we found the value $2.7e$ which agrees pretty well with the value $2.65e$ found by Ewing and Seitz. However, the figures are not strictly comparable, since the normalization is different in the two cases. The *s*-sphere approximation does not seem to be so useful in lattices of the NaCl-type as in the simple metals, where the atomic polyeder lies rather close to the surface of the *s*-sphere. Here the spheres will overlap in a rather large part of the crystal volume and in the overlapping regions the charge density will not have a unique value, if the continuity conditions are only satisfied on the surface of the spheres.

---

[1] That means here the total distribution minus the density of the free lithium ions.

From measurements of X-ray reflections AHMED [11] has concluded that LiH has only about 25 % ionic character with limiting values 50 % ionic character of complete covalency. The possibility of determining the state of ionization from X-ray measurements has recently been discussed by BIJVOET and LONSDALE [12] and WALLER and LUNDQVIST [13], who independently found that the X-ray method cannot give reliable information about the state of ionization in LiH. It seems also rather difficult to decide about the ionic condition from a mere knowledge of the charge distribution, unless the experimental accuracy is extremely high and the results are compared with the results of careful theoretical calculations. It must be emphasized that the quantum mechanical description of a ionic crystal, which we have used here differs widely from the classical picture, where the ions are regarded as essentially non-overlapping. As the charge density of the negative ion often is appreciable in a volume of the same magnitude as the unit cell, it is clear that we cannot divide the lattice into space-filling polyedra in such a way, that the whole charge cloud of a free negative ion is confined within one of them and that the total charge of a free positive ion will be found in the other. The same is true even when starting from the neutral atoms, as the contribution to the charge density from the valence electron of the metal atom will be appreciable in the whole cell. In the case of LiH the charge in each of the atomic polyedra would probably be approximately the same in a purely covalent state as in the ionic state and therefore it must be rather difficult to estimate the degree of ionization from a mere knowledge of the charge distribution.

VI. Comments

The agreement between the theoretical and experimental value of the binding energy is not so good as in the earlier treatments. One must remember, however, that the situation is inherently simpler in crystals like e.g. NaCl and KCl than in LiH. In these crystals the wave functions of the different orbitals in the free negative ions tend faster towards zero, which means that the probability of an electron in a certain orbital to be at distances from the nucleus comparable with the interionic distance in the crystal is much smaller than for the electrons of a free hydrogen ion. Accordingly the overlap integrals are much smaller, and investigating the expression for the charge density we find that the charge distribution deviates rather little from the superposition of the densities of the free ions, whereas in LiH the deformation is large. Already these facts indicate, that one cannot expect to get a very good agreement unless the deformation of the negative ions in the field of the crystal is explicitly taken into account. In a first approximation the electrons of the lithium ions can be assumed to be unaffected by the crystal binding; the problem then consists in finding the wave functions of the remaining two electrons per unit cell. We note that the amplitude of the hydrogen ion wave functions are rather large in the neighbourhood of the surrounding positive ions. However, in the neighbourhood of a lithium ion, the field due to that ion constitutes the largest part of the field acting on the electron and it seems reasonable to assume that in this region the wave function should have some similarity to a 2s-function of a neutral lithium atom. When constructing crystal orbitals from the orbitals of free hydrogen ions we neglect completely this deformation, which must be considered as a very crude approximation. The result could be improved e.g. by introducing a number of parameters in the wave functions, or by including configuration interaction, or by making a new attempt to solve the Hartree-Fock equations for the crystal, but unfortunately the numerical calculations in all cases would be formidable. Here we had to consider the overlap between a certain negative ion and its 80 nearest neighbours and between a positive ion and its 38 nearest neighbours. The numerical calculations already in this approximation have been very tedious and if carrying through an investigation in a higher approximation simpler formulae and methods of computation must necessarily be used. Possibly the simplified expression for the energy, which has recently been derived by Löwdin can be used, if accurate enough for this problem.

Regarding the approximations used in the earlier treatments our results suggest, that one might neglect the terms of the third and the higher orders in the overlap integrals even if the series expansion of the matrix $\boldsymbol{P}$ is not convergent. The value of the binding energy agrees rather well with that obtained when using the complete expression, and the lattice constant is fairly close to the observed value, if the interaction between neighbours up to the fourth order is taken into account. If we use the conventional approximation and neglect the error introduced on using wave functions, which are only approximations to the Hartree-Fock functions, the binding energy agrees rather well with the experimental value. However, such an approximation must be considered inadmissible, since E_{II} is not a constant term, but varies with the interionic distance, tending to zero when the lattice constant tends to infinity; it must therefore be included in the cohesive energy and in fact it constitutes a rather large part of the repulsive potential.

I wish to acknowledge my sincere gratitude to Professor I. Waller for suggesting this investigation and for his continued interest and very valuable advice during the course of the present work. I am also much indebted to Dr. P. O. Löwdin for his kind interest and for many stimulating discussions on these matters. This investigation has been made possible through financial support from Nobelstiftelsen and Statens Naturvetenskapliga Forskningsråd. Part of the tedious numerical work has been carried out by Fil. mag. T. Eriksson and Fil. kand. S. Holmqvist, to whom I wish to express my grateful thanks for their valuable assistance.

Institute of Mechanics and Mathematical Physics, University of Uppsala.

APPENDIX

Calculation of integrals

1. Two-centre integrals

A number of different methods have been developed for computing molecular integrals.[1] When the wave functions are given numerically, the method introduced by Coolidge [14] and later developed by Landshoff [2] and Löwdin [3], [15] seems to be the most advantageous. For analytical wave functions the integrals have hitherto usually been evaluated by using elliptical coordinates. The evaluation of all types of two-centre integrals occurring in molecular problems is now systematically investigated [16] and tables, from which all integrals can be calculated, are being prepared.

---

[1] See e.g. the references found in [15].

When the wave functions are of the simple form used here, the method of elliptical coordinates offers certain advantages. Simple expressions can be found for all two-centre integrals except the exchange integrals in terms of the integrals

$$A_n(\alpha) = \int_1^\infty e^{-\alpha x} x^n \, dx$$

and

$$B_n(\beta) = \int_{-1}^{+1} e^{-\beta x} x^n \, dx$$

where $n = 0, 1, 2 \ldots$, and β depend on the interionic distance and the effective nuclear charges.

The coulomb and hybrid integrals are reduced to one electron integrals by means of the formula[1]

$$\int \frac{|\psi_g(\boldsymbol{r}')^2|}{|\boldsymbol{r}-\boldsymbol{r}'|} d\boldsymbol{r}' = \frac{1}{|\boldsymbol{r}-\boldsymbol{r}_g|} - \frac{\omega_g(|\boldsymbol{r}-\boldsymbol{r}_g|)}{2|\boldsymbol{r}-\boldsymbol{r}_g|}$$

where

$$\omega_g(r) = 8\pi \{ \int_r^\infty |\psi_g(x)|^2 x^2 \, dx - r \int_r^\infty |\psi_g(x)|^2 x \, dx \}$$

All types of two-centre integrals occurring in our calculation can be found in [5]. As the reduction of the integrals to the auxiliary quantities $A_n^{(\alpha)}$ and $B_n(\beta)$ is easily performed, the explicit formulae are not given here.

The exchange integrals are more difficult to compute. We have used the Neumann expansion of $|\boldsymbol{r}_1 - \boldsymbol{r}_2|^{-1}$ in elliptical coordinates [17]. For the integrals between unequal neighbours an infinite expansion is obtained, whereas the expansion reduces to two terms in the case of equal ions. The terms in the series expansion were calculated from a few auxiliary quantities by means of recursion formulae. This procedure of computation is rather awkward because of the loss of significant figures in the repeated use of the recursion formulae. Therefore only the first five terms could be computed using ordinary calculating machines. Fortunately the series expansion seemed to converge rapidly and thus the accuracy seemed to be sufficient for our purpose.

All auxiliary quantities necessary to compute these integrals can be found in the extensive tables computed by KOTANI, AMEMIYA, and SIMOSE [18]. Unfortunately these tables have been completely unnoticed in the literature until recently and we did not know about their existence until the calculations were already finished.

2. Three- and four-centre integrals

The most important three-centre integrals appearing in the S^2-approximation are of the type

$$(g' g'' g) = \int \frac{\psi_{g'}^*(\boldsymbol{r}) \, \psi_g(\boldsymbol{r})}{|\boldsymbol{r}-\boldsymbol{r}_{g''}|} d r$$

and occur in the sum

$$\sum_{g''}^{(g)} \varepsilon_{g''} (g' g'' g)$$

---

[1] Cf. ref. [3] eq. (9.7–9.9).

Here $\varepsilon_{g''}$ denotes the valency of the ion at the lattice point g. When g or g' has reference to a positive ion a simple approximate formula can be used. We note that the product $\psi^*_{g'}(\boldsymbol{r})\,\psi_g(\boldsymbol{r})$ vanishes outside a small region about the lattice point of the positive ion. Expanding the denominator in spherical harmonics with the origin at the lattice point of the positive ion, we find that the contributions from the higher moments can be neglected and we get the simple formula[1]

$$(g'\,g''\,g) \approx \frac{S_{g'g}}{|\boldsymbol{r}_g - \boldsymbol{r}_{g''}|}$$

if g denotes the lattice point of the positive ion.

The calculation of $\sum\limits_{g''}^{(g)} \varepsilon_{g''}\,(g'\,g''\,g)$ in the case where g and g' refer to two neighbours of the second order is more complicated. Because of the large overlap these terms must be calculated with the highest possible accuracy. Fortunately this integral can be expressed in a closed form when using the Neumann expansion of the denominator, as the infinite expansion reduces to two terms. However, the integral tends to zero so slowly when r_{gg} and $r_{g'g}$ increase, that the summation over g has to be performed over the whole lattice. Therefore, when the lattice point g is well outside the region, where the overlap density $\psi^*_{g'}(\boldsymbol{r})\,\psi_g(\boldsymbol{r})$ is different from zero, we expand the denominator in spherical harmonics with the origin at the centre of gravity of $\psi^*_{g'}(\boldsymbol{r})\,\psi_g(\boldsymbol{r})$ i.e. the midpoint between the lattice points g and g'. Summing over all points g'', whose distance R from this point is constant, we get

$$\sum_{g''} \varepsilon_{g''} = 0 \quad (R = \text{const.})$$

Introducing the series expansion into $\sum\limits_{g''} \varepsilon_{g''}\,(g'\,g''\,g)$ we find that the first term vanishes, the second term vanishes since the origin is at the centre of charge, the leading term is the third which varies as R^{-3}. We now computed $\sum\limits_{g''} \varepsilon_{g''}\,(g'\,g''\,g)$ $(R = \text{const.})$ for increasing values of R, using the exact expression, until we found that the first non-vanishing term in the expansion approximated the correct value with sufficient accuracy. We had to use the exact formula when summing over the first four values of R. The case where g and g' refer to neighbours of the fourth order was treated analogously.

In E_3 (4 c) and E_4 (4 d) two-electron integrals of three- and four-centre type appear. The calculation of such integrals presents considerable difficulties and they have not yet been fully investigated. Some three-centre integrals have been evaluated in elliptical coordinates, but the results were confined to special configurations of the nuclei [19]–[22]. All integrals of this type can be obtained as infinite series expansions by expanding $|\boldsymbol{r}_1 - \boldsymbol{r}_2|^{-1}$ in spherical harmonics [15]. However, when computing an expression like E_4 (4 d) it is not sufficient to have formulae, which give the values of the integrals for each possible configuration, because the number of integrals occurring is so tremendously large, but some method has to be used by means of which the summations can be carried out in a convenient manner. In this respect the method of expanding the integrand into spherical harmonics is rather useful, because some of the summations can be performed under the integral signs, and therefore the resulting integrals will be formally reduced to the two-centre type. Furthermore the symmetry of the crystal reduces the number of terms in the series expansion. An alternative method has been used by LÖWDIN, introducing the idea of "combined orbitals" [23]. We have tried both methods, but unfortunately none of them seemed to work very well in our case. The expansions with the origin at the lattice point of a hydrogen ion did not seem to converge fast enough, partly because of the strong maxima in the overlap densities at the surrounding positive ions.

---

[1] Cf. ref. [3], Chapter V.

Instead we have used an idea due to LÖWDIN [24] to approximate each product $\psi_g(\boldsymbol{r})\,\psi_{g'}(\boldsymbol{r})$ by

$$\psi_g(\boldsymbol{r})\,\psi_{g'}(\boldsymbol{r}) \approx \lambda_g\,|\,\psi_g(\boldsymbol{r})\,|^2 + \lambda_{g'}\,|\,\psi_{g'}(\boldsymbol{r})\,|^2$$

where λ_g and $\lambda_{g'}$ are determined so as to give the correct charge and moment. Introducing this approximate formula into E_4 and the last sum in E_3, the summations can be carried out by combining the quantities λ_g and $\lambda_{g'}$ with the elements $p_{g\,g'}$ and simplifying the formulas as far as possible before the numerical evaluation.

Since the three- and four-centre integrals of the type considered here have been evaluated only in very special cases and only for special configurations of the nuclei we cannot draw any decisive conclusions with regard to the validity of this approximation. In the following table we have compared the integrals $(a\,b\,b\,c)$ and $(a\,b\,a\,c)$, where a, b, and c denote three hydrogen atoms in the corners of an equilateral triangle with the side R, with the values calculated by HIRSCHFELDER and WEYGANDT [22].

The three-centre integrals $(a\,b\,b\,c)$ *and* $(a\,b\,a\,c)$ (*in a.u.*).

	$(a\,b\,b\,c)$		$(a\,b\,a\,c)$	
R	Hirschfelder–Weygandt	Löwdin's formula	Hirschfelder–Weygandt	Löwdin's formula
2.0	0.1698	0.1636	0.2584	0.2498
2.5	0.0954	0.0909	0.1777	0.1688
3.0	0.0509	0.0481	0.1192	0.1115

We have also calculated a number of two-centre exchange and hybrid integrals using LÖWDIN's formulae and compared the results with the correct values. The agreement was rather good — for the exchange integrals between two negative neighbours the accuracy of the approximate formula was very high. It seems therefore that this approximation could be used without any significant loss of accuracy. We also tested the formula on the one electron two- and three-centre integrals, but for these integrals the accuracy was not high enough, and therefore it seemed to be more safe to evaluate these integrals by direct methods.

REFERENCES

1. E. A. HYLLERAAS, Z. f. Phys. *63,* 771 (1930).
2. R. LANDSHOFF, Z. f. Phys. *102,* 201 (1936); Phys. Rev. 52, 246 (1937).
3. P. O. LÖWDIN, Thesis, Uppsala 1948, Cf. also Arkiv f. mat., astr. o. fysik 35 A, N:o 30, J. Chem. Phys. *18,* 365 (1950).
4. D. H. EWING and F. SEITZ, Phys. Rev. *50,* 760 (1936).

5. S. O. Lundqvist and P. O. Fröman, Arkiv f. fysik *2*, 431 (1950).
6. S. O. Lundqvist, Arkiv f. fysik *3*, 25 (1952).
7. H. Bethe, Z. f. Phys. *57*, 815 (1929).
8. J. Yamashita, J. Phys. Soc. of Japan, *7*, 284 (1952).
9. J. Yamashita and M. Kojima, J. Phys. Soc. of Japan, *7*, 261 (1952).
10. D. G. Bell, D. M. Hum, L. Pincherle, D. W. Sciama, and P. M. Woodward, Proc. Roy. Soc. A, *217*, 71 (1953).
11. M. S. Ahmed, Phil. Mag. *42*, 997 (1951).
12. J. M. Bijvoet and K. Lonsdale, Phil. Mag. *44*, 204 (1953).
13. I. Waller and S. O. Lundqvist, Arkiv f. fysik 7, 121 (1953).
14. A. S. Coolidge, Phys. Rev., *42*, 189 (1932).
15. S. O. Lundqvist and P. O. Löwdin, Arkiv f. fysik *3*, 147 (1951).
16. Reports from the Conference on Quantum-mechanical Methods in Valence Theory, Shelter Island (1951).
17. C. Neumann, Vorlesungen über die Theorie des Potentials, p. 341 (1887).
18. M. Kotani, A. Amemiya, and T. Simose, Proc. Phys.-Math. Soc. Japan 20, Extra No. (1938), ibid., 22, Extra No. (1940).
19. J. Hirschfelder, H. Eyring, and N. Rosen, J. Chem. Phys. *4*, 121 (1936).
20. J. Hirschfelder, H. Diamond, and H. Eyring, J. Chem. Phys. *5*, 695 (1937).
21. D. Stevenson and J. Hirschfelder, J. Chem. Phys. *5*, 933 (1937).
22. J. Hirschfelder and O. Weygandt, J. Chem. Phys. *6*, 806 (1938).
23. P. O. Löwdin, J. Chem. Phys. *19*, 1579 (1951).
24. ——, J. Chem. Phys. *21*, 374 (1953).

Tryckt den 24 augusti 1954

Uppsala 1954. Almqvist & Wiksells Boktryckeri AB

ARKIV FÖR FYSIK Band 8 nr 18

Communicated 14 April 1954 by Bengt Edlén

Relative intensities of Stark effect components in the arc spectrum of helium

By L. Minnhagen and U.-B. Nordberg

With 4 figures in the text

Relative intensities of the Stark effect components of the helium group $2\,^1P$–$4\,^1Q\,(Q=P,D,F)$ have been measured at field strengths ranging from 110 to 350 kV/cm on spectrograms which were obtained in connection with a similar investigation on $2\,^3P$–$4\,^3Q$ (1).

The light-source was a canal-ray tube with field-condenser designed by Ryde (2) and the spectrograms were obtained with a glass prism spectrograph, the dispersion at λ 4922 *A* being 21 *A*/mm (Fig. 1). A fairly wide slit was used (0.1–0.2 mm) which is advantageous when measuring intensities. The directions of canal-ray, field and observation were all at right angles to each other. To obtain the field strengths the splittings of $2\,^1P$–$4\,^1Q$ and $2\,^3P$–$4\,^3Q$ were measured and compared with Sjögren's (3) observations.

As the components of $2\,^1P$–$4\,^1Q\,(Q=P,D,F)$ are spread over about 100 *A* at the fields investigated, it was necessary to use heterochromatic photometry when measuring their relative intensities. For this purpose every photographic plate was standardized by using a ribbon filament lamp. The lamp was run with different currents and produced a series of continuous spectra on the plate, each corresponding to a known colour temperature. The emissivity of the tungsten ribbon being known (4), the energy distribution in the actual spectral range was determined from Planck's law. The densities were measured with a Moll microphotometer through running parallel to the dispersion direction across the Stark effect components (Fig. 2) and at right angles across the continuous spectra at the wave-length of every Stark component. The product of peak value and half-width of the energy distribution curve of a component was used as a measure of its intensity. From the relative intensities, properly corrected (1), the relative oscillator strengths were determined by division by ν^4 (ν = wave number) (Table 1).

The theoretical π pattern of λ 4922 *A* has six components, one pair from each of $2\,^1P$–$4\,^1P$, $2\,^1P$–$4\,^1D$ and $2\,^1P$–$4\,^1F$. On the spectrograms—obtained with a spectrograph of moderate resolving power and, for these experiments, with a wide slit—the $2\,^1P$–$4\,^1P$ components are resolved at every field strength, whereas the $2\,^1P$–$4\,^1D$ components as well as the $2\,^1P$–$4\,^1F$ components are unresolved. This pattern is in agreement with Sjögren's (3) observations (Fig. 3). It appears (Table 1 and Fig. 4) that the intensities of the "forbidden" $2\,^1P$–$4\,^1P$

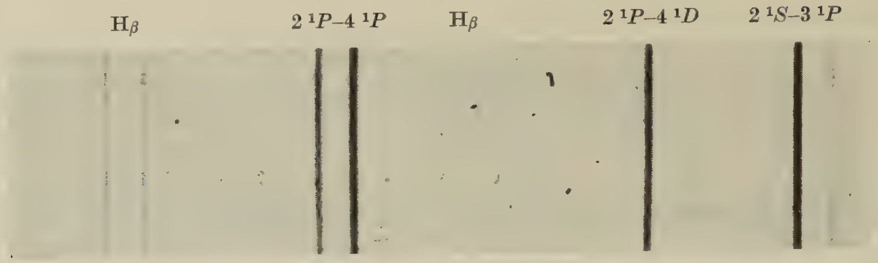

Fig. 1. Stark effect spectrogram of $2\,{}^1P$–$4\,{}^1Q$; π components; field strength 347 kV/cm (× 10).

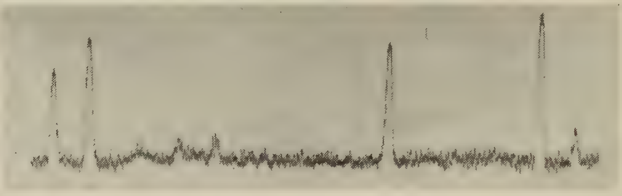

Fig. 2. Microphotometer record of the above spectrogram.

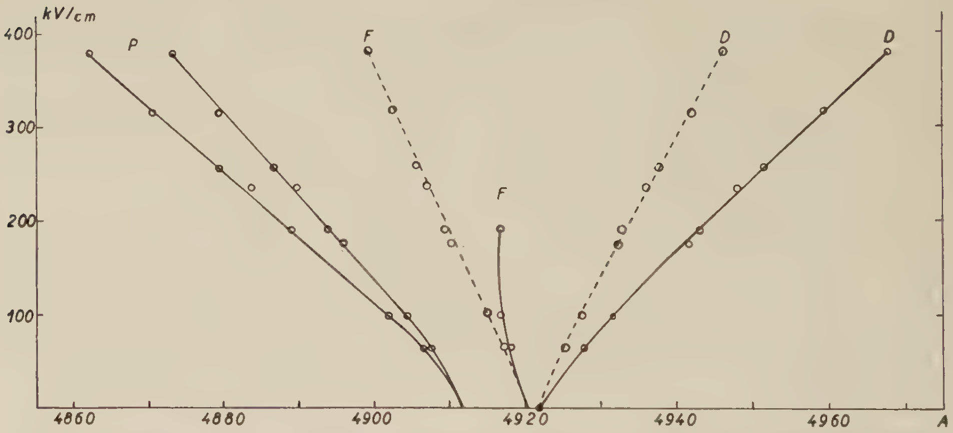

Fig. 3. Shift-field relation based on SJÖGREN's observations (3); dashed curves represent $m: 2 \to 1$ components.

components increase in relation to $2\,{}^1P$–$4\,{}^1D$ in the whole range of field strengths investigated. The intensities of the $2\,{}^1P$–$4\,{}^1F$ components—also "forbidden"—as computed by LANGSTROTH (5) on the basis of FOSTER's (6) theory rise to a maximum at about 30 kV/cm and then decrease. At the weakest field now investigated (113 kV/cm) the intensity sum of the two unresolved components is still measurable, but the line is not visible on the spectrograms obtained at higher fields. SJÖGREN could not observe the line above 190 kV/cm (Fig. 3).

The theoretical σ pattern has eight components, six of them having the same shifts as the π components. The remaining components, viz. $2\,{}^1P$–$4\,{}^1D$, m: $2 \to 1$ and $2\,{}^1P$–$4\,{}^1F$, m: $2 \to 1$ are the strongest ones in the σ pattern at the fields investigated, and they are clearly resolved from other components.

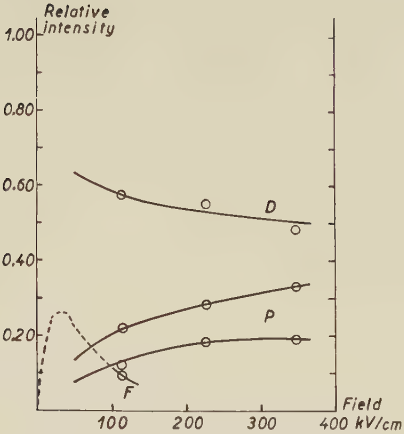

Fig. 4. Observed intensity-field relation for π components; theoretical $2\,^1P$–$4\,^1F$ curve dashed.

The observations show that the intensities of the $2\,^1P$–$4\,^1D$ and $2\,^1P$–$4\,^1F$, m: $2 \to 1$ components are only slightly affected by increasing the field from 110 kV/cm to 220 kV/cm; $2\,^1P$–$4\,^1P$ gets stronger and the intensity sum of the remaining $2\,^1P$–$4\,^1F$ components gets smaller to such an extent that the line could not be observed at 220 kV/cm.

The relative intensities of the $2\,^1P$–$4\,^1Q$ components have been measured earlier at weaker fields. THORNTON (7) attained 130 kV/cm using the canal-ray method. The agreement between his observations and the theoretical intensities according to FOSTER's (6) theory is not too good. There are also some discrepancies between the intensities observed by LANGSTROTH (5) at a maximum field of about 60 kV/cm and the theoretical ones. This is most pronounced in the case of the $2\,^1P$–$4\,^1P$ components which are much stronger than predicted by theory. For a similar comparison with the present observations the theoretical relative oscillator strengths at the lowest fields investigated are given in Table 2, the sum of the strengths being given for unresolved components. The agreement with the theory is decidedly better than in the works cited, but also in

Table 1. Observed relative oscillator strengths of $2\,^1P$–$4\,^1Q$ components. The sum of the strengths of the π and σ components are each made equal to one.

π components					σ components				
Field kV/cm	$m \to m$	$2\,^1P$–$4\,^1P$	$2\,^1P$–$4\,^1D$	$2\,^1P$–$4\,^1F$	Field kV/cm	$m \to m$	$2\,^1P$–$4\,^1P$	$2\,^1P$–$4\,^1D$	$2\,^1P$–$4\,^1F$
113	$0 \to 0$ $1 \to 1$	0.12 0.22	0.57	0.10	110	$0 \to 1$ $1 \to 0$ $2 \to 1$	weak 0.12	0.25 0.32	0.05 0.26
225	$0 \to 0$ $1 \to 1$	0.18 0.28	0.55	–	220	$0 \to 1$ $1 \to 0$ $2 - 1$	– 0.16	0.25 0.32	– 0.27
347	$0 \to 0$ $1 \to 1$	0.19 0.33	0.48	–					

Table 2. Theoretical relative oscillator strengths of $2\,^1P$–$4\,^1Q$ components. The sum of the strengths of the π and σ components are each made equal to one.

π components					σ components				
Field kV/cm	$m \to m$	$2\,^1P$–$4\,^1P$	$2\,^1P$–$4\,^1D$	$2\,^1P$–$4\,^1F$	Field kV/cm	$m \to m$	$2\,^1P$–$4\,^1P$	$2\,^1P$–$4\,^1D$	$2\,^1P$–$4\,^1F$
113	0→0	0.13	0.59	0.10	110	0→1	0.03	0.24	0.04
	1→1	0.19				1→0	0.09		
						2→1		0.33	0.27

the present case $2\,^1P$–$4\,^1P$ is stronger than predicted by theory. As the relative intensities of Stark components are influenced by the experimental conditions (2) it is not astonishing that different investigations are not in close agreement. As to the discrepancy between experiment and theory, especially as regards $2\,P$–$4\,P$, it should be noticed that it is assumed in the theory that the number of atoms excited to the different states of the same total quantum number is the same. This assumption appears not to be valid for the light-sources used. The excitation conditions have been discussed by LANGSTROTH (5) who pointed out that a greater excitation probability to the $4\,P$ states should be expected, the enhancement being more pronounced for $4\,^3P$ than for $4\,^1P$. In order to test this statement, the present results for $2\,^1P$–$4\,^1P$ were compared with those previously given for $2\,^3P$–$4\,^3P$ (1) which were obtained under the same experimental conditions. It appears that the $2\,^3P$–$4\,^3P$ strength and the $2\,^1P$–$4\,^1P$ strength are both greater than those predicted by FOSTER's theory, and that the excess is greater for the triplet than for the singlet transition in agreement with LANGSTROTH's ideas.

Physics Laboratory, University of Lund.

REFERENCES

1. MINNHAGEN, L., ZS. f. Phys. *113*, 292 (1939).
2. RYDE, N., ZS. f. Phys. *109*, 108 (1938).
3. SJÖGREN, K., Experimentelle Untersuchungen des Stark-Effekts bei Wasserstoff und Helium. Diss. Lund 1934.
4. HAMAKER, H. C., Reflectivity and emissivity of tungsten. Diss. Amsterdam 1934.
5. LANGSTROTH, G. O., Proc. Roy. Soc. (A) *129*, 70 (1930).
6. FOSTER, J. S., Proc. Roy. Soc. (A) *117*, 137 (1928).
7. THORNTON, R. L., Proc. Roy. Soc. (A) *150*, 259 (1935).

Tryckt den 24 augusti 1954

Uppsala 1954. Almqvist & Wiksells Boktryckeri AB

ARKIV FÖR FYSIK Band 8 nr 19

Communicated 14 April 1954 by RAGNAR LILJEBLAD and LISE MEITNER

A peak height comparison method for mass spectrometry

By C. TAYLOR

With 6 figures in the text

1. Introduction

The amplitudes of two mass peaks are best compared by the double-collector method, which has the great advantage of measuring instantaneously the ratio of the two ion currents, so that fluctuations in those currents are of no account (1). Some difficulties arise however if the peaks to be compared are not adjacent, or if other peaks lie close by. Special collector assemblies can be designed to meet these problems, but for spectra which are complicated, and when the highest precision is not required, it is usual to display all the peaks on a self-balancing potentiometric recorder such as the Leeds and Northrup "Speedomax".[1]

The limitations of this method are the accuracy with which the recorder can be read, and the unsteadiness of the ion beams. Fluctuations are important, because there is considerable delay between the scannings of the two peaks while the recorder wastes time tracing the sides of the peaks and the spaces between them. Information about their heights only is required, however, and an improvement can be made by switching the spectrometer between the tops of the two peaks, with a short scan at each, as was done by HERCUS and MORRISON (2) in their work on ionization efficiencies. The circuit described in the present paper, which uses a similar scan, switches an attenuator at the same time as it switches the spectrometer, thereby bringing the two mass peaks to the same height. This gives some of the advantages of a null method, as the role of the recorder is reduced to showing when there is no difference in peak height. Fluctuations in ion current are still a disadvantage, but their effect is reduced, since repeated comparisons are made in a short time.

The method may be understood with reference to Fig. 1, which shows traces which might be obtained on the recorder when studying a typical spectrum. After scanning the whole mass range in the usual way (*a*), a circuit is brought in which selects only the two peaks of interest, jumping across any intermediate peaks (*b*). A relay driven by the switching circuit couples in a precision potential divider when the larger of the two peaks is being scanned, and in this way the peaks are brought to exactly the same height (*c*). Since the tops of the peaks follow each other alternately close together on the paper, this adjustment can be made very precisely. The amplitude ratio is read off directly from the setting of the potential divider.

---

[1] The recorder referred to throughout this article was a Speedomax Type G, Model S, 60000 series.

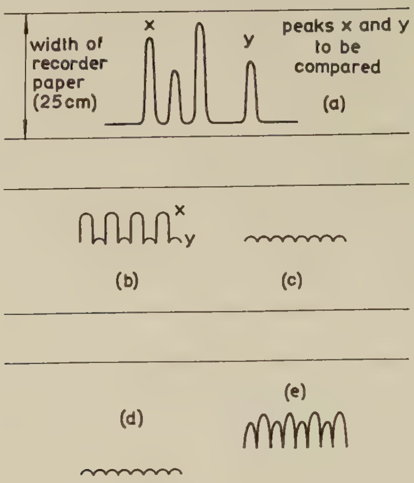

Fig. 1. Types of recorder traces, illustrating the method. — (*a*) Whole spectrum. (*b*) Only peaks of interest scanned. (*c*) Peaks equalized. (*d*) Recorder backed-off. (*e*) Sensitivity increased, revealing small error in equalization.

One may increase the accuracy of the recorder as a null indicator by backing it off so that the tops of the peaks lie near its zero position, and then increasing the gain of the amplifier. This is shown in Fig. 1 at (*d*) and (*e*). A small difference in peak height becomes easily visible, and a fine adjustment can be made to the potential divider. If the apparatus is sufficiently stable it may be useful to make a further increase in gain, first reducing the scan amplitude to keep the excursions of the recorder within reasonable bounds. When working in this way a difference in peak height of 1 % may correspond to as much as 20 mm on the record, and the limit of accuracy is no longer set by the recorder, but by instabilities in the other units of the spectrometer.

2. Switching circuit

This circuit (Fig. 2) modulates the acceleration voltage of the spectrometer. The switching from one mass peak to the other is done by a pair of contacts on the relay RL2, which short-circuit a small fraction of the input potential divider of the acceleration voltage stabilizer. This fraction is variable by means of P7 and P8, which control the separation between the two peaks selected. The scan across each peak is obtained from the long time-constant grid circuit of the asymmetric multivibrator V2, and is added to the 170 V reference voltage supplied by the voltage regulator tubes VR1 and VR2. The comparison valve VS in the stabilizer is used to mix the two modulation signals, which can be adjusted quite independently of each other.

The switching circuit must also disconnect the recorder at the moment of change from one peak to the other, as otherwise there will be severe transients, especially when high sensitivity is used. The cut-out and scan wave-forms have twice the frequency of the switching wave-form, since there are two change-overs

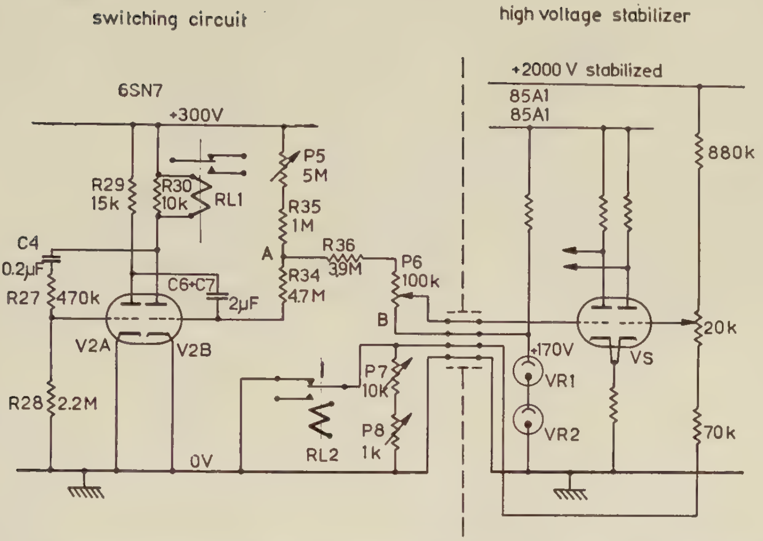

Fig. 2. Essentials of switching circuit, showing connection to high-voltage stabilizer.

in each switch cycle, and each switch position must be covered by a scan. This leads to a scale-of-two arrangement.

In the present circuit, the multivibrator V2 provides the scan (normally 6 seconds) and fixes the cut-out period (1 second), during which it excites the coil of relay RL1. A pair of contacts on this relay breaks the lead to the recorder, and its other contacts are coupled with RL2 in such a way that the relays together form a scale-of-two, RL2 opening and closing with half the frequency of RL1. As well as switching the high-voltage stabilizer, RL2 carries sets of contacts which contribute to the scale-of-two circuit, switch the precision potential divider, and operate signal lamps showing which peak is being scanned.

The wave-forms are shown in Fig. 3. Part of the sawtooth current in the grid return of V2B flows through the scan amplitude control P6, adding a sawtooth to the reference voltage. P6 is tapped into the grid return at a point *A* chosen so that no current flows through P6 when the scan reaches its mid-point, and thus the slider of P6 has at this moment the same voltage as that across the regulator tubes (point *B*), whatever its setting. If this were not the case, a change in scan amplitude would shift the scan from the top of the peak. P5 is included so that the desired condition may be obtained.

The relays, which are of the telephone type, have 15 K windings and close at 3 mA. R27 is included in the grid circuit of V2A because otherwise C4 and RL1 form a ringing circuit through the low impedance offered by the grid of V2A when it is driven positive, and under these conditions the circuit ceases to function as a multivibrator but oscillates with a frequency which is almost independent of the V2B grid circuit constants.

The relay scale-of-two is shown in Fig. 4. The large condenser C3 provides the memory required by all such circuits. If RL2 stands open, C3 charges through R22 to + 300 V. If RL2 stands closed, C3 discharges itself completely through

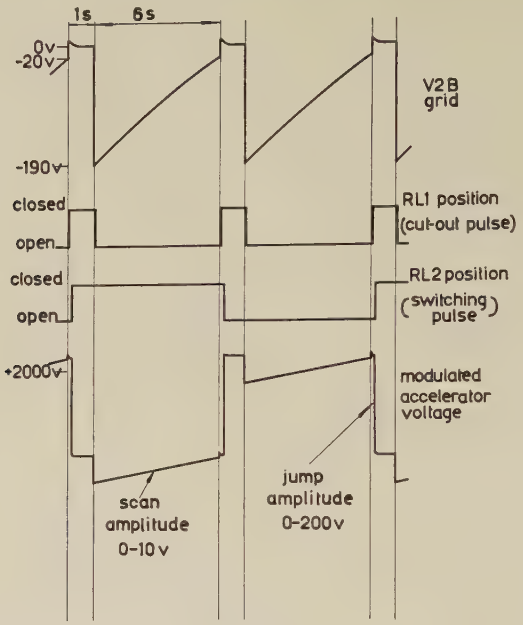

Fig. 3. Wave-forms.

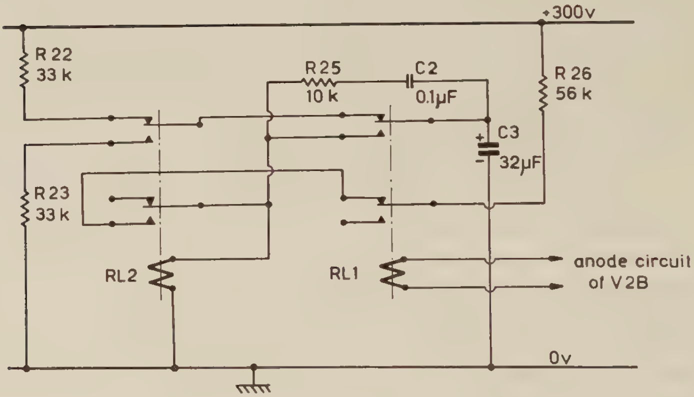

Fig. 4. Scale-of-two using relays.

R23. Each time RL1 is energized, C3 is connected across the coil of RL2, which therefore changes position: C3 is so large that the new position is held until RL1 opens again. At those change-overs when RL2 closes, it continues to be held by current flowing from R26 through holding contacts on both relays. The components R25 and C2 are included to suppress sparking at the contacts switching C3.

It will be noticed that since RL1 drives RL2, the recorder is cut out by the closing of RL1 before RL2 can switch the stabilizer and potential divider.

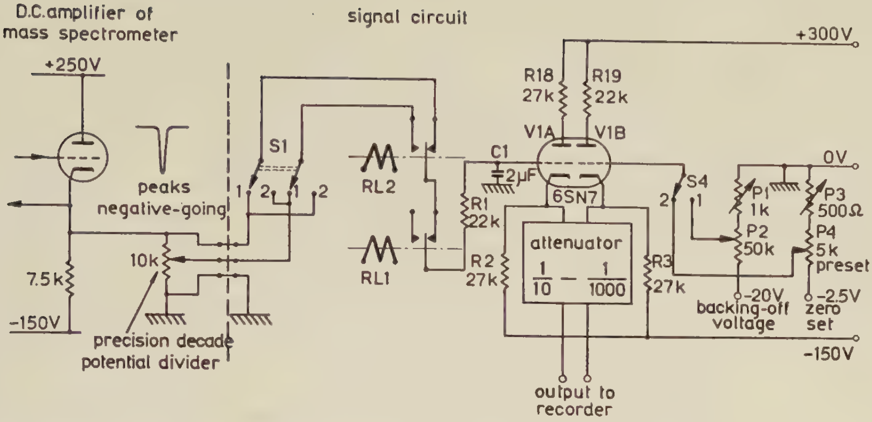

Fig. 5. Essentials of signal circuit, showing connection to DC amplifier of mass spectrometer.

The necessary delay between cut-out and switching is thus ensured without the need for further timing elements. The cut-out also covers the fly-back of the sawtooth, since it is this part of the wave-form which cuts off V2B and initiates the release of RL1 (see Fig. 3, where the delays in opening and closing of the relays are exaggerated).

In a magnetic sector spectrometer the relation between the focused mass and the acceleration voltage is $dm/m = -dV/V$. The modulation provided by the present circuit gives a maximum scan of 0.5 %, and can work with peaks separated by up to 10 %. This is in general sufficient for comparing the isotopes of any one element. There is of course some mass discrimination when this method of switching is used, and accurate measurements of abundance ratios can only be made by comparison with a standard. If it is desired to increase the switching range, the relay contacts should be used to control the magnet current stabilizer instead of the acceleration voltage stabilizer.

3. Signal circuit

The switching circuit was built for use with an existing spectrometer which was normally run with a double-collector. This spectrometer has a precision potential divider of 10 K total resistance at its output, for comparing the ion currents by NIER's method (1). The same potential divider is used when the spectrometer is run with the switching circuit.

It is necessary to match the recorder, which is originally designed for use in low-impedance thermocouple circuits, to the relatively high impedance of the potential divider. When it has reached equilibrium, the recorder draws no current, since its input circuits are potentiometric, and it could therefore be connected directly to the slider of the divider without disturbing its calibration. The time taken by the recorder to reach equilibrium is however dependent on the driving impedance, since it has an input filter of large capacitance. The difference in driving impedance when the two peaks are being scanned may be anything up to 10 K, depending on the amplitude ratio, and the way the divider is connected.

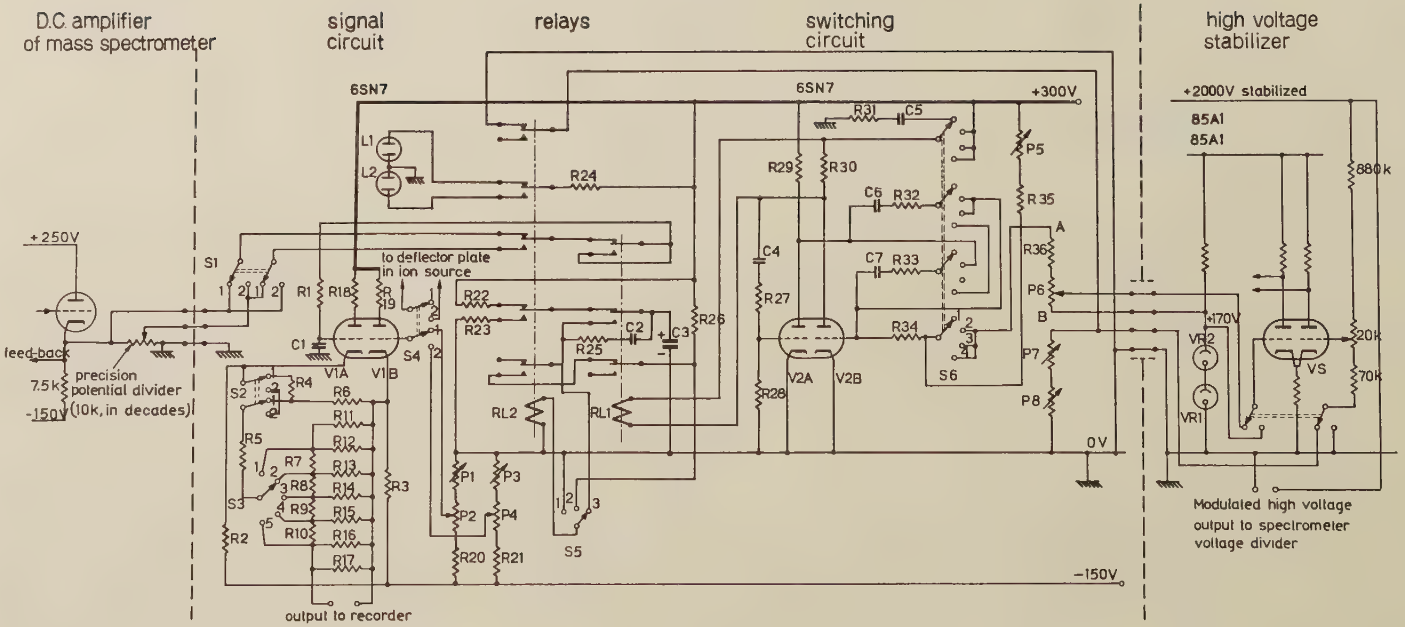

Fig. 6. Complete circuit.

Tests show that when the recorder is driven by an impedance of a few ohms it can make a 10 cm trace and settle to its final position in less than a second, while for an impedance of 5 K the time required is about 3 seconds. In a scan lasting 6 seconds the recorder would thus follow the form of one peak more closely than that of the other, and an error would result.

For this reason the recorder is isolated from the divider by the cathode follower V1A, as shown in Fig. 5. The backing-off voltage, set by potentiometers P1 and P2, is supplied by a second cathode follower V1B: the resulting symmetric drive helps to minimize the effect of heater and cathode variations. The sensitivity of the recorder is controlled by an attenuator which presents an impedance of 11 K to the cathodes of V1, and of 1 K to the recorder. This attenuator reduces the signals from the DC amplifier (which may be several volts) to the 10 mV level needed by the recorder. Since the attenuator comes after V1 it also helps to reduce the effects of drifts in this valve, and of any contact potential effects at the relay contacts in its grid circuit.

When the cut-out contacts on RL1 open, the grid of V1A is left floating. Grid current charging the capacities at this point during the 1 second cut-out period produces an unwelcome transient on the recorder, but this is kept small (about 0.5 mV at full sensitivity) by the large condenser C1. Together with R1 this condenser also serves as a low-pass filter. S1 is included so that the circuit may be used with spectra in which either the lighter or the heavier of the two peaks is the more abundant. At the other grid, S4 serves to remove the backing-off voltage without disturbing the settings of P1 and P2. This is useful for checking the zero-setting of the DC amplifier in the course of a measurement, as described in the next section.

The signal circuit shown was designed for the 10 K potential divider which

---

Components in Fig. 6

R1	22 K
R2, R3	27 K (2 W)
R4, R5	10 K
R6–R10	1.2 K
R11, R17	2.7 K
R12–R16	3.9 K
R18	27 K (2 W)
R19	22 K (2 W)
R20, R21	330 K
R22	33 K (1 W)
R23	33 K
R24	470 K
R25	10 K
R26	56 K (2 W)
R27	470 K
R28	2.2 M
R29	15 K (3 W)
R30	10 K (2 W)
R31	22 K
R32, R33	2.2 K
R34	4.7 M
R35	1 M
R36	3.9 M

C1	2 μF
C2	0.1 μF
C3	32 μF (450 V)
C4	0.2 μF
C5	0.1 μF
C6, C7	1 μF
P1	1 K
P2	50 K
P3	0.5 K
P4	5 K
P5	5 M
P6	100 K
P7	10 K
P8	1 K
RL1, RL2	Telephone-type relay. (Svenska Reläfabrik type RT, coil resistance 15 K, closing at 3 mA, not slugged)
L1, L2	Neon signal lamp
V1, V2	6SN7

All resistors ±10 %, rated ½ W unless otherwise stated.

List of controls

Control	Position	Function
S1		Largest peak
	1	*M* largest
	2	*m* largest
S2		Sensitivity (coarse)
	1	× 1/100
	2	× 1/10
S3		Sensitivity (fine)
	1–5	× 0.58 per step
S4		Recorder Bias
	1	Backing off
	2	Zero-setting
S5		Switch circuit
	1	*m*
	2	*M*
	3	Switching
S6		Scan
	1	No scan
	2	Scan time 6 sec.
	3	,, ,, 3 ,,
	4	,, ,, 1.5 ,,
P1		Backing-off (fine)
P2		Backing-off (coarse)
P3		Zero-setting (fine)
P4	Preset	Zero-setting (coarse)
P5	Preset	Scan centering
P6		Scan amplitude
P7		Switch amplitude (coarse)
P8		Switch amplitude (fine)

happened to be available. A better solution would be to start with a potential divider of low impedance (1 K) driving the recorder directly. V1 can then be omitted, the sensitivity attenuator being placed between the DC amplifier and the divider: this scheme will be used in the switching circuit now being made for a second spectrometer. Careful attention to this part of the circuit is needed if systematic errors are to be avoided, because of the non-linear input impedance of the chopper circuit in the recorder, and the non-linear time response of the writing mechanism itself. A simple test is to measure an abundance ratio using two different scan rates.

4. Operation

The complete circuit is shown in Fig. 6. The functions of the various controls are listed in the table, where *m* refers to the peak of lower mass and *M* to that of higher mass.

The preset potentiometer P5 is set by connecting a volt-meter between points *A* and *B* in the figure, and adjusting P5 so that there is no voltage between them when the scan reaches its mid-point. P4 is set so that the recorder can be brought on scale when zero-setting at maximum sensitivity.

To make a measurement, the mass spectrum is first run through in the ordinary way with the automatic sweep of the spectrometer, so that the focusing and general appearance of the spectrum may be checked. This is done with S5 set to *m*, and the scan switched off. The automatic sweep is then stopped as near as possible to *m*, which is brought to its maximum by fine adjustment of the accelerating voltage. This control, not shown in the figure, is normally included in the control panel of the spectrometer.

S5 is next set to *M*, and the switch amplitude control P7 slowly increased, tracing the spectrum through any intermediate peaks until the peak of higher mass is reached. The automatic scan and switch may then be brought in, the peaks equalized, and the recorder backed off as described above. It will be necessary from time to time to make small corrections to the acceleration voltage, to keep the scans at the tops of the peaks.

It is important that the zero level of the DC amplifier should be set so that in the absence of ion current there is no current through the precision divider. Any such current will give different deflections at the recorder as the divider is switched between its maximum and its slider, and when a measurement is being made these deflections constitute spurious additions to the peak heights, the error so caused being greatest for large abundancy ratios. To set the amplifier, the ion beam is suppressed and the backing-off voltage removed (both operations being done by S4), and the precision potential divider is turned down to its minimum position. The automatic switch will now couple the recorder from one end of the divider to the other, and the trace will show the amount of unbalance. The amplifier is corrected by its usual zero-setting controls, which are not shown in the figure.

After completing an abundance ratio measurement it is advisable to check whether the zero level of the amplifier has drifted. The ratio of the potential divider is first increased by say 1 % for a few cycles, to determine the inequality in peak height corresponding to this amount. The beam is then suppressed with S4, and if the zero has drifted the recorder will trace a square-wave showing to what extent the supposed equality in height was due to unbalance current through the divider. If this is small it can be corrected for without repeating the measurement. As with the double-collector method, there is no need for the zero-setting to be exact, but one has to know exactly by how much it is in error.

If in practice transients occur on the record at the change-over between peaks, the high voltage stabilizer is probably too slow, so that the switching is not complete before the end of the 1 second cut-out period. The feed-back bleeder in voltage stabilizer circuits is often over-compensated for AC, to reduce hum, and the large time-constants involved slow down the response of the circuit to modulation.

The DC amplifier should also be suspected, especially in double-collector instruments, where speed is not normally necessary, and an array of alternative collectors and high resistors at the input may result in a large input capacity. If it is not found possible to eliminate the transients by speeding up the unit responsible for the delay in the switch-over, it will be necessary to lengthen the cut-out period by increasing C4 and C3.

Positions (3) and (4) of S6 provide more rapid scans, which are especially useful for following changes in the height of a single peak. Mass peak 31, for example, which is particularly sensitive to ether, may be scanned repeatedly in this way and used as an indicator for leak-hunting, or any peak may be selected as an indicator during adjustment of the ion source for maximum ion current.

Although there are a fair number of controls one soon learns to use them without difficulty. It is worth planning the lay-out of the panel with care, and arranging the sense of rotation of the controls in a logical manner. The unit should be mounted directly beneath the recorder.

5. Conclusion

The circuit described serves the double purpose of eliminating the recorder as a source of error, and making a better use of the information supplied by the spectrometer. Although the effect of fluctuations in ion current is reduced, these fluctuations remain the limiting factor, and thus the accuracy obtained in a given problem lies between that obtainable with a double collector, and that of a conventional scan through the whole spectrum.

The method was developed during work with mercury samples in which small changes in isotopic constitution had been produced (3). The spectrometer was a 6″ all-metal 90° Nier-type instrument, built at this laboratory by Dr. Hans von Ubisch.

Summary

A circuit is described which scans alternately the tops of two mass peaks whose amplitude is to be compared, and couples in a precision potential divider when the larger of the two peaks is being scanned. The divider is adjusted by hand so that the peaks, which are displayed on a potentiometric recorder, are brought to the same height, and their amplitude ratio is then read off directly from the setting of the divider. By backing off the recorder, the gain may be increased while still keeping the peaks on scale, and in this way a change in ratio of 1 % may be expanded to 20 mm or more on the paper of the recorder. The device can be used for mass pairs which may be widely separated, and may lie anywhere in the range of the spectrometer.

A.B. Atomenergi, Department of Physics, Stockholm, Sweden.

REFERENCES

1. Nier, A. O., Ney, E. P. and Inghram, M. G., Rev. Sci. Instrum. *18*, 294 (1947).
2. Hercus, G. R. and Morrison, J. D., Rev. Sci. Instrum. *23*, 118 (1952).
3. Haeffner, E., Nature *172*, 775 (1953).

Tryckt den 24 augusti 1954

Uppsala 1954. Almqvist & Wiksells Boktryckeri AB

ARKIV FÖR FYSIK Band 8 nr 20

Communicated 12 May 1954 by BENGT EDLÉN

The vacuum-ultraviolet spectrum of Cl I

By STIG AVELLÉN

In order to get a more precise value of the ground term $3s^2\,3p^5\;{}^2P$ and to find the unknown $3s^2\,3p^4\,5s$ and $3s^2\,3p^4\,3d$ terms of Cl I, the vacuum-ultraviolet spectrum of chlorine has been investigated.

The only previous investigation of the vacuum-ultraviolet spectrum of Cl I seems to be that by TURNER [1] in 1926. He reported 7 lines of which 5 coincided with lines that he had also obtained with a bromine light source. In 1928 BOWEN [2] and LAPORTE [3] interpreted these lines as resulting from the electron transition $3p-4s$ in Cl I.

The spectrograph used in the present investigation was the same as previously described by ARVIDSSON [4]. It is of the grazing incidence type with a N.P.L. metal grating having 567 lines/mm and a ruled surface of 32 × 19 mm. The radius of curvature is 1538 mm and the dispersion at 1350 A is 4.7 A/mm. A water-cooled hollow-cathode light source having a cathode area of about 10 cm^2 was directly attached to the spectrograph by means of a ground joint. Helium at a pressure of 1 to 5 mm Hg was circulated in the conventional manner. Nickel or copper was used as cathode material, and a powder of LiCl, NaCl, $FeCl_3$, Cu_2Cl_2 or $CuCl_2$ was smeared on to the inner wall of the cathode. In some experiments a small amount of CCl_4 was circulated through the light source. The current was varied from 0.2 to 1 amp. and the exposure time from 5 to 60 min. Schumann plates from Hilger and Q1 and Q2 plates from Ilford were used. Lines of Cu II, O I, H I, N I and N II have been used as standards of wavelength.

The transitions $3p\;{}^2P-4s\;{}^4P, {}^2P$ (Table 1) and $3p\;{}^2P-4s\;{}^2D$ (Table 2) appeared with great intensity. Assuming the term values for $4s\;{}^4P, {}^2P$ given by KIESS [5] as correct, the level values for $3p\;{}^2P_{1\frac{1}{2}}$ and ${}^2P_{\frac{1}{2}}$ are calculated from the observed transitions as shown in Table 1 with estimated limits of error of about ± 0.25 K. The combination with $4s\;{}^2D$ has not been used in this calculation as it falls in a region with few standards.

A number of lines arising from combinations of previously known terms with the ground term have been observed in the region 980 A – 1050 A. In addition, some twenty-five lines have been measured in the region 1080 A – 1110 A. They must be interpreted as arising from transitions to the ground term from the unknown $5s$ and $3d$ terms, but it appears that a detailed and unambiguous identification of these levels will require a knowledge of their combinations with the $4p$ terms. These lines should fall in the region 10,000 A – 20,000 A. KIESS [5] gives a table of Cl I lines extending to 10,427 A in the infrared, but it does not

Table 1.

Transition	Int.	λ	σ	$3p\,^2P_{\frac{1}{2}}$	$3p\,^2P_{1\frac{1}{2}}$	Turner's λ-values
$3p\,^2P_{\frac{1}{2}} - 4s\,^4P_{1\frac{1}{2}}$	8	1396.527	71606.21	104113.01		1396.5
$3p\,^2P_{\frac{1}{2}} - 4s\,^4P_{\frac{1}{2}}$	6	1389.961	71944.46	104112.82		1389.9
$3p\,^2P_{1\frac{1}{2}} - 4s\,^4P_{2\frac{1}{2}}$	6	1389.688	71958.60		104995.60	
$3p\,^2P_{1\frac{1}{2}} - 4s\,^4P_{1\frac{1}{2}}$	11	1379.529	72488.51		104995.31	1379.6
$3p\,^2P_{1\frac{1}{2}} - 4s\,^4P_{\frac{1}{2}}$	4	1373.118	72826.95		104995.31	
$3p\,^2P_{\frac{1}{2}} - 4s\,^2P_{1\frac{1}{2}}$	10	1363.449	73343.41	104112.97		1363.5
$3p\,^2P_{\frac{1}{2}} - 4s\,^2P_{\frac{1}{2}}$	10	1351.657	73983.27	104113.03		1351.7
$3p\,^2P_{1\frac{1}{2}} - 4s\,^2P_{1\frac{1}{2}}$	12	1347.238	74225.93		104995.49	1347.2
$3p\,^2P_{1\frac{1}{2}} - 4s\,^2P_{\frac{1}{2}}$	9	1335.723	74865.82		104995.58	1335.8
			Mean value	104112.96	104995.46	

Table 2.

Transition	Int.	λ	$\sigma_{\text{obs.}}$	$\sigma_{\text{calc.}}$
$3p\,^2P_{\frac{1}{2}} - 4s\,^2D_{1\frac{1}{2}}$	11	1201.358	83239.13	83239.34
$3p\,^2P_{1\frac{1}{2}} - 4s\,^2D_{1\frac{1}{2}}$	12	1188.768	84120.70	84121.84
$3p\,^2P_{1\frac{1}{2}} - 4s\,^2D_{2\frac{1}{2}}$				84120.14

seem to contain any such transitions. It will therefore be necessary to reinvestigate the chlorine spectrum in the region beyond 10,000 A before the 5*s* and 3*d* terms can be definitely established.

The Physical Laboratory, University of Lund, April 1954.

REFERENCES

1. L. A. Turner, Phys. Rev. *27*, 397, 1926.
2. I. S. Bowen, Phys. Rev. *31*, 497, 1928.
3. O. Laporte, Nature *121*, 1021, 1928.
4. G. Arvidsson, Diss. Uppsala 1932; Ann. d. Physik *12*, 787, 1932.
5. C. C. Kiess, B. S. Jour. Research *10*, 827, 1933.

Tryckt den 24 augusti 1954

Uppsala 1954. Almqvist & Wiksells Boktryckeri AB

ARKIV FÖR FYSIK Band 8 nr 21

Communicated 10 March 1954 by MANNE SIEGBAHN

The reaction energy of $O^{17}\,(d, \alpha)\,N^{15}$

By ROLF PAULI, KATARINA AHNLUND and CURT MILEIKOWSKY

With 4 figures in the text

Introduction

O^{17} is the rarest of the stable oxygen isotopes, with an isotopic abundance of 0.04 %. It has not until now been available as target nucleus for precision measurements of nuclear energy levels.

Thin targets of this isotope have been produced and the first reaction established is the ground state transition $O^{17}(d, \alpha)N^{15}$. The reaction energy was measured with the Cockcroft-Walton accelerator (ref. 1) and heavy particle spectrometer (ref. 2) of the Nobel Institute. The reaction has not been reported previously.

Experimental procedure

The O^{17}-targets were obtained from a quantity of gaseous oxygen enriched by diffusion in O^{17} and O^{18}, kindly put at our disposal by Professor K. CLUSIUS, Zürich. The gas contained some percent of the isotope 17. Our first O^{17}-targets, used in the earlier parts of the work reported here, were produced by oxidation. At a gas pressure of about 1 mm Hg clean Cu-disks were HF-heated to get a suitable thin oxide layer. Oxide thicknesses of a few keV were obtained as estimated from the line-widths of the $O^{18}(p, \alpha)N^{15}$-peaks from the targets.

An electromagnetic separation procedure has later been developed in order to get stronger O^{17}-targets, as will be described in a further report.

By deuteron bombardement of O^{17} we obtained an α-particle group whose energy fell in the region expected from the nuclear masses of the components in the ground state transition $O^{17}(d, \alpha)N^{15}$. We controlled the identity of the group by varying the angle between the incident deuteron beam and the detector, and by making a special comparison with $F^{19}(d, \alpha)O^{17}$, which gives an α-group in the same region.

The Q-value was measured in three different runs. Deuteron energy, angles, and thickness of layer on target were determined by the same methods as in previous work in this laboratory (ref. 3). The α-particles leaving the target within an angle of 3.4° at 134.7° to the deuteron beam were analysed by the magnetic spectrometer and detected in nuclear emulsion plates. In the first

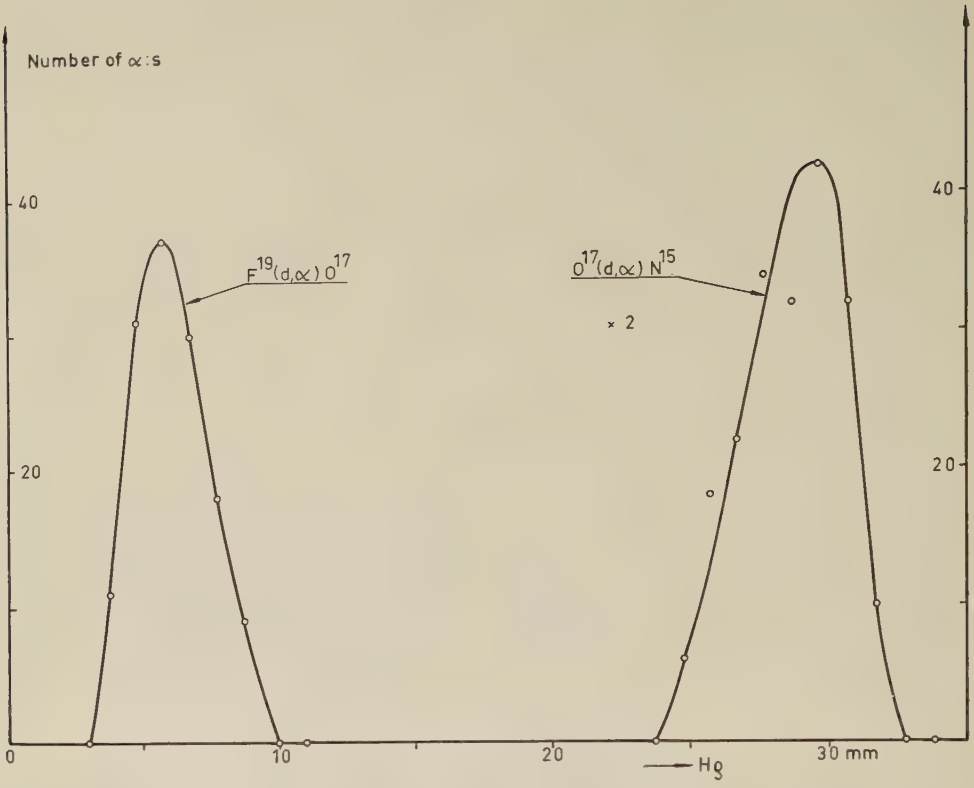

Fig. 1. Spectra of α-particles from $F^{19}(d,\alpha)O^{17}$ Q_1 and from $O^{17}(d,\alpha)N^{15}$ detected in nuclear track plates placed after the nuclear spectrometer. Both reactions are studied at the angle $\theta = 134.7°$ to the incident 855 keV deuteron beam with the angular width $2\,\Delta\,\theta = 3.4°$. The bombardment on F^{19} was 800 μC and on O^{17} 3200 μC. The number of α-tracks per 0.8 mm of the plate is shown in the figure. 1 mm in the plate corresponds to 9.8 keV α-energy.

run the energy scale of the spectrometer was calibrated with α-particles from $F^{19}(d,\alpha)O^{17}$, $Q_1 = 9167 \pm 11$ keV (ref. 4) at 134.7° and in the later runs with $N^{14}(d,\alpha)C^{12}$, $Q_1 = 9137 \pm 6$ keV (ref. 5) at 61.0°. In run 1 an oxidized O^{17}-target on Cu was used in comparison with an evaporated F^{19}-target on Ag. In run 2 we used O^{17} oxidized on Cu and separated N^{14} in Ta, and in run 3 separated O^{17} in Fe and NH_3NO_3 precipitated on Ag.

Results

The experimental α-groups are shown in Figs. 1–3. The peaks were read at the high-energy edges using minimum angle and external layer correction. We get

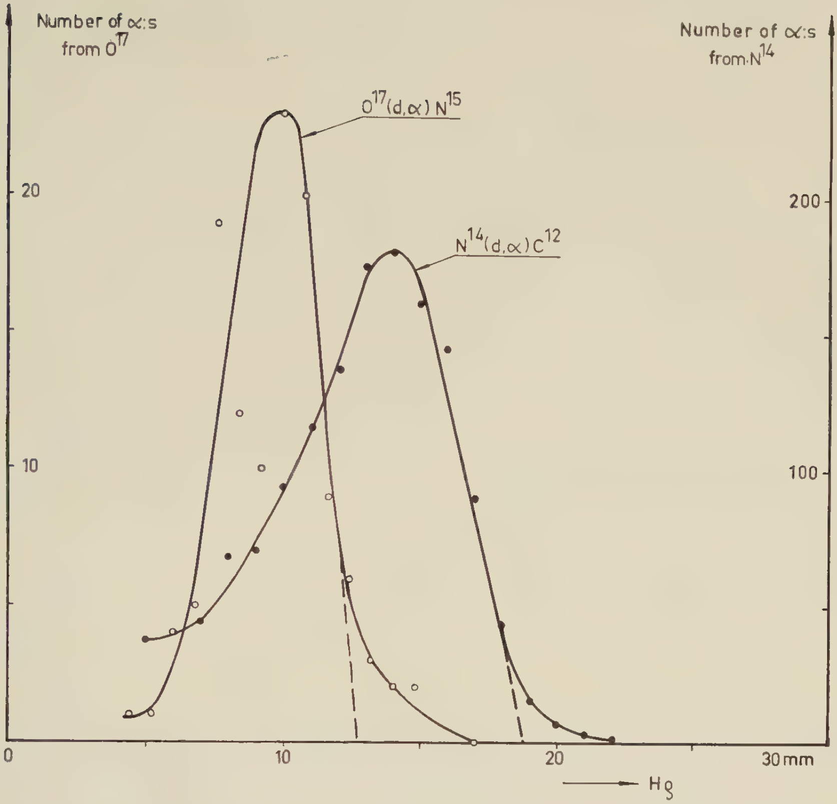

Fig. 2. Spectra of α-particles from $O^{17}(d,\alpha)N^{15}$ at $\theta = 134.7°$ and from $N^{14}(d,\alpha)C^{12}$ Q_1 at $\theta = 61.0°$ $2\Delta\theta = 3.4°$. Deuteron energy 856 keV. Bombardment 2400 μC for both reactions. Number of tracks per 0.8 mm plate is given for O^{17} and per 0.4 mm plate for N^{14}. 1 mm = 9.8 keV.

	Run 1	Run 2	Run 3
Q in keV	9787.7	9810.0	9812.3

The total probable errors in the Q-values are composed of the partial errors shown in the table below. The contributions to the error in Q are given for the various partial errors.

Source of error	Run 1	Run 2	Run 3
Q of calibration reaction	11.2	6.1	6.1
Deuteron energy	2.5	3.4	2.5
Angle measurement	0.4	6.7	6.7
Reading of α-peaks	15.0	16.0	6.7
Dispersion in plate	7.5	2.5	2.5
Total probable error	20	19	12

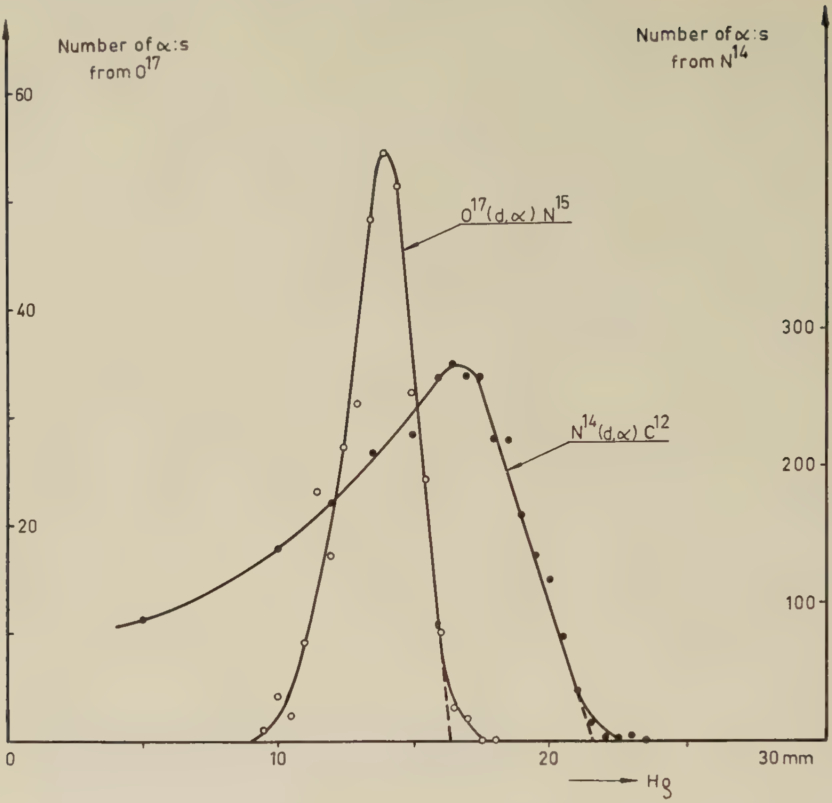

Fig. 3. Spectra of α-particles from $O^{17}(d,\alpha)N^{15}$ at $\theta = 134.7°$ and from $N^{14}(d,\alpha)C^{12}$ Q_1 at $\Theta = 61.0°$ $2\Delta\Theta = 3.4°$. Deuteron energy 832 keV. Bombardment 2400 μC for both reactions. Number of tracks per 0.4 mm is given. 1 mm = 9.8 keV.

We compare our results with the Q-value calculated from the atomic masses of the components of the reaction $O^{17}(d,\alpha)N^{15}$:

O^{17}:	17.004533	(± 7)	a.m.u.
d:	2.014735	(± 6)	
α:	4.003873	(±15)	
N^{15}:	15.004863	(±12)	(ref. 6)

From the mass difference $O^{17} + d - (\alpha + N^{15})$ we get the Q-value 9817 ± 20 keV. We also calculate a Q-value from the experimental Q-values in the nuclear reaction cycle:

$O^{16}(d,p)O^{17}$	$Q_a = 1917 \pm 4$ keV	
$O^{16}(d,\alpha)N^{14}$	$Q_b = 3115 \pm 5$	
$N^{14}(d,p)N^{15}$	$Q_c = 8615 \pm 9$	(ref. 7)
$O^{17}(d,\alpha)N^{15}$	Q_d	

from which $Q_d = Q_b + Q_c - Q_a = 9813 \pm 11$ keV.

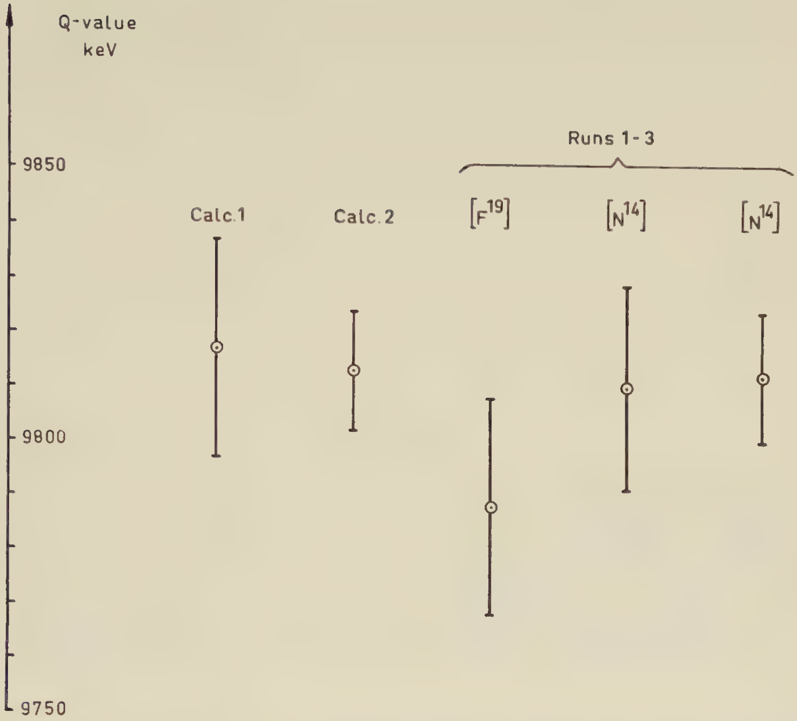

Fig. 4. Q-value of $O^{17}(d,\alpha)N^{15}$. Calc. 1 is the value expected from the atomic masses of the components. Calc. 2 is calculated from the experimental Q-values in the nuclear reaction cycle mentioned in the text. The experimental values 1–3 are obtained from the curves in Figs. 1–3.

In Fig. 4 the various Q-values are placed together. Our experimental values thus show a good agreement with the values calculated from other experimental data. Our value calibrated with F^{19} seems to lie somewhat low. A discussion of the Q-value determination for $F^{19}(d,\alpha)O^{17}$ which is given in ref. 4 should perhaps be considered here. In connection with the agreement between the last two runs one may recollect that different types of target of both O^{17} and N^{14} were used in these runs. The mean of the three runs is $Q = 9807 \pm \pm 12$ *keV*.

ACKNOWLEDGEMENTS

We are very grateful to Professor Klaus Clusius, Zürich, for presenting the enriched oxygen gas, and to Professor Manne Siegbahn for continuous interest in our work.

REFERENCES

1. Mileikowsky, C., and Pauli, R. T., Ark. f. Fys. *4*, nr 12, 287 (1952).
2. Mileikowsky, C., Ark. f. Fys. *4*, nr 16, 337 (1952).
3. —— Ark. f. Fys. *7*, nr 8, 89 (1953).
4. Watson, H. A., and Buechner, W. W., Phys. Rev. *88*, 1324 (1952).
5. Malm, R., and Buechner, W. W., Phys. Rev. *81*, 519 (1951).
6. Ajzenberg, F., and Lauritsen, T., Rev. Mod. Phys. *24*, 321 (1952).
7. Van Patter, D. M., M. I. T. Technical Report 57 (1952).

Tryckt den 25 augusti 1954

Uppsala 1954. Almqvist & Wiksells Boktryckeri AB

ARKIV FÖR FYSIK Band 8 nr 22

Communicated 25 November 1953 by Manne Siegbahn and Erik Hulthén

The decay of As^{71}

By Sigvard Thulin, Jean Moreau[1], and Hugo Atterling

With 7 figures in the text

Abstract:

The decay of 65 hr As^{71} has been studied using electromagnetically separated samples. The isotope decays by K-capture and positron emission. The probability ratio of K-capture to positron emission is 2.1 ± 1. It was found that at least 97 % of the positrons correspond to a β^+ transition of energy 813 ± 10 keV. Two γ-rays of energies 23.3 ± 0.3 and 174.5 ± 0.4 keV were recorded by means of their conversion electrons. The $K/(L+M)$ ratios are respectively 5.4 ± 0.8 and 8.9 ± 1. $\gamma - e^-$- and $\gamma - \beta^+$-coincidence measurements were performed. A decay scheme is proposed.

Introduction

The 65 hr As^{71} isotope is formed together with several other strong arsenic activities when germanium is bombarded with deuterons. The yield of As^{71} is in fact only a small part of the total active arsenic yield (cf Fig. 1). Moreover, the half lives of the other arsenic species are inconvenient for making a unique time analysis of the measured data. A successful study of the decay of As^{71} therefore seems to be very difficult unless the As^{71} is separated from the bulk activity. As the decay data on As^{71} were incomplete (1) the present investigation was taken up, using electromagnetically separated samples of As^{71}. A preliminary report on the β-measurements has been published elsewhere (3). Meanwhile, an investigation of the As^{71} β-spectrum was published by P. H. Stoker and Ong Ping Hok (2). Their results, obtained by a time analysis of the β-spectra of As^{71}, As^{72} and As^{74}, are in accordance with ours except that they did not find the conversion electrons of the 23.3 keV γ-ray. This discrepancy is, however, explained below.

Preparation of β-sources

Metallic germanium, fused onto a water-cooled copper plate, was bombarded with 25 MeV deuterons in the 225-cm cyclotron (4) (about 1000 μAhr).

The irradiated germanium metal was converted to the sulfate and dissolved in H_2SO_4 (1 : 7) together with a few milligrams of arsenic carrier. The arsenic was then

---

[1] On leave from Centre d'Etudes Nucléaires, Saclay, France.

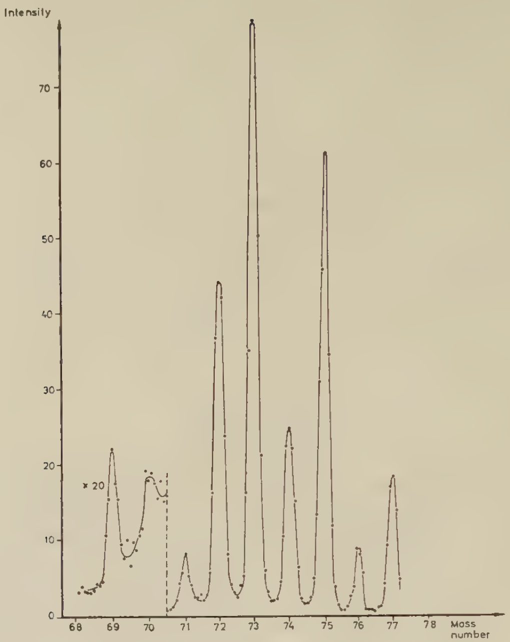

Fig. 1. Activity spectrum of arsenic isotopes, deposited on a collector foil in the isotope separator.

reduced by means of zinc. The mixture of AsH_3 and H_2 formed was dried and passed through a pyrex spiral, immersed in liquid air to condense the AsH_3 gas. From our experience it seems to be important to eliminate the presence of oxygen in the apparatus, and hydrogen was therefore passed through it for some time before the reduction of the arsenic was started. The glass spiral also had to be thoroughly cleaned to avoid decomposition of AsH_3 on the walls.

The spiral, containing AsH_3 mixed with H_2, was connected to the ion source of the isotope separator via a needle valve. The arsenic mass spectrum as seen on the fluorescent screen consisted of four visible lines due to As^+, AsH^+, AsH_2^+ and AsH_3^+ of the stable As^{75}. Weaker lines of lower mass numbers, probably due to germanium, were also present. The target used consisted of an aluminium plate having an elliptical aperture (5 × 6.5 mm) at the position where ions of mass number 71 were focused. Behind this aperture a standard β-sample holder was mounted, this being covered with an aluminium backing foil of thickness 0.15 mg/cm². On this foil the As^{71} isotope was collected.

The separations lasted for 0.5–2 hr and the total collector current was 2–8 μA.

In a separate run the activities deposited on mass numbers 69–77 were studied in the following manner. The ions were collected on an aluminium foil of thickness 2.5 mg/cm². After the separation the foil was cut into strips 1 mm broad, parallel to the direction of the mass spectrum lines. The activity of each strip was measured with a GM-counter (window thickness 3.7 mg). Fig. 1 shows a plot of the intensity as a function of distance along the collector. It is seen that the activity on mass number 71 is very weak compared with the activities of the other lines. Even a very weak tail from the activity at neighbouring mass numbers will cause an observable contamination in the As^{71} activity. The β-sources of As^{71} later prepared did in fact contain a contamination of As^{72}, which had to be corrected for (cf. below).

The very weak activity at mass number 69 is probably due to Ge^{69}. This assignment is supported by the measured half life of about 30 hr.

The half life of the activity at mass number 71 was found to be 65 ± 5 hr.

β-spectrometer measurements

The β-spectum of As^{71} was studied in the intermediate image β-spectrometer (5), adjusted to 3.5 % resolution. As already mentioned, the source backing had a thickness of 0.15 mg/cm^2. In the final measurements we used a GM-counter window having a "cut-off" less than 5 keV.

Fig. 2 shows the β-spectrum of As^{71} obtained by using a helical baffle, transmitting only positrons. The corresponding Fermi plot appears in Fig. 3. These plots have been corrected for a contamination of As^{72} positrons having an upper limit of ~ 2.4 MeV and amounting to about 10 % of the total intensity (cf. above). This contamination was shown to decay with a half life of about 30 hr. The residual positron spectrum (Fig. 2) was analyzed into two components of energies 813 ± 10 keV and 250 keV and intensities 97 % and 3 % respectively. The question arises whether the weak low-energy component is real or not. In fact, measurements on the positron-emitting Kr^{79} in the same β^--spectrometer indicate that the low-energy part of a positron distribution might be somewhat distorted because of scattering when the ring focus slit is large. Another reason why the 250 keV β^+-component may be non-existent will be given below (p. 225).

Fig. 4 shows the low-energy electron lines (cf. 3) of As^{71}, measured in the intermediate image spectrometer with the positrons baffled off. The K and $(L+M)$ conversion lines of the 174.5 keV γ-ray (cf. 2, 3) shown in Fig. 5 were recorded in the double focusing spectrometer with higher resolution. Table I gives the energy data and the interpretation of the lines.

Table I

Line energy keV	Interpretation	Calculated γ-ray energy keV	GM-window absorption correction	Relative intensity
8.4	KLL		4.0	9.7
9.6	KLM		2.5	2.5
12.2	K_{23}	23.3	1.56	1.0
21.9	$(L+M)_{23}$	23.1	1.0	1.9
163.4	$(K+L)_{175}$		1.0	1.7
163.4	K_{175}[1]	174.5		1.5
173.5	$(L+M)_{175}$[1]	174.7		0.2

[1] Measured in the double focusing spectrometer.

According to our β-measurements, there are two γ-rays of energies 23.3 ± 0.3 and 174.5 ± 0.4 keV respectively in the decay of As^{71}.

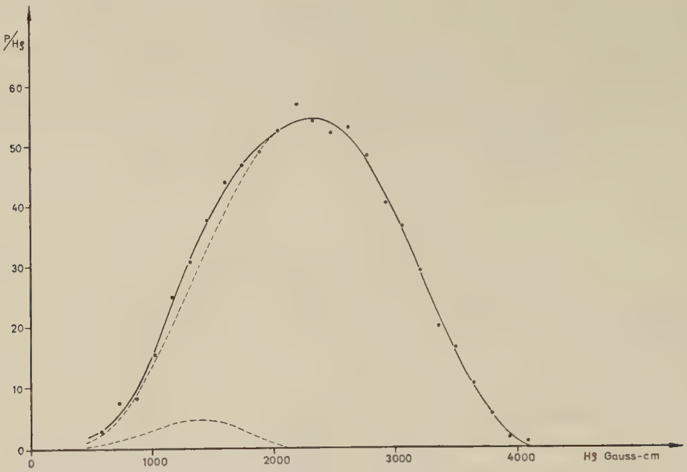

Fig. 2. Positron spectrum of As^{71}.

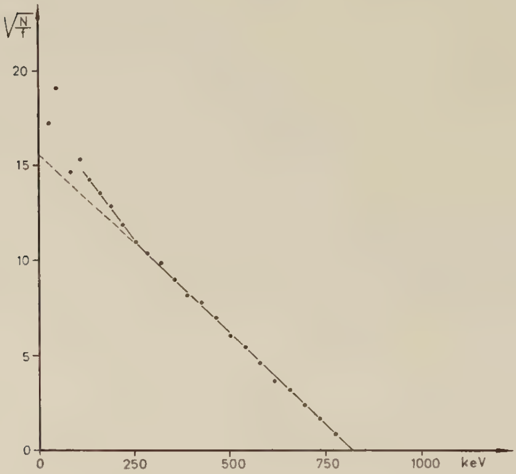

Fig. 3. Fermi plot of the positron distribution of As^{71}. (Upper energy limit 813 KeV).

It is earlier mentioned (p. 219) that STOKER and ONG PING HOK (2) did not find the 23.3 keV γ-ray. This seems to be due to the fact that their samples contained a relatively strong admixture of As^{73}. The L- and M-conversion lines of the 13 keV γ-ray of this isotope would certainly have obscured the weak K-line of the 23.3 keV γ-ray in As^{71}.

The half lives of the various lines and of the β^+ continuum were checked by several measurements during a period of 10 days. All of them, except the Auger lines, decayed with a half life consistent with that found for As^{71} (cf. p. 221). The decay curve of the Auger lines was found to be complex, containing a component with an appreciably longer half life than that of As^{71}. It seems probable that the long lived part of the Auger lines is due to 11 d Ge^{71}, formed in the decay of As^{71}.

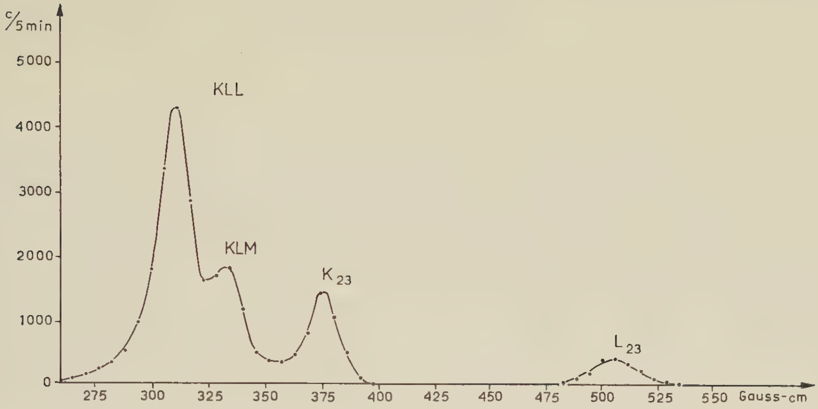

Fig. 4. Electron spectrum of As^{71} as recorded in the intermediate image β spectrometer.

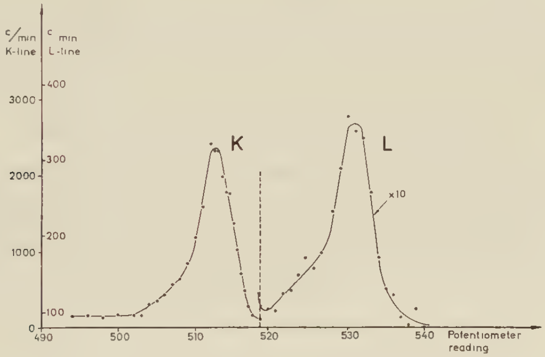

Fig. 5. K- and $(L + M)$-lines resolved in the double focusing β-spectrometer.

Intensity comparisons

In order to calculate the $K/(L + M)$ ratio of the low-energy γ-ray, and estimate the relative intensities of K-capture and positron emission, an absorption correction curve for the GM-window was needed. For this purpose the Co^{60} β-continuum was measured using a Co^{60} source on a very thin nylon backing. The straight line deviation of the Kurie plot in the low-energy region was considered to be mainly due to absorption in the GM-window. The corresponding absorption corrections, as calculated for the different lines, are given in Table I.

Intensity comparisons were performed both by means of the areas under the electron lines and the β^+-continuum and by means of peak heights. In Table I are given relative areas obtained in the final β-spectrometer measurement. $K/(L + M)$ ratios of the 23.3 and 174.5 keV γ-rays were estimated by both methods mentioned above, with a higher weight given to the former. The following mean values were obtained from different β-measurements.

$$\left(\frac{K}{L+M}\right)_{23} = 5.4 \pm 0.8$$

$$\left(\frac{K}{L+M}\right)_{175} = 8.9 \pm 1 .$$

The errors given are believed to include the uncertainties in GM-window absorption. Our value of $K/(L+M)_{175}$ is in accordance with the value 8.3 reported by STOKER and ONG PING HOK (2). According to the semi-empirical K/L curves of GOLDHABER and SUNYAR (6), the 23.3 keV γ-ray should be due to an M2 transition. The 175 keV γ-ray, however, cannot be classified unambiguously in this way. It might correspond to an M2, E2 or E3 type transition. A decision between these alternatives might be obtained by comparing the experimentally determined internal conversion coefficient with the theoretical values obtained from the tables of ROSE *et al.* (7). Accepting the decay scheme of Fig. 7, which seems to be experimentally established, we calculate $\alpha_{175} = 0.07$. In Table II this value is compared with the theoretical values.

Table II

	E1	E2	E3	M1	M2	Experimental
$a_{K_{175}}$	0.012	0.082	0.52	0.017	0.110	0.07

The experimental value of α_K is calculated with the assumption that the intensity of L-electron capture is negligible. It is seen that the most probable alternative is that the 175 keV γ-ray corresponds to an E2 or E2 + M1 transition.

The probablitity ratio of K-capture to positron emission, C/β^+ was calculated from the formula

$$\frac{C}{\beta^+} = \frac{\Sigma A}{\beta^+ (1-\omega_K)} - \frac{K_{23}+K_{175}}{\beta^+}$$

where β^+ = area of the positron spectrum
ΣA = total area of Auger lines due to As^{71}.
K_{23} and K_{175} = area of corresponding K-conversion lines
ω_K = fluorescence yield for Ge. We use the value $\omega_K = 0.46$ (8).

In estimating the Auger line intensity due to As^{71}, the following possible contaminations should be considered: 1. Auger lines due to the contamination with As^{72}. According to measurements by McCOWN *et al.* (9) the ratio C/β^+ is approximately the same (~ 2) for As^{71} and As^{72}. The presence of positrons from As^{72}, amounting to 10 % of the positron intensity of As^{71}, therefore also entails a contamination of 10 % intensity in the K-capture part of the Auger lines. 2. The presence of Auger lines from Ge^{71} collected as Ge^{71} ions in the arsenic separation. From the very low intensities of stable Ge lines in the mass spectrum, and from the decay curve of the Auger lines, we conclude that the contribution to the Auger line intensity from Ge^{71} initially present in the sample can be neglected. 3. The growth of Ge^{71} from As^{71} gives an increasing contribution from Ge^{71} to the Auger line intensity. However, if the intensity comparisons are made soon after the preparation of the β-source, this contribution can be neglected.

After correction for the As^{72} Auger lines, we obtain

$$\frac{C}{\beta^+} = 2.1 \pm 1 .$$

Every additional correction discussed above will decrease this value.

The large error is mainly due to uncertainties in the corrections for GM-window absorption applied to the Auger lines (cf. Table I). The value obtained is in agreement with the value $C/\beta^+ \sim 2$ reported by McCown *et al.* (9).

In spite of the large error in our value of C/β^+, it is useful in a computation of $\log ft$ values for the two β^+-transitions in As^{71}. Using this value of C/β^+, the observed half-life of 65 hr, and the relative intensities obtained for the β^+-components, we calculate $\log ft = 5.2$ for the 250 keV β^+-transition and $\log ft = 5.9$ for the 813 keV β^+ transition.

These values classify both transitions as belonging to the allowed group (10). It is then possible to obtain theoretical values for the ratio of K-capture to positron emission. From the curves of Feenberg and Trigg (11) we get $C/\beta^+ = 2$ and ~ 200 for the 815 keV and 250 keV components respectively. The latter value means that the 250 keV K-capture branch would have an intensity about 6 times stronger than the total positron intensity. This is, however, in contradiction with our value 2.1 for C/β^+. This is another reason for regarding the existence of a weak low-energy component as doubtful (cf. p. 221).

Scintillation spectrometer measurement

The pulse distribution of As^{71} was recorded with a scintillation spectrometer (12) employing a NaJ(Tl) crystal. Two lines appeared, at 179 and 535 ± 40 keV. The instrument was calibrated by means of the 175 keV γ-ray of Sb^{125} and the 661 keV γ-ray of Cs^{137}. The strong 179 keV γ-line in the As^{71} spectrum is interpreted as being due to the 175 keV γ-ray already established. The very weak 535 keV line may be due to annihilation radiation.

Coincidence measurements

In order to get information about the decay scheme of As^{71} some coincidence measurements were performed in the intermediate image spectrometer. A scintillation counter (photomultiplier EMI 5311 and a NaI(Tl) crystal) was mounted behind the β-sample. Coincidences were recorded between pulses from the GM-counter of the spectrometer and γ-pulses of selected energies. The resolving time of the coincidence circuit was 5×10^{-7} sec. The coincidence arrangement is described in more detail in ref. (13).

$\beta^+ \gamma$-coincidences were recorded between β^+ particles of selected energies and γ-quanta of 174.5 keV energy. The Fermi plot of the coincidence spectrum thus obtained is shown Fig. 6. The β^+-continuum in coincidence with the 174.5 keV γ-ray has an upper limit of 790 ± 30 keV.

$e^- \gamma$-coincidences were measured between K-conversion electrons of the 23.3 keV γ-ray and γ-quanta of energy 174.5 keV. The coincidence rate obtained indicates that all K-conversion electrons of the 23.3 keV γ-ray are followed by a 175 keV γ-quantum in cascade. This result is based on the known total efficiency ε for recording the 174.5 keV γ in the crystal. (A value of $\varepsilon = 6 \times 10^{-3}$ was obtained in the $\beta^+ \gamma$-coincidence measurement described above.)

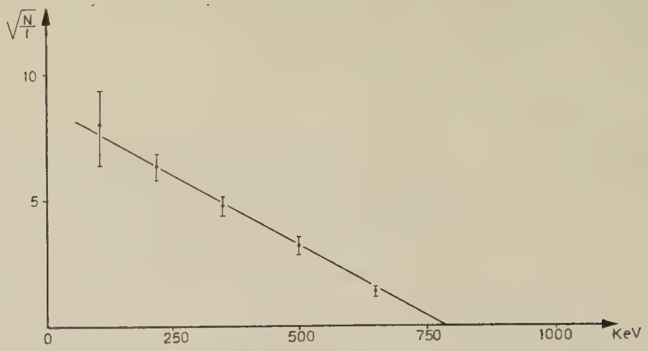

Fig. 6. Fermi plot of intensity distribution for $\beta^+\gamma_{175}$-coincidences.

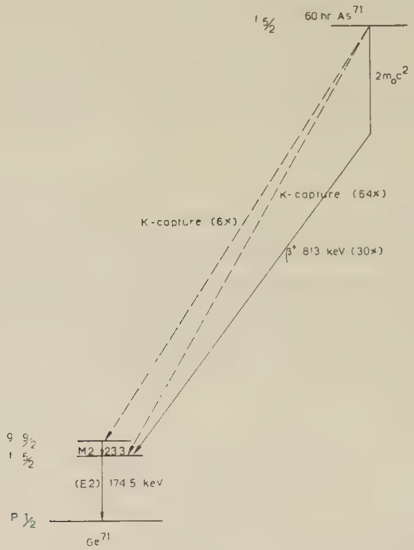

Fig. 7. Proposed decay scheme for As^{71}.

Decay scheme

The following experimental data form the basis for our discussion of the decay scheme of 65 hr As^{71}. The isotope decays by K capture and positron emission. The branching ratio is found to be $C/\beta^+ = 2.1 \pm 1$. At least 97 % of the positron transitions occur with a total particle energy of 813 ± 10 keV. The log ft value (5.9) for the positrons corresponds to an allowed ($\Delta I = 0, 1$, no) transition. Two γ-transitions of energies 23.3 ± 0.2 and 174.5 ± 0.4 keV occur in Ge^{71}. The $K/L + M$ ratios are 5.4 ± 0.8 and 8.9 ± 1 respectively. The former transition is most probably of the M2 type, and the latter might be of E2 type. The 175 keV γ-ray is shown to be in coincidence both with the 23.3 keV γ-ray and the positrons. The total intensity of the 23.3 keV transition is lower than that of the 174.5 keV transition.

The experimental results lead to the decay scheme shown in Fig. 7. The branching ratio given in the figure is obtained as follows. The measured intensity of the $K + L + M \ldots$ electrons of the 23.3 keV γ-ray is 15 % of the total positron intensity, that is 5.5 % of the total decay intensity. Since the theoretical value of the internal conversion coefficient for this M2 transition is ~ 500 the intensity of 23.3 keV γ-quanta can be neglected compared with the conversion electron intensity. Thus 5.5 % of all As^{71} nuclei decay to the 197.8 keV level in Ge^{71}.

The data may also be used for a comparison of the decay scheme with the level predictions for Ge^{71} and As^{71} obtained from the strong spin-orbit coupling model (14). According to this theory, the ground state of $^{39}_{32}$Ge^{71} should be $p_{1/2}$, analogous to the nuclei Y^{89} and Se^{73}, which also have an odd nucleon number of 39, and whose spins have been measured to be 1/2. An investigation by SARAF *et al.* (15) on the continuous gamma-ray spectrum accompanying orbital electron capture in Ge^{71} gives experimental support to this prediction. Possible excited states would be $g_{9/2}$ and $f_{5/2}$. An M2 transition (the 23.3 keV γ-ray) can only occur between the $g_{9/2}$ and the $f_{5/2}$ levels. The 174.5 keV γ-transition is probably of E2 type and would occur between the $f_{5/2}$ and $p_{1/2}$ levels. The level scheme for Ge^{71} shown in Fig. 9 is then justified experimentally.

The ground state of $^{38}_{33}$As^{71} might be $p_{3/2}$ or $f_{5/2}$. The assumption of a $p_{3/2}$ state would lead to the following difficulties. First, the transition to the $p_{1/2}$ ground state of Ge^{71} would be allowed and have high intensity, in contradiction to the experimental evidence. Secondly, the transition to the $g_{9/2}$ level in Ge^{71} would be highly forbidden, with $\Delta I = 3$ yes. If we assume an $f_{5/2}$ ground state of As^{71}, however, the experimental branching ratio becomes more plausible. The positron transition to the $f_{5/2}$ level in Ge^{71} would be allowed ($\Delta I = 0$, no), in accordance with the experimental log ft value 5.9. The transition to the $g_{9/2}$ level then proceeds with a spin difference of 2 units and parity change and the experimental value of log $(W_0^2 - 1)ft$ should be 9–10. This condition is fullfilled if the branching ratio C/β^+ for the 792 keV β^+-transition is assumed to be 50. For a corresponding allowed transition this value is 2 (11).

A comparison of the experimental value of $C/\beta^+ = 2.1$ and the theoretical value $C/\beta^+ = 2.4$ for the 813 keV positron component indicates that K-capture transitions to the ground state of Ge^{71} are of low intensity.

The level scheme of Fig. 9 may also explain why no isomeric state has hitherto been observed in Ge^{71} (cf. 1 and 15), as it has been in the cases of Zn^{69}, and Y^{89} which also have an odd nucleon number of 39. The total half life of the 23.3 keV $g_{9/2} - f_{5/2}$ transition should be of the order of 10^{-3} sec. according to the formula of WEISSKOPF (16). GOLDHABER and SUNYAR's plot of half lives as a function of energy for M1, M2 and E2 transitions (6) indicates that the 23.3 keV transition might have a half-life $\geq 10^{-6}$ sec.

Finally, the possibility of the existence of a weak 250 keV positron component should be discussed in connection with the decay scheme of Fig. 9. If it were real, it is plausible to assume the weak 535 keV line in the scintillation spectrum to be partly due to a γ-ray. Another branch might then be constructed in the decay scheme of As^{71}: a 250 keV positron component would feed a high energy level, which would decay to one of the 174.5 or 197.8 keV levels in Ge^{71} by emission of a 535 keV γ-quantum. The establishment of such a decay branch would require an improved coincidence equipment and stronger samples.

It is a great pleasure for one of the authors (J. MOREAU) to express his sincere thanks to Professor MANNE SIEGBAHN for the hospitality he has received at the Nobel Insititute of Physics, and also to thank all the members of this institute for helping him in every possible way.

Nobel Institute of Physics, Stockholm 50, Sweden.

REFERENCES

1. J. M. HOLLANDER, I. PERLMAN and G. T. SEABORG, UCRL-1928.
2. P. H. STOKER and ONG PING HOK, Physica *19*, 279 (1953).
3. H. ATTERLING and S. THULIN, Nature *171*, 927 (1953).
4. H. ATTERLING and G. LINDSTRÖM, Nature *169*, 432 (1952).
5. H. SLÄTIS and K. SIEGBAHN, Ark. f. Fysik *1*, 339 (1949).
6. M. GOLDHABER and A. W. SUNYAR, Phys. Rev. *83*, 906 (1951).
7. M. E. ROSE, G. H. GOERTZEL, B. J. SPINRAD, J. HARR, and P. STRONG, Privately circulated tables on K-conversion coefficients, cf. Phys. Rev. *83*, 79 (1951).
8. E. H. S. BURHOP, The Auger effect, Cambridge Univ. Press, p. 48 (1952).
9. D. A. MCCOWN, L. L. WOODWARD, and M. L. POOL, Phys. Rev. *74*, 1315 (1948).
10. S. A. MOSZKOWSKY, Phys. Rev. *82*, 35 (1951).
11. E. FEENBERG and G. TRIGG, Rev. Mod. Phys. *22*, 399 (1950).
12. B. ÅSTRÖM, Ark. f. Fysik *7*, 241 (1954).
13. J. MOREAU, Ark. f. Fysik (in press).
14. M. G. MAYER, Phys. Rev. *75*, 1969 (1949), O. HAXEL, J. H. D. JENSEN, and H. E. SUESS, Phys. Rev. *75*, 1766 (1949).
15. B. L. SARAF, J. VARMA and C. E. MANDEVILLE, Phys. Rev. *91*, 1216 (1953).
16. V. F. WEISSKOPF, Phys. Rev. *83*, 1073 (1951).

Tryckt den 25 augusti 1954

Uppsala 1954. Almqvist & Wiksells Boktryckeri AB

ARKIV FÖR FYSIK Band 8 nr 23

Communicated 25 November 1953 MANNE SIEGBAHN and ERIK HULTHÉN

The decay of Kr^{79}

By SIGVARD THULIN, JEAN MOREAU[1] and HUGO ATTERLING

With 7 figures in the text

Abstract

The β-spectrum of 34.5 h Kr^{79} has been remeasured. The positron spectrum was found to be complex, with two components of energies 598 ± 5 and 325 ± 20 keV and intensities 93 and 7 % respectively. In addition to two earlier reported gamma rays (1) the conversion electrons of 13 more gamma rays have been found. $\beta^+\gamma$- and $e^-\gamma$-coincidence measurements have been performed. Tentative level schemes are given.

Introduction

The β-spectrum of Kr^{79} was studied in 1951 by I. BERGSTRÖM (1). He then used electromagnetically separated sources of Kr^{79}, produced by the Kr^{78} (n, γ) reaction. As the abundance of Kr^{78} is only 0.34 %, the Kr^{79} samples were rather weak. The positron spectrum was found to have an upper energy limit of 590 keV. Two gamma-rays of energy 44 and 263 keV were reported and the ratio of K-capture to β^+-emission, C/β^+, was estimated to be 8 ± 4. A tentative decay scheme was proposed.

Later P. RADVANYI (2) has made a calculation of the ratio C/β^+ from cloud chamber measurements. His value is $C/\beta^+ = 14.1 \pm 4$. Radvanyi proposed a decay scheme different from that given by BERGSTRÖM. He also remeasured the half life and found the value 34.5 ± 0.2 h (3).

A third possibility of fitting the known data into a term scheme has been suggested by M. GOLDHABER and R. D. HILL on the basis of shell theory considerations (4). Fig. 1 shows the different decay schemes proposed.

The present investigation was undertaken in order to check these decay scheme alternatives.[2] For this purpose coincidence measurements in a β-spectrometer were planned. However, a remeasurement of the electron line spectrum, using strong Kr^{79} sources, led to the discovery of several new converted γ-rays. The decay therefore appears to be very complicated. In spite of this our coincidence measurements give some information on the decay scheme of Kr^{79} (cf. p. 237).

---

[1] On leave from Centre d'Etudes Nucléaires, Saclay.

[2] Later Dr. S. Frankel at the University of Pennsylvania has informed us that the decay scheme of Kr^{79} is of interest also because of recent medical application. In a scintillation spectrometer investigation of Kr^{79}, Dr. Frankel has shown the presence of several γ-rays.

Preparation of β-sources

The Kr^{79} isotope was produced by bombarding potassium bromide with 25 MeV deuterons in the 225 cm cyclotron at this institute (5). The bromide was fused into grooves in a copper target plate. The deuteron beam was limited to 10 μA in order to avoid destruction of the bromide target. After irradiation for 1–5 hr the target plate was cut away from the cooling tubes and placed in a vacuum-tight brass chamber. After evacuation a small amount of stable krypton was introduced into the chamber. The irradiated potassium bromide was then dissolved in some few ml of water, introduced by means of a separation funnel. In this way the whole Kr^{79} content of the irradiated bromide was extracted. The active krypton gas was fed to the ion source of the isotope separator through a needle valve, and ions of Kr^{79} were collected on aluminium foils. The technique of collection has been described elsewhere (6). The separations lasted for about half an hour. It should be noticed that in this case the isotope separator has been used solely for the preparation of β-sources, since the Kr gas contained only one active isotope.

Two types of sources were prepared, one with 0.15 mg/cm^2 aluminium backing (sample diameter 4 mm), and another with 2.5 mg/cm^2 aluminium backing (size 2×15 mm). They were used in different β-spectrometers (see below).

Positron spectrum and K-capture

The positron spectrum of Kr^{79} was measured in the intermediate image spectrometer (7), adjusted for 3 % resolution. The G.M.-counter window transmitted electrons of energy above 4.6 keV, as was found by a measurement of the Co^{60} β-spectrum. An estimate of the absorption correction as a function of energy for the counter window was also obtained from this measurement (cf. ref. 1). The spectrometer was calibrated by means of the F line of ThB.

As backings for the Kr^{79} β^+-sources we used aluminium foils of thickness 0.15 mg/cm^2. It has earlier been shown that back-scattering from similar β^--sources in the same spectrometer is negligible above 35–50 keV (8).

Fig. 2 shows the β-spectrum of Kr^{79}, obtained by using a helical baffle, which transmitted only positrons. A Fermi plot (9) of the data is shown in Fig. 3. The straight high energy part of the line corresponds to a β^+-component of allowed shape, having an energy limit of 598 ± 5 keV. An analysis of the Fermi plot gives another β^+-component of energy 325 ± 20 keV and intensity 7 % of the total positron intensity. The corresponding β^+-distributions, as calculated from the Fermi plot, are shown in Fig. 2 (broken lines).

A calculation of the ft values of the β^+-components presumes a knowledge of the branching ratio, C/β^+, of K capture and positron emission. This ratio was estimated from the areas under the Auger lines, the K-conversion lines (see below) and the β^+-continuum, using the formula

$$\frac{C}{\beta^+} = \frac{\Sigma A}{\beta^+ (1-\omega_K)} - \frac{\Sigma K}{\beta^+}$$

where ΣA is the total area of the Auger lines, corrected for absorption in G.M.-counter window, β^+ is the area under the β^+-continuum, and ΣK is the total areas

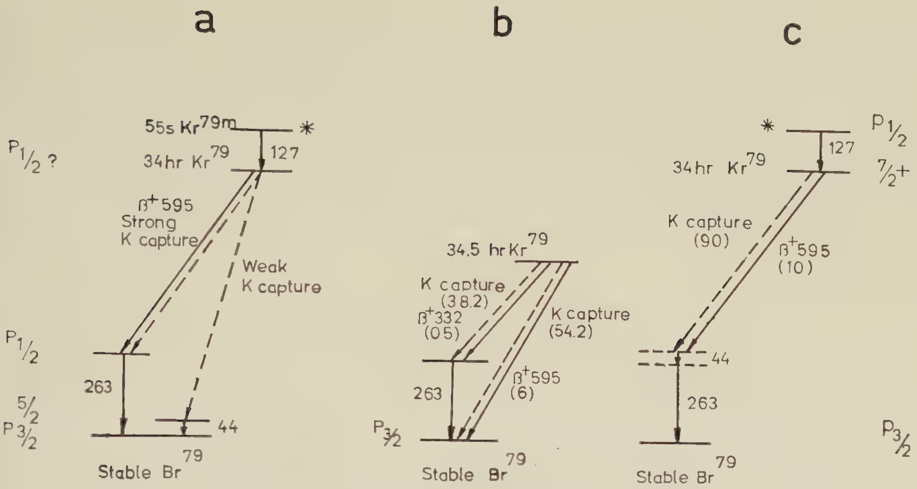

Fig. 1. Proposed decay schemes for Kr^{79}: a. I. BERGSTRÖM (1), b. P. RADVANYI (2), c. M. GOLDHABER and R. D. HILL (4).

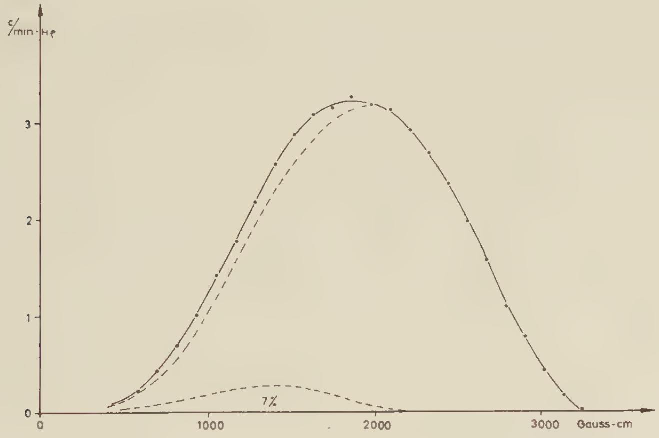

Fig. 2. Positron spectrum of Kr^{79}. (Upper energy limits 325 and 598 keV.)

of all K conversion lines. ω_K is the fluorescence yield for Br. Using $\omega_K = 0.57$ (10) and absorption corrections calculated from Co^{60} β-measurements, we obtain $C/\beta^+ = 9.5 \pm 3$. Later the measurement of relative intensities of Auger lines and positron spectrum has been repeated, using a GM-counter window of cut-off 1.9 keV. This window is assumed to have negligible absorption at Auger line energy. In this case we obtained a branching ratio $C/\beta^+ = 9.2 \pm 2$. We accept the mean value

$$\frac{C}{\beta^+} = 9.3 \pm 2.$$

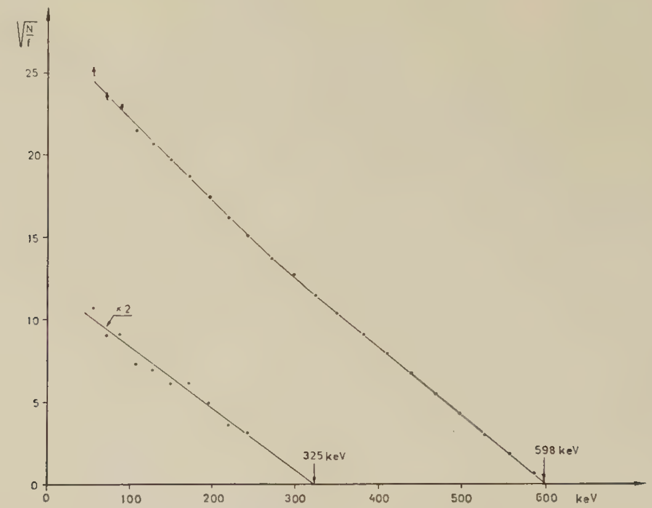

Fig. 3. Fermi plot of positron distribution for Kr^{79}.

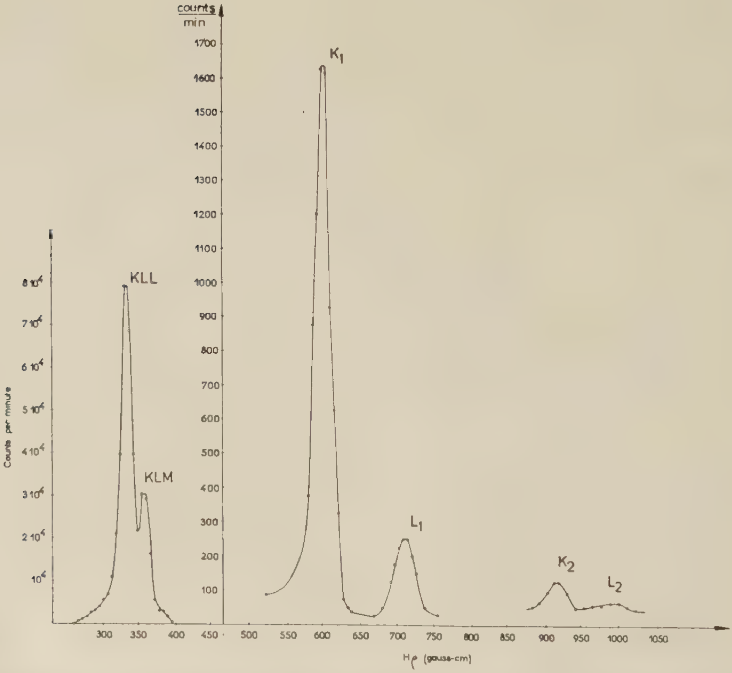

Fig. 4. Auger lines and conversion lines from 44.5 and 84.0 keV γ-rays measured in the intermediate image β-spectrometer.

From this value of the branching ratio, the observed half life, and the relative intensities of the two β^+-components, we calculate log ft values of 5.5 and 5.4 for the 598 and 325 keV β^+-component respectively. These values classify both spectra in the groups of allowed transitions (11), occuring with no change in parity and with a spin difference 0 or ± 1 according to the Gamow-Teller selection rules.

In accordance with the results of BERGSTRÖM (1) there was no indication of positrons of energy > 598 keV, even in our strong sources. The 1 meV positron component, reported by some investigators, have definitely been due to contaminations.

Electron conversion lines

With the relatively strong β-sources available to us, a systematic search for electron conversion lines was undertaken. The intermediate image β-spectrometer was used to scan the whole energy region up to about 1200 keV. In this way rough energy values were obtained, and intensity ratios were estimated for all resolved lines (thin counter window). In the double focusing spectrometer (12) most of the conversion lines could be resolved and accurate energy determinations were performed. Because of the thick GM-counter window, lines of energy less than 100 keV were not measured in this spectrometer.

The double focusing spectrometer was provided with a double GM-counter, which could be used for coincidence detection. In this way the background was decreased, and low intensity lines could be measured. Due to scattering and absorption in the window of the first counter, the coincidence method was applied only for lines of energy greater than 300 keV. For lower energy lines the first counter was used separately.

Fig. 4 shows the low energy part of the conversion electron spectrum of Kr^{79} obtained with the intermediate image spectrometer. The Auger lines and the K_1, L_1, K_2 and L_2 lines were measured only in this spectrometer. Figs 5 and 6 show the electron lines measured in the double focusing spectrometer. The resolving power was generally 0.2 %. Some weak lines were measured with lower resolution, as indicated in the figures.

The decay of the K electron lines was followed for about four half-lives. No significant deviations from the 35 hr period were found.

The energy data of all the lines are collected in Table I. The interpretations given in column 3 are justified mainly by the good internal consistency of the γ-energy values obtained from the K and L lines respectively (cf. column 4). For most γ-rays the $K/(L+M)$ ratio is estimated. In four cases (γ-rays 4, 10, 13, and 15) the $(L+M)$-lines were too weak for measurement. In the case of γ_{11}, the $(L+M)$-line is not resolved from the K_{12} line. This fact will not seriously affect the estimated $K/(L+M)$ ratio of γ_{12}, even if the ratio $K/(L+M)_{11}$ would be abnormally low, since the intensity of the K_{11} line is only ~ 20 % of the K_{12} line. In the last column of Table I are given rough values of relative line intensities. They are obtained by comparing the areas under the lines measured in the two spectrometers.

The $K/(L+M)$ ratio of the 84.0 keV γ-ray is regarded as uncertain, for the following reason. In two different measurements we find the center of the $(L+M)$-line to lie at an energy which is 1.4 keV too low in one case and 1.7 keV too low in the other. The $(L+M)$-line also appears somewhat broadened. Therefore we cannot exclude

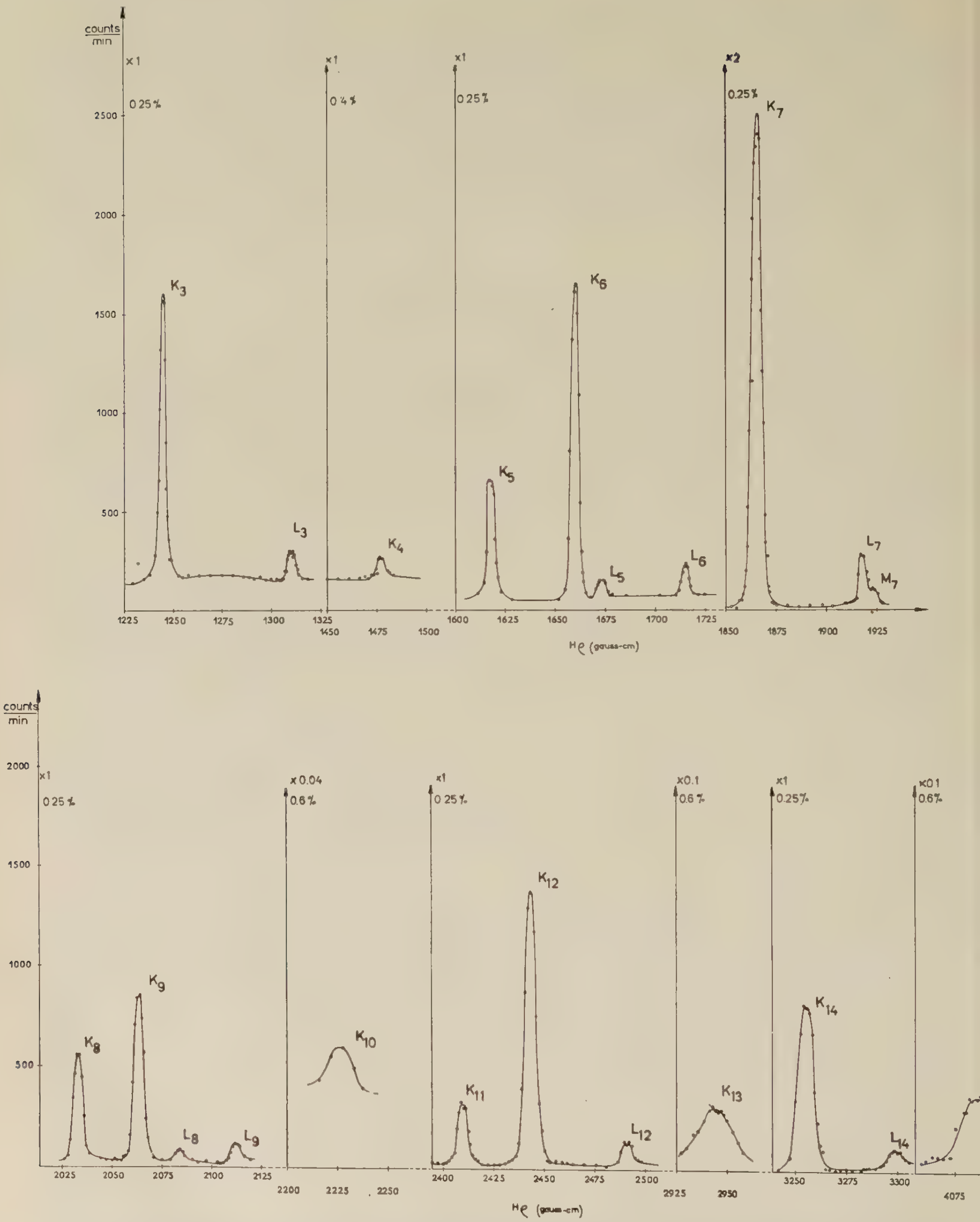

Fig. 5 and 6. Internal conversion spectrum of Kr^{79}, measured in the double focusing spectrometer. The resolution values and scale factors given at the top of the vertical lines apply to the regions to the right of the lines.

the possibility that this conversion line is a superposition of the $(L + M)$-line of the 84 keV γ-ray and another conversion line. This superposed line would then probably be a K-line. If it were an $(L + M)$-line we would have been able to detect the corresponding K-line.

Table I

γ-ray	Electron energy keV	Interpretation	γ-ray energy keV	Final γ-ray energy keV	$K/(L+M)$ ratio	Estimated intensity of K electron lines
0	9.6±0.4 11.1±1	KLL KLM				16 200
1	31.2 43.1	K_1 L_1	44.5±0.4 44.6±0.5	44.5±0.4	7.2	100
2	70.5 80.6	K_2 L_2	84.0±0.6 82.3	84.0±0.6	5 ?	4
3	122.6 134.5	K_3 L_3	136.1±0.2 136.2±0.3	136.1±0.2	8.6	15
4	167.0	K_4	180.5±0.4	180.5±0.4		1
5	195.1 206.9	K_5 L_5	208.6±0.3 208.6±0.5	208.6±0.3	6.9	6
6	203.8 215.5	K_6 L_6	217.3±0.2 217.2±0.4	217.3±0.2	10.6	17
7	247.8 259.6	K_7 L_7	261.3±0.2 261.3±0.3	261.3±0.2	8.0	51
8	286.3 298.1	K_8 L_8	299.8±0.2 299.8±0.3	299.8±0.2	10.8	6
9	293.4 304.9	K_9 L_9	306.9±0.2 306.6±0.5	306.9±0.2	9.4	9
10	332.0	K_{10}	345.5±0.8	345.5±0.8		0.2
11	375.7	K_{11}	389.2±0.4	389.2±0.4		3
12	384.2 396.2	K_{12} L_{12}	397.7±0.4 397.9±0.5	397.7±0.4	10.1	15
13	512.7	K_{13}	525.9±0.6	525.9±0.6		0.3
14	592.9 605.0	K_{14} L_{14}	606.4±0.5 606.7±0.7	606.4±0.5	7.8	9
15	819.9	K_{15}	833.4±0.7	833.4±0.7		0.4

Coincidence measurements

Our study of the β-spectrum of Kr^{79} has shown that the decay of this isotope is complicated. It therefore seems at present very difficult to establish a unique decay scheme by means of coincidence measurements. However, some important information might be obtained, as for example whether the main β^+-transition goes to the ground state of Br^{79} or not. As mentioned before, three hypothetical possibilities for the final level of the 598 keV β^+-component have been proposed (1, 2, 4). Further-

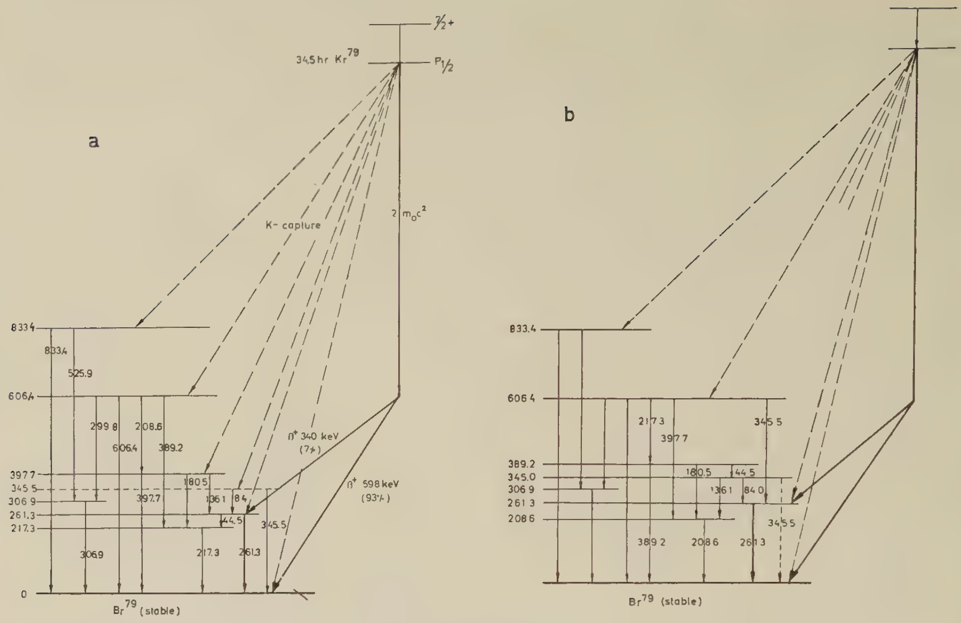

Fig. 7. Proposed alternative decay schemes of Kr^{79}. Energy values are given in keV.

more, the accurate determination of most γ-ray energies made it possible to construct only a few probable energy level diagrams (Cf. Fig. 7 and discussion on page 237). We also tried to check some other details of this scheme.

Our coincidence measurements were performed in the intermediate image β-spectrometer using a GM-counter for β-particle detection. A scintillation counter was mounted behind the sample, at a distance (~ 3.5 cm) where it was easy to arrange magnetic shielding for the photomultiplier. This arrangement is described in some detail in ref. (13). The resolving time of the coincidence circuit was $3 \cdot 10^{-7}$ sec.

$\beta^+\gamma$-coincidences were recorded between positrons of selected energies and γ-quanta of all energies. The coincidence rate as a function of positron energy showed a small coincidence effect only for positrons of energy lower than 300 keV. The coincidence rate for 350 keV positrons was less than 3 % of the effect to be expected if these positrons were in cascade with a γ-ray in the energy region round 200 keV. We therefore conclude that the 598 keV β^+-component goes to the ground state of Br^{79}.

$e^-\gamma$-coincidence measurements were performed by focusing a K-conversion line in the GM-counter and recording coincidences with γ-quanta of energy higher than a selected value. In this way the K-conversion lines of the 44.5 and 84.0 keV γ-rays were examined. No coincidences were found between either of these lines and any γ-ray of energy higher than 300 keV. This result is in accordance with the decay schemes of Fig. 7.

A more detailed study of $e^-\gamma$ and $\beta^+\gamma$-coincidences with an improved NaI crystal arrangement is in progress.

Decay scheme of Kr^{79}

The energy determination of most of the γ-rays is of an accuracy which makes it possible to construct only a few probable alternative decay schemes. Two of them are shown in Fig. 7. The internal energy consistency corresponds to the errors in the γ-energy determinations.

The position of the 84.0 and 345.5 keV γ-rays in the decay scheme of Fig. 7a is somewhat arbitrary. The corresponding level is therefore drawn with a broken line. A 345.1 keV γ-transition may also occur between the 606.4 and 261.3 keV levels. In the latter case the 84 keV γ-ray may feed any level in the decay scheme. The coincidence data are in accordance with both alternatives of Fig. 7.

According to our coincidence measurements the 598 keV β^+-transition leaves the Br^{79} nucleus in its ground state. This fact eliminates the tentative decay scheme of BERGSTRÖM (cf. Fig. 1a). The β^+ transition is of the allowed type (cf. p. 233) with a spin change of 0 or ± 1 and no parity change. As the ground state of Br^{79} is known to have the spin 3/2, the spin of the ground state of Kr^{79} would then be 1/2, 3/2 or 5/2. A comparison with nuclear shell theory predictions (14) gives the terms $p_{3/2}$ and $p_{1/2}$ for the ground states of Br^{79} and Kr^{79} respectively. This result makes the term scheme proposed by GOLDHABER and HILL impossible (cf. Fig. 1c). Their assignment of $p_{1/2}$ and $7/2+$ levels in Kr^{79} should be interchanged. In their paper these authors give a plot (Fig. 77, (4)) of energy differences between $7/2+$ and $p_{1/2}$ levels in various nuclei as a function of Z. The point corresponding to the $7/2+$ and $p_{1/2}$ level separation for Kr^{79} should be plotted with opposite sign as a consequence of the level interchange.

For the excited levels in Br^{79} no unique spin and parity assignments can be obtained at present. Unfortunately, the $K/(L+M)$ ratio of most γ-rays gives no unique indication as to the multipole character of the radiation, when compared with GOLDHABER and SUNYAR's semi-empirical curves (15). The extreme one-particle shell model (14) is apparently not valid for the excited levels of Br^{79}, since there are more levels than predicted by this model.

It may be of interest to compare the experimental ratio, C/β^+, of K-capture to positron emission, with that predicted by theory (16). Both the 598 and 325 keV β^+ transitions are of the allowed type. The corresponding theoretical C/β^+ ratios are respectively 8 and ~ 80. Thus the total C/β^+ ratio would be 13.4. Moreover, there is K-capture branching to energy levels in Br^{79} which are not reached by positron emission. Our experimental value for the total ratio C/β^+, $9{,}3 \pm 2$, is therefore to be compared with a theoretical value higher than 13.5. The discrepancy, if significant, may be partly explained by the assumption that our value for the intensity of the low energy β^+ component is too high.

It is to be noticed that the measurements on the long-lived Se^{79} fits in with the decay scheme alternatives of Fig. 7. This isotope decays to the ground state of Br^{79} by emission of β^--particles of energy ~ 150 keV (17). No γ-rays are found. This might be explained by the assumption that the first excited level in Br^{79} has an excitation energy higher than 150 keV, as is the case in the schemes of Fig. 7.

It is a great pleasure for one of the authors (J. MOREAU) to express his sincere thanks to Professor MANNE SIEGBAHN for the hospitality he has received at the Nobel Institute of Physics, and also to thank all the members of this institute for helping him in every possible way.

Nobel Institute of Physcis, Stockholm 50, Sweden.

REFERENCES

1. I. Bergström, Ark. f. fysik. *5*, nr 14, 191 (1952).
2. P. Radvanyi, Compt. Rend. *235*, 289 (1952).
3. ——Compt. Rend. *234*, 1275 (1952).
4. M. Goldhaber and R. D. Hill, Rev. Mod. Phys. *24*, 188 (1952).
5. H. Atterling and G. Lindström, Nature *169*, 432 (1952).
6. S. Thulin, Ark. f. fysik. 4, 363, (1952).
7. H. Slätis and K. Siegbahn, Ark. f. Fysik. *1*, 339 (1949).
8. I. Bergström and S. Thulin, Phys. Rev. *79*, 537 (1950).
9. NBS. AMS 13 (1952).
10. E. H. S. Burhop, The Auger Effect, Cambridge University Press, p. 48 (1952).
11. S. A. Moszkowski, Phys. Rev. *82*, 35 (1951).
12. A. Hedgran, Ark. f. Fyik. *5*, 1 (1952).
13. J. Moreau, Ark. f. fysik (in press).
14. M. G. Mayer, Phys. Rev. *75*, 1969 (1949), O. Haxel, J. H. D. Jensen and H. E. Suess, Phys. Rev. *75*, 1766 (1949).
15. M. Goldhaber and A. W. Sunyar, Phys. Rev. *83*, 906 (1951).
16. E. Feenberg and G. Trigg, Rev. Mod. Phys. *22*, 399 (1950).
17. J. M. Hollander, I. Perlman, and G. T. Seaborg, Rev. Mod. Phys. *25*, 469 (1953).

Tryckt den 25 augusti 1954

Uppsala 1954. Almqvist & Wiksells Boktryckeri AB

ARKIV FÖR FYSIK Band 8 nr 24

Communicated 10 February 1954 by OSKAR KLEIN

Ionic and covalent contributions to the hydrogen bond. Part I

By C. A. COULSON* and U. DANIELSSON**

With 2 figures in the text

1. Introduction

Previous calculations of the energy of the hydrogen bond, particularly as it occurs in the O–H ... O case of ice and water, have almost entirely treated the problem as if it were electrostatic. The fact that a satisfactory heat of sublimation of ice can be obtained if we replace each H_2O molecule by a plausible set of positive and negative electric charges at appropriate places in the molecule, has tended to confirm this picture. So also has the almost unchanged OH valence vibration frequency and internuclear distance between steam and ice. Our object in these two papers is to test the validity of this model, and, in particular, to discover whether or not there is any significant degree of covalent binding in the O–H ... O region.

It is well known that the O ... O distance in such bonds is not always the same. There are both long (2.8 Å) and short (2.5 Å) bonds, as well as intermediate values. Since the O–H distance is practically constant in all these, it follows that there are substantial changes in the H ... O distance, which must vary between about 1.5 and 1.8 Å. It would not be surprising if the short H ... O bond, which is only 0.5 Å longer than a normal O–H distance, were rather more covalent than the long one. We shall show that this is the case.

A further problem which is of interest is to estimate how the degree of covalent bonding in the H ... O region varies when the proton is moved to different points along the O ... O direction. We shall suppose throughout this calculation that the three atoms lie on a straight line, and we shall discuss the variation in the covalent and ionic contributions as the H atom moves along this line.

A complete discussion of the hydrogen bond as it occurs in ice, is clearly impossible. Severe approximations must be made. One of the most drastic of those which we make is to deal only with a single $\diagdown$O–H ... O$\langle$ system. Even if this is not directly applicable to ice, it should provide a first approximation to that situation, and it does occur frequently in the association of alcohols and acids and in organic crystals.

---

* Mathematical Institute, Oxford.

** Swedish Cement and Concrete Research Institute, Stockholm.

In paper I we use two distinct assumptions in order to make our calculations. Essentially they both involve the inferences that we feel entitled to make from the actual internuclear distances in O–H and H . . . O. Neither of the assumptions which we use is likely to be exactly correct, though one of them has been found useful [1] in the theory of metals and alloys. The other assumption is, at least, plausible, and we shall see that the agreement between the two sets of conclusions, while far from perfect, is adequate to justify us in coming to fairly definite conclusions about ionic and covalent contributions.

In paper II we fall back on the well-developed technique of covalent-ionic resonance, recently summarised by WARHURST [2]. To make the necessary calculations the discussion now has to be much more intimate, and the detailed analytical form of the various wave functions used has to be specified. Where these are not known, they can be estimated. The agreement of our final values here with those of paper I is satisfactory.

2. Model

We regard the $\diagdown\text{O–H} \ldots \text{O}\langle$ system as represented by a resonance hybrid of (I), (II) and (III) below,

(I) $\qquad \diagdown\text{O–H}\quad \text{O}\langle\ \psi_1$

(II) $\qquad \diagdown\overset{-}{\text{O}}\ \overset{+}{\text{H}}\quad \text{O}\langle\ \psi_2$

(III) $\qquad \diagdown\overset{-}{\text{O}}\ \text{H—}\overset{+}{\text{O}}\langle\ \psi_3.$

Thus the wave function for the system is of the form

$$\psi = C_1\psi_1 + C_2\psi_2 + C_3\psi_3. \tag{1}$$

We define the weights of these three component structures by the relation

$$\omega_1 : \omega_2 : \omega_3 = C_1^2 : C_2^2 : C_3^2, \tag{2}$$

and

$$\omega_1 + \omega_2 + \omega_3 = 100. \tag{3}$$

Structure (I) is a result of a purely covalent pairing of an oxygen orbital and a hydrogen orbital. (II) is the corresponding ionic structure, and (III) is the result of a covalent bond across the long H . . . O distance. This means that we are particularly interested in the weight ω_3. The definition of the weights ω_ν in (2) shows that we are neglecting the transitional structures recently introduced by SYRKIN and DYATKINA [3]. Our chief reason for leaving these out is that their inclusion considerably complicates the situation and destroys its simple pictorial character. Since the assumptions and approximations which we are compelled to make are so numerous, it follows that our final accuracy cannot be very great. All that we can hope to do, therefore, is to determine whether or not the covalent structure (III) is significant, and to estimate its approximate weight. The introduction of transitional structures would not be justified by any corresponding gain in accuracy.

We shall use $L_1 + L_2$ to represent the O ... O distance, and L_1, L_2 for the $\diagdown$O–H and H ... O$\langle$ bond lengths respectively.

In order to get the weights ω_1, ω_2 and ω_3 we require two relations in addition to (3). We shall call these the dipole-moment and bond-length relations, since these are the quantities which we use.

The dipole-moment relation is found at once if we suppose that the ratio of the weights of structures (I) and (II) is the same as it is in a free steam molecule, and is determined in such a way as to give the experimental dipole moment (1.87 D). More precisely we suppose that the dipole moment of (I) is zero, and of (II) is $e L_1$, the direction of this moment being along the line of the bond. If μ_{steam} is the dipole moment of a steam molecule, and if θ is the bond angle, and if we take L_1 to be effectively the same in steam as in the hydrogen bond, this gives

$$\frac{\omega_2}{\omega_1 + \omega_2} \cdot 2 e L_1 \cdot \cos \frac{1}{2} \theta = \mu_{\text{steam}} . \tag{4}$$

The angle θ is slightly different in steam from the tetrahedral value appropriate to ice. But the alteration is unimportant for the purposes of (4), where we shall take $\theta = 105°$.

One comment is necessary on the validity of this dipole-moment relation. As COULSON [4] and POPLE [5] have shown, the oxygen orbital which is used to form the electron-pair bond in (I) is almost certainly a hybrid of $2s$ and $2p$, so that the so-called covalent structure does in fact possess a dipole moment. Notwithstanding this objection we believe, as WARHURST [2] has claimed, that this type of analysis will give its best results when it is not scrutinised too closely regarding the detailed form of the orbitals used. In fact, there is a real sense in which equation (4) may be regarded as a simple statement that the ionic character of the O–H bond is not greatly altered as a result of hydrogen bond formation. Infra-red data suggests that the dipole moment is not changing very rapidly as the O–H bond length alters slightly from its equilibrium value; for that reason we accept the validity of (4) even when L_1 is not the equilibrium bond length. Such a situation arises when the H atom is moved along the O ... O line.

We must now discuss the second relation between the weights ω_1, ω_2 and ω_3. This is what we have previously called the bond-length relation. We have chosen two distinct forms for this relation. Let us call them relation A and relation B.

Relation A uses the formula connecting atomic radius R in a bond and the bond order p, which was introduced by PAULING [1] and which has the form

$$R(p) = R(1) - C \log_e p. \tag{5}$$

C is a constant assumed to be equal for all the elements. If suffixes O and H refer to oxygen and hydrogen respectively, then

$$L(p) = R_{\mathrm{O}}(p) + R_{\mathrm{H}}(p)$$

$$L(1) = R_{\mathrm{O}}(1) + R_{\mathrm{H}}(1),$$

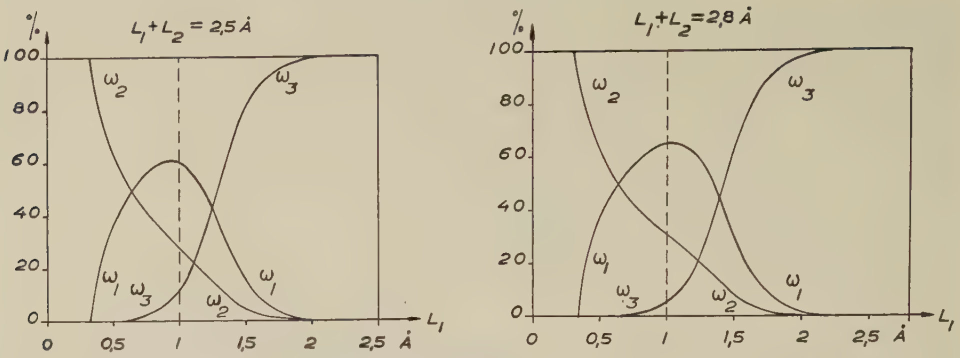

Fig. 1. The weights ω_1, ω_2 and ω_3 as functions of the O–H distance calculated with use of relation A.

so that

$$L(p) = L(1) - 2C \log_e p. \tag{6}$$

We assume that this formula is valid both for the short bond in structure (I) and the long bond in structure (III). This assumption enables us to obtain bond orders p_1 and p_2 for the O–H and H ... O bonds. Then, if we use the relation

$$\frac{\omega_1}{\omega_3} = \frac{p_1}{p_2},$$

which expresses the fact that the weights of the structures (I) and (III) are proportional to the appropriate bond orders, it follows that

$$\frac{\omega_1}{\omega_3} = e^{-(L_1-L_2)/2C}. \tag{7}$$

The numerical value of C is found by applying (5) to the carbon–carbon bonds in diamond ($R = 0.771$ Å), ethylene ($R = 0.670$ Å) and acetylene ($R = 0.602$ Å). (The ethylene value, about which some uncertainty still persists, is discussed more fully by COULSON, DAUDEL and ROBERTSON [6].) The best fit for these three cases is obtained when $2C = 0.2995$ Å, though we have verified that if Thompson's value for ethylene (0.665 Å) is used, no appreciable alterations are caused in ω_1, ω_2 and ω_3. Equations (3), (4) and (7) now provide sufficient information to determine the weights for any assumed values of L_1 and L_2. Fig. 1 shows the way in which ω_1, ω_2 and ω_3 vary as H moves, for the short and long hydrogen bonds where $L_1 + L_2 = 2.5$ Å and 2.8 Å, respectively. In this figure the equilibrium position of the H atom is marked by a dotted vertical line. The corresponding weights are given in Table 1. Before discussing these results, however, we must outline relation B, which replaces (7) and enables an independent estimate of the weights to be made.

Here we assume that the energy of a covalent bond as a function of the distance between the bonded atoms may be described by a Morse function

$$E(L) = D\left\{e^{-2a(L-L_e)} - 2e^{-a(L-L_e)}\right\}, \tag{8}$$

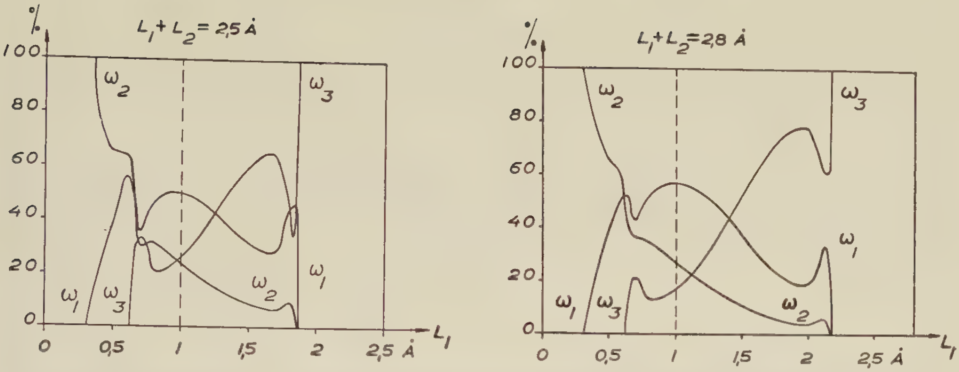

Fig. 2. The weights ω_1, ω_2 and ω_3 as functions of the O–H distance calculated with use of relation B.

Table 1. The weights ω_1, ω_2 and ω_3 at the equilibrium position of the hydrogen atom calculated with use of relation A.

	$L_1+L_2=2.5$ Å	$L_1+L_2=2.8$ Å
ω_1	60.3 %	64.9 %
ω_2	28.4 "	30.6 "
ω_3	11.3 "	4.5 "

where D is the bond energy and a is some constant. If, now, it is further assumed that the weights ω_1 and ω_3 are proportional to the corresponding bond energies, and that the same Morse function (8) can be used for both structures in spite of the fact that in (III) the bonded oxygen is a positive ion, then the required relation is

$$\frac{\omega_1}{\omega_3} = \frac{E(L_1)}{E(L_2)}. \tag{9}$$

It is practically certain that this method will exaggerate the importance of (III). If this is so, it may be regarded as providing an upper limit to ω_3. Fig. 2 shows the corresponding variation of ω_1, ω_2 and ω_3, for the short and long hydrogen bonds, as in Fig. 1. Table 2 gives the weights at the equilibrium configuration.

Table 2. The weights ω_1, ω_2 and ω_3 at the equilibrium position of the hydrogen atom calculated with use of relation B.

	$L_1+L_2=2.5$ Å	$L_1+L_2=2.8$ Å
ω_1	50.2 %	56.8 %
ω_2	23.6 "	26.7 "
ω_3	26.2 "	16.5 "

3. Discussion

There is a fairly good agreement from this work that in the equilibrium configuration the long bond is essentially electrostatic, the covalent contribution $\diagdown\overset{-}{\mathrm{O}}\ \mathrm{H}{-}\overset{+}{\mathrm{O}}\!<$ amounting only to a few percent. This is in excellent agreement with some work of Pauling [7], who suggested weights ω_1, ω_2 and ω_3 equal respectively to 65, 33 and 2 %. Our work suggests, however, that as the H atom moves toward the far oxygen atom an increasing covalency appears. With the short hydrogen bond this covalency is beginning to be appreciable, even in the equilibrium configuration. It seems probable that a purely electrostatic model for this situation would be hardly fair. In particular if, as in ice, the charge displacements associated with $\mathrm{H} \ldots \overset{+}{\mathrm{O}}$ covalency may be "relayed" cooperatively to adjacent bonds, it becomes entirely plausible that such covalency should be more important. If it is, we may begin to understand the mechanism which permits the migration of hydrogen atoms in organic crystals such as those of the purines and pyrimidines. It does not seem possible to be more explicit than this until more detailed calculations have been made of this cooperative migration.

REFERENCES

1. Pauling, L., J. Amer. Chem. Soc. *69*, 542 (1947).
2. Warhurst, E., Proc. Roy. Soc. A, *207*, 32 (1951).
3. Syrkin, Y. K., and Dyatkina, M. E., Structure of Molecules and the Chemical Bond, London 1950, Chapter 10.
4. Coulson, C. A., Proc. Roy. Soc. A, *207*, 63 (1951).
5. Pople, J. A., Proc. Roy. Soc. A, *202*, 323 (1950); *205*, 163 (1951).
6. Coulson, C. A., Daudel, R., and Robertson, J. M., Proc. Roy. Soc. A, *207*, 306 (1951).
7. Pauling, L., J. Chim. phys. *46*, 435 (1949).

Tryckt den 25 augusti 1954

Uppsala 1954. Almqvist & Wiksells Boktryckeri AB

ARKIV FÖR FYSIK Band 8 nr 25

Communicated 10 February 1954 by Oskar Klein

Ionic and covalent contributions to the hydrogen bond. Part II

By C. A. Coulson* and U. Danielsson**

With 4 figures in the text

1. Introduction

In this part we continue our study of the O–H ... O system, using the three structures (I), (II) and (III) of Part I, but attempting a semi-wave-mechanical treatment in order to estimate the weights ω_1, ω_2 and ω_3 with which they occur in the resonance wave function. Our method is essentially a development of that used so successfully by Warhurst [1] for diatomic and certain symmetrical polyatomic molecules. We shall first describe the method and the results which it yields. Afterwards we shall comment on the reliability and significance of these values.

2. Method

We seek for a wave function to represent the system O–H ... O. Even neglecting the other groups bonded to the oxygen atoms, there are 17 electrons here. We are obviously obliged to simplify our problem, and must do so fairly drastically. We therefore restrict ourselves to the 4 electrons which are involved in the bond formation. In the covalent structure (I), two of these electrons comprise the O–H bond, covalently paired together, and the other two are non-bonding electrons on the second oxygen atom. In (II) both of the first pair of electrons are on the first oxygen atom, and the second pair are still on the other oxygen. In (III) the second pair are covalently paired to form the H–O bond.

(I) $$\diagdown O_A{-}H \quad O_B\langle \quad \psi_1$$

(II) $$\diagdown \overset{-}{O}_A \quad \overset{+}{H} \quad O_B\langle \quad \psi_2$$

(III) $$\diagdown \overset{-}{O}_A \quad H{-\!-}\overset{+}{O}_B\langle \quad \psi_3.$$

---

* Mathematical Institute, Oxford.

** Swedish Cement and Concrete Research Institute, Stockholm.

The wave function for these four electrons takes the form

$$\psi = C_1 \psi_1 + C_2 \psi_2 + C_3 \psi_3, \tag{1}$$

where the wave functions for the component structures are

$$\begin{aligned}
\psi_1 &= N_1 [\mathrm{Det}\,\{A\,\bar{H}\,B\,\bar{B}\} - \mathrm{Det}\,\{\bar{A}\,H\,B\,\bar{B}\}] \\
\psi_2 &= N_2\,\mathrm{Det}\,\{A\,\bar{A}\,B\,\bar{B}\} \\
\psi_3 &= N_3 [\mathrm{Det}\,\{A\,\bar{A}\,H\,\bar{B}\} - \mathrm{Det}\,\{A\,\bar{A}\,\bar{H}\,B\}].
\end{aligned} \tag{2}$$

In these expressions the N's are normalising factors, A and B are oxygen atomic orbitals and H is a hydrogen atomic orbital. The notation Det stands for a determinant in which only the leading diagonal term is shown, and in which the arguments of the four functions are always in the sequence 1, 2, 3, 4. The bar denotes an orbital with negative spin. Its absence implies positive spin.

The appropriate values of the coefficients C_ν and the energy E follow in a familiar way from the secular equations. The secular determinant for the energy may be be written

$$\begin{vmatrix}
\mathrm{H}_{11} - E & \mathrm{H}_{12} - E\,\Delta_{12} & \mathrm{H}_{13} - E\,\Delta_{13} \\
\mathrm{H}_{21} - E\,\Delta_{21} & \mathrm{H}_{22} - E & \mathrm{H}_{23} - E\,\Delta_{23} \\
\mathrm{H}_{31} - E\,\Delta_{31} & \mathrm{H}_{32} - E\,\Delta_{32} & \mathrm{H}_{33} - E
\end{vmatrix} = 0, \tag{3}$$

where

$$\begin{aligned}
\mathrm{H}_{\mu\nu} &= \int \psi_\mu^* \,\mathrm{H}\, \psi_\nu \, d\tau \\
\Delta_{\mu\nu} &= \int \psi_\mu^* \psi_\nu \, d\tau,
\end{aligned} \tag{4}$$

and H is the Hamiltonian for the four electrons. The normalising condition requires that

$$\sum_{\mu\nu} C_\mu C_\nu \Delta_{\mu\nu} = 1, \tag{5}$$

and the weights of the three structures are defined by

$$\omega_\mu = 100 \frac{C_\mu^2}{C_1^2 + C_2^2 + C_3^2}. \tag{6}$$

Just as in Part I, we have neglected all transitional structures. Our plan is to estimate values for the $\mathrm{H}_{\mu\nu}$ and $\Delta_{\mu\nu}$, and hence to derive the coefficients C_μ and the weights ω_μ.

It is quite straightforward to calculate the N's. They are given by

$$\begin{aligned}
N_1^{-2} &= 2 \cdot 4! \cdot (1 + S_1^2 - S_2^2), \\
N_2^{-2} &= 4!, \\
N_3^{-2} &= 2 \cdot 4! \cdot (1 - S_1^2 + S_2^2),
\end{aligned} \tag{7}$$

where

$$S_1 = \int A\, H\, d\tau, \qquad S_2 = \int H\, B\, d\tau, \tag{8}$$

and we have arbitrarily neglected $S_3 = \int A\, B\, d\tau$. Our justification for this neglect is that for $L = 2.8$ Å, and p-orbitals on the oxygen nuclei, $S_3 = 0.010$; for tetrahedral hybrids instead of p-orbitals, $S_3 = 0.014$. When $L = 2.5$ Å the corresponding values are 0.023 and 0.034. Since every S always occurs multiplied either by itself or some other function of the same order of magnitude, the neglect of S_3 is justified.

The $\Delta_{\mu\nu}$ follow from (4) and (7). They are

$$\begin{aligned}
\Delta_{12} &= \sqrt{\frac{2}{1 + S_1^2 - S_2^2}} \cdot S_1, \\
\Delta_{23} &= \sqrt{\frac{2}{1 - S_1^2 + S_2^2}} \cdot S_2, \\
\Delta_{13} &= \Delta_{12}\, \Delta_{23}.
\end{aligned} \tag{9}$$

The only other quantities which occur in (3) are the $\mathrm{H}_{\mu\nu}$. These may be expressed quite simply in terms of matrix elements of H with respect to individual elements of the determinants (2) rather than, as in their definition, with respect to the determinants themselves. In writing down the appropriate formulae (10) we have neglected exchange between the oxygen orbitals A and B. This is justified on the same grounds as the neglect of S_3.

$$\begin{aligned}
\mathrm{H}_{11} &= \frac{(A\,H\,B\,B\,|\mathrm{H}|\,A\,H\,B\,B) + (A\,H\,B\,B\,|\mathrm{H}|\,H\,A\,B\,B) - (A\,H\,B\,B\,|\mathrm{H}|\,A\,B\,B\,H)}{1 + S_1^2 - S_2^2} \\
\mathrm{H}_{22} &= (A\,A\,B\,B\,|\mathrm{H}|\,A\,A\,B\,B) \\
\mathrm{H}_{33} &= \frac{(A\,A\,H\,B\,|\mathrm{H}|\,A\,A\,H\,B) - (A\,A\,H\,B\,|\mathrm{H}|\,A\,H\,A\,B) + (A\,A\,H\,B\,|\mathrm{H}|\,A\,A\,B\,H)}{1 - S_1^2 + S_2^2} \\
\mathrm{H}_{12} &= \sqrt{\frac{2}{1 + S_1^2 - S_2^2}}\,(A\,H\,B\,B\,|\mathrm{H}|\,A\,A\,B\,B) \\
\mathrm{H}_{23} &= \sqrt{\frac{2}{1 - S_1^2 + S_2^2}}\,(A\,A\,B\,B\,|\mathrm{H}|\,A\,A\,B\,H) \\
\mathrm{H}_{13} &= \sqrt{\frac{2}{1 - (S_1^2 - S_2^2)^2}}\,(A\,H\,B\,B\,|\mathrm{H}|\,A\,A\,H\,B)
\end{aligned} \tag{10}$$

The notation $(A\,H\,B\,B\,|\mathrm{H}|\,A\,H\,B\,B)$ denotes the integral

$$\int A^*(1)\, H^*(2)\, B^*(3)\, B^*(4)\, \mathrm{H}\, A(1)\, H(2)\, B(3)\, B(4)\, d\tau^4,$$

and similarly for the other elements.

3. Choice of orbitals

Further progress is not possible until we specify the atomic orbitals being used. For hydrogen we use the isolated atom orbital

$$H = \psi_H(1s) = \frac{e^{-r}}{\sqrt{\pi}} \tag{11}$$

using atomic units of length, mass and charge. For the oxygen orbitals the choice is more difficult. The orbitals with which we are concerned belong to the L-shell, but they may be hybrids of s and p ranging from pure p to tetrahedral sp^3. According to COULSON [2] and POPLE [3] they are more likely to resemble the latter than the former. In view of this uncertainty, we have made our numerical calculations for both cases. Thus, choosing familiar Slater functions, we have

$$\begin{aligned} A = \psi_A\,(\text{hybrid}) &= \cos\beta \cdot \psi(2s) + \sin\beta \cdot \psi(2p) = \\ &= \sqrt{\frac{c^3}{3\pi}} \cdot r_A\, e^{-c r_A} \{\cos\beta + \sqrt{3} \cdot \sin\beta \cos\theta_A\}, \end{aligned} \tag{12}$$

where r_A, θ_A are polar coordinates (see Fig. 1), c is a constant related to the effective nuclear charge at the oxygen nuclei, and supposed to have the same value 2.275 a.u.$^{-1}$ for A and B. This value is strictly correct according to Slater's prescriptions for a neutral oxygen atom, as in ψ_1. A different value (strictly, two different values) would be required in ψ_2 and ψ_3. Since ψ_1 predominates, we have felt it justifiable to maintain this one value of c throughout. Changing c would add very considerably to the calculations, and would be unlikely to affect the weights ω_ν in any really significant manner. The parameter β in (12) determines the hybridisation. Pure p-orbitals correspond to $\beta = \frac{\pi}{2}$, tetrahedral hybrids to $\beta = \frac{\pi}{3}$.

Values of S which result from this choice of orbital are found from the tables of MULLIKEN, RIEKE, ORLOFF and ORLOFF [4]. They were made for three different O…O distances, viz. $L = 2.80$ Å (the long bond), $L = 2.50$ Å (the short bond), and $L = 2.65$ Å. In each case three different positions of the proton have been considered, in which $L_1 = 0.8$, 1.0 and 1.2 Å, so that the effect of motion of the proton along the line of centres could be studied. The $\Delta_{\mu\nu}$ follow immediately from the S integrals, according to (9).

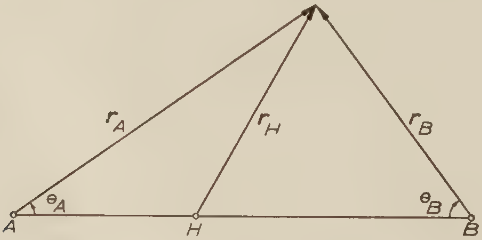

Fig. 1. The polar coordinates used in the atomic wave functions.

4. The integrals $H_{\mu\mu}$

With the explicit expressions (11) and (12) for the atomic orbitals it becomes possible in principle to evaluate all the integrals $H_{\mu\nu}$. Such an evaluation is very tedious, and it seems to us in keeping with the spirit of this type of calculation that we should use other distinct experimental information to estimate them. In this respect the diagonal terms $H_{\mu\mu}$ are easier than the off-diagonal terms $H_{\mu\nu}$. The integral $H_{\mu\mu}$ is the energy for the pure state ψ_μ. We estimate these energies as follows: H_{11} is obtained by using Pauling's geometrical mean formula for the energies of pure covalent bonds. This value of H_{11} refers to the equilibrium covalent distance. Other distances are covered by a Morse function, so that

$$H_{11} = D_{\text{G.M.}} \{e^{-2a(L_1-L_e)} - 2e^{-a(L_1-L_e)}\}, \tag{13}$$

where

$$D_{\text{G.M.}} = \sqrt{D\,(O\text{–}O) \cdot D\,(H\text{–}H)} = 60.07 \text{ kcal. mole}^{-1},$$

and where a and L_e may be taken to be the same as for a real O–H bond; so $a = 2.23$ Å^{-1} and $L_e = 0.97$ Å. The values for an ideal covalent O–H bond will almost certainly differ slightly from these. But this would scarcely affect our final conclusions.

For ψ_2 the energy H_{22} is determined from (a) the energy needed to remove an electron from atom H to atom A, (b) the electrostatic attraction between H^+ and A^-, and (c) a Born repulsion term. Thus

$$H_{22} = I_H - E_A - \frac{e^2}{L_1} + b\,e^{-\frac{L_1}{\varrho}}. \tag{14}$$

The polarization of B in the field of A and H^+ ought to be taken into account. Choosing a reasonable value for the polarizability, this appears to be a small quantity, and so, in view of the difficulty of knowing just which polarizability we ought to choose, we have neglected it completely. The value of ϱ is chosen as 0.4 Å, which figure Warhurst [5] finds to give good results in the case of the hydrogen halides. The energy b is given the value $b = 346.8$ kcal. mole^{-1}. This is chosen to make H_{22} a minimum for $L_1 = 1.76$ Å, the univalent ionic radius for oxygen. $I_H = 312.0$ kcal. mole^{-1}, and $E_A = 50.7$ kcal mole^{-1}, according to a paper by Mulliken [6]. This is the valence state affinity, and we have used it for pure p and for sp^3 hybrids, even though, according to Moffitt [7], a variation in E_A would be expected.

For ψ_3 the energy H_{33} is estimated by taking into account (a) the electrostatic attraction between A and B^+, (b) the covalent binding energy H–B^+, (c) the work required to transfer one electron from B to A and (d) the energy of polarization of the bond in the field of the ion A^-. Thus

$$H_{33} = -\frac{e^2}{L_1 + L_2} + D_{\text{G.M.}} \{e^{-2a(L_2-L_e)} - 2 \cdot e^{-a(L_2-L_e)}\} + I_B - E_A - \frac{1}{2} \cdot \frac{e^2\,\alpha_{\text{O-H}}}{\left(L_1 + \frac{L_2}{2}\right)^4}. \tag{15}$$

Just as in H_{22} the polarization of the lone pair on atom A in the field of the ion B^+ is neglected. For $D_{G.M.}$, a and L_e the same values are used as in H_{11}, even though the oxygen atom is now ionized. According to MULLIKEN [6] $I_B = 312.5$ kcal. mole ^{1}. The polarizability of bonds has been studied by DENBIGH [8] who gives an average polarizability for O–H equal to 0.681×10^{-24} cc. We require the longitudinal polarizability. This is unknown, but if we assume that the ratio of longitudinal to transverse polarizabilities is the same (1.31) as in H–C, we get $\alpha_{O-H} = 0.81 \times 10^{-24}$ cc. This is the value which we have used in our calculations.

5. The integrals $H_{\mu\nu}$

The integrals $H_{\mu\nu}$ are more difficult to estimate than are the $H_{\mu\mu}$, since they do not represent the energy of any single structure, but a coupling between two of them. On the other hand a knowledge of their values is important since the resonance energy depends more strongly on these terms than on any other. Our procedure has been to calculate H_{12} by the aid of experimental data, and estimate H_{13} and H_{23} by familiar methods.

H_{12} is calculated from properties of the bond O–H. For this bond only ψ_1 and ψ_2 occur in the wave function analogous to (1). If we suppose that H_{11} and H_{22} are unaffected by the removal of the atom B, then it follows that

$$H_{12} = \Delta_{12} E' - \sqrt{(H_{11} - E')(H_{22} - E')}, \tag{16}$$

where E' is the O–H bond energy. We put

$$E' = D\{e^{-2a(L_1 - L_e)} - 2e^{-a(L_1 - L_e)}\} \tag{17}$$

with

$$D = \text{dissociation energy} = 110.2 \text{ kcal. mole}^{-1}.$$

In this way H_{12} is found as a function of L_1.

For H_{13} and H_{23} no similar method is available. We have employed an approximation used earlier by several authors (e.g. MULLIKEN). We suppose that the ratios $H_{12} : H_{13} : H_{23}$ are independent of the zero from which energy is measured. This is equivalent to replacing the overlap charge distributions AH and HB by $S_1 AA$ and $S_2 BB$ respectively. We find, from (10)

$$\begin{aligned} H_{23} &= \sqrt{\frac{1 + S_1^2 - S_2^2}{1 - S_1^2 + S_2^2}} \cdot \frac{S_2}{S_1} \cdot H_{12} \\ H_{13} &= \sqrt{\frac{2}{1 - S_1^2 + S_2^2}} \cdot S_2 \cdot H_{12} . \end{aligned} \tag{18}$$

In this manner all the necessary terms are found.

6. Results

We are now in a position to solve the secular determinant (3). The values which are obtained are shown in Table 1 below.

Table 1. The energy E and the weights ω_1, ω_2 and ω_3 as functions of the O–H distance L_1.

	L_1+L_2 in Å	L_1 in Å	E in kcal. mole^{-1}	ω_1 in %	ω_2 in %	ω_3 in %
pure p-orbitals	2.50	0.8	− 91	87.8	10.4	1.8
		1.0	−120	83.1	13.0	3.9
		1.2	−107	81.3	12.8	5.9
	2.65	0.8	− 90	88.5	10.3	1.2
		1.0	−117	84.8	12.7	2.5
		1.2	−103	83.4	12.4	4.2
	2.80	0.8	− 88	89.1	10.2	0.7
		1.0	−114	85.8	12.5	1.7
		1.2	−100	85.3	11.9	2.8
sp^3 tetrahedral orbitals	2.50	0.8	− 94	86.5	10.1	3.4
		1.0	−125	81.6	12.3	6.1
		1.2	−112	80.0	12.0	8.0
	2.65	0.8	− 92	87.6	10.1	2.3
		1.0	−120	83.5	12.3	4.2
		1.2	−107	82.2	11.8	6.0
	2.80	0.8	− 90	88.5	10.1	1.4
		1.0	−117	84.9	12.2	2.9
		1.2	−103	84.2	11.6	4.2

The main conclusions to which this table leads are:

(a) the weight ω_3 varies with position of the H atom (L_1) and with O...O distance (L_1+L_2) in a manner extremely similar to that found in Part I, but its absolute value is rather smaller, of the order of one half. This is interesting because, despite all the assumptions made, it does confirm the general picture of Part I.

(b) the use of tetrahedral hybrids instead of pure p-orbitals for the oxygen bonding orbitals increases the weight ω_3 by a factor between 1.5 and 2. This is obviously related to the greater overlapping power of hybrids.

(c) for any chosen $L\,(=L_1+L_2)$ there is a certain position of the proton (value of L_1) for which the energy is least. We have called this L_{1e}. It is shown in Table 2. This table also shows the length $L_{1e}-L_e$, where L_e is the normal O–H equilibrium length. $L_{1e}-L_e$ is the increase in O–H distance as a result of hydrogen bonding. These increases are almost independent of the choice of atomic orbital on the oxygen atom, and are of the same order of magnitude as the distances calculated on electrostatic grounds by Verwey [9] and found experimentally by Ubbelohde [10]. The equilibrium O–H distance (0.983 Å, for p-bonds, 0.986 Å, for tetrahedral ones) for the long bond $L_1+L_2=2.8$ Å agrees excellently with the experimental value 0.986 Å [11]. Table 2 also shows the minimum energy for each of the three O...O distances, and after subtracting the energy of an O–H bond, the dissociation energy D

Table 2. The stretch of the O–H distance, the dissociation energy D and the weights ω_1, ω_2 and ω_3 for the hydrogen bond at the equilibrium position of the hydrogen atom.

	$L_1 + L_2$ in Å	L_{1e} in Å	$L_{1e} - L_e$ in Å	E in kcal. mole^{-1}	D in kcal. mole^{-1}	ω_1 in %	ω_2 in %	ω_3 in %
pure p-orbitals	2.50	0.994	0.024	−120.0	9.8	83.2	12.9	3.9
	2.65	0.988	0.018	−116.6	6.4	85.0	12.6	2.4
	2.80	0.983	0.013	−114.6	4.4	86.1	12.3	1.6
sp^3 tetrahedral hybrids	2.50	0.997	0.027	−124.6	14.4	81.7	12.2	6.1
	2.65	0.992	0.022	−120.2	10.0	83.7	12.2	4.1
	2.80	0.986	0.016	−117.0	6.8	85.2	12.0	2.8

of the hydrogen bond. It is clear that this energy increases rapidly as the O…O distance is decreased. Fig. 2 shows this variation, together with the experimental energies of the hydrogen bond for ice, alcohol and formic acid. These are taken from PAULING's book, *The Nature of the Chemical Bond.* It is surprising how closely these points lie on our theoretical curves. Finally Table 2 shows the equilibrium values of the weights ω_ν. It is clear that the energy curves which we have obtained for the motion of the proton could be used to discuss the change in O–H vibration frequency on association. There is no need to do this calculation because we have shown that the bonding is essentially electrostatic, and therefore any other conclusions which depend on this fact must follow automatically. Such calculations, based on an electrostatic model, have been made by COGGESHALL [12], by BAUER and MAGAT [13] and by VERWEY [9] and are in agreement with experiment in this respect.

One single example of this may be given. COGGESHALL writes down an expression for the energy of the O–H…O system by using a Morse function for the O–H bond, and then superposes an electrostatic energy term $q E_p (L_1 - L_e)$ in our notation, where q is the net charge on the H atom and E_p is the electrostatic field at the H atom due chiefly to the non-bonded oxygen neighbours. He shows that the presence of this extra term provides an explanation of the change in valence vibration frequency on association, and also an increase in the extinction coefficient. But it may also be shown to result in an increase in the O–H bond length. For if the Morse potential is

$$D\left\{e^{-2a(L_1-L_e)} - 2e^{-a(L_1-L_e)}\right\}$$

as in equation (17), then the equilibrium value of L_1 in association is given by the stationary value of the sum of the Morse energy and the electrostatic energy term. It is easy to show that this occurs when L_1 has the value L_{1e}, where in the first approximation,

$$L_{1e} - L_e \simeq \frac{q E_p}{2 D a^2}. \qquad (19)$$

If we substitute the numerical values of q and E_p used by COGGESHALL it follows that, when O…O equals 2.70 Å,

$$L_{1e} - L_e = 0.013 \text{ Å}.$$

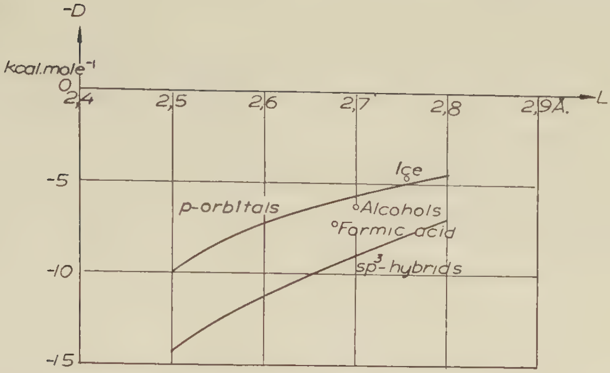

Fig. 2. The dissociation energy of the hydrogen bond as function of the O . . . O distance.

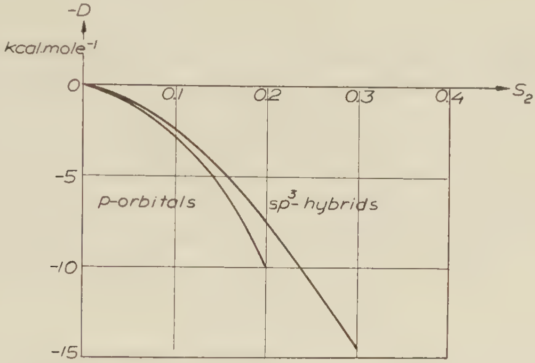

Fig. 3. The dissociation energy of the hydrogen bond versus the overlap integral S_2.

The agreement between this value and the two values 0.016 and 0.020 Å interpolated from column 4 of Table 2 shows that our theory leads to essentially the same conclusions as COGGESHALL's theory, and may be said to justify the model which he had to assume without proof on physical grounds.

Although the curves in Fig. 2 appear to fit so excellently with the observed energy, it is necessary to point out that there is a serious omission. For according to these curves (and the data in column 5 of Table 2), we should expect a resultant force tending to draw the two oxygen atoms closer and closer together. In reality this cannot be the case. Evidently we have left out all mention of a repulsive term which prevents the oxygens approaching too closely. This term is the repulsion between the lone-pair on atom B and the electrons of the O–H bond and should have been included in H_{11} and H_{22}. There is a similar term omitted from H_{33}. It is difficult to see how these terms could be estimated, and presumably, since they come into play rather suddenly when the relevant charge-clouds begin to overlap, their effect on the internuclear distances in equilibrium is not large. But this is a serious objection to our treatment.

It has recently been proposed [14, 15] that the dissociation energy of a bond between two atoms is approximately proportional to the overlap integral be-

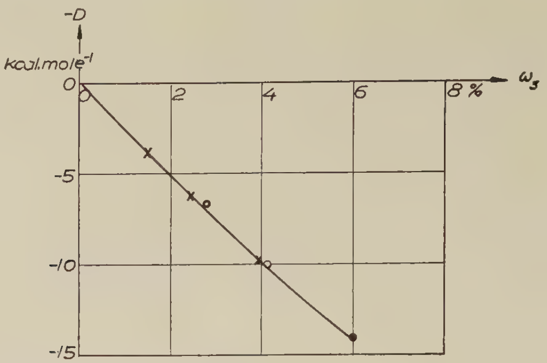

Fig. 4. The dissociation energy versus the weight ω_3.
× = p-orbitals, ○ = $s\,p^3$-hybrids.

tween the appropriate atomic orbitals. We should not expect such a simple relationship to hold for an essentially ionic type of binding as in our case; but it is interesting to notice, from Fig. 3, that a relation of this general kind still persists. It does not, however, appear to be linear, and it differs slightly according to the type of hybrid orbital used for the oxygen atom. It is worth mentioning that there appears to be a unique relationship, independent of hybrid type, between the energy of the hydrogen bond and the weight ω_3. This is shown in Fig. 4.

7. Conclusions

Before concluding we must make some comments on the above discussion. The most important comment is a recognition of the empirical nature of the theory which is used. In recent times it has been made very clear (e.g. WARHURST [1], COULSON [16]) that the theoretical basis on which the calculations are based, is exceedingly shaky. But nevertheless the theory has given excellent numerical results in other cases: it seems at least reasonable to expect a similar situation here. It is probable that the close liaison with experiment required in estimating the various matrix elements $H_{\mu\nu}$ is the primary cause of this. For it implies that, even though it is not theoretically provable, the basic idea is essentially a form of calculus by which valid predictions may be obtained. These predictions are more likely to be correct when they refer to a sequence of behaviour, or to a qualitative conclusion, than when we try to use them for exact quantitative purposes. For example, although we should not wish to claim any final accuracy for any of our numerical work in this paper, we do believe that our conclusions are qualitatively correct. They may be stated in the following way:

(1) Using the model of three resonating structures for the hydrogen bond in O–H ... O, it appears that except for the short bond (O ... O equal to 2.5 Å) the bonding is essentially electrostatic. But with the short bond we notice the beginning of a significant covalent contribution.

(2) As the O ... O distance is shortened, the O–H equilibrium distance increases, in a manner found experimentally. Similarly the energy increases.

(3) As the hydrogen atom moves, the two oxygen atoms remaining fixed, the covalent character of H ... O increases rapidly as this distance decreases.

(4) The use of hybrid atomic orbitals on the oxygen atoms makes only a minor difference to the numerical values involved.

(5) Despite its essentially electrostatic character, the energy of the hydrogen bond varies smoothly with the weight of the covalent structure O ... H–O.

One of us (U. D.) is grateful to the Swedish Natural Science Research Council for a grant which made it possible for this work to be done in London, at a time when the senior author was at King's College, London.

REFERENCES

1. Warhurst, E., Proc. Roy. Soc. A, *207*, 32 (1951).
2. Coulson, C. A., J. Chim. phys. *46*, 198 (1949).
3. Pople, J. A., Proc. Roy. Soc. A, *202*, 323 (1950).
4. Mulliken, R. S., Rieke, C. A., Orloff, D., and Orloff, H., J. chem. Phys. *17*, 1248 (1949).
5. Warhurst, E., Trans. Faraday Soc., *45*, 461 (1949).
6. Mulliken, R. S., J. chem. Phys. *2*, 792 (1934).
7. Moffitt, W. E., Proc. Roy. Soc. A, *202*, 534, 548 (1950).
8. Denbigh, K. G., Trans. Faraday Soc. *36*, 936 (1940).
9. Verwey, E. J., Recueil Trav. chim. Pays-Bas *60*, 887 (1941).
10. Ubbelohde, A. R., J. Chim. phys. *46*, 429 (1949).
11. Bauer, E., and Magat, M., J. Physique *9*, 319 (1938).
12. Coggeshall, N. D., J. chem. Phys. *18*, 978 (1950).
13. Bauer, E., and Magat, M., C. R. Acad. Sci. [Paris] *201*, 667 (1935).
14. Maccoll, A., Trans. Faraday Soc. *46*, 369 (1950).
15. Mulliken, R. S., J. Amer. Chem. Soc. *72*, 4493 (1950).
16. Coulson, C. A., Proc. Roy. Soc. A, *207*, 63 (1951).

Tryckt den 23 september 1954

Uppsala 1954. Almqvist & Wiksells Boktryckeri AB

ARKIV FÖR FYSIK Band 8 nr 26

Communicated 14 April 1954 by Erik Hulthén and G. Borelius

Ionization and fragmentation of N_2 by bombardment with atomic ions. Dissociation energy of N_2

By Einar Lindholm

In previous papers [1, 2, 3] collisions between molecules and atomic ions were investigated using magnetic analysis of the collision products. In the present paper the investigation has been continued with N_2 molecules. As the results of these measurements seem to be of value for the determination of the dissociation energy of nitrogen, which has been discussed in many papers [4, 5, 6], the measurements will be described in some detail.

The apparatus has been described earlier [1, 3]. All parts of the apparatus are placed inside a large vacuum container. The atomic ions (marked A) are produced in an ion source of Nier type, are analysed in a semicircular inhomogeneous permanent magnet A with a radius of 75 mm, enter the collision chamber that is filled with N_2 gas at a pressure of $2 \cdot 10^{-4}$ mm Hg, and, after leaving the collision chamber, are collected and measured by means of the electrometer tube amplifier A. In the collision chamber ionized fragments (marked B) are obtained from N_2. The ions B are drawn out through one side of the collision chamber, are accelerated and analysed in a permanent magnet B similar to magnet A, and are finally collected and measured with the electrometer tube amplifier B.

The energy of the ions A during the collision in the collision chamber has been 500 eV as during the previous measurements. The calibration of the apparatus has been carried out as before [1] by comparison with the cross section for charge exchange that has been measured by Hasted [7] for the collisions of A^+ ions with A atoms. In the previous papers the fear was expressed that the uncertainty of this calibration might be considerable owing to the strong defocussing caused by the secondary electron repeller plates. In the present work on N_2 the defocussing of the ion beam between the collision chamber and the collector A has been eliminated in the following manner. The electrometer tube amplifier A, which was previously earthed, is now very well insulated and connected to the collision chamber which has the potential 1500 V. The ions A pass directly from the collision chamber to collector A. It therefore seems probable that the unit of the cross section (cm^{-1}) that is used in the table can be taken as being more reliable than before.

The nitrogen was obtained from sodium azide.

The result of the measurements are given in the table. The first column gives the incident atomic ions, arranged according to their ionization potentials. In the two following columns the cross sections are given for the formation of the fragments N_2^+ and N^+. The last column gives the recombination energy (RE) that is probably responsible for the formation of the fragment in question. As N_2^+ may be formed in different ways the different processes are referred to by the letters *x*, *a*, *b*, *d*. Below the cross sections the mass spectrum of N_2 that is obtained by electron bombardment is given. At the foot of the table the appearance potentials (AP) for each fragment are given. For N_2^+ three values are given, corresponding to the three known ionization potentials for the three processes *x*, *a*, and *b*.

The RE for the different atomic ions have been tabulated and discussed previously [3]. In the present measurements two more ions have been used for which the RE are given below. The symbol (^2S ^1S) means that the ion is in the ^2S state before the collision and goes over into the atomic state ^1S during the charge exchange.

He^+ from He. 24.58 (^2S–^1S).

S^{++} from H_2S. 20.36 (^3P–^2P). 21.57 (^3P–^2D). 21.76 (^1D–^2P). 22.97 (^1D–^2D). 23.40 (^3P–^4S). 23.73 (^1S–^2P).

O^+. Previously [3] it has been found that the O^+ ions that are obtained from CO_2, CO and N_2O have different properties. The ions from CO_2 are mainly in the ^4S state, but from CO and N_2O many ions are also obtained in the ^2D or ^2P states. This difference may be observed with a better sensitivity than before by means of N_2. In this way it will probably be possible to investigate the dependence of the state of the O^+ ion, obtained from say CO, on the electron energy.

Kr^+. The small cross sections prove that the high metastable states $4p^4\,4d$ $^4D_{3\frac{1}{2}}$, $^4F_{4\frac{1}{2}}$, $^4F_{3\frac{1}{2}}$, $^2F_{3\frac{1}{2}}$ with the RE 15.89–18.31 are absent in the ion beam.

Cl^+. The small cross sections prove that the state ^1S with the RE 16.36 and 16.47 are absent in the ion beam.

Ion	N_2^+	N^+	RE (number) and AP (*x*, *a*, *b*, see below).	
A^{++}	3	20	N: 27.6, 29.3, 31.7, process *d*?	
Kr^{++}	3	6	N: 23.9, 24.5, 24.6, 25.2, *e*.	
He^+	2	40	N: 24.58, *e*.	
Ne^+	1	20	N: 21.56, 21.66, *f*.	
S^{++}	30	6	N_2: 20.36, *b*.	
F^+	50	20	N_2: 17.42, *x*, *a*; 20.01, *b*. N: 22.98, *f*.	
A^+	60	2	N_2: 15.76, 15.94, *x*.	
N^+	8	2	N_2: 15.03, *x*.	
Kr^+	1	1	All RE below 14.67.	
O^+	100	6	N_2: 16.67, 16.94, *a*; 18.64, *b*.	From CO
	20	3		From CO_2
	40	3		From N_2O
Cl^+	3	1	All RE below 14.45.	
Br^+	1	0.5	All RE below 13.25.	
C^+	10	2	N_2: 16.58, *x*, *a*.	
S^+	1.5	0.3	All RE below 12.20.	
Se^+	—	—	All RE below 11.45.	
B^+	1.5	0.5	All RE below 12.92.	
N_2^+	90	2		
Electrons	100	10		
AP:	*x*: 15.576	*e*: 24.297		
	a: 16.694	*f*: 21.914		
	b: 18.746			

Earlier investigations

Nitrogen has according to MULLIKEN [8, 9] (cf. MCDOWELL [10]) the following electron configuration

$$\begin{array}{cccccc}
KK & (\sigma_g\,2\,s)^2 & (\sigma_u\,2\,s)^2 & (\pi_u\,2\,p)^4 & (\sigma_g\,2\,p)^2 & {}^1\Sigma_g^+ \\
 & & 18.746 \text{ eV} & 16.694 \text{ eV} & 15.576 \text{ eV} & \\
 & & B\,{}^2\Sigma_u^+ & A\,{}^2\Pi_u & X\,{}^2\Sigma_g^+ & \\
 & d & b & a & x &
\end{array}$$

Below the electron configuration the ionization potentials for the electrons in the three lowest orbitals are given, then the states of the molecular ions that are obtained in this manner, and our notations x, a, b, d for the different ionization processes.

Process x has been observed as a Rydberg series by WORLEY and JENKINS [11, 12] and has been investigated mass spectrometrically as well [13, 14, 15, 6]. The state $X\,{}^2\Sigma_g^+$ is well known [16, 17, 18] and 21 vibrational levels have been observed.

Process a has been observed as a Rydberg series by WORLEY [19] and the $A^2\Pi_u \rightarrow X^2\Sigma_g^+$ bands have been measured by DOUGLAS [20]. Vibrational levels up to $v = 14$ of the A state have been established as perturbations in the B state [16]. The process a has not yet been detected by the mass spectrometer. However, MCDOWELL [10] has pointed out a change in slope of the ionization efficiency curve for the N_2^+ ion in Fig. 8 of HAGSTRUM's paper [6] which may possibly correspond to process a.

Process b has been observed as a Rydberg series by HOPFIELD [21], but has not yet been found in any electron impact studies. The state $B^2\Sigma_u^+$ is well known from investigations of the 1st negative nitrogen bands $B^2\Sigma_u^+ \rightarrow X\,{}^2\Sigma_g^+$ and 29 vibrational levels are known [16, 17, 18]. Process b corresponds to the removal of an antibonding electron from the ground state of N_2.

Process d has never been observed. Its ionization potential has been estimated to 30 eV by MULLIKEN [9].

An electronic state $C^2\Sigma_u^+$ has been observed by means of band spectra at 23.586 eV [22, 23, 24, 25, 18], but it is improbable that this state can correspond to process d as it is odd (cf. [23] and [10]).

The fragmentation of the nitrogen molecule by electron impact has been studied by a number of investigators [26, 27, 14, 6]. They have obtained 24.3 ± 0.2 eV as the value of the AP for formation of N^+. HAGSTRUM [6] has been able to show that the N^+ ions which are formed at this electron energy have zero kinetic energy. From this it follows that there exists a dissociation limit at this energy. DOUGLAS [18] has been able to show that the $B^2\Sigma_u^+$ state dissociates into this limit.

From spectroscopic determinations the accurate value of the energy corresponding to this dissociation limit is found to be 24.297 eV above the ground state of N_2 [4, 5, 28, 18]. This determination is based on the ionization potential for N and on the fact that the dissociation energy for N_2 seems to be either 7.373 eV or 9.756 eV.

The two values of the dissociation energy for N_2 correspond to the uncertainty as to the states of the fragments that are obtained in the dissociation limit 24.297 eV. LOZIER [27] and HAGSTRUM [6] have given reasons for the assumption that the N atom is excited and the dissociation process at this voltage is

$$N_2\,(X\,{}^1\Sigma_g^+) + 24.297 \text{ eV} \rightarrow N^+\,({}^3P) + N\,({}^2D). \qquad (e)$$

It appeared impossible to prove the statement by direct argument from the measurements on nitrogen. HAGSTRUM has obtained his result by comparing appearance potential measurements on CO, N_2, NO and O_2. But other authors have got deviating results and the topic is the subject of much discussion [4, 5, 28, 18].

If process *e* is assumed to be correct, the consequence must be the existence of a dissociation limit with lower energy. But the process

$$N_2\,(X\,^1\Sigma_g^+) + 21.914\text{ eV} \rightarrow N^+\,(^3P) + N\,(^4S) \qquad (f)$$

has not yet been observed in any electron impact studies and it appeared to be impossible to prove that any of the states of N_2^+ converge towards this limit [18].

Discussion of the new measurements

Regarding the interpretation of the measurements of the cross sections in the table, reference may be made to [3] where there are similar discussions of several molecules.

The new measurements give a good illustration of the observation in [3] that when RE is smaller than AP the cross section will diminish rapidly with increasing energy deficit. When bombarding with A^+ (RE 15.76 and 15.94) the cross section for formation of N_2^+ (AP 15.58) is large as RE and AP are equal. With N^+ the cross section is smaller owing to the energy deficit 0.55 eV. With Kr^+ and Cl^+ the cross sections are small as the energy deficits amount to 0.9 eV and 1.1 eV.

When bombarding with ions whose RE is higher than 15.58 the energy excess will be absorbed as vibrational energy by the molecular ion that is formed during the process, or possibly the molecular ion will be formed in one of the higher electronic states of N_2^+. Large cross sections for formation of N_2^+ will therefore be obtained with F^+, O^+ and S^{++}. As each of these ions has several RE and as the AP for the processes *x*, *a* and *b* lie relatively close together, it is impossible to give any reliable correlation of the different AP and RE.

The cross section for formation of N^+ is large when bombarding with He^+ (RE 24.58). The explanation seems to be straightforward. The process must be the well-known process *e*. The small energy excess 0.28 eV will be absorbed as initial kinetic energy by the two fragments N^+ and N. The cross section for formation of N_2^+ is small, which proves that the N_2^+ ions, which probably are the primary products of the process, immediately dissociate.

The large cross section for formation of N^+ makes possible an explanation of the activation methods that have been used in the investigations of the spectrum of N_2^+. It has appeared that, when using a discharge through helium, containing a trace of nitrogen, the N_2^+ bands are strong compared with the N_2 bands [20, 29, 17, 18]. In the $C\,^2\Sigma_u^+ \rightarrow X\,^2\Sigma_g^+$ system, the bands $v' = 3$ have a high intensity, the bands $v' = 4$ and $v' = 5$ have a rapidly decreasing intensity and the bands $v' < 3$ have not been observed under these conditions [22, 24, 25].

WATSON and KOONTZ [22] tried to explain the anomalous intensity distribution in the $C \rightarrow X$ bands by assuming that excited N_2^+ ions with the energy 24.3 eV or a little higher are formed during a collision of the second kind between He^+ and N_2. As the $v = 3$ level of the *C* state will get an anomalously high population owing to its mode of formation, the corresponding bands will be strong. TANAKA [25], however, has pointed out that a more accurate comparison of the energies shows that the $v = 4$ level should get the highest population.

Douglas [18] has recently given another explanation. He assumes that the high population of the $v=3$ level depends upon inverse predissociation when an N^+ ion and an N atom come together, as at the dissociation limit they may undergo radiationless transition into the $v=3$ level. If the gas in the discharge tube contains a large number of nitrogen ions and atoms, we may expect a high intensity of the bands $v'=3$.

With the new measurements of the cross sections at our disposal it seems to be possible to make a decision as to which of the two explanations is the correct one. Watson and Koontz's explanation is probably not correct as our measurements of the cross sections show that the N_2^+ ions that are obtained in the collision immediately dissociate. It is true that the mass spectrometric analysis of the fragments takes about 10^{-6} sec. and during this time it would of course be possible for the molecular ion to transmit radiation. But in that case the result of the transition would have been an N_2^+ molecular ion in the ground state $X\,^2\Sigma_g^+$ and we would of course have observed this ion in the mass spectrometer. On the other hand, Douglas's explanation is supported by our result that the cross section for formation of N^+ is large, for this shows that the gas in the discharge tube must contain a large number of nitrogen ions and atoms.

The cross section for formation of N^+ is large when bombarding with Ne^+ (RE 21.56 and 21.66). This is surprising, for if the fragmentation takes place according to process *e*, the energy deficit would amount to as much as 2.6 eV. We have shown above and in [3] that when the energy deficit amounts to more than about 0.5 eV, the cross section will be very small. The reason for this is that, when the kinetic energy of the incident atomic ion takes part in the energy balance, the molecular ion and the fragments from it will have a certain initial velocity. Owing to the discrimination in mass spectrometer *B*, the fragments with an initial velocity larger than a certain amount will not reach collector *B* [30]. Therefore it seems to be impossible to explain the cross sections with Ne^+ by means of process *e*. (There is of course a theoretical possibility that in the case of process *e* most of the initial kinetic energy may be taken up by the atom so that the initial kinetic energy of the ion will be small. But as the probability of this is likely to be small, it will be impossible to explain in this way why the cross sections with Ne^+ and He^+ only differ by a factor 2.)

Another conceivable explanation might be that Ne^+ has a RE higher than 21.56 and 21.66 owing to some metastable state of Ne^+. But there is no such state in Ne^+ as the only possibility, $3s\ ^4P$, probably has a life time of the order 10^{-8} sec. owing to the strong transition to the ground state of Ne^+ [31]. Further, a large cross section for formation of N^+ is also obtained with F^+ (RE 22.98).

It therefore seems necessary to assume the existence of a process with an AP lower than 24.3 eV, and the only possibility seems to be process *f*. No explanation can be given for the fact that this process is important when bombarding with Ne^+ and F^+ but unimportant when bombarding with electrons. This is probably due to our incomplete knowledge of the spectrum of N_2^+.

Our explanations for the cross sections with He^+ and Ne^+ are in good agreement with the experimental results that Wolf [32] has obtained for the same collision processes. For He^+ he found a large cross section that was increasing for decreasing velocity of the ion, which proves that the resonance is exact. And that is just the case for process *e*, for the small energy excess 0.28 eV is absorbed by the fragments. For Ne^+ the cross section was a little smaller and decreasing for decreasing velocity. This velocity dependence shows that the resonance is imperfect. Since a small energy excess always will be absorbed, Wolf's measurements prove that in the collisions of Ne^+ with N_2 there is a small energy deficit. That agrees with our explanation as RE 21.66 for Ne^+ is smaller than AP 21.914 for process *f*.

Takamine, Suga and Tanaka [24] have investigated the spectrum of N_2^+ in ultra violet by means of a discharge tube containing Ne instead of He. The intensity distribution in the $C \rightarrow X$ band system was in this case quite different from the distribution with He. The bands $v' = 0$ were now the strongest and the bands $v' = 1$ only a little weaker. For $v' = 2$ the intensity was small and for higher values of v' the bands were very weak. Takamine, Suga and Tanaka tried to explain the intensity distribution by assuming a three-body collision of the second kind

$$Ne^+ + N_2 + N\,(^2D) \rightarrow Ne + N_2^+ + N\,(^4S).$$

In this process the nitrogen molecule takes up energy from both the Ne^+ ion and the metastable N atom. Recently this explanation has been questioned by Tanaka [25] who has pointed out that the levels $v' = 1$ and $v' = 2$ are closer to the sum of the ionization potential of Ne and the excitation energy of $N\,(^2D)$ than the level $v' = 0$, and therefore we should expect the bands $v' = 1$ and $v' = 2$ to be the strongest. Further, Douglas [18] has pointed out that the low intensity for $v' \geq 3$ may be due to predissociation into the dissociation limit 24.297 eV. Finally, the new measurements of the cross sections seem to show that Takamine, Suga and Tanaka's explanation cannot be correct as collision between Ne^+ and N_2 results in dissociation of N_2.

On the other hand, it is difficult to give a better explanation. Probably any new explanation will have to be founded on the assumption of the existence of a large number of $N\,(^4S)$ atoms and $N^+\,(^3P)$ ions in the discharge tube. When these come together an N_2^+ ion will be formed, but nothing can be said about the details of this process, for Takamine, Suga and Tanaka have investigated only the bands in the vacuum ultraviolet. Probably an investigation of the spectrum for longer wavelengths, with neon in the discharge tube, will reveal deviations from the spectrum that is obtained with helium, and in this way the activation process may possibly be determined. Further, it may perhaps be possible to get information about the electronic states that arise from the dissociation limit 21.914 eV. These have not yet been observed (cf. Douglas [18]).

The existence of the low dissociation limit 21.914 eV that seems to proved by the measurements of the cross sections appears to support Hagstrum's view that excited products are obtained from N_2 by electron impact, and it follows that the measurements in this paper favour the values 6.338 eV and 7.373 eV for the dissociation energies for N_2^+ and N_2.

It must be stressed that, in some respects, measurement by means of collisions with atomic ions must be considered to be more reliable than measurement of appearance potentials by means of electron impact. In the latter case an ion current is observed which is so weak that it may barely be detected. The result of the measurement will therefore depend, to a certain extent, on the sensitivity of the apparatus and may be affected by small quantities of impurities, as has been stressed by the critics of the method (Gaydon, l.c.). On the other hand, in measurement by means of atomic ions, only the strong peaks are taken into consideration and therefore impurities are of no importance. A further advantage of the method is that the spectroscopic values for the recombination energies may be used directly, whereas in the appearance potential measurements they are used only indirectly during the calibration of the apparatus by means of, say, argon.

Summary

The charge exchange in collisions between atomic ions and nitrogen molecules has been investigated. The fragments N_2^+ and N^+ from the molecule have been analysed in a second mass spectrometer. The measurements confirm the earlier result that when the recombination energies of the ion are appreciably lower than the appearance potentials of the molecule, the cross section for the charge exchange is small. In the collisions of He^+ the cross section for formation of N^+ is large, which explains the high intensity of the N_2^+ bands in the spectrum from a discharge through a mixture of He and N_2. In the collisions of Ne^+ the cross section for formation of N^+ is large, too. As the recombination energy for Ne^+ is 21.6 eV, this shows that the N_2^+ molecular ion may dissociate when it has absorbed about 6 eV, and this means that the values for the dissociation energies 6.338 eV for N_2^+ and 7.373 eV for N_2, given by HERZBERG and HAGSTRUM, seem to be proved. The desirability of further spectroscopic investigations using a discharge through a mixture of Ne and N_2 is pointed out.

I wish to express my gratitude to Prof. E. HULTHÉN for helpful criticism of the manuscript and to Ing. F. TORSTENSSON for valuable technical assistance.

Department of Physics, Chalmers University of Technology, Gothenburg.

REFERENCES

1. E. LINDHOLM, Proc. Phys. Soc. A *66*, 1068, 1953.
2. E. LINDHOLM, Institute of Petroleum, Conference on Applied Mass Spectrometry, London 1954, in print.
3. E. LINDHOLM, Zeits. f. Naturforsch. *9a*, 535, 1954.
4. A. G. GAYDON, Dissociation Energies and Spectra of Diatomic Molecules, London 1953.
5. G. HERZBERG, Molecular Spectra and Molecular Structure. I. Spectra of Diatomic Molecules. New York 1950.
6. H. D. HAGSTRUM, Rev. Mod. Phys. *23*, 185, 1951.
7. J. B. HASTED, Proc. Roy. Soc. A *205*, 421, 1951.
8. R. S. MULLIKEN, Rev. Mod. Phys. *4*, 1, 1932.
9. R. S. MULLIKEN, Phys. Rev. *46*, 549, 1934.
10. C. A. McDOWELL, Institute of Petroleum, Conference on Applied Mass Spectrometry, London 1954, in print.
11. R. E. WORLEY and F. A. JENKINS, Phys. Rev. *54*, 305, 1938.
12. R. E. WORLEY, Phys. Rev. *64*, 207, 1943.
13. J. T. TATE, P. T. SMITH and A. L. VAUGHAN, Phys. Rev. *48*, 525, 1935.
14. H. D. HAGSTRUM and J. T. TATE, Phys. Rev. *59*, 354, 1941.
15. R. E. HONIG, J. Chem. Phys. *16*, 105, 1948.
16. D. COSTER and H. H. BRONS, Zeits, f. Phys. *73*, 747, 1932;
    W. H. J. CHILDS, Proc. Roy. Soc. A *137*, 641, 1932;
    H. H. BRONS, Physica *1*, 739, 1933.
17. A. E. PARKER, Phys. Rev. *44*, 90 and 914, 1933;
    F. H. CRAWFORD and P. M. TSAI, Proc. Am. Acad. Arts Sci. *69*, 407, 1935.
18. A. E. DOUGLAS, Can. J. Phys. *30*, 302, 1952. (An energy level diagram of the N_2^+ molecule is given in this paper.)
19. R. E. WORLEY, Phys. Rev. *89*, 863, 1953.
20. A. E. DOUGLAS, Astrophys. J. *117*, 380, 1953.
21. J. J. HOPFIELD, Phys. Rev. *36*, 789, 1930;
    R. S. MULLIKEN, Phys. Rev. *46*, 144, 1934.
    T. TAKAMINE, T. SUGA and Y. TANAKA, Sci. Papers Inst. Phys. Chem. Res. (Tokyo) *34*, 854, 1938.

22. W. W. Watson and P. G. Koontz, Phys. Rev. *46*, 32, 1934;
R. B. Setlow, Phys. Rev. *74*, 153, 1948.
23. P. Baer and E. Miescher, Helv. Phys. Acta *26*, 91, 1953.
24. T. Takamine, T. Suga and Y. Tanaka, Sci. Papers Inst. Phys. Chem. Res .(Tokyo) *36*, 437, 1939.
25. Y. Tanaka, J. Chem. Phys. *21*, 1402, 1953.
26. A. L. Vaughan, Phys. Rev. *38*, 1687, 1931.
27. W. W. Lozier, Phys. Rev. *44*, 575, 1933; *45*, 840, 1934.
28. A. E. Douglas and G. Herzberg, Can. J. Phys. *29*, 294, 1951.
29. T. R. Merton and J. G. Pilley, Phil. Mag. *50*, 195, 1925.
30. C. E. Berry, Phys. Rev. *78*, 597, 1950.
31. C. E. Moore, Ultraviolet Multiplet Table, Circ. Nat. Bur. Std. 488, 1950.
32. F. Wolf, Ann. d. Phys. *30*, 313, 1937.

Tryckt den 23 september 1954

Uppsala 1954. Almqvist & Wiksells Boktryckeri AB

ARKIV FÖR FYSIK Band 8 nr 27

Communicated 10 March 1954 by Erik Hulthén and G. Borelius

The blue band-system of niobium oxide

By Ulla Uhler

With 3 figures in the text

Abstract

A new rotational analysis of the blue band-system of niobium[1] oxide has been carried out. The bands are shaded to the red and represent a $^2\Delta$–$^2\Delta$ transition $(A^2\Delta$–$(X)^2\Delta)$. Both $^2\Delta$-states show a moderate multiplet splitting and have large γ-values. The 0,0, 0,1, 1,2, 1,0, 2,1, 2,0 and 3,1 bands have been analysed.

The band-origins are represented by the relation

$$\sigma = 21\,385.3_1 + 850.4_8\ (v'+\tfrac{1}{2}) - 3.3_7\ (v'+\tfrac{1}{2})^2 - 989.0_3\ (v''+\tfrac{1}{2}) + 3.8_3\ (v''+\tfrac{1}{2})^2.$$

The rotational analyses gave the following constants:

$$\begin{array}{ll}
B_e'' = 0.4321\ \mathrm{K} & B_e' = 0.4001\ \mathrm{K} \\
B_0'' = 0.4310 & B_0' = 0.3992 \\
B_1'' = 0.4289 & B_1' = 0.3973 \\
B_2'' = 0.4269 & B_2' = 0.3954 \\
 & B_3' = 0.3932 \\
\alpha'' = 0.0021 & \alpha' = 0.0019 \\
D'' = 0.22\cdot 10^{-6} & D' \sim 0.27\cdot 10^{-6} \\
|A''| \approx 15 & |A'| \approx 14 \\
\gamma'' \sim 1 & \gamma' \sim 1 \\
r_e'' = 1.691\cdot 10^{-8}\ \mathrm{cm} & r_e' = 1.757\cdot 10^{-8}\ \mathrm{cm}
\end{array}$$

The present analysis is completely at variance with the one performed by K. S. Rao.

I. Introduction

The band-spectrum of niobium oxide was first studied by V. R. Rao [1]. He found an extensive spectrum and divided the bands into three systems, *A*, *B* and *C*. Vibrational constants were given and the possible electronic transitions were discussed. Systems *B* and *C* (in the green-yellow and red regions respectively) have a very complicated appearance: every band has four heads and the two systems overlap. In system *C* only the sequence $\Delta v = +1$ has been identified. The rest of the system lies further in the infra-red. The blue system has a simpler appearance: each band has only one head. V. R. RAO considers the three systems *A*, *B* and *C* to be $^4\Pi$–$^4\Pi$, ($^4\Sigma$)–$^4\Pi$ and $^4\Sigma$–$^4\Pi$ respectively, with the lower state in common.

---

[1] This element is usually known as Columbium. The International Union of Chemistry has adopted Niobium as the official name of element 41.

In 1952 K. S. RAO [2] published a short notice of a rotational analysis of the blue 0,0, 0,1 and 1,0 bands (system *A*). Last year V. R. RAO and D. PREMASWARUP [3] published an investigation of system *C*, extended further to the red. They stress the fact that the system *C* and *A* probably have the lower state in common. They also concur with K. S. RAO in his suggestion that the lower state of system *A* is a quartet term.

The *B*-values reported by K. S. RAO seem to be too high for such a heavy molecule. Thus it seemed worth while to repeat the rotational analysis of system *A*. Rotational analyses have been carried out on the 0,0, 0,1, 1,2, 1,0, 2,1, 2,0 and 3,1 bands. It was possible to check the analysis through the existence of some perturbations. The vibrational analysis agrees with the one given by V. R. RAO, but the derived constants differ somewhat.

II. Experimental

The spectrum of the NbO molecule is very easily excited. The bands appear strongly in the flame surrounding a D.C. arc (220 V, 5 A) between graphite electrodes fed by niobium oxide or a niobium salt. The arc burns more steadily if the lower electrode is positive. A still better source of light is an arc between niobium rods run at 220 V, 2 A D.C. (The rods were supplied by *Metallografiska Institutet*, Stockholm.) The spectrum obtained in this way was very free from impurities. This source was used for the final exposures. For a general survey the bands were photographed in a large quartz spectrograph (the dispersion in the blue region is about 7.5 Å/mm). The final spectrograms were taken in a Wood's 21 ft. concave grating in the first order (165,000 lines in all). The dispersion is about 1.24 Å/mm. Ilford Thin Film Half Tone plates were used. The exposure time of the grating spectrograms was 1 hour. Iron lines served for comparison. Their wave-lengths were taken from HARRISON's Tables [4].

III. The blue system

The structure of the bands

The appearance of the blue system is shown in Figs. 1 and 2. The bands are degraded to longer wave-lengths. The vibrational assignment is comparatively easy, as the sequences do not overlap. Every band has only one head.

The 1,1 band has such a low intensity that the head cannot be seen, and consequently the 0,0 band lies very free. The rotational structure is not fully resolved in the vicinity of the heads. The *R*-lines have not been identified before the turn of the head.

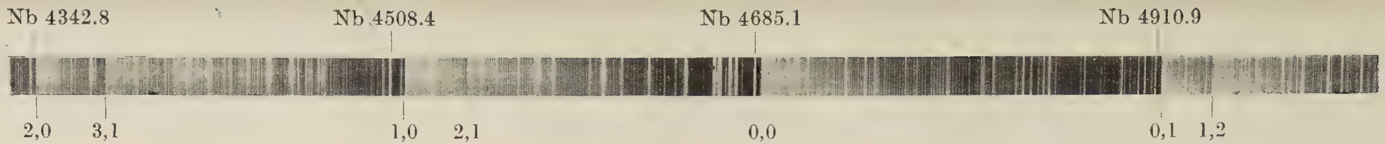

Fig. 1 a. The blue band-system of NbO.

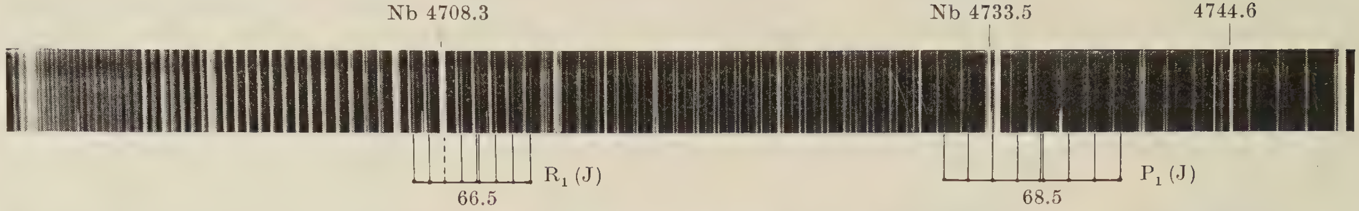

Fig. 1 b. Reproduction of the 0,0 band.

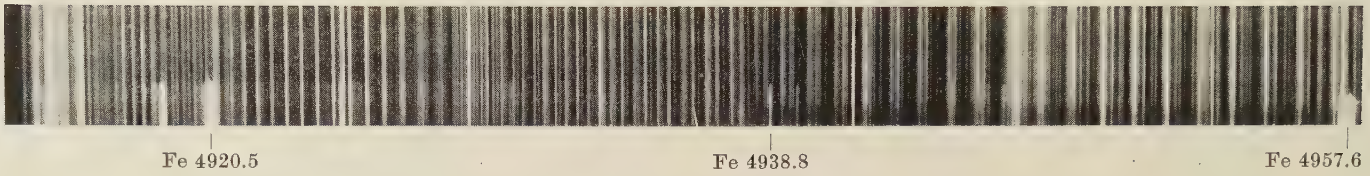

Fig. 2 a. The 0,1 band.

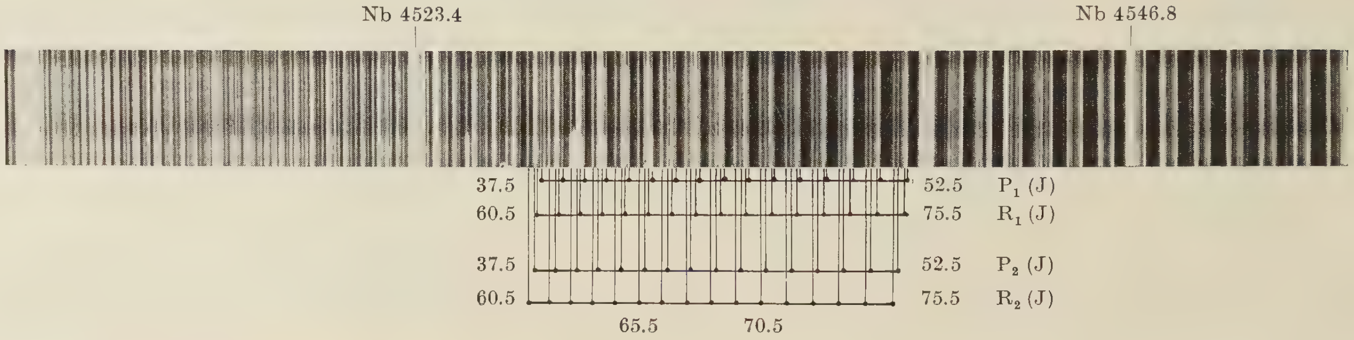

Fig. 2 b. The 1,0 band.

Each band consists mainly of four branches of equal intensity. In some of the bands very weak satellite branches were observed. In the 0,0 band a small perturbation was observed in two of the four strong branches. The same irregularity was found in the 0,1 band but not in the 1,0 band. Consequently, there is a perturbation in the upper state $v' = 0$, which gives the connection between one R and one P branch. The other two branches were found to be another pair of R and P branches. The correctness of this assumption is verified by another small perturbation occurring in the level $v' = 2$. Thus two R and two P branches have been identified.

The nature of the transition

The molecule NbO has an odd number of electrons. Consequently, electronic terms of even multiplicities are to be expected. The band-systems may be doublet-doublet or quartet-quartet transitions. The possibility of intercombination systems must also be considered. For heavy molecules the rule $\Delta S = 0$ is no longer valid, and the intercombination systems may have intensities quite comparable with those of the allowed transitions. (Compare the $^4\Sigma^-$–$^2\Pi$ system in GeH and SnH [5].)

The absence of strong Q-branches in the blue bands indicates that $\Delta \Lambda = 0$. V. R. RAO's suggestion that the transition is a $^4\Pi$–$^4\Pi$ must be ruled out. In such a case one should have at least eight branches, four R and four P branches of equal intensity. It is highly improbable that they coincide in such a way that only four branches remain. Another fact that militates against this assumption is the absence of Λ-type doubling. In the 0,0 band the branches can be followed up to $J \sim 115.5$ but even at such high J-values no doubling of the lines can be detected. Thus $^4\Pi$–$^4\Pi$ must be excluded. Niobium consists of one stable isotope only, and consequently there is no isotope splitting in the branches either. Other transitions involving terms of higher multiplicity than four, quartet transitions and intercombinations between doublet and quartet terms, are also ruled out, because in all these cases there should be more than four strong branches. There remain the doublet-doublet transitions $^2\Pi$–$^2\Pi$, $^2\Sigma$–$^2\Sigma$ and $^2\Delta$–$^2\Delta$. As every band has only one head, the coupling cases cannot be very far from Hund's case b. The conditions of case b are progressively fulfilled with increasing rotation. $^2\Pi$ (case b) has a Λ-type doubling proportional to $J(J+1)$, which should definitely be detectable for high J-values, even if one might expect to observe only the difference between the Λ-type doublings of the upper and lower states. Thus the system cannot be a $^2\Pi$–$^2\Pi$ transition. To distinguish between the remaining possibilities, $^2\Sigma$–$^2\Sigma$ and $^2\Delta$–$^2\Delta$, one has to regard the second differences of the levels F_1 and F_2. In a $^2\Sigma$–$^2\Sigma$ transition Hund's case b is valid for low as well as for high J-values, while a $^2\Delta$-term may belong to case b for high rotational quantum numbers and go over into case a or an intermediate coupling case for low J-values. If the term belongs to case b, the difference between $\Delta_2 F_1(K)$ and $\Delta_2 F_2(K)$ will be constant over the whole range, and equal to 2γ, a splitting constant due to the magnetic interaction of $\boldsymbol{K}$ and $\boldsymbol{S}$. In the present case the difference is constant for high J-values, where case b is to be expected, but increases at the beginning. The increase at the beginning is caused by the coupling between the spin, $\boldsymbol{S}$, and the component of the orbital angular momentum along the internuclear axis, Λ. This is possible only in the case of a $^2\Delta$–$^2\Delta$ transition. Consequently, the blue band-system is considered to be a $^2\Delta$–$^2\Delta$ transition.

The lowest $^2\Delta$-state (called $(X)\ ^2\Delta$) of NbO is not necessarily the ground state of the molecule. If both the atoms are placed in their ground states, viz, Nb (^{6}F) and O (^{3}P), it is impossible to obtain a doublet term. The $(X)^2\,\Delta$-state probably dissociates into O (^{3}P) and some excited state of the Nb atom.

Rotational analysis

Tables 1–4 give the wave-numbers of the 0,0, 0,1, 1,0, 2,0, 2,1, 1,2 and 3,1 bands. Overlapping lines are marked with an asterisk. Table 5 gives a part of the combination differences, $R(J-1)-P(J+1)$, of the lower level of the 0,0, 1,0 and 2,0 bands. The agreement is good. The errors in the measurements of the lines do not as a rule exceed 0.05 K.

The rotational energies of the components of a doublet state have been calculated for any coupling case between *a* and *b* by HILL and VAN VLECK [6]:

$$\begin{aligned} J = K + \tfrac{1}{2}\quad F_1(J) &= B\left[(J+\tfrac{1}{2})^2 - \Lambda^2 - \tfrac{1}{2}\sqrt{4(J+\tfrac{1}{2})^2 + Y(Y-4)\Lambda^2}\right] - D J^4 \\ J = K - \tfrac{1}{2}\quad F_2(J) &= B\left[(J+\tfrac{1}{2})^2 - \Lambda^2 + \tfrac{1}{2}\sqrt{4(J+\tfrac{1}{2})^2 + Y(Y-4)\Lambda^2}\right] - D(J+1)^4, \end{aligned} \tag{I}$$

where $Y = \dfrac{A}{B}$.

The effect of the K, S interaction should be added to F_1 and F_2, viz, $+\tfrac{1}{2}\gamma K$ and $-\tfrac{1}{2}\gamma(K+1)$ respectively.

The B and D values are obtained graphically from the equation:

$$\frac{\Delta_2 F_1(J) + \Delta_2 F_2(J)}{2(J+\tfrac{1}{2})} = 4B - 8D(J+\tfrac{1}{2})^2.$$

When $\dfrac{\Delta_2 F(J)_{\text{mean}}}{J+\tfrac{1}{2}}$ was plotted against $(J+\tfrac{1}{2})^2$ straight lines were obtained, giving $4B$ as the intersection with the ordinate and $8D$ as the inclination of the line. The estimated values for $v'=3$ are less accurate, as the line in this case was rather short. The upper state is denoted $A\,^2\Delta$. The following values were obtained:

$(X)\ ^2\Delta$	$A\ ^2\Delta$
$B_0'' = 0.4310$ K	$B_0' = 0.3992$ K
$B_1'' = 0.4289$	$B_1' = 0.3973$
$B_2'' = 0.4269$	$B_2' = 0.3954$
	$[B_3' = 0.3932]$
$D_0'' = 0.22 \cdot 10^{-6}$ K	$D_0' = 0.26 \cdot 10^{-6}$ K
$D_1'' = 0.22 \cdot 10^{-6}$	$D_1' = 0.27 \cdot 10^{-6}$
$D_2'' = 0.22 \cdot 10^{-6}$	$D_2' = 0.29 \cdot 10^{-6}$
	$[D_3' = 0.33 \cdot 10^{-6}]$.

Table 1. Wave-numbers of the 0,0 band.

J	R_1	P_1	R_2	P_2	J	R_1	P_1	R_2	P_2
25.5		21 274.44*		21 274.44*	70.5	211.16	098.41	212.51	100.06
26.5		71.93*		71.93*	71.5	07.32	93.04	08.71	094.69
27.5		69.37*		69.37*	72.5	03.40	87.56	04.91	89.26
28.5		66.73*	21 312.21	66.73*	73.5	199.37	82.02	00.95	83.76
29.5	21 312.58	64.05*	11.20	64.05*	74.5	95.42	76.42	196.99	78.21
30.5	11.37	61.31*	10.11*	61.31*	75.5	91.31	70.63	92.78*	72.60
31.5	10.11*	58.48*	08.85*	58.48*	76.5	87.16	65.02	88.69*	66.91
32.5	08.85*	55.62*	07.71	55.62*	77.5	82.91	59.26	84.49*	61.19*
33.5	07.41	52.71*	06.40	52.71*	78.5	78.63	53.40	80.24*	55.39*
34.5	05.98	49.72*	05.01	49.72*	79.5	74.28	Nb	75.94*	49.47*
35.5	04.48	46.67*	03.62	46.67*	80.5	69.83	41.50	71.58*	43.50*
36.5	02.88	43.52*	02.14	43.52*	81.5	65.35	35.44	67.13*	37.46*
37.5	01.25	40.25*	00.58	40.45*	82.5	60.78	29.39	62.65*	31.47
38.5	299.55	36.97*	298.96	37.23*	83.5	56.16	23.14	58.06*	25.33
39.5	97.81	Nb	97.29	33.93*	84.5	51.49	16.91	53.44*	19.08
40.5	95.99	30.23	95.53	30.57*	85.5	46.72	10.62	48.75*	12.83
41.5	94.09	26.77	93.70	27.11*	86.5	41.90	04.23	44.00*	06.47
42.5	92.14	23.24	91.78	23.67	87.5	37.00	20 997.80	39.16*	00.08
43.5	90.09	19.65	89.92	20.13	88.5	32.05	91.30	Nb	20 993.62
44.5	87.97*	16.03*	87.97*	16.56	89.5	27.03	84.73	29.18	87.12
45.5	85.87*	12.31	85.87*	12.87	90.5	21.94	78.07	24.10	80.49
46.5	83.69*	08.52	83.69*	09.11	91.5	16.76	71.38	Nb	73.81
47.5	81.44*	04.66	81.44*	05.30	92.5	11.49	64.65	13.79	67.08
48.5	79.12*	00.79	79.12*	01.43	93.5	06.25	57.80	08.54	60.30
49.5	76.62	196.80	76.80*	197.49	94.5	00.87	50.96	03.21	53.44
50.5	74.19	92.78*	74.44*	93.52	95.5	095.40	43.99	097.82	46.51
51.5	71.64	88.69*	71.93*	89.45	96.5	89.92	36.90	92.33	39.51
52.5	69.07	84.49*	69.37*	85.33	97.5	84.37	29.83	86.83	32.44
53.5	66.39	80.24*	66.73*	81.12	98.5	78.73	22.64	81.22	25.31
54.5	63.63	75.94*	64.05*	76.86	99.5	73.02	15.45*	75.55	18.12
55.5	60.87	71.58*	61.31*	72.55	100.5	67.31	08.15	69.87	10.85
56.5	58.02	67.13*	58.48*	68.18	101.5	61.19*	00.80	64.01	03.53
57.5	55.11	62.65*	55.62*	63.71	102.5	55.39*	893.30	58.17	896.12
58.5	52.11	58.06*	52.71*	59.21	103.5	49.47*	85.79	52.18	88.64
59.5	49.05	53.44*	49.72*	54.62	104.5	43.50*	78.29	46.22	81.13
60.5	45.91	48.75*	46.67*	50.02	105.5	37.46*	70.65	40.12	73.54
61.5	42.76	44.00*	43.52*	45.32	106.5	31.27	62.91	34.03	65.85
62.5	39.64	39.16*	40.45*	40.56	107.5	24.86	55.19	27.78	58.14
63.5	36.20	34.30	37.23*	35.71	108.5	18.58	47.30	21.51	50.34
64.5	Nb	29.42	33.93*	30.81	109.5	12.26	39.47	15.16	42.49
65.5	29.38	24.44	30.57*	25.85	110.5	05.83	31.49	08.73	34.54
66.5	26.08 25.73	19.37	27.11*	20.85	111.5	20 999.32	23.48	02.25	26.60
67.5	22.27	14.23	23.67*	15.72	112.5	92.70	15.37	20 995.72	18.54
68.5	18.64	09.35 08.92	20.13*	10.58	113.5	86.01	07.25	89.08	10.40
69.5	14.93	03.73	16.26	05.36	114.5	79.31	799.01	82.39	02.22
					115.5	72.52	90.77	75.65	793.97

Table 2. Wave-numbers of the 0,1 and 1,0 bands.

J	The 0,1 band				The 1,0 band			
	R_1	P_1	R_2	P_2	R_1	P_1	R_2	P_2
23.5		20 299.29		20 298.69*		22 121.31		22 122.12
24.5		96.93		96.47*		18.87		19.69
25.5		94.62	20 334.88	94.21		16.36	22 157.77	17.20
26.5		92.25	34.18*	91.89		13.67	56.82	14.65
27.5		89.80	33.45	89.48		11.12	55.75	12.13*
28.5	20 334.18*	87.31	32.59	87.00		08.41	54.68	09.41*
29.5	33.24	84.76	31.66	84.50	22 153.96	05.63	53.51	06.58*
30.5	32.18	82.10	30.71	81.91	52.64	02.77	52.25	03.74*
31.5	31.07	79.41	29.66	79.26	51.30	099.88	50.93	Nb
32.5	29.88	76.63*	28.60*	76.63*	49.67*	96.88	49.67*	Nb
33.5	28.60*	73.83*	27.36*	73.83*	48.22	93.83	48.22*	094.75*
34.5	27.36*	71.00*	26.23	71.00*	46.69*	90.58	46.69*	91.61*
35.5	25.97	68.09*	24.93	68.09*	45.06*	87.43	45.06*	88.41*
36.5	24.56	65.13*	23.57	65.13*	43.38*	84.17	43.38*	85.26
37.5	23.07	62.11*	22.18	62.11*	41.61	80.84	41.76	82.03
38.5	21.53	58.97	20.74	59.13	39.74	77.44	39.96	78.62
39.5	19.94	55.78	19.22	56.05	37.80	73.97	38.09	75.14
40.5	18.28	52.55	17.65	52.84	35.81	70.41	36.15	71.70
41.5	16.56	49.26	16.00	49.60	33.77	66.80	34.15	68.01
42.5	14.78	45.92	14.32	46.28	31.65	63.12	32.09	64.33
43.5	12.97	42.52	12.56	42.92	29.65	59.37	29.93	60.62
44.5	11.08	39.05	10.74	39.49	27.20	55.54	27.71	56.83
45.5	09.06	35.54	08.87	35.99	24.88	51.66	25.46	52.96
46.5	06.97*	31.94	06.97*	32.44	22.49	47.70	23.12	49.03
47.5	04.94*	28.30	04.94*	28.85	20.03	43.67	20.68	45.02
48.5	02.85*	24.59	02.85*	25.17	17.51	39.59	18.20	40.96
49.5	00.65	20.81	00.81	21.44	14.91	35.41	15.68	36.82
50.5	298.42	16.98	298.69*	17.66	12.13*	31.18	13.03	32.67
51.5	96.11	13.10	96.47*	13.82	09.41*	26.88	10.35	28.34
52.5	93.72	09.12	94.01	09.98	06.58*	22.50	07.60	24.00
53.5	91.25	05.14	91.61	05.99	03.74*	18.08	04.73	19.52
54.5	88.77	01.06*	89.14	02.00*	Nb	13.57	01.88	15.10
55.5	86.23	196.91*	86.64	197.81*	Nb	08.95	098.87	10.51*
56.5	83.60	92.71*	84.08	93.67	094.75*	04.37*	95.83	05.95
57.5	80.93	88.50	81.48	89.52*	91.61*	21 999.60*	92.73	01.18
58.5	78.19	84.17	78.79	85.28	88.41*	94.83*	89.52	21 996.44
59.5	75.38	79.82	76.09	80.94*	85.02	89.92*	86.27	91.60
60.5	72.52	75.34*	73.27	76.61*	81.65	84.95*	82.95	86.65
61.5	69.59	70.91*	70.41	72.05*	78.20	79.99*	79.58	81.76
62.5	66.62	66.38*	67.48	67.54*	74.71	74.86*	76.10	76.72
63.5	63.58	61.78*	64.47	62.95*	71.15	69.84	72.57	71.65*
64.5	60.49	57.03*	61.41	58.50*	67.50	64.69*	68.98	66.51*
65.5	57.32	52.35*	58.28	53.71	63.80	59.36	65.30	61.19*
66.5	54.32 53.98	47.52	55.13	48.93*	60.02	54.05*	61.59	55.92*
67.5	50.78	42.71	51.90	44.14	56.19	48.57*	57.72	50.56*
68.5	47.45	37.95* 37.59*	48.59	39.26*	52.26	43.10*	53.86	45.09*
69.5	44.03	32.77*	45.23	34.30	48.26	37.59	49.90	39.50*

Table 2. (cont.)

J	The 0,1 band				The 1,0 band			
	R_1	P_1	R_2	P_2	R_1	P_1	R_2	P_2
70.5	240.56	127.73	241.81	129.29	044.17	931.91*	045.86	934.00
71.5	37.02	22.60*	38.34	Nb	40.03	26.32	41.76	28.31*
72.5	33.41	17.43*	34.77	19.16*	35.86	20.53	37.62	22.53*
73.5	29.79	12.32	31.08	13.92*	31.59	14.67	33.38	16.78
74.5	26.05	07.15	27.49	08.71	27.25	08.79	29.07	10.91
75.5	22.28	01.61	23.78	03.39	22.88	02.83	24.69	04.96*
76.5	18.42	096.23	19.96	098.04	18.36	896.77	20.29	899.00
77.5	14.57	90.84*	16.11	92.63	13.82	90.77	15.73	92.95*
78.5	10.55	85.29	12.21	87.11*	09.09*	84.54*	11.13	86.85*
79.5	06.52*	79.73	08.15	81.60	04.37*	78.25*	06.54*	80.62
80.5	02.43	74.08*	04.18	76.01	21 999.60*	71.96	01.74	74.30
81.5	198.34	68.32*	00.03*	70.34*	94.83*	65.58	21 996.96*	67.79
82.5	94.11*	62.51	195.90	64.65	89.92*	59.13	92.08*	61.62
83.5	89.93	56.70	91.66	58.79*	84.95*	52.54*	Nb	55.02*
84.5	85.49	50.84	87.35	52.99	79.99*		82.29	
85.5	80.94*	44.92	82.94	47.08*	74.86*		77.11	
86.5	76.61*	38.99	78.71	41.12*	69.60		72.01	
87.5	72.05*	32.83*	74.13	35.11	64.33		66.66	
88.5	67.54*	26.74	69.60	28.98*	59.02		61.39	
89.5	62.95*	20.51	64.88		Nb		55.92*	

The B-values can be combined in the equations

$$B_v'' = 0.4321 - 0.0021\ (v'' + \tfrac{1}{2})$$

$$B_v' = 0.4001 - 0.0019\ (v' + \tfrac{1}{2}).$$

The internuclear distances are:

$$r_e'' = 1.691 \cdot 10^{-8}\ \text{cm}$$

$$r_e' = 1.757 \cdot 10^{-8}\ \text{cm}.$$

The B-values can be approximately obtained from GUGGENHEIMER's formula [7]. For a diatomic molecule with a double bond the B-value is given within 10 per cent by

$$\omega = 2.976 \cdot 10^3\,(Z_1 \cdot Z_2)^{\frac{1}{4}} \cdot \mu^{-\frac{1}{2}} \cdot r_e^{-1.23} \quad \text{and} \quad B_e = \frac{h}{8\pi^2 c\,\mu\,r_e^2}.$$

Z_1 and Z_2 are the numbers of electrons in the outer shells of the two atoms.

For the lower state $(X)^2\Delta$ the formula gives $B_e'' \sim 0.433$ ($\omega_e'' = 989$ K), in good agreement with the experimental value given above. K. S. RAO's [2] result $B_e'' = 0.6557$ shows a clear disagreement with the expected value.

Perturbations

Two small perturbations have been found, one in the level $v' = 0$ and the other in $v' = 2$.

Table 3. Wave-numbers of the 2,0 and 2,1 bands.

J	The 2,0 band				The 2,1 band			
	R_1	P_1	R_2	P_2	R_1	P_1	R_2	P_2
28.5					22 010.41	21 963.85	22 010.62*	21 965.66
29.5	22 988.48	22 940.41*	22 989.20	22 942.36	09.09*	61.14*	09.56	62.70
30.5	Nb	37.40	87.74	39.31	07.83	58.22	08.35	59.93
31.5	85.54	34.35*	86.21	36.31	06.54*	55.29	06.93	57.09
32.5	83.97	31.12*	84.67	33.24	05.09	52.29	05.67	54.05*
33.5	82.33	27.94*	83.14	Nb	03.58	49.30	04.29	51.09
34.5	80.51	24.85	81.46	26.80	01.93	46.18	02.69	48.03*
35.5	78.80	21.50	79.73	23.43	00.37	43.10	01.18	44.83
36.5	76.99	18.12	77.93	20.13	21 998.67	39.73	21 999.51	41.60
37.5	75.05	14.64	76.04	16.63	96.96*	36.42	97.67	38.28
38.5	73.07	11.07	Nb	13.05	94.97	33.04	95.91	34.88
39.5	71.00	07.43	72.13	09.48	93.13	29.58	94.07	31.42
40.5	68.83	03.74	69.97	05.76	91.12	26.06	92.08*	27.92*
41.5	66.65	899.99	67.95	02.04	89.11	22.53*	90.31	24.34
42.5	64.33	96.18	65.69	898.19	Nb	18.77	88.24	20.66
43.5	61.97	92.23	63.46	94.36	84.88	15.04	86.16	17.15*
44.5	59.51	88.25	60.37	90.53	82.56	11.24	83.14	13.38*
45.5	57.01	84.16	57.98	86.54	80.17	07.36	81.13	09.55*
46.5	54.44	80.04	55.53	81.71	77.83	03.42	78.87	04.96*
47.5	51.81	75.83	52.92	77.61	75.39	899.52	76.40	00.99
48.5	49.04	71.52	50.26	73.38	72.86	95.43*	73.95*	897.06
49.5	46.21	67.14	47.49	69.06	70.24	91.21*	71.37	92.95*
50.5	43.34	62.74	44.68	64.67	67.59	86.85*	68.77	88.79*
51.5	40.41*	58.22	41.84	60.22	64.69*	82.64*	66.09	84.54*
52.5	37.40*	53.60	38.79	55.66	62.03	78.25*	63.36	80.16*
53.5	34.35*	48.88	35.84	51.04	59.36	73.83*	60.51	75.79*
54.5	31.12*	44.22	32.62	46.31	56.24	69.31*	57.61	71.20*
55.5	27.94*	39.32*	29.43	41.59*	53.38	64.81	54.59	66.68*
56.5	24.53	34.57	26.12	36.66*	50.11	60.19*	51.58	62.13*
57.5	21.17	29.71	22.76	31.74	46.96	55.47	48.57	57.26*
58.5	17.66	24.64	19.36	26.66	43.72	50.65*	45.34	Nb
59.5	14.14	19.58	15.87	21.76	40.46		42.03	
60.5	10.55	14.39*	12.24	16.57*	37.00*		38.66	
61.5	06.83	09.06	08.61	11.28	33.73*		35.33	
62.5	03.05	03.66	04.82	06.01	30.16		31.91	
63.5	899.24	798.40	01.01	00.62	26.61		28.31*	
64.5	95.29	92.98	897.17	795.16	23.01		24.70	
65.5	91.39	87.43	93.20	89.65	19.20		21.05	
66.5	87.26	81.78	89.16	Nb	15.50		17.15*	
67.5	83.13	76.15*	85.12 (Nb)	78.33*	11.64		13.38*	
68.5	78.88	70.36	80.84	72.67	07.68*		09.55*	
69.5	74.57	64.58*	76.56	66.78	03.74		05.54	
70.5	70.18	58.73	72.22	60.94*	899.52*		01.48*	
71.5	65.78	52.67	67.87	54.95*	95.43*		897.49	
72.5	61.29	46.59	63.31	48.92	91.21*		93.14	
73.5	56.71	40.44	58.77	42.91	86.85*		88.79*	
74.5	Nb	34.27	54.14	36.66	82.64*		84.54*	
75.5	47.38	27.99	49.42	30.41	78.25*		80.16*	
76.5	42.55	21.59	44.62	24.04	73.83*		75.79*	
77.5	37.63	15.13	39.85	17.64	69.31*		71.20*	
78.5	32.73	08.68	Nb	11.06	64.62		66.68*	
79.5	27.84	02.12		04.62	59.82		62.13*	
80.5				697.90			57.26*	

Table 4. Wave-numbers of the 1,2 and 3,1 bands.

J	The 1,2 band				The 3,1 band			
	R_1	P_1	R_2	P_2	R_1	P_1	R_2	P_2
25.5		20 164.23*		20 164.88*		22 800.06*		22 802.76*
26.5		61.78*		62.44		797.31*		00.06*
27.5		59.38*		60.20*		94.54*		797.31*
28.5		56.95*	20 202.84*	57.52		91.76*		94.54*
29.5	20 202.84*	54.40*	02.00*	55.00		88.78*	22 838.07	91.76*
30.5	01.75	51.89	01.06*	52.35*	Nb	85.88	36.66*	88.78*
31.5	00.65	49.24	00.03*	49.86	22 833.80*	82.83	Nb	85.60*
32.5	199.35	46.53	198.89	47.07	32.21*	79.84	33.80*	82.57*
33.5	98.19	43.75	97.81*	44.43	30.63	76.60	32.21*	79.42*
34.5	96.91*	40.93*	96.66	41.60	28.97	73.41	30.42	76.15*
35.5	95.54*	37.95*	95.26	38.63*	27.19	70.08	28.70	72.94
36.5	94.11*	34.97	94.11*	35.87*	25.29	66.78	26.74	69.45
37.5	92.71*	31.93	92.71*	32.77*	23.42	63.24	24.92	65.93
38.5	91.13*	28.87*	91.13*	29.72	21.41	59.72	22.99	62.31
39.5	89.52*	25.74*	89.52*	26.57	19.35	56.08	20.95	Nb
40.5	87.92*	22.60*	87.92*	23.34	17.25	52.43	18.84	54.95*
41.5	86.23*	19.16*	86.23*	20.09	15.00	48.65	16.57*	51.27
42.5	84.47*	15.90	84.47*	16.79	12.71	44.82	14.39*	47.44
43.5	82.61	12.32	82.61*	13.47*	10.32	40.93	12.13	43.50
44.5	80.74	09.05	80.94*	10.04*	07.89	36.92	09.69	39.55
45.5	78.58	05.55	79.13	06.53	05.40	32.92	07.18	35.60
46.5	76.61*	01.96	77.16	03.09	02.76*	28.76	04.60	31.44
47.5	74.70	098.35	75.14	099.37*	00.06*	24.56	01.97	27.23
48.5	72.56	94.61	73.09	95.80	797.31*	20.32	799.28	22.89
49.5	70.38	90.84*	70.91*	92.06	94.54*	15.98	96.51	18.50
50.5	68.14	87.11*	68.77	88.23	91.76*	11.53	93.72	14.12
51.5	65.82	83.22	66.38*	84.36	88.78*	07.04	90.78	09.66
52.5	63.43	79.25	64.23*	80.43	85.60*	02.45	87.68	05.09
53.5	61.01	75.25	61.78*	76.43	82.57*	697.90	Nb	00.46
54.5	58.80*	71.20	59.38*	72.52	79.42*		Nb	
55.5	55.96	67.09	56.95*	68.47	76.15*		78.33*	
56.5	53.32*	62.94	54.40*	64.42				
57.5	50.69*	58.79*	51.67	60.13				
58.5	47.93	54.41	48.93*	55.87				
59.5	45.16	50.03	46.22	51.50				
60.5	42.24	45.63	43.54*	47.08*				
61.5	39.26*	41.12*	40.49	42.71				
62.5	36.38	36.60	37.59*	38.21				
63.5	33.44	32.01	34.62	33.63				
64.5	30.26	27.38	31.52	28.98*				
65.5	27.08	22.74	28.44	24.48				
66.5	Nb		25.23	19.66				

Table 5. The combination differences $\Delta_2 F''(J)$ $(v''=0)$.

J	$\Delta_2 F_1''(J)$			$\Delta_2 F_2''(J)$		
	From 2,0	From 1,0	From 0,0	From 2,0	From 1,0	From 0,0
32.5	57.60	57.47	57.40	–	56.18	56.14
33.5	59.12	59.09	59.13	57.87	58.06	57.99
34.5	60.83	60.79	60.74	59.71	59.81	59.73
35.5	62.39	62.52	62.46	61.33	61.43	61.49
36.5	64.16	64.22	64.23	63.10	63.03	63.17
37.5	65.92	65.94	65.91	64.88	64.76	64.91
38.5	67.62	67.64	–	66.56	66.62	66.65
39.5	69.33	69.33	69.32	–	68.26	68.39
40.5	71.01	71.00	71.04	70.09	70.08	70.18
41.5	72.65	72.69	72.75	71.78	71.82	71.86
42.5	74.42	74.40	74.44	73.59	73.53	73.57
43.5	76.08	76.11	76.11	75.14	75.26	75.22
44.5	77.81	77.99	77.78	76.92	76.97	77.05
45.5	79.47	79.50	79.45	78.66	78.68	78.86
46.5	81.18	81.20	81.21	80.37	80.44	80.57
47.5	82.92	82.90	82.90	82.15	82.16	82.26
48.5	84.67	84.62	84.64	83.86	83.86	83.95
49.5	86.30	86.33	86.34	85.59	85.53	85.60
50.5	87.99	88.03	87.93	87.27	87.34	87.35
51.5	89.74	89.63	89.70	89.02	89.03	89.11
52.5	91.53	91.33	91.40	90.80	90.83	90.81
53.5	93.18	93.01	93.13	92.48	92.50	92.50
54.5	95.03	94.79	94.81	94.25	94.22	94.18
55.5	96.55	–	96.50	95.96	95.93	95.87
56.5	98.23	–	98.22	97.69	97.69	97.60
57.5	99.89	99.92	99.96	99.46	99.39	99.27
58.5	101.59	101.69	101.67	101.00	101.13	101.00
59.5	103.27	103.46	103.36	102.79	102.87	102.69
60.5	105.08	105.06	105.05	104.59	104.51	104.40
61.5	106.89	106.79	106.75	106.23	106.23	106.11
62.5	108.43	108.36	108.46	107.99	107.93	107.81
63.5	110.07	110.02	110.22	109.66	109.59	109.64
64.5	111.81	111.79	111.76	111.36	111.38	111.38
65.5	113.51	113.45	–	–	113.06	113.08
66.5	115.24	115.23	115.15	114.87	114.74	114.85
67.5	116.90	116.92	116.73 116.81	116.49	116.50	116.53
68.5	118.55	118.60	118.54	118.34	118.22	118.31
69.5	120.15	120.35	120.23	119.90	119.86	120.13
70.5	121.90	121.94	121.93	121.61	121.59	121.57
71.5	123.59	123.64	123.60	123.30	123.33	123.25
72.5	125.34	125.36	125.30	124.96	124.98	124.95
73.5	127.02	127.07	126.98	126.65	126.71	126.70
74.5	128.72	128.76	128.74	128.36	128.42	128.35
75.5	–	130.48	130.40	130.10	130.07	130.08
76.5	132.25	132.11	132.05	131.78	131.74	131.59
77.5	133.87	133.82	133.76	133.56	133.44	133.30
78.5	135.51	135.57	–	135.23	135.11	135.02
79.5		137.13	137.13		136.83	136.74

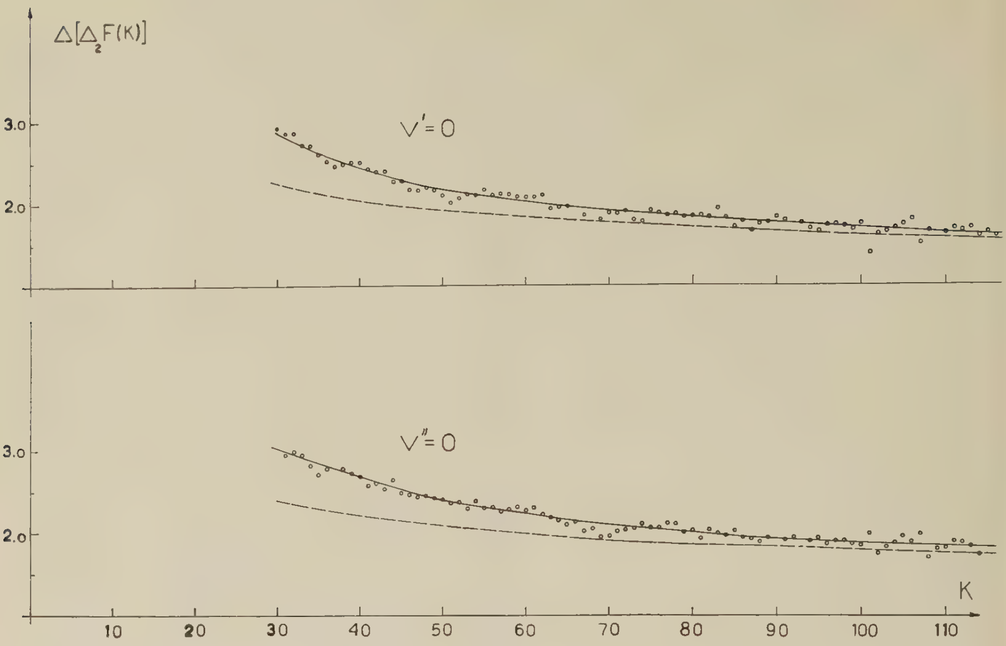

Fig. 3. $\Delta_2 F_1(K) - \Delta_2 F_2(K)$ plotted against K for $v'' = 0$ and $v' = 0$.

In $v' = 0$ the F_1-level $J = 67.5$ is perturbed. Each one of the lines $R_1(66.5)$ and $P_1(68.5)$ consists of two components, one stronger and the other rather weak. The displacement from the regular position is small, only ~ 0.2 K, but quite definite. In the F_2-level of $v' = 2$ another small perturbation has been observed round $J \sim 44.5$. No extra lines were detected.

Probably there are many more perturbations, e.g. in the levels $v' = 1$ and $v' = 3$, but the errors in the measurements possibly correspond to the magnitude of the displacements, and may therefore conceal the perturbations.

Unfortunately, the perturbations cannot be treated in greater detail as the material is so small.

The coupling constants

The magnetic coupling between $\boldsymbol{K}$ and $\boldsymbol{S}$ causes a splitting of the F_1 and F_2 levels, which, at a first approximation, increases linearly with K. The splitting constant is denoted γ. To this splitting the effect of the multiplet splitting should be added. The coupling constant A (see eq. (I)) is a measure of the strength of the coupling between the spin, $\boldsymbol{S}$, and the component of the electronic orbital angular momentum along the internuclear axis, $\boldsymbol{\Lambda}$.

In the present case it is impossible to obtain the splitting $\Delta F(K) = F_1(K) - F_2(K)$ directly, as the satellite branches have not been identified. The coupling conditions have to be studied from the second combinations, which gives a small accuracy in the determination of the constants.

The rotational energy is represented by ($\Lambda = 2$):

$$F_1(K) = B\left[(K+1)^2 - 4 - \sqrt{(K+1)^2 + Y(Y-4)}\right] + \tfrac{1}{2}\gamma \cdot K$$

$$F_2(K) = B\left[\quad K^2 \quad - 4 + \sqrt{\quad K^2 \quad + Y(Y-4)}\right] - \tfrac{1}{2}\gamma \cdot (K+1).$$

The effect of the D-values is excluded. The expression

$$\Delta[\Delta_2 F(K)] = \Delta_2 F_1(K) - \Delta_2 F_2(K) = 2\gamma + B\left[4 - \sqrt{(K+2)^2 + Y(Y-4)} - \right.$$
$$\left. - \sqrt{(K+1)^2 + Y(Y-4)} + \sqrt{K^2 + Y(Y-4)} + \sqrt{(K-1)^2 + Y(Y-4)}\right]$$

is plotted against K in Fig. 3.

The influence of Y is small for large K-values and $\Delta[\Delta_2 F(K)]$ approaches 2γ. It is difficult to determine values of the two constants, γ and Y, which describe the coupling completely. The above expressions of the rotational energy do not seem to be exactly fulfilled for the $^2\Delta$-terms of the NbO molecule. One way of correction is to adopt a variation in γ, assuming that γ decreases with increasing K-values.

As is seen from Fig. 3 the curves of $v' = 0$ and $v'' = 0$ are very similar. γ' is smaller than γ'' but the influence of the $\mathbf{S}$, $\mathbf{\Lambda}$-coupling is about the same. If one assumes the value $Y(Y-4) = 1200$ for both the upper and the lower state, $2\gamma'$ and $2\gamma''$ vary in the way shown in Fig. 3 (dotted lines). γ' varies from 1.1 K at $K \sim 30$ to 0.8 K at high K-values and γ'' is 1.2–0.9 K. The γ-values appear to be very high, but they are of the same magnitude as those of $^2\Delta$ SnH [8], $\gamma = 0.69$, and $^2\Delta$ GeH [9], $\gamma = 0.47$. Such high γ-values have never been observed for Σ-terms, which is another reason for assuming the transition to be a $^2\Delta$–$^2\Delta$.

For Y two roots are obtained

$$Y_1 = +37 \text{ and } Y_2 = -33,$$

giving $A_1'' = +16$, $A_2'' = -14$, $A_1' = +15$, $A_2' = -13$.

It is hardly possible to decide whether the terms are regular or inverted, as the branches cannot be followed to the lowest rotational quantum numbers.

It must be stressed that the values given above are only tentative. It is possible to adopt other values of the coupling constants, which gives different γ-values. As the influence of Y on $\Delta[\Delta_2 F(K)]$ cannot be separated from that of γ, it is difficult to get certain values of the constants.

Rotational analyses with treatment of the coupling conditions have been performed only for the $^2\Delta$-terms of the CH group, e.g. SnH [8], GeH [9], SiH [10] and CH [11]. In the case of CH and SiH, the coupling obeys HILL-VAN VLECK's expressions. The values of the constants are very small. A similar departure from the formulas, as was found in the present case, was observed for the $^2\Delta$-terms of GeH and SnH. SnH shows a larger disagreement than GeH. For both molecules the discrepancy could be compensated by the assumption of a decreasing value of γ. Thus it seems to me that HILL-VAN VLECK's formula does not adequately describe the coupling conditions in the $^2\Delta$-terms of heavier molecules.

It must be mentioned, though, that there is another version of the analysis giving negative values of γ'' and γ'. If the numbering is increased for F_1 by one unit and simultaneously decreased by one unit for F_2, the value $\gamma'' \sim -0.70$ is obtained. The B and D values would remain unchanged, but the A-values would be somewhat altered. This alternative has been rejected for the following reason.

It has earlier been mentioned that weak satellite branches have been observed but not identified. It is difficult to predict the intensities of the satellite branches, as the coupling case is neither case *a* nor case *b*. However, possible satellite branches are $^SR_{21}$, $^RQ_{21}$, $^QR_{12}$, $^QP_{21}$, $^PQ_{12}$ and $^OP_{12}$, and of these, $^QR_{12}$ and $^QP_{21}$ will probably be strongest. On the basis of the obtained values of γ and Y, the positions of the satellite lines could be approximately calculated. In the case of $\gamma \sim -0.70$ some of the lines fall in front of the head. Using the value $\gamma \sim 1.2$, the positions of the branches coincide well with the region of the observed weak lines. The numbering giving $\gamma \sim +1$ has therefore been chosen.

Origins of the bands

The origins of the bands were calculated in the following way:

$$4\,\sigma = R_1\,(J-1) + P_1\,(J) + R_2\,(J-1) + P_2\,(J) = 4\,\sigma_0 + 4\,(B' - B'')\,J^2 -$$

$$- 4\,(D' - D'')\,J^2\,(J+1)^2.$$

Plotting $4\,\sigma\ - 4\,\Delta\,B\,J^2 + 4\,\Delta\,D\,J^2\,(J^2+1)$ against J^2 and extrapolating to $J = 0$, $4\,\sigma_0$ was obtained as the intersection with the ordinate. The correction term involving $\Delta\,D$ has to be added, as the J-values are high. The results are given in Table 6.

Table 6. Scheme of the band origins.

v' \ v''	0	1	2
0	$21\,316.1_7$ (-0.02)	$20\,334.8_0$ (-0.02)	
1	$22\,159.8_0$ $(+0.09)$		$20\,204.8_2$ (-0.01)
2	$22\,996.9_6$ (-0.07)	$22\,015.5_4$ (-0.02)	
3		$22\,845.7_5$ $(+0.03)$	

The vibrational constants

The vibrational constants have been calculated from seven equations of the type

$$\sigma_0 (v' v'') = \sigma_e + \omega_e' (v' + \tfrac{1}{2}) - \omega_e' x_e' (v' + \tfrac{1}{2}) - \omega_e'' (v'' + \tfrac{1}{2}) + \omega_e'' x_e'' (v'' + \tfrac{1}{2})^2$$

by means of the method of least squares. The results are

$$\sigma_e = 21385.3_1 \text{ K}$$

$$\begin{array}{llll} \omega_e'' & = 989.0_3 & \omega_e' & = 850.4_8 \\ \omega_e'' x_e'' & = 3.8_3 & \omega_e' x_e' & = 3.3_7 \end{array}$$

The differences between calculated and observed values of σ_0 are given in brackets in Table 6.

ACKNOWLEDGEMENTS

I am much indebted to Professor ERIK HULTHÉN for the keen interest with which he has followed my work. I wish also to thank Dr. ALBIN LAGERQVIST for suggesting this problem to me and for his valuable help. To Dr. BENGT KLEMAN I am also most grateful for many helpful discussions.

Physics Department, University of Stockholm, February 1954.

REFERENCES

1. RAO, V. R., Ind. J. Phys. *24*, 35, 1950.
2. RAO, K. S., Nature *170*, 670, 1952.
3. RAO, V. R., and PREMASWARUP, D., Ind. J. Phys. *27*, 399, 1953.
4. HARRISON, G. R., Wavelength Tables. New York 1939.
5. KLEMAN, B., Investigations in the bandspectra of some diatomic hydrides. Dissertation, Stockholm 1953.
6. HILL, E. and VAN VLECK, J. H., Phys. Rev. *32*, 250, 1928.
7. GUGGENHEIMER, K. M., Proc. Phys. Soc. *58*, 456, 1946.
8. WATSON, W. W., and SIMON, R., Phys. Rev. *55*, 358, 1939.
9. KLEMAN, B., and Werhagen, E., Ark. f. Fysik *6*, 359, 1953.
10. ROCHESTER, G. D., Zeit. f. Phys. *101*, 769, 1936.
11. GERÖ, L., Zeit f. Phys. *118*, 27, 1941.

Tryckt den 24 augusti 1954

Uppsala 1954. Almqvist & Wiksells Boktryckeri AB

ARKIV FÖR FYSIK Band 8 nr 28

Communicated 14 April 1954 by MANNE SIEGBAHN and ERIK HULTHÉN

The rotational analysis of the α and γ systems of zirconium oxide

By A. LAGERQVIST, U. UHLER and R. F. BARROW

With 4 figures in the text

Abstract

New rotational analyses of the 0,0 bands of the α and γ systems of ZrO have been made. Earlier analyses, which led to an improbably small value of the internuclear distance, appear to be incorrect. The values of the constants derived are as follows:

State	B_0 K[1]	D_0 K	r_e cm
C	0.3927	0.26×10^{-6}	1.775×10^{-8}
A	0.4035	0.33×10^{-6}	1.752×10^{-8}
X	0.4146	0.32×10^{-6}	1.728×10^{-8}

The nature of the electronic states is discussed: it is concluded that states X and C are $^3\Delta$, state A $^3\Phi$.

Introduction

Although a considerable amount of work has been devoted to the study of the band-spectrum of zirconium oxide (see, for example, LOWATER [1] and AFAF [2]) much of which has been stimulated by the astrophysical importance of the molecule, a number of unsolved problems remain. The position is especially unsatisfactory in respect of the rotational analysis of the ZrO bands. Analyses of bands of two of the strongest systems, the blue α-bands and the red γ-bands have been put forward by LOWATER [3] and by TANAKA and HORIE [4] respectively. The results of these analyses are at the least surprising, in that they lead to a value of the internuclear distance of about 1.42 Å, which is 0.2 Å *less* than the well-established value for the *lighter* molecule TiO. Doubts about the correctness of these analyses are not lessened when they are examined in greater detail: for example, the impression is given by LOWATER's excellent print of the 0,0 band of the α-system (C–X) that she may have picked out the branches incorrectly.

We have therefore studied the rotational structure of the 0,0 bands of the α and γ systems afresh: as a result, we have come to new conclusions about these bands, which are reported in this paper.

---

[1] In this paper, K (Kayser) will be used for cm^{-1}.

Experimental

The source of light was a carbon arc, whose lower positive electrode contained pure zirconium oxide. It was run at a current of 10 to 12 A from a 220 V. D.C. supply. The spectrograms were taken in a first order of a Wood's 21 ft. concave grating (165,000 lines in all). The dispersion in the blue region is about 1.25 and in the red 1.19 Å/mm. Ilford Thin Film Half Tone and Thin Film Half Tone Panchromatic plates were used. The systems are very strong, and an exposure of 30 minutes sufficed for the blue bands: the red system was well developed after an exposure of 1 hour. Iron lines, whose wavelengths were taken from the M.I.T. Tables (1939) were used for comparison. Both systems were photographed twice, and two sets of independent measurements were made.

Structure of the bands

The appearance of the bands is shown in Figures 1 and 2.

The 0,0 band of the γ-system consists of three equidistant well-separated sub-bands, degraded to longer wavelengths. Each sub-band has two heads, obviously one R and one Q head. A P-branch could be identified in each sub-band in the regions remote from the sub-band origins. The structure in these regions is very complex, for not only is the isotope effect appreciable, but also there is overlapping by lines of the 1,1 sub-bands.

The 0,0 band of the α-system also consists of three sub-bands degraded to longer wavelengths. Each band possesses only one head, an R-head. These heads are disposed irregularly (at 21639.9, 21556.1 and 21543.2 K) and the sub-bands overlap considerably. The 0,0 sub-band at shortest wavelength (21639.9 K) consists of a long series of lines, which in LOWATER's analysis were assigned alternately as P and R branch lines. From the spacing elsewhere in the band, it appeared that it was in fact more probable that these lines constituted a single series of *overlapping* P and R lines, and this is confirmed by the analysis.

The agreement between their vibrational intervals indicates that the red and blue systems have a common lower state. It seemed convenient to start with the analysis of the red bands, as the presence of Q-branches usually helps. Plotting $\Delta Q(J)$ against J, the numbering of the Q-branch could be determined within a couple of units. It was then comparatively easy to find the first combination differences between R–Q and Q–P, which completed the analysis. The first differences agreed within the errors of the measurements; that is, no Λ-type doubling was found. The values of $\Delta_2 F'(K)$ derived from the three sub-bands are not equal: thus the upper level A cannot be a $^3\Sigma$-state. This is confirmed by the absence of satellite branches. As no Λ-type doubling could be detected, it seems probable that neither state is $^3\Pi$. The most likely view is that the red band system represents a $^3\Phi$–$^3\Delta$ transition.

The knowledge of the second combination differences of the $X\,^3\Delta$-state considerably facilitated the analysis of the blue bands. Only two branches could be identified in each sub-band, one P and one R branch: in the violet sub-band, the R and P branches happen to coincide. The second differences $\Delta_2 F''(J)$ proved to fit very well for the appropriate sub-bands. No Λ-type doubling was observed in any sub-band. The absence of strong Q-branches

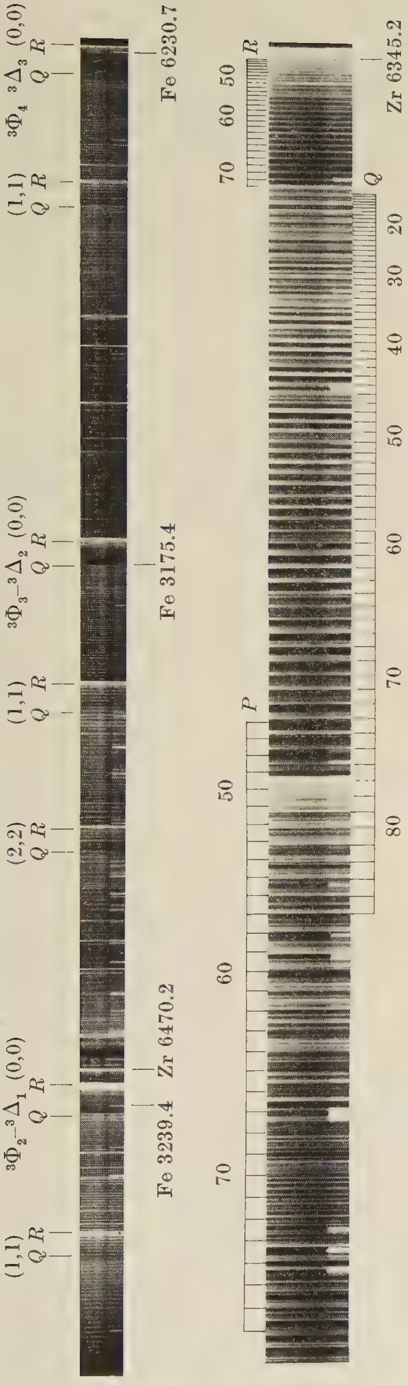

Fig. 1. *a.* The 0,0 band of $A\,^3\Phi-X\,^3\Delta$. The appearance of the reproduction in front of Zr 6470.2 Å is spoilt by a joint of the plates. — *b.* The $^3\Phi_3-^3\Delta_2$ sub-band.

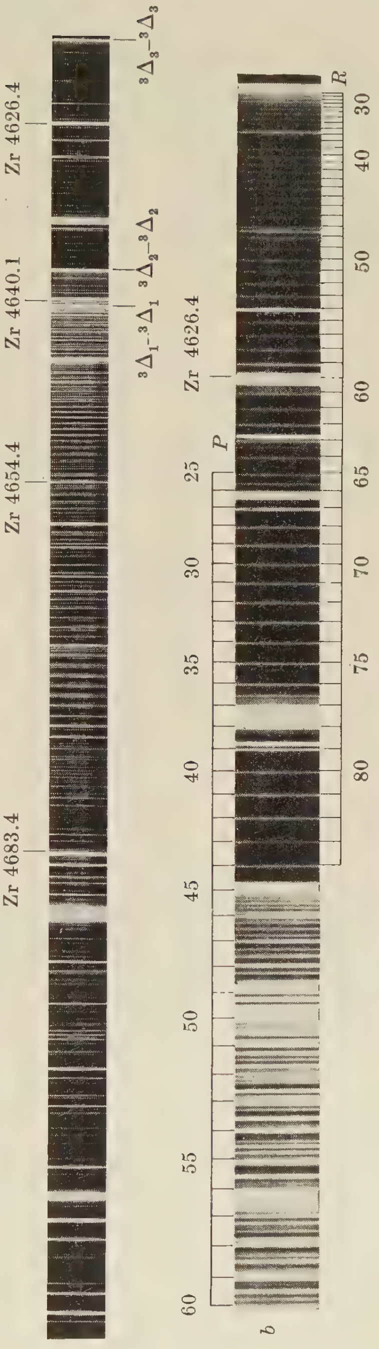

Fig. 2. *a.* The 0,0 band of $C\,^3\Delta-X\,^3\Delta$. *b.* The $^3\Delta_3-^3\Delta_3$ sub-band.

indicates $\Delta\Lambda = 0$ for the transition; taking the lower state to be $^3\Delta$, the C–X system is then a $^3\Delta$–$^3\Delta$ transition.

There is a further reason for adopting the present assignment of the eletronic transitions. A rotational analysis of the 0,0 band of the β-system B–X has recently been completed by one of us (UHLER [5]). The β-bands contain strong Q-branches, i.e. $|\Delta\Lambda| = 1$. Two of the three sub-bands exhibit considerable Λ-type doubling leading to a doubling of all branches. These facts exclude every possibility except $^3\Pi$–$^3\Delta$ for the B–X system: the sub-band in which no Λ-type doubling was detected is clearly $^3\Pi_2$–$^3\Delta_3$. Thus the state X must be a $^3\Delta$ state, which settles the assignments of the α and γ systems given above.

Rotational analysis of the γ-system

Evaluation of the constants

Tables 1–3 give the wave-numbers of the 0,0 γ-band, overlapped lines are marked with an asterisk. BUDÓ [6] gives the following expressions for the rotational term values for triplet states for any degree of spin uncoupling:

$$\begin{aligned} F_1(J) &= B_v\,[J(J+1) - \sqrt{Z_1} - 2Z_2] - D_v\,(J-\tfrac{1}{2})^4 \\ F_2(J) &= B_v\,[J(J+1) + 4Z_2] \qquad - D_v\,(J+\tfrac{1}{2})^4 \\ F_3(J) &= B_v\,[J(J+1) + \sqrt{Z_1} - 2Z_2] - D_v\,(J+\tfrac{3}{2})^4 \end{aligned} \tag{1}$$

where

$$Z_1 = \Lambda^2\,Y(Y-4) + \tfrac{4}{3} + 4\,J(J+1)$$

$$Z_2 = \frac{1}{3\,Z_1}[\Lambda^2\,Y(Y-1) - \tfrac{4}{9} - 2\,J(J+1)]$$

and

$$Y = \frac{A}{B_v}.$$

A is a measure of the strength of the coupling of the spin to internuclear axis. In the present case all states are near to Hund's coupling case *a* (or case *c*), i.e. the A-values are all large. In case *a*, the effective B-values of the sub-bands are approximately given by

$$B_{\text{eff}} = B_v\left[1 \pm \frac{2\,B_v}{A\,\Lambda}\right]. \tag{2}$$

The + sign refers to $\Sigma = +1$, the − sign to $\Sigma = -1$: these signs are correct for A positive, i.e. for normal terms. For the central sub-band ($\Sigma = 0$) the effective B-value is equal to the true B_v-value. Thus we have for normal states $B_{^3\Delta_3} > B_{^3\Delta_2} > B_{^3\Delta_1}$ and $B_{^3\Phi_4} > B_{^3\Phi_3} > B_{^3\Phi_2}$. The violet sub-band has the largest combination differences and the red sub-band has the smallest. Consequently the violet sub-band is $^3\Phi_4$–$^3\Delta_3$, the central one $^3\Phi_3$–$^3\Delta_2$, and the red one $^3\Phi_2$–$^3\Delta_1$. This assignment is entirely in agreement with the analysis of the β-system [5].

The true rotational constants have been determined graphically using the expressions

Table 1. Wave-numbers of $A\,^3\Phi_2$–$X\,^3\Delta_1$ (0,0).

J	Q_1	Q_1^{94}	R_1	P_1	J	Q_1	Q_1^{92}	Q_1^{94}	R_1	P_1
0					50	15 400.53		15 400.83	15 441.41	15 360.40
1	15 425.44*				51	399.47		399.74	41.16	58.50
2	25.21				52	98.38		98.68	40.86	56.66
3	24.95				53	97.29		97.61	40.54	54.77
4	24.65				54	96.16		96.31	40.21	52.85
5	24.34				55	95.02		95.29	39.86	50.91
6	24.04				56	93.82		94.11	39.52	48.93*
7	23.67*				57	92.65		93.09	39.09	46.99*
8	23.32				58	91.40		91.75	38.68	44.96
9	22.93				59	90.19		90.55	38.23	42.91*
0	22.57*				60	88.95		89.32	37.77	40.90
1	22.10				61	87.68		88.02	37.27	38.82
2	21.65*				62	86.37		86.76	36.78	36.67
3	21.16				63	85.05		85.48	36.25	34.64
4	20.69*				64	83.68	15 383.92	84.14	35.70	32.54
5	20.16				65	82.30		82.69	35.13	30.23
6	19.61*				66	80.93	81.09	81.35	34.52	28.11
7	19.07				67	79.49	79.66	79.93	33.91	25.89
8	18.54*				68	78.07		78.40	33.24	23.69
9	17.89				69	76.62	76.85	77.04	32.56	21.46
0	17.29				70	75.12		75.50	31.87	19.19
1	16.64				71	73.65	73.84	74.08	31.15	16.88
2	15.98				72	72.09	72.28	Zr	30.40	14.67
3	15.29*				73	70.54	70.80	71.06	29.64	12.25
4	14.61				74	68.98		69.40	28.85	09.89
5	13.87				75	67.38	67.60	67.85	28.05	07.51
6	13.15				76	65.76	65.99	66.34	27.20	05.06
7	12.37				77	64.11*	64.35	64.60	26.33	02.68
8	11.63				78	62.47	62.71	62.96	25.44*	00.25
9	10.81				79	60.76	60.92	61.21	24.52	297.75
0	09.98	15 410.16			80	59.02	59.33	59.60	23.67*	95.23
1	09.15	09.32			81	57.28	57.56	57.87	22.57*	92.76
2	08.24	08.50			82	55.55	55.79	56.15	21.65*	90.20
3	07.36	07.61			83	53.78	54.04	54.35	20.69*	87.58
4	06.42	06.64			84	51.94	52.25	52.56	19.61*	85.04
5	05.52	05.71			85	50.15	50.29	50.66	18.54*	82.45
6	04.55	Zr		15 367.85	86	48.29	48.62	48.93*	17.52	
7	03.58	03.91	15 442.11	65.99*	87	46.38	46.71	46.99*		
8	02.61		41.91	64.11*	88	44.49	44.83	45.14		
9	01.59		41.67	62.21	89	42.56	42.91*	43.22		

$$\frac{\sum_{i=1}^{3} \Delta_2 F_i(J)}{3\,(J+\frac{1}{2})} = 4\,B - 8\,D\,(J+\tfrac{1}{2})^2.$$

The effective B and D values have also been determined for every sub-level separately. Values of the rotational constants obtained from $\Delta_1 F(J)/(J+1)$

Table 2. Wave-numbers of $A\,{}^3\Phi_3$–$X\,{}^3\Delta_2$ (0,0).

J	Q_2	Q_2^{94}	R_2	P_2	J	Q_2	Q_2^{92}	Q_2^{94}	R_2	P_2
10					50	15 712.80		15 713.10	15 753.85	15 672.6
11	15 739.80				51	11.68		11.97	53.49	70.6
12	39.61*				52	10.48		10.78	53.10	68.6
13	39.27				53	09.33		09.65	52.69	66.8
14	38.98				54	08.06		08.38	52.34*	64.6
15	38.69*				55	06.83		07.20	51.82	62.7
16	38.30				56	05.57		05.96	51.35	60.6
17	37.87*				57	04.36		04.69	50.85	58.5
18	37.46				58	02.97		03.30	50.33	56.4
19	37.10*				59	01.64		02.00	49.78	54.3
20	36.67				60	00.26		00.66	49.23	52.1
21	36.33				61	698.89		699.33	48.65	50.0
22	35.82				62	97.48		97.86	48.04	47.7
23	35.17				63	96.05	15 696.25	96.54	47.41	45.5
24	34.63				64	94.58	94.76	95.03	46.70	43.3
25	34.04				65	93.10	93.33	93.54	46.04	41.0
26	33.49				66	91.61	91.76	92.04	45.34	38.7
27	32.91				67	90.07	90.36	90.56	44.61*	36.4
28	32.27				68	88.54	88.77	89.04	43.83	34.1
29	31.64				69	86 96	87.29	87.50	43.04	31.7
30	30.97				70	85.36	85.58	85.84	42.25	29.3
31	30.22				71	83.75*	84.00	84.23	41.38	26.9
32	29.55				72	82.06*	82.36	82.58	40.52*	24.5
33	28.81				73	80.43	80.67	80.97	39.61*	22.0
34	28.06				74	78.76	79.00	79.28	38.69*	19.6
35	27.27				75	77.02	77.33	77.59	37.87*	17.2
36	26.45	15 726.68			76	75.28	75.56	75.84	37.10*	14.5
37	25.61	25.82			77	head	73.78	74.10	36.15	12.0
38	24.83				78	71.72	71.99	72.30		
39	23.90	24.13			79	69.91	70.29	70.51		
40	23.02	23.28			80	68.08	68.35	68.67*		
41	22.07	22.30			81	66.20	66.50	66.80*		
42	21.15	21.46			82	64.31	64.68*	64.97		
43	20.18	20.42			83	62.41	62.70*	63.02		
44	19.25	19.51		15 683.75*	84	60.46	60.80	61.03		
45	18.20	18.49	15 755.23	82.06*	85	58.50*	58.87	59.18		
46	17.16	17.45	55.01	80.12	86	56.49*	56.83	57.19		
47	16.10	16.45	54.75	78.29	87	54.48	54.86	55.17		
48	15.04	15.32	54.47	76.42	88	52.46	52.86	53.19		
49	13.96	14.25	54.17	74.53	89	50.40	50.88	51.14		
					90	48.29	48.69	49.08		
					91	46.18	46.48	46.98		
					92	44.05	44.36	44.74		
					93	41.85	42.19	42.68		

are in close agreement with those from $\Delta_2 F(J)/(J+\frac{1}{2})$ which provides additional confirmation of the analysis.

As only the 0,0 band has been analysed no experimental value of α can be derived. An estimate of α can, however, be obtained from the expression by PEKERIS [7]

Table 3. Wave-numbers of $A\,{}^3\Phi_4$–$X\,{}^3\Delta_3$ (0,0).

J	Q_3	Q_3^{94}	R_3	P_3	J	Q_3	Q_3^{92}	Q_3^{94}	R_3	P_3
10					50	16 004.62		16 004.82	16 045.65	15 964.41*
11	16 032.30				51	03.47		03.84	45.28	62.38
12	32.07				52	02.31		02.74	44.89	60.45
13	31.73*				53	01.02			44.47	58 39
14	31.43				54	15 999.78		00.11	44.01	56.36
15	31.12				55	98.50		15 998.87	43.55	54.26
16	30.74*				56	97.21		97.54	43.06	Zr
17	30.32				57	95.93		96.34	42.54	50.03*
18	29.82*				58	94.56		95.00	42.00	47.80*
19	29.48				59	93.19	15 993.33	93.57	41.42	45.66*
20	29.01*				60	91.79	91.99	92.26	40.84	43.56*
21	28.56				61	90.37	90.58	90.84	40.20	41.41*
22	28.07*				62	88.95	89.10	89.34	39.55	39.13
23	27.55				63	87.48		87.89	38.88	36.86*
24	27.04*				64	86.00	86.25	86.44	38.21	34.63*
25	26.42				65	84.49	84.70	84.97	37.43	32.35
26	25.82				66	82.93		83.42	36.71	29.97
27	25.23				67	81.38	81.57	81.82	35.94	27.51*
28	24.61				68	79.79	80.06	80.23	35.12	25.21
29	23.88				69	78.17	78.44	78.70	34.29	22.85
30	23.20				70	76.55			33.49*	20.48
31	22.47*				71	74.89	75.17	75.41	32.57	17.92
32	21.79				72	73.23	73.43	73.75*	31.73*	15.51
33	21.02				73	71.49	71.73	72.04*	30.74*	13.02
34	20.23*				74	69.76	70.07*	70.33	29.82*	10.48
35	19.46*				75	67.99	68.27*	68.53	29.01*	08.03
36	18.61				76	66.27*	66.51	66.85	28.07*	05.39
37	17.80*				77	64.41*	64.73	65.10	27.04*	02.78
38	16.96				78	62.60		63.22	25.99	00.21
39	16.02				79	60.74	61.05	61.30	24.83	897.60
40	15.13	16 015.35			80	58.87	59.22	59.46	23.60	
41	14.15	14.35	16 048.07	15 981.05	81	56.95	57.26	57.57	22.47*	
42	13.22*		47.88	79.32	82	55.01	55.37	55.78	21.26	
43	12.20	12.48	47.64	77.53	83	53.04	53.38	53.69		
44	11.15		47.41	75.73	84	51.04	51.28	51.71		
45	10.17	10.53	47.19	73.75*	85	48.99	49.36	49.77		
46	09.10	09.40	46.89	72.04*	86	46.99	47.33	47.80*		
47	08.04	08.32	46.65	70.07*	87	44.93	45.27	45.66*		
48	06.92	07.16	46.34	68.27*	88	42.85	43.26	43.56*		
48	05.80	06.09	46.01	66.27*	89	40.70	40.94	41.41*		
					90	38.57	39.02	39.33		
					91	36.41	36.86*	37.25		
					92	34.20	34.63*	35.03		
					93	31.96	32.46	32.84		
					94	29.73	30.18	30.64		
					95	27.51*	28.04	28.40		

$$\alpha_e = \frac{6\sqrt{\omega_e\, x_e\, B_e^3}}{\omega_e} - \frac{6\, B_e^2}{\omega_e}.$$

The values of the constants are collected in Table 4.

Table 4. Summary of constants for the 0,0 bands of the systems A–X and C–X.

Values of B and D

State	$B_{0\mathrm{eff}}$ K	B_0 K	$D_{0\mathrm{eff}} \times 10^6$ K	$D_0 \times 10^6$ K
$C\,^3\Delta_3$	0.3953	0.3927	0.24	0.26
$C\,^3\Delta_2$	0.3926		0.18	
$C\,^3\Delta_1$	0.3896		0.35	
$A\,^3\Phi_4$	0.4046	0.4035	0.38	0.33
$A\,^3\Phi_3$	0.4040		0.39	
$A\,^3\Phi_2$	0.4027		0.31	
$X\,^3\Delta_3$	0.4156	0.4147	0.31	0.33
$X\,^3\Delta_2$	0.4148		0.33	
$X\,^3\Delta_1$	0.4134		0.31	

Values of α, D and r_e

State	α (PEKERIS) K	$D \times 10^6$ (KRATZER) K	$r_e \times 10^8$ cm
$C\,^3\Delta$	0.0021	0.36	1.775
$A\,^3\Phi$	0.0021	0.36	1.752
$X\,^3\Delta$	0.0021	0.32	1.728

Values of σ_0

A–X

$^3\Phi_4$–$^3\Delta_3$: 16033.85 K
$^3\Phi_3$–$^3\Delta_2$: 15741.36
$^3\Phi_2$–$^3\Delta_1$: 15426.78

C–X

$^3\Delta_3$–$^3\Delta_3$: 21631.48 K
$^3\Delta_2$–$^3\Delta_2$: 21548.46
$^3\Delta_1$–$^3\Delta_1$: 21536.36

The isotope effect

Zirconium has the following five stable isotopes $\mathrm{Zr}^{90}:\mathrm{Zr}^{91}:\mathrm{Zr}^{92}:\mathrm{Zr}^{94}:\mathrm{Zr}^{96}$ with the relative abundances 51.46 : 11.23 : 17.11 : 17.40 : 2.80 [8]. The main lines are thus due to the molecule $\mathrm{Zr}^{90}\mathrm{O}$. Lines arising from $\mathrm{Zr}^{92}\mathrm{O}$ and $\mathrm{Zr}^{94}\mathrm{O}$ have been identified in the Q-branches only. The weak lines from the isotope Zr^{91} are generally masked by the strong main lines and for this reason we have refrained from publishing the observed ones.

The isotopic shift is the sum of the vibrational and the rotational displacements. The vibrational shift can be written

$$\Delta\,\sigma_v = \sigma_v - \sigma_v^i = (1-\varrho)\,[(v'+\tfrac{1}{2})\,\omega' - (v''+\tfrac{1}{2})\,\omega''],$$

where $\varrho = \sqrt{\dfrac{\mu}{\mu_i}}$ (μ = the reduced mass of the molecule). Here no index refers to the molecule $\mathrm{Zr}^{90}\mathrm{O}^{16}$. The vibrational displacements in the 0,0 band are $+0.06_6$ and 0.12_9 K for the $\mathrm{Zr}^{92}\mathrm{O}$ and $\mathrm{Zr}^{94}\mathrm{O}$ respectively.

The rotational isotope displacement can be obtained from the expression

$$\Delta\,\sigma_r = \sigma_r - \sigma_r^i \sim (1-\varrho^2)\,[\sigma - \sigma_{\mathrm{origin}}].$$

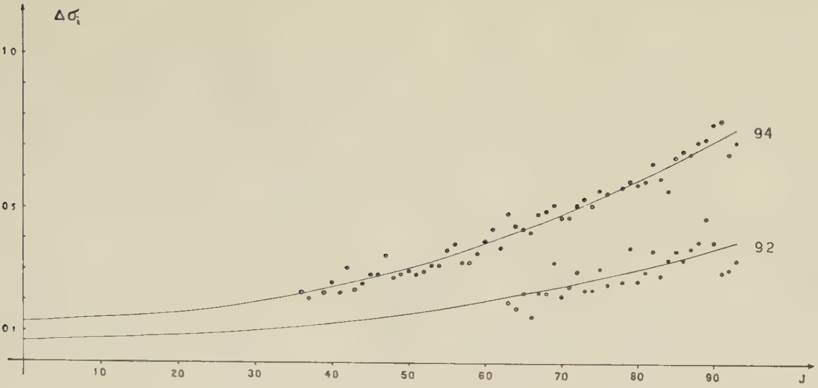

Fig. 3. The isotope shifts for the Q-lines of $^3\Phi_3$–$^3\Delta_2$.

Fig. 3 gives the observed values of the isotope shifts of the Q_2-lines. The lines correspond to the theoretical shifts using $\varrho = 0.99836$ ($Zr^{92}O^{16}$) and $\varrho = 0.99678$ ($Zr^{94}O^{16}$). The agreement between the experimental and the theoretical values is satisfactory.

Calculation of the origins

The origins of the sub-bands have been determined by plotting

$$\sigma_0 = Q(J) - (B' - B'')\, J(J+1) \quad \text{against} \quad J(J+1).$$

The intercept gives σ_0.

Rotational analysis of the α-system

Evaluation of the constants

The wave-numbers of the 0,0 band are given in Table 5. The rotational constants were determined graphically as above.

For the lower state $X\,^3\Delta$ the means of the second combination differences of the γ and α systems have been used. They agree very well.

The origins were obtained from the R and P lines according to the expression:

$$R(J-1) + P(J) - 2(B' - B'')\, J^2 = 2\,\sigma_0.$$

Plotting the left-hand side expression against J^2, $2\,\sigma_0$ is obtained as the intercept.

The Q-branches

In a $^3\Delta$–$^3\Delta$ transition weak Q-branches may be observed for the lowest J-values. The intensities of the Q-branches are proportional to the Ω-values of the sub-bands. In the present case the ratios are 1 : 4 : 9. The positions of the first Q-lines have been calculated using the B, D and σ_0 values but no sign of weak lines could be detected on the plates, even for $^3\Delta_3$–$^3\Delta_3$.

Table 5. Wave-numbers of $C\,^3\Delta - X\,^3\Delta$.

J	R_1	P_1	R_2	P_2	R_3	P_3
20					21 639.91* H	
21		21 509.00*		21 521.94		
22	21 542.20	07.18		20.16		
23	41.92*	05.33		18.35		
24	41.57*	03.41		16.62*		
25	41.14	01.43	21 554.68	14.67		21 598.86
26	40.65	499.42	54.34	12.71	39.20	97.08
27	40.14	97.35	53.93	10.79*	38.87	95.27
28	39.60	95.22	53.47	08.77	38.51	93.34
29	39.00*	93.09	52.99	06.68	38.13	91.41
30	38.33	90.89	52.47	04.56	37.72	89.41
31	37.61	88.68*	51.87	02.47*	37.31	87.42
32	36.89*	86.30*	51.27	00.23*	36.84	85.38
33	36.09*	83.98	50.58	498.15*	36.25	83.31
34	35.22	81.57	49.95*	95.78*	35.75	81.17
35	34.32*	79.15*	49.11	93.46	35.12	79.01
36	33.34*	76.65	48.31	91.07	34.49	76.83
37	32.37	74.08	47.49	88.68*	33.81	74.57
38	31.44*	71.46*	46.64	86.30*	33.06	72.31
39	30.16	68.85	45.70	83.79	32.29	69.99
40	29.10	66.17	Zr	81.21*	31.48	67.62
41	27.90	63.49	Zr	78.65*	30.69	65.20
42	26.67	60.66*	42.66	76.05	29.81	62.76
43	25.45*	57.84	41.57*	73.45	28.90	60.31
44	23.97	54.98	40.52	70.77	27.96	57.80
45	22.68	52.03	39.28	67.98*	26.96	55.28
46	21.23	49.08	38.15	65.20	25.93	52.62
47	19.73	46.06	36.89*	62.45	24.90	49.95
48	18.22*	42.99	35.65	59.59	23.75	47.28
49	16.62*	39.92	34.32*	56.73	22.59	Zr
50	15.00*	36.72	32.89	53.78	21.38	41.92*
51	13.32	33.49	31.44*	50.81	20.16	39.00*
52	11.62	30.17	30.24*	47.80	18.87	36.09*
53	09.90*	26.77	28.56	Zr	17.58	33.34*
54	08.02*	23.55	27.04	41.70	16.18*	30.24*
55	06.16*	Zr	25.45*	38.56	14.86	27.40
56	04.20*	16.68	23.93	35.43	13.43	24.40
57	02.25*	13.18	22.24	32.22	11.95	21.42
58	00.23*	09.60	20.60	29.03	10.47	18.22*
59	498.15*	06.02	18.94	25.75	08.99*	15.00*
60	96.10*	02.35	17.17	22.46	07.35	12.13
61	93.86	398.64	15.41	19.14	05.73	09.00*
62	91.62	94.96*	13.62	15.80	04.08	05.70
63	89.35	91.12	11.77	12.38	02.37	02.47*
64	87.06	87.35	09.90*	09.00	00.62	499.21
65	84.68	83.42	08.02*	05.47	598.86	95.78*
66	82.20*	79.43	06.16*	02.00	97.08	92.47
67	79.76	75.46	04.20*	398.50	95.27	89.10
68	77.25	71.42	02.25*	94.96*	93.34	[85.71]
69	74.68	67.34	00.23*	91.39	91.41	82.20*

Table 5 (cont.)

J	R_1	P_1	R_2	P_2	R_3	P_3
70	21 472.11	21 363.19	21 498.15*	21 387.80	21 589.41	21 478.65*
71	69.48*	59.04	96.10*	84.12	87.42	75.04
72	66.71	54.81	93.99	80.54	85.38	71.46*
73	Zr	50.52	91.98	76.79	83.31	67.98*
74	61.11		89.81	73.14	81.17	Zr
75	58.24		87.65	69.42	79.01	60.66*
76			85.55	65.72	76.83	56.92*
77			83.33	61.90	74.57	
78			81.21*	58.15	72.31	
79				54.33	69.99	
80				50.52	67.62	

Discussion

Earlier analyses

As mentioned in the introduction Lowater analysed the blue α-system C–X. The wave-numbers of the lines measured by her agree very well with ours. That Lowater obtained such large values of B derives from the fact that she picked out the lines for the R and P branches wrongly, choosing branches with a double interval between the lines as compared with the branches given here. She considered the transition to be a $^3\Pi$–$^3\Pi$. In such a transition the sub-bands $^3\Pi_1$–$^3\Pi_1$ and $^3\Pi_2$–$^3\Pi_2$ may contain weak Q-branches, which have lines of appreciable intensity only for low J-values. The Q-branch of $^3\Pi_2$–$^3\Pi_2$ should be more intense than that of $^3\Pi_1$–$^3\Pi_1$. Lowater asserted that she had found a Q-head in the 0,1 band of $^3\Pi_2$–$^3\Pi_2$, but not in the 0,0 band. If her analysis were correct, the Q-branch of the 0,0 band should have the same strength as that of the 0,1 band. Lowater also gives the lines corresponding only to the isotope Zr^{94}. It is remarkable that she did not give the lines corresponding to the isotope Zr^{92}. The relative abundance between $Zr^{94} : Zr^{92}$ is 17.40 : 17.11.

Tanaka and Horie have carried out an analysis of the 0,0 and 1,1 bands of the γ-system A–X. They maintained that the transition is $^3\Sigma$–$^3\Pi$. The lower state is in common with the lower state of the α-system $^3\Pi$–$^3\Pi$. It is clear that Tanaka and Horie have had several difficulties in completing this analysis, as it is based on Lowater's scheme. A major difficulty is their treatment of the Q-heads. Lowater correctly reported that each sub-band has double heads and she attributed one head to the Q-branch. These heads did not fit into the analysis of Tanaka and Horie. They mention first that these heads cannot be clearly seen on their plates—on their reproduction of "$^3\Sigma$–$^3\Pi_2$" this head is, however, very apparent—then they introduce a perturbing state responsible for these heads and for an assumed perturbation in the beginning of the band. In addition, our measurements of the lines agree poorly with those of Tanaka and Horie. Finally, the present value of r_e'' fits well with that for TiO, the preceding molecule in this group, whereas the Lowater value is incompatible with that for TiO: thus

TiO $r_e'' = 1.620 \times 10^{-8}$ cm (CHRISTY [9])
ZrO $r_e'' = 1.416$ (LOWATER [3])
ZrO $r_e'' = 1.728$ (this analysis).

Correlation between atomic and molecular states

The ground state of zirconium is a ^3F-state, the lowest excited state, ^3P, lies at about 4000 K above ^3F. The ground state of oxygen is ^3P, the nearest state lying about 16,000 K higher. It is natural to correlate $X\,^3\Delta$ with Zr (^3F) + + O (^3P). The state $A\,^3\Phi$ must also dissociate to yield the same atom pair, as Zr (^3P) + O (^3P) cannot give rise to a $^3\Phi$ molecular state. $C\,^3\Delta$ may dissociate into Zr (^3P) + O (^3P), which is assumed below, or into higher excited atom pairs. The irregular term $C\,^3\Delta$ cannot be explained as belonging to Hund's coupling case *a*; it seems as if it approaches Hund's coupling case *c*.

The dissociations energies

The dissociation energies have been calculated from the formula

$$D_e = \frac{\omega_e^2}{4\,\omega_e\,x_e}.$$

The values obtained with this method are often too high, but are in this case the only ones available. AFAF's [2] values of the vibrational constants have been used. The values of the dissociation energies are as follows:

$C\,^3\Delta$ $D_C = 51{,}000$ K. $= 6.3$ e.V.
$A\,^3\Phi$ $D_A = 54{,}000$ $= 6.7$
$X\,^3\Delta$ $D_X = 66{,}000$ $= 8.2$

From the term level scheme (Fig. 4) it is possible to determine the value of the energy of dissociation of the ground state D_X. Using $D_A = 54{,}000$ K we obtain $D_X = 70{,}000$ K, using $D_C = 51{,}000$ K we obtain $D_X = 69{,}000$ K. The mean value of D_X is 68,000 K = 8.4 e.V.

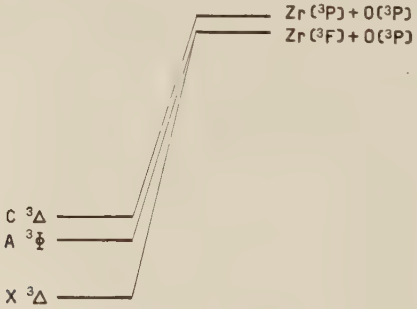

Fig. 4. Atomic and molecular states.

Physics Department, University of Stockholm. April 1954.
Physical Chemistry Laboratory, University of Oxford.

REFERENCES

1. LOWATER, F., Proc. Phys. Soc. *44*, 51, 1932.
2. AFAF, M., Proc. Phys. Soc. *63*, 1156, 1950.
3. LOWATER, F., Phil. Trans. Roy. Soc. London, A, *234*, 355, 1935.
4. TANAKA, T. and HORIE, T., Proc. Phys.-Math. Soc. Japan, *23*, 464, 1941.
5. UHLER, U., Ark. f. Fysik Bd. *8*, 295, 1954.
6. BUDÓ, A., Zeit. f. Phys. *96*, 219, 1935.
7. PEKERIS, C. L., Phys. Rev. *45*, 98, 1934.
8. HOLLANDER, J. M., PERLMAN, I. and SEABORG, G. T., Rev. Mod. Phys. *25*, 469, 1953.
9. CHRISTY, A., Phys. Rev. *33*, 701, 1929.

Tryckt den 24 augusti 1954

Uppsala 1954. Almqvist & Wiksells Boktryckeri AB

ARKIV FÖR FYSIK Band 8 nr 29

Communicated 14 April 1954 by MANNE SIEGBAHN and ERIK HULTHÉN

The rotational analysis of the β-system of zirconium oxide

By ULLA UHLER

With 2 figures in the text

Abstract

The 0,0 band of the system β $(B\text{–}X)$ of zirconium oxide has been made the subject of a rotational analysis. Λ-type doubling was observed in two of the three sub-bands and the transition was found to be $^3\Pi\text{–}^3\Delta$. The constants derived are:

$B\,^3\Pi$	$B_0' = 0.4016$ K[1]	$D_0' = 0.38 \times 10^{-6}$ K	$r_e' = 1.755 \cdot 10^{-8}$ cm
$X\,^3\Delta$	$B_0'' = 0.4145$	$D_0'' = 0.30 \times 10^{-6}$	$r_e'' = 1.728 \cdot 10^{-8}$

Introduction

In 1932 LOWATER [1] published a vibrational analysis of the visible part of the band spectrum of zirconium oxide. She divided the extensive spectrum into three systems, namely the α-system $(C\text{–}X)$, the β-system $(B\text{-}X)$ and the γ-system $(A\text{–}X)$. Rotational analyses have earlier been performed of the α and γ systems by LOWATER [2] and TANAKA and HORIE [3] respectively. The rotational constants derived were unexpectedly large and their analyses appear to be incorrect. A new rotational analysis of the systems α and γ has recently been carried out by LAGERQVIST, UHLER and BARROW [4], giving entirely different, but acceptable, values of the constants.

LOWATER's vibrational analysis showed that the β-system probably has the lower state in common with α and γ and the present analysis confirms this conclusion. She regarded the transition as $^3\Sigma\text{–}^3\Pi$. My rotational analysis of the 0,0 band of the β-system shows, however, that the system is due to a $^3\Pi\text{–}^3\Delta$ transition. The significant observation is that two of the three sub-bands show Λ-type doubled branches.

Zirconium has five isotopes, Zr^{90}, Zr^{91}, Zr^{92}, Zr^{94} and Zr^{96} in the relative abundances 51.46 : 11.23 : 17.11 : 17.40 : 2.80 [5]. The analysis refers to the most abundant molecule $Zr^{90}O^{16}$. Weak lines of the molecules $Zr^{92}O^{16}$ and $Zr^{94}O^{16}$ can be seen in the spectrum at the expected positions but they have been omitted from the analysis.

---

[1] Note: In this paper, K (Kayser) will be used for cm^{-1}.

Experimental

A carbon arc fed with zirconium oxide was used as source of light. The current was 10–12 A from 220 V D.C. output. The spectrum was photographed in a 21 ft. concave grating (165,000 lines) with a dispersion in the yellow-green region of 1.22 Å/mm in a first order. Ilford Thin Film Half Tone Panchromatic plates were used. An exposure time of one hour and a half was sufficient. Iron lines served for comparison: their wave-lengths were taken from HARRISON's Wavelength Tables [6].

The structure of the bands

Fig. 1 shows the appearance of the 0,0 band of the β-system (B–X). The band structure is very dense and moreover the 0,0 bands are overlapped by other bands, some of which belong to the α-system. The bands of the β-system are degraded to the red.

The red sub-band, which is the simplest one, has two heads, one R and one Q head. Three branches could be identified, namely an R, a P and a Q branch. An approximate numbering of the Q-branch was found by plotting $\Delta Q(J)$ against a relative J-numbering. As the first combination differences were known from the analysis of the γ-system [4] it was comparatively easy to find the connected Q–R and Q–P lines.

The central sub-band shows three heads, one weak Q-head and two narrow, distinct R-heads. Six branches were identified, two R, two P and two Q branches. The combination differences known for the lower central state proved to fit very well on both sets of R, P and Q branches. The doubling of all branches is obviously due to Λ-type doubling. The fact that only one Q-head can be seen indicates that the doubling is zero for $J = 0$ and then rapidly increases. A weak perturbation has been found in the upper state at $J = 55$ (the c-level only).

The violet sub-band consists of six branches: double R, P and Q branches. Two R-heads can be seen, the splitting of which is larger than in the central sub-band. It is difficult to decide whether there are two Q-heads or only one as there are atomic lines in the neighbourhood. The remaining combination differences of the lower state agreed very well with the ones obtained from this sub-band.

The Λ-type doubling in a $^3\Pi_2$-state is expected to be very small, while $^3\Pi_1$ shows a splitting proportional to $J(J+1)$. The splitting of $^3\Pi_0$ should be largest and independent of J to a first approximation. The Λ-type doubling of a $^3\Delta$-state is negligible. These conditions seem to be fairly well fulfilled in the present case. Thus a $^3\Pi$ state must be either the upper or lower state. Strong Q-branches give $|\Delta\Lambda| = 1$, i.e. the other state must be either $^3\Sigma$ or $^3\Delta$. The number of branches and the doubling of R, Q and P branches in the red sub-bands give $^3\Delta$ as the only possibility. From the character of the Λ-type doubling described above one can thus conclude that the B–X system is either a $^3\Delta$–$^3\Pi$ or a $^3\Pi$–$^3\Delta$ transition. The band systems α (A–X) and γ (C–X) have the lower state in common with the β-system (B–X). No analogous Λ-type doubling exists in those bands. Consequently it is natural to assume the lower state to be a $^3\Delta$-state and the transition B–X to be $^3\Pi$–$^3\Delta$.

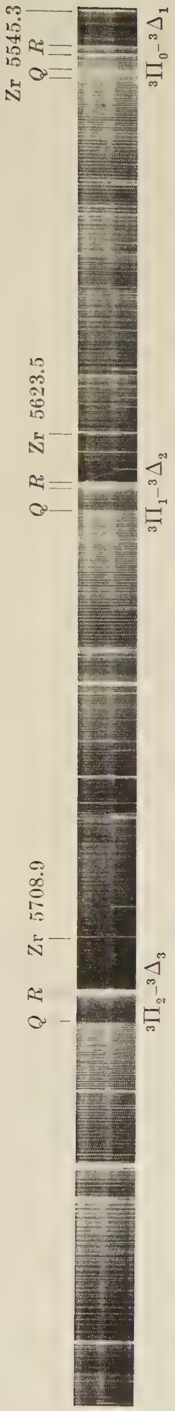

Fig. 1 *a*. The 0,0 band of the β-system.

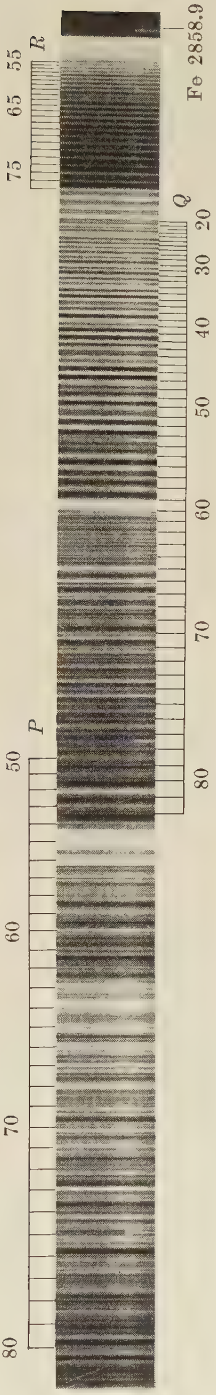

Fig. 1 *b*. The $^3\Pi_2 - ^3\Delta_3$ sub-band.

Rotational analysis

Evaluation of the constants

The expressions for the rotational term-values for any degree of spin uncoupling have been given by Budó [7].

$$\begin{aligned} F_1(J) &= B_v[J(J+1)-\sqrt{Z_1}-2Z_2]-D_v(J-\tfrac{1}{2})^4 \\ F_2(J) &= B_v[J(J+1)+4Z_2] \qquad -D_v(J+\tfrac{1}{2})^4 \\ F_3(J) &= B_v[J(J+1)+\sqrt{Z_1}-2Z_1]-D_v(J+\tfrac{3}{2})^4 \end{aligned} \qquad \text{(I)}$$

where

$$Z_1=\Lambda^2 Y(Y-4)+\frac{4}{3}+4J(J+1)$$

$$Z_2=\frac{1}{3Z_1}\left[\Lambda^2 Y(Y-1)-\frac{4}{9}-2J(J+1)\right]$$

and

$$Y=\frac{A}{B_v}.$$

A is a measure of the strength of the coupling of the spin to the internuclear axis.

If the triplet state approaches Hund's case a, i.e. the A-value is large, the effective B-values of the sub-states are approximately given by

$$B_{\text{eff}}=B_v\left[1\pm\frac{2B_v}{A\Lambda}\right]. \qquad \text{(II)}$$

The positive sign refers to $\Sigma=+1$, the negative sign to $\Sigma=-1$ if A is positive. For the central sub-band ($\Sigma=0$) the effective B-value is equal to the true B_v-value.

The wave-numbers of the three sub-bands are given in Tables 1–3. Owing to the dense structure of the bands it has not been possible to follow the R-lines much further than to the Q-heads. Nor have the R-lines been identified before the turn of the head. Consequently the bands analysed are rather short. Furthermore, as may be seen from the tables, the three sub-bands are not analysed for the same J-values. The overlapping region is very small and for this reason it was necessary to calculate the true B-value as a mean of the separate B_{eff}-values instead of from a mean of the combination differences.

The combination differences of the lower state agree very well with the ones of the α and γ-systems [4], as is seen from Table 4.

Plotting $\frac{\Delta_2 F(J)}{J+\frac{1}{2}}$ against $(J+\frac{1}{2})^2$, one obtains a straight line, giving $4B_{\text{eff}}$ as the intersection with the ordinate. The slope of the line is $8D_{\text{eff}}$.

Table 1. Wave-numbers of $^3\Pi_2$–$^3\Delta_3$ (The 0,0 band).

J	Q_3	J	R_3	Q_3	P_3
13	17 464.56	48	17 482.61	443.02	17 404.25
14	64.28	49	82.36	42.02	02.49
15	63.97*	50	82.13	41.03	00.64
16	63.72	51	81.86	39.89	398.82
17	63.37	52	81.52	38.84	97.00
18	62.96	53	81.24	37.75	94.90
19	62.67*	54	80.90	36.56	92.93
20	62.31	55	80.52	35.38	90.97
21	61.86	56	80.14	34.29	88.97
22	61.44*	57	79.73	33.01	87.02
23	61.03	58	79.31	31.77	84.94
24	60.52	59	78.87	30.52	82.91
25	60.06	60	78.40	29.27	80.95
26	59.55	61	77.88	27.94	78.77
27	59.06	62	77.38	26.67	76.70
28	58.45	63	76.74	25.92	74.51
29	57.92	64	76.17	23.83	72.24
30	57.33	65	75.55	22.42	70.06
31	56.73	66	74.91	21.02	67.84
32	56.05	67	74.23	19.47	65.65
33	55.44	68	73.54	18.04	63.50
34	54.72	69	72.82	16.52	61.06
35	54.07	70	72.04	15.01	58.68
36	53.36	71	71.25	13.37	56.38
37	52.56	72	70.43	11.80	54.01
38	51.81	73	69.58	10.20	51.59
39	51.09	74	68.68	08.56	49.11
40	50.35	75	67.80	06.83	46.59
41	49.54	76	66.89	05.11	44.13
42	48.57	77	65.90	03.40	41.60
43	47.66	78	64.93	01.67	39.08
44	46.86	79	63.97*	399.78	36.45
45	45.92	80	62.76*	98.01	33.79
46	44.99	81	61.44*	96.12	31.19
47	44.02	82		94.25	28.55
		83		92.34	25.81
		84		90.42	
		85		88.40	

The B_{eff} and D_{eff} values may also be calculated from the first differences:

$$\frac{\Delta_1 F(J)}{J+1} \sim 2B - 4D(J+1)^2.$$

Table 2. Wave-numbers of $^3\Pi_1$–$^3\Delta_2$ (The 0,0 band).

J	R_{2c}	R_{2d}	Q_{2c}	Q_{2d}	P_{2c}	P_{2d}
19				17 740.69*		
20			17 740.69*	40.25*		
21			40.25*	39.88*		
22			39.88*	39.29*		
23			39.29*	38.77*		
24			38.77*	38.27*		
25			38.27*	37.64*		
26			37.64*	37.09*		
27			37.09*	36.41*		
28			36.41*	35.78*		
29			35.78*	35.14*		
30			35.14*	34.42*		
31			34.42*	33.65*		
32			33.65*	32.86*		
33			32.86*	32.09*		
34			32.09*	31.12		
35			31.28	30.00		
36			30.45	28.92		
37			29.55	28.09		
38			28.72	27.06		
39		17 757.94	27.78	26.11		
40		57.59	26.85	25.02		
41		57.32	25.86	23.90*		
42		57.13	24.85	22.78*		17 688.90*
43		56.76*	23.90*	21.68*		87.10*
44		56.45	22.78*	20.61*		85.29*
45		56.18*	21.68*	19.40*		83.33*
46		55.74*	20.61*	18.24*		81.28
47		55.30*	19.40*	17.03*		79.30
48		54.92*	18.24*	15.80*		77.24
49		54.53	17.03*	14.52*	17 677.62	75.26
50	17 756.76*	54.10*	15.80*	13.31*	75.69	73.14
51	56.18*	53.52*	14.52*	11.97*	73.73	71.08
52	55.74*	52.93*	13.31*	10.62*	71.67	69.01
53	55.30*	52.41	11.97*	09.31	69.60	66.83
54	54.92*	51.78	10.61*	07.91*	67.50	64.64
55	54.10*	51.15	09.62	06.45*	65.37	62.44
56	53.52*	50.40	07.91*	04.74	63.35	60.03
57	52.93*	49.49	06.45*	03.14	60.88	57.68
58	52.14	48.50	05.05	01.52	58.60	55.25
59	51.44	47.52*	03.57	699.84	56.36	52.73
60	50.75	46.66*	02.02	98.10	54.06	50.35
61	50.04	45.71	00.50	96.39	51.74	47.76
62	49.15	44.60	698.89	94.54	49.38	45.15
63	48.37	43.59*	97.28	92.71	46.96	42.45
64	47.60*	42.41*	95.65	90.84	44.56	39.99

Table 2 (cont.)

J	R_{2c}	R_{2d}	Q_{2c}	Q_{2d}	P_{2c}	P_{2d}
65	746.76*		694.02	688.90*	642.07	637.27
66	45.92		92.33	87.10*	39.58	34.34
67	44.79		90.59		37.10	
68	43.82*		88.90*		34.58	
69	42.79*		87.10*		31.99	
70	41.77*		85.29*		29.51	
71	40.69*		83.33*		26.79	
72	39.62		81.41		24.14	
73			79.59*		21.48	
74					18.80	

The values of both methods agreed, which confirms the analysis.

The true B_v and D_v values are obtained as a mean of the constants of the three sub-bands.

The following values were obtained.

$$\begin{array}{llll}
 & {}^3\Pi_2 & B_{\text{eff}}=0.4058\ \text{K} & D_{\text{eff}}=0.39\times10^{-6}\ \text{K} \\
 & {}^3\Pi_{1c} & B_{\text{eff}}=0.4036 & D_{\text{eff}}=0.53\times10^{-6} \\
B\,{}^3\Pi & {}^3\Pi_{1d} & B_{\text{eff}}=0.4027 & D_{\text{eff}}=0.54\times10^{-6} \\
 & {}^3\Pi_0 & B_{\text{eff}}=0.3960 & D_{\text{eff}}=0.24\times10^{-6} \\
 & & B_v\ =0.4016 & D_v\ =0.38\times10^{-6} \\
 & {}^3\Delta_3 & B_{\text{eff}}=0.4154 & D_{\text{eff}}=0.24\times10^{-6} \\
X\,{}^3\Delta & {}^3\Delta_2 & B_{\text{eff}}=0.4145 & D_{\text{eff}}=0.29\times10^{-6} \\
 & {}^3\Delta_1 & B_{\text{eff}}=0.4136 & D_{\text{eff}}=0.37\times10^{-6} \\
 & & B_v\ =0.4145 & D_v\ =0.30\times10^{-6}
\end{array}$$

The values of B_v'' and D_v'' for $X\,{}^3\Delta$ agree excellently with the ones obtained from the α and γ systems [4]. The individual D''-values are in poorer agreement, no doubt because of the shortness of the analysed branches.

An estimate of α can be obtained from PEKERIS' formula [8]

$$\alpha=\frac{6\sqrt{\omega_e x_e B_e^3}}{\omega_e}-\frac{6\,B_e}{\omega_e}.$$

This gives $\alpha'=0.0023$ and $\alpha''=0.0021$ using LOWATER's [1] vibrational constants.

The internuclear distances are $r_e'=1.755\cdot10^{-8}$ cm and $r_e''=1.728\cdot10^{-8}$ cm for the upper and lower state respectively.

The relative magnitude of the B-values of the sub-levels ($B_{^3\Pi_2}>B_{^3\Pi_1}>B_{^3\Pi_0}$) indicates that $B\,{}^3\Pi$ like $X\,{}^3\Delta$ is regular (compare [4]).

Table 3. Wave-numbers of $^3\Pi_0$–$^3\Delta_1$ (The 0,0 band).

J	R_{1c}	R_{1d}	Q_{1c}	Q_{1d}	P_{1c}	P_{1d}
15			17 989.43			
16			88.86*			
17			88.33*			
18			87.77*			
19			atomic line			
20			86.34*			
21			85.52*			
22			84.70*			
23			83.90*			
24			83.08			
25			82.16*			
26			81.27*			
27			80.34	17 984.40*		
28	18 002.35		79.37	83.48		
29	02.11*	18 006.14	78.36	82.48		17 959.40*
30	01.85	05.81	77.31	81.45	17 953.74*	57.63*
31	01.54*	05.47	76.19	80.19	51.73*	55.83
32	01.21	05.09	75.15	78.98	49.86*	53.74*
33	00.87*	04.69	73.98*	77.81	47.86*	51.73*
34	00.50	04.24	72.84*	76.54	45.99	49.71
35	00.12*	03.71	71.65	75.37	43.91	47.76*
36	17 999.70	03.22	70.39	73.98*	42.05	45.58*
37	99.19	head	69.13	72.72*	39.84*	43.55*
38	98.72*	02.11*	67.87	71.26	37.81*	41.33
39	98.12*	01.54*	66.53	69.93	35.65*	39.09
40	97.61	00.87*	65.06	68.52	33.55*	36.79
41	96.88	00.18	63.74	67.04	31.33	34.60
42	96.33*	17 999.54	62.40*	65.54	29.15	32.37
43	95.70	98.81*	60.93*	64.09	26.83	30.08
44	94.98	98.12*	59.40*	62.40*	24.59	27.81
45	94.30	97.29	57.89	60.93*	22.36	25.47
46	93.59	96.41*	56.40	59.40*	20.03	22.97
47	92.74*	95.56	54.79	57.70*	17.60	20.64
48	91.93*	94.75	53.20	56.08	15.27	18.21
49	91.00*	93.78	51.58	54.33	12.81*	15.76
50	90.20	92.82*	49.86*	52.62	10.38	13.18
51	89.26	91.93*	48.20	50.87	07.91*	10.60
52	88.33*	90.94*	46.55	49.12	05.48*	07.97*
53	87.31	89.96*	44.76	47.28	02.88*	05.48*
54	86.34*	88.86*	42.94	45.50*	00.38*	02.88*
55	85.43*	87.77*	41.16	43.55*	897.73*	00.38*
56	84.40*	86.67	39.32	41.73	95.07	897.73*
57	83.25*	85.52*	37.44	39.84*	92.41	94.85
58	82.16*	84.40*	35.59*	37.81*	89.78	92.04
59		83.25*	33.55*	35.87	87.04	89.30
60				33.91	84.32	86.56

Table 4. Values of $\Delta_2 F''(J)$.

System Sub-band	α Red	β Blue	γ Red	α Central	β Central	γ Central	α Blue	β Red	γ Blue
J									
45	74.89	75.05		75.32	(75.17)		75.34		75.37
50	83.13	83.14	83.17	83.51	(83.45)	83.48	83.59	83.54	83.63
55	91.34	91.27	91.28	91.61	91.66	91.72	91.78	91.93	—
60	99.51		99.41	99.80	99.73	99.74	99.99	100.10	100.01
65	107.63		107.59	107.90	108.05	107.96	108.15	108.33	108.24
70	115.64		115.68	116.11	(116.00)	116.09	116.37	116.44	116.37
75			123.79	124.09		124.11	124.25	124.55	124.43

The Λ-type doubling

The Λ-type doubling expected theoretically for a $^3\Pi$-term (Hund's case *a*) has been described above. For $^3\Pi_2$ it is usually small, for $^3\Pi_0$ constant and for $^3\Pi_1$ it is proportional to $J(J+1)$.

No doubling has been observed in the sub-band $^3\Pi_2$–$^3\Delta_3$. The Λ-type doubling in a $^3\Delta$-term is negligible. The splitting in $^3\Pi_1$ is derived from

$$\Delta\sigma_{cd} = Q_{2c}(J) - Q_{2d}(J) = (B_c - B_d)\, J(J+1).$$

The plot of $\Delta\sigma_{cd}$ against $J(J+1)$ (see Fig. 2) is roughly linear, passes through the origin and has a slope of 0.0010_6. This value of $B_c - B_d$ is in good agreement with the one obtained directly from the *B*-values (0.0009). As no $^3\Sigma$-term combining with the $^3\Pi$-state is known it is impossible to get the symmetry; the notations *c* and *d* of the two sets of levels are chosen arbitrarily.

According to the theoretical treatment the splitting in $^3\Pi_0$ (case *a*) should be constant to a first approximation. This is not the case here. The splitting decreases with increasing *J*-values. One possible explanation is that the $^3\Pi$-state does not belong to pure case *a* but is an intermediate case *a*–*b* for higher *J*-values. A confirmation of this view, is that the B'_{eff}-values differ from one another more than the B''_{eff}-values.

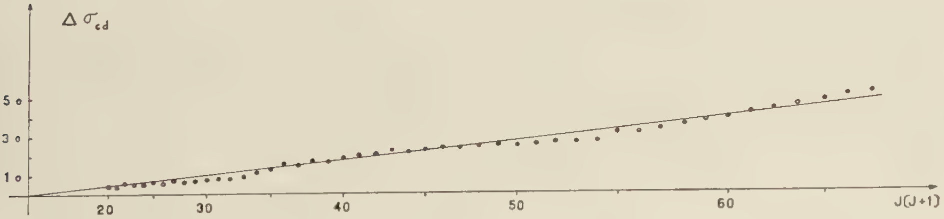

Fig. 2. The Λ-type doubling of $^3\Pi_1$ as a function of $J(J+1)$.

The origins of the bands

The origins of the sub-bands are obtained as

$$Q(J)_{\text{mean}} = \sigma_0 + (B' - B'')\,J(J+1).$$

Plotting $Q(J)_{\text{mean}}$ against $J(J+1)$, one obtains σ_0 as the intersection with the ordinate.

The results are:

$^3\Pi_2 - {}^3\Delta_3 \qquad \sigma_0 = 17466.3_0$ K
$^3\Pi_1 - {}^3\Delta_2 \qquad \sigma_0 = 17745.2_5$
$^3\Pi_0 - {}^3\Delta_1 \qquad \sigma_0 = 17995.8_5$.

Arrangements of the sub-levels

It is not possible to obtain accurate values of the coupling constants A' and A''. Assuming the ground state to obey Budó's formula, one obtains an approximate A-value for $X\,^3\Delta$ (eq. II).

The value is:

From the β-system : $A_X \sim 190$
From the α and γ systems [4]: $A_X \sim 160$.

From the ground state multiplet splitting ($A_X \cdot \Lambda \sim 350$ K) and the σ_0-values approximate values of the upper coupling constants can be derived. Alternatively A_A, A_B and A_C can be estimated from the difference of the B_{eff}-values (eq. II). The agreement between the values given in Table 5 is poor. Thus no reliable values of the coupling constants can be obtained. Besides, no significant A-values are derivable as the sub-band intervals are irregular. Especially in the case of $C\,^3\Delta - X\,^3\Delta$ the deviations from Budo's formulas are considerable.

Table 5.

State	A (from σ_0)	A (from ΔB)
$C\,^3\Delta$	~200	55
$B\,^3\Pi$	~ 85	65
$A\,^3\Phi$	~220	115
$X\,^3\Delta$	(175)	175

Physics Department, University of Stockholm. April 1954.

REFERENCES

1. Lowater, F., Proc. Phys. Soc. *44*, 51, 1932.
2. Lowater, F., Phil. Trans. Roy. Soc. London, A, *234*, 355, 1935.
3. Tanaka, T. and Horie, T., Proc. Phys.-Math. Soc. Japan, *23*, 464, 1941.
4. Lagerqvist, A., Uhler, U. and Barrow, R. F., Ark. f. Fysik, Bd. *8*, 281, 1954.
5. Hollander, J. M., Perlman, I. and Seaborg, G. T., Rev. Mod. Phys. *25*, 469, 1953.
6. Harrison. G. R., Wavelength Tables. New York, 1939.
7. Budó, A., Zeit. f. Phys. *96*, 219, 1935.
8. Pekeris, C. L., Phys. Rev. *45*, 98, 1934.

Tryckt den 25 augusti 1954

Uppsala 1954. Almqvist & Wiksells Boktryckeri AB

ARKIV FÖR FYSIK Band 8 nr 30

Communicated 14 April 1954 by MANNE SIEGBAHN and BENGT EDLÉN

Photo-electric mass determinations in nuclear emulsions

Part II. A new correction for local variations in the emulsion with a report on the photo-electric identification of K-particles

By STEN VON FRIESEN

With 2 figures in the text

Introduction

The photo-electric method of determining the mass of charged particles brought to rest in nuclear emulsions has been very thoroughly examined and several improvements have been introduced. In part I of this paper, KRISTIANSSON[1] has studied the accuracy with which the masses can be measured in an emulsion of average quality. He has found that the mass of a particle with a residual range of 4000–5000 microns of approximately protonic mass can be determined with a standard error of 10 per cent. A large part of this error seems to be due to extended irregularities in the emulsion over regions which are large compared to the measured distance along the tracks. A complete elimination of the irregularities would reduce the standard error of a mass-determination to 5 to 6 per cent. Part II of the paper deals with an examination of the possibility to eliminate the influence of the extended irregularities. It also gives an account of the finding, in the course of this work, of heavy mesons which come to rest in the emulsion without any visible secondaries.

The new correction

The emulsion used for this investigation is a 400 micron Ilford G 5 flown near Lund. It reached 34,000 metres, and remained above 29,000 metres for 7 hours. The measurements were made in a plate which seems to have been at one of the corners of the poured region, when the plates were made. This can be seen in Fig. 1 where the variation of the thickness of the emulsion is shown. The lower left hand corner is nearly 20 per cent thinner than the diagonally opposite part of the emulsion. The general background is higher than that of KRISTIANSSON's plates which belong to the 1952 Sardinian plates. The extended irregularities are more pronounced. The usual corrections for depth in the emulsion are very similar in both cases, thus indicating that the development has been essentially the same in both batches.

The plate has been scanned for proton-like tracks stopping in the emulsion. All tracks measured lie between the depths of 40 and 370 microns in the undeveloped

---

[1] K. KRISTIANSSON, Ark. f. Fysik *8*, 311, 1954.

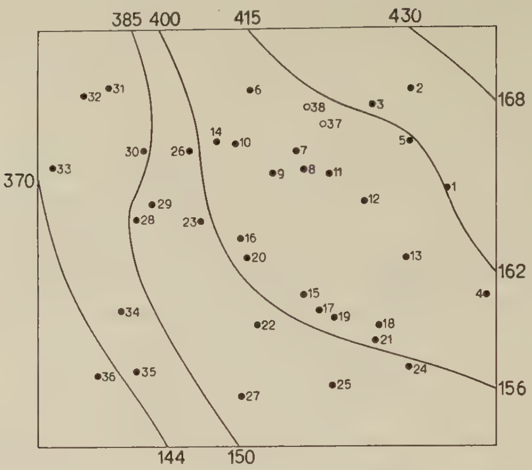

Fig. 1. Map of the plate showing the relative position of the tracks. The high numbers at the edges give the thickness of the emulsion before development, the lower values the thickness after development.

emulsion. A length of 5000 microns has been used when possible. The lower limit has been 3000 microns and the average value 4400 microns. The masses have been measured by means of the method which has been published in an earlier paper[1], with certain modifications described in Parts I[2] and III[3] of the present paper.

The distribution of the mass values was unusually wide ($\sigma = 14$ per cent), and there were certain regions of the plate where the masses were high. Such apparently high mass values must be due to larger grains in the developed emulsion or increased sensitivity in those regions. It is reasonable to assume that the corresponding effect would appear in an investigation of the electron background. If this can be shown to be true, a study of the local properties of the background would then enable us to apply a correction to the mass values of particles which we measure in that region.

In order to study the background, the transparency of the plate and the thickness of the emulsion have been determined. From the data obtained an absorption coefficient k has been calculated according to the formula $I = I_0 \cdot e^{-kx}$, where I_0 and I are the light intensity before and after the passage through x cm of emulsion. The transparency was studied by placing the plate on the same microscope as that used for the mass measurements. The slit was replaced by a circular aperture, and a suitable objective gave a field of view with a diameter of 1.7 millimetres in the plane of the emulsion. The light falling on the photo-multiplier tube gave rise to a photo-current, which was amplified and recorded on a Speedomax recorder, as described in Part III. The stage was driven slowly past the objective by a synchronous motor. The plate was scanned along lines 2 millimetres apart. The thickness of the emulsion was measured very carefully by means of the depth-focussing adjustment of the microscope with a 100 power oil immersion objective. Measurements were made over the plate in a grid with 2 millimetre meshes. Since the thickness of

---

[1] S. v. FRIESEN and K. KRISTIANSSON, Ark. f. Fysik *4*, 505, 1952.

[2] K. KRISTIANSSON, l.c.

[3] S. v. FRIESEN and L. STIGMARK, Ark. f. Fysik *8*, 121, 1954.

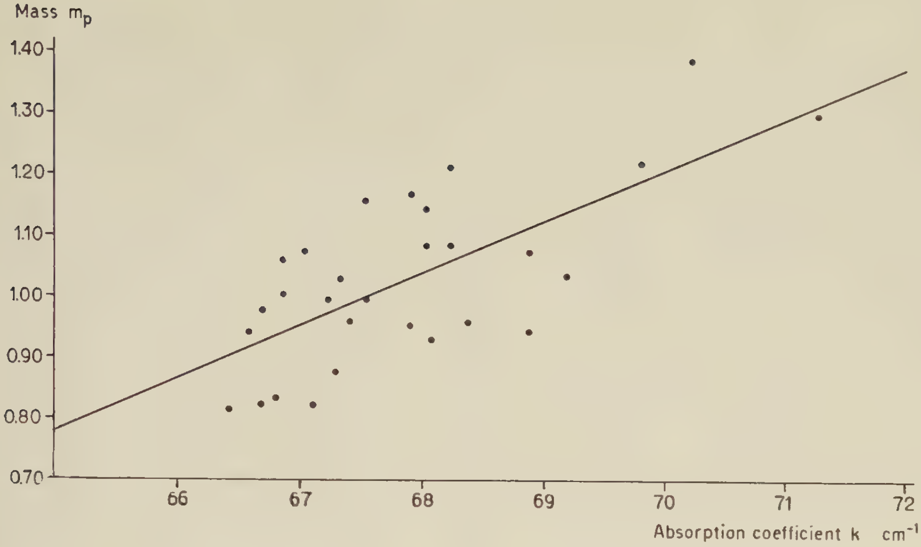

Fig. 2. Measured mass values for protons *v.* background absorption.

the emulsion is very sensitive to its state of humidity, special precautions had to be taken to make sure that the conditions were uniform. To achieve this, the surface of the emulsion was cleaned with xylene to remove all traces of immersion oil. After the cleaning, the plate was stored for several days at a constant humidity of 60 per cent. When a state of equilibrium had been reached, the whole surface was covered by a thin layer of immersion oil to prevent any change of humidity occurring during the measurements. The influence of the glass was taken into account when calculating the coefficient *k*. The greater part of the error in *k* was due to difficulties in measuring the thickness of the emulsion, which might result in an error of one micron or more.

The diagram in Fig. 2 shows the relation between the mass of the protons determined in the usual manner and the absorption *k* of the corresponding region. Certain areas of the plate near the edges show a dark stain at the surface of the emulsion, thus preventing a reliable determination of the absorption. Tracks situated in such areas should not be included when a study is made of the absorption-mass relation. It is not possible to estimate exactly the extension of the stain and therefore some unambiguous criterion had to be adopted in deciding what values should be discarded. Since the discolorations are concentrated in the thin regions of the emulsion it was decided to select only those particles which were situated in places where the emulsion had a thickness of more than 150 microns after development. The extreme values were 140 and 170 microns.

Corrections to be applied to the mass values have been found by fitting a straight line to the points in Diagram 2 by the method of least squares. Table 1 shows the results of the measurements. Column 6 gives the corrected values. Column 7 gives corrected values for the protons lying in those parts of the emulsion which are more than 156 microns thick. It can be seen from the table that the uncorrected masses show great variations and that the corrections are able to compensate for the variations.

Table I. Protons

Track No.	x microns	I/I_0	k cm^{-1}	mass M_p	corrected mass 1–29	corrected mass 1–21
1	164	0.335	66.8	0.831	0.891	0.890
2	164	0.328	67.9	0.951	0.920	0.916
3	162.5	0.331	68.0	1.088	1.042	1.037
4	161.5	0.332	68.2	1.088	1.026	1.022
5	161	0.334	68.1	0.929	0.888	0.885
6	161	0.339	67.3	0.876	0.897	0.894
7	161	0.341	66.9	1.004	1.065	1.065
8	161	0.342	66.7	0.821	0.888	0.885
9	161	0.342	66.6	0.940	1.025	1.024
10	161	0.343	66.4	0.812	0.901	0.900
11	160	0.341	67.3	1.030	1.050	1.047
12	159.5	0.341	67.4	0.960	0.973	0.970
13	159.5	0.341	67.5	0.996	0.997	0.993
14	158.5	0.345	67.1	0.820	0.853	0.852
15	158.5	0.348	66.7	0.976	1.055	1.052
16	158	0.347	67.0	1.078	1.129	1.126
17	158	0.348	66.8	1.060	1.129	1.128
18	158	0.342	67.9	1.170	1.134	1.129
19	157.5	0.347	67.2	0.995	1.023	1.019
20	157	0.346	67.5	1.160	1.161	1.157
21	156.5	0.340	68.9	1.073	0.961	0.956
22	155	0.347	68.2	1.211	1.142	
23	154.5	0.350	68.0	1.143	1.095	
24	154.5	0.338	70.2	1.393	1.131	
25	153.5	0.343	69.8	1.221	1.014	
26	153	0.351	68.4	0.957	0.893	
27	152	0.339	71.3	1.305	0.986	
28	151.5	0.352	68.9	0.943	0.845	
29	151	0.352	69.2	1.035	0.905	

$I = I_0 \cdot e^{-kx}$

Standard deviation

1–29 uncorrected $\sigma = 13.8$ %, 1–29 corrected $\sigma = 9.6$ %
1–21 uncorrected $\sigma = 10.8$ %, 1–21 corrected $\sigma = 9.2$ %

The standard deviations computed from the distributions of the mass values are $\sigma = 13.8$ per cent and $\sigma = 9.6$ per cent in the uncorrected and corrected case, respectively, for the tracks 1–29, and $\sigma = 10.8$ per cent and $\sigma = 9.2$ per cent for tracks 1–21. The results clearly show the importance of the new correction. It is also evident that when no corrections are applied, the most reliable mass determinations are obtained when comparing the unknown particle with known particles in its immediate vicinity in the emulsion. Under these circumstances an even lower value of σ can be expected.

Hitherto, it has not been possible to decide whether the differences between different parts of a plate are due to variations of grain density or grain size, or possibly both. A very careful determination of the grain density of relativistic tracks might provide the answer to this question. Since the variations of the properties of the grains are smaller by a factor of 6 to 8 than the mass variations, such an investigation would involve the counting of a very large number of grains.

Identification of slow K-particles showing no decay and no visible interaction

In the course of the present mass determinations two particles were found with a mass of approximately 1000 electron masses. The remaining particles consisted of 29 protons and 5 deuterons. A similar determination by ALINDER[1] on another plate yielded one K-particle, 36 protons, 5 deuterons and 3 tritons. All three particles stop in the emulsion with no sign of any decay or interaction. The $g_{\min.}$ of the plate studied by ALINDER was very low, $g_{\min.} \sim 15$ grains per 100 microns. On the other hand two particles were found in an emulsion where $g_{\min.}$ was equal to 25 grains per 100 microns, which would enable decay particles to be quite easily recognized. These particles are the only ones that are exceptional. All others fall well within the normal distributions for protons, deuterons, and tritons. Owing to this and to the fact that the particles belong to two different batches of plates, which have been manufactured, exposed and developed on different occasions, it seems unlikely that they are faded protons. This cannot, however, be stated with certainty. One of the tracks comes from a star, but the other prongs are too short to be measured photo-electrically. In view of the difficulties existing where the behaviour of negative K-mesons is concerned, it was considered of interest to other workers in this field to describe the present particles in some detail. Table 2 gives the main data.

Table 2. K-particles

Particle	Mass		Range microns	Measured by
	Uncorrected	Corrected		
K_{Ld_1}	905 ± 85	905 ± 70	3450	v. FRIESEN
K_{Ld_2}	984 ± 85	960 ± 70	3300	,,
K_{Ld_3}	890 ± 90	—	5700	ALINDER

The errors given are standard errors.

ALINDER has not yet finished his measurements and no correction of the kind described in this paper has been applied to K_{Ld3}. His proton values show a somewhat wider distribution ($\sigma \sim 12$ per cent) than usual. On the other hand, the range of K_{Ld3} is great.[2] Thus, the limits of error of K_{Ld3} are only slightly wider than those of K_{Ld1} and K_{Ld2} before the correction has been applied. K_{Ld1} and K_{Ld2} are situated in the most favourable part of the emulsion (37 and 38 in Fig. 1). K_{Ld2} is ejected from a star of type $5 + 0$ n.

The mass has been computed in two different ways. One consisted in comparing the unknown particles directly with the protons 1–21, without any corrections. The other way was to apply the correction described earlier in this paper. The k-values of K_{Ld1} and K_{Ld2} were 67.3 and 67.6 cm^{-1}, respectively. The limits of error are standard errors based on the known distribution of the protonic mass values, the relatively greater length of the K-particles having been taken into consideration ($\sim$ 6500–7000 microns when reduced to protonic mass. See Part I p. 317).

---

[1] Unpublished. Plate from the 1952 Sardinian expedition. Altitude of flight 27,000 metres.

[2] Small-angle scattering *v.* range gives a mass value 1100 ± 185 M_e for this particle (ALINDER and NORLIND).

All three values are more than five standard deviations removed from the mass of a proton. They agree very well with each other. A search for electron pairs around the stopping point of the particles has been unsuccessful. If such pairs are created the probability of finding one would, however, be only 1:10.

It is well known that the majority of the K-mesons hitherto found seem to be positively charged. Several possible ways of explaining this circumstance were discussed at the Bagnères de Bigorre conference in July 1953.[1] Professor POWELL suggested that the nuclear stars that have been observed might be produced by nuclear absorption of negative τ-mesons, whereas the absorption of negative $\varkappa$-mesons might not lead to star production. Professor ROSSI pointed out that as in the case of negative μ-mesons most of the energy could be thought to escape as neutrinos. The fact that $\varkappa$-mesons seem to be much more common than τ-mesons is in good agreement with the suggested explanation. It does not appear unreasonable to assume that our K-particles, which show neither decay nor visible interaction at the end of their range, are examples of negative $\varkappa$-mesons if we accept POWELL's explanation of the apparent anomaly.

It would be very difficult to observe such slow negative $\varkappa$-mesons by means of any other method than that of photo-electric mass determination.

Summary

A correlation has been shown to exist between the density of the general background in a nuclear emulsion and the photo-electrically determined mass values of protons in the same region, by means of which it will be possible to improve the mass determinations of particles of unknown mass.

In the course of the work K-particles have been found which show neither decay nor visible interaction at the end of their range.

Department of Physics, University of Lund, February 1954.

---

[1] Comptes-Rendus du Congrès International sur le Rayonnement Cosmique. Bagnères de Bigorre, Juillet 1953.

Tryckt den 25 augusti 1954

Uppsala 1954. Almqvist & Wiksells Boktryckeri AB

ARKIV FÖR FYSIK Band 8 nr 31

Communicated 14 April 1954 by MANNE SIEGBAHN and BENGT EDLÉN

Photo-electric mass determinations in nuclear emulsions

Part I. An investigation of the accuracy of mass determinations

By KRISTER KRISTIANSSON

With 8 figures in the text

Introduction

The accuracy with which a determination of the mass of a particle can be made through measurements of the number of grains in a track in a photographic emulsion is fixed by the quality of the emulsion, and particularly by the accuracy with which the grain density of the track can be measured. Such a measurement can be made by a direct count of the number of grains in the track. However, in order to reduce the subjective factor and thereby increase the reproducibility and reliability of the measurements, in many laboratories working in this field photo-electric apparatus have been constructed for grain density determinations [1, 2, 3, 4, 5, 6, 7].

The principle in all these devices is that in the image plane of the eye piece of a microscope a slit is inserted and above this there is a photo-multiplier tube which registers the beam of light passing through the slit. This beam depends in some way on the grain density of the track. Such measuring devices have been employed in investigations of the grain density in tracks of different kinds and in mass determinations of heavy mesons. However, the present knowledge of the photo-electric measuring technique is incomplete. For this reason the author has decided to investigate this technique and particularly to determine the accuracy with which a mass determination can be made. The measurements have been carried out on tracks in G 5 emulsions with the apparatus constructed by VON FRIESEN and KRISTIANSSON [2].

The investigation has been divided into three parts: the first deals with details in apparatus and measuring technique which are important for accuracy and reproducibility, the second with the accuracy in the determination of the mean width of a track, and the third, finally, with the accuracy in a mass determination.

Experimental arrangement and method of measurement

Improvements in the apparatus

The photo-electric apparatus, which has been employed in the measurements, and the measuring technique have previously been described in detail [2]. Some improvements have been made, however, which will be briefly mentioned. The main object has been to increase the speed of measurement, so that now it amounts to 3,500 to 4,000 μ per hour.

The dermination of the mean width of a track is made from three measurements. Firstly the light passing the slit is measured with the track focussed in the slit and, secondly, the light from the background on both sides of the track. The displacement of the field of view in relation to the slit, which is necessitated by these three measurements, is carried out by means of a plane parallel glass plate placed about halfway between the objective and the eye piece and revolvable around an axle parallel to the longitudinal direction of the slit to three fixed positions. The thickness of the plate is 9 mm and its normal coincides in the central position with the optical axis of the microscope. The total displacement of the field of view from the measurement of the track to the measurement of the background is approximately 3 μ, measured in the objective plane, which corresponds to an angular deviation of approximately 8° of the plate. The change in the amount of transmitted light resulting from the altered angle of incidence is negligible.

A rotation of the glass plate involves a slight change in the direction of the beam of light through the slit and consequently the spot of light on the surface of the photo-multiplier has a somewhat different position in the three settings. If the sensitivity of the cathode surface is not constant the current will depend upon the position of the spot of light and an error arises which is encountered in every measurement. A suitable choice of photo-multiplier, a careful adjustment of this so that the spot of light falls in a place on the surface of the cathode where the sensitivity is constant over a greater area, and placing a piece of frosted glass below the cathode have eliminated this error to such an extent that the photo-currents from the three different settings of the glass plate agree to within 0.1 per cent if the illumination of the objective plane is uniform.

For registration of the measurements a Leeds and Northrup Speedomax typ G recorder was employed, which was connected to the photo-multiplier tube via a cathode-follower. The linearity in this registering system is very high, a reduction of the photo-current to one half decreases the registration of the recorder to one half with an error that is less than 0.5 per cent. A detailed description of this part of the apparatus and the measuring technique involved will be presented in the report by von Friesen and Stigmark [8].

Slit dimensions

One detail of great significance for the measurements is the dimensions of the slit employed. The width is particularly important. The photo-electric apparatus constructed up to this time differ considerably in this respect in that the slit employed in some apparatus is narrower than the image of the track in the eye piece and others have a slit which is appreciably wider than the track. In the apparatus used in this investigation the slit has always been wider than the track; the image of the track covers about 20 per cent of the surface of the slit. The measurements are made when the slit is in a fixed position in relation to the track.

The slit width is determined chiefly by three factors. The slit must not be too wide for then the surface occupied by the image of the track becomes small in relation to the surface of the slit itself and the accuracy of measurement is reduced. On the other hand, it must not be too narrow so that difficulties arise in the adjustment of the track in the slit. In such a case the speed of measurement is greatly reduced.

Furthermore, if the slit is too narrow sections occur in the tracks of particles with low energy which exhibit so great a scattering that the entire image of the track cannot be covered by the slit and the measurement gives too low a value.

An approximate estimate of the minimum width permissible for the slit can be obtained if we make it a condition for minimum slit width that a track of a meson with a residual range of approximately 100 μ and a scattering of 3 $\bar{\alpha}$, where $\bar{\alpha}$ is the mean value of the angle of scattering for this range, can be completely covered by the surface of the slit. Such a slit has a width of 2.5 μ measured in the objective plane if the length is 30 μ and if the maximum diameter of the track is 1.2 μ (twice the diameter of the grains).

A control measurement has been made with slit widths of 2 and 3 μ at the end of proton and meson tracks (residual range $30\ \mu < R < 500\ \mu$). The measurements with the two slits did not show any difference in the mean track width of the proton track, whereas in the meson tracks, which within the same range interval have comparatively large scattering, the 2 μ slit gave as the mean value of a large number of measurements 2 per cent lower mean track width than the 3 μ slit. The conclusion, that can be drawn from the measurements, is that the error resulting from too large scattering of tracks of particles with greater energy than about 3 MeV is insignificant even for a 2 μ slit (from the agreement of the proton measurements). With this slit, however, there occurs a minor error in the energy interval below 3 MeV (the meson measurements). A somewhat wider slit is thus desirable, which has also been demonstrated in the earlier discussion. Most of the measurements described in the following have been made with a slit with the dimensions 2.4 × 30 μ.

Significance of the inclination of the track

There are different reports in the literature on how the result of a photo-electric measurement of a track is dependent upon the inclination of the latter in relation to the plane of the slit. CECARELLI and ZORN observe that they have not found that the measurements are affected to any higher degree if the track inclines a few degrees towards the horizontal plane [3]. KAYAS and MORELLET have shown, on the other hand, that the results are strongly dependent upon the dip and they correct their measurements accordingly [4]. VAN ROSSUM has made the same observation and tries to eliminate this correction by erecting a stage that can be inclined so that the track can always be placed at right angles to the optical axis of the microscope [7]. The measurements which had been made in Lund did not show any correlation between mean track width and dip. At that time, however, only tracks that incline less than 10° towards the horizontal plane in undeveloped emulsions were measured.

In order to determine the dependence of the mean track width on the dip, the end of tracks of singly charged particles heavier than mesons and with different angles of dip have been measured in the interval $R = 30$–$1{,}000\ \mu$. The mean track width has been corrected for the degree of development to the middle of the emulsion according to a method which has been described in an earlier paper [9]. In order to make the measurements of the mean track width at different places in the track directly comparable, a measurement at a place in the track with the residual range R has been multiplied by a factor $S(R=0)/S(R)$, where $S(R=0)$ is the average value of the mean track width at the end of a proton track and $S(R)$ is the mean track width of the same track in a place with the residual range R. The factor can be readily computed from the relation between mean track width and residual range for protons in the emulsion. The error which arises as a result of assuming that all the particles are protons is probably insignificant since the majority of tracks of this type are proton tracks. There is no possibility of determining whether the particles are protons, deuterons or tritons, since on account of the dip they are too short to be identified. The measurements have been made with two slits with the dimensions $2\ \mu \times 30\ \mu$ and $3\ \mu \times 30\ \mu$.

In Fig. 1, which shows the result of the measurement, the mean track width is plotted as a function of tan α, where α is the angle between the track and the horizontal plane in an undeveloped emulsion. Inasmuch as the measurement takes place after the development the result will be to a certain degree dependent upon the shrinkage factor of the emulsion, which in the emulsions employed was approximately 2.6. The mean track width $S(R=0)$ at the end of a horizontal track of a singly charged particle has here and in all subsequent diagrams been set at 100. It can be seen from the figure that as soon as the dip is slight ($\tan \alpha < 0.2$) the mean track width is independent thereof. At a greater dip the mean track width depends on the slit width so that with a $3\ \mu$ slit the mean track width increases, while with a $2\ \mu$ slit it decreases.

The cause of the diverging results which have been obtained in different laboratories is undoubtedly the width of the slit employed. KAYAS and MORELLET and VAN ROSSUM, who have found an appreciable decrease in the mean track width with increased dip, are working with a narrow slit, whereas CECARELLI and ZORN and the present author, working with a wide slit, have found that the mean track width changes only slightly with dip. The reason why the results with a wide slit are not affected to any great extent by the dip is not difficult to understand. A measurement of a track in the slit is not a measurement of the black area discernible in the microscope which the track occupies in the slit but a measurement of the amount of light belonging to the image-forming rays, which is absorbed by the track. This amount of light absorbed is not dependent upon the focusing of the track in the slit but is always the same. A prerequisite for a correct result, which in the first approximation is independent of the dip, is that if a grain belonging to the track lies below the image of the slit in the objective plane all rays which are absorbed by the grain should be able to pass through the image of the slit if the grain had not been there. If the grain lies above the image of the slit all the incident rays which are absorbed should have passed within the limits of the image of the slit. The permissible interval in depth within which the track must lie will be dependent on the slit width and the optical properties of the microscope, but it is not limited by the depth of focus in the direct observations of the track through the microscope.

The slight increase in mean track width which the $3\ \mu$ slit shows for a large dip of the track depends on the following. The slit is sufficiently wide so that the beam of light which is absorbed by the track fulfils the above-mentioned conditions of lying within the limits of the image of the slit. The number of grains in a track, where the length of the horizontal projection is constant, increases as $\cos^{-1} \alpha$. The mean track width should increase as this function, but part of the increase is compensated by the fact that the overlapping of the grains becomes greater when the dip increases. Consequently the mean track width increases more slowly than $\cos^{-1} \alpha$. Since the degree of overlapping depends upon the grain density the appearance of curves for the same slit will depend on the grain density, although they never can lie above $\cos^{-1} \alpha$. The decrease in the mean track width for the narrower slit with a large dip of the track depends on the fact that the slit is not wide enough so that

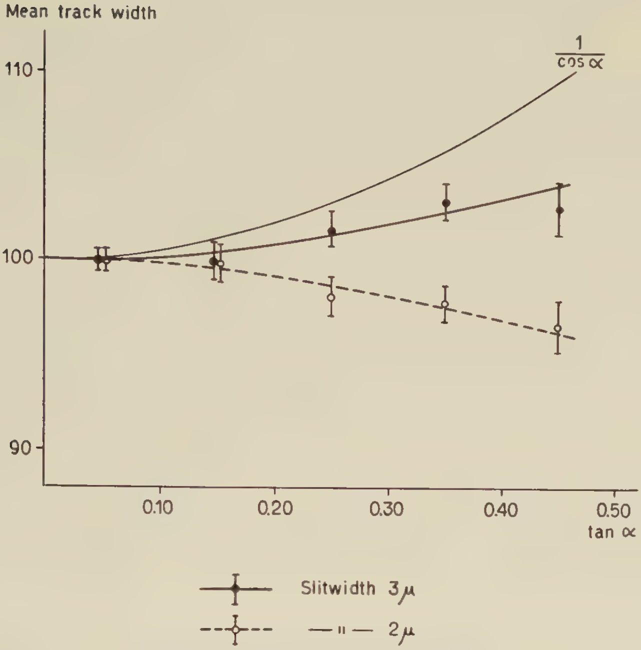

Fig. 1. Mean track width *v.* dip.

part of the previously mentioned beam of light passes in the objective plane outside the limits of the image of the slit. The decrease in the mean track width from this cause is not compensated for by the increase which comes from the greater number of grains with increased dip.

It is evident that a slit of approximately 2.5 μ is suitable for use in the measurement of tracks with about the same grain density as the end of proton tracks and with the optical arrangement which is employed in Lund. For such a slit width the increase in the number of grains and the decrease in the mean track width, as a result of effects at the edge of the slit, almost completely compensate each other so that the mean track width becomes independent of the dip of the track.

Thus no correction for light losses due to the dip of the track is necessary if $\tan \alpha < 0.5$. On the other hand, with a large dip consideration must be taken of the error in measurements of the residual range which arises from the fact that the length of the projection of the track is measured in the microscope. As soon as the error in measurements of the residual range has exceeded 2 per cent the figures have been corrected.

Accuracy in measurements of the mean track width

Reproducibility of the measurements

The reproducibility of measurements of the mean track width has been investigated on repeated occasions by measuring the same track more than once. If the integrated mean track width from different measurements of a track, which is 3,000 to 4,000 μ long, are compared the agreement is always very good. The standard deviation is less than 0.3 per cent.

Uncertainty in measurements of the background

The error which arises in the determination of the mean track width depends on, errors from the adjustment of the microscope, errors from the recording of each measurement, and the error from the measurement of the illuminated background. The correct background, which belongs to the site of the track, diverges from the mean value of the measured backgrounds on both sides of the track, if the amount of light passing through the slit is not linearly dependent upon a displacement to both sides from the track.

In order to determine the error resulting from this necessarily approximate determination of the background measurements have been made with a blank central position and the difference between the measurement in the central position and the mean value of the measurement in the outer positions has been ascertained. The standard deviation, which results from the error in the background in a determination of the mean track width, has been found in this way to be 9 per cent on one single section of a track for a slit with the dimensions $2.4 \times 30\ \mu$. This standard deviation depends to a high degree upon the density of background grains and slow electrons and it probably could be reduced considerably if the time between the production and the development of the emulsion were decreased. For the emulsions employed this time amounted to about ten weeks.

Correction for uneven development

The value of the mean track width which is obtained in the measurement of a track is not uniquely determined by the ionization, but depends also on the position of the track in the emulsion since the degree of development and the transparency of the emulsion vary with the coordinates of the track. It is usually possible to make a correction for the depth in an emulsion by measuring tracks of the same kind at different depths, comparing the mean track witdhs and computing from them a correction factor for each depth. All mean track widths are multiplied by such a factor and thereby reduced to the same depth. The significance of such a correction is clearly shown in an earlier report, where also a method for its determination is described [9].

It has proved to be possible to increase the accuracy in the determination of the correction factor by using protons in the whole interval $R = 0\text{–}3000\ \mu$. In this case the function which indicates the dependence of the mean track width on the distance to the surface is determined by successive approximations in the following manner. An approximate depth-mean track width curve is drawn with the help of tracks of protons, deuterons and tritons in the interval $R = 0\text{–}1\,000\ \mu$. The correction which is determined in this way is sufficiently good for differentiating protons from deuterons and tritons and a comparatively good mean track width relation for protons can be determined. A better depth-mean track width curve is constructed from the protons only ($R < 3{,}000$) when the variation of the mean track width with the range is taken into consideration in such a way that each value of the mean track width is multiplied by the factor $S(R=0)/S(R)$. This, as previously pointed out, makes it directly comparable to the mean track width for the range $R = 0$.

If in a $400\ \mu$ emulsion the correction is computed from about 20 protons which are fairly evenly distributed at different depths the error in the corrected values of the mean track width caused by an incorrectly drawn depth-mean track width curve will

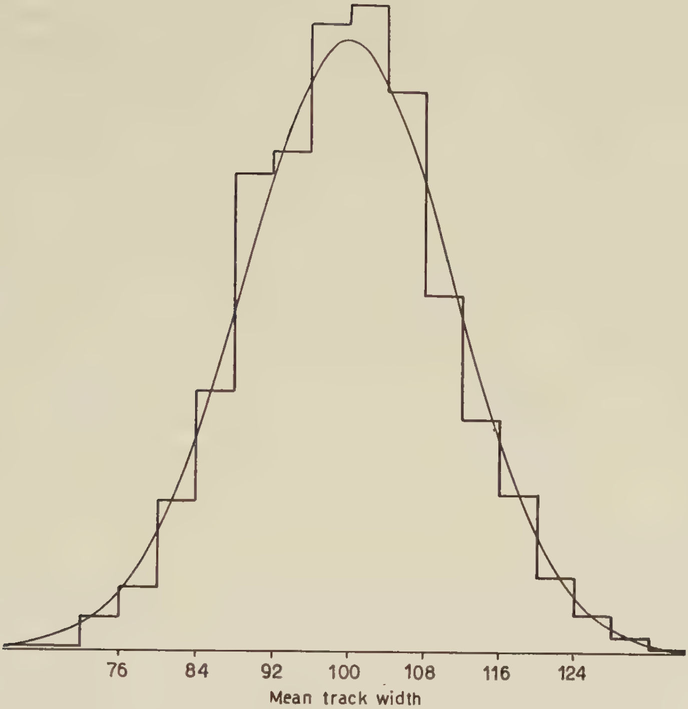

Fig. 2. The distribution of measurements of mean track width in proton tracks.

hardly be greater than 1 per cent at any depth. Since a track which is to be corrected almost always passes obliquely through the emulsion the errors from the correction will cancel each other and the error in the integrated mean track width from faulty correction is then negligible in comparison with other errors.

Distribution of the measurements around the mean value

The histogram in Fig. 2 shows how measurements with a 30 μ long slit are distributed around the mean value. The distribution has been determined from measurements on 12 protons ($R < 3{,}000$) where every measurement of the mean track width has been corrected to the middle of the emulsion and multiplied by the factor $S(R = 0)/S(R)$. The distribution, as is shown by the figure, agrees well with the normal frequency distribution. The standard deviation (σ_{total}) has been calculated to 11 per cent. This standard deviation depends partly on the variation in grain density in the track and partly on the error from the determination of backgrounds. Since these errors are independent of each other the following relation is valid

$$\sigma^2_{\text{total}} = \sigma^2_{\text{background}} + \sigma^2_{\text{grain}}$$

and σ_{grain} can be computed to 7 per cent. This is the standard deviation of the measurement of the projected area of the grains in one section if the length of the intervals is 30 μ and the track is a proton track with $R \leq 3{,}000$ μ. This distribution is dependent upon the total number of grains in the slit but the above result is applicable without any appreciable error to the entire interval of mean track width which is investigated in this paper ($R = 0$–$6{,}000\ \mu$ for protons and $R = 0$–$1{,}500\ \mu$ for mesons).

If the standard deviation of the measurements is compared with the standard deviation of the number of grains (N) in a slit length which could be expected if the distribution of the grains were a Poisson distribution, it is found that the measured standard deviation is considerably less than the calculated ($\sqrt{N}$), even if the known distribution of the grain diameters in a G 5 emulsion is taken into consideration [2]. Similar observations on thinner tracks have been made by Hodgson and by DELLA CORTE, RAMAT and RONCHI [10, 11]. Hodgson has shown that this is caused by the fact that the distance which is occupied by grains in an interval in the track is not negligible in relation to the length of the interval itself. The same condition prevails to a still greater extent in the tracks used in this investigation. The number of grains per slit length can be estimated to about 50 and the Poisson distribution would thus correspond to an error of 14 per cent. The experimentally determined distribution is only about one half as great as that which can be estimated theoretically.

Correlations between measurements in a track

A question which has been raised in investigations of the distribution of grains in a track is whether there is any relation between the grain density in different parts of the track in addition to that which is determined by the ionization. Such a dependence can conceivably be caused by some form of periodicity in the sensitivity of the emulsion, by irregularities in the distribution of grains of varying size, or by variations in the efficiency of the development. A study of the distribution of grains in thin tracks has been carried out by COATES [12]. He divided the tracks into cell-lengths of 3.3 μ and studied how the number of grains varied between the cells. No periodicity was observable when cell-lengths of this size were employed.

The slit length which was used in measurements of the mean track width is about ten times greater than COATES' cell-length. Furthermore, there is a difference between grain counting and photo-electric measurements in that in the first case the number of grains is determined and in the second the projected area of the grains. It can, therefore, be of interest to repeat the investigation by means of photo-electric measurements and attempt to determine possible correlation between mean track widths in 30 μ sections at different distances from one another. If widespread irregularities exist they are important for all determinations of grain density. Each measurement should embrace a length of the track which is much greater than the diameter of these irregularities.

For the calculation of coefficients of correlation between measurements at different distances, protons from the same plate have been chosen and the interval $R = 30$–$2{,}880\ \mu$ has been employed for all of them. The measurements have been reduced to the middle of the emulsion and multiplied by the factor $S(R=0)/S(R)$ in the usual manner.

The coefficient of correlation $r(d)$ for measurements at the distance of d slit lengths from one another has been computed from the following formula:

$$r(d) = \frac{\sum_{i=1}^{22} \sum_{k=1}^{96-d} \Delta S_{k,i} \cdot \Delta S_{k+d,i}}{22\,(96-d)\,\sigma^2}.$$

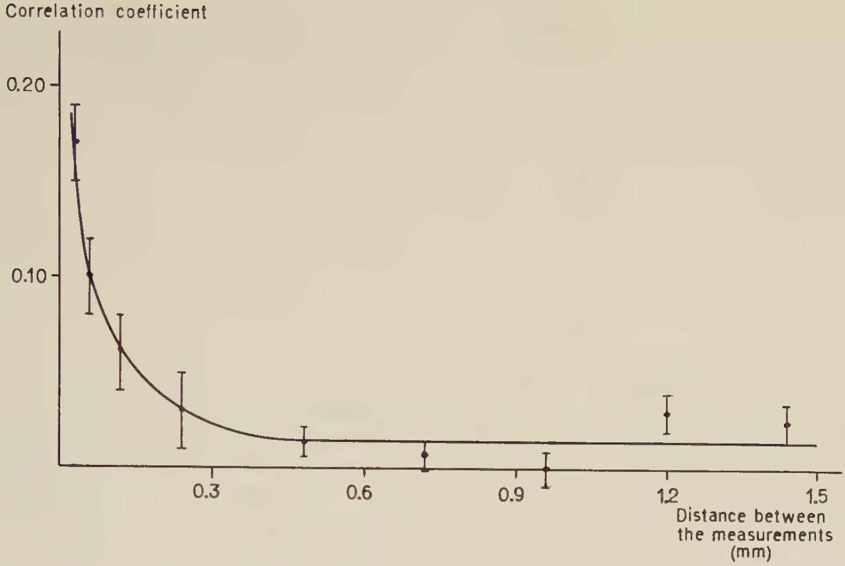

Fig. 3. The correlation coefficient between measurements at different distances.

$\Delta S_{k,i}$ and $\Delta S_{k+d,i}$ are the deviation of the measurements of mean track width from the mean value in the slit k and $k+d$ of track i. The total number of tracks is 22 and in each track 96 slit lengths are employed. σ is the standard deviation of the mean track widths. The diagram in Figure 3 shows the result, where $r(d)$ is plotted as a function of d.

The calculations of the coefficients of correlation indicate that there is some correlation between measurements of mean track width of sections of the track at different distances from one another. The coefficient decreases at first relatively quickly when the distance between the measurements increases, but attains a value at a distance of about 10 slit lengths which remains constant within the limits of error and seems to lie somewhat above zero. The correlation between measurements close to each other depends on irregularities in the track or emulsion which are of small linear dimensions in relation to the measured track length. Any certain estimate of the magnitude of the disturbances is difficult to make since the coefficients of correlation do not give any information as to their character.

A very rough estimate of the maximum diameter of these disturbances is obtained if the mean track width in a track is approximated to a sine wave superimposed upon the smooth mean track width-range curve and the disturbance is regarded as half a wave-length of such a sine wave. The greatest diameter which a disturbance can have in such a case is equal to twice the distance between the measurements whose mutual distance is such that the coefficient of correlation between them is zero. If the steeply sloping part of the curve in Figure 4 is approximated to a straight line it cuts the R-axis at some point between $R = 0.2$ and 0.3 mm depending on how one draws the line. The maximum diameter of the disturbances thus can not very well exceed 0.5 mm. The mean diameter must be considerably less, but it cannot be estimated with certainty from the available data.

How great a part of the spread of the measurements depends upon this periodicity and the magnitude of its mean amplitude can be computed from differences between measurements at varying distances. Each such difference can be regarded as a sum of one part which is independent of the periodicities of the emulsion and another part which does depend upon them. The size of the latter depends on the mutual distance of the measurements (d). If the differences are calculated from consecutive measurements ($d = 1$) the contribution from the periodicities is extremely small, whereas in differences from measurements at a great distance ($d = 16$) it reaches a maximum value corresponding to the entire amplitude of the disturbance. The component of the spread which depends on these disturbances has been found from such calculations to be 4 per cent of the total mean track width at the end of a proton track.

The conclusion that can be drawn from this investigation is that the periodicity in unfavourable cases can exert a certain influence on the accuracy in the determination of the ionization by means of a grain density measurement in a track the length of which is of the same order of magnitude as the diameter of the disturbances. As soon as the track length is great in relation to the extension of the disturbances they lose their significance. In such a case waves of too high and too low mean track width will compensate each other more or less completely.

The constant value slightly above zero which the coefficient of correlation assumes for great slit distances depends on a certain variation in the average level of the mean track width in different parts of the emulsion. In the calculation of the coefficients of correlation for $d \geqq 16$ each proton track has been divided into intervals with 8 measurements in each. The average of the mean track width has been computed for each interval and the correlation between those mean values has been determined. It has been recalculated to the value corresponding to the correlation coefficient which one gets without the formation of averages. The mean value of $r(d)$ in this region ($d \geqq 16$) is 0.014 ± 0.004. The spread in the average level of the mean track width to which this correlation coefficient corresponds amounts to (1.3 ± 0.2) per cent. A similar variation of the mean level has been observed in measurements by VON FRIESEN in another emulsion, which indicates that the effect is not a peculiarity of the emulsion studied here but more likely a normal property of nuclear emulsions [13].

Total error in a photo-electric measurement

The most significant errors in a measurement of the mean track width have been discussed and a brief summary is advisable. In order to give an idea of the real significance of errors in a measurement of the mean width of a track with a suitable length for a mass determination, the errors have been calculated for a track of 4,000 μ and such a grain density that it corresponds to a proton track with a residual range of exactly 4,000 μ. The main causes of the spread of the measurements are the following:

1. Errors from flaws in experimental arrangement, method of measurement and correction for uneven development.
2. Normal statistical variations in the number of grains in a track.
3. Errors from irregularities in the emulsion.

The error in the mean track width from defects in the measuring technique is composed of errors from the adjustment of the microscope and from the readings of the recorder chart and an error from the determination of the background. The total error amounts to 0.8 per cent in the track which we considered above. The relative significance of the error changes with the length of the track (L) as $1/\sqrt{L}$. The error from the depth correction has been previously discussed and was assumed to be very small in comparison with other errors.

The standard deviation of the total number of grains in a track with a range (L) changes approximately as $\sqrt{L}$. Thus the relative standard deviation decreases as $1/\sqrt{L}$. This amounts to 0.6 per cent in the same track.

Finally the irregularities in the emulsion, which have been examined by calculations of the correlation coefficients between the measurements at different distances, give rise to errors. They can be regarded as partly a periodicity in the mean track width and partly as a variation in the average level of the mean track width. The periodicity first mentioned is important only in a track whose length is of the same order of magnitude as the wave-length. If the track is longer the waves will compensate each other. The error in the mean track width from these periodicities decreases as $1/L$ when L increases and for a 4,000 μ track it is negligible in comparison with other errors.

The variation in the average level of the mean track width, the existence of which has been demonstrated by the correlation coefficient for widely separated measurements, is independent of the length of the track and will have a relatively greater influence the longer the track is. The computations have shown that the standard deviation of the average level of the mean track width amounts to (1.3 ± 0.2) per cent of the total mean track width.

The sum of these errors in the measurement of the mean track width of a 4,000 μ track is (1.7 ± 0.2) per cent. This is therefore the standard deviation in a photoelectric measurement of the integrated mean track width in the aforementioned track.

Accuracy in the determination of the mass of a particle

Selection of tracks

The errors, which arise in the measurement of the mean track width and which have been previously discussed, will determine the accuracy with which a mass determination can be made in tracks which end in the emulsion. Since the knowledge of these errors in spite of the investigation just described cannot be regarded as complete, it is difficult to calculate with certainty the true accuracy of a mass determination. For this reason a direct experimental investigation has been made by measuring approximately 70 tracks of singly charged particles, protons, deuterons, tritons, and π- and μ-mesons.

The emulsions from which the tracks have been selected are two Ilford G 5 emulsions with the dimensions 5×7.5 cm and with a thickness of 400 μ. They were exposed during a balloon flight at an altitude of approximately 27 km for 6 hours and developed in Id 19 according to a method of temperature development with the warm stage at 12°C for 2 hours.

The only condition in the selection of a track for measurement has been that it should end in the emulsion and have a certain minimum length. The tracks of π- and μ-mesons have been at least 800 μ and the tracks of the heavier particles at least 3,000 μ. All measurements have been made with a slit with the dimensions 30×2.4 μ. The correction has been computed from the protons in the interval $R = 0$–3,000 μ. Each emulsion has been treated separately when correction and mass determinations were made.

Method of calculation

Every calculation of the mass of a particle from determinations of the grain density in a track is only relative and is always based on the fact that the ionization of charged particles is a function of only the charge and velocity of the particle. It is, however, possible to compute the mass from the experimental data in various ways. It seems advantageous in photo-electric measurements to calculate the mean track width-range relation for every particle by the method of least squares and to determine the ratio between the masses of the particles by comparing the curves obtained by this procedure.

The mean track width $S(R, m)$ in a track of a particle with a mass m at a point with the residual range R is a definite function of the ionization (J) as soon as the velocity (v) of the particle falls below that which corresponds to minimum ionization. Consequently we write

$$S(R, m) = f_1(J).$$

For a singly charged particle the following is valid:

$$J = f_2(v) = f_3(R/m).$$

Combination of these equations yields

$$S(R, m) = f(R/m).$$

It is impossible to obtain a simple analytical expression of the function $f(R/m)$ due to the fact that the appearance of the function depends on the emulsion and the development in a complicated way. The function, however, can with advantage be expanded into a power series.

$$S(R, m) = S_0 + A\, R/m + B(R/m)^2 + - - - - -$$

The constant coefficents S_0, A, B, $- - -$ in the expansion depend on the quality of the emulsion and the degree of development but are independent of the mass of the particle. They can be determined from measurements of particles of known mass and conveniently found by the method of least squares.

The necessary number of terms in an expansion which will give an approximation of the mean track width-range relation with an accuracy not less than the accuracy of the measurements is determined for a certain emulsion by the measured length of the tracks. In the G 5 emulsions employed with the grain density of 20 grains per 100 μ in tracks of minimum ionizing particles it is sufficient to use three terms for a proton track which has a residual range not exceeding 6,000 μ. A meson track with a length of 1,500 μ requires an additional term.

Before presenting the result of these calculations it is advisable to call attention to a couple of details in the computations. The measurements have been made with

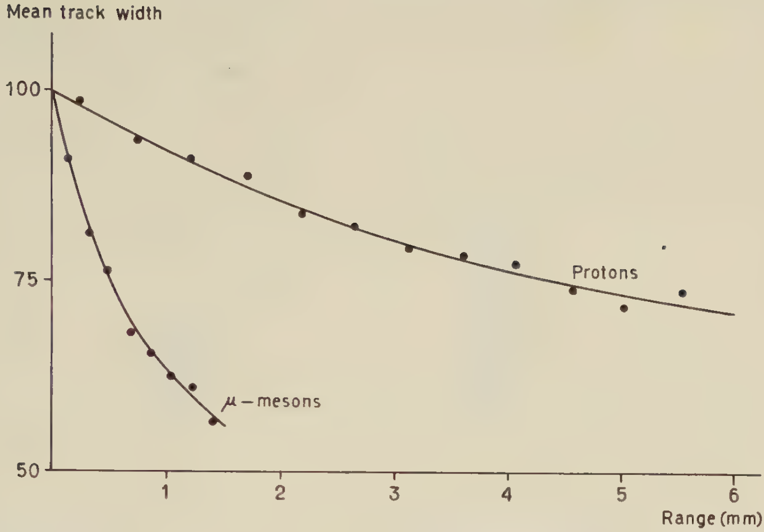

Fig. 4. Mean track width *v.* residual range for protons and μ-mesons in a G 5 emulsion.

a 30 μ long slit. In the correction of the mean track width to the middle of the emulsion 60 μ intervals have been employed as the unit. In the calculations with the method of least squares interval lengths of 240 μ have been used for protons, deuterons and tritons and 60 μ for mesons.

Since the measurements take place independent of all disturbances in the track certain single values will be influenced to a high degree by black spots and other irregularities in or around the track. In order to eliminate at least to some extent such disturbances all measurements which deviate from the mean value in the track by more than 20 per cent for 60 μ intervals have been excluded in the mass determinations. The number of rejections is about 1 per cent of the number of single measurements.

Fig. 4 shows the mean track width-range relations for protons and μ-mesons in one of the emulsions. The proton curve is of the second and the meson curve of the third degree. It is seen that the curves fit well the inscribed points which are the mean values of 20 protons divided into 480 μ intervals and 10 μ-mesons in 180 μ intervals. The equations of the curves are, if R is measured in mm,

$$S(R, P) = 100 - 8.37\,R + 0.623\,R^2 \text{ protons}$$

$$S(R, \mu) = 100 - 70.2\,R + 47.3\,R^2 - 13.7\,R^3 \text{ } \mu\text{-mesons.}$$

A good check on the equations can be obtained by a direct determination of the ratio between the mass of the μ-meson and of the proton from the coefficents. Such a calculation gives the mass ratio 0.119, if the coefficients of the R-terms are employed. If the coefficients of the R^2-terms are employed one gets 0.115. The best determination of this mass ratio, which has been made by SMITH and his co-workers in Berkeley, has given 0.1127 [14]. Any better agreement between the values which have been computed from the coefficients of these calculations and the measure-

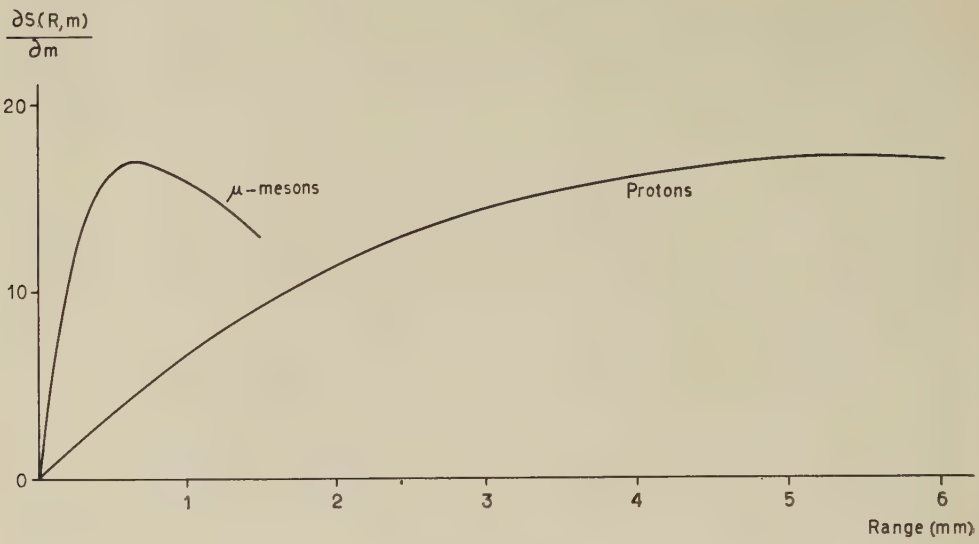

Fig. 5. The resolving power $\partial S(R,m)/\partial m$ *v.* residual range for protons and μ-mesons.

ments in Berkeley can hardly be expected, since the proton and μ-meson curves are approximations of different degree and, moreover, are calculated for residual ranges which are nowhere near proportional to the masses.

When the mass of an unknown particle is to be computed the foregoing expansion of $S(R, m)$ is applied with S_0, A, B, — — — determined from known standard particles and with the mass as a variable. The mass is calculated by the method of least squares with the condition that the sum of the squares of the deviation from $S(R, m)$ of the measurements shall be minimum.

The mean track width-range relation of a particle with the mass m can be written

$$S(R, m) = S_0 + A\,R\frac{1}{m} + B\,R^2\left(\frac{1}{m}\right)^2 + \ldots$$

The above-mentioned condition for the determination of the mass is that

$$\Delta = \sum_n (S_i - S(R_i, m))^2 \text{ shall be minimum.}$$

$$0 = \frac{\partial\,\Delta}{\partial\,m} = 2\sum_n (S_i - S(R_i, m))\frac{\partial\,S(R_i, m)}{\partial\,m}$$

S_1, R_1; S_2, R_2; … S_i, R_i … S_n, R_n represent measurements.

If it is sufficient to approximate $S(R, m)$ by an expansion of the second degree, the equation which determines the mass is of the third degree and can easily be solved graphically.

Another improvement in the method of calculation could be made if each measurement was given a weight in proportion to the value of the measurement for the

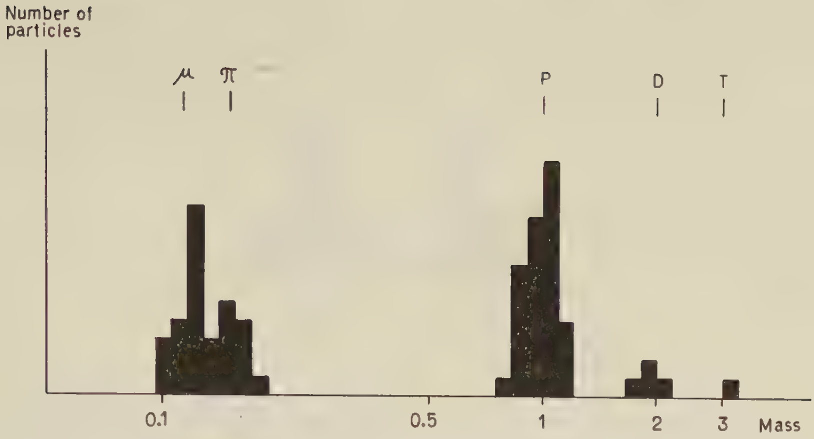

Fig. 6. The mass spectrum of mesons, protons, deuterons and tritons (second degree approximation).

mass determination. Such a weight must, however, include the mass of the particle. This would raise the degree of the equation from which the mass is computed and render the entire method of calculation very cumbersome without appreciably increasing the accuracy in the mass determination.

The last equation, however, may be regarded as an ordinary mean value computation where $\partial S(R, m)/\partial m$ indicates the statistical weight which should be assigned to each measurement. The representation of the statistical weight of a measurement by $\partial S(R, m)/\partial m$ has a certain justification since this derivative stands for the resolving power of the emulsion for a particle with the mass m at the residual range R. $\partial S(R, m)/\partial m$ is given in Fig. 5 as a function of R for μ-mesons and protons. It has been calculated from the mean track width-range relation for μ-mesons.

Mass spectrum

The distribution of the masses of the measured particles is shown in the histogram in Fig. 6. The mass determination has been made by an approximation of the second degree of the mean track width-range relation with the coefficients determined from the proton tracks. This approximation permits residual ranges of not more than about 700 μ for μ-mesons and about 1,000 μ for π-mesons and ranges of this size have been employed in the calculations of the masses of the mesons in the histogram. The ranges of the protons, deutrons, and tritons vary between 3,000 and 5,800 μ. This histogram answers two important questions in connection with mass determinations:

1. Do systematic errors possibly exist in a determination of mass according to this method?
2. What is the accuracy of a mass determination?

Separation of π- and μ-mesons

Before the discussion of these important points an investigation of the possibility of separating π- and μ-mesons will be undertaken. The histogram in Fig. 6 contains

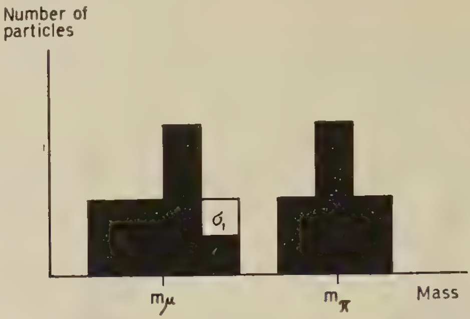

Fig. 7. Separation of π- and μ-mesons.

one group of mesons, in which there is a suggestion of separation into two. It can be noted that the group corresponding to the lower mass contains partly μ-mesons identified by electron decay and partly unidentified particles, while the other group contains π-mesons identified by π-μ decay and σ-stars and a couple of unidentified particles. The separation between the groups is incomplete due to the fact that the track length used for the mass determinations has been too small.

The histogram in Fig. 7 shows the mass distribution of 18 mesons with a mean residual range of 1,360 μ. The mass is computed by a third degree approximation of the mean track width-range relation on a somewhat simplified manner. $\partial S(R, m)/\partial m$ has been kept constant, thereby reducing the equation which determines the mass to the third degree. In this histogram the groups are separated. The standard error amounts to 7 per cent, which means that the probability of incorrect identification of a meson is only about 2 per cent if the boundary between the π- and μ-mesons is placed half-way between the groups.

In the μ-meson group there is one σ-meson. This can be a π-meson with extremely low mean track width caused by some irregularity in the emulsion, but it is more likely a negative μ-meson which has given a star [15, 16]. The star has one prong only, a proton track, which leaves the emulsion after about 200 μ. The grain density and scattering indicate that the track cannot be much longer. Since μ-meson stars have exactly this appearance it is likely that this σ-meson is a μ-meson.

Systematic errors

If the photo-electric method of measurement or the calculations were impaired by any error, which had a tendency to displace the masses in one or the other direction in relation to the proton mass, it would imply that the mass relationship com-

Table 1.

Particle	Number of particles	Calculated mass
μ-Mesons	19	$213 \pm 6\ m_e$
π-Mesons	11	$285 \pm 10\ m_e$
Protons	34	$1.00\ M_p$
Deuterons	4	$1.94 \pm 0.10\ M_p$
Tritons	1	$3.08\ M_p$

puted from the mean values of the particle groups in the histogram in Fig. 6 would be incorrect. In Table 1 the mean values for the masses of the particles in the different groups are presented. The results show that there is no reason for assuming any systematic error in the mass determinations in the region between the μ-meson mass and the triton mass, that is within the region where photo-electric measurements have so far been employed.

Standard deviation in a mass determination

The standard error of a mass determinaton has been calculated from the distribution of masses in the proton group in Fig. 7 and amounts to 10 per cent. It is probable that a mass determination even for particles with other masses can be made with an accuracy of about 10 per cent by measuring tracks with a length which is proportional to the mass, and corresponding to the lengths of the proton tracks used in this investigation. If the length of the track is increased the error will decrease. As previously mentioned the standard deviation of the masses of the π- and μ-mesons is 7 per cent calculated from tracks with a mean length of 1,360 μ.

Relations between the standard deviations in mean track width and mass

The accuracy with which the mean track width can be measured has been determined by an analysis of the component sources of error, and the distribution which can be expected in a mass determination has been determined from direct measurements of the masses of particles. The results of the two investigations should correspond even if they are expressed in different units. A comparison is a good check of the measurements, particularly valuable in controlling the analysis of the errors in the mean track width. The problem which must be solved before such a check is possible is what relations are valid between the standard deviation of the mean track width and the standard deviation of the mass.

For this calculation the problem has been somewhat simplified assuming that the total error in the mean track width is distributed along the entire track in such a manner that the integrated mean track width can be written

$$(1+\alpha)\int_0^R S(R,m)\,dR$$

where $\int_0^R S(R,m)\,dR$ is the mean value of the integrated mean track width of tracks with the residual range R of particles with the mass m, and $\alpha\int_0^R S(R,m)\,dR$ the integrated contribution from the errors. This will determine the error Δm of the computed mass.

The previously described method of determining the mass of a particle could be regarded as a calculation of the mean value of the measurements of mean track width around a function $S(R,m)$, where the statistical weight of every measurement was determined by the resolving power $\partial S(R,m)/\partial m$. It is therefore suitable to insert the factor $\partial S(R,m)/\partial m$ in the integral for the integrated contribution of the errors, so that the calculation can follow the method of mass determination as closely as possible. The integral of this product determines the "effective" increase in the integrated mean track width ΔI_{eff}:

$$\Delta I_{\text{eff}} = \alpha \int_0^R \frac{\partial S(R, m)}{\partial m} S(R, m)\, dR.$$

ΔI_{eff} can also be computed in another manner, viz. as the difference in integrated mean track width for particles with the mass m and $m + \Delta m$. Since the change in the weight of a measurement is insignificant if the mass increases by the amount Δm, ΔI_{eff} can be written:

$$\Delta I_{\text{eff}} = \int_0^R \frac{\partial S(R, m)}{\partial m} (S(R, m + \Delta m) - S(R, m))\, dR.$$

This integral determines Δm. If terms including higher degrees than the first of Δm are omitted $\frac{\Delta m}{\alpha}$ can be determined from the equation

$$\alpha \int_0^R \frac{\partial (S R, m)}{\partial m} S(R, m)\, dR = \Delta m \int_0^R \left(\frac{\partial S(R, m)}{\partial m}\right)^2 dR.$$

Both the integrals can be calculated numerically for different masses and different residual ranges. The component function for μ-mesons and protons of the integrands are given in Fig. 4 and 5. The values for $\frac{\Delta m}{\alpha}$ computed for proton tracks with different residual ranges are given in Table 2.

Table 2.

Residual range (mm)	$\frac{\Delta m}{a}$
2	10.0
4	6.6
6	5.5
8	5.0

Influence of track length on the accuracy of a mass determination

The error of the integrated mean track width in a measurement of a track has been earlier discussed, as well as the variation of the components of this error with the measured track length. Combining these results with $\frac{\Delta m}{\alpha}$ which is known from a previous calculation it is possible to estimate the standard error of a mass value as a function of the measured track length for different particles. Fig. 8 shows the result of such a computation for protons and μ-mesons. The two points marked in the diagram are the standard deviations of the direct measurements of protons and of π-

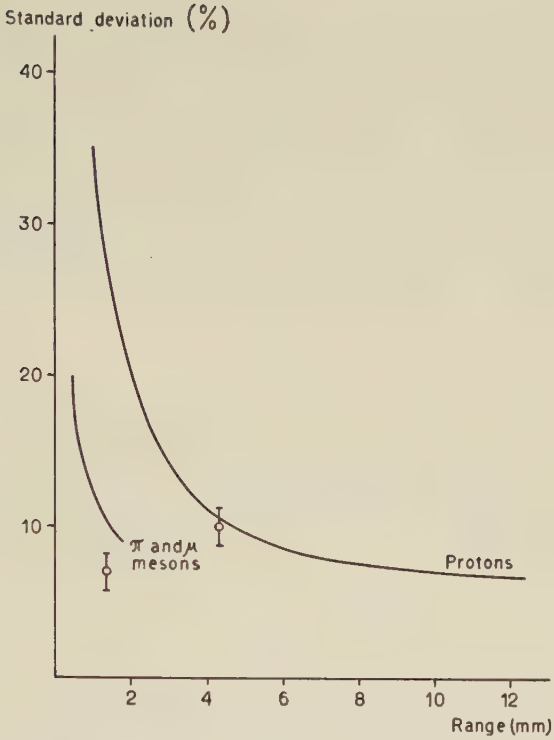

Fig. 8. The standard deviation of a mass determination *v.* residual range.

and μ-mesons (combined in one point). As is seen both the measurements lie somewhat below the corresponding curves. This can be interpreted as an over-estimate of some of the errors from which the curves are calculated.

The general form of the curves shows that the accuracy in a mass determination increases rapidly with increased range at the beginning and goes up very slowly for great ranges. For the short ranges the error is dominated by errors in the measurements and statistical variations in the number of grains. Both these errors diminish relatively quickly with increasing track length. In long tracks the error from the emulsion itself dominates. The magnitude of this depends upon the quality of the developed emulsion.

Possibilities of reducing the error

If the areas in the emulsion which have the same average level of the mean track width are large the error in a mass determination of an unknown particle can be reduced by selecting the particles of known mass for comparison in the same region in which the track of the unknown particle is found. In such a case the irregularities of the emulsion will be more or less completely compensated. Whether such a choice is at all possible depends on the size of the regions and no information on this can be obtained from the present material. Other measurements, however, have indicated that there is reason to assume that the regions are so large that in general it is possible to choose particles for the comparison from a region with similar properties [13]. As a rule the limits of the different regions in the emulsion cannot be determined, but if the particles of known mass are selected around the track of the unknown particle as near as possible, the error from the variation in the level of the mean track width will be reduced quite considerably. If the errors from the emulsion are completely eliminated the calculated standard deviation for a 4 mm proton track becomes 7 per cent instead of 11 and for a 6 mm long track 5 per cent instead of 8.5. If the variations in the average level of the mean track width in the emulsion can be eliminated the standard deviation in a mass determination will lie about 40 per cent below the standard deviations determined in this investigation.

Discussion

By means of photo-electric measurements of the grain density in tracks of an unknown particle it is, therefore, possible in favourable cases to determine the mass of this particle with a standard error of only about 6 per cent. ($R = 5$ mm.)

It can be appropriate here to compare the photo-electric method with the other methods of mass determination now in use for particles whose tracks end in the photographic emulsion, i.e., the methods where the residual range is one of the two parameters measured. The other parameter which can be determined is either the coulomb-scattering of the particle or its ionization by means of gap measurements.

The suitability of the scattering method for mass determinations has been discussed in many papers. MENON and ROCHAT measured a mixture of protons, deuterons and tritons in a plate exposed to cosmic radiation and found that the mass spectrum of these particles computed from measurements of the scattering was continuous from about the mass $M_p/2$ (M_p = the proton mass) to the mass 4 M_p without pronounced maxima in those places where according to the calculations one would expect protons, deuterons and tritons to fall [17]. HOLTEBEKK, ISACHSEN and SÖRENSEN have more recently made a similar investigation with the same result [18]. This implies that the standard error in a mass determination by means of scattering measurements is at least 20 to 25 per cent which has been confirmed by NORLIND [19]. Furthermore, MENON and O'CEALLAIGH have shown in a review of the determination of the scattering constant that it may possibly be somewhat incorrect, which would imply that every mass determination by this method will contain systematic errors [20].

The gap measurement is a measurement of the ionization [21]. It measures that part of the track which lacks grains while the photo-electric method measures the grains in the track. As a matter of principle about the same amount of useful information from the track should be obtained by both methods. The gap measurement is, however, much more subjective than the photo-electric measurement and the reliability in the measurements is thereby greatly reduced. Measurements by RITSON have demonstrated that with a special arrangement for the measurement of the total length of the gap the reproducibility is such that the total length of the gaps in a track can be measured in relation to the total length of the gaps in another track with an error that is less than 4 per cent [22]. If errors from the development and emulsion are added to this error a mass determination with a standard error of less than 10 to 15 per cent is probably not possible.

The photo-electric measurement of the mean track width of a track and the determination from this measurement of the mass of a particle is superior to both the scattering method and the gap measurement method in respect to accuracy. The photo-electric measurements are considerably slower than the measurements of scattering since it is necessary in each plate to measure many known particles for comparison. The speed of the gap measurements and the photo-electric measurements, on the other hand, do not differ greatly.

From the foregoing it is evident that the photo-electric method of measurement is particularly suitable for use in mass determinations of heavy mesons and hyperons, i.e., in measuring tracks of particles which occur infrequently and where the greatest possible precision is desirable.

Summary

An investigation is described of the accuracy of mass determinations of singly charged particles ending in a nuclear emulsion. The standard deviation amounts to 10 per cent of the mass for protons with a residual range of 4,000 microns. The greater part of this error is due to extended irregularities in the emulsions. The mass of an unknown particle can be determined with higher accuracy through a suitable choice of known particles for comparison.

ACKNOWLEDGEMENT

The author wishes to express his sincere appreciation to Professor S. von Friesen for his encouraging interest in this investigation

Department of Physics, University of Lund, February 1954.

REFERENCES

1. Blau, Rudin, and Lindenbaum, Rev. Scient. Instr. *21*, 978, 1950.
2. von Friesen and Kristiansson, Ark. f. Fysik. *4*, 505, 1951.
3. Cecarelli and Zorn, Phil. Mag. *43*, 356, 1952.
4. Kayas and Morellet, Comp. rend. *234*, 1359, 1952.
5. Della Corte and Ramat, Nuovo Cimento *9*, 605, 1952.
6. Demers and Mathieu, Can. J. Phys. *31*, 97, 1953.
7. van Rossum, Comp. rend. *236*, 2234, 1953.
8. von Friesen and Stigmark, Ark. f. Fysik. *8*, 121, 1954.
9. Kristiansson, Phil. Mag. *44*, 268, 1953.
10. Hodgson, Br. J. of Appl. Phys. *3*, 11, 1952.
11. Della Corte, Ramat, and Ronchi, Nuovo Cimento *10*, 509, 1953.
12. Mitchell, Fundamental of Photographic Sensitivity. London 1951, p. 321.
13. von Friesen, Ark. f. Fysik, *8*, 305, 1954.
14. Smith, Birnbaum, and Barkas, Phys. Rev. *91*, 765, 1953.
15. George and Evans, Proc. Phys. Soc. *64 A*, 193, 1951.
16. Fry, Phys. Rev. *85*, 676, 1952.
17. Menon and Rochat, Phil. Mag. *42*, 1232, 1951.
18. Holtebekk, Isachsen, and Sörensen, Phil. Mag. *44*, 1037, 1953.
19. Norlind, Ark. f. Fysik, *8*, 155, 1954.
20. Menon and O'Ceallaigh, Phil. Mag. *44*, 1291, 1953.
21. Hodgson, Phil. Mag. *41*, 725, 1950.
22. Ritson, Phys. Rev. *91*, 1572, 1953.

Tryckt den 23 oktober 1954

Uppsala 1954. Almqvist & Wiksells Boktryckeri AB

ARKIV FÖR FYSIK Band 8 nr 32

Communicated 14 April 1954 by MANNE SIEGBAHN and ERIK HULTHÉN

The band-spectrum of the Cu_2-molecule

By BENGT KLEMAN and STIG LINDKVIST

With 2 figures in the text

In a King's furnace loaded with copper there appear two strong band-systems, one extended system in the green region and one shorter in the blue region. A vibrational analysis of these systems showing that they have a common final state has been made. By means of the vibrational isotope effect in the green system it is shown that the emitter is Cu_2. The blue system is identical with a system which has earlier been ascribed to CuI (MULLIKEN's *B*-system) [1].

The existence of band-spectra obtained with silver and gold under similar experimental conditions is reported. These spectra have been presumed to be due to Ag_2 and Au_2.

Introduction

In the course of an investigation of the appearance of the band-spectra from metal oxides excited in a King's furnace we observed, when the furnace was loaded with copper, silver or gold, some unknown molecular band-systems which did not seem to be due to the oxides. In the meantime a paper by ZEEMAN [2] has appeared, in which he describes a band-spectrum obtained in emission from a King's furnace with aluminium. The presence of the spectrum was independent of the atmosphere in the furnace, but was found to depend on whether the aluminium metal was placed in a liner of carbon or in one of zirconium oxide. This led him to conclude that the spectrum was due to AlC, despite the smallness of the ω-values obtained from the vibrational analysis, which pointed to a somewhat heavier molecule.

The green systems with copper and gold, obtained under very similar conditions, show sequences of the same length and ω-values of the same order of magnitude as the spectrum obtained with aluminium by ZEEMAN.

In the present paper we start with copper, since the isotope effect in the extended green system makes it possible to conclude that the emitter is the Cu_2-molecule. Some band-systems obtained from copper salts in a flame have been ascribed to Cu_2 by SINGH [3]. There are, however, in this case no rigorous proofs that the bands are really due to Cu_2, and we do not find any agreement between our constants for the Cu_2-molecule and those obtained by SINGH.

Experimental

The emission from a King's furnace loaded with copper has been investigated. At a temperature of 1900°–2000° C there appear two strong band-systems in the visual region, one extended green system and a shorter blue system. The emission of

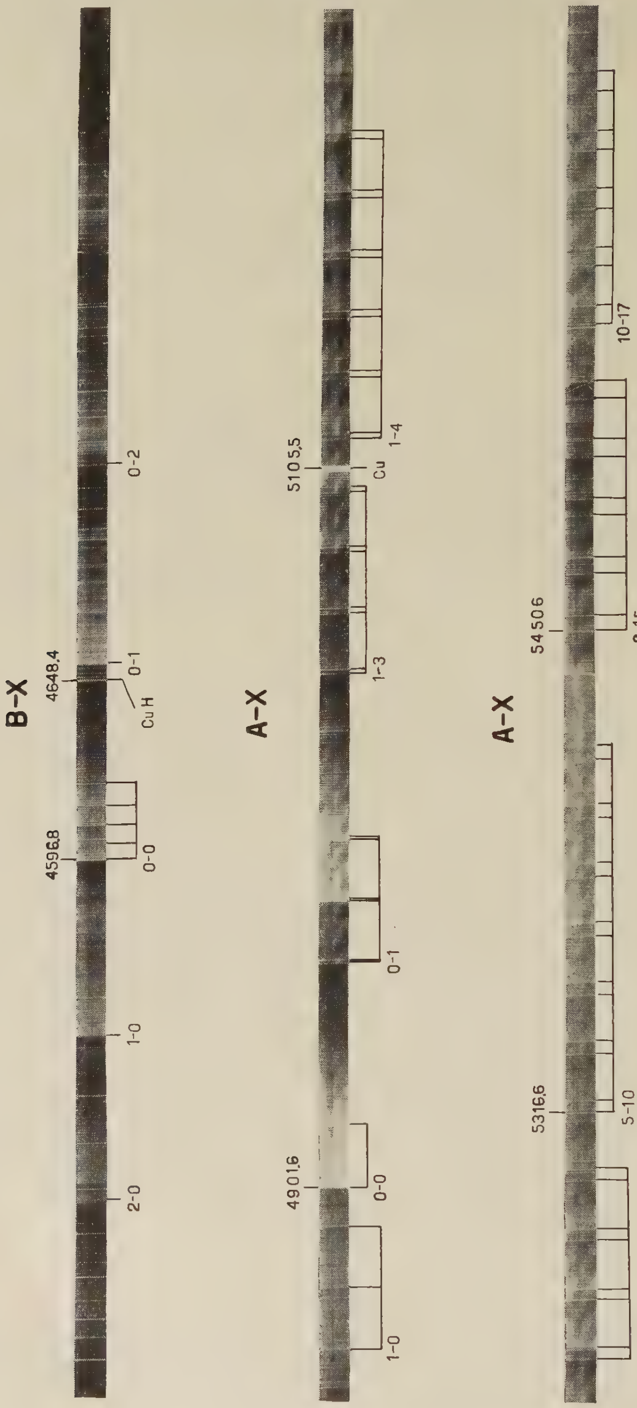

Fig. 1. The green A–X and the blue B–X band-systems of Cu_2.

Table 1. Wave-numbers of the band-heads A–X

Δv	$v' v''$	$Cu^{63}Cu^{63}$	$Cu^{63}Cu^{65}$	Δv	$v' v''$	$Cu^{63}Cu^{63}$	$Cu^{63}Cu^{65}$
+1	1,0	20586.2		−5	4,9	18851.2	18862.4
	2,1	20513.6			5,10	18792.5	18803.8
	3,2	20441.2			6,11	18734.1	18746.6
					7,12	18676.6	18689.4
0	0,0	20396.1			8,13	18619.1	18632.4
	1,1	20323,6			9,14	18562.7	18575.9
					10,15	18506.6	18520.0
−1	0,1	20131.5	20133.7		11,16	18450.5	18464.6
	1,2	20060.7	20063.9				
	2,3	19991.3	19994.2	−6	7,13	18437.2	18451.5
					8,14	18381.7	18396.9
−2	1,3	19800.9	19805.6		9,15	18326.8	18341.6
	2,4	19732.9	19738.2		10,16	18272.7	18288.1
	3,5	19666.4	19671.8		11,17	18218.2	18233.7
	4,6	19600.8	19607.0		12,18	18164.2	18179.6
					13,19	18109.5	18125.8
−3	0,3	19609.8	19615.6		14,20	18054.8	18071.5
	1,4	19543.2	19549.3				
	2,5	19476.9	19484.1	−7	10,17	18040.5	18057.8
	3,6	19412.4	19420.0		11,18	17988.2	18005.2
	4,7	19349.1	19356.8		12,19	17935.9	17953.8
	5,8	19286.4	19294.3		13,20	17883.3	17900.5
	6,9	19223.8	19232.6		14,21	17830.7	17848.9
					15,22	17777,9	17796.6
−4	3,7	19161.3	19170.3				
	4,8	19099.4	19109.0	−8	9,17	17861.3	
	5,9	19038.3	19048.2		10,18	17811.0	
	6,10	18978.0	18988.4		11,19	17760.0	17777.9
	7,11	18919.1	18929.6		12,20	17709.8	17728.4
	8,12	18859.6	18870.5		13,21	17659.0	17678.3
	9,13	18801.3	18812.5		14,22	17608.7	17627.9
					15,23	17557.3	17577.4
					16,24	17506.7	17526.3
					17,25	17453,8	17475.0
					18,26	17403.0	17423.2

the systems seems to be independent of the atmosphere in the furnace, and we obtain them equally well with hydrogen, nitrogen or argon. Neither do they in any critical way depend on the pressure of the gas, but we have in most of our exposures maintained an argon-pressure of about 500 torr in order to diminish the evaporation of the metal.

Preliminary exposures were made in a Hilger Medium Quartz spectrograph. The final spectrograms were taken in the first order of a plane grating in Littrow mounting with a dispersion of about 5 Å/mm. In this spectrograph the region 4000–6000 Å was photographed on Ilford Thin Film Half Tone and Thin Film Panchromatic Half Tone plates. The exposure times were varied from five minutes in the violet to one hour in the orange.

The green system

We will denote the green system A–X and the blue system B–X. The assumption that the common final level X is the ground-state of Cu_2 seems very plausible in view of the low energy of exitation in the light source.

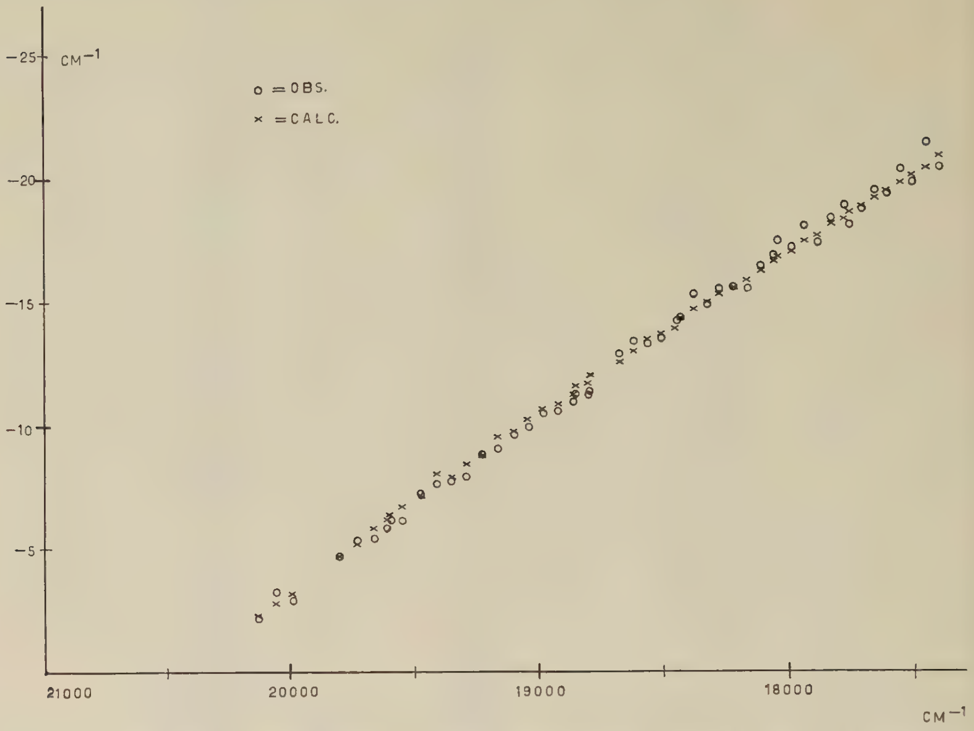

Fig. 2. The vibrational isotope splitting between $Cu^{63}Cu^{63}$ and $Cu^{63}Cu^{65}$ in the *A–X* system of Cu_2 plotted against the wave-numbers of the band-heads of $Cu^{63}Cu^{63}$. The calculated splitting has been obtained by applying the theoretical ϱ-value to the equation for the band-heads of $Cu^{63}Cu^{63}$ [subtraction of equations (1) and (2)].

The 0,0-band of *A–X* is easily recognised in Fig. 1 and the assignment of the vibrational quantum numbers of the bands present little difficulty. There are two isotopes of copper Cu^{63} and Cu^{65}, with a relative abundance of 69 and 31 per cent respectively. We thus expect the three molecules $Cu^{63}Cu^{63}$, $Cu^{63}Cu^{65}$ and $Cu^{65}Cu^{65}$ to be present in a ratio of about 10 : 9 : 2. We have been able to measure the band-heads of the rarest isotope molecule $Cu^{65}Cu^{65}$ only for a few bands, since they are mostly lost in the partly resolved rotational structure of the stronger bands. Table 1 gives the position of the band-heads $Cu^{63}Cu^{63}$ and $Cu^{63}Cu^{65}$.

The vibrational analysis has been carried out for the $Cu^{63}Cu^{63}$-molecule and gives the following equation for the band-heads:

$$Cu^{63}Cu^{63} : \sigma_{v'v''} = 20396.0_0 + [191{,}5_0 v' - 0.375_0 v'^2 - 0.018_0 v'^3] - \\ - [265.1_1 v'' - 1.023_4 v''^2 + 0.0008_0 v''^3]. \quad (1)$$

The constants have been determined graphically.

If we calculate the equation for the band-heads of $Cu^{63}Cu^{65}$ from the equation (1) by applying the theoretical ϱ-value 0.99228 and make use of the relations

$$\omega_e^i = \varrho\,\omega_e,\ \omega_e^i x_e^i = \varrho^2 \omega_e x_e \text{ and } \omega_e^i y_e^i = \varrho^3 \omega_e y_e,$$

we get

$$\mathrm{Cu}^{63}\mathrm{Cu}^{65}: \sigma_{v'v''} = 20396.2_9 + [190.0_2 v' - 0.369_0 v'^2 - 0.017_6 v'^3] - \\ - [263.0_7 v'' - 1.007_6 v''^2 + 0.0007_8 v''^3]. \qquad (2)$$

This equation gives the band-heads of $\mathrm{Cu}^{63}\mathrm{Cu}^{65}$ with about the same accuracy as equation (1) gives them for $\mathrm{Cu}^{63}\mathrm{Cu}^{63}$, as may be seen from a comparison of the observed and calculated isotope splitting in Fig. 2.

The isotope effect thus proves that the Cu_2-molecule is the carrier of the observed spectrum, and at the same time it serves as a check on the correctness of the vibrational analysis.

An estimation of the B' and B'' values from the relations by GUGGENHEIMER [4] shows that the band-heads lie very near the origins, and it is thus to be expected that the equation for the origins should be very nearly approximated by the equation for the band-heads.

The blue system

In the blue system, contrary to the green system, the heads are not very marked, and it is difficult to localize them exactly. By looking at the bands in an *à vision directe* one gets an impression of diffuseness in the last observable sequences $\Delta v = -4, -3, +3$ and $+4$, and we are not able to fix the positions of the heads in these sequences. The ω-values for the upper and lower states are more equal in the system B–X than in A–X, and if a predissociation occurs in the B-term the branches in the last observed bands may be cut off before they form a head. The rotational structure in B–X is in parts well-resolved and this increases the difficulty of measuring the heads. It has not been possible to distinguish the heads due to the different isotopes. The measurements of the band-heads of B–X are given in Table 2. The positions of the heads may be represented by the following equation:

$$\mathrm{Cu}_2: \sigma_{v'v''} = [21747.5 + 243.8 v' - 2.0 v'^2 - 0.02 v'^3] - [265.2 v'' - 1.0 v''^2]. \qquad (3)$$

This system is obviously identical with a system measured by MULLIKEN in his study of CuI and ascribed to CuI by him [1]. MULLIKEN gives the following equation for the heads:

$$(B\text{–}X \text{ of CuI}): \sigma_{v'v''} = 21748.3 + [241.8 v' - 1.88 v'^2] - [265.4 v'' - 1.0 v''^2].$$

MULLIKEN excited the CuI-molecule with active nitrogen, getting five band-systems which he ascribed to CuI. Of these, the system under discussion, B–X, was the weak-

Table 2. Wave-numbers of the band-heads B–X.

$\Delta v = -2$		$\Delta v = -1$		$\Delta v = 0$		$\Delta v = +1$		$\Delta v = +2$	
0.2	21222.1	0.1	21483.5	0.0	21747.5	1.0	21989.4	2.0	22227.3
				1.1	21725.1			3.1	22196.1
				2.2	21700.5				
				3.3	21673.9				
				4.4	21644.6				

Table 3. Constants (in Kaysers) of the $Cu^{63}Cu^{63}$-molecule obtained from the vibrational analysis.

	Ground state *X*	*Upper states*	
		A	*B*
σ_e	0	20433.0	21757.8
		$A \rightarrow X$	$B \rightarrow X$
σ_{00}		20396.0	$21747._5$
ω_e	266.1	191.9	$245._8$
ω_0	265.1	191.5	$243._8$
$\omega_e x_e$	1.025	0.348	2.0
$\omega_0 x_0$	1.023	0.375	2.0
$\omega_e y_e = \omega_0 y_0$	0.0008	−0.018	−0.02

est, and it also gave the poorest agreement with the constants of the ground state of CuI. Ritschl [5], in his work on the copper halogenides in absorption, did not observe the B–X system, though he did obtain the other four. Unfortunately, the ω-value of the ground state of CuI is only slightly less than that of Cu_2, and the precision in the measurements of the B–X-system does not admit of a decision as to which of the two molecules is the carrier of these bands. We are thus left to decide this by assessing the experimental conditions under which the system appears. The blue system which appears in a King's furnace is of a dominating strength, stronger than the green system of Cu_2, and we find the simultaneous absence of the four known systems of CuI to be adequate proof that the blue system does not belong to CuI. We thus conclude that the emitter of the blue system is Cu_2.

Energy of dissociation

An estimate of the energy of dissociation of the ground-state of Cu_2 is obtained by the formula

$$D_0 = \frac{\omega_0^2}{4\,\omega_0 x_0}.$$

This gives us the value $D_0^0 = 2.1$ eV.

Gold and silver

The band-spectra from a King's furnace loaded with gold and silver have also been recorded.

With gold there appears in emission an extended green system stretching from about 4800 to 6400 A. This band-system gives a regular impression and resembles the A–X system of Cu_2.

The band-spectra obtained with silver seem to be of a more complicated nature. There is a strong continuum having its long-wave-length limit at about 5000 A. There also appears a strong short system with sharp heads in the region 4300–4500 A.

The whole region from 4000–6000 A is covered with numerous faint and mostly diffuse bands.

We make the preliminary assumption that the related band-spectra are due to Au_2 and Ag_2. These will be discussed in later papers.

Physics Department, University of Stockholm. April 1954.

REFERENCES

1. Mulliken, R. S., Phys. Rev. *26*, 1, 1925.
2. Zeeman, P. B., Can. J. Phys. *32*, 9, 1954.
3. Singh, N. L., Proc. Ind. Acad. *25 A*, 1, 1946.
4. Guggemheimer, K. M., Proc. Phys. Soc., London, *58*, 456, 1946.
5. Ritschl, R., Z. f. Phys. *42*, 172, 1927.

Tryckt den 23 oktober 1954

Uppsala 1954. Almqvist & Wiksells Boktryckeri AB

ARKIV FÖR FYSIK Band 8 nr 33

Communicated 12 May 1954 by ERIK HULTHÉN

Microwave spectrum of chlorobenzene

By GUNNAR ERLANDSSON

The spectrum of monochlorobenzene has been investigated in the K-band microwave region. The lines arising from the rotational transitions $J=7$–8 and $J=8$–9 of $C_6^{12}H_5Cl^{35}$ have been identified and used for evaluation of rotational constants and moments of inertia.

In Table 1 observed frequency values are listed together with values calculated from the following rotational constants

$$A=5.6667 \qquad B=1.5769 \qquad C=1.2333 \quad \text{kMc/sec}$$

and the asymmetry parameter $\varkappa=-0.8450$. Calculated and observed values agree within the limits of error (± 5 Mc/sec). The corresponding moments of inertia are

$$I_A=89.19 \qquad I_B=320.5 \qquad I_C=409.8 \quad \text{AÅ}^2.$$

Table 1. $C_6^{12}H_5Cl^{35}$

Transition	$\nu_{\text{calc.}}$	$\nu_{\text{obs.}}$	Transition	$\nu_{\text{calc.}}$	$\nu_{\text{obs.}}$
$7_{0.7}-8_{0.8}$	21149	21151	$8_{0.8}-9_{0.9}$	23584	23584
$7_{1.7}-8_{1.8}$	20781	—	$8_{1.8}-9_{1.9}$	23303	23308
$7_{1.6}-8_{1.7}$	23342	23339	$8_{1.7}-9_{1.8}$	26064	26063
$7_{2.6}-8_{2.7}$	22231	22233	$8_{2.7}-9_{2.8}$	24926	24923
$7_{2.5}-8_{2.6}$	23556	23554	$8_{2.6}-9_{2.7}$	26615	26616
$7_{3.5}-8_{3.6}$	22642	22642	$8_{3.6}-9_{3.7}$	25481	25483
$7_{3.4}-8_{3.5}$	22829	22830	$8_{3.5}-9_{3.6}$	25811	25807
$7_{4.4}-8_{4.5}$	22624	22628	$8_{4.5}-9_{4.6}$	25483	25483
$7_{4.3}-8_{4.4}$	22632		$8_{4.4}-9_{4.5}$	25502	25502
$7_{5.3}-8_{5.4}$	22583	22578	$8_{5.4}-9_{5.5}$	25428	25427
$7_{5.2}-8_{5.3}$	22583		$8_{5.3}-9_{5.4}$	25428	
$7_{6.2}-8_{6.3}$	22560	22560	$8_{6.3}-9_{6.4}$	25395	25395
$7_{6.1}-8_{6.2}$	22560		$8_{6.2}-9_{6.3}$	25395	
$7_{7.1}-8_{7.2}$	22546	—	$8_{7.2}-9_{7.3}$	25376	25375
$7_{7.0}-8_{7.1}$	22546	—	$8_{7.1}-9_{7.2}$	25376	
			$8_{8.1}-9_{8.2}$	25363	25359
			$8_{8.0}-9_{8.1}$	25363	

Table 2. $C_6^{12}H_5Cl^{37}$

Transition	$\nu_{calc.}$	$\nu_{obs.}$	Transition	$\nu_{calc.}$	$\nu_{obs.}$
$8_{0.8}-9_{0.9}$	23083	—	$8_{5.4}-9_{5.5}$	24774	24776
$8_{1.8}-9_{1.9}$	22781	—	$8_{5.3}-9_{5.4}$	24774	
$8_{1.7}-9_{1.8}$	25435	—	$8_{6.3}-9_{6.4}$	24744	24746
$8_{2.7}-9_{2.8}$	24323	24318	$8_{6.2}-9_{6.3}$	24744	
$8_{2.6}-9_{2.7}$	25883	—	$8_{7.2}-9_{7.3}$	24727	—
$8_{3.6}-9_{3.7}$	24828	24827	$8_{7.1}-9_{7.2}$	24727	—
$8_{3.5}-9_{3.6}$	25110	25114	$8_{8.1}-9_{8.2}$	24715	—
$8_{4.5}-9_{4.6}$	24824	24827	$8_{8.0}-9_{8.1}$	24715	—
$8_{4.4}-9_{4.5}$	24839	24834			

The value of I_A may be compared to the corresponding value found for fluorobenzene [1], $I_A = 89.230$ and for benzonitrile [2], $I_A = 89.39$. The present value is less accurate than for fluorobenzene, and the difference cannot be considered significant. The results thus indicate that the benzene skeleton is fairly undisturbed by the substitutions. Assuming this structure to be regularly hexogonal and putting $d_{CH} = 1.050$ Å and $d_{CC} = 1.404$ Å (cf. ref. [1]) the C–Cl bond distance may be calculated to $d_{CCl} = 1.706$ Å.

From the above results the rotational constants for $C_{12}^6H_5Cl^{37}$ have been calculated to

$$A = 5.6667 \qquad B = 1.5320 \qquad C = 1.2063 \quad \text{kMc/sec}$$

and the asymmetry parameter $\varkappa = -0.8537$. Expected absorption frequencies for $J = 8–9$ have been calculated from these constants and compared to observed frequencies. The results are found in Table 2. Observations have been made with the naturally occurring concentration of the isotope. The lines are then, with present technique, barely above noise level, and the results are therefore not fit for detailed analysis. The agreement seems, however, to be satisfactory.

Department of Physics, University of Stockholm, April 1954.

REFERENCES

1. G. Erlandsson, Arkiv för Fysik 7 nr 17 (1953).
2. —, Journ. Chem. Phys. (Awaiting publication).

Tryckt den 23 oktober 1954

Uppsala 1954. Almqvist & Wiksells Boktryckeri AB

ARKIV FÖR FYSIK Band 8 nr 34

Read 14 April 1954

Diffraction gratings in immersion

By E. HULTHÉN and H. NEUHAUS

With 7 figures in the text

Introduction

At the London Optical Conference in 1950 it was suggested [1] that the resolving power R of diffraction gratings might be increased by immersing the grating in a transparent medium of high refracting index μ_i. Thus

$$R = \frac{2\,W \sin \alpha}{\lambda} \cdot \mu_i, \tag{1}$$

where W is the ruled width of the grating and where α applies to the case of autocollimation of incidence and diffraction. The idea is a strict parallel to that of the immersion microscope, the optical resolving power in both cases being determined by the effective or numerical aperture of the instrument expressed in wave-length units. The application of the immersion principle to spectroscopy was further developed [2] in accordance with Fig. 1 a and b.

Fig. 1 a applies to the case in which a fine-ruled grating is brought into optical contact with a plane glass plate through an immersion-oil of high refracting index. Obviously, the diffraction angle α will in this case remain unmodified by the glass plate, which serves only to protect the surface of the immersion and make it optically plane. Thus, assuming unity for the refracting index of air, one gets:

$$\mu_i \sin \alpha = \mu_g \sin \beta = \sin \gamma \tag{2}$$

and

$$m\lambda = 2\sigma \cdot \mu_i \sin \alpha.$$

Here α stands for the angle of incidence and diffraction in the immersion, β and γ for the angles of refraction in the glass plate and in the air. The diffraction at the compound grating therefore still obeys the ordinary grating equation:

$$m\lambda = 2\sigma \sin \gamma \tag{3}$$

as indicated by the dotted ray in Fig. 1 a. Consequently, the spectrum produced by an immersion grating will coincide in all orders with the spectrum produced by the

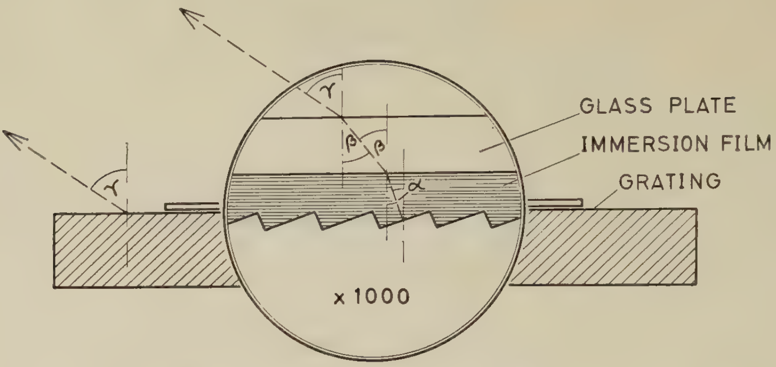

Fig. 1 a. The immersion of a fine-ruled grating with blaze angle $\alpha < 20°$.

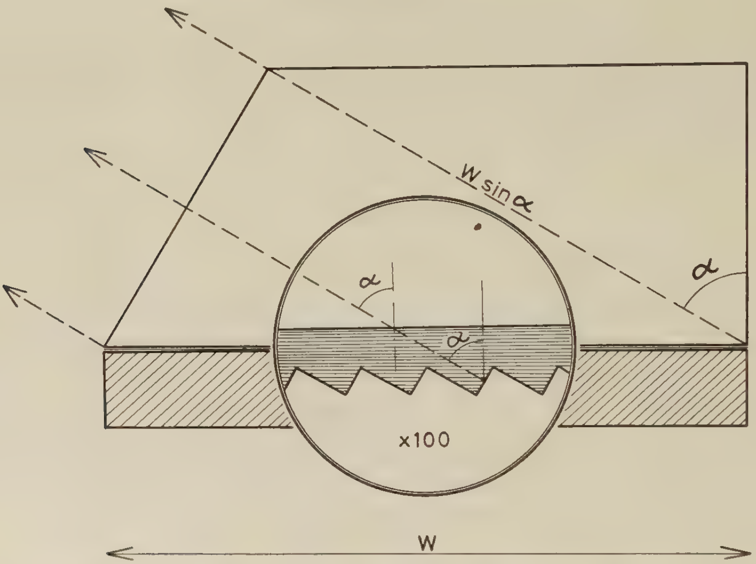

Fig. 1 b. The immersion of a coarse-ruled grating with blaze angle $\alpha \simeq 60°$ and combined with a prism. It is assumed that the refracting indices of the immersion and the prism are nearly identical, $\mu_i \simeq \mu_g$.

ordinary grating. Both kinds of spectra will, however, exhibit great differences in intensity, as the immersion spectra are produced at a steeper angle of incidence α than the angle of incidence γ occurring at the uncovered surface:

$$\sin \gamma = \mu_i \sin \alpha. \tag{4}$$

These relations will be demonstrated in § 1.

Fig. 1 a refers to the ordinary dense-ruled grating in immersion where the blaze generally appears in the first or second orders of spectrum, corresponding to angles of incidence of less than 20°. In the coarse-ruled gratings, however, the blaze sometimes appears at high angles of incidence $\simeq 60°$. When applying the method to a grating of this type, it is advantageous to let the beam pass through a prism or a side-facet in the glass plate as indicated in Fig. 1 b. This case differs in many respects from the relations holding in case 1 a, and will be treated in § 2 and 3.

§ 1. Observations on the intensity shift in the diffraction produced by an immersion grating according to Fig. 1 a

The statement derived above, concerning the angular coincidence in all orders of the spectra produced by the grating in immersion and the uncovered grating, follows directly from Snell's law of refraction and needs no further elucidation here.

The essential feature of this type of immersion grating is, however, its capacity to push the intensity into higher orders in the spectrum. Thus a grating characterized by a blaze at the angle of α will according to equation (4) have the blaze shifted into the angle γ when it is used as an immersion grating. This corresponds to a shift of blaze from an order m into the range of $\mu_i \cdot m$. Striking illustrations of this effect were obtained from photographs of the grating surface according to the arrangement shown in Fig. 2. Thus a coverglass fastened to the grating with an immersion-oil

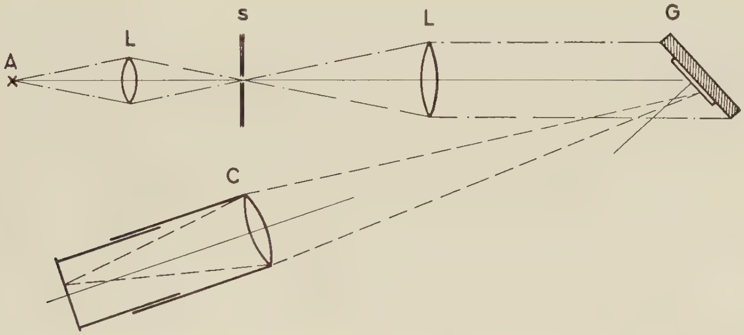

Fig. 2. Recording the intensity shift produced by an immersion grating according to Fig. 1 a. *A*: Light-source, *LL*: lenses, *S*: slit, *G*: plane grating, partly screened by a coverglass, immersed to the grating surface, *C*: a telescope or camera, imaging the grating surface.

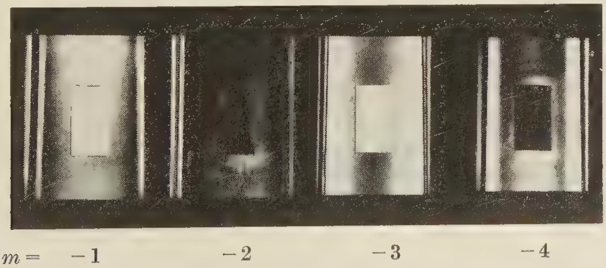

Fig. 3. Contrast patterns of the grating illuminated in different spectral orders $m = -1, -2, -3, -4$, according to Tab. 1.

Table 1. Photoelectric recordings of the intensity shifts of Hg λ 5461 in different spectral orders from a plane grating ruled with 288 grooves/mm, uncovered and immersed in α-bromnaphthalene according to Figs. 1 a, 2 and 3.

Spectral order	*Grating*	
	uncovered	immersion
6	3.2	2.2
5	6.1	10.1
4	14.1	42.5
3	10.6	44.3
2	82.5	29.2
1	77.0	31.4
0	100.0	100.0
−1	63.8	96.7
−2	3.1	2.0
−3	6.2	13.3
−4	5.1	4.3
−5	9.2	1.7
−6	8.5	3.2

appears in high or dark contrast to the uncovered part of the grating when illuminated in different orders of monochromatic light, Fig. 3.

Some photographs of the contrast images taken with the camera C, Fig. 2, are shown in Fig. 3. A series of corresponding photoelectric measurements of the intensity relations between the contrast images are given in Table 1. These recordings support our assumptions regarding the intensity shift into higher orders in the spectrum produced by grating in immersion. Including high orders ($m = 10$), the spectral lines produced by the grating immersed in α-bromnaphthalene appeared sharp and distinct. The blurring effects due to the immersion-oils earlier reported [2] probably constitute no serious hindrance to the attainment of a high spectroscopic resolution in the way indicated in Fig. 1 a. The flexibility of the method makes it attractive for further investigations.

§ 2. The échelle grating in immersion

A Harrison échelle grating from Bausch and Lomb Optical Co. enabled us to test the immersion principles at very high spectroscopic resolutions, according to the scheme shown in Fig. 1 b.

The Bausch and Lomb échelle grating, marked 154 A-9, is an aluminized replica on glass, covering an area of 102 × 203 mm^2 with 80 grooves per mm. When used near its blaze angle, $\alpha = 63° 40'$, the grating exhibits the high efficiency of 50 % of the mercury green light in its 41th order, far beyond that of an ordinary grating used at this angle. The blaze is, however, limited to a very narrow angle, Table 2.

This means that the échelle has to be used in a Littrow mounting of autocollimation ($\alpha \simeq \beta$). The grating was temporarily mounted on a heavy stone table, 5 × 1 meters, the light-beam from the slit made parallel by reflection from a concave mirror of 450 cm facal length. The light-beam to and from the échelle was thus twice re-

Table 2. Photoelectric recordings of the intensity shifts of Hg λ 5461 in different spectral orders from an échelle grating with 80 grooves/mm, uncovered and immersed in α-bromnaphthalene according to Fig. 1 b.

Échelle uncovered			Échelle in immersion	
Order	Diffraction angle	Intensity	Order	Intensity
37	–	5.3	M – 4	1.2
38	–	9.4	M – 3	0.9
39	58°26′	7.8	M – 2	2.5
40	60°54′	3.4	M – 1	8.8
41	63°35′	*100.0*	M	*100.0*
42	66°34′	5.5	M + 1	*64.7*
43	69°55′	1.1	M + 2	0.2

$\mu \simeq 1.66,\ M = \mu_i \cdot m \simeq 68$

flected by the mirror and brought to focus close to the slit. The 18 meter light-path of this mounting, including three reflections, made it, however, rather exposed to aerial and mechanical disturbances.

When applied for immersion the échelle was combined with a 30°/60° flint-glass prism according to Fig. 1 b. In order to reduce the light path and the number of interfering reflections, the front face of the prism was ground spherically convex with a curvature corresponding to the 4.5 meter focal length of the mounting already existing, Fig. 4. The simplified construction of the optics, together with an effective reduction of the mechanical disturbances attained by resting the stone table on spongy rubber, greatly increased the efficiency of the spectrograph. Well-defined spectral images of very high dispersion, ≃ 5–8 mm/Å, were obtained with this instrument, even when the exposures were prolonged up to one hour.

The slit-width and the illumination of the slit are important conditions for the attainment of a high optical purity in the spectrum. These problems have been investigated in detail by VAN CITTERT [3], who distinguished the cases of coherent and incoherent illuminations of the slit. When no condensing lens was used, the coherent illumination desired was obtained by placing the light-source at such a distance

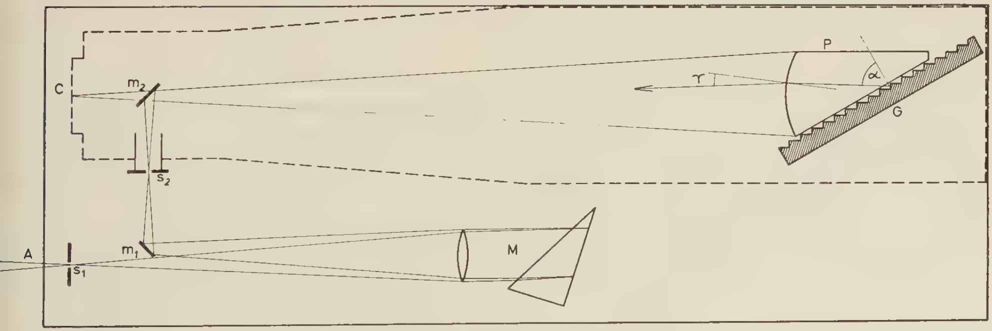

Fig. 4. The échelle grating in immersion according to 1 b. S_1: narrow slit to the monochromator M, S_2: open entrance-slit of the échelle spectrograph, G–P: échelle grating combined with a 30°/60° prism with convex front aperture, C: focal plane.

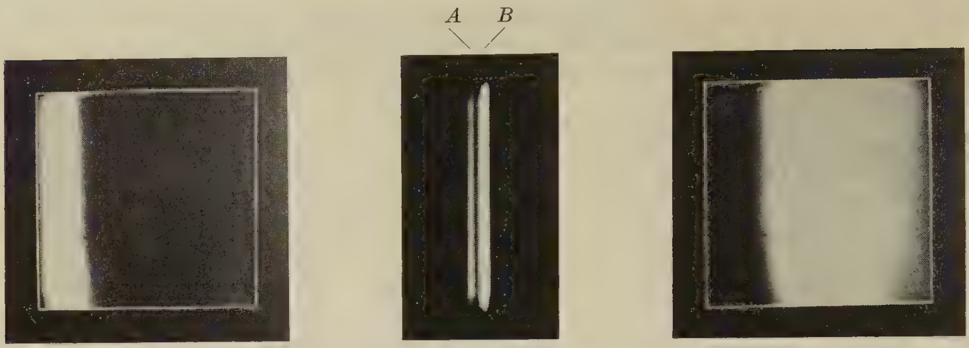

a. b. c.

Figs. 5 a, b, c. Fig. 5 b. Cd λ 5086, split into two components *A* and *B*, according to an exposure of the échelle grating, unscreened. Figs. 5 a and 5 c show the contrast patterns of the grating when illuminated by *A* and *B* respectively.

from the slit that the beam of light passing through a wide-open slit covered only 2/3 of the grating aperture (= 7.5 cm). With successive narrowing of the slit the illumination spread out over the entire aperture of the grating by diffraction. The optimal slit-width was set according to the relation:

$$s=\tfrac{3}{2}\Omega^{-1}\lambda,$$

where Ω^{-1} indicated the inverse angular aperture of the grating ($\Omega^{-1}\simeq 60$).

The crowding of overlapping orders in the spectrum of the échelle-immersion grating (Table 2) was eliminated by placing a monochromator M in front of the entrance-slit S_2. This arrangement was preferred, as being more efficient than interference filters. The spectral lines produced by the monochromator thus acted as a set of coherently illuminated slits within the wide-open entrance-slit S_2 of the échelle spectrograph.

It may be added that the increased crowding of the spectral orders within the blaze angle of the échelle grating in immersion as well as the increase of the dispersion, necessarily entail a corresponding decrease in the light-power of the instrument.

From strioscopic investigations, to be published later, it appeared that the grating and the prism suffer from some optical imperfections. Thus the spectral images produced by the échelle were badly marred by a ghost-line, Fig. 5, sharing $\simeq 20\%$ intensity of the main line. When the échelle was viewed in a telescope placed close behind the spectral line, the impaired parts of the grating were brilliantly illuminated when the main line was masked, Fig. 6 a. Conversely, the perfect parts of the grating were brilliantly illuminated when the ghost-line was masked, Fig. 6 b. Consequently, when the impaired parts of the échelle were masked, the ghost disappeared completely. Through this procedure of masking, the useful width of the grating and the prism in combination was reduced to 15 cm.

The joining of the échelle and the prism entails heavy temperature disturbances in connection with the unavoidable handling, so that the spectral images produced are at first very poor. The high spectroscopic dispersion and optimal resolution were therefore somewhat delayed, as it took several hours before the thermal state of the instrument was stabilized.

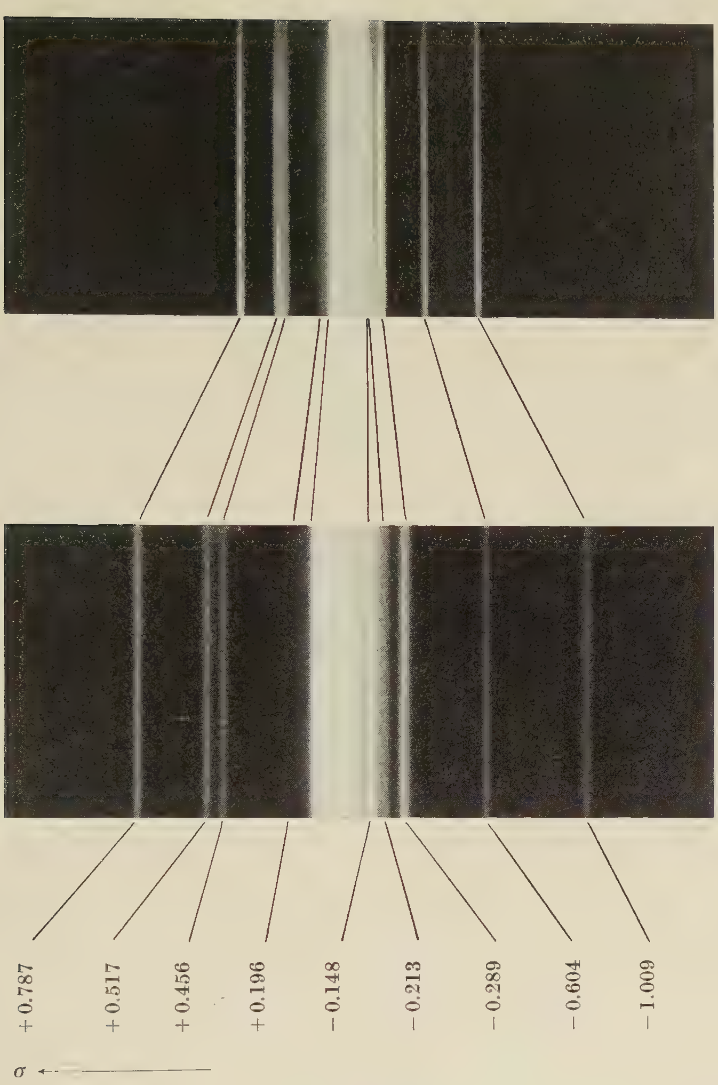

Fig. 6 a.

§ 3. The resolving power and the dispersion of the échelle grating in immersion

An immersion spectrograph built according to Fig. 4 is composed of a grating and a prism, each contributing to the resolving power and the dispersion of the instrument. The optical qualities of both components must therefore be of a very high standard. The optimal aperture of the compound system are attained when the incoming and the diffracted beams of light propagate along the optical axis of the instrument. Disregarding some inconsiderable effects arising from the light refractions between the immersion film, α-bromnaphthalene, and the glass prism

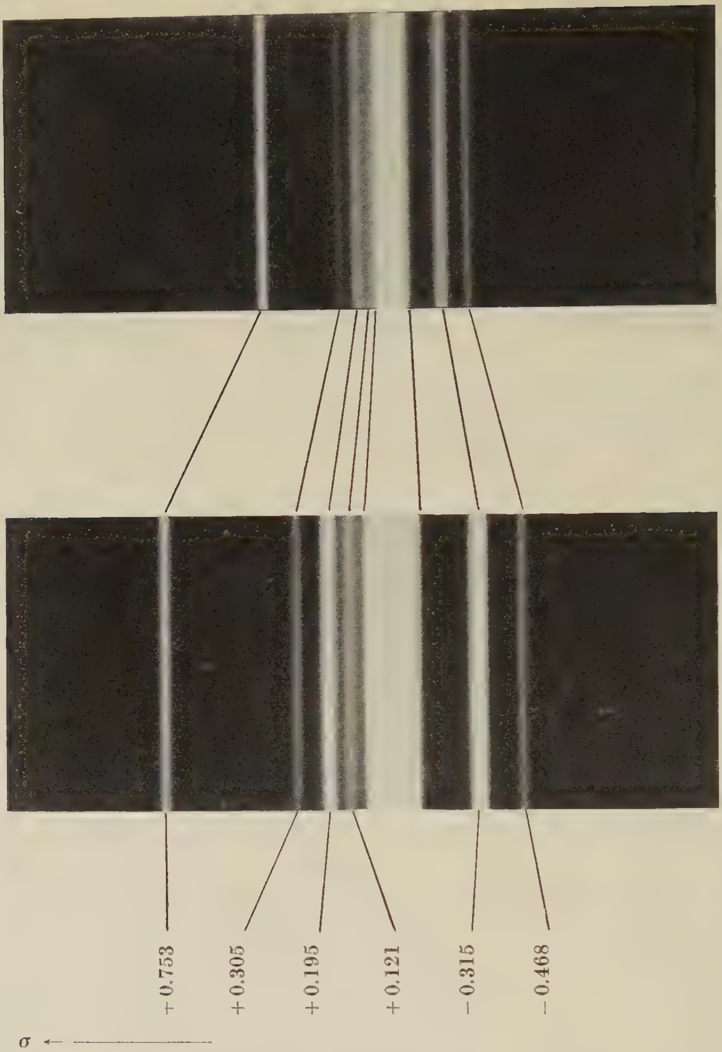

Fig. 6 b.

Figs. 6 a and b. The hyperfine structures of Hg λ 4358 and 5461 from exposures of the échelle grating uncovered and in immersion. Light-source: an end-on discharge tube cooled by air. The linear dispersion measured at λ 4358: $D_i = 7.70$ mm/Å, $D_0 = 3.60$ mm/Å, $D_i/D_0 = 2.14$; linear dispersion at λ 5461: $D_i = 5.86$ mm/Å, $D_0 = 3.33$ mm/Å, $D_i/D_0 = 1.76$.

($\mu_i \neq \mu_g$, Fig. 1 a), the resolving power of the instrument will here be derived from general considerations concerning the total light-path difference H between the bordering rays when expressed in wave-number units. Thus

$$H = \frac{2\,W \sin\beta}{\lambda} \cdot \mu_g \tag{4}$$

and

$$\delta H = \frac{2\,W \sin\beta}{\lambda}\mu_g\left(\frac{\lambda}{\mu_g}\cdot\frac{d\mu_g}{d\lambda}-1\right)\delta\lambda.$$

Applying the Raleigh criterion for spectroscopic resolution:

$$|\delta H| = 1, \tag{5}$$

one gets

$$R = \left|\frac{\lambda}{\delta\lambda}\right| = \frac{2\,W \sin\beta}{\lambda}\mu_g\left(1-\frac{\lambda}{\mu_g}\cdot\frac{d\mu_g}{d\lambda}\right). \tag{6}$$

The dispersion factor in the bracket may be calculated from the Cauchy-formula:

$$\mu_g = A + \frac{B}{\lambda^2} + \frac{C}{\lambda^4} + \cdots.$$

Thus, according to equations (6) and (2):

$$R = \frac{2\,W \sin\alpha}{\lambda}\cdot\mu_i\left(1+\frac{1}{\mu_g}\cdot\frac{2\,B}{\lambda^2}+\cdots\right). \tag{7}$$

The prevailing increase of the resolving power of the immersion grating is due to the refracting index, $\mu_i \simeq 1.67$ at λ 5000 Å, while the contribution from the prismatic dispersion factor $\frac{1}{\mu_g}\cdot\frac{2\,B}{\lambda^2}$ increases from 0.06 at λ 7000 Å to 0.21 at λ 4000 Å. The theoretically expected resolving power of the spectrograph here described ($W = 15$ cm, $\lambda = 5000$ Å) amounts to $\simeq 1 \cdot 10^6$.

The angular dispersion $\frac{d\gamma}{d\lambda}$ of the compound system considered here is related to the resolving power R and the aperture A according to

$$R = A\cdot\frac{d\gamma}{d\lambda}. \tag{8}$$

Here, A corresponds to the front aperture of the prism:

$$A = W \cos\beta.$$

Again, applying equation (6) to (8) we get:

$$\frac{d\gamma}{d\lambda} = \frac{2\,\mu_g \operatorname{tg}\beta}{\lambda}\left(1-\frac{\lambda}{\mu_g}\cdot\frac{d\mu_g}{d\lambda}\right). \tag{9}$$

The linear dispersion of the spectrograph at the focus $f = 450$ cm increases according to (9) from 4.5 mm/Å in the red to 9.5 mm/Å at the violet end of the spectrum.

Although reliable estimates of the spectroscopic resolution can be obtained only by direct testing, good agreement was found between the observations on the hyperfine structure of some atomic lines reproduced in Figs. 6 a, b, and the simple theory

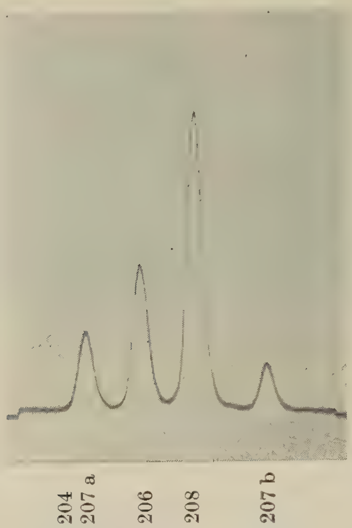

Fig. 7. Hyperfine structure of Pb II, λ 5372, ordinary lead, recorded with IP 21 photomultiplier. Light-source: hollow cathode with Helium of 5-mm pressure. The Pb^{204} component is masked by Pb^{207} a.

of the échelle immersion grating outlined above. Especially does the perfect resolution of the narrow doublet 0.517/0.456 in the hyperfine structure of Hg λ 4358 Å serve as an excellent illustration of the high resolution obtained.

The observed increases of the dispersion gained by the immersion, 1.76 and 2.14 are also in agreement with the values to be expected from equation (9).

The échelle grating in immersion here described is an instrument with a rather limited application. The main purpose of our investigation, however, has been to demonstrate the high resolution to be gained by introducing the immersion principle in spectroscopy. For this purpose the instrument offers great advantages also in photoelectric recordings, Fig. 6 c, of the hyperfine structure and the isotopic constitution of suitable elements.

The application of the immersion principle is not, however, limited to the case of plane gratings here discussed. In this connection the concave grating will be the object of further investigations now in progress.

Summary

In accordance with previous suggestions the immersion principle has been tested for grating in two cases. In the first case a fine-ruled grating was brought into optical contact with a glass plate through an immersion-oil of high refracting index. A characteristic intensity shift of the blaze order into higher orders in the spectrum was observed. In the second case the principle was applied to a coarse-ruled échelle grating by combining it with a flint prism. The considerable increase of the resolving power and the dispersion of this new instrument is demonstrated. Strioscopic meth-

ods have been used in tracing optical irregularities in gratings and prisms, and the importance of a coherent illumination of the spectroscope slit is stressed. The application of the immersion principle has been restricted to plane gratings.

Our investigations were supported by a grant from the Swedish Committee for Scientific Research.

Physics Department, University of Stockholm. April 1954.

REFERENCES

1. HULTHÉN, E., Proc. London Opt. Conference 1950, p. 111.
   The basic idea of combining the grating with an immersion of high refracting index has already been suggested by G. L. ROGERS, Nature *160*, 25, 1947. However, no indications as to the possibility of increasing the resolving power of the grating in this way were given by him. It is not our intention to discuss here the possibilities of constructing an immersion grating according to the suggestion proposed by ROGERS.
2. HULTHÉN, E., Ark. Fys. *2*, 439 (1950).
   HULTHÉN, E. and NEUHAUS, H., Nature *173*, 442, 1954.
3. VAN CITTERT, P. H., Zeitsch. Phys. *65*, 547, 1930; *69*, 298, 1931. Physica *I*, 201, 1934.

Tryckt den 21 oktober 1954

Uppsala 1954. Almqvist & Wiksells Boktryckeri AB

ARKIV FÖR FYSIK Band 8 nr 35

Read 24 February 1954

The determination of electric discharge fields with a special klydonograph

By H. Norinder and O. Salka

With 9 figures in the text

1. Introduction

If a metal rod is situated in an electric field, charge is induced in it, and this charge in its turn gives rise to a field which modifies the original one. If we consider a rod in the form of a prolate spheroid with its major axis parallel to the field, the rod acquires the same potential as would exist at the position coinciding with its centre if the rod were absent. If we consider a disc in the form of an oblate spheroid, situated so that the two major axes lie in an equipotential surface of the undisturbed field, the disc acquires the same potential. Such a rod and disc might be regarded as the basic elements of a klydonograph, with the rod perpendicular to the disc but separated from it by a thin insulating disc. The rod and plate have different potentials, corresponding to their different positions in the field and relative to one another. However, these potentials are not the same as those the rod or plate would have alone in the absence of the other. The potential difference between the two electrodes is the decisive factor for the Lichtenberg figures in the klydonograph, and it would therefore be desirable to derive it theoretically. But the exact treatment of this problem encounters great difficulties which necessitate a number of simplifying assumptions. Since the plate is thin, and takes the potential of the equipotential in which it lies, with very little alteration of the original field, we attribute the greater part of the field disturbance to the rod, and for a first approximation neglect the existence of the plate.

The potential due to prolate spheroid, with the equation

$$\frac{\varrho^2}{b^2} + \frac{z^2}{c^2} = 1$$

(where ϱ, z are cylindrical coordinates, and b, c the semi-axes), introduced into a uniform field parallel to the z axis is, according to Smythe [1],

$$V = E\,z\left(1 - \frac{\cot h^{-1}\eta - \dfrac{1}{\eta}}{\cot h^{-1}\eta_0 - \dfrac{1}{\eta_0}}\right) \tag{1}$$

where

$$\eta_0 = \frac{c}{\sqrt{c^2 - b^2}}$$

and

$$\frac{\varrho^2}{c_2^2(\eta^2 - 1)} + \frac{z^2}{c_2^2 \eta^2} = 1$$

$$c_2 = \sqrt{c^2 - b^2}.$$

E is the field intensity of the uniform field.

This formula may be tested by measurements obtained with the klydonograph connected directly to a voltage source.

Formula (1) indicates that the voltage on the klydonograph is proportional to the field intensity, and increases as the length of the "point" electrode increases. It is obvious, however, that a longer point disturbs the original field to a greater extent. The point should be just sufficiently long for the field investigated to give Lichtenberg figures of adequate size. When the point is aligned with the field the klydonograph potential is a maximum. When the point is at right-angles to the field direction, both electrodes have the same potential, so the potential across the klydonograph is zero.

2. Construction of the klydonograph and measurements with it

The klydonograph used consists of a pressed cylindrical bakelite box (diameter 40 mm, height 20 mm), on the bottom of which there is a thin metal disc A (Figure 1 a), backed by three springs. A bakelite disc 0.75 mm thick (B) lies next to the metal disc, and on top of it is the film (C) (diameter 39 mm). The insulating ring (D) presses the film against the bakelite disc, to prevent air gaps between them. The greatest care was observed throughout the experiments to ensure that such intervening air layers were absent and that the point made proper contact with the film. A brass rod 6 mm in diameter (point electrode) is fastened to the lid of the box with an insulating nut (F) at one end, and the other end is shaped like a prolate spheroid. A point 17 mm long (the standard klydonograph) was used for most of the experiments, but points 12 mm and 7 mm long were also used in a few instances. The smallest electrode used was a steel ball 4 mm in diameter.

The klydonograph was suspended in the field to be investigated by means of nylon threads, so that the point was orientated in the direction of the field. This provides

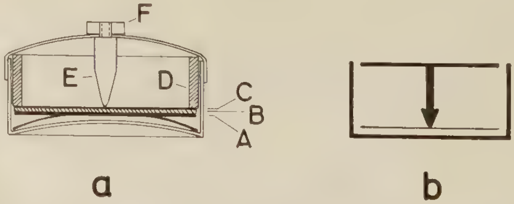

Fig. 1. Construction of the klydonograph. — a: the standard klydonograph, with metal plate (A), insulating disc (B), film (C), insulating ring (D), point electrode (E), and insulating nut (F). — b: a klydonograph (schematic) with the box of metal, used for supplementary experiments.

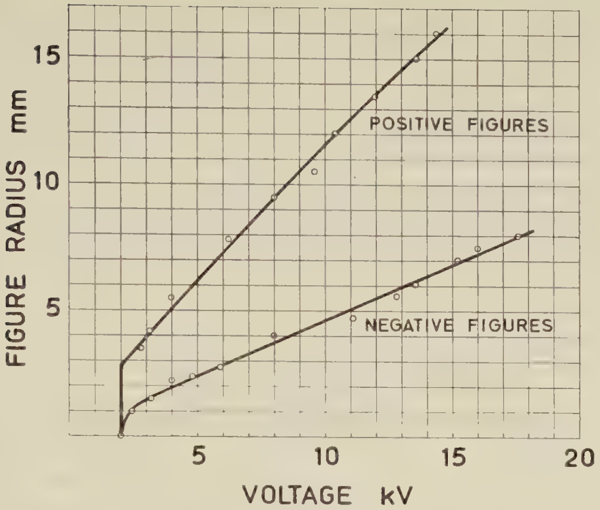

Fig. 2. Calibration curves for the klydonograph: the variation of the radius of the figure with the applied voltage (wave 1/60 μsec).

two possibilities: (1) the usual position with the point uppermost, and (2) the reverse position, with the point underneath. When a negative impulse is applied to the arrangement, negative Lichtenberg figures appear in the first case and positive in the second.

When deciding on the shape of the impulse voltage wave to be used, the effect of the wave shape on the figure is an important consideration. Recent experiments [2], [3] have shown that the wave front is the only factor deciding the size and shape of the figure. The duration of the wave tail is the sole determinant of the back figure. Accordingly, the wave front was kept constant throughout the experiments, at a value of about 1 μsec. No particular attention was paid to the wave tail; for most experiments it was about 1000 μsecs., though a few measurements were carried out with wave tails of 60 μsecs.

As regards the polarity of the surge, the following properties of discharges are of importance: the negative discharge is insensitive to local concentrations of the field in the vicinity of the high voltage electrodes (e.g. owing to the presence of the klydonograph), whereas with positive discharges a local increase in the field intensity near the positive electrode leads to a discharge even when the general field is of low intensity. Negative impulses were therefore chosen for all experiments.

The polarity of the Lichtenberg figure is always open to choice by suspending the klydonograph in the appropriate manner. It was verified experimentally that simultaneous reversal of both the applied voltage and the orientation of the klydonograph had no effect on the figures, neither as to size nor as to shape.

As is well known, the Lichtenberg figures exhibit a considerable scattering effect. In order to lessen the effect of this, the films were always exposed to five successive surges, following each other at five second intervals. Preliminary experiments had shown the later figures were not effected by those preceding them. The klydonograms thus obtained, with 5 superposed figures, permit an easier measurement of the longer branches.

Finally, a characteristic of the klydonograph, the size of the figure as a function of the potential difference, was determined. For this purpose the plate of the klydonograph was earthed and an impulse of 1/60 μsec applied to the point. The curves for both polarities are reproduced in Fig. 2. As will be seen, the klydonograph takes voltages up to 15 kV when the point is positive, and up to 18 kV when it is negative. For higher voltages there is a sliding spark from the point across the film to the plate. It may be remarked in this connection that the positive figure covers almost the whole of the film just before the sparkover voltage is reached, while with the negative figure the discharge occurs when the figure has extended to no more than half the radius of the film.

3. The klydonograph in uniform fields

The field was produced with a plate-plate arrangement. The upper electrode was a disc 60 cm in diameter with a rounded edge of 16 cm radius. A plate 200 × 200 cm was the lower electrode. In order to ensure a uniform field, the distance between the electrodes was only 20 cm. It could then be assumed that the field intensity was practically constant along the central axis. It might be suspected that the introduction of the klydonograph with its point 17 mm long (8.5 per cent of the total gap) could disturb the field to some extent. There is also the danger that with the point near to the upper or lower electrode the original plate-plate arrangement might be changed to a point-plate arrangement. In order to examine these possibilities, klydonograms were taken for three different klydonograph positions: near the upper plate electrode, in the centre of the gap, and near the lower plate electrode, the klydonograph in each case being in the central axis, with its point in the direction of the field. The resulting figures (Fig. 3) show that there are some differences in the size of the figures in these three positions. Two reasons are conceivable. Either the field is not the same in the three positions, or the point of the klydonograph disturbs the originally uniform field. If the former were the case, all figures for the position "high voltage electrode" would be larger than those for the position "earthed electrode", so more as the field at such a considerable distance (20 cm) must be considered as slightly divergent. From the curves follows that the negative figures have a tendency towards increasing in the position "high tension electrode", the positive figures on the other hand in the position "ground plate". If we bear in mind that the negative figure was obtained with the klydonograph suspended in the usual direction, and the positive with it reversed, it is clear that the figures were larger when the point was directed away from the neighbouring plate. This leads us to conclude that the difference between the figures is to be ascribed to the disturbing effect of the klydonograph point, and that the central position corresponds to the least disturbance. Accordingly, the curves in Fig. 3 are drawn for the centre of the gap. The measuring range for our klydonograph with the 17 mm point was between 2.5 and 15 kV/cm in this position. The figures disappear below the lowest value, and somewhat above the highest the discharge gap breaks down. The figure radii are then: 3 mm for the negative and 8 mm for the positive (by comparison, the diameter for the film was 39 mm). In addition, the curves show that the figures of the two polarities have different features. In the first place there is the property of the Lichtenberg figures which has longest been known – that the range of the negative figure seems to go down to zero, while the range of positive has

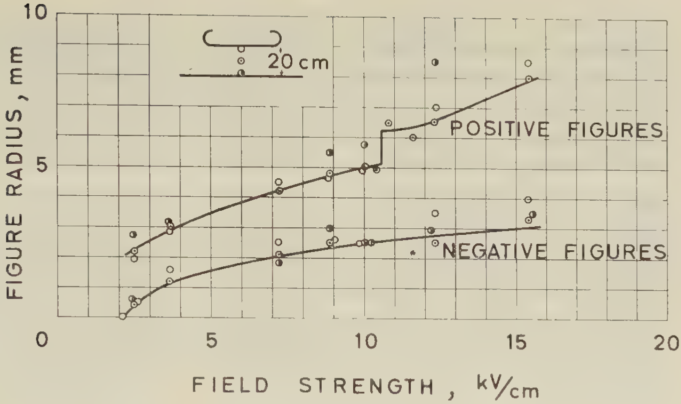

Fig. 3. The klydonograph characteristic in a uniform field: the variation of the radius of the figure with the field intensity.

at the start a definite value (the initial step) – in our case a little more than 2 mm from the centre. Among more than a hundred klydonograms there was no positive figure with a radius of less than 2 mm, i.e. without the initial step. Secondly, the positive figures were found to have a new property, not observed with the ordinary type of klydonograph: as the field intensity increased, the figures increased continously in size till about 10 kV/cm was reached, where there was a "jump", after which the figures again increased continuously.

Both the discontinuities of the positive figure are formed in the same way; when the field intensity decreases, the radius of the figure diminishes and the number of branches decreases. In the limiting case there is often no more than a single branch with a length exceeding a minimum value. The only difference between the two discontinuities is that the figure consists of just a few branches near the initial step (Fig. 4 a), whereas at the second it has the regular rosette form of the continuously increasing Lichtenberg figures, with one or more advanced branches. All these branches also exceed a minimum value (Fig. 4 e). They make the figure unsymmetrical, and seem not to appear until after the regular branches, so they must grow out between the regular branches. The number of these branches increases as the field intensity rises further. The figure then becomes more symmetrical again, but it is still possible to distinguish the two parts – the inner regular rosette and the outer more irregular branches, as may be seen from Figs 4 f, g, h (single impulse) and Fig. 5 (five superposed impulses).

Finally, in order to determine the effect of an inclination of the klydonograph on the figures, klydonograms were taken with the klydonograph axis at various angles to the field. The klydonograph was still situated in the middle of the interelectrode gap. The voltage, and consequently the field, were maintained constant (8.8 kV/cm), and the direction of the klydonograph point altered in steps of 10°. Fig. 6 gives the variation of the figure radius with the angle of inclination. As was to be expected, the figures were negative between 0° and 90° (the normal range of suspensions), and positive between 90° and 180° (reverse suspension). The largest figures occurred in the two extreme cases (0° and 180°), with the klydonograph axis in the direction of the field. The angular variation through 90° is accompanied by a shrinking in figures of both polarities. In the 90° position, where the point of the klydonograph is at right angles to the field, the klydonogram exhibits no figure.

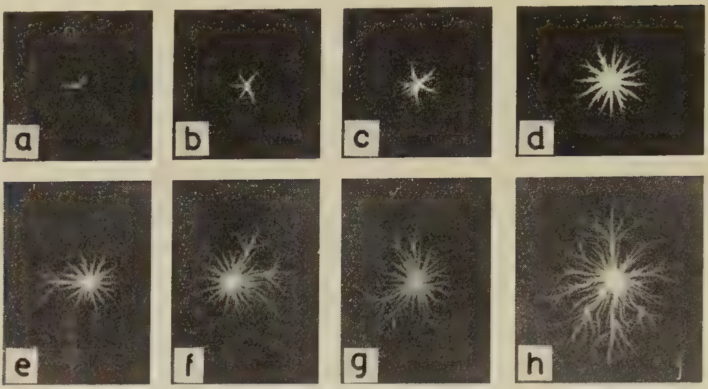

Fig. 4. The stages of development for the Lichtenberg figures from a single impulse. — a–d: symmetrical Lichtenberg figures. — e–h: unsymmetrical Lichtenberg figures. — a: the initial step. e: the step at a field intensity of 10 kV/cm.

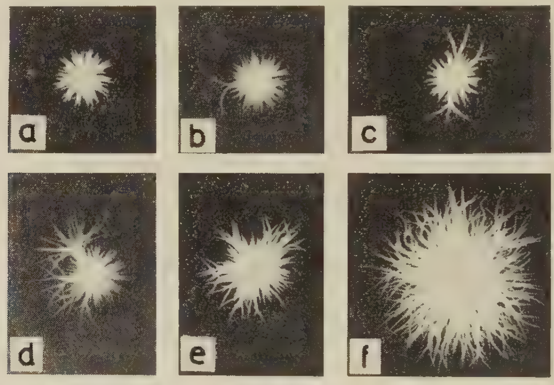

Fig. 5. The stages of development of unsymmetrical Lichtenberg figures for 5 consecutive impulses. — a: symmetrical figures. — b: the step at a field instensity of 10 kV/cm.

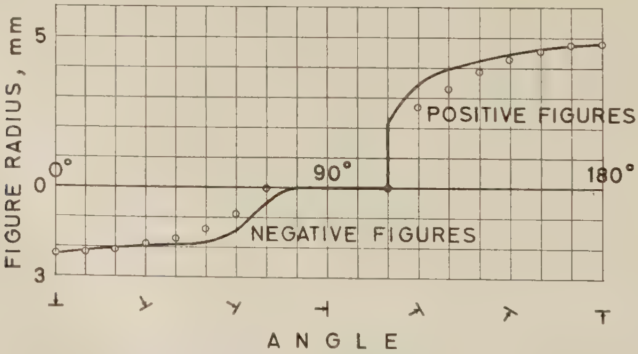

Fig. 6. Variation of the figures on turning the klydonograph through 180°. The points shown are calculated from $V = V_{\max} \cos \varphi$.

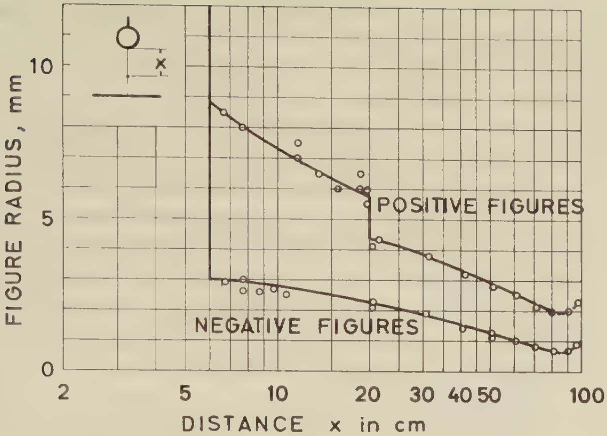

Fig. 7. The klydonograph characteristic for a non-uniform field (sphere-plate arrangement): the variation of the figure radius with the distance (x) from the sphere.

4. The klydonograph in non-uniform fields

A sphere-plate arrangement is suitable for the production of a non-uniform field. It is then possible to calculate the field along the axis of symmetry, allowing a comparison between theoretical and experimental values. The sphere used was 50 cm in diameter, and its height 100 cm above the earthed plate, which was 200 × 200 cm. Negative surge voltages were used in this case also. The onset voltage for corona with this arrangement was about 700 kV. In order to avoid corona, i.e. space charge, the highest voltage employed was 665 kV. At this voltage, the axial field intensity is theoretically 30.6 kV/cm at the surface of the sphere and 2.4 kV/cm at the plate. The Lichtenberg figures were taken with the same impulse voltage throughout, and the klydonograph hung in various positions along the vertical central axis, with point in the direction of the field. With the ordinary suspension the figures were negative, and in the reverse direction positive. In Fig. 7, the radius of the figures is plotted against the distance between the klydonograph and the surface of the sphere. As with the uniform field, there is a step in the middle of the positive figures. Besides this, both curves exhibit a "jump" at about 6 cm from the sphere, where the field intensity was about 20 kV/cm. For higher intensities, the figures of both polarities are instable, and suddenly cover the whole film. The upper limit for measurements with this klydonograph is thus 20 kV/cm.

The fact that both curves appear to rise slightly at a distance of 90 to 100 cm, i.e. near the earthed plate, is presumably attributable to the field disturbance produced by the klydonograph.

5. Evaluation of results

The next step was to compare the experimentally determined figure sizes in the uniform field with the calibration curve of the klydonograph. For the uniform field, the figures correspond to the klydonograph potential induced by the field. This potential is not experimentally measurable, though the intensity of the original

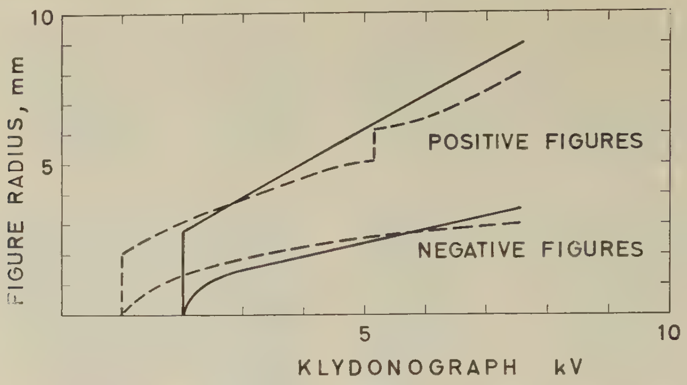

Fig. 8. Comparison of the klydonograph characteristic for a uniform field (broken line) with the calibration curve (solid line) of the klydonograph.

field is. However, the impulse voltage applied to the klydonograph for calibration provides a direct means of determining this potential. In order to obtain a common axis of abscissae for the curves in the two cases, it is necessary to know the klydonograph potential in terms of the field intensity. The formula given in the introduction may be used for this purpose, to a first approximation. For our klydonograph,

$$c = 0.85 \text{ cm} \qquad b = 0.3 \text{ cm}$$

and the shortest distance between the point and the plate $z - c = 0.1$ cm (thickness of insulating disc 0.75 mm and of the film 0.25 mm). The potential of the plate, i.e. the potential difference between point and plate is, according to the formula,

$$V = 0.49\ E \text{ (kV)} \qquad (E \text{ in kV/cm}).$$

The transformation from E to V for a uniform field (Fig. 3) has been carried out in Fig. 8, and the calibration curves are also included (from Fig. 2). The fact should not be neglected that the formula quoted is derived for a spheroid alone in a uniform field. In our case, the point is not completely ellipsoidal in shape, and a metal disc is also introduced into the field. In view of this, the agreement between the curves for the uniform field (broken line) and the calibration curves (solid line) cannot be regarded as poor. The lack of conformity regarding the initial potential is presumably due to the simplifications mentioned above. A striking feature of the positive curve for the uniform field is the step at about 5 kV, which has no equivalent in the calibration curve.

The curves for the uniform field cannot be compared immediately with those for the non-uniform field. The axis of abscissae for the former is the field intensity, for the latter the distance of the klydonograph from the sphere. The variation of the field intensity along the symmetry axis of a sphere-plate arrangement may be calculated by means of the formula [4]

$$E = V \frac{2\,\delta\,[\delta^2\,(f+1) + y^2\,(f-1)]}{[\delta^2\,(f+1) - y^2\,(f-1)]^2}$$

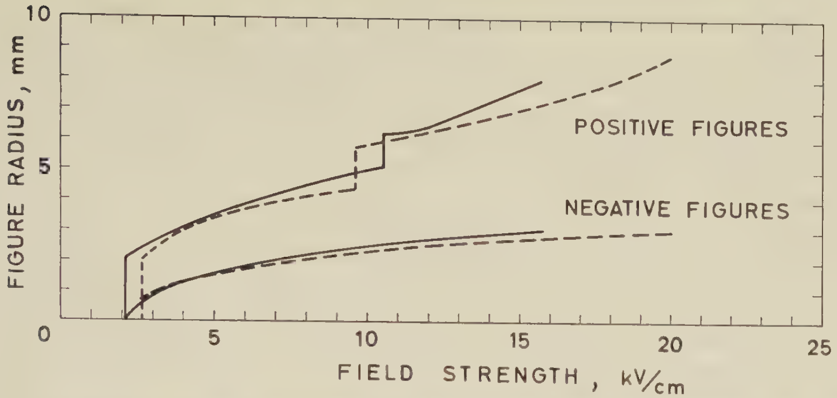

Fig. 9. Comparison of the klydonograph characteristics for uniform (solid line) and non-uniform fields (broken line).

where: E is the field intensity at the point y

δ the length of the discharge gap

$f = \frac{1}{4}\left[(2p-1) + \sqrt{(2p-1)^2+8}\right]$

$p = 1 + \frac{\delta}{R}$; V voltage

R is the radius of the sphere.

The values of the field intensity calculated for various points on the axis of symmetry enabled the curves for the non-uniform field at 665 kV (Fig. 7) to be redrawn with the field intensity along the axis of abscissae (Fig. 9). The curves for the uniform field from Fig. 3 are also reproduced for comparison purposes. The agreement between the curves is satisfactory; even the steps in the positive curves occur at approximately equal field intensities, at about 10 kV/cm.

It is interesting to see whether the klydonograph potential varies as the cosine of the angle of inclination when the klydonograph is turned through 180°. To this end, the largest figure radii of Fig. 6 were selected: 2.2 mm for the negative ($\varphi = 0$) and 4.8 mm for the positive ($\varphi = 180°$). These correspond according to the calibration curves (Fig. 2) to klydonograph potentials $V_{\max} = 4.5$ kV for the negative figures and $V_{\max} = 3.8$ kV for the positive. The potentials $V = V_{\max} \cos \varphi$ were calculated for each 10° variation in the angle of inclination, and then interpreted as figure radii from the calibration curve (Fig. 2), giving the points shown in Fig. 6. Since the experimental values are larger than the calculated for the curves of each polarity, we must assume either that the klydonograph potential does not follow a simple law as the angle of inclination is changed, or that the difference is due to inaccuracies in the calibration curve for the klydonograph.

Discussion

Before embarking on the discussion, it should be emphasised that all the present measurements were carried out with a wave front of 1 μsec, and in a field where no corona was visible (discharge-free field). A special investigation of the effect of different wave-fronts was not undertaken.

Although there is at present no exact mathematical solution of the problem at hand, these experiments show beyond doubt that in an impulsive electric field the potential between the electrodes of a klydonograph is determined by the field intensity and the angle between the field direction and the klydonograph point. This potential may be assumed to vary conformally with the field and the impulse voltage, and must be the primary cause of the Lichtenberg figures. It is hardly conceivable that there is any scattering effect in this potential when the other parameters—field intensity, size, shape and position of the klydonograph—remain unaltered. But, as we know, the measurement of voltage by means of Lichtenberg figures is rendered difficult by the large scatter of the results. In addition to random variations in the discharge process, there is a certain variability in the insulation and the film of the klydonograph. Consequently, the accuracy of klydonograph measurements cannot be expected to be better than some 20 per cent for a single measurement. For greater accuracy, several measurements must be carried out.

Regarding the question as to which polarity of the figures is preferable for the measurement of field intensity, we may consider briefly the properties of the two polarities. Positive figures:

1) larger diameters
2) steeper radius/field intensity curve for higher field intensities
3) a step at about 10 kV/cm field intensity
4) large scattering
5) sensitivity to small air gaps between the electrode and the film and between the film and the insulator disc.

Negative figures:

1) smaller diameters
2) continuous increase in size
3) flatter radius/field intensity curve for higher field intensities
4) smaller scattering.

The last three properties constitute considerable disadvantages for the positive figures. Near the step, the scattering is especially large, since any small variation of the conditions may suffice to shift the figure from one branch of the curve to the other; the transition is not at all sharp. It follows from this that the decision is in favour of the negative figures.

If the voltage gradient is to be measured, it is obvious that the klydonograph must have its point in the direction of the field lines; any other orientation would give only a field component in the corresponding direction. This circumstance is a disadvantage when it comes to measuring fields of undefined direction. In such cases, the direction of the field must first be determined by preliminary experiments. On the other hand, it is not really essential that the klydonograph be orientated exactly, since the flatness of the curve (Fig. 6) near the maximum means that errors of ± 20° in the orientation make no great difference to the figures. On account of this flat maximum, it is better to determine the direction of the equipotentials than of the field, since the null method may be employed for this purpose.

On account of the difficulties which beset the mathematical treatment, it is not yet possible to derive a calibration curve for the klydonograph theoretically. The approximate formula given in the introduction may be used as a guide, however. In practice, there is no other way than to calibrate each klydonograph, i.e. to determine the variation of the figure radius with the field intensity experimentally. The plate-plate arrangement is the most suitable for this purpose. In order to make the disturbance of the field's uniformity as small as possible, the distance between the plates should be large compared with the length of the klydonograph point. It is doubtful whether such a calibration curve is applicable to the measurement of markedly non-uniform fields. Since the point has a certain length, the question arises as to which point of space the measured field intensity corresponds to. It is customary to identify this point with the mid-point of the point electrode. For a markedly non-uniform field, the mid-point of the point electrode and the point to which the measurement refers no longer coincide, the latter point being displaced towards the field of greater intensity. This displacement can never exceed half the length of the point electrode. It is unfortunately impossible to determine it experimentally, and since it may be considerable for long point electrodes in markedly non-uniform fields, it becomes yet another factor lowering the accuracy of the measurements. The potential induced across the klydonograph gives rise to a local field under the influence of which the Lichtenberg figures develop. It is also possible that the primary field affects the figures, especially when it is not at right angles to the film. The experiments with the inclined klydonograph show that the Lichtenberg figures only change in size when the klydonograph is inclined to the field, and retain their shape and symmetry. If the primary field exercised an influence on the figures, they would be oval for all angles other than 0° and 180°. Experiments were performed with a klydonograph in which the interior of the instrument was completely screened from the primary field. This klydonograph was of the same shape and size as our standard klydonograph, except that the box and lid were of metal instead of bakelite. An annular slit 2 mm wide was left between the box and the lid (Fig. 1 b). The only difference between the figures obtained with this instrument and with the standard klydonograph was in the size, the shape and structure being the same. These experiments lead us to conclude that the primary field has no appreciable effect on the formation of the Lichtenberg figures. Only the local field within the klydonograph, between the point and the plate, is significant.

We will now consider the detailed structure of the Lichtenberg figures obtained. The negative figures do not differ in this respect from those described in the literature. The positive figures, on the other hand, are different from the classical Lichtenberg figures. For weak fields (up to 10 kV/cm) these figures are divided up more or less uniformly by radial branches that are not sharply forked, with a nearly circular outer boundary (Figs. 4 d and 5 a)—that is to say, the form which is described [5] as the pure, simple, regular positive Lichtenberg figure, and which will be referred to here as the symmetrical figure. Their size increases continuously with the intensity of the field. At intensities of about 10 kV/cm (in our experiments using a point length of 17 mm), single longer branches begin to extend outwards from the symmetrical figure (Figs. 4 e and 5 b). These go between the branches of the symmetrical figure, and seem to appear after the formation of the latter. They are considerably longer than the radius of the symmetrical figure, and they therefore represent a discontinuity in the development. The longer branches extend singly outwards from the circular region—e.g. only one such branch may occur in five superposed figures (Fig. 5 b). The outer boundary of the figure then deviates a great deal from the circular form. Although the number of these branches increases as the field intensity increases, the figure never regains the symmetry of those taken at less than 10 kV/cm; we will therefore refer to these figures as unsymmetrical (Figs.

4 h and 5 f). A striking characteristic is that the figures for the highest possible field intensity retain a small symmetrical rosette around the centre. The branches of this rosette are of the same length as in the symmetrical figure at 10 kV/cm field intensity. Consequently, we may conclude that the Lichtenberg figure is formed in two stages —first the symmetrical central rosette up to 10 kV/cm, then, above this intensity, the longer, more irregular branches.

It is of interest to compare our two types of figure (the symmetrical and unsymmetrical) with those of other authors. For this purpose, we may select three fairly recent publications.

1. PRAETORIUS [6] determined the variation of the figure with gas pressure. His positive figure of form 1 corresponds to our symmetrical, and form 2 (though without what he calls the "spark channels" in the centre of the figure) to our unsymmetrical. PRAETORIUS found that form 1 does not persist beyond 200 mm Hg.
2. ANSTEY [2] calls the figures resembling our symmetrical figures "Type *A* figures", and those resembling our unsymmetrical figures "Type *B* figures". He states that the former are obtained with average slope of wave front greater than 7.9 kV/μs, and the latter with slope less than 5 kV/μsec.
3. AMIN [3] says that the so-called normal Lichtenberg figures (corresponding to our symmetrical) occur with steepfronted waves and comparatively small voltages, while "intermediate figures" (corresponding to our unsymmetrical) occur when the front is steep and the voltages somewhat below the limit at which the Toepler (spark) figures appear.

The statement of the last of these three authors accords well with our results. The discontinuity in the growth of our figures may be regarded as the initiation of Toepler figures. Since the charge was presumably insufficient for the formation of proper Toepler figures, the channels are similar in appearance to the branches of the ordinary Lichtenberg figures. The second discontinuity in both types of figures, which is observable at a field intensity of 20 kV/cm with the sphere-plate arrangement (Fig. 7), may be regarded as a transition to fully develop Toepler figures. There are two striking facts to be observed. Firstly, the first discontinuity (at about 10 kV/cm) occurs only with the positive figures, while the negative increase continuously. Secondly, neither figure evidences a discontinuity in the calibration of the klydonograph with directly coupled voltages, both figures then retaining the normal form up to the highest possible voltages. This leads us to suppose that some factor or factors effecting the development of the figures in our case is as yet not understood. Further results bearing on this question are being collected.

It should be noted that as a rule no inverse figures occurred in the experiments described here. Traces of such figures were observed in only a few exceptional cases. But in some preliminary experiments with chopped wave, i.e. with rapidly sloping wave tail, the inverse figures were prominent. It is known that these inverse figures are caused by a discharging of the space charge, left on the emulsion (in the Lichtenberg figures) to the point electrode after the collapse of the potential, [7], [2], [3].

It is interesting to weigh the advantages and disadvantages of the methods mentioned here for the measurement of fields of considerable spatial extent. At present, two methods are available for the measurement of impulsive fields [8]. One is the sounding condenser method. In addition to the sound, auxiliary apparatus is required, and this introduces undesirable disturbances. The sound and its connections disturb the original field, so that the original discharge may be altered. For instance, there may be a sparkover to the sound. In addition, there are errors arising from the fact that the method actually measures the potential at a particular point. In order to measure the field intensity at a point it is therefore necessary to carry out measurements in its neighbourhood, and since these positions must lie along a line of force, it is necessary to know the direction of the field beforehand. As a consequence of these disadvantages, this method has found very little application in the measurement of the electric field in atmospheric discharge gaps.

The second method employs as measuring device a small glow tube (about 15 mm long), for which the onset field may vary from 300 to 3,000 V/cm, according to the pressure of the contained gas. The field intensity is not measured directly, the voltage on the electrodes being raised until the tube lights up. The field intensity corresponding to other electrode voltages may then be found by computation. The accuracy of measurements is about 10–15 per cent. As the tube need not have electrodes, the disturbance of the measured field is reduced to a minimum.

The method described in this paper is at present the only one by which the field intensity in a single process may be measured directly and without intermediate operations. It is probably also possible to determine the onset of a space charge in the field. Only a small disturbing object is introduced into the field, since the klydonograph requires no connections. The main source of disturbance is the point. Since the point must be 1–2 cm long to obtain sufficiently large figures in fields of up to 20 kV/cm, the method is suitable only for fields of considerable extent. The measuring range of the instrument lies between 2.5 and 20 kV/cm. Longer points allow measurements to be made at lower field intensities; but a greater disturbance of the original field is then unavoidable. The apparatus is simple and inexpensive. Serious disadvantages are:

1. the inaccuracy—the error may amount to 20 per cent, and
2. the effect of the steepness of the wave front on the measurement. However, this latter disadvantage is accompanied by the advantage that it may be possible to gain some information about the development of the discharge process.

Thus, when measurements of the field due to rapidly changing atmospheric discharges are required, the klydonograph serves not only to measure the field intensity (e.g. measurement of lightning fields) but also to provide information about the development of the discharge process.

Summary

A special klydonograph may be used for the measurement of field intensities even single impulses. It allows the field intensity to be measured directly, without intermediate operations. It is not possible to calibrate the klydonograph theoretically; it must be done experimentally. It is preferable to employ negative figures for measuring purposes, since they increase continuously. The positive figures do not increase in size continuously with the field intensity: there is a discontinuity, at about 10 kV/cm in the present case. Figures of both polarities reach a stage of instability at about 20 kV/cm, after which the figures cover the whole film disc. The measuring range of our standard klydonograph (with a point electrode 17 mm long) is from 2.5 to 20 kV/cm. However, this range may be extended upwards or downwards by a suitable choice of point length. The error of the measurements is about 20 per cent. The klydonograph may also be used to determine the direction of the field. Furthermore, the klydonograph provides information about the steepness of the impulse front.

REFERENCES

[1] Smythe, W. R., Static and Dynamic Electricity (Second edition). McGraw-Hill Book Company, New York 1950, p. 169.

[2] Anstey, F. B., A study of the Lichtenberg Figures and an experimental and mathematical investigation of the surge generator used therein. Thesis, University of London, 1946.

[3] Amin, M. A., Lichtenberg Figures. Their characteristics and practical applications. Thesis, University of London, 1947.

[4] Norinder, H., and Salka, O., Mechanism of positive spark discharges with long gaps in air at atmospheric pressure. Arkiv för fysik, Vol. 3, Nr 19, p. 347, Stockholm 1951.

[5] Pedersen, P. O., On the Lichtenberg Figures Part III. Det Kgl. Danske Videnskabernes Selskab. Mathematisk-fysiske Meddelelser, Kopenhagen 1929, p. 7.

[6] Praetorius, G., Untersuchung der Druckabhängigkeit von Gleitentladungen auf Photoplatten. Arch. Electrotechn., Bd. 34, S. 83, 1940.

[7] Merril, F. H., and von Hippel, A., The atomphysical interpretation of Lichtenberg Figures and their application to the study of gas discharge phenomena. Journ. Appl. Phys., Vol. 10, p. 873, 1939.

[8] Strigel, R. Ausmessung von elektrischen Feldern. Verlag und Druck G. Braun, Karlsruhe, 1949, S. 17 und S. 50.

Tryckt den 20 oktober 1954

Uppsala 1954. Almqvist & Wiksells Boktryckeri AB

ARKIV FÖR FYSIK Band 8 nr 36

Communicated 2 June 1954 by BENGT EDLÉN

A delayed disintegration of a heavy nucleus

By B. WALDESKOG

With 1 figure in the text

During the last few years some remarkable events have been found in photographic emulsions, which can be explained by assuming the presence within a nucleus of a hyperon. A hyperon is a particle with mass between that of the neutron and that of the deuteron.

The original discovery of a hyperon bound within a nucleus was due to DANYSZ and PNIEWSKI (1). They observed a heavy nuclear fragment emitted from a disintegration in a photographic emulsion. The charge of the fragment was ~ 5 e. The particle appeared to reach the end of its range in the emulsion, where it disintegrated into 4 particles. Several similar events have now been discovered (2, 3). The highest value of the charge for the reported events is ~ 5 e.

A new event of the same type was found in a stack of *G*-5 emulsions, 400 μ thick, exposed in a balloon flight at geomagnetic latitude 56°N. The maximum altitude was 34,000 m. A micro-photograph of the event is shown in Fig. 1. The heavy particle comes out of the glass and has a range of 1,400 μ in the emulsion. The charge of the particle was determined by the photoelectric method for heavy particles described by the author (4). It was found to be a track of a particle with charge 9 e. The energy of the particle when entering the emulsion is ~ 700 MeV. From the photoelectric measurements it can be calculated that the disintegration occurred not at the end of the heavy track but 5–10 μ from the end. This can be done by comparing the measurements for this track with those of a normal track, the charge of which has been determined to 9 e. The kinetic energy of the particle is certainly small at the point of disintegration compared with the energy necessary to produce the star *A*. Therefore, it seems most likely that this event represents a disintegration in flight of the heavy particle rather than a usual star. The lifetime for the heavy particle in the emulsion is $\sim 2\times10^{-11}$ s.

In the star *A* there are three visible tracks. The results of the analysis of the star are given in the following table:

Track	Range	Grain density	Identity	Energy
1	400 μ	Black	α	34 MeV
2	—	7–8	p, d, t	10–15 MeV assumed p
3	4–5 μ	Black	Z>2	—

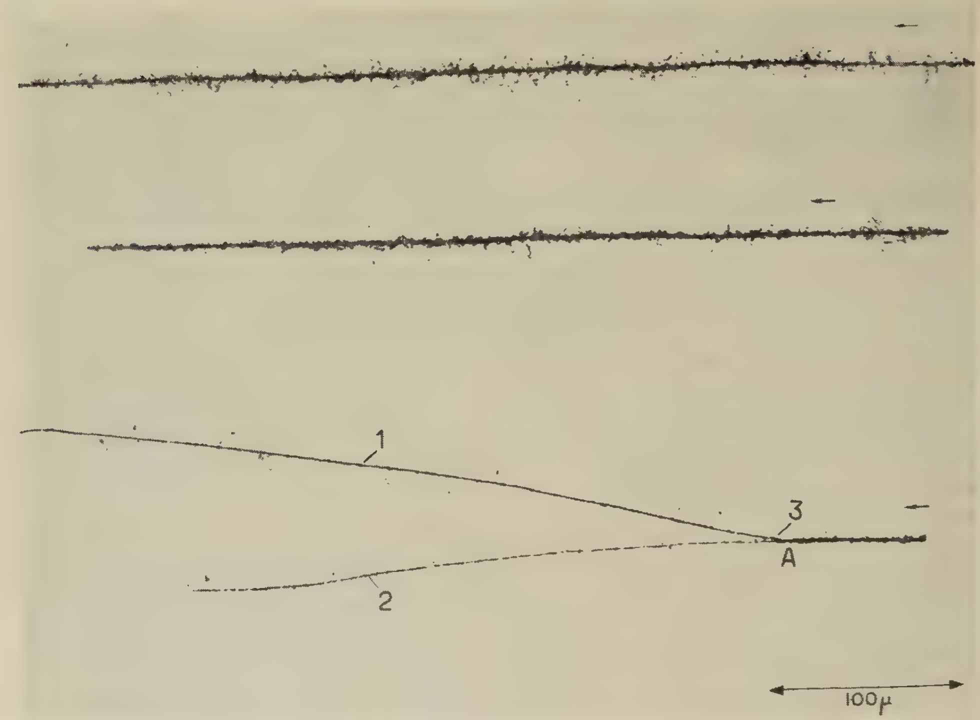

Fig. 1. Microphotograph of a heavy track with charge 9 e disintegrating very near the end.

Track 1 was determined by photoelectric measurements to be the track of an α-particle. Track 2 leaves the emulsion. It is impossible to determine the type of particle because the track is too short. Track 3 is very short one, 4–5 μ, and its charge and energy are impossible to determine. The total energy of the visible tracks in star *A* is, if particle 2 is assumed to be a proton, at least 45 MeV and this energy is too large to explain the disintegration as a collision between the heavy particle and a nucleus of the emulsion.

The explanation for this event seems to be the same as that given for the event described by Danysz and Pniewski. There must exist among the nucleons of the heavy nucleus a hyperon, which causes the particle to disintegrate in flight.

REFERENCES

1. M. Danysz and J. Pniewski, Phil. mag. Ser. 7, *44*, 348 (1953).
2. D. A. Tidman, G. Davis, A. J. Herz, and R. M. Tennent, Phil. mag. Ser. 7, *44*, 350 (1953).
3. J. Crussard and D. Morellet, C.R. de l'Acad. Sci. Paris, *236*, 64 (1953).
4. B. Waldeskog, Arkiv för Fysik *7*, 475 (1954).

Tryckt den 20 oktober 1954

Uppsala 1954. Almqvist & Wiksells Boktryckeri AB

ARKIV FÖR FYSIK Band 8 nr 37

Communicated 26 May 1954 by AXEL E. LINDH and G. HÄGG

The reflection and transmission of X-rays in quartz near the Bragg angle

By GÖSTA BROGREN

With 7 figures in the text

Introduction

In an earlier publication the present author and Ö. ADELL have studied the anomalous intensities of the transmitted and reflected X-ray beams in the region near the Bragg angle in a calcite crystal [1–2]. The problem was treated both theoretically and experimentally and the shapes and forms of the intensity curves of the reflected and transmitted beams were calculated by means of the dynamical theory of X-ray diffraction in perfect crystals. These curves were also determined experimentally. A very good qualitative and quantitative agreement was obtained.

The anomalous X-ray transmission through crystals was first found by BORRMAN [3] who investigated the transmission of the copper $K\alpha$ radiation through quartz plates cut for Laue reflection. These investigations were purely qualitative and cannot be used for a quantitative comparison with theoretical calculations. As no newer determinations have been carried out on quartz, the author extended the investigation on the anomalous X-ray transmission near the Bragg angle to the quartz crystal too. The present work comprises experimental determinations of the intensity curves of the reflected and transmitted radiation in the symmetric Laue case as well as theoretical calculations of these curves.

Experimental

The investigation was carried out with a double crystal spectrometer. The same experimental method as earlier was used. Plane parallel quartz plates with the dimensions $25\times15\times0.45$ mm were used as monochromator and analyser crystals. The parallel surfaces 25×15 were very carefully ground and polished. The monochromator crystal was always cut for symmetric Bragg reflection with the reflecting atomic planes parallel to the plane surface. The analyser crystal was cut for symmetric Laue reflection (the reflecting planes were perpendicular to the plane surface and parallel to surface 15×0.45 or 25×0.45).

Measurements were made using atomic planes $10\bar{1}0$ and $11\bar{2}0$. Before use all crystals were etched in hydrofluoric acid in order to remove possible surface defects. The intensities of the transmitted and the Laue reflected radiation were registered simultaneously by means of two Geiger-Müller counters, whose relative sensitivity was carefully determined for every wavelength used. The intensity of the beam that was reflected from the monochromator crystal against the analyser crystal was measured with both Geiger-Müller counters before and after every registration of the intensity curves. The time of registration was 30 seconds/point. 3—5 runs were made for every experimental arrangement and wavelength. In order to avoid overlapping from higher orders, the voltage of the X-ray tube was always kept below the double excitation potential of the wavelength used.

Theoretical discussion

The quartz crystal, the structure of which is well known [4–5], belongs to space group D_3^4 or D_3^6. The influence of surface treatment and the perfection of the quartz crystal have been studied previously by an investigation of the X-ray diffraction with a double crystal spectrometer in $(1, -1)$ position, where both crystals were adjusted and cut for symmetric Bragg reflection [6]. There too the two planes $10\bar{1}0$ and $11\bar{2}0$ were used. It was found that the properties of the etched quartz crystals were very nearly the same as the dynamical theory of the X-ray diffraction in perfect absorbing crystals states. The agreement with the theory was better than what was found with the calcite crystal. The quartz crystal should thus be very suitable for an experimental study of the anomalous X-ray transmission as this effect exists only in perfect, absorbing crystals.

The theoretical calculation of the intensity patterns presents certain difficulties. All theoretical publications about the anomalous X-ray transmission restrict themselves to crystal lattices having an inversion center and to strong reflecting atomic planes. The latter condition is easily realized for the quartz crystal, which, however, has no inversion center. The geometrical structure factor is real in a crystal with an inversion center and it attains the same value for the two planes (hkl) and $(\bar{h}\bar{k}\bar{l})$. For this reason the Fourier components ψ_H and $\psi_{\bar{H}}$ of these planes are also identical in such a crystal. (The notation is given in the earlier paper and is the same as is used by ZACHARIASEN [7].)

If the crystal lattice has no inversion center, the geometrical structure factor is as a rule complex. If we provisionally further assume that the whole actual wavelength range is so much shorter than the critical K absorption wavelengths of the elements which build up the crystal that the anomalous contribution to the atomic scattering power from the K electrons can be neglected, we have for the structure factors of the planes (hkl) and $(\bar{h}\bar{k}\bar{l})$

$$F_H = A + jB \tag{1}$$

$$F_{\bar{H}} = A - jB \tag{2}$$

where

$$|F_H| = |F_{\bar{H}}| \tag{3}$$

hence

$$F_H = |F_H|\,(\alpha + j\beta) \tag{4}$$

$$F_{\bar{H}} = |F_H|\,(\alpha - j\beta). \tag{5}$$

If we work within a wavelength range where the anomalous contribution to the atomic scattering power due to the K electrons cannot be neglected, this can be calculated from the formulas developed by HÖNL [8–9]. The atomic scattering factor is then

$$f = f^{\circ} + f' + j f'' = f_r + j f_j. \tag{6}$$

In order to study the influence of the anomalous scattering due to the K electrons, we compute the structure factor so that the contributions from the real and the imaginary parts of the atomic scattering factor are obtained separately. We get for planes $(h k l = H)$ and $(\bar{h} \bar{k} \bar{l} = \bar{H})$

$$F_H = F_r\ (a + j b) + j F_j\ (a_1 + j b_1) \tag{7}$$

$$F_{\bar{H}} = F_r\ (a - j b) + j F_j\ (a_1 - j b_1) \tag{8}$$

where

$$F_r\ (a + j b) = \sum_x f_{r_x}\ (A_x + j B_x) \tag{9}$$

$$F_j\ (a_1 + j b_1) = \sum_x f_{j_x}\ (A_x + j B_x) \tag{10}$$

The summation is extended over all atoms in the unit cell. In the wavelength range this investigation comprises f_r is much larger than f_j. Then $F_r \gg F_j$. If we assume that the complex numbers can be replaced by their moduli it is possible to obtain an analogy with the conditions valid for crystals with an inversion center. By substituting

$$\varkappa = \left| \frac{F_J}{F_R} \right| = \left| \frac{F_j}{F_H} \right| \quad (\text{as } |F_R| \approx |F_H|) \tag{11}$$

we obtain

$$F_H = |F_H|\ (1 + j \varkappa) \tag{12}$$

and

$$\psi_H\ \psi_{\bar{H}} \approx |\psi_H|^2\ (1 + 2 j \varkappa). \tag{13}$$

This relation is identical with the corresponding expression for crystals with an inversion center and the theoretical treatment for these can be applied directly to crystals without a center of symmetry by means of the assumption above.

Calculations

The crystal plates that were used as Bragg monochromators were so thick that the conditions for Equation 30 in the earlier paper were fulfilled and it could be used for calculating the Bragg diffraction patterns. The intensity distribution of the transmitted and the reflected radiation in the symmetric Laue case was obtained from Equations 27 and 28.

The geometrical structure factor $A_x + j B_x$ for space group D_3^4 or D_3^6 can be calculated from well-known relations by inserting the coordinates for the atomic positions. (See for instance Ref. 10, p. 465–6.) The latter are: $x_{\mathrm{Si}} = 0.465$, $x_{\mathrm{O}} = 0.415$, $y_{\mathrm{O}} = 0.272$, $z_{\mathrm{O}} = 0.120$. [5.]

Then the structure factor F is given by

$$F = (A_{\mathrm{Si}} + j B_{\mathrm{Si}})\, f_{\mathrm{Si}} + (A_{\mathrm{O}} + j B_{\mathrm{O}})\, f_{\mathrm{O}} \tag{14}$$

where

$$f = f^{\circ} + f' + j f''. \tag{15}$$

Table 1. The constants, used in the calculat

The thickness of the t

Line	Wave-length in X.U.	Bragg angle ϑ_B	$\cos 2\vartheta_B$	$\delta \cdot 10^6$	μ_l cm^{-1}	f°_{Si}	f'_{Si}	f''_{Si}	f°_{O}	f''_{O}	$F_{10\bar{1}0}$
Au $L\alpha_1$	1274	8° 38′	0.9887	5.86	57	10.7	0.20	0.23	6.6	0.032	$-15.4\,(1+j\,0.01$
Au $L\beta_1$	1081	7° 18′	0.9919	4.20	36	10.7	0.16	0.18	6.6	0.028	$-15.4\,(1+j\,0.01$
Mo $K\alpha_1$	708	4° 47′	0.9965	1.80	10.5	10.7	0.09	0.08	6.6	0.018	$-15.4\,(1+j\,0.00$

Table 2. The constants, used in the calculat

The thickness of the t

Line	Wave-length in X.U.	Bragg angle ϑ_B	$\cos 2\vartheta_B$	$\delta \cdot 10^6$	μ_l cm^{-1}	f_{Si}	f'_{Si}	f''_{Si}	f_{O}	f''_{O}	$\psi'_0 \cdot 10^6$	$\psi''_0 \cdot 10^6$
Cu $K\alpha_1$	1537	18° 16′	0.8035	8.60	98	9.4	0.25	0.36	5.3	0.039	−17.2	−0.24
Au $L\alpha_1$	1274	15° 4′	0.8649	5.86	57	9.4	0.20	0.23	5.3	0.032	−11.72	−0.115
Au $L\beta_1$	108	12° 43′	0.9031	4.20	36	9.4	0.16	0.18	5.3	0.028	− 8.40	−0.062
Mo $K\alpha_1$	708	8° 18′	0.9583	1.80	10.5	9.4	0.09	0.08	5.3	0.018	− 3.60	−0.0118

The normal atomic scattering factor f° is taken from the tables calculated by James and Brindley [11]. For f' and f'' we have according to Hönl

$$f' = \frac{2^7 e^{-4}}{9} \left\{ \frac{4x^2}{(1-\Delta_K)^2} \ln \left| \frac{1}{x^2} - 1 \right| - \frac{1}{(1-\Delta_K)^3} \left(2x^2 + x^3 \ln \left| \frac{1-x}{1+x} \right| \right) \right\} \tag{16}$$

$$f'' = \frac{2^7 e^{-4} \pi}{9} \left\{ \frac{4x^2}{(1-\Delta_K)^2} - \frac{x^3}{(1-\Delta_K)^3} \right\} \quad \text{if } x < 1 \tag{17}$$

$$= 0 \qquad\qquad \text{if } x > 1$$

$$\Delta_K = \frac{(Z-s)^2 - I_K/Rhc}{(Z-s)^2} \tag{18}$$

where Z is the atomic number (or the nuclear charge), I_K the ionisation energy of the K level, R Rydberg's constant, h Planck's constant, c the velocity of light, $x = \lambda/\lambda_K$, λ the wavelength and λ_K the wavelength of the K absorption edge, and s a correction that must be applied to Z in order to obtain the effective nuclear charge. This correction is nearly constant and equal to about 0.3 The critical K absorption wavelength is for oxygen 23,500 X.U. and for silicon 6,730 X.U. The value of Δ_K is calculated to 0.27 for Si and to 0.30 for O.

The spacings of the atomic planes used are $d_{10\bar{1}0} = 4246.02$ X.U. and $d_{11\bar{2}0} = 2451.44$ X.U., which gives $\sin\vartheta/\lambda = 0.118$ and 0.204 respectively.

ψ'_0 and ψ''_0 were calculated from experimental data of the refractive index and

the transmission patterns for plane $(10\bar{1}0)$.
sion crystal was 0.045 cm.

$\cdot 10^6$	$\psi_0'' \cdot 10^6$	$\varkappa$	$\psi_H' \cdot 10^6$	A_n	A_p	$(\varkappa A)_n$	$(\varkappa A)_p$	y_n		y_p		g_n	g_p
								radians $\cdot 10^6$	sec. of arc	radians $\cdot 10^6$	sec. of arc		
1.7	−0.115	0.0157	2.00	22.1	21.1	0.346	0.332	6.75	1.39	6.45	1.33	−0.058	−0.061
8.40	−0.062	0.0125	1.44	18.8	18.2	0.235	0.228	5.73	1.18	5.54	1.14	−0.043	−0.044
3.60	−0.0118	0.0059	0.62	12.3	12.1	0.072	0.072	3.72	0.77	3.69	0.76	−0.019	−0.019

the transmission patterns for plane $(11\bar{2}0)$.
sion crystal was 0.045 cm.

j	$\varkappa$	$\psi_H' \cdot 10^6$	A_n	A_p	$(\varkappa A)_n$	$(\varkappa A)_p$	y_n		y_p		g_n	g_p
							radians $\cdot 10^6$	sec. of arc	radians $\cdot 10^6$	sec. of arc		
76	0.0272	3.28	31.0	25.0	0.844	0.678	5.51	1.14	4.44	0.92	−0.073	−0.091
06	0.0175	2.27	26.2	22.7	0.461	0.397	4.54	0.93	3.93	0.81	−0.051	−0.059
40	0.0138	1.63	21.8	19.7	0.301	0.272	3.80	0.78	3.44	0.71	−0.038	−0.042
09	0.0063	0.70	14.1	13.6	0.089	0.085	2.45	0.51	2.35	0.49	−0.017	−0.018

the absorption coefficient. Where no direct experimental values were available, these constants were obtained by extrapolation.

The thicknesses of the crystals were determined by direct measurement before they were inserted in the spectrometer. The values obtained were controlled by absorption measurements with Mo $K\alpha$ radiation for which the absorption coefficient is very accurately known.

All values of the parameters and constants used are given in Tables 1–2.

Results

The geometrical structure factor for plane $(10\bar{1}0)$ in quartz is real. For this reason the geometrical structure factors of planes $(10\bar{1}0)$ and $(\bar{1}010)$ are identical, and consequently $F_H = F_{\bar{H}}$. The Fourier components ψ_H and ψ_H are then identical. In cases like this the theory for the anomalous X-ray transmission that was developed for crystal lattices with an inversion center will be valid without any restriction, and is directly applicable to plane $(10\bar{1}0)$.

Experimental determinations of the intensity curves of the transmitted and the reflected radiation in the Bragg-Laue arrangement were carried out for three emission lines, viz., Au $L\alpha_1$, Au $L\beta_1$ and Mo $K\alpha_1$. The measurements were made in such areas of the transmission crystal where the thickness control gave the same value as the earlier determined (0.045 cm). In order to facilitate a comparison between the experimental curves and the theoretical ones, these two have been brought together with the calculated curves to the left.

Measurements with plane $(1\,1\,\bar{2}\,0)$ were carried out with the three above emission lines and with Cu $K\alpha$ radiation in the same way as before. Plane $(1\,1\,\bar{2}\,0)$ has a complex geometrical structure factor so that the calculations were made under the above assumptions. The results are given in Figs. 4–7.

In order to make a qualitative and quantitative comparison easier, some characteristic data have been calculated from the curves and brought together in Tables 3–4.

The experimental curves obtained in the investigations with plane $(1\,0\,\bar{1}\,0)$ are nearly identical with the calculated ones (see Figs. 1–3). The qualitative agreement is very good, as a direct comparison between the curves indicates. This appears also from the data in Table 3, where the pure qualitative quantities such as the angular distances Δ and Δ' from the peak of the reflection curve to the maximum and minimum of the transmission curve are equal within the experimental limits of error. This is also the case for the more quantitative data. Calculated and experimental values of the full width of the reflection curve, of the maximum intensity of this curve, and of the integrated reflection are equal within the experimental error. As to the corresponding quantities in the transmission curve similar relations are valid, though the differences between calculated and experimental values are greater. In the wavelength range used the ratio λ/λ_K for Si is small, so that $\varkappa$ and $\varkappa A$ attain small values. The corresponding transmission curves have broad and rather low peaks. This makes it rather difficult to draw a correct curve through the experimental points, so that the uncertainties in the widths and in the integrated transmission must be greater than in the corresponding reflection values. With respect to this fact the qualitative agreement must be considered good also for the transmission curves.

The results of the investigations with plane $(1\,1\,\bar{2}\,0)$ appear from Figs. 4–7 and Table 4. A good agreement is obtained here too, though it is inferior to that with plane $(1\,0\,\bar{1}\,0)$. The experimental values of the widths of the reflection curves are larger and the experimental maximum intensities of these curves smaller than the corresponding calculated values. The experimental and calculated values of the integrated reflection are nearly equal, so that the above deviations seem to compensate each other. The experimental transmission curves here deviate more from the theoretical curves than was the case with the above plane. Their maximum intensities are lower and their minimum intensities higher than the calculations indicate. The deviations are greatest at the longest wavelength (at the Cu $K\alpha$ line, see Fig. 4). However, the integrated transmission is the same within the errors of measurements, so that the deviations here too compensate each other. (It should be mentioned that these are rather large because a slight error in the position of the dotted line indicating the normal transmission causes a relatively great change in the integrated transmission. The error in the integrated reflection is considerably less.)

The qualitative agreement between the shapes of the curves and between the angular relations must be considered good, as is seen from the values of the angular distances from the peaks of the reflection curves to the maxima and minima in the transmission curves.

It was found in an earlier investigation of the X-ray diffraction in quartz, carried out with both crystals in the Bragg position, that quartz reflects very nearly as a perfect crystal [6.] The experimental values of the double crystal coefficient of reflection were identical with the calculated ones within the limits imposed by

Table 3. The results obtained in the investigation with plane $(10\bar{1}0)$.

W_R is the full width of the reflection curve at half maximum intensity, measured in sec. of arc; W_T is the full width of the maximum in the transmission curve at half maximum intensity, measured in sec. of arc. (The maximum is measured from a base line that indicates the normally transmitted intensity at angles off the Bragg angle, where no anomalous transmission takes place.) $W_{\min}$ is the full width of the minimum in the transmission curve at half minimum intensity (measured as above); $R_{\max}$ is the maximum intensity of the reflection curve; $T_{\max}$ is the maximum and $T_{\min}$ the minimum intensity of the transmission curve, all given in per cent of the intensity incident upon the transmission crystal; Δ is the angular distance from the peak of the reflection curve to the maximum of the transmission curve and Δ' the distance from the peak in the reflection curve to the minimum in the transmission curve, both measured in sec. of arc; $\int_{-\infty}^{\infty} R\,d\vartheta$ is the area under the reflection curve and is here called the integrated reflection; $\int_{-\infty}^{+\infty} (T-T_0)\,d\vartheta$ is the area between the transmission curve and the line that indicates the normally transmitted intensity. It is here called the integrated transmission. The last two quantities are both measured in radians.

Emission line	Wave-length X.U.	W''_R		W''_T		$W''_{\min}$		$R_{\max}\cdot 10^2$		$T_{\max}\cdot 10^2$		$T_{\min}\cdot 10^2$		$10^6\cdot\int R\,d\vartheta$		$10^6\cdot\int(T-T_0)\,d\vartheta$		Δ		Δ'	
		t	exp	t	exp	t	exp	t	exp	t	exp	t	exp	t	exp	t	exp	t	exp	t	exp
Au $L\alpha_1$	1274	4.7	4.6	8.0	7.0	5.8	6.0	2.7	2.8	8.8	8.7	4.5	4.6	0.86	0.80	−0.52	−0.75	2.8	3.0	1.2	1.6
Au $L\beta_1$	1081	3.9	4.0	10.0	8.0	4.3	5.2	7.0	7.1	21.2	21.2	12.5	12.8	1.76	1.94	−1.43	−1.71	3.4	4.0	1.0	0.8
Mo $K\beta_1$	708	2.7	2.8			2.6	2.5	21.4	23.0	63.0	63.0	40.0	38.8	3.66	4.03	−3.47	−3.68	7.1	5.5	0.3	0.3

Table 4. The results obtained in the investigations of the transmission through a quartz plate cut for Laue reflection. Reflecting plane: $(11\bar{2}0)$. Notations as in Table 3.

Emission line	Wave-length X.U.	W''_R		W''_T		$W''_{\min}$		$R_{\max}\cdot 10^2$		$T_{\max}\cdot 10^2$		$T_{\min}\cdot 10^2$		$10^6\cdot\int R\,d\vartheta$		$10^6\cdot\int(T-T_0)\,d\vartheta$		Δ		Δ'	
		t	exp	t	exp	t	exp	t	exp	t	exp	t	exp	t	exp	t	exp	t	exp	t	exp
Cu $K\alpha_1$	1537	3.3	3.6	4.0	6.0	4.2	4.4	0.66	0.65	1.75	1.46	0.53	0.62	0.13	0.14	0.09	0.08	1.4	1.2	1.6	1.8
Au $L\alpha_1$	1274	2.9	3.0	4.4	5.8	3.6	3.6	2.87	2.95	8.60	8.20	4.05	4.45	0.51	0.57	0.19	−0.12	1.8	2.4	0.8	0.8
Au $L\beta_1$	1081	2.5	2.8	5.0	3.6	2.8	2.8	6.80	6.35	20.8	20.2	11.4	11.6	1.10	1.16	−0.82	−1.25	2.2	2.6	0.5	0.7
Mo $K\alpha_1$	708	1.8	2.3			1.8	1.8	20.4	18.8	62.6	62.8	42.4	45.5	2.32	2.52	−2.22	−2.20	4.4	4.0	0.2	0.3

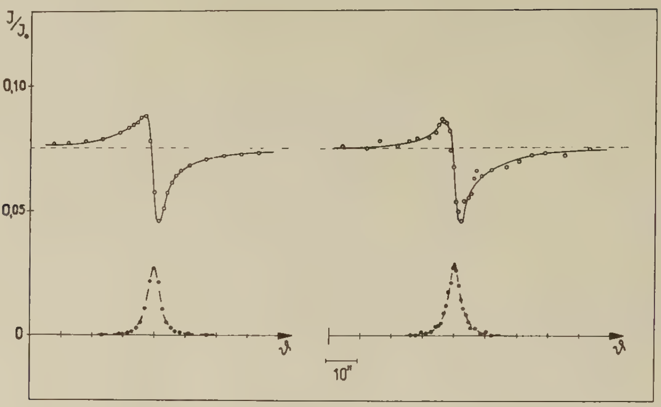

Fig. 1.

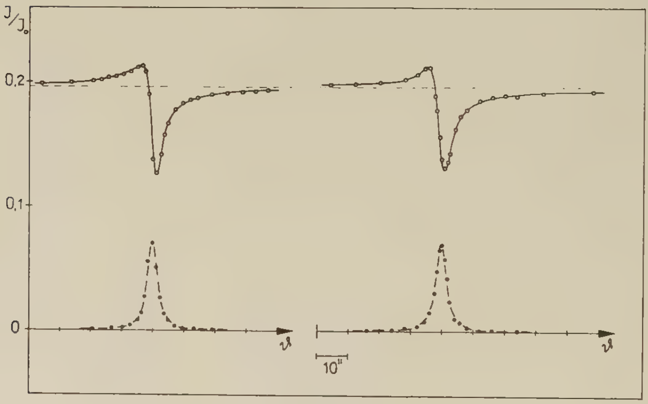

Fig. 2.

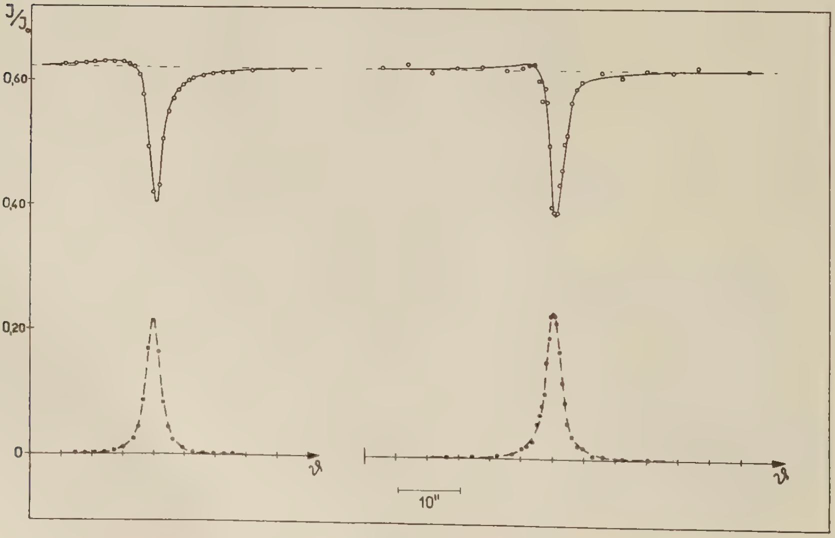

Fig. 3.

experimental errors and the uncertainties in some of the values used in the theoretical calculations. The experimental values of the widths of the rocking curves were greater and those of the percent reflection (the peak intensity of the rocking curve) smaller than the corresponding theoretical values. In the above investigation we studied the diffraction from the two planes that have been used in the present investigation. It was found that the experimental values from plane $(1\,0\,\bar{1}\,0)$ were in better agreement with theory than those from plane $(1\,1\,\bar{2}\,0)$. The crystals used there were used as monochromator crystals in the present investigation. The broadening of the experimental transmission curves may thus wholly or partly depend on defects in the monochromator crystals. However, the broadening are much smaller here than in the Bragg-Bragg arrangement.

In summarizing the results of the above comparisons and discussions we find that all recordings with plane $(1\,0\,\bar{1}\,0)$ have given a very satisfactory agreement with theory. All quantitative determinations are very close to the theoretical values and the shapes of the experimental and the theoretical intensity curves are the same. In the recordings with plane $(1\,1\,\bar{2}\,0)$ the agreement is not equally good because the experimental curves are broader than the theoretical ones. The broadening increases with decreasing wavelength but it is much less than what was earlier found in the investigations of the transmission through calcite. It is not probable that the difference in curve width arises from the fact that plane $(1\,1\,\bar{2}\,0)$ has a complex geometrical factor which necessitated the above assumption before the theory could be applied to this plane. The good agreement between the experimental and theoretical values of the integrated reflection and between the shapes of the theoretical and experimental curves seem to indicate that this assumption leads to correct results. The qualitative and quantitative agreement for this plane is as good as or better than that obtained with calcite. With plane $(1\,0\,\bar{1}\,0)$ where the theory is valid without any restriction the agreement is excellent.

The agreement with the theoretical diffraction and transmission patterns is much better than that obtained with calcite, which verifies the earlier observation that quartz is more nearly a true perfect crystal than any other crystal hitherto found.

Acknowledgement

The work has been financially supported by a grant from the Swedish Natural Science Research Council, which is gratefully acknowledged. This made it possible to carry out the tedious numerical calculations. I also want to thank fil. mag. ÖVED ADELL for valuable assistance with the experimental investigation and fil. mag. CARL NORDLING for assistance with the numerical calculations.

The Physical Institute, University of Uppsala, Sweden. April 1954.

Figs. 1–3. Transmitted and reflected intensities through a 0.45 mm thick quartz crystal, cut for symmetric Laue reflection. Monochromator crystal cut for symmetric Bragg reflection. Reflection plane $(1\,0\,\bar{1}\,0)$. In this and following figures the left-hand curves give the theoretical patterns, the right-hand ones those experimentally obtained.

Fig. 1. Au $L\alpha_1$ radiation. Fig. 2. Au $L\beta_1$ radiation. Fig. 3. Mo $K\alpha_1$ radiation.

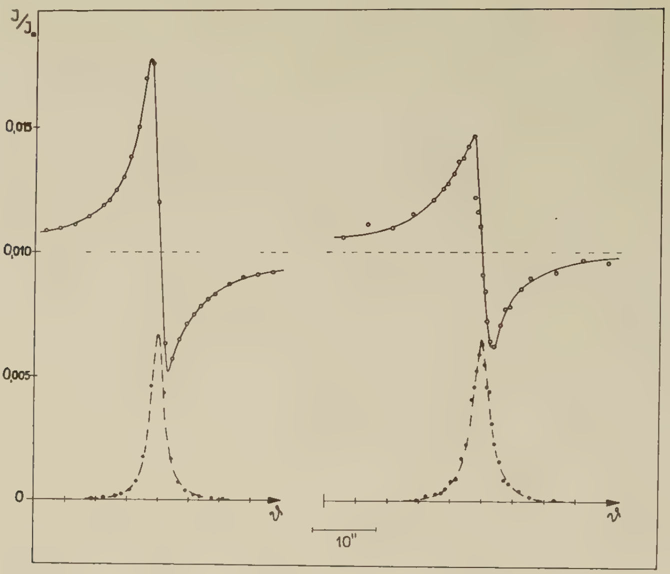

Fig. 4.

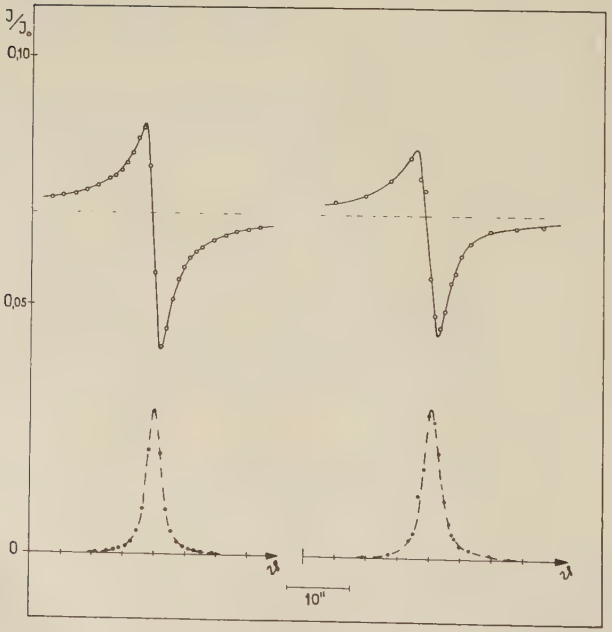

Fig. 5.

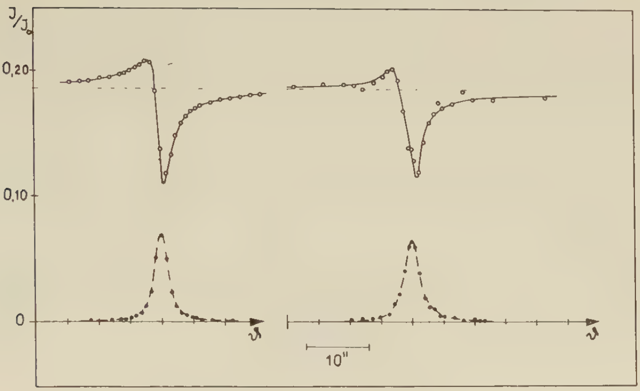

Fig. 6.

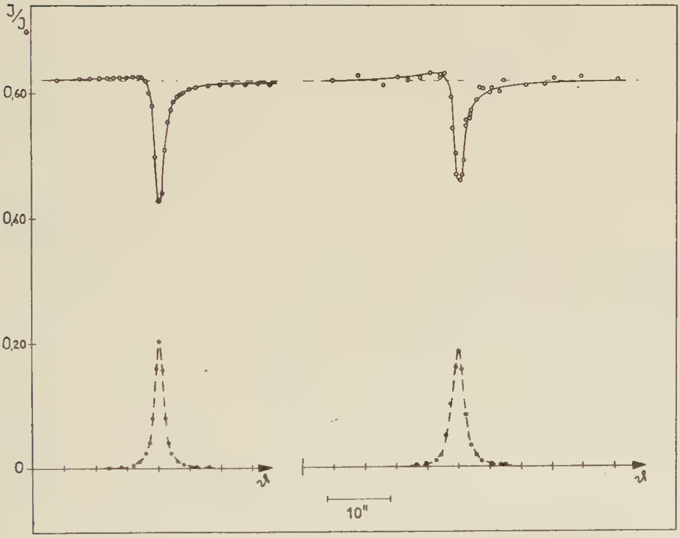

Fig. 7.

Figs. 4–7. Transmitted and reflected intensities through a 0.45 mm thick quartz crystal, cut for symmetric Laue reflection. Monochromator crystal cut for symmetric Bragg reflection. Reflections from plane $(1\,1\,\bar{2}\,0)$.

Fig. 4. Cu $K\alpha_1$ radiation. Fig. 5. Au $L\alpha_1$ radiation. Fig. 6. Au $L\beta_1$ radiation. Fig. 7. Mo $K\alpha_1$ radiation.

REFERENCES

1. G. BROGREN and Ö. ADELL, Ark. f. Fys. *8*, 97, 1954.
2. G. BROGREN and Ö. ADELL, *Ib.* *8*, 501, 1954.
3. G. BORRMAN, Phys. Zs. *42*, 157, 1941.
4. P. H. WEI, Zs. f. Krist. *92*, 355, 1935.
5. R. BRILL, C. HERMANN and C. PETERS, Ann. d. Phys. *41*, 233, 1941.
6. Ö. ADELL, G. BROGREN and L.-E. HAEGGBLOM, Ark. f. Fys. *7*, 197, 1953.
7. W. H. ZACHARIASEN, Theory of X-ray Diffraction in Crystals. John Wiley & Sons, Inc. New York 1945.
8. H. HÖNL, Zs. f. Phys. *84*, 1, 1933.
9. H. HÖNL, Ann. der Phys. *18*, 625, 1933.
10. International Tables for X-ray Crystallography. Vol. I. The Kynoch Press. Birmingham, 1952.
11. R. W. JAMES and G. W. BRINDLEY, Phil. Mag. *12*, 81, 1931.

Tryckt den 20 oktober 1954

Uppsala 1954. Almqvist & Wiksells Boktryckeri AB

ARKIV FÖR FYSIK Band 8 nr 38

Communicated 14 April 1954 by Erik Hulthén and G. Borelius

On the origin of unsymmetrical Rowland ghosts in optical gratings

By Erik Djurle

With 5 figures in the text

1. Introduction

The formation of the so-called Rowland ghosts in optical gratings was treated in 1893 by Rowland [1] and later by Runge [2]. These and later papers on the subject treat periodic errors in the groove spacing and the contributions to the ghosts of the different periodicities. The theory shows that the ghosts should have a symmetrical intensity distribution around the parent line. However, it is a fact well-known to spectroscopists that the ghosts sometimes show an unsymmetrical intensity distribution. As a complement to a previous paper [3] dealing with experimental tests of gratings, it should be of some interest to present a detailed theoretical treatment of the subject.

The ghost intensity is measured above the continuous background, so the asymmetry cannot be due to an incoherent unsymmetrical background. The effect must be due to a superposition of coherent light scattered into the positions of the ghosts. This light can have its origin in the imperfections of the optical system of which the grating is a part. In practically all cases it is found that spherical aberration, astigmatism, coma, and curvature of the slit [4], only broaden the image of the entrance slit by an amount of less than 1/100 of the distance to the nearest ghost. The asymmetry, accordingly, is due to diffraction effects at the grating surface.

The application of phase contrast methods to the analysis of optical gratings has given us a fuller knowledge of the properties of the grating surface and of the light diffracted from it than could be obtained using earlier methods, such as knife-edge and out-of-focus tests. Several papers, including some from this laboratory, describe the application of the phase contrast method and give examples of phase curves for different gratings [5, 6, 7, 3]. The curves show a periodic variation due to the superposition of harmonic frequences caused by the screw of the ruling machine, and also random variations. The interference in the spectral plane of coherent light originating from these two types of error, periodic and random, can give rise to unsymmetrical ghosts.

2. The formation of ghosts according to diffraction theory

A coherent, monochromatic, and plane wave front that falls on a plane reflexion or transmission grating undergoes diffraction. The phase of the diffracted light is determined by the properties of the grating surface and the angle of diffraction, the light vectors from the grating being Fourier transformed [8]. The transform gives the amplitude of the light vectors in the reciprocal Fourier plane, which in the case of an optical grating corresponds to the plane of its spectrum.

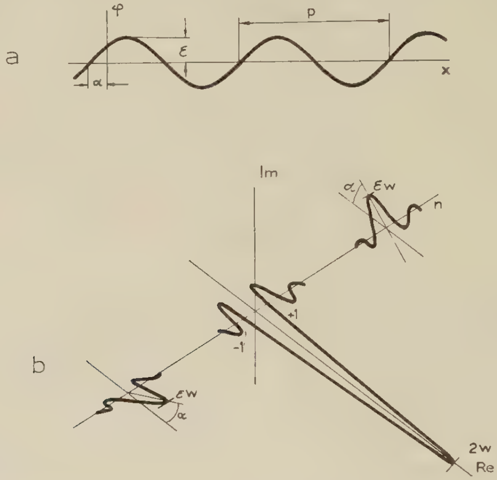

Fig. 1. Schematic view of the periodic wave front and its vectors in the diffraction plane.

The vector amplitude $G(u)$, in a direction that makes a small angle u with the normal to the plane wave-front from the grating, is obtained by multiplying the vector $F(x)$ at the position x on the grating surface by exp $(ikux)$, and integrating over the surface $2w$, $k=2\pi/\lambda$, i.e.

$$G(u)=\int_{-w}^{+w} F(x)\ \exp\ (ikux)\,dx. \tag{I}$$

$F(x)$ is usually normalized, and for an ideal grating all vectors have the same direction, i.e. $F(x)=1$. An actual grating shows phase differences between the vectors from the different parts of the surface, i.e $F(x)=$ exp $(i\varphi)$, where φ is the registered phase curve for the grating. As mentioned above, φ has periodic and random components. As the higher periodicities of the basic periodic error only complicate the calculations and do not contribute to the first ghost on either side of the parent line, the function φ will be chosen as

$$\varphi(\varepsilon,\delta)=\varepsilon\sin(2\pi x/p+\alpha)+\delta(x),$$

where ε is the periodic error amplitude, p the period length, α the phase angle of the periodic error, and $\delta(x)$ the random error, cf. Fig. 1 where only the periodic part is indicated.

The evaluation of integral (I) is made in two steps.

$$G(u) = \int_{-w}^{+w} \exp\,[i\,k\,u\,x + i\,\varphi(\varepsilon, 0)]\,d\,x + \\ + \int \exp\,(i\,k\,u\,x)\,[\exp\{i\,\varphi(\varepsilon,\delta)\} - \exp\{i\,\varphi(\varepsilon, 0)\}]\,d\,x. \qquad \text{(II)}$$

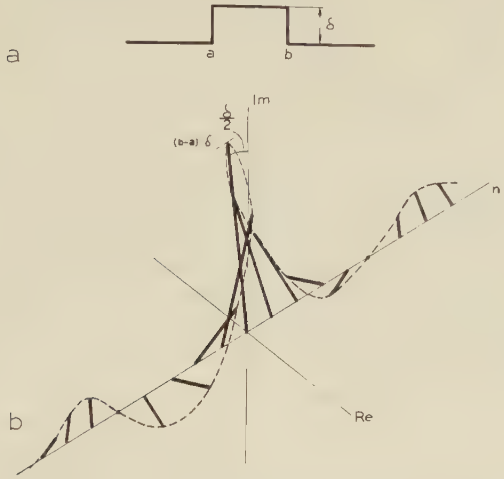

Fig. 2 a. Random anomaly type *A*. b. Vector contribution from the anomaly in the diffraction plane.

The second integral is taken over all parts of the grating surface showing phase irregularities. This calculation is very tedious for un actual phase curve, which includes the $\delta(x)$ term, so only the influence of some typical forms of the anomaly $\delta(x)$ are calculated here.

If the amplitude ε of the periodic term is small, as is the case for all modern gratings, its square can be neglected and the first integral in II gives

$$G_1(u) = 2\,w \left\{ \frac{\sin n\,\pi}{n\,\pi} + \frac{\varepsilon}{2}\,e^{i\,\alpha}\,\frac{\sin\,(n + 2\,w/p)\,\pi}{(n + 2\,w/p)\,\pi} + \right. \\ \left. + \frac{\varepsilon}{2}\,e^{i\,(\pi-\alpha)}\,\frac{\sin\,(n - 2\,w/p)\,\pi}{(n - 2\,w/p)\,\pi} \right\}, \qquad \text{(III)}$$

where n is the "diffraction unit" [3], $n = 1$ corresponding to the first zero-point for the diffraction curve due to the whole grating aperture. The amplitude distribution is shown in Fig. 1.

The evaluation of the second integral is done for two types of non-periodic anomalies shown in Figs. 2 a and 3 a. These are representative for the random anomalies found in actual phase curves [3, 6, 7].

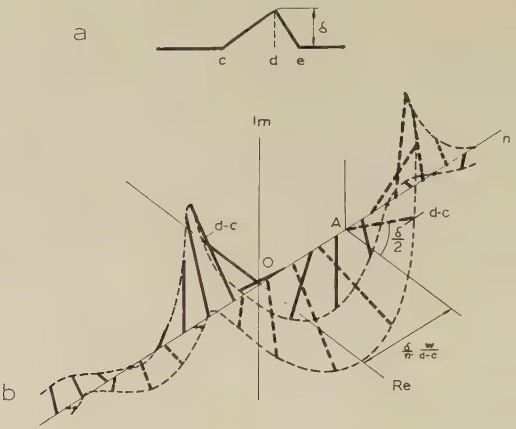

Fig. 3 a. Random anomaly type *B*. b. Vectors in the diffraction plane due to the anomaly. Only contributions from the part *c–d* are shown.

The anomaly in Fig. 2 a is supposed to be extended from a to b, its phase δ being constant within this interval. The second integral in II gives two diffraction figures lying on helical surfaces with an angle $\pi - \delta$ between them. The resultant vector can be written, if terms of the second order are omitted,

$$\Delta_1 G(u) = e^{i[n\pi(b-a)/2w+(\pi+\delta)/2]}\,(b-a)\,2\sin\frac{\delta}{2}\,\frac{\sin n\pi(b-a)/2w}{n\pi(b-a)/2w}. \tag{IV}$$

As $(b-a) < 2w$, the amplitude varies slowly with n. The diffraction figure is shown in Fig. 2 b.

The anomaly type shown in Fig. 3 a gives a contribution of the same kind, the resultant vector consisting of terms from four diffraction figures, two with their maxima displaced from the origin 0 to A, Fig. 3 b. If the anomaly is extended between c and e

$$\begin{aligned}\Delta_2 G(u) = {} & (d-c)\,e^{in\pi(d+c)/2w}\left\{e^{i\delta/2}\,\frac{\sin[n\pi(d-c)/2w+\delta/2]}{n\pi(d-c)/2w+\delta/2} - \right.\\ & \left. -\frac{\sin n\pi(d-c)/2w}{n\pi(d-c)/2w}\right\} + (e-d)\,e^{in\pi(e+d)/2w}\left\{e^{i\delta/2}\,\frac{\sin[n\pi(e-d)/2w-\delta/2]}{n\pi(e-d)/2w-\delta/2} - \right.\\ & \left. -\frac{\sin n\pi(e-d)/2w}{n\pi(e-d)/2w}\right\}.\end{aligned} \tag{V}$$

The vector amplitude in the spectral plane is $G(u) = G_1(u) + \Sigma\,\Delta_1 G(u) + \Sigma\,\Delta_2 G(u)$, the vectors in the two sums generating helical surfaces when n varies. The turning velocity $(b+a)/2w$ in $\exp\, i n\pi(b+a)/2w$ depends on the position of the anomaly. The turning of the vector within the n-region ± 1 unit in which the ghost has appreciable intensity is less than $\pm\pi$, as $(b+a) < 2w$. In the

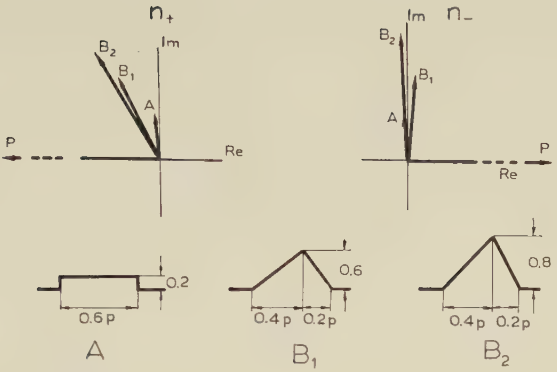

Fig. 4. Some typical anomalies and their vector contributions to the n_+ and n_- ghosts. P is the vector contribution from the periodic error.

calculations, the vector position for the n-value corresponding to maximum intensity of the ghost is used, as the turning only modifies the shape of the ghost.

The superposition of the vectors at the position of the ghost is done for the constant n-values $n_\pm = \pm 2\,w/p$. We get for n_+

$$\Delta_1 G(u) = e^{i[\pi(b+a)/p+(\pi+\delta)/2]}\,(b-a)\,2\sin\frac{\delta}{2}\,\frac{\sin\pi(b-a)/2w}{\pi(b-a)/2w} \tag{VI}$$

$$\begin{aligned}\Delta_2 G(u) = e^{i\pi(c+e)/p}\Bigg[(d-c)\Bigg\{&e^{i[\pi(d-e)/p+\delta/2]}\,\frac{\sin[\pi(d-c)/p+\delta/2]}{\pi(d-c)/p+\delta/2} - \\ &- e^{i\pi(d-e)/p}\,\frac{\sin\pi(d-c)/p}{\pi(d-c)/p}\Bigg\} + (e-d)\Bigg\{e^{i[\pi(d-c)/p+\delta/2]}\,\frac{\sin[\pi(e-d)/p-\delta/2]}{\pi(e-d)/p-\delta/2} - \\ &- e^{i\pi(d-c)/p}\,\frac{\sin\pi(e-d)/p}{\pi(e-d)/p}\Bigg\}\Bigg].\end{aligned} \tag{VII}$$

The amplitude of the additional vector due to the anomaly is determined by its extension and δ-value, the direction being determined by its position on the grating surface, $\exp\, i\pi(b+a)/p$. A large extension of the anomaly has only a small influence on the ghost, as the diffraction figure in this case is narrow. The extension should be of the order of p or less. The displacement of the anomaly a distance p along the grating surface causes the vector to rotate one turn. For a given anomaly it is only its position in relation to the periodic structure that determines its effect on the ghost intensity.

3. Experimentally obtained anomalies and the ghost intensity

The addition of vectors VI and VII for the two ghosts n_+ and n_- is indicated in Fig. 4. The two periodical ghost vectors are symmetrical about the imaginary axis, Fig. 1. The vectors from the random anomalies are turned

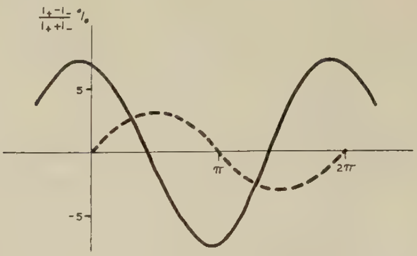

Fig. 5. Difference between I_+ and I_- for one anomaly B_1, as a function of the anomaly position in relation to the periodic error (dotted curve).

through equal angles in the positive and negative directions from their positions for $n = 0$, see Figs. 2 and 3. The phase angle α can thus be omitted. The condition for unsymmetrical ghosts is that the additional vectors be unsymmetrical relative to the periodic vector for n_+ and n_-. Asymmetry of the order of 10 % in vector amplitude has been observed experimentally in records of the intensity distribution in the spectral plane.

The vectors A in Fig. 4 correspond to anomalies of the type shown in Fig. 2. The vector makes an angle $\delta/2$ with the imaginary axis. The condition for influencing the ghost intensity is that the above-mentioned asymmetry in the vectors must be relatively large, i.e. δ must be large. A δ-value of 0.2 radians and an extension of the anomaly of 0.6 p, Fig. 4, gives in its most favourable position an asymmetry of some tenths of a per cent in intensity. The chosen δ-value, 0.2 radians, is a maximum for this kind of anomaly. The asymmetry can thus not be due exclusively to this type of anomaly, even if there should be many of them. Of course, they give some contribution to the asymmetry.

The type of anomalies shown in Fig. 3 gives rise to unsymmetrical vectors larger than the preceding anomaly and can thus be the origin of the asymmetry in ghost intensity. This is partly due to their asymmetry about the mid-point, and partly to the displacement along the n-axes of two of the diffraction figures, building up the resultant vector. The phase curves for various gratings tested shows that the δ-value in this case can be considerable, 0.6 to 0.8 radians. B_1 and B_2 in Fig. 4 correspond to anomalies with extension 0.6 p and $\delta = 0.6$ and 0.8 radians respectively. The turning exponent of the vector is a multiple of 2π, e.g. the midpoint of the anomaly lies at the origin, or a whole number of periods from it.

The behaviour of the ghost intensity for anomaly B_1 is shown in Fig. 5, where $(I_+ - I_-/I_+ + I_-)$ is plotted as a function of the position of the mid-point of the anomaly relative to the periodic variation. The amplitude of the periodic variation corresponds to a ghost intensity of 0.16 per cent.

If the anomalies of this type are randomly distributed over the grating surface, the sum of the vectors in Fig. 4 gives no contribution to the ghost intensity, as the anomaly vector polygon is closed in this case. Because of the ruling technique used it is possible that anomalies of this kind may appear with some periodicity in relation to the periodic error. An addition of vectors distributed in a small angular region in Fig. 4 would produce a resultant causing the observed asymmetry.

If the resultants are for example as large as 4 B_1 and the periodic error corresponds to a ghost intensity of 0.16 per cent, we get an intensity of 0.23 and 0.19 per cent for the two ghosts. The mean intensity is 0.21 per cent and the asymmetry 23 per cent, or in amplitude about 11 per cent.

The interference of coherent light originating from periodic and random errors thus causes, under certain conditions, an asymmetry in the ghosts. The calculations also show that the general relation between the ghost intensity and the amplitude of the periodic error [1, 2] is modified, a matter which should be taken into account when compensating for periodical errors.

Summary

The ordinary theory of Rowland ghosts shows that they should be symmetrical in intensity, but it is nevertheless a well-known fact that they are sometimes unsymmetrical. A study of the way they are built up, according to diffraction theory, shows that their asymmetry is explained by certain anomalies present in the phase structure of the grating. Such anomalies have been found in gratings when examined by the phase contrast method.

I wish to express my thanks to Dr. E. Ingelstam for suggesting this study and for his valuable advice in the course of the work.

Optics Laboratory, Royal Institute of Technology, Stockholm 70, March 1954.

REFERENCES

1. H. A. Rowland, Phil. Mag. *5*, 397, 1893.
2. C. Runge, Ann. der Physik *71*, 178, 1923.
3. E. Ingelstam and E. Djurle, J. O. S. A. *43*, 572, 1953.
4. H. G. Beutler, J. O. S. A. *35*, 311, 1945.
5. A. M. Camus, M. Françon, E. Ingelstam and A. Marechal, Rev. Opt. *30*, 121, 1951.
6. E. Ingelstam and E. Djurle, Arkiv för Fysik *4*, Nr 27, 1952.
7. E. Ingelstam and E. Djurle, Arkiv för Fysik *6*, Nr 44, 1953.
8. P. M. Duffieux, L'Integral de Fourier et ses applications à l'optique. Rennes 1946.

Tryckt den 29 oktober 1954

Uppsala 1954. Almqvist & Wiksells Boktryckeri AB

ARKIV FÖR FYSIK Band 8 nr 39

Communicated 28 April 1954 by AXEL E. LINDH and G. HÄGG

A note on the widths of X-ray emission lines

By GÖSTA BROGREN

With 2 figures in the text

The full width of an emission line at half maximum intensity is the sum of the widths of the initial and the final energy levels between which the transition takes place. Hence, it is possible to derive the width of an emission line if the widths of the levels are known. A large number of line width determinations has also been carried out with different kinds of X-ray spectrometers. The highest accuracy is ascribed to those made with double crystal spectrometers, as the resolving power is higher for such instruments than for any others. After it had been shown that the reflecting qualities of calcite are in excellent agreement with what is predicted by the dynamical theory for the X-ray diffraction in crystals, the measurements carried out with the cleavage surface of this crystal have been considered the most accurate. It is, however, uncertain whether the measured width of a spectral line is the real width or whether it is necessary to apply a correction. EHRENBERG and MARK [1] calculated the "true" wavelength width of an X-ray line assuming the shape to be that of the Gaussian error curve both for the line and for the diffraction pattern of the single crystal. If D is the dispersion of the two-crystal spectrometer, w_A the angular width of the rocking curve in position $(n_A - n_A)$, w_B that in position $(n_B - n_B)$, and w_1 the angular width of the spectral line obtained in position $(n_A + n_B)$, they found that the width w_λ of the line should be

$$w_\lambda = \frac{1}{D}\sqrt{w_1^2 - \frac{w_A^2 + w_B^2}{2}}\,. \tag{1}$$

As the correction given by (1) is commonly only a few per cent, and as the above assumption about Gaussian error curve shape is not correct (the diffraction pattern for an absorbing perfect crystal is asymmetric), usually no correction is applied to the experimental values obtained. Hitherto, the results from the first order reflections from calcite 211 (= the cleavage plane) have been considered the most accurate.

In connection with an investigation of the reflection properties of some atomic planes in quartz, which are suitable to be used as crystal gratings in X-ray spectroscopy, the contour curve of the copper Kα_1 line was registered with a double crystal spectrometer. The crystal specimens used had the surfaces ground and polished parallel to the desired atomic plane. The exact orientation of this plane as to the very surface was determined by a method of adjustment that permitted an accurate parallelism of the atomic planes in the two reflecting crystal plates [2].

Table 1. The width of the Cu Kα_1-line.

w_c is the full width of the rocking curve at half maximum intensity, w_0 is the full width of the contour curve in position (1 + 1) or the experimental line width, and $\lambda/d\lambda = 2 \tan \vartheta / w_c$ is the resolving power of the two-crystal spectrometer in position (1 + 1).

Crystal grating	w_0 X.U.	w_c X.U.	$\lambda/d\lambda$ $.10^{-4}$	$w_0 - w_c$ X.U.
Quartz $10\bar{1}0$	0.56	0.10	1.51	0.46
,, $10\bar{1}\bar{1}$	0.58	0.14	1.11	0.44
,, $11\bar{2}0$	0.47	0.04	4.0	0.43
,, $11\bar{2}\bar{2}$	0.45	0.03	6.0	0.42
,, $20\bar{2}\bar{3}$	0.43	0.01	14.0	0.42
,, $22\bar{4}0$	0.44	0.01	15.1	0.43
Calcite 211	0.58	0.15	1.06	0.43
,, 422	0.45	0.02	10.1	0.43

Before the measurements were carried out, the crystals were etched with hydrofluoric acid until the reflectivities (= the full width of the rocking curve at half maximum intensity, the percent reflection and the double crystal coefficient of reflection) were not influenced by subsequent etching. It was also checked that the reflectivities were uniform over the surfaces of the specimens used.

The heights of the horizontal slits were always less than one mm. As the distance between them was 300 mm, the vertical divergency φ_m was less than 1/300 radians, and the geometric resolving power larger than 360,000. This value is so high that the forms and widths of the curves to be measured are not affected by the vertical divergency.

The results appear from Table 1. Fig. 1 gives the obtained line width as a function of the resolving power of the spectrometer. When this increases, the line width decreases asymptotically towards a value of about 0.43 X.U. The dotted line in the figure represents the difference between the width in position (1 + 1) (the experimental line width) and that in position (1 − 1) (the width of the rocking curve). The difference was always between 0.46 and 0.42 X.U. Hence, the difference seems to have a constant value, equal to the obtained width of the line when the resolving power is very large.

It should be mentioned that with calcite 211 we got the width 10.2″ (0.15 X.U.) of the rocking curve and a line width for Cu Kα_1 of 0.58 X.U. The corresponding values of plane 422 (second order of 211) were 2.3″ (0.02 X.U.) and 0.45 X.U. respectively. Hence, the same change with the resolving power is found with calcite. As appears from Fig. 1, the calcite values also fit the curves.

The above results indicate that the true width of the copper Kα_1 line is the difference between the measured width of the line and the width of the diffraction pattern of the spectrometer used. It must be emphasised that the present accepted values of the widths of X-ray emission lines—as a rule obtained with calcite 211—are too great, which implies that the X-ray energy levels are smaller than has been assumed. New determinations are necessary, but they must be preceded by a thorough investigation of the relation between the measured line width and the resolving power of the spectrometer. This should be done for different crystal gratings and different emission lines.

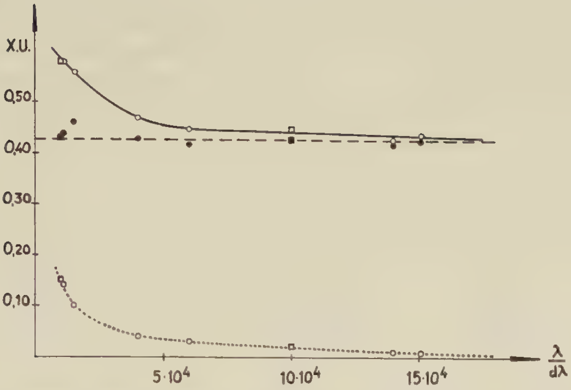

Fig. 1. The relation between the experimental width of the Cu Kα_1 line and the resolving power of the two-crystal spectrometer. ——— is the experimental width w_0 (obtained in position $(1 + 1)$). · · · · · · is the width w_c of the rocking curve in position $(1 - 1)$. – – – – – is the difference between the two above values.

It has been observed previously that the line width depends on the properties of the crystal grating used. In 1935 PARRATT [3] made an experimental investigation of the problem. He used sixteen different crystal pairs in a double spectrometer for measuring the widths of four different emission lines, viz. the Kα_1 lines of Mo, Cu, and Ti, and the Lα_1 line of Ag. When he had established a criterion for "perfect crystal pairs", he used the values from such pairs to find the true line width W_T from the full width W_C of the rocking curve at half maximum intensity in position $(n - n)$, and the observed line width W_0 in position $(n + n)$. He formulated the relation

$$W_T = W_0 - 2.9\ W_C^{1.7}. \tag{2}$$

He discussed several factors which may affect the line-width determinations. For the purpose of comparison, his values of the width of the copper Kα_1 line are given in Table 2.

Our experience is that the best criterion for the perfection of a crystal is the comparison between theoretical and experimental values of the reflectivities. The best agreement is obtained for the coefficient of reflection, which for good specimens deviates only slightly from the theoretical values. The experimental value of the width of the rocking curve is generally slightly larger and that of the percent reflection slightly smaller than the respective theoretical values. The deviations are larger for the calcite crystal than for the quartz crystal. It should be borne in mind that the coefficient of reflection by itself is not a criterion of perfection [4]. Since no values are given on the coefficient of reflection, the qualities of the different crystal pairs have been judged from the widths of the rocking curves for Cu Kα_1 and Mo Kα_1. In our previous work with calcite and quartz crystals, we found that when the deviation from the calculated width of the rocking curve was larger than about ten per cent, a considerable broadening often appeared for position $(n + n)$, due to deficiencies in the crystal. With this criterion of perfection, only three of PARRATT's crystal pairs are perfect, viz. quartz $(11\bar{2}0)$ and calcite A_4B_4 and $A_{15}B_{15}$. The crystal

Table 2. The width of the Cu Kα_1 line owing to PARRATT.

w_0 is the experimental line width, w_c is the full width of the rocking curve at half maximum intensity. $w_0 - w_c$ is introduced when the crystal pair can be considered perfect.

Crystal grating	w_0		w_c		$w_0 - w_c$ X.U.	Asymmetry	PARRATT's crystal notation
	sec.	X.U.	sec.	X.U.			
Quartz $11\bar{2}0$ . . .	42.0	0.475	3.4	0.038	0.44	1.15	
,, $22\bar{4}0$ . . .	95.0	0.44	2.2	0.010	0.43	1.15	
,, $10\bar{1}0$ . . .	33.5	0.68	10.7	0.217			
,, $20\bar{2}0$ . . .	49.5	0.475	4.0	0.04			
Calcite 211 . . .	52.0	0.74	13.0	0.185			A_1B_1
,, 211 . . .	59.0	0.84	15.0	0.214			A_2B_2
,, 211 . . .	45.0	0.64	10.6	0.15			A_3B_3
,, 211 . . .	39.5	0.56	10.0	0.142	0.42	1.15	A_4B_4
,, 422 . . .	72.0	0.455	1.9	0.012	0.44	1.15	A_4B_4
,, 211 . . .	45.4	0.64	13.4	0.19			A_5B_5
,, 422 . . .	74.2	0.47	7.0	0.044			A_5B_5
,, 211 . . .	45.0	0.64	11.3	0.16			$A_{10}B_{10}$
,, 211 . . .	70.0	0.995	25.0	0.35			$A_{11}B_{11}$
,, 211 . . .	41.0	0.58	10.0	0.142	0.44	1.13	ALLISON [6] ($A_{15}B_{15}$)
,, 211 . . .	40.0	0.567	9.8	0.14	0.43	1.13	BEARDEN & SHAW [7]
,, 422 . . .	72.5	0.458	2.4	0.015	0.44	1.10	,, ,, ($A_{16}B_{16}$)
,, 211 . . .	37.8	0.54	9.8	0.14	0.40		BEARDEN & ROSEBERRY [8]

pairs $A_{16}B_{16}$ and $A_{17}B_{17}$, for which only determinations with the Cu Kα_1 line are given, must also be considered perfect, as the rocking curve widths obtained with these agree excellently with the calculations.

In the measurements with crystal pairs where there are larger deviations from the theoretical values of the width of the rocking curve, the experimental line width increases with increasing width of the rocking curve. No simple relation exists between them, as may be seen for instance from the results with A_1B_1 and A_5B_5. In the copper case the rocking curve widths are 0.185 X.U. and 0.19 X.U. respectively but the line widths determined are 0.74 X.U. and 0.64 X.U. resp. With Mo Kα_1 the corresponding values are 0.13 X.U. and 0.162 X.U. resp. and 0.40 X.U. and 0.39 X.U. resp. Since the reason for the broadening of the rocking curves is not known, no explanation of the above results can be advanced. Our own investigations of various lattice planes in quartz and calcite showed that the higher orders rocking curves were very often asymmetric because of crystal defects, but that these effects only caused a broadening in the first order curves. Such defects may affect the form and width of the contour curve of an emission line (= width in position 1 + 1) in various ways, depending on the type and orientation of the defects in the crystal plates. The defects are not amenable to calculation, and it is therefore not possible to use imperfect crystals for measurements to which some kind of correction is subsequently applied.

Table 3 and Fig. 2 give some measurements on the Kα_1 lines of Mo, Fe and Ti. All have been carried out with crystal pairs which must be considered perfect due to the above criterion. The last column gives the difference between the observed width W_0 in position (1 + 1) and the width of the rocking curve W_C, which for the Cu Kα_1 line was found to be the true line width W_T. It will be seen that this differ-

Table 3. The widths of the $K\alpha_1$-lines of Ti, Fe and Mo.

w_0 is the experimental line width in position $(1+1)$, w_c is the full width of the rocking curve at half maximum intensity.

Line	Crystal grating	w_0 X.U.	w_C X.U.	$w_T = w_0 - w_C$	Results obtained from
Ti $K\alpha_1$	Quartz $11\bar{2}0$ . . .	0.91	0.075	0.84	PARRATT
	Calcite 211 . . .	1.09	0.22	0.87	,,
	,, 422 . . .	0.88	0.017	0.86	,,
	,, 211 . . .	1.05	0.23	0.82	BEARDEN & SHAW [8]
	Mean			0.85	
Fe $K\alpha_1$	Quartz $11\bar{2}0$ . . .	0.82	0.04	0.78	BROGREN
	Calcite 211 . . .	1.00	0.19	0.81	ALLISON [7]
	Mean			0.80	
Mo$K\alpha_1$	Quartz $11\bar{2}0$ . . .	0.27	0.029	0.24	PARRATT
	,, $11\bar{2}0$ . . .	0.263	0.027	0.24	BROGREN
	Calcite 211 . . .	0.306	0.076	0.23	PARRATT, crystal A_4B_4
	,, 422 . . .	0.264	0.008	0.26	,, ,, ,,
	,, 211 . . .	0.29	0.075	0.22	ALLISON [7]
	Mean			0.24	

ence is a constant within the experimental limits of error, which is a further proof that the relation

$$W_T = W_0 - W_C \tag{3}$$

is valid for perfect crystals.

The above results indicate that when the width of a line is determined in a double crystal spectrometer, using perfect crystal specimens, the true width W_T of the line may be obtained from the full width W_0 of the contour curve in position $(n+n)$ and the full width W_C of the rocking curve at half maximum intensity in position $(n-n)$ by the relation (3). Further experimental verification is necessary, however, before this can be considered definitely established.

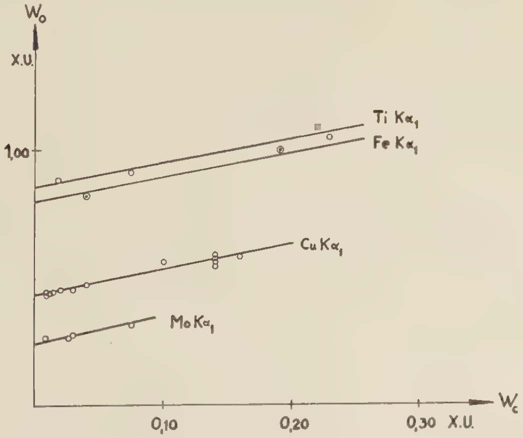

Fig. 2. The experimental line width w_0 as a function of the width w_c of the rocking curve.

One of the factors influencing the width of the lines is the asymmetry of the diffraction pattern. No method has yet been devised for determining the real shape of the single crystal diffraction pattern experimentally. The dynamic theory of X-ray diffraction has been applied to the diffraction pattern from the double spectrometer, and gave excellent agreement with experiment for position $(n-n)$. The predicted form of the single crystal diffraction pattern is asymmetric, as is also that of the diffraction pattern in position $(n+n)$. Indirect evidence for the dynamic theory is provided by the fact that asymmetric "rocking curves" were obtained with the two-crystal spectrometer when the first calcite crystal had the surface parallel to atomic plane 211, and the second had the surface perpendicular to this plane [5]. The latter crystal was in the position for internal reflection, in which case the dynamic theory predicts symmetric single crystal diffraction pattern. Calculation shows that the resultant diffraction pattern should be asymmetric, which was found to be the case experimentally.

It appears from PARRATT's results, however, that the effect of the asymmetric diffraction pattern in position $(n+n)$ is very slight or nil. Quartz $11\bar{2}0$ and calcite 211 have diffraction patterns with different asymmetry. If there were an interaction between this asymmetry and the contour of the line, it should be apparent if the asymmetry of the line is changed. PARRATT found that the asymmetry of the Cu $K\alpha_1$ line was exactly the same when the line was recorded with quartz $11\bar{2}0$ and calcite 211 (using the perfect pair A_4B_4), and the same holds for the Ti $K\alpha_1$ line. This indicates, that the effect of the asymmetric diffraction pattern is negligible in this wavelength range. This result was verified in the above registrations with various quartz and calcite gratings, where no change in the asymmetry was observed.

Theoretical discussion

It is, however, possible to analyse how the shape and width of an emission line is influenced by the diffraction pattern.

According to the classical theory the natural line width is a direct consequence of the damping of an electronic oscillator [12]. Its energy E and amplitude A decrease exponentially with time and are given by

$$E = E_0 \cdot e^{-\gamma t} \tag{4}$$

$$A = A_0 \cdot e^{-\frac{\gamma t}{2}} \tag{5}$$

where E_0 and A_0 are the energy and the amplitude at time $t=0$ and γ a constant defined by

$$\gamma = 8\pi^2 e^2 \nu_0^2 / 3 m c^3. \tag{6}$$

ν_0 is the frequency of the oscillator, e the charge of the electron, m its mass and c the velocity of light.

The elongation x is

$$x = A_0 \cdot e^{-\frac{1}{2}\gamma t} \cos(2\pi\nu_0 t + \alpha). \tag{7}$$

The radiation that is emitted during the damping is not strictly monochromatic but has a certain spectral distribution I (ν). A Fourier analysis of the emitted radiation gives

$$I(\nu) = \frac{\gamma}{2\pi} \cdot \frac{1}{4\pi^2(\nu_0 - \nu)^2 + \left(\frac{\gamma}{2}\right)^2} \tag{8}$$

or

$$I(\nu) = \frac{I_0}{1 + \frac{16\pi^2(\nu_0 - \nu)^2}{\gamma^2}}, \tag{9}$$

where I_0 is the intensity when $\nu = \nu_0$.

Eq. (9) is the classical expression for the form of a spectral line. The full width w_ν at half maximum intensity is

$$w_\nu = \frac{\gamma}{2\pi} = \frac{4\pi e^2 \nu_0^2}{3mc^3} \tag{10}$$

or, if it is measured in wavelength units

$$w_\lambda = \frac{w_\nu \cdot \lambda}{\nu_0} = w_\nu \frac{c}{\nu_0^2} = \frac{4\pi e^2}{3mc^2}. \tag{11}$$

Inserting the values of the constants we obtain

$$w_\lambda = 0.116 \text{ X.U.} \tag{12}$$

Hence the classical theory predicts a line width that is independent of the wavelength. This is in contradiction to the experimental results. The observed natural line widths are several times larger than is to be expected from the classical theory and they are not independent of the wavelength. We also know that they depend on the properties of the energy levels involved in the emission of the lines. Thus, the width of the Mo Kα_1 line is about 0.26 X.U. and that of U Lβ_3 0.76 X.U., though they have almost exactly the same wavelength.

This fact is taken into account in the quantum mechanical treatment of the problem. According to this theory the energy levels must have a certain breadth. As an excited energy level A has a mean lifetime t_A it must have a certain breadth ΔE_A according to Heisenberg's uncertainty principle ($\Delta E \cdot \Delta t \approx h$, where h is the Planck constant).

The mean lifetime of an excited state A of an atom is determined by two factors, viz., the probability per unit of time for a transition to take place from level A to another level C with lower energy and with a simultaneous emission of a photon, and the probability per unit of time for a transition to a lower energy level without emission (Auger effect).

If Γ_A represents the probability for both transitions and t_A is the mean lifetime of the excited state A, we have

$$\Gamma_A = \frac{1}{t_A}. \tag{13}$$

Weisskopf and Wigner [9] have shown by quantum mechanical considerations that the spectral energy distribution of level A is given by

$$I_A(\nu)\,d\nu = \frac{\Gamma_A}{2\pi} \cdot \frac{d\nu}{4\pi^2(\nu_A-\nu)^2+\left(\frac{\Gamma_A}{2}\right)^2}, \tag{14}$$

where E_A is the energy of level A, and

$$\nu_A = \frac{E_A}{h} \tag{15}$$

A spectral line is emitted when a radiative transition takes place from level A to another lower energy level B. The latter level is characterized by the spectral energy distribution $I_B(\nu)$, given by

$$I_B(\nu)\,d\nu = \frac{\Gamma_B}{2\pi} \frac{d\nu}{4\pi^2(\nu_B-\nu)^2+\left(\frac{\Gamma_B}{2}\right)^2}, \tag{16}$$

where Γ_B is the transition probability for level B,

E_B the energy of the state, and $\nu_B = \frac{1}{h} E_B$.

As is easily seen the levels A and B have the widths $\Gamma_A/2$ and $\Gamma_B/2$ at half maximum.

The special distribution of the line emitted in the transition from A to B is then

$$I_{AB}(\nu) = \int_0^\infty I_A(\nu')\,I_B(\nu'-\nu)\,d\nu' \tag{17}$$

which gives after integration

$$I_{AB}(\nu) = \frac{\Gamma_A+\Gamma_B}{2\pi} \frac{1}{4\pi^2(\nu_{AB}-\nu)^2+\left(\frac{\Gamma_A+\Gamma_B}{2}\right)^2}, \tag{18}$$

where $\nu_{AB} = \frac{1}{h}(E_A - E_B)$.

This line has the same shape as was calculated from the classical theory. Its width, however, is equal to the sum of the widths of the initial and the final states (contrary to the predictions from the classical theory). The level width can be obtained quantum mechanically by complicated calculations, but this is of no importance for the present problem.

In the above account we have assumed that the states involved are not influenced by outer disturbances, which is not always the case. In X-ray spectroscopy the influence of Doppler effect and of the collisions between atoms can be neglected contrary to what is the case in optical spectroscopy. On the other hand the influence of the electric field of adjacent atoms on the energy levels often plays an important rôle which cannot be neglected. This influence can cause a displacement in the wavelength and in the shape of the emission line. A displacement due to the influence of chemical combination has been experimentally established for the Kα lines (transition KL_{II} or KL_{III}) up to the element 25 Mn and for the Kβ_1 line (transition $KM_{II,\,III}$) up to 27 Co [10]. Similar displacements have been found in the L series. HAGLUND [11] observed no displacement for the Lα_1 and Lβ_1 lines (transitions $L_{III}\,M_V$ and $L_{II}M_{IV}$) for the elements above 40 Zr but could follow it for the Lβ_2 line (transition $L_{III}N_{IV,\,V}$) up to 46 Pd. Sometimes a simultaneous change in the shape of the lines was observed, so that lines that were asymmetric in the pure elements (metals) because of overlapping of the levels, became symmetric for some oxides. The latter are isolators where there are no unoccupied levels immediately above the filled valency levels.

However, sometimes the lines are asymmetric for reasons not accurately known. This is for instance the case for the elements 20 Ca – 30 Zn, where the Kα lines are asymmetric and where the asymmetry is influenced by the entrance of electrons into the $M_{IV,\,V}$ shell. In the wavelength range below 2000 X.U. the asymmetry is not greater than the shape of the line can be represented by Eq. [18].

As was mentioned earlier, registering the line necessitates the use of a spectrometer with a crystal grating. The shape and width of the line are influenced by the diffraction pattern of the instrument employed. The double crystal spectrometer is the most suitable instrument for this type of investigation because it is capable of registering both the resultant diffraction pattern (the rocking curve) and the contour curve of the line. It has been shown that the calcite and the quartz crystals reflect as perfect crystals within the limits imposed by experimental error and the uncertainty in the values used in the theoretical calculations. For these crystals it has been found that the theoretical and the experimental rocking curves have the same shape as is found for an emission line, so that the rocking curve is represented by

$$I = \frac{I_0}{1 + \frac{4\,(\lambda - \lambda_0)^2}{w_R^2}} \quad \text{or} \quad I = \frac{I_0}{1 + \frac{4\,(\nu - \nu_0)^2}{w_{R_\nu}^2}}, \tag{19}$$

where w_R is the full width of the rocking curve at half maximum intensity in X.U. and w_{R_ν} the corresponding value in frequency units.

If the resultant diffraction pattern for position $(1+1)$ is calculated theoretically, it is found to have the same shape as the rocking curve when the absorption in the crystal is low. When the absorption increases the peak of the curve is asymmetric but the rest of the curve remains nearly unchanged. (See ref. 12, p. 734.) The deviations are so small that the curve can be represented by Equation (19) for wavelengths below about 2000 X.U. for both calcite and quartz gratings.

If the contour curve of a line of the above shape is recorded in a double crystal spectrometer where perfect crystals are used, the reflected intensity $I(l)$ is determined by

$$I(l) = \text{const} \int_{-\infty}^{+\infty} \frac{d\,x}{\left(1 + \frac{4\,x^2}{w_r^2}\right)\left(1 + \frac{4\,(x-l)^2}{w_\lambda^2}\right)}, \tag{20}$$

where w_r is the full width of the rocking curve at half maximum intensity, w_λ the full width of the natural line at half maximum intensity, and l the distance between the peaks of the line and the rocking curve. Equation (20) thus represents the contour curve that is obtained experimentally. The full width w_l of this curve at half maximum is

$$w_l = w_\lambda + w_r\,. \tag{21}$$

Hence the full width of the line registered is equal to the sum of the true line width and the width of the rocking curve. This relation is identical with the relation (2), which was found experimentally.

Institute of Physics, University of Uppsala, Sweden, March 1954.

REFERENCES

1. W. Ehrenburg and H. Mark, Zs. f. Phys. *42*, 807 (1927).
2. G. Brogren, Arkiv f. Fysik *3*, 507 (1951).
3. L. G. Parratt, Rev. Sci. Instr. *6*, 387 (1935).
4. Ö. Adell, G. Brogren and L.-E. Haeggblom, Arkiv f. Fysik *7*, 197 (1953).
5. G. Brogren and Ö. Adell, Arkiv f. Fysik (in print).
6. S. K. Allison, Phys. Rev. *44*, 63 (1933).
7. J. A. Bearden and C. H. Shaw, Phys. Rev. *48*, 18 (1935).
8. J. A. Bearden and H. H. Roseberry, Phys. Rev. *48*, 110 (1935).
9. W. Weisskopf and E. Wigner, Zs. f. Phys. *63*, 54 (1930).
10. V. H. Sanner, Dissertation. Uppsala 1940.
11. Ph. Haglund, Arkiv f. Mat., Astr. o. Fy. *28 A*. No. 18 (1941).
12. K. H. Compton and S. K. Allison, X-ray in Theory and Experiments. Second Edition, 1935. (D. Van Nostrand and Co.)

Tryckt den 29 oktober 1954

Uppsala 1954. Almqvist & Wiksells Boktryckeri AB

ARKIV FÖR FYSIK Band 8 nr 40

Communicated 14 April 1954 by Axel E. Lindh and I. Waller

The anomalous X-ray transmission in calcite

II. Investigations in the wavelength range 558 X.U–1932 X.U.

By Gösta Brogren and Öved Adell

With 23 figures in the text

In an earlier report [1] the authors treated the anomalous X-ray transmission through calcite in the region near the Bragg angle theoretically, and derived expressions for the intensities of the reflected and the transmitted radiation for symmetric Laue reflection (reflections in a crystal where the reflecting atomic planes are perpendicular to the two parallel boundary surfaces of the crystal). The effect of the diffraction pattern of the monochromator crystal was also taken into consideration by a double integration procedure applied to the intensity patterns of the analyser and monochromator crystals. The results attained were checked by experimental determinations of the intensity curves of the reflected and the transmitted radiation in a double crystal spectrometer. The tedious and elaborate graphical and numerical calculations made it necessary to limit the investigation to only one wavelength, 1537 X.U. (the Cu Kα_1 line), with which measurements were carried out for three different arrangements. The investigation has now been extended to five further wavelengths, for which both theoretical and experimental intensity curves have been determined.

Experimental

The investigation was carried out with a double crystal spectrometer in which two types of monochromator crystals could be used, one cut for symmetric Bragg reflection and the other for symmetric Laue reflection. The first-order reflection from the cleavage plane (the 211 plane) of calcite was used. Details of the apparatus, the method, and the notation used were given in the above paper, and only some supplementary details are given here. In the experiments with the Laue monochromator, the transmission was investigated for only one thickness of the analyser crystal, while three different thicknesses of this crystal were used in combination with the Bragg monochromator. In the latter case the monochromator crystal could be considered thick for all the wavelengths used. The thickness of the transmission crystal was determined before it was inserted in the spectrometer. It was then checked by calculating the thickness from the ratio between the intensities of the transmitted and incident radiation under normal transmission conditions. As the crystals were etched before use, the thickness varied somewhat over the surface. This caused an uncertainty in the value of the thickness where the normal transmission was slight; when it was large enough to allow a determination directly from the registered transmission curves, this kind of error was eliminated.

The intensities of the transmitted and reflected beams were measured simultaneously with two Geiger-Müller counters. 3–5 successive runs were made. The intensity of the beam incident upon the analyser crystal was determined before and after each registration of the transmitted and reflected intensities with both counters. Great care was taken that the radiation was incident on the same parts of the counters as when they were in their normal positions. When necessary, the direct intensity was reduced by means of absorption foils, whose absorption had been carefully determined. The relative sensitivity of the counters was checked for each wavelength.

Table 1.

The atomic scattering factors for the atoms in the $CaCO_3$ molecule and the crystal structure factor for plane 211 in calcite. The scattering factors are given by the relation $f_x = f_x^0 + f_x' + i f_x''$. f_x^0 is the normal scattering factor, calculated by JAMES and BRINDLEY [7], f_x' and f_x'' are the anomalous contributions due to the K electrons, which can be calculated from the formulas developed by HÖNL [8–9]. The crystal structure factor is given by the relation $F_{211} = 2\,(f_{Ca} + f_C + f_O)$. For the wavelength range investigated f_O', f_C' and f_C'' are so small that they can be neglected.

Emission line	Wavelength X.U.	Ca			O		f_C^0	F_{211}	$\varkappa$
		f_{Ca}^0	f_{Ca}'	f_{Ca}''	f_O^0	f_O''			
Fe K α_1. .	1932	15.3	0.09	1.805	6.0	0.049	3.4	$49.5 + i \cdot 3.69$	0.0745
Co K α_1. .	1785	15.3	0.15	1.571	6.0	0.045	3.4	$49.7 + i \cdot 3.23$	0.065
Cu K α_1. .	1537	15.3	0.28	1.21	6.0	0.039	3.4	$49.9 + i \cdot 2.50$	0.050
Au L α_1. .	1274	15.3	0.32	0.85	6.0	0.032	3.4	$50.0 + i \cdot 1.76$	0.0352
Au L β_1. .	1081	15.3	0.31	0.63	6.0	0.028	3.4	$50.0 + i \cdot 1.32$	0.0264
Mo K α_1. .	708	15.3	0.21	0.29	6.0	0.018	3.4	$49.8 + i \cdot 0.62$	0.0124
Ag K α_1. .	558	15.3	0.16	0.18	6.0	0.014	3.4	$49.7 + i \cdot 0.40$	0.0080

The values of the parameters used in the calculations. The param

Line	Wavelength X.U.	Bragg angle ϑ_B	$\cos 2\vartheta_B$	μ_0 cm^{-1}	$\psi_0' \cdot 10^6$	$\psi_0'' \cdot 10^6$	$\psi_H' \cdot 10^6$	y_n	
								radians $\cdot 10^5$	sec a
Fe K α_1 . .	1932	18°35.8′	0.7966	370	−27.55	−1.14	−13.60	2.25	4.
Co K α_1 . .	1785	17° 8.2′	0.8264	295	−23.52	−0.840	−11.70	2.08	4.
Cu K α_1 . .	1537	14°42.1′	0.8712	193	−17.44	−0.473	− 8.65	1.75	3.
Au L α_1 . .	1274	12° 8.4′	0.9115	120	−11.98	−0.244	− 6.00	1.46	3.
Au L β_1 . .	1081	10°16.2′	0.9365	76	− 8.56	−0.130	− 4.28	1.22	2.
Mo K α_1 . .	708	6°42.6′	0.9728	23.4	− 3.70	−0.0264	− 1.95	0.80	1.
Ag K α_1 . .	558	5°17.1′	0.9830	12.1	− 2.30	−0.0107	− 1.15	0.63	1.

First the Bragg-Laue arrangement was used, with successive transmission crystals of thicknesses 0.47 mm, 0.91 mm, and 0.34 mm; finally both crystals were in the Laue position. The monochromator was checked before and after the first two series of measurements. A Bragg analyser was then inserted, and the rocking curves of the Mo Kα_1 and Cu Kα_1 radiation registered. The full widths at half maximum intensities were found to be 5.2″ and 10.2″, in good agreement with the theoretical values for a perfect calcite crystal (4.6″ and 9.8″).

Calculations

The diffraction pattern of the radiation from the Bragg monochromator is obtained from eq. (30) and the intensity curves for the reflected and transmitted intensities in the Laue case from eqs. (26) and (27) in the previous paper. The values of the constants that are necessary for the calculations are given in Tables 1–2. The notation is as given in the above publication.

Results

In earlier comparative work [2–3], a direct comparison was made between experimental curves and those calculated for the symmetrical Laue case on the assumption that the incident radiation was parallel and monochromatic. In Fig. 1 we give the shapes of the reflection and transmission curves for the normally polarized component of Au Lβ_1 radiation. Calculations have been carried out for thicknesses 2.0 mm, 0.91 mm, 0.47 mm, 0.34 mm, and 0.00 mm. The three intermediate ones are those experimentally investigated. The theory indicates that the shapes depend on $(\varkappa A)$ rather than on the thickness, and the Au Lβ_1 wavelength was chosen only in order to study the effect of a variation in $(\varkappa A)$.

In Fig. 1 the normal transmission is indicated by the dotted line. The two thickest crystals absorb practically all incident radiation for angles off the Bragg angle, and only a maximum appears in the transmission curve. For the 2 mm crystal the maximum intensity is nearly the same for the reflection and trans-

defined by relations given in the earlier publication [1].

y_p		g_n	g_p	$t_0 = 0.034$ cm		$t_0 = 0.047$ cm		$t_0 = 0.091$ cm	
dians 10^5	sec. of arc			$(\varkappa A)_n$	$(\varkappa A)_p$	$(\varkappa A)_n$	$(\varkappa A)_p$	$(\varkappa A)_n$	$(\varkappa A)_p$
.79	3.70	−0.0839	−0.105	5.95	4.76	8.25	6.60	16.0	12.80
.72	3.55	−0.0717	−0.0866	4.63	3.95	6.60	5.46	12.80	10.60
.52	3.15	−0.0548	−0.0628	3.10	2.70	4.30	3.74	8.35	7.26
.33	2.75	−0.0407	−0.0447	1.80	1.64	2.50	2.28	4.85	4.42
.14	2.35	−0.0306	−0.0327	1.12	1.05	1.55	1.45	3.01	2.82
.78	1.60	−0.0143	−0.0147	0.337	0.327	0.466	0.454	0.905	0.880
.62	1.27	−0.00932	−0.0095	0.177	0.174	0.245	0.241	0.475	0.468

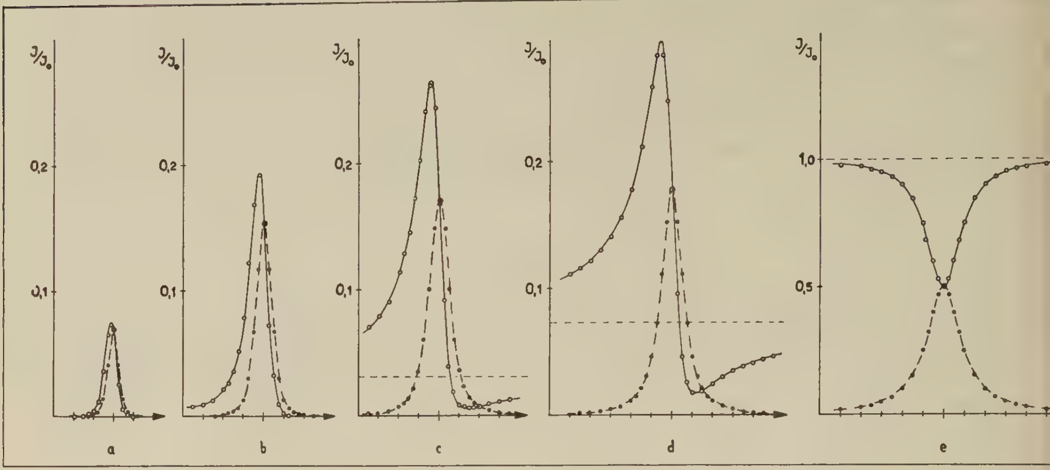

Fig. 1. The theoretical values of the transmitted and reflected intensities of Au $L\,\beta_1$ through calcite crystals, cut with the reflection planes (the 211 plane) perpendicular to the surface. The incident beam is assumed to be parallel and normally polarized. The thicknesses of the crystals are: *a*, 2.0 mm; *b*, 0.91 mm; *c*, 0.47 mm; *d*, 0.34 mm; and *e*, 0.0 mm. The solid curve gives the transmitted intensities, the dotted one the reflected. The normal transmission is indicated by dotted lines, parallel to the angular axis.

mission curves, but the latter has a greater width at half maximum intensity and is asymmetric. When the thickness decreases, the widths and heights of both curves increase. For the 0.47 mm and 0.34 mm crystals a minimum has appeared in the transmission curve. As the crystal thickness decreases the minimum becomes more and more pronounced while the maximum is weakend. For very thin crystals, where $(\varkappa A) = 0$, the maximum has completely disappeared, so that there is only a minimum in the transmission curve.

The reflection and transmission curves cut each other at the peak of the reflection curve (for $\vartheta = \vartheta_B$), and the intensity of the transmitted beam is consequently less than that of the reflected in a small region where $\vartheta > \vartheta_B$. When the crystal is thick the two maxima nearly coincide. For decreasing thickness the angular distance between them increases. If the thickness is very small, $(\varkappa A \approx 0)$, the angular position of the transmission minimum and the reflection maximum coincide, the two integrals $\int R\,d\,\vartheta$ and $\int (T - T_0)\,d\,\vartheta$ are equal and there is a pure extinction effect in the transmitted intensity.

The full widths of the reflection curves at half maximum intensity are, in the order of decreasing crystal thickness, 1.5″, 2.0″, 3.1″, 3.4″, and 5.0″. The corresponding value of the diffraction pattern of the Bragg monochromator is 5.4″. In the derivation of the equations for the reflection and transmission curves we made the assumption that the incident beam was monochromatic and parallel. The above values show that it is not possible to fulfil the latter condition experimentally since the angular divergence of the monochromatized beam is larger than the width of the pattern to be investigated. The resultant pattern can only be obtained by combined integration of the diffraction pattern of the monochromator with the reflection and transmission curves of the Laue crystal.

Since the Bragg diffraction pattern of an absorbing crystal is asymmetric and its width exceeds the corresponding value for the analyser crystal, the resultant curves will deviate very much from those in Fig. 1. (This is easily seen by comparing Fig. 1 with Figs. 3, 8 and 13.) The peak intensities will be depressed and the widths increased. For a thin crystal, for instance, where normally a relatively large part of the incident radiation passes through the crystal, the whole of the resultant reflection curve lies below the transmission curve, and they do not intersect. This makes it impossible to draw conclusions from a comparison between experimental curves and theoretical curves like those in Fig. 1.

If the monochromator crystal is cut for Laue reflection, the experimental conditions are improved. The reflection curve is then symmetric and has a smaller width at half maximum intensity than the corresponding curve in the Bragg case. There will be less change in the shapes of the transmission intensity curves. There is, however, one great disadvantage; the intensity of the beam from the monochromator is less, particularly when the absorption coefficient is great. This restricts the use of the Laue monochromator.

The transmission measurements were carried out on three different calcite specimens with various thicknesses, and not on a single crystal whose thickness was successively reduced by etching. This procedure permitted us to perform supplementary determinations where necessary. For this reason the results from all measurements with one crystal combination are listed together, which makes it easier to trace the effect of any crystal deficiencies that may occur.

Results from the investigations with a Bragg monochromator

The transmission through 0.91 mm calcite

The measurements on the transmission through the thickest calcite crystal were carried out with three emission lines, viz. Au Lα_1, Au Lβ_1, and Mo Kα_1. Figs. 2–4 give the calculated and the experimental intensity curves, and Table 3 some characteristic data.

The investigations with Au Lα_1 radiation show that there is a qualitative agreement between the shapes of the theoretical and experimental curves. The distance Δ between the maxima of the transmission and reflection curves is 0.0″ and 0.4″, the full width of the reflection curve at half maximum intensity 6.6″ and 6.7″, and that of the transmission curve 6.7″ and 6.4″. (Here and in the following the experimental value is given first.) The intensity of the reflection curve is in both cases greater than that of the transmission curve in the same angular region. However, the experimental intensities are less than the theoretical. This is particularly so for the transmission curve, which is much closer to the reflection curve in the experimental case, making the experimental ratio between the maximum intensities of the reflected and transmitted radiation 0.91, as against 0.82 for the calculated curves.

The shapes of the experimental curves differ a good deal from those of the calculated ones. The values obtained for the integrated reflection and the integrated transmission are considerably less than the theoretical ones. The inte-

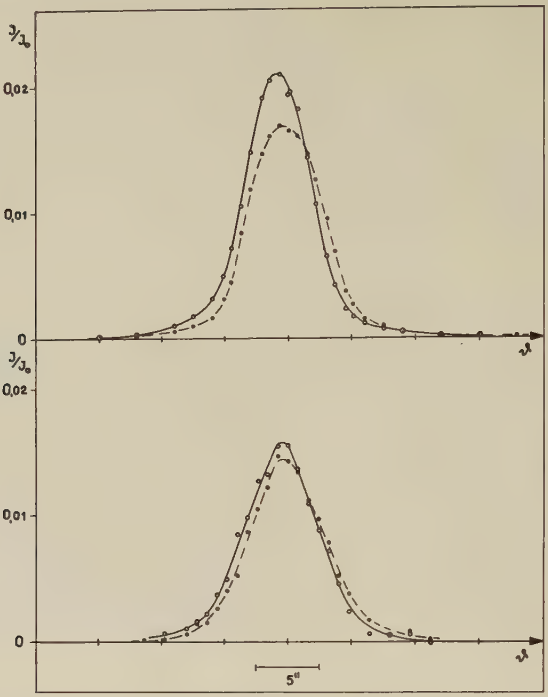

Fig. 2. Transmitted and reflected intensities for Au Lα_1 through a 0.91 mm calcite crystal. Monochromator in Bragg position. The intensity I_0 incident upon the analyser crystal was 69,000 counts/min.

In Figs. 2–19 the following designations are used:

———————— is the transmitted intensity, - - - - - - - - - - - is the reflected intensity.

The normal transmission is indicated by means of a thin, dotted line parallel to the angular axis. The theoretical curves are given above or to the left in the figures.

grated reflection is defined by the integral $\int_{-\infty}^{+\infty} R\,d\vartheta$ and the integrated transmission by $\int_{-\infty}^{+\infty} (T-T_0)\,d\vartheta$, where T_0 is the normal transmission off the Bragg angle.

On the whole, the results from the determinations with Au Lβ_1 radiation verify the above observations. The widths of the experimental curves are considerably greater than those of the calculated curves, for instance, the width of the experimental reflection curve is 7.7″, whereas that of the calculated is only 5.6″. The experimental intensities are less than the calculated, as is also the case for the integrated reflection and the integrated transmission. The intensity of the transmission curve is relatively less in the experimental case, where the ratio $R_{\max}/T_{\max}$ has the value 0.78, against 0.66 calculated.

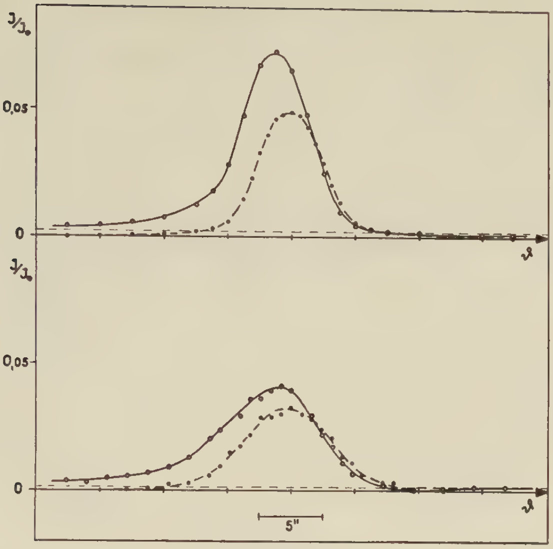

Fig. 3. Transmitted and reflected intensities for Au Lβ_1 through a 0.91 mm thick calcite crystal. Monochromator in Bragg position. $I_0 = 30{,}000$ counts/min.

Table 3.

Results from the measurements of the anomalous transmission through the 0.91 mm calcite crystal. Monochromator in the Bragg position. w_R is the full width of the reflection curve at half maximum intensity; w_T the full width of the transmission curve at half maximum intensity; $R_{\max}$ is the peak intensity of the reflection curve and $T_{\max}$ the maximum intensity of the transmission curve, both measured in per cent of the radiation incident upon the transmission crystal. $\int R\,d\vartheta$ is the area under the reflection curve, which is here called the integrated reflection, and $\int (T-T_0)\,d\vartheta$ the area between the transmission curve and the line that indicates the normally transmitted intensity. $\int (T-T_0)\,d\vartheta$ is here called the integrated transmission. Δ is the angular distance from the peak of the reflection curve to the peak of the transmission curve and Δ' the angular distance from the peak of the reflection curve to the minimum of the transmission curve. The integrated reflection and the integrated transmissicn are measured in radians, the other angular quantities in seconds of arc. The above notation is also used in Tables 4–7.

e	Wave-length X.U.	w''_R		w''_T		$R_{\max} \cdot 10^2$		$T_{\max} \cdot 10^2$		R_m/T_m		$10^6 \int R\,d\vartheta$ radians		$10^6 \int [T-T_0]\,d\vartheta$ radians		Δ sec. of arc		Δ' sec. of arc	
		t	exp	t	exp	t	exp	t	exp	t	exp	t	exp	t	exp	t	exp	t	exp
α_1	708	5.0	6.0	—	—	10.1	9.5	25.1	20.4	0.40	0.47	3.16	4.41	2.52	0.81	2.8	3.0	3.0	3.4
β_1	1081	5.6	7.7	6.2	8.4	4.90	3.30	7.41	4.20	0.66	0.78	1.62	1.41	2.71	1.94	1.2	0.8	—	—
α_1	1274	6.7	6.6	6.4	6.7	1.70	1.44	2.09	1.58	0.82	0.91	0.65	0.52	0.73	0.55	0.4	0.0	—	—

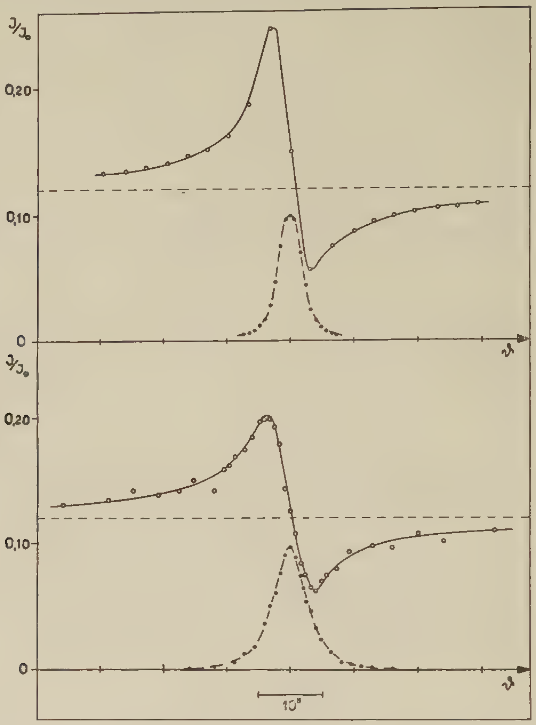

Fig. 4. Transmitted and reflected intensities for Mo Kα_1 through a 0.91 mm thick calcite crystal. Monochromator in Bragg position. $I_0 = 11{,}600$ counts/min.

The measurements with Mo Kα_1 radiation also gave curves with lower maximum intensities and greater widths than the calculated curves. (See Fig. 4.) The difference in intensity appears very distinctly from the peak in the transmission curve where the experimental value is 0.20 against 0.25 in the calculated curve. Consequently the experimental value of the integrated transmission is much less than the theoretical ($0.8 \cdot 10^{-6}$ radians against $2.5 \cdot 10^{-6}$ radians). The width of the experimental reflection curve exceeds that of the calculated (6.0″ against 5.0″), which compensates for the lower intensity so that the integrated reflection is about the same in both cases. Apart from these details, the agreement is good. Thus the distance from the peak of the reflection curve to that of the transmission curve is 3.0″, against the value 2.8″ obtained from the calculations, and the distance to the minimum in the latter curve is 3.4″, against 3.0″.

The most reliable among the above measurements are those carried out with Mo Kα_1 radiation, where the thickness could be determined directly from the recorded curves, so that it was accurately known. The Bragg monochromator had been used in a previous investigation of the properties of calcite 211 in the double crystal spectrometer [4]. With both crystals in the Bragg position the full width of the rocking curve at half maximum intensity was found to be 5.2″ for Mo Kα_1 (theoretical value 4.6″), and the integrated reflection (= the double crystal coefficient of reflection) $2.3 \cdot 10^{-5}$ radians (theoretical value $2.0 \cdot 10^{-5}$ rad.). The glancing angle is 6° 42′. At this small glancing angle a length of about 15 mm of each crystal was irradiated. There is a great probability that such a surface contains several crystallites, which should increase the width of the rocking curve as well as the integrated reflection. This is taken to be the reason for the deviation from the calculations. Such defects of the monochromator must also smooth the curves obtained with the Bragg-Laue arrangement, increasing the widths and decreasing the maximum intensities. However, the deviations from the calculations are greater than can be explained by imperfections in the monochromator crystal. The main reason seems to be defects in the analyser crystal. This is verified by the results obtained with the Au lines. A crystal in the Bragg position appears to improve with increasing wavelength, because the increased absorption coefficient decreases the penetration depth and because the irradiated area of the crystal surface decreases. For a Laue crystal a slight imperfection will have a considerable effect on the anomalous transmission, and this effect may increase with the wavelength. This seems to be the case for the above crystal specimen.

Transmission through the 0.47 mm crystal

The measurements with the crystal of medium thickness (0.47 mm) were carried out with five emission lines, viz., Co Kα_1, Cu Kα_1, Au Lα_1, Au Lβ_1, and Mo Kα_1. The results are given in Table 4 and Figs. 5–9. With the first two lines the absorption in the crystal was so great that the thickness could not be determined directly from the recordings. This may introduce some uncertainty into the determination of the thickness, which in its turn causes an uncertainty in the calculated intensities. However, the shapes of the calculated curves are very little influenced by a slight variation of the thickness.

The measurements with the copper line have been published previously. They gave a very good qualitative agreement between theory and experiment but inferior quantitative agreement, as both the experimental intensities and the experimental values of the integrated transmission and reflection were lower than the corresponding theoretical quantities. The difference was about ten per cent, which is wholly explained by the above uncertainty in the thickness.

Table 4.

Results from the measurements of the anomalous transmission through the 0.47 mm thick calcite crystal. Monochromator in Bragg position. Notation as in Table 3.

ne	Wave-length X.U.	w''_R		w''_T		$R_{\max} \cdot 10^2$		$T_{\max} \cdot 10^2$		R_m/T_m		$10^6 \int R\, d\vartheta$ radians		$10^6 \int [T - T_0]\, d\vartheta$ radians		Δ sec. of arc		Δ' sec. of arc	
		t	exp	t	exp	t	exp	t	exp	t	exp	t	exp	t	exp	t	exp	t	exp
K α_1	708	5.0	5.8	—	—	15.3	16.8	45.2	40.2	0.34	0.42	5.39	5.98	−0.85	−1.30	2.7	4.0	2.4	2.4
L β_1	1081	6.4	6.5	6.8	8.2	7.50	6.90	14.8	13.1	0.51	0.47	2.80	2.76	4.52	5.22	2.0	1.8	7.2	7.2
L α_1	1274	6.8	6.6	7.2	8.0	3.87	3.90	6.28	6.35	0.62	0.62	1.55	1.45	2.90	3.00	1.8	1.6	14.4	16.0
K α_1	1537	8.0	8.2	8.3	8.4	2.35	2.03	3.21	2.68	0.74	0.76	1.09	0.94	1.48	1.33	1.6	1.4	—	—
K α_1	1785	8.6	9.0	9.0	9.2	1.07	0.93	1.28	1.07	0.84	0.87	0.56	0.47	0.67	0.54	0.8	0.8	—	—

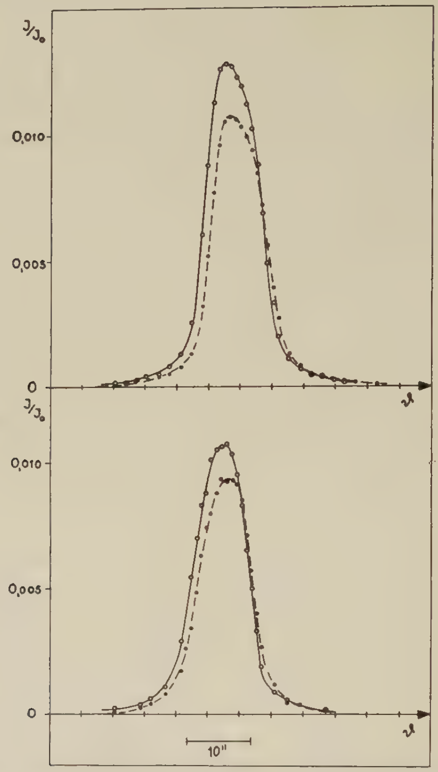

Fig. 5. Transmitted and reflected intensities for Co Kα_1 through a 0.47 mm thick calcite crystal. Monochromator in Bragg position. $I_0 = 300{,}000$ counts/min.

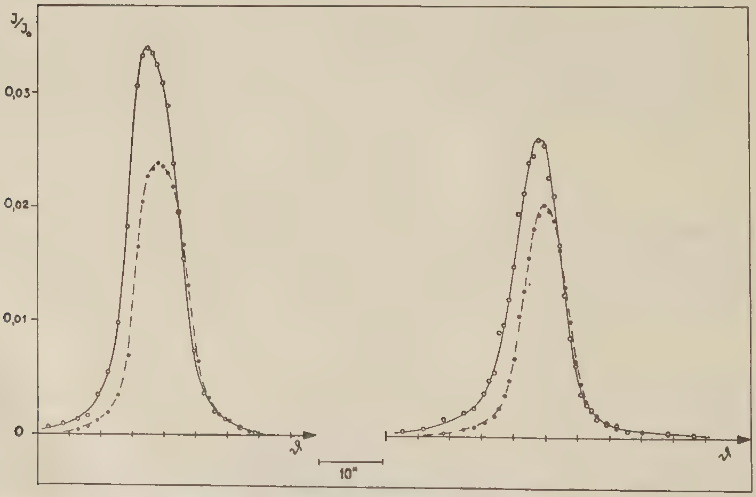

Fig. 6. Transmitted and reflected intensities for Cu Kα_1 through a 0.47 mm thick calcite crystal. Monochromator in Bragg position. $I_0 = 280{,}000$ counts/min.

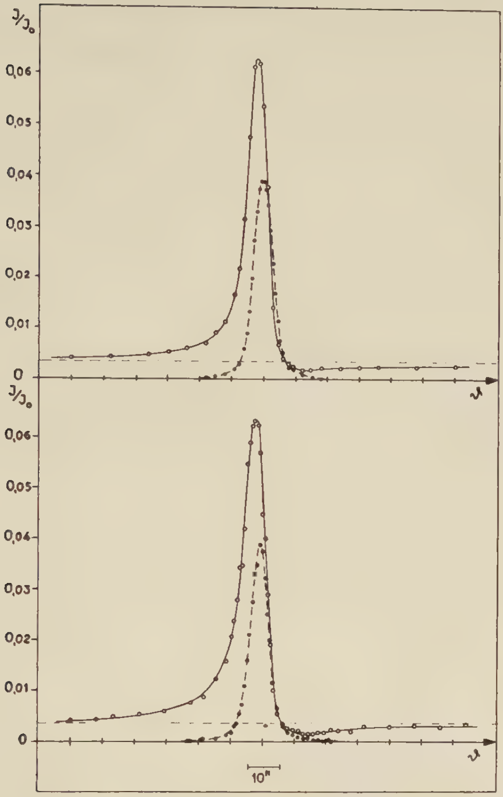

Fig. 7. Transmitted and reflected intensities for Au Lα_1 through a 0.47 mm thick calcite crystal. Monochromator in Bragg position. $I_0 = 148,000$ counts/min.

The results obtained with the Co Kα_1 radiation verify these observations. The general shapes of the curves agree, the characteristic qualitative data—the widths of the reflection and transmission curves, the distance between their maxima, and the ratio of their maximum intensities—are identical within the experimental limits of error. The experimental values of the intensities and of the integrated reflection and transmission are less than the calculated ones in this case as well, but again the difference is not greater than can be explained by the uncertainty in the thickness. The asymmetric flattening of the reflection curve due to the Bragg monochromator also appears, but owing to the lower intensity it is not so clearly observable as with copper radiation.

The results obtained with the two Au lines and with the Mo Kα line can be discussed together. The general agreement between experimental and theoretical curves is very good. In the measurements with the Au Lα_1 line it must be considered excellent, as all figures given in Table 4 except one are identical within the experimental limits of error. The exception is the width of the transmission curve, where the experimental value is about ten per cent larger. With Au Lβ_1 radiation the experimental widths of both curves are larger than the

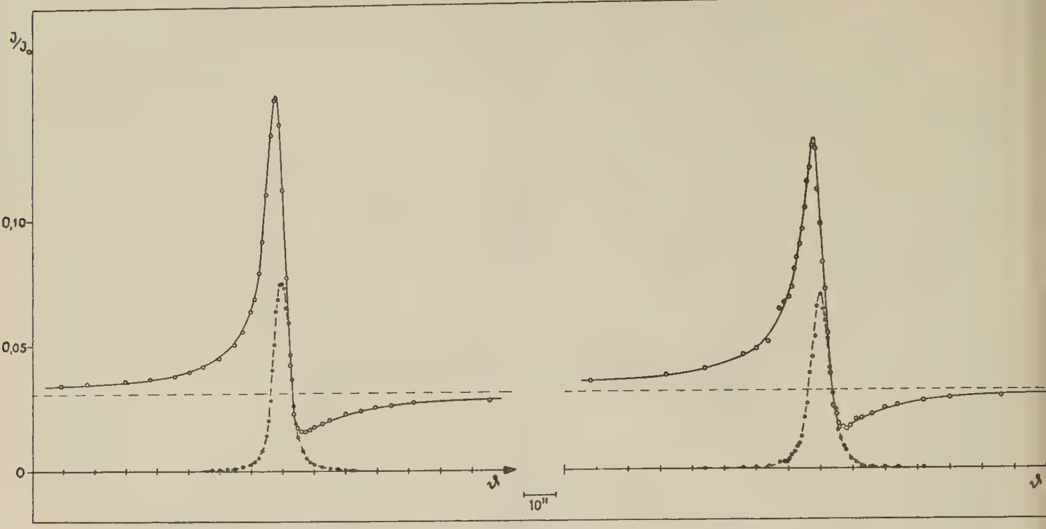

Fig. 8. Transmitted and reflected intensities for Au Lβ_1 through a 0.47 mm thick calcite crystal. Monochromator in Bragg position. $I_0 = 80{,}000$ counts/min.

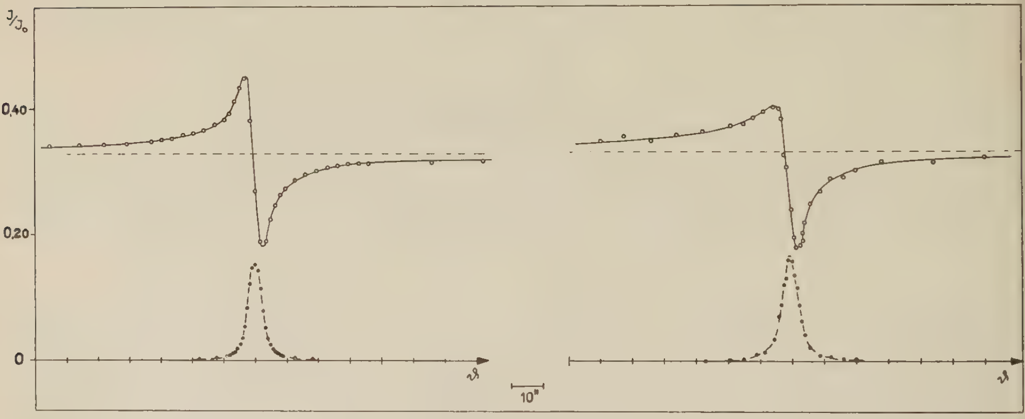

Fig. 9. Transmitted and reflected intensities for Mo Kα_1 through a 0.47 mm thick calcite crystal. Monochromator in Bragg position. $I_0 = 11{,}300$ counts/min.

calculated ones, but here the broadening is accompanied by a decrease of the maximum intensities of the curves. These effects compensate each other in the reflection curve, so that the two values of the integrated reflection are nearly the same. The experimental value of the integrated transmission exceeds the calculated by 15 percent. The depression of the transmission maximum is still more pronounced in the registrations with molybdenum radiation, where the form of the maximum deviates very much from the predictions. The minimum of the transmission curve as well as the whole reflection curve have the predicted shapes, however. In this case also the width of the experimental reflection curve is somewhat larger than that of the calculated.

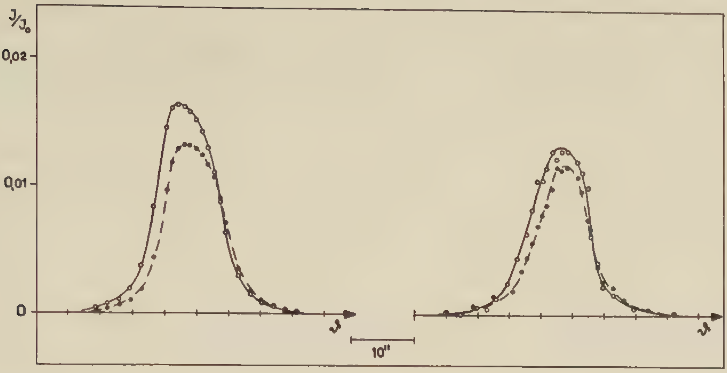

Fig. 10. Transmitted and reflected intensities for Fe Kα_1 through a 0.34 mm thick calcite crystal. Monochromator in Bragg position. $I_0 = 27{,}500$ counts/min.

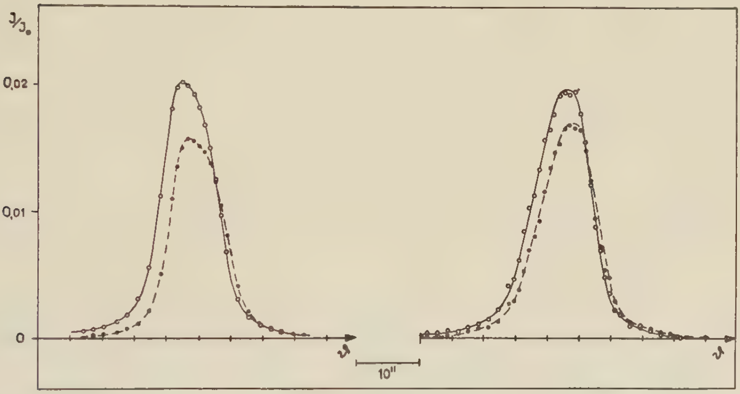

Fig. 11. Transmitted and reflected intensities for Co Kα_1 through a 0.34 mm thick calcite crystal. Monochromator in Bragg position. $I_0 = 96{,}000$ counts/min.

Transmission through 0.34 mm calcite

The transmission through the thinnest crystal (0.34 mm thick) was investigated with the Kα_1 lines of Fe, Co, and Cu, and with the Au Lβ_1 line. The qualitative agreement is very good for all measurements, as can be seen in Figs. 10–13 and Table 5. With the first three lines, where the normal transmission is too low for a determination of the thickness to be possible, the widths of the experimental curves are identical with the calculated values within the experimental limits of error. For Fe Kα_1 and Co Kα_1 radiation the intensity of the transmission curve is somewhat too low in comparison with that of the reflection curve. The uncertainty in the thickness appears from the fact that the experimental intensity is less than the calculated with Fe and Cu radiation, but greater than the calculated with Co radiation. With these three emission lines the asymmetrical flattening of the peak of the reflection curve due to the asymmetrical Bragg diffraction pattern appears distinctly. The general shapes

Table 5.

Results from the measurements of the amonalous transmission through a 0.34 mm thick calcite crystal. Monochromator in Bragg position. Notation as in Table 3.

Line	Wave-length X.U.	w''_R		w''_T		$R_{\max} \cdot 10^2$		$T_{\max} \cdot 10^2$		R_m/T_m		$10^6 \int R\,d\vartheta$ radians		$10^6 \int [T - T_0]\,d\vartheta$ radians		Δ sec. of arc		sec
		t	exp	*t*	exp	*t*	exp	*t*	exp	*t*	exp	*t*	exp	*t*	exp	*t*	exp	*t*
Au L β_1	1081	6.8	7.6	8.1	8.5	8.49	8.6	19.4	17.8	0.44	0.48	3.26	3.86	3.86	3.11	2.4	2.8	6.0
Cu K α_1	1537	8.8	9.0	9.0	9.0	3.8	2.24	5.69	4.34	0.67	0.68	1.85	1.39	2.94	2.43	1.4	1.6	—
Co K α_1	1785	9.6	9.8	9.9	10.2	1.58	1.66	2.02	1.96	0.79	0.84	0.84	0.90	1.18	1.09	1.2	1.2	—
Fe K α_1	1932	10.1	9.8	10.5	10.1	1.33	1.18	1.62	1.32	0.82	0.89	0.77	0.61	0.93	0.72	0.9	0.6	—

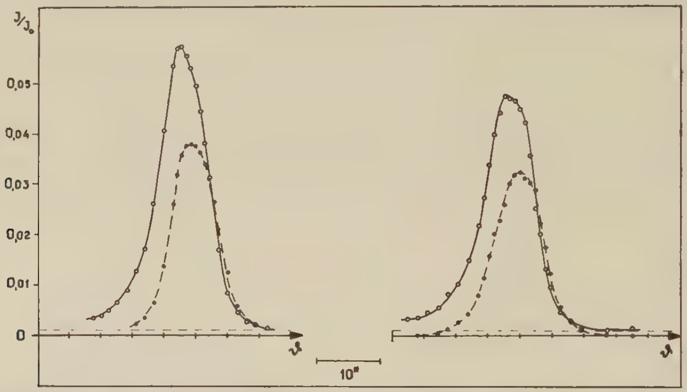

Fig. 12. Transmitted and reflected intensities for Cu Kα_1 through a 0.34 mm thick calcite crystal. Monochromator in Bragg position. $I_0 = 80{,}000$ counts/min.

of the curves and their relative positions agree very well with what has been calculated. The good agreement between theory and experiment appears most clearly by studying the correspondence within the regions where the reflection and transmission curves cut or nearly cut each other.

A slight difference between experimental results and calculations is found in the recordings with Au Lβ_1, where the peak of the transmission curve is lower than expected and the experimental widths of both curves are larger than the calculated ones. The broadening is not greater than can be ascribed to the broadening in the Bragg diffraction pattern, which was discussed earlier.

Results from the investigations with the monochromator in the Laue position

The above measurements were all carried out with the monochromator in the Bragg position. From earlier investigations with two crystals in the Bragg position it is known that the experimental rocking curves are broader than the calculated ones, and that this broadening increases with decreasing wavelength.

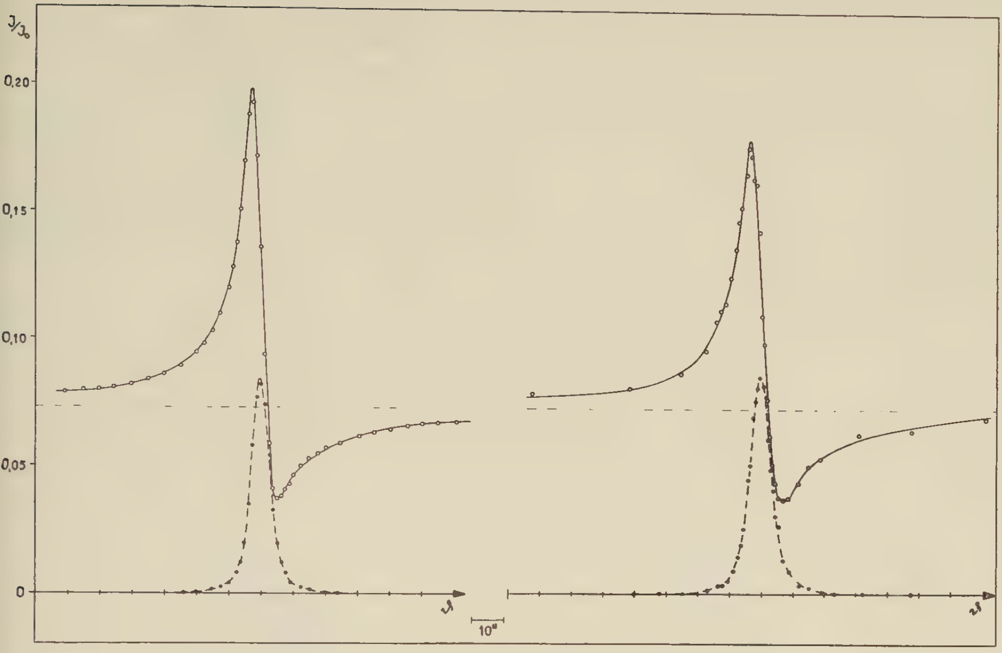

Fig. 13. Transmitted and reflected intensities for Au Lβ_1 through a 0.34 mm thick calcite crystal. Monochromator in Bragg position. $I_0 = 23{,}300$ counts/min.

Such a difference also appears in the reflection curves obtained with the Bragg-Laue arrangement, as well as the wavelength dependence. In order to get further information about this broadening and in order to utilize the lower angular divergence of a beam reflected from a Laue monochromator, a series of measurements was carried out with two crystals cut for symmetric Laue reflection. All details about methods of adjustment etc. were given in the previous

Table 6.

Results from the measurements of the anomalous transmission through a 0.34 mm thick calcite crystal. Monochromator in Laue position with the same crystal thicknes as the analyser. Notation as in Table 3.

ne	Wave length X.U.	w''_R		w''_T		$R_{\max} \cdot 10^2$		$T_{\max} \cdot 10^2$		R_m/T_m		$10^6 \int R\,d\vartheta$ radians		$10^6 \int [T - T_0]\,d\vartheta$ radians		Δ sec. of arc		Δ' sec. of arc	
		t	exp	t	exp	t	exp	t	exp	t	exp	t	exp	t	exp	t	exp	t	exp
K α_1	558	5.4	7.2	—	—	18.4	15.6	68.4	68.4	0.27	0.13	6.7	6.7	−6.0	−6.6	9.6	11.2	0.4	0.4
K α_1	708	5.9	7.0	—	—	13.8	13.5	34.2	32.2	0.41	0.42	6.17	6.37	−4.28	−5.84	4.8	6.8	2.8	3.0
L β_1	1081	5.6	6.3	6.8	7.9	9.0	9.1	20.0	20.1	0.45	0.45	3.49	3.38	4.57	4.11	2.4	2.4	5.8	6.4
L α_1	1274	5.5	5.9	7.6	7.6	7.80	7.91	13.1	12.5	0.60	0.63	2.48	2.60	4.43	4.69	1.6	2.0	16	18.5
K α_1	1537	5.3	5.5	15.6	5.9	7.31	6.72	10.1	9.0	0.73	0.75	2.09	2.01	3.30	2.93	1.3	1.5	—	—
K α_1	1785	5.2	5.2	5.2	5.2	4.3	5.5	5.3	6.5	0.81	0.85	1.12	1.48	1.46	1.70	0.8	0.5	—	—

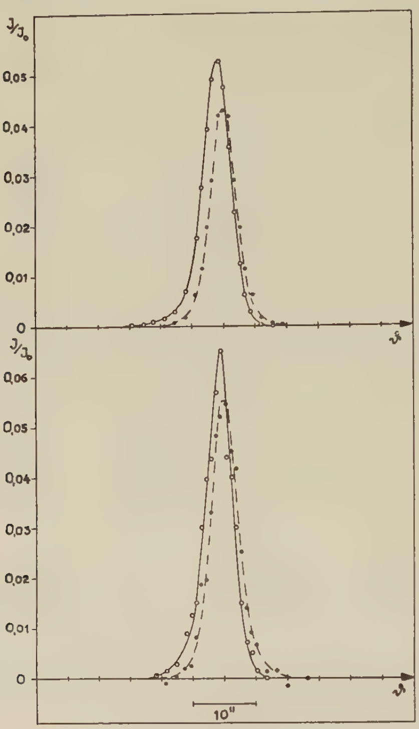

Fig. 14. Transmitted and reflected intensities for Co K α_1 through calcite. Monochromator in Laue position. Both crystals 0.34 mm thick. $I_0 = 5{,}850$ counts/min.

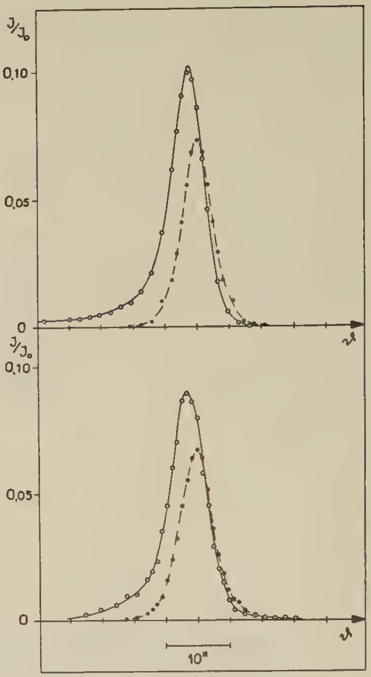

Fig. 15. Transmitted and reflected intensities for Cu K α_1 through calcite. Monochromator in Laue position. Both crystals 0.34 mm thick. $I_0 = 31{,}000$ counts/min.

report [1]. The crystals were obtained by etching two crystal plates one mm thick until they were reduced to the desired thickness. This procedure does not give smooth surfaces, so the thickness is variable over the surface. When the adjustment is changed from one emission line to another, it is not certain that the reflections will take in exactly the same parts of the crystals as before. In consequence, some uncertainty must be ascribed to the thickness value used in the calculations. As to the analyser crystal, the normal transmission could sometimes be used during the adjustments, so that the desired thickness was obtained, but this method could not be used for the monochromator crystal. This uncertainty influences the intensity, but the shapes and widths of the curves remain almost unchanged. For this reason no great significance should be attached to an intensity difference between experimental and calculated curves, if it is not too great.

The investigations were carried out with the following emission lines: Co K α_1, Cu K α_1, Au L α_1, Au L β_1, Mo K α_1, and Ag K α_1. The results are given in Table 6 and Figs. 14–19. With the first two lines the absorption in the analyser was too great to permit a checking of the thickness directly from the transmission curves, so that the difference between calculated and obtained intensities may be much greater than in the other recordings.

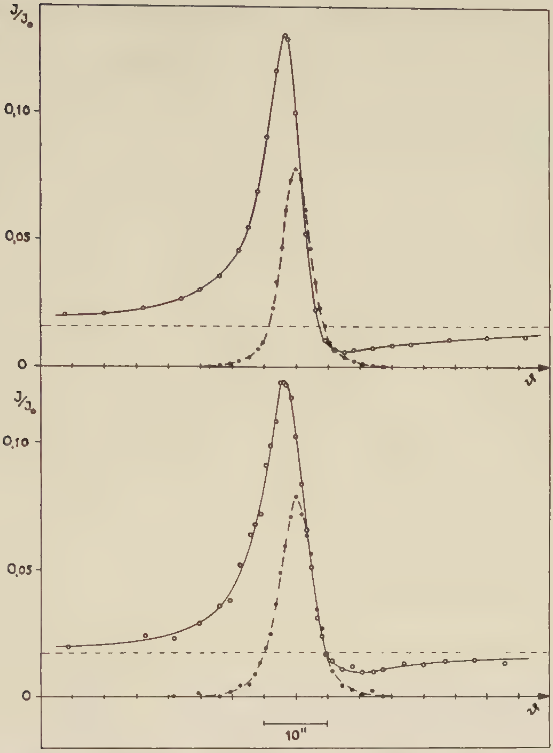

Fig. 16. Transmitted and reflected intensities for Au Lα_1 through calcite. Monochromator in Laue position. Both crystals 0.34 mm thick. $I_0 = 19{,}000$ imp./min.

The registrations with the Co Kα_1 radiation gave a higher intensity than was calculated. The qualitative agreement is very good. The full width at half maximum intensity is 5.2″ for all curves. The distance Δ between the maxima of the curves is 0.5″ as against the calculated 0.8″, and the ratio between the maximum intensities ($R_{\max}/T_{\max}$) 0.85 as against 0.81. The advantages of the Laue monochromator are easily seen if Fig. 14 is compared with Fig. 11. In the latter the same transmission crystal is investigated with the same radiation, but a Bragg monochromator is used. In the latter case the width of the reflection curve is 9.8″ and the width of the transmission curve 10.2″, i.e. they have nearly twice the value obtained with a Laue monochromator. The maximum intensities are about five times less with the Bragg monochromator. As the Laue diffraction pattern is much narrower and symmetric, the resultant curves are less broadened and more like the curves in Fig. 1. In the present figure, the transmission curve intersects the reflection curve near its maximum (on the long wave side of it) and then runs inside it, distinctly separated from it. The shapes of the experimental and calculated curves are practically identical, except that the experimental intensities, as well as the integrated reflection and the integrated transmission, are somewhat higher than expected. The reflection curve is symmetric, but the transmission curve asymmetric in the way the theory predicts.

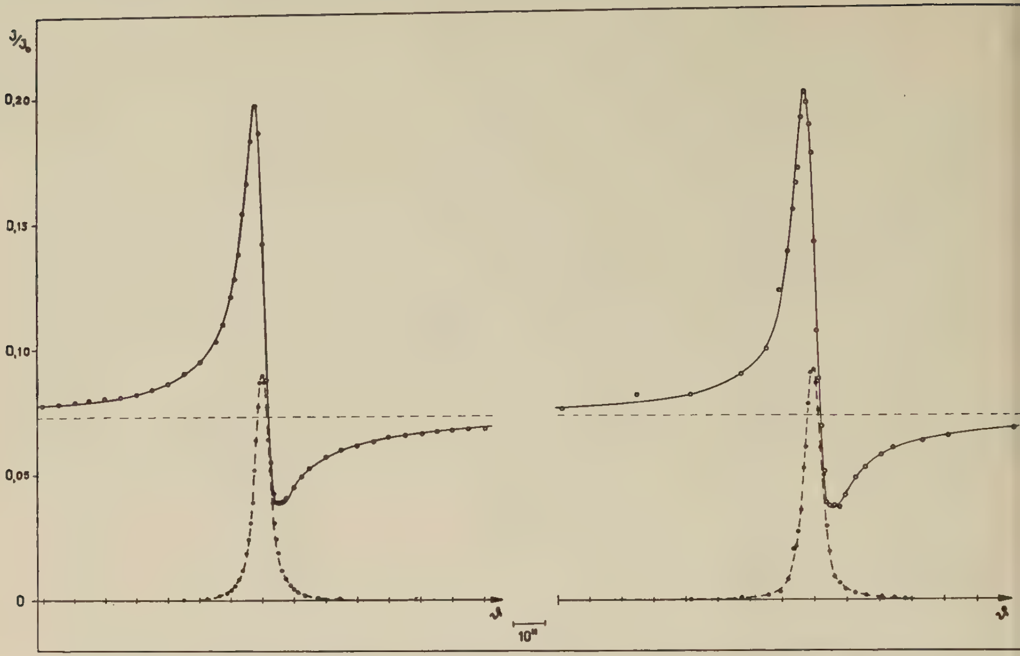

Fig. 17. Transmitted and reflected intensities for Au L β_1 through calcite. Monochromator in Laue position. Both crystals 0.34 mm thick. $I_0 = 18{,}000$ counts/min.

The measurements with copper radiation give the same good agreement as to the shapes and qualitative data (general characteristics) of the curves. The quantitative data on the other hand (maximum intensities, integrated reflection and integrated transmission) are less than the calculated values. It should be noted that the experimental width of the reflection curve, 5.5″, exceeds the calculated width, 5.3″, by 0.2″, a difference which seems to be real though it is of the same order of magnitude as the experimental error.

In the recordings with the other four emission lines the thickness of the analyser crystal could be determined directly from the transmitted intensity, so that measurements could be carried out in a crystal region which had the desired thickness. The results obtained with Au L α_1, Au L β_1, and Mo K α_1 agree both qualitatively and quantitatively with the calculations. (See Figs. 16–18.) The only exception occurs in the widths of the reflection and the transmission curves. The experimental values are greater than the theoretical, and the experimental broadening increases with decreasing wavelength.

The measurements with Ag K α_1 radiation (Fig. 19) give a qualitative and in some respects also a quantitative agreement with the calculations. This is particularly the case with the maximum in the transmission curve, which is very broad, with a maximum intensity only 2–3 per cent above the normal transmitted intensity. The reflection curve is broadened and has lower maximum intensity; the transmission curve is broadened, too, and has higher minimum intensity than the corresponding calculated curves. The broadening is

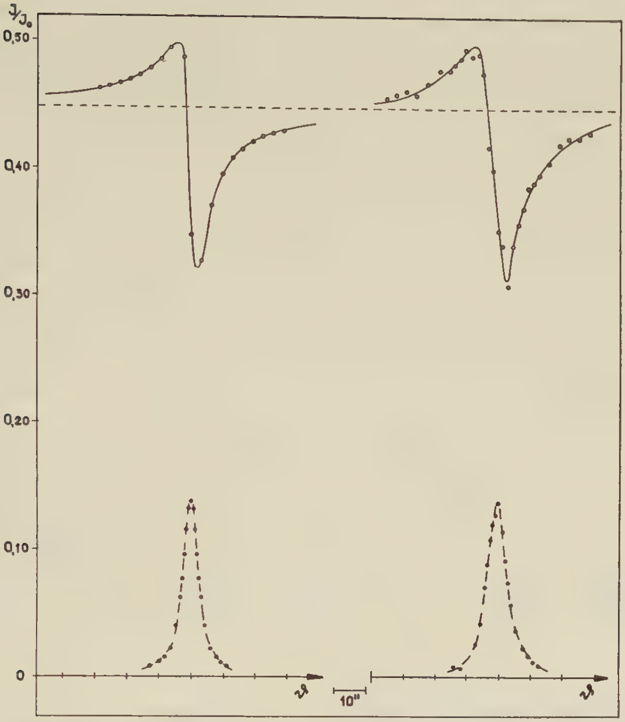

Fig. 18. Transmitted and reflected intensities for Mo Kα_1 through calcite. Monochromator in Laue position. Both crystals 0.34 mm thick. $I_0 = 23{,}500$ counts/min.

greater than in the case of Au Lβ_1, but since the transmission maximum is flat, it is not possible to observe any change in it. The integrated reflection and transmission remain unchanged and agree with the calculated values within the limit of error. In these curves the integrated transmission has nearly the same numerical value as the integrated reflection, but with the opposite sign, so that the anomalous transmission here has become a pure extinction effect.

All investigations with the Laue-Laue arrangement thus show a very good qualitative agreement between the calculated and the experimental curves. The quantitative agreement must also be considered good. Within the limits of error the theoretical and experimental values of the integrated reflection, of the integrated transmission, of the distance from the peak of the reflection curve to the maximum and the minimum of the transmission curve, and of the ratio $R_{\max}/T_{\max}$, are equal. The shapes of the calculated curves in the angular regions where the reflected intensity exceeds the transmitted are practically identical with those obtained experimentally. Our method, in which two Geiger-Müller counters were used for a simultaneous registration of both the transmitted and the reflected radiation and where the two counters were very carefully calibrated against each other so that their relative sensitivity was accurately known, makes it possible to determine the relative positions of the two curves with high

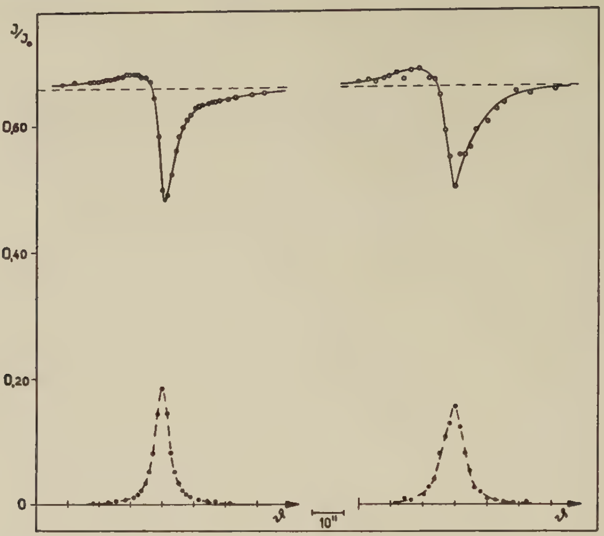

Fig. 19. Transmitted and reflected intensities for Ag Kα_1 through calcite. Monochromator in Laue position. Both crystals 0.34 mm thick. $I_0 = 7{,}500$ counts/min.

accuracy. The excellent agreement in this respect is perhaps the best experimental proof of the dynamical theory.[1]

In one respect there is a deviation between experiments and calculations which is too great to be attributed to experimental errors and to uncertainties in the calculations. This is the broadening of the experimental curves, which has already been mentioned. With Co Kα_1 radiation we obtained identical experimental and theoretical widths, but in the other recordings the experimental curves were broader than the calculated ones. In the reflection curves the broadening was 0.2″ for Cu Kα_1, 0.4″ for Au Lα_1, 0.7″ for Au Lβ_1, 1.1″ for Mo Kα_1, and 1.8″ for Ag Kα_1. Similar broadenings were observed in the curves obtained with the Bragg-Laue arrangement, where they could be partly explained by the earlier observed broadening for the Bragg-Bragg arrangement. The broadening for the Laue-Laue arrangement increases with decreasing wavelength and decreasing glancing angle. For Ag Kα_1 the latter is 5° 17′. As the incident beam is then nearly perpendicular to the surface, the reflecting volume of the crystal is a minimum when the broadening is greatest. The theoretical width of the reflection curve is nearly the same for all radiation used.

---

[1] The only previous experimental investigation of the relative positions of the curves was made with an instrument, where the transmitted and the reflected intensities were registered with the same Geiger–Müller counter, which had to be moved between two positions [5].

However, the sensitivity to X-rays is not the same in different parts of a counter. For this reason it is absolutely necessary to choose the two positions so that the incident beam enters exactly the same region of the counter in both positions. Otherwise the two registrations are carried out with different sensitivity and no certain conclusions can be drawn from the results. In the above work by BROWN, ROGOSA and SCHWARZ, such a mistake must have been made, as the maximum intensity of the reflected radiation is greater than that of the transmitted radiation in the two curves reproduced. This cannot occur when a crystal is cut for symmetric Laue reflection, in which case the transmitted intensity must always be greater than the reflected.

If the absorption is neglected, and if the broadening is supposed to be due to small imperfections in the crystal structure it ought to be the same for all wavelengths. However, when $(\varkappa A)$ is large the normal absorption is also great. If we have a crystallite of small dimensions, the maximum reflection and transmission in it will correspond to directions in the rest of the crystal to be passed, where the absorption is so high that the influence from the disorientated crystallite cannot be experimentally observable. For this reason the effect of defects ought to be more pronounced with decreasing values of wavelength and $(\varkappa A)$. The measurements with a Bragg monochromator seem to indicate that the broadening increases with decreasing thickness of the transmission crystal. However, further experimental material is needed before an explanation can be given.

General discussion

Hitherto all angles have been measured in seconds of arc. In the theoretical discussion of the transmission the intensities R_L of the reflected radiation and T_L of the transmitted radiation in the symmetrical Laue case, and R_B of the reflected radiation in the symmetric Bragg case, were obtained from the relations

$$R_L(y) = e^{-\frac{\mu_0 t_0}{\gamma_0}} \frac{\cosh \frac{2\varkappa A}{\sqrt{1+y^2}}}{2(1+y^2)} \tag{1}$$

$$T_L(y) = \frac{e^{-\frac{\mu_0 t_0}{\gamma_0}}}{2(1+y^2)} \left\{ (1+2y^2) \cosh \frac{2\varkappa A}{\sqrt{1+y^2}} + 2y\sqrt{1+y^2} \sinh \frac{2\varkappa A}{\sqrt{1+y^2}} \right\} \tag{2}$$

$$R_B(y) = L - \sqrt{L^2 - (1+4\varkappa^2)}, \tag{3}$$

$$\text{where } L = \sqrt{(-1+y^2-g^2)^2 + 4(gy-\varkappa)^2} + y^2 + g^2. \tag{4}$$

The incident beam is here assumed to be parallel, monochromatic, and of unit intensity. The derivation of the equations was given in the previous publication.

The angular coordinate y is proportional to the wavelength and chosen in such a way that the full width of the Bragg diffraction pattern of the normal polarized component is nearly the same for all wavelengths if it is expressed in y coordinates. Within the wavelength range where the investigations with a Bragg monochromator have been carried out, the width of the Bragg diffraction pattern can be considered constant if it is expressed in the y coordinate that corresponds to the wavelength in question.

The influence of the analyser crystal (the transmission crystal) is determined by equations (1) and (2), where the exponential factor only influences the intensity and is independent of the angular coordinate. The shape of the intensity curves is determined by the value of the parameter $(\varkappa A)$, and will be independent of the wavelength, if here too we express the angular coordinate in terms

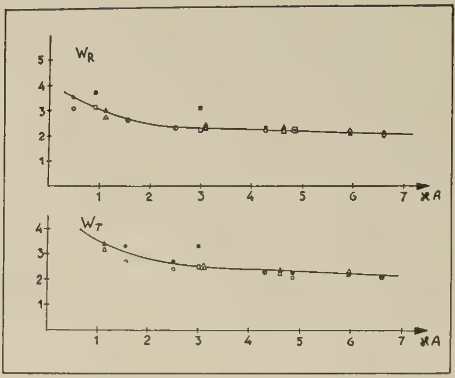

Fig. 20. The full widths w_R of the reflection curves and w_T of the transmission curves as functions of ($\varkappa A$). The widths are measured in the y coordinate for the normal polarized component belonging to the wavelength with which the point was obtained. All measurements are made with the monochromator in Bragg position.

In Figs. 20–22 open points indicate theoretical values; the square points were obtained with a 0.91 mm thick analyser crystal, the triangular ones with a 0.47 mm and the circular ones with a 0.34 mm thick analyser crystal. The great deviation obtained with the 0.91 mm crystal is easily observable.

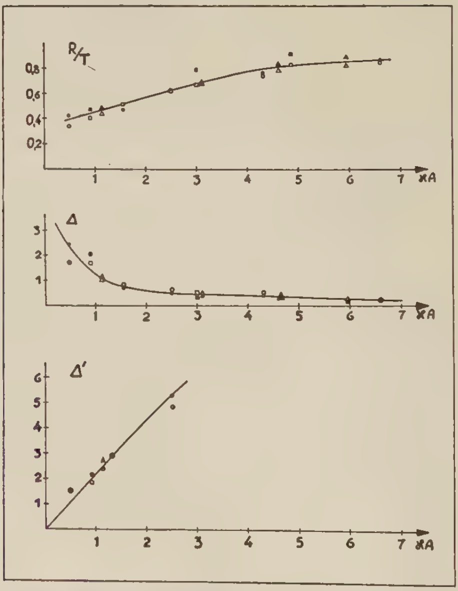

Fig. 21. $R_{\max}/T_{\max}$ (in the figure abbreviated to R/T) and the angular distances Δ and Δ' from the peak of the reflection curve to the peak and to the minimum of the transmission curve as functions of ($\varkappa A$). Δ and Δ' are given in y_n units. The results were obtained with the monochromator in Bragg position.

Table 7.

Results from the determinations of the angular quantities, when they are all expressed in terms of the y-coordinate for the normal polarization. The values of $(\varkappa A)$ refer to the same polarization. Notation as in Table 3. I–III are the determinations with a Bragg monochromator. The thickness of the analyser was 0.91 mm for I, 0.47 mm for II and 0.34 mm for III. IV refers to the investigations with both crystals in Laue position.

up	Line	$(\varkappa A)_n$	w_R		w_T		$R_{\max} \cdot 10^2$		$T_{\max} \cdot 10^2$		R_m/T_m		$\int R\,dy$		$\int (T-T_0)\,dy$		Δ		Δ'	
			t	exp	t	exp	t	exp	t	exp	t	exp	t	exp	t	exp	t	exp	t	exp
	Au Lα_1	4.85	2.2	2.2	2.1	2.2	1.70	1.44	2.09	1.58	0.82	0.91	0.22	0.17	0.24	0.18	0.1	—	—	—
	Au Lβ_1	3.01	2.2	3.1	2.5	3.3	4.90	3.30	7.41	4.20	0.66	0.78	0.64	0.56	1.08	0.77	0.5	0.3	—	—
	Mo Kα_1	0.91	3.1	3.7	—	—	10.1	9.5	25.1	20.4	0.40	0.47	1.92	2.08	1.53	0.50	1.7	2.0	1.8	2.1
	Co Kα_1	6.60	2.0	2.1	2.1	2.1	1.07	0.93	1.28	1.07	0.89	0.87	0.13	0.11	0.16	0.13	0.2	0.2	–	—
	Cu Kα_1	4.30	2.2	2.3	2.3	2.3	2.35	2.03	3.21	2.68	0.74	0.76	0.30	0.26	0.41	0.37	0.5	0.4	–	—
	Au Lα_1	2.50	2.3	2.2	2.4	2.7	3.87	3.90	6.28	6.35	0.62	0.62	0.51	0.48	0.97	1.00	0.6	0.5	4.8	5.3
	Au Lβ_1	1.55	2.6	2.6	2.7	3.3	7.50	6.90	14.8	13.1	0.51	0.47	1.12	1.10	1.80	2.08	0.8	0.7	2.9	2.9
	Mo Kα_1	0.47	3.1	3.5	—	—	15.3	16.8	45.2	40.2	0.34	0.42	3.29	3.64	-0.52	-0.79	1.7	2.4	1.5	1.5
I	Fe Kα_1	5.95	2.2	2.1	2.3	2.2	1.32	1.18	1.62	1.32	0.82	0.89	0.17	0.13	0.20	0.16	0.2	0.1	—	—
	Co Kα_1	4.63	2.2	2.3	2.3	2.4	1.58	1.66	2.02	1.96	0.79	0.84	0.20	0.21	0.27	0.25	0.3	0.3	—	—
	Cu Kα_1	3.10	2.4	2.5	2.5	2.5	3.80	2.94	5.69	4.34	0.67	0.68	0.51	0.39	0.81	0.67	0.4	0.4	—	—
	Au Lβ_1	1.12	2.7	3.0	3.2	3.4	8.5	8.6	19.4	17.8	0.44	0.48	1.30	1.54	1.54	1.24	1.0	1.1	2.4	2.7
	Co Kα_1	4.63	1.2	1.2	1.2	1.2	4.3	5.5	5.3	6.5	0.81	0.85	0.26	0.34	0.34	0.40	0.2	0.1	—	—
	Cu Kα_1	3.10	1.5	1.5	1.6	1.6	7.31	6.72	10.1	9.0	0.73	0.75	0.58	0.58	0.91	0.81	0.4	0.4	—	—
	Au Lα_1	1.80	1.8	2.0	2.5	2.5	7.80	7.91	13.1	12.5	0.60	0.63	0.83	0.86	1.47	1.56	0.5	0.7	5.3	6.1
	Au Lβ_1	1.12	2.2	2.5	2.7	3.1	9.0	9.1	20.0	20.1	0.45	0.45	1.39	1.35	1.78	1.64	1.0	1.0	2.3	2.6
	Mo Kα_1	0.34	3.6	4.3	—	—	13.8	13.5	34.2	32.2	0.41	0.42	3.78	3.83	-2.62	-3.56	2.9	4.2	1.7	1.8
	Ag Kα_1	0.18	4.2	5.6	—	—	18.4	15.6	68.4	68.4	0.27	0.23	5.20	5.20	-4.67	-5.14	7.5	8.2	0.3	0.3

of the y coordinate corresponding to the wavelength in question. If all angular quantities which are given in the tables in seconds of arc, are transformed to the y coordinate corresponding to the wavelength in question (we have taken the appropriate one for the normal polarized component), they can be plotted in diagrams as functions of $(\varkappa A)$. In this way all measurements obtained with the Bragg-Laue arrangement can be directly compared in spite of the fact that three transmission crystals with different thicknesses were used, and a simple graphical check on both theory and crystal perfection is obtained.

Figs. 20–22 give the full width w_R of the reflection curve, w_T of the transmission curve, the distances Δ and Δ' from the peak of the reflection curve to the maximum and to the minimum of the transmission curve respectively, and the ratio $R_{\max}/T_{\max}$ as functions of $(\varkappa A)$. The experimental values are indicated by solid points, the calculated ones by rings. In all the diagrams the points can be joined by lines that form smooth curves, although they were obtained under different experimental conditions and with various transmission crystals. There are some experimental points which do not fit the curves. They all come from determinations with the thickest transmission crystal, which verifies the previous observation that the crystal specimen used there was not perfect. It should be mentioned that the first preliminary investigation gave relatively narrow reflection

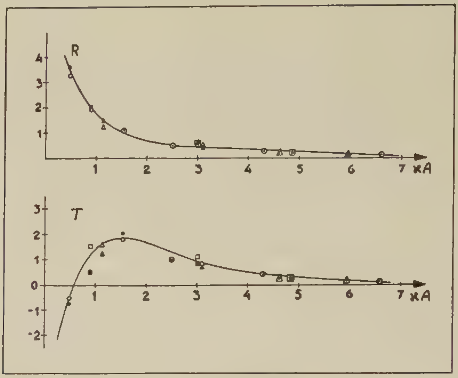

Fig. 22. The integrated reflection $\int R\,dy$ (abbreviated to R) and the integrated transmission $\int (T-T_0)\,dy$ (abbr. to T) as functions of $(\varkappa A)$. The ordinate is given in y units for the normal polarization. The results were obtained with the monochromator in Bragg position.

curves. With a Bragg monochromator and a Laue crystal 0.41 mm thick we obtained for the full width of the reflection curve at half maximum intensity the value 4.9″ with Mo Kα_1 radiation. This value may be compared with the registration with the 0.47 mm transmission crystal. On that occasion we used cleft calcite specimens and the internal reflections took place in planes which made an angle of about 75° with the surface (asymmetric Laue reflection). Since the crystals were not ground or polished, their quality was perhaps better. In the present investigation, where the crystal specimens were both ground and polished in the preparation, defects *may* have arisen during the preparation which were not eliminated by etching. This may be the reason for the observed deviations from the curves and for the differences between experimental results and calculations.

The integrated reflection and the integrated transmission can also be transformed from radians to y units and then plotted in diagrams as functions of $(\varkappa A)$. If the surface under the Bragg diffraction curve is put equal to unity for Mo Kα_1, it is 0.98 for Au Lβ_1, 0.93 for Au Lα_1, 0.89 for Cu Kα_1, 0.83 for Co Kα_1, and 0.76 for Fe Kα_1. The two factors $\frac{\mu_0 t_0}{\gamma_0}$ and $(\varkappa A)$ vary in the wavelength range concerned in the same way (both are approximately proportional to λ^3). For this reason the integrated reflection and the integrated transmission should be functions of $(\varkappa A)$ rather than of the wavelength, and should attain approximately the same value for different wavelength values if $(\varkappa A)$ is kept constant, with y as the angular coordinate. In the diagrams (Fig. 22) the R values form a smooth curve and the points fit the curve very well. The differences between experimental and calculated points are small, because the broadening of the reflection curve is compensated by the simultaneous decrease in maximum intensity, which leaves the integrated area nearly unchanged. The graphical reproduction of the integrated transmission gives in some cases larger deviations between the experimental points and the calculated ones, but these are obtained from the molybdenum curves in which the transmission maximum was very deformed.

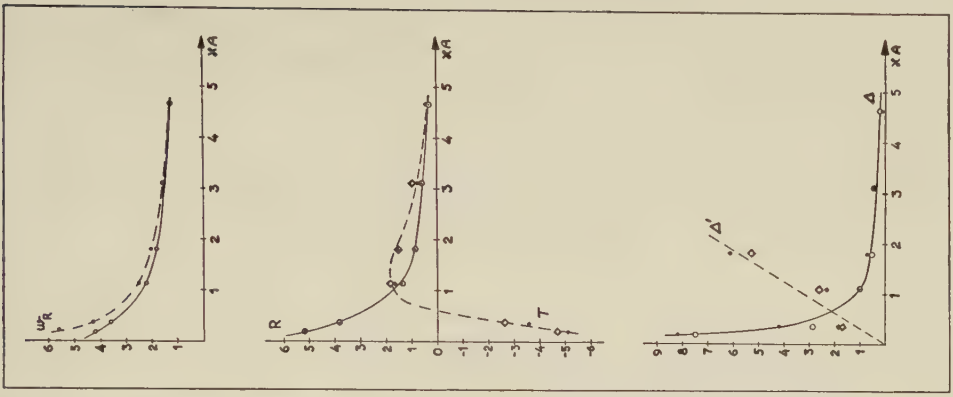

Fig. 23. The collected results obtained with both crystals cut for symmetric Laue reflection. Notation as in Figs. 20–22. Solid points represent experimental values. The systematic increase of the experimental width of the reflection curve as compared with the theoretical values is easily seen. The deviations between theoretical and experimental values of Δ and Δ' are mostly due to the fact that the maximum and minimum of the transmission curve cannot be determined accurately enough from the curves owing to the fact that the distances between the points in these regions are too great.

In view of the fact that the new way of expressing the results in y units is taken directly from the theoretical treatment of the transmission, the good adaptation to the curves in Figs. 20–22 must be considered a good indication of the correctness of the theory.

The results from the Laue-Laue determinations are not so well fitted for this way of representing the determined quantities graphically, as the width of the diffraction pattern of the Laue monochromator and the area under it depend on the value of $(\varkappa A)$. The angularly dependent quantities, however, are functions of $(\varkappa A)$, and can here easily be studied graphically, because both crystals had the same thickness. w_R, w_T, Δ, Δ', the integrated reflection and the integrated transmission are given in diagrams in Fig. 23. The good agreement between theoretical and experimental points and the smooth connecting curves verify the earlier conclusion that the present theory seems to account for the experimental observations.

Summary

The previously developed theoretical treatment of the anomalous X-ray transmission through perfect absorbing crystals in the region near the Bragg angle has been checked experimentally with calcite crystals in a double crystal spectrometer. With the monochromator crystal cut for symmetric Bragg reflection the transmission through three analyser crystals has been investigated in the wavelength range 558–1932 X.U. The analyser crystals were cut for symmetric Laue reflection. The transmission was also studied with a monochromator crystal cut for symmetric Laue reflection. The theoretical shapes of the intensity curves of the transmitted and reflected beams have been calculated and compared with

the experimentally obtained patterns. A very satisfactory agreement between theory and experiment was obtained. It was also possible to verify the theoretically predicted asymmetry of the Bragg diffraction pattern for a perfect absorbing crystal.

The investigation has been supported by a grant from the Swedish Natural Science Research Council, which made it possible to carry out all calculations.

The Physical Institute, University of Uppsala, Sweden. March 1954.

REFERENCES

1. G. Brogren and Ö. Adell, Arkiv för Fysik *8*, 97 (1954)
2. P. B. Hirsch, Acta Cryst. *5*, 176 (1952).
3. G. N. Ramachandran, J. Appl. Phys. *23*, 500 (1952).
4. G. Brogren, Arkiv för Fysik *6*, 479 (1953).
5. L. C. Brown, G. L. Rogosa and G. Schwarz, J. Appl. Phys. *23*, 1054 (1952).
6. G. Brogren and Ö. Adell, Arkiv för Fysik *7*, 1 (1953).
7. R. W. James and G. W. Brindley, Phil. Mag. *12*, 81 (1931).
8. H. Hönl, Zs. f. Phys. *84*, 1 (1933).
9. H. Hönl, Ann. der Phys. *6*, 479, (1933).

Tryckt den 22 november 1954

Uppsala 1954. Almqvist & Wiksells Boktryckeri AB

ARKIV FÖR FYSIK Band 8 nr 41

Mitgeteilt am 2. Juni 1954 durch MANNE SIEGBAHN und ERIK HULTHÉN

Über die Höhe der angeregten Elektronenzustände von CaO, SrO und BaO

Von ALBIN LAGERQVIST und LENNART HULDT

Mit 6 Figuren im Text

§ 1. Einführung

Die bisher beobachteten Bandenspektren von CaO und SrO sind einander sehr ähnlich und bestehen beide aus mehreren Systemen, welche sich von dem ultravioletten Gebiet bis in das ultrarote erstrecken. Von beiden Molekülen sind je drei Systeme in den ultravioletten, blauen und ultraroten Gebieten rotationsanalysiert[1-5]. Alle drei Systeme haben denselben unteren Zustand $X'^1\Sigma$. Ausserdem sind im sichtbaren Spektralgebiet eine Anzahl starker Banden vorhanden, die wegen ihrer verwickelten Struktur bis heute noch nicht analysiert worden sind.

Von BaO ist nur ein einziges System im Sichtbaren gefunden worden, das einem $^1\Sigma$-$^1\Sigma$-Übergang entspricht[6].

Die Grundterme ^1S im Erdalkaliatom und ^3P im Sauerstoff können nicht einen $^1\Sigma$-Term ergeben. Der unterste gefundene Molekülterm in den drei Oxyden muss daher in ein Atompaar dissoziieren, in welchem das eine Atom oder beide angeregt sind. Eine lineare Extrapolation der spektroskopischen Daten ergibt für die Höhe der Dissoziationsgrenze für CaO 3,5 eV, für SrO 3,3 eV und für BaO 6,7 eV. Wird hiervon die möglichst niedrigste Anregungsenergie der Dissoziationsprodukte abgezogen, erhält man in Ordnung 1,6, 1,5 und 5,5 eV, welche Werte folglich die Dissoziationsenergien darstellen würden, wenn man die erwähnten $^1\Sigma$-Terme als die Grundzustände annimmt.

Die niedrigen Werte für CaO und SrO sind kaum mit der auffälligen Stabilität dieser Moleküle zu vereinbaren. Auch ergeben termochemische Bestimmungen[7, 8] sowie eine flammenspektroskopische Methode[9] Dissoziationsenergien von 4,9 eV (CaO), 4,7 eV (SrO) und 5,5 eV (BaO). Der $^1\Sigma$-Term von BaO kann somit wohl der Grundzustand des Moleküls sein. Dieses lässt sich dagegen für die anderen beiden Moleküle nur mit Bedenken annehmen, obwohl die spektroskopischen

---

[1] M. HULTIN u. A. LAGERQVIST, Ark. f. Fys. *2*, 471, 1951.

[2] A. LAGERQVIST, Ark. f. Fys. *8*, 83, 1954.

[3] G. ALMKVIST u. A. LAGERQVIST, Ark. f. Fys. *1*, 477, 1949.

[4] J. KOVÁCS u. A. BUDÓ, Ann. d. Phys. *12*, 17, 1953.

[5] G. ALMKVIST u. A. LAGERQVIST, Nature *170*, 885, 1952; Ark. f. Fys. im Erscheinen.

[6] A. LAGERQVIST, E. LIND u. R. F. BARROW, Proc. Phys. Soc. A *63*, 1132, 1950.

[7] G. DRUMMOND u. R. F. BARROW, Trans. Faraday Soc. *47*, 1275, 1951.

[8] L. BREWER u. D. F. MASTICK, J. Amer. Chem. Soc. *73*, 2045, 1951.

[9] L. HULDT u. A. LAGERQVIST, Ark. f. Fys. *2*, 333, 1950.

Werte wegen der langen Birge-Sponer-Extrapolation unsicher sind. Man müsste daher bei CaO und SrO einen tieferen Term erwarten, der wahrscheinlich ein Triplett wäre, aus Ca(Sr) ^1S und O ^3P gebildet.

Die nicht analysierten Banden von CaO und SrO im Sichtbaren werden von einigen Forschern Ca_2 und Sr_2 zugeordnet.

Da die üblichen spektroskopischen Methoden bis jetzt zur Klärung der genannten Fragen versagt haben, wird hier ein Versuch gemacht, aus der Abhängigkeit der Bandenintensitäten von der Temperatur die Bandensysteme in Niveauschemata einzuordnen.

§ 2. Methodisches

In einer thermischen Lichtquelle ist die Besetzung eines Molekülniveaus der Höhe E oberhalb des Grundterms durch den Ausdruck gegeben:

$$N_E = N \frac{g e^{-E/kT}}{\sum g_i e^{-E_i/kT}}, \tag{1}$$

wo N_E = Anzahl der Moleküle im Niveau E,
N = Gesamtzahl der Moleküle,
g = Statistisches Gewicht des Niveaus E,
k = Boltzmannsche Konstante,
T = Absolute Temperatur.

In der von uns früher[9] benutzten Luft-Acetylenflamme ist die Temperatur zwischen etwa 2 100 und 2 400° K einstellbar. Wir massen damals die Intensität einer Atomlinie, um dadurch die Dissoziationsenergie des Moleküls zu bestimmen. Der Dissoziationsgrad ist aber klein und kann in erster Annäherung vernachlässigt werden. Die Banden des betreffenden Oxydes treten stark hervor. Durch Messung der Intensität einer Bande, die in Abwesenheit von Selbstabsorption proportinal N_E ist, kann die Abhängigkeit der Besetzung N_E von der Temperatur bestimmt werden, wodurch nach gleichung (1) E erhältlich ist. Ist die Intensität einer Bande I_1 bei der Temperatur T_1 und I_2 bei der Temperatur T_2, wird

$$\frac{I_1}{I_2} = e^{\frac{E}{k}\left(\frac{1}{T_2} - \frac{1}{T_1}\right)}, \tag{2}$$

vorausgesetzt, dass N sich nicht nennenswert mit der Temperatur verändert.

Dieses Verfahren haben wir für die Erdalkalioxydbanden verwendet. Die Temperatur wird dabei, wie vorher, durch Natriumlinienumkehr bestimmt. Eine Wolframbandlampe wird hinter der Flamme aufgestellt und die Stromstärke so variiert, dass man die Linienumkehr der gelben Natriumdublette in einem Spektroskop beobachten kann. Ist die Intensität des Lampenkontinuums beim Umkehrpunkt und bei der Wellenlänge λ der Natriumlinien I_{Na}, so gilt nach dem Planckschen Gesetz

$$I_{\mathrm{Na}} = \mathrm{Konst} \times e^{-hc/\lambda kT} = \mathrm{Konst} \times e^{-E_{\mathrm{Na}}/kT}, \tag{3}$$

da, weil der untere Term der Na-Linie der Grundzustand ist, $hc/\lambda = E_{\mathrm{Na}}$ = die Anregungsenergie der Na-Resonanzdublette (= 17 000 K* = 2,11 eV).

---

* 1 K (Kayser) = 1 cm^{-1}.

Wenn in Gleichung (1) N und die Zustandsumme im Nenner als annähernd konstant angenommen werden, folgt aus (1) für die Intensität der Bande:

$$I = \text{Konst} \times e^{-E/kT}. \tag{4}$$

Aus (3) und (4) kann jetzt die Temperatur eliminiert werden, wonach

$$\log I = \frac{E}{E_{\text{Na}}} \log I_{\text{Na}} + \text{Konst.} \tag{5}$$

Wird $\log I$ als Ordinate gegen $\log I_{\text{Na}}$ als Abszisse aufgetragen, erhält man also aus einer Reihe von Messungen bei verschiedenen Temperaturen eine Gerade, deren Neigung $E/(17\,000\ \text{K})$ ist.

Werden bei verschiedenen Temperaturen Messungen der Intensitäten I_1 und I_2 zweier Banden mit den Anregungsenergien E_1 und E_2 von einem oder auch von zwei verschiedenen Molekülen gemacht, erhält man aus Gleichung (4) nach Eliminieren von T

$$\log I_1 = \frac{E_1}{E_2} \log I_2 + \text{Konst.} \tag{6}$$

Ist E_2 bekannt, lässt sich, ähnlich wie oben, E_1 graphisch bestimmen, ohne dass Temperaturmessungen erforderlich sind. Wenn beide Banden demselben Molekül zugehören, fällt der eventuelle Fehler fort, der darauf beruht, dass sich zufolge einer möglichen Dissoziation die Konstante in Gleichung (6) mit der Temperatur etwas ändert.

Die letzte Methode ist grundsätzlich die gleiche, die einer von uns[10] für Atomlinien angewandt hat. Eine etwas abweichende Entwicklung des Prinzips ist von Phillips[11] für das TiO-Spektrum benutzt worden.

§ 3. Experimentelles

Das Licht der mit Erdalkalisalzlösung gespeisten Flamme wurde durch einem Monochromator (Hilger-Glasspektrometer mit konstanter Ablenkung) spektral zerlegt. Zur Messung der Lichtstärke dienten Sekundär-Elektronen-Vervielfacher, und zwar für das sichtbare Gebiet ein RCA 931 A und für das ultrarote ein Cintel MS 20. Der Photostrom wurde, wenn erforderlich nach Verstärkung, mit einem Multiflex-Galvanometer gemessen. Die Temperatur der Flamme wurde durch Änderung der Acetylenzufuhr geregelt. Die Luftzufuhr wurde dagegen konstant gehalten, damit die Lösungsmenge pro Sekunde unverändert blieb.

§ 4. Ergebnisse

Für jede der untersuchten Banden wurde der Photostrom für eine Anzahl verschiedener Konzentrationen der Salzlösung und bei verschiedenen Temperaturen der Flamme an dem Galvanometer abgelesen. Die Figuren 1 und 2 stellen die Resultate der Ablesungen für die CaO-Banden bei rund 6 220 Å und für die

---

[10] L. Huldt, Ark. f. Fys. *2*, 353, 1950.

[11] J. G. Phillips, Astrophys. Journ. *115*, 567, 1952.

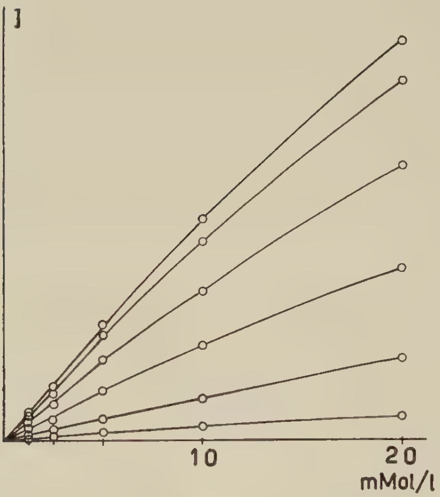

Fig. 1. Intensität des CaO-Spektrums bei 6 220 Å gegen Konzentration der Calciumnitratlösung.

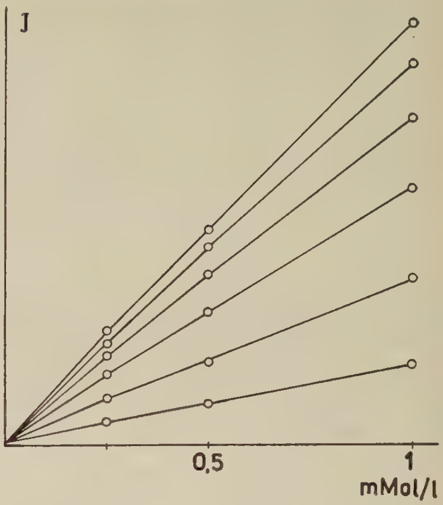

Fig. 2. Intensität des SrO-Spektrums bei 6 860 Å gegen Konzentration der Strontiumnitratlösung.

SrO-Banden bei rund 6 860 Å dar. Die Kurven zeigen, dass die Banden nicht dem Molekül Ca_2 bzw. Sr_2 zugeschrieben werden können. In einem solchen Fall würde nämlich die Intensität nicht linear sondern etwa quadratisch mit der Konzentration anwachsen, was aus dem Massenwirkungsgesetz abgeleitet werden kann. Die Linearität der Kurven ist ein Kriterium dafür, dass die Selbstabsorption gering ist, und dass der Sättigungsdruck des Oxydes nicht erreicht ist. Bei höheren Konzentrationen sollen aber die Kurven zufolge der Selbstabsorption immer konkav nach unten werden, was auch in Fig. 1 ersichtlich ist.

Einige Beispiele der Anwendung der Gleichung (5) zeigt Fig. 3. Die Neigung der BaO-Gerade ist ungefähr 1 und dasselbe gilt auch für die Bande des Vanadiumoxyds, welches wir zum Vergleich mitaufgenommen haben. Die Banden von CaO und SrO zeigen ihrerseits ein ganz abweichendes Verhalten. Diese Geraden haben alle grössere Neigungen als 1, was ganz hohen Anregungsenergien entspricht. Die Beziehungen der verschiedenen Banden miteinander nach Gleichung (6) werden in Fig. 4 und 5 gezeigt.

Für die Bariumoxydbanden haben wir aus vierzehn Messreihen als Wert der Anregungsenergie $E = 17\,300 \pm 1\,000$ K erhalten. Dieses ist mit der Annahme verträglich, dass der untere Zustand das Grundniveau ist, da die Wellenzahl dieser Banden rund 16 700 K beträgt. Bei den Untersuchungen der übrigen Oxyde haben wir häufig deren Bandintensitäten mit denjenigen des Bariumoxydbandes verglichen, und so nach Gleichung (6) die Anregungsenergie berechnet mit $E_{\mathrm{BaO}} = 16\,700$ K. Ausserdem sind die verschiedenen Banden eines Moleküls miteinander verglichen worden, was das Verhältnis zweier Anregungsenergien eines Moleküls lieferte.

Die erhaltenen Energien erwiesen sich bis auf einige tausend K reproduzierbar. Die Ergebnisse für die verschiedenen Moleküle und Spektralgebiete waren:

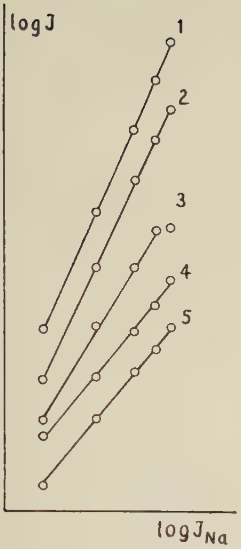

Fig. 3. Bandenintensitäten gegen Intensität des Kontinuums bei Umkehr der Na-Linien. — 1. CaO 5 475 Å. 2. SrO 5 470 Å. 3. SrO 6 100 Å. 4. VO 5 700 Å. 5. BaO 6 000 Å.

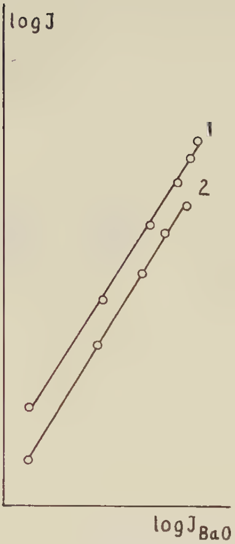

Fig. 4. 1. Intensität des SrO-Spektrums bei 6 830 Å. 2. Intensität des CaO-Spektrums bei 8 650 Å gegen die Intensität des BaO-Spektrums (0–0-Bande).

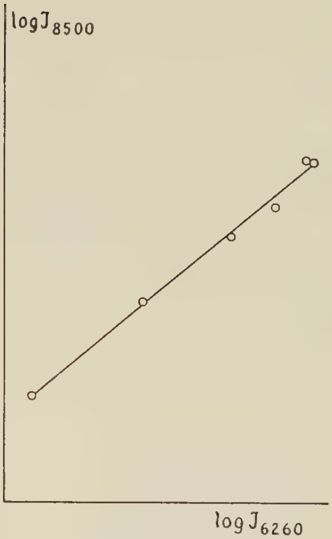

Fig. 5. Abhängigkeit zweier CaO-Bande (6 260 Å und 8 500 Å) von einander.

Calciumoxyd:	Ultrarot, Wellenzahl	11 500 K : $E = 27\,000$ K
	Orange,	16 000 K : $E = 32\,000$ K
	Grün,	18 000 K : $E = 36\,000$ K
Strontiumoxyd:	Ultrarot,	10 900 K : $E = 24\,000$ K
	Rot,	15 000 K : $E = 27\,000$ K
	Gelb,	16 500 K : $E = 28\,000$ K
	Grün,	18 000 K : $E = 37\,000$ K
	Violett,	26 000 K : $E = 38\,000$ K
Bariumoxyd:	Grün,	16 700 K : $E = 17\,300$ K
Vanadiumoxyd:	Grün,	17 400 K : $E = 19\,000$ K

§ 5. Diskussion

Die Ziffern für die Strontium- und Calciumoxyde zeigen das unerwartete Resultat, dass keine der starken Banden mit dem Grundzustand kombinieren. Es ist jedoch kaum anzunehmen, dass dieses Resultat einem Mangel in der Methode zuzuschreiben ist, da ja BaO und VO das erwartete Auftreten zeigen, und da das ultrarote und das violette System von SrO, deren Endzustand gemeinsam ist, gut übereinstimmen. Um eine Auffassung von der Absolutintensität des gelben SrO-Systemes zu erhalten, verglichen wir den Galvanometerausschlag für dieses System mit dem der Sr-Linie bei 4 607 Å. Unter Heranziehung unserer früheren Daten[9] der Dissoziation und unter Berücksichtigung der Selektivität der Photozelle konnten wir dann errechnen, dass die Stärke des Überganges für das Bandsystem von der gleichen Grössenordnung wie für die Atomlinie ist. Unsere Er-

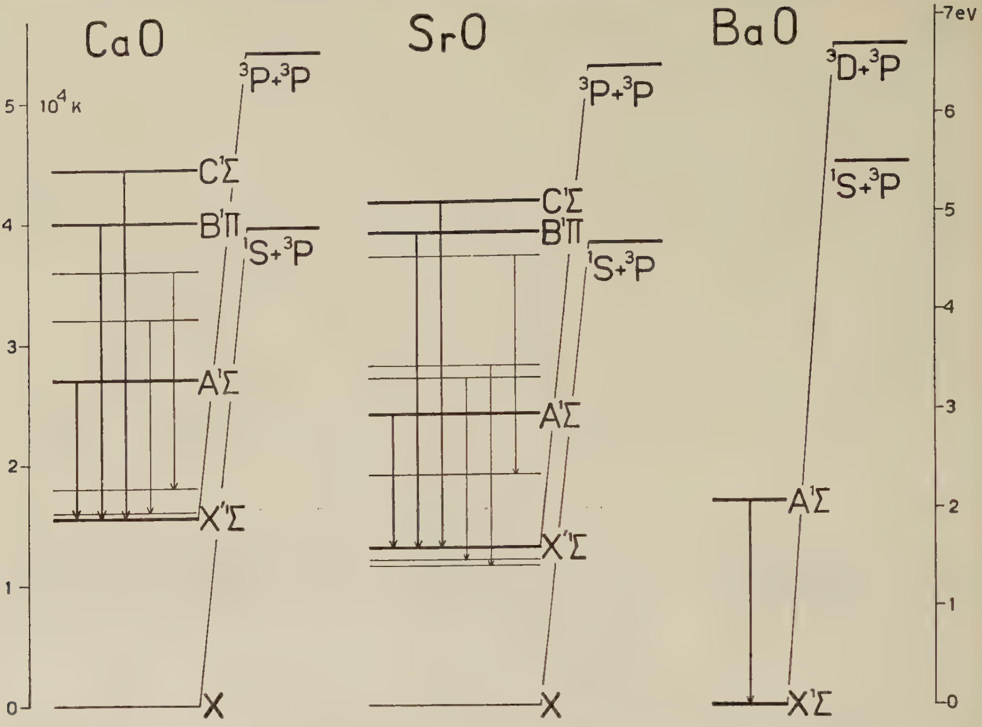

Fig. 6. Termschemata von CaO, SrO und BaO nach Ergebnissen dieser Arbeit. Die rechtsseitigen Niveaus sind diejenigen der Atome (Erdalkaliatom + Sauerstoff).

gebnisse müssen somit so gedeutet werden, dass die sichtbaren Banden im SrO- und CaO-Spektrum starke Übergänge zwischen hochliegenden Termen sind.

Mit unseren hier gefundenen Daten sind die Termschemata der drei Erdalkalioxyde in Fig. 6 gezeichnet worden. Die analysierten Terme sind mit dicken Linien gezogen, die nicht analysierten mit feinen Linien. Es wird bemerkt, dass die letzteren um einige tausend K unsicher sind. Der niedrigste bekannte $^1\Sigma$-Term in CaO und SrO ist hier mit X', nicht X, bezeichnet. Die unteren Zustände der intensiven, nicht analysierten Banden dieser Moleküle sind gesondert gezeichnet, obwohl es natürlich sehr nahe liegt, sie sich als ein einziges, mit X' identisches Niveau vorzustellen.

Da nunmehr die X'-Terme in CaO und SrO nicht die Grundzustände darstellen, liefern die in § 1 genannten Birge-Sponer-Extrapolationen mit den termischen Daten etwas besser übereinstimmende Werte. Unter Hinzufügung des Abstandes X–X' ergeben sich jetzt als die bandenspektroskopischen Werte der Dissoziationsenergie für CaO 3,5 eV und für SrO 3,1 eV.

Stockholm, Physikalisches Institut der Universität, Juni 1954.

Tryckt den 22 november 1954

Uppsala 1954. Almqvist & Wiksells Boktryckeri AB

ARKIV FÖR FYSIK Band 8 nr 42

Communicated 2 June 1954 by MANNE SIEGBAHN and ERIK HULTHÉN

Ionization and fragmentation of CO by bombardment with atomic ions. Dissociation energy of CO. Heat of sublimation of carbon

By EINAR LINDHOLM

With 3 figures in the text

In connection with investigations [1, 2, 3] of collisions between some simple molecules and atomic ions, the collisions between N_2 and atomic ions were investigated [4] using magnetic analysis of the collision products. The result of that work was a contribution to the discussion concerning the dissociation energy of N_2. As the dissociation energy of CO also has been much discussed (for reviews see [5, 6, 7]) it was decided to carry out measurements for this molecule too, to see whether it might be possible by means of the new method to decide between the values for the dissociation energy that have been obtained by spectroscopic, mass spectrometric and other methods. The result of the work is that HAGSTRUM's [7] value 9.6 eV is supported against GAYDON's [5] value 11.111 eV. From this it follows that the value 135.7 kcal/mol for the heat of sublimation of carbon is preferable in the light of the new measurements.

The apparatus has been described earlier [1, 2, 3, 4]. The atomic ions are produced in an ion-source of Nier type, are analysed in a semicircular magnet, enter the collision chamber which is filled with CO gas at a pressure of $2 \cdot 10^{-4}$ mm Hg, and, after leaving the collision chamber, are collected and measured. In the collision chamber ionised fragments are obtained from CO. These are drawn out through one side of the collision chamber, are accelerated and analysed in another semicircular magnet, and are finally collected and measured with an electrometer tube amplifier. The kinetic energy of the incident atomic ions was 500 eV as during the previous measurements. The CO was obtained from a lecture-size tank from the Matheson Company. Mass spectrometer analysis of the gas in the collision chamber revealed only minute impurities of H_2O.

The results of the measurements are given in the table. The first column gives the incident atomic ions, arranged according to their ionisation potentials. The following three columns give the cross-sections for the formation of the fragments CO^+, O^+ and C^+. The last column gives the recombination energy (RE) for the process that is probably responsible for the formation of the fragment in question. The different fragmentation processes are referred to by the letters *x*, *a*, *b*, *c*, *d*, *f*, *g*, *h*. Below the cross-sections the mass spectrum of CO that is obtained by electron bombardment is given. At the foot of the table the appearance potentials for each fragment are given.

The RE for the different atomic ions have been tabulated and discussed previously [3, 4].

O^+: It has previously been stated [3] that O^+ ions from CO_2 seem to be mainly in the ^4S state. This has been verified in the present work by a study of the velocity dependence of the cross-sections in a manner that will be discussed later in this paper. When bombarding CO with O^+ from CO_2 the energy deficit amounts to 0.4 eV for formation of CO^+. As the velocity of the ion decreases we may expect the cross-section to decrease. It appeared, in fact, that for an ion energy of 50 eV the cross-section was only $^1/_6$ of the cross-section at 500 eV. On the other hand, when O^+ ions from N_2O were used, no decrease of the cross-section was observed.

Br^+: The small cross-sections prove that the state ^1S with the RE 14.87 and 15.32 is absent in the ion beam.

P^+: $POCl_3$ is a more convenient material than P_4S_3 for the production of P^+ ions. The properties of the P^+ ions from P_4S_3 and $POCl_3$ seem to be equivalent. The small cross-sections prove that the state ^5S with the RE 17.50 is absent.

Ion	CO^+	O^+	C^+	RE (number) and AP (*x*, *a*, *b* . . ., see below).
A^{++}	1	0.5	10	C: 27.6, 29.3, 31.7.
Kr^{++}	15	0.4	15	CO: 25.2 25.7, 26.4, *c*. C: 23.9 . . . 26.4, *d*.
He^+	2	4	30	C: 24.58, *d*. O: 24.58, *g*.
Ne^+	0.8	0.8	10	C: 21.56, 21.66, *f*.
F^+	150	2	30	CO: 17.42, *a*; 20.01, *b*. C: 22,98, *d*; 17.42, *h*.
A^+	15	0.2	8	CO: 15.76, 15.94, *x*. C: 15.76, 15.94, *h*.
N^+	50	0.3	3	CO: 14,06, 14.54, 15,03, *x*.
Kr^+	40	—	2	CO: 14.00, 14,67, *x*.
O^+	120	—	10	CO: 14.45, 14.98, 16.67, 16.94, 18.64, *x*, *a*. C: *h*. From N_2O and CO.
	120	0.5	10	CO: 13.62, *x*. C: *h*. From CO_2.
Cl^+	10	0.05	2	CO: 14.45, 14.34, *x*.
Br^+	1	—	2	All RE below 13.25.
C^+	10	0.1	2	CO: 16.58, *a*.
P^+	3	—	0.3	All RE below 11.32.
S^+	2	—	0.8	All RE below 12.20.
B^+	15	—	0.8	CO: 12,92, *x*.
CO^+	150	0.1	4	
Electrons	100	2.5	10	

AP: *x*: 14.009 *g*: 23.2 *f*; 20.9.
a: 16.532 *d*: 22.8.
b: 19.670.
c: 25.5 ± 0.5.

Earlier investigations

Carbon monoxide has, according to Mulliken [8, 9] (cf. Moffitt [10] and Long and Walsh [11]), the following electron configuration:

KK	$(z\sigma)^2$	$(y\sigma)^2$	$(w\pi)^4$	$(x\sigma)^2$	$^1\Sigma^+$
	25.5 ± 0.5 eV	19.670 eV	16.532 eV	14.009 eV	
		$B\ ^2\Sigma$	$A\ ^2\Pi$	$X\ ^2\Sigma$	
	c	*b*	*a*	*x*	
		1.17 Å	1.24 Å	1.12 Å	

The figures below the electron configuration are the ionization potentials for the electrons in the four lowest orbitals, below them the states of the molecular ions that are obtained by these ionizations, our designations x, a, b, c for the different ionization processes, and internuclear distances r_e for the different states (for CO $r_e = 1.13$ Å) [12].

Process x has been observed as a Rydberg series by TAKAMINE, TANAKA and IWATA [13], and has also been investigated mass spectrometrically [14, 15, 16, 17, 7]. Recently the state $X\,^2\Sigma$ has been investigated by RAO [18]. 14 vibrational levels have been found [19].

Process a has been observed as a Rydberg series by TANAKA [20], but has not yet been detected by the mass spectrometer. The state $A\,^2\Sigma$ has been investigated using both the comet-tail bands (A–X) [21] and the Baldet-Johnson bands (B–A) [22]. 12 vibrational levels have been observed [23].

Process b has been observed as a Rydberg series by TANAKA [20] but not with the mass spectrometer. 12 vibrational levels of the state $B\,^2\Sigma$ are known from investigations of the Baldet-Johnson bands and the first negative bands (B–X) [18, 19].

Process c has never been observed. Its IP has been estimated by MULLIKEN [9] as 32 eV.

The fragmentation of CO by electron impact may take place in several manners. The most important process has AP 22.8 eV and gives C^+ ions and O atoms [14, 15, 24, 17, 7]. HAGSTRUM [7] has been able to show that the C^+ ions which are formed at this electron energy have zero kinetic energy. From this it follows that there exists a dissociation limit for CO^+ at this energy.

Regarding the states of the fragments which are formed in this process several views have been advanced. HAGSTRUM [7, 25] has given reasons for the assumption that the O atom is excited and the dissociation process at this voltage is

$$\mathrm{CO}\,(X\,^1\Sigma^+) + 22.8\ \mathrm{eV} \rightarrow C^+\,(^2P) + \mathrm{O}\,(^1D). \qquad (d)$$

From measurements of this and other appearance potentials HAGSTRUM has determined the dissociation energy of CO to be 9.6 eV. On the other hand, GAYDON [26, 5], using spectroscopic methods, has obtained the value 11.111 eV for the dissociation energy of CO, and therefore explains the process at 22.8 eV by supposing that the O atom is formed in its ground state ^3P.

Another fragmentation process with AP 20.9 eV also gives C^+ ions [24, 17, 7]. For the same AP O^- ions are also observed, and LOZIER [24] has shown that the numbers of positive and negative ions formed for electron energies between 20.9 and 22.8 eV are equal. In LOZIER's measurements the only ions registered were those for which the initial energies were higher than a certain variable limiting value. LOZIER inferred from this that the formation of C^+ and O^- occurs at the same time in a primary process. Using the value 9.6 eV for the dissociation energy of CO LOZIER's computations showed that the AP 20.9 eV for the fragments C^+ and O^- agrees with the appearance potential calculated for the corresponding products with uncharged O. He therefore assumed that the O^- ion is formed in an excited state, so that the excitation energy equals the electron affinity of oxygen, 2.2 eV. The fragmentation process is thus, according to LOZIER and HAGSTRUM,

$$\mathrm{CO}\,(X\,^1\Sigma^+) + 20.9\ \mathrm{eV} \rightarrow \mathrm{C}^+\,(^2P) + \mathrm{O}^{-*}\,(2.2). \qquad (e)$$

The existence of an excited state of the negative oxygen ion is by no means proved. Theoretical computations have not been successful [27]. HASTED [28] has recently questioned its existence in connection with his work on the detachment of electrons from negative O^- ions in collisions with rare gas atoms. In his measurements the same cross-sections are obtained for O^- ions undoubtedly in the ground state and for O^- ions that according to LOZIER and HAGSTRUM should be in the excited state. HASTED has therefore discussed the possibility that the fragmentation process instead of process *e* may be the following

$$\mathrm{CO}\,(X\,{}^1\Sigma^+) + 20.9\ \mathrm{eV} \rightarrow \mathrm{C}^+\,({}^2P) + \mathrm{O}\,({}^3P), \qquad (f)$$

and that the O^- ion is formed in a secondary process involving radiative attachment. But this is not established by HASTED's measurements because an alternative explanation may be given by the assumption that the lifetime of the excited state may be so short that it has decayed to the ground state before entering HASTED's collision chamber.

GAYDON, using the higher value for the dissociation energy of CO, assumes that at 20.9 eV the fragments C^+ (^2P) and O^- (^2P) are obtained. In this way he avoids difficulties with the excited state of O^-, but a consequence is that the agreement between the computed and measured AP is not quite satisfactory.

A third fragmentation process has AP 23.2 eV and gives O^+ ions.

$$\mathrm{CO}\,(X\,{}^1\Sigma^+) + 23.2\ \mathrm{eV} \rightarrow \mathrm{C}\,({}^3P) + \mathrm{O}^+\,({}^4S). \qquad (g)$$

In this case the fragments possess initial kinetic energies [17, 7] and therefore the intensity of the O^+ ion current is low and it has been necessary to use the retarding potential method for the determination of the AP. With HAGSTRUM's value 9.6 eV for the dissociation energy of CO the computed AP for process *g* agrees well with the measured value [25, 7], but using GAYDON's value it is impossible to obtain agreement. GAYDON [5] has therefore suggested the possibilities that O^+ may be obtained from impurities or that C^- may be obtained as the other fragment in the process. But neither explanation seems to be probable [29, 7].

Discussion of the new measurements

Regarding the interpretation of the measurements of the cross-sections in the table, reference may be made to [3] and [4] where there are similar discussions of several molecules.

Process *x* (AP 14.009) seems to be responsible for the large cross-sections for formation of CO^+ in the collisions with Kr^+, N^+, O^+, and Cl^+. In the collisions with A^+ (RE 15.76 and 15.94) the cross-section for formation of CO^+ is comparatively small. This is probably due to the fact that the energy excess in this case amounts to 1.8 eV. As the internuclear distances for CO and CO^+ $X\,{}^2\Sigma$ are roughly the same, the probability for absorption of this energy excess will be small according to the Franck-Condon principle. In the collisions with B^+ (RE 12.92) the energy deficit for the formation of CO^+ amounts to 1.1 eV. The correctness of this interpretation has been proved by varying the velocity of the incident ion. As the velocity decreased the cross-section decreased rapidly.

Process *a* (AP 16.532) seems to account for the cross-section for formation of CO^+ in the collisions with C^+.

Process *b* (AP 19.670) gives a large cross-section for formation of CO^+ in the collisions with F^+ (RE 20.01). Process *a* is probably of importance as well, because the slightly greater internuclear distance for $A\ ^2\Pi$ than for CO should make it possible for the energy excess 0.9 eV to be absorbed as vibrational energy.

Process *c* may possibly be the cause of the large cross-section for formation of CO^+ in collisions with Kr^{++} (RE 23.9 . . . 26.4). If this is the case, it should be possible to deduce the AP for process *c* from these experiments. The small cross-section with A^{++} (RE 27.6, 29.3, and 31.7) shows that the AP must be considerably lower than 27.6. The small cross-section with He^+ (RE 24.58) shows that it is at least 1.0 eV higher than 24.58. The probable value for the AP for process *c* is thus $25.5 \pm \pm 0.5$ eV. This is much lower than MULLIKEN's estimate, 32 eV.

In collisions with He^+ (RE 24.58) the cross-section is very large for formation of C^+, and also for the formation of O^+ the cross-section is larger than with other atomic ions. It is immediately evident that the fragmentation occurs according to the processes *d* and *g*. Process *d* seems also to be responsible for part of the cross-section for formation of C^+ in collisions with F^+ (RE 22.98). (The pressure dependence of the ratio C^+/CO^+ showed that process *h* is also of importance.)

In collisions with Ne^+ (RE 21.56 and 21.66) the cross-section for formation of C^+ is rather large. This is surprising, for if the fragmentation takes place according to process *d*, the energy deficit would amount to as much as 1.1 eV. Previously [4], a similar result referring to the collisions between Ne^+ and N_2 has been discussed in some detail, and it was pointed out that for an appreciable energy deficit the cross-section will be small. Further it was mentioned that Ne^+ has no metastable states and therefore only RE 21.56 and 21.66. It seems therefore necessary to assume the existence of a fragmentation process giving C^+ ions and with AP below 21.66 eV. At first sight the only possibility seemed to be the process marked *e* above, which has been studied by LOZIER and HAGSTRUM. But on taking into consideration the manner in which the activation energy is supplied to the molecule it became clear that we cannot explain the cross-sections in this way. For in the ionic collision the energy is obtained from the neutralisation of the atomic ion and therefore during the primary process a molecular ion is formed which immediately afterwards dissociates into a positive ion and a neutral atom. But in process *e* we have quite the contrary: a highly excited neutral molecule is assumed to dissociate into a positive and a negative ion. The only possible explanation of the cross-section with Ne^+ seems therefore to involve the assumption of the existence of process *f*.

To obtain confirmation of the correctness of this interpretation the variation of the cross-section with the velocity of the incident ion was investigated. If the fragmentation occurs according to process *f*, the energy excess will amount to 0.7 eV, which will be absorbed by the fragments as kinetic energy. We may therefore consider the energy resonance in the collision process to be exact and may expect increasing cross-sections for decreasing velocity [30]. But, on the other hand, if the fragmentation occurs according to process *d*, the energy deficit will amount to 1.1 eV, and we will expect decreasing cross-sections for decreasing velocity.

Owing to the discrimination in the collision chamber the present apparatus is not all suited for accurate determinations of cross-sections. It is therefore necessary to calibrate the apparatus using a collison process for which the energy defect is known. A suitable process is the bombardment of N_2 with Ne^+ ions. The energy

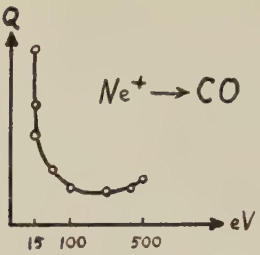

Fig. 1.

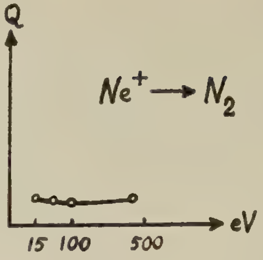

Fig. 2.

Fig. 1. Cross-sections for the process $Ne^+ + CO \rightarrow C^+$ as a function of the kinetic energy of the Ne^+ ion. The large cross-sections for low velocities show that the resonance is exact. Fig. 2. Cross-sections for the process $Ne^+ + N_2 \rightarrow N^+$ as a function of a kinetic energy of the Ne^+ ion. The cross-sections for low velocities are small owing to the energy energy deficit 0.25 eV.

deficit for this process amounts to 0.25 eV [4] and as the mass of the N^+ ion roughly equals the mass of the C^+ ion we can expect reliable results from this comparison.

Fig. 1 shows clearly that with CO the cross-section is large for low velocity and Fig. 2 shows that with N_2 the cross-section does not increase noticeably for decreasing velocity. From the comparison it is clear that the energy deficit for N_2 is greater than for CO, and this definitely implies that the fragmentation cannot take place according to process *d*. The measurements were made rapidly, first with CO, then with N_2, and finally with CO again. The measurements were thus not affected by surface potentials or other possible disturbances.

From these measurements it therefore seems to be proved that fragmentation of CO may occur according to process *f*. This means that the present work favours HAGSTRUM's view that the O atoms from the dissociation process *d* at 22.8 eV are excited, and in addition, HAGSTRUM's values for the dissociation energy of CO, 9.605 eV, and the heat of sublimation of carbon, 5.887 eV (135.7 kcal/mol) (cf. [6, 7, 31, 32, 33]).

It remains to explain the origin of the negative O^- ions at 20.9 eV in LOZIER's and HAGSTRUM's works. Several possibilities are conceivable. The first possibility is, of course, that both processes exist and process *e* occurs in electron impact and process *f* in collisions with Ne^+. The second possibility is that process *e* does not exist, and that the negative ions are formed in a separate process from an excited state of CO^-. McDOWELL [34] has discussed similar processes for O_2. The last possibility is that the negative ions are formed in a secondary process involving radiative attachment from the $O^+ (^3P)$ atoms that are obtained in process *f*. This has been discussed by HASTED (loc. cit.) in connection with his criticism of the excited state of the negative O^- ion. If this last possibility is the correct one it seems probable that the corresponding processes in NO and O_2 [7, 28] may be explained in the same way. It would therefore be of interest to investigate these molecules in the same manner as the present work with CO. The difficulty will be to find suitable atomic ions for this purpose.

A noteworthy result of the present measurements is that the C^+ fragment is often surprisingly abundant. This is especially clear from the cross-sections with A^+ (RE 15.76 and 15.94). With this low RE we should not expect any C^+ ions at all, as the energy deficit amounts to as much as 5 eV. The explanation is probably a secondary process in the collision chamber. This has already been observed by HOGNESS and HARKNESS [14].

$$CO^+ + CO \rightarrow C^+ + CO_2. \tag{h}$$

They were able to show that these C^+ ions were formed in another part of the ion source than the normal C^+ ions and that the ratio of the intensities of the C^+ peak and the CO^+ peak increased with pressure. Fig. 3 shows that the ratio of the C^+ peak and the CO^+ peak obtained with A^+ in the present work also increases with pressure. The variation is smaller than in the work of HOGNESS and HARKNESS, however, probably owing to the smaller dimensions of our collision chamber.

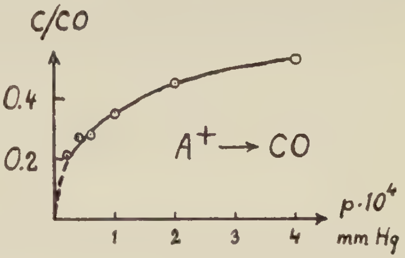

Fig. 3.

By considering the energy necessary for process *h* we may obtain some information as to process *f*. The heats of formation for CO_2 and CO are 94.4 and 26.4 kcal/mol and the dissociation energy for O_2 117.2 kcal/mol. If D denotes the least energy that must be absorbed by the CO^+ ion before it can dissociate to $C^+ + O$, we obtain

$$\begin{array}{lll} CO^+ + D & = C^+ + O & \\ & O = \frac{1}{2}\,O_2 + \frac{1}{2} \times 117.2 & \\ CO & + 26.4 = C + \frac{1}{2}\,O_2 & \\ C & + O_2 \quad = CO_2 + 94.4 & \\ \hline CO^+ + CO & = C^+ + CO_2 + 126.2 - D & \end{array}$$

The condition for the process to be energetically allowed is $D \leq 126.2$ kcal/mol, i.e. $D \leq 5.48$ eV. As CO^+ has been formed in the collision with A^+, the CO^+ ion has the initial energy 15.94 eV compared with the ground state of CO. The process *h* will therefore be allowed if dissociation may take place for an energy less than $15.94 + 5.48 = 21.42$ eV. Only by presuming the existence of process *f* can the large cross-section for formation of C^+ in the collisions with A^+ be explained. (As a check the ratio C^+/CO^+ was measured with low velocity of the incident ion and was found to be independent of the velocity. This proves that the initial energy of the CO^+ ion is 15.94 eV and not appreciably higher.) Further we observe that in collisions with Kr^+ C^+ is very weak compared with CO^+, which shows that the energy $14.67 + +5.48 = 20.15$ eV is too low for process *h*.

In this connexion it should perhaps be mentioned that the variation of the cross-sections with pressure shows that process *h* does not occur in the collisions with Ne^+ and Kr^{++} but is of importance in the collisions with F^+, N^+, and O^+.

Summary

The charge exchange in collisions between atomic ions and CO molecules has been investigated. The fragments CO^+, O^+, and C^+ from the molecule have been analysed in a second mass spectrometer. The fragmentation processes are discussed on the

basis of the known ionization potentials of CO and the known appearance potentials of O^+ and C^+. In collisions with Ne^+ the cross-section for formation of C^+ is rather large. As the recombination energy for Ne^+ is 21.6 eV, the fragmentation process must correspond to the appearance potential 20.9 eV for C^+. Previously it has been assumed that in this process an excited O^- ion is formed, but as the primary process in the present experiments is charge exchange, the other fragment must be a neutral O atom. These results support the value 9.605 eV for the dissociation energy of CO and 135.7 kcal/mol for the heat of sublimation of carbon given by LOZIER and HAGSTRUM but, on the other hand, they throw doubt on their assumption concerning the existence of an excited state of O^-.

I wish to express my gratitude to Ing. F. Torstensson for valuable technical assistance.

Department of Physics, Chalmers University of Technology, Gothenburg.

REFERENCES

1. E. LINDHOLM, Proc. Phys. Soc. A *66*, 1068, 1953.
2. E. LINDHOLM, Institute of Petroleum, Conference on Applied Mass Spectrometry, London 1954, in print.
3. E. LINDHOLM, Zeits. f. Naturforsch. *9a*, 535, 1954.
4. E. LINDHOLM, Ark. Fys. 1954, in print.
5. A. G. GAYDON, Dissociation Energies and Spectra of Diatomic Molecules. London 1953.
6. H. D. SPRINGALL, Research *3*, 206, 1950.
7. H. D. HAGSTRUM, Rev. Mod. Phys. *23*, 185, 1951.
8. R. S. MULLIKEN, Rev. Mod. Phys. *4*, 1, 1932.
9. R. S. MULLIKEN, Phys. Rev. *46*, 549, 1934.
10. W. MOFFITT, Proc. Roy. Soc. A *196*, 524, 1949.
11. L. H. LONG and A. D. WALSH, Trans. Farad. Soc. *43*, 342, 1947.
12. G. HERZBERG, Molecular Spectra and Molecular Structure I. Spectra of Diatomic Molecules. New York 1950.
13. T. TAKAMINE, Y. TANAKA, and M. IWATA, Sci. Pap. Inst. Phys. Chem. Res. (Tokyo) *40*, 371, 1943.
14. T. R. HOGNESS and R. W. HARKNESS, Phys. Rev. *32*, 936, 1928.
15. A. L. VAUGHAN, Phys. Rev. *38*, 1687, 1931.
16. J. T. TATE and P. T. SMITH, Phys. Rev. *39*, 270, 1932.
17. H. D. HAGSTRUM and J. T. TATE, Phys. Rev. *59*, 354, 1941.
18. K. N. RAO, Astrophys. J. *111*, 50, 1950.
19. H. BISKAMP, Zeits. f. Phys. *86*, 33, 1933.
20. Y. TANAKA, Sci. Pap. Inst. Phys. Chem. Res. (Tokyo) *39*, 447, 1942.
21. K. N. RAO, Astrophys. J. *111*, 306, 1950.
22. K. N. RAO and K. S. SARMA, Mem. Soc. Roy. Sci. Liège *13*, 181, 1953.
23. H. BULTHUIS, Diss. Groningen, 1935.
24. W. W. LOZIER, Phys. Rev. *46*, 268, 1934.
25. H. D. HAGSTRUM, Phys. Rev. *72*, 947, 1947.
26. A. G. GAYDON and W. G. PENNEY, Proc. Roy. Soc. A *183*, 374, 1945.
27. H. S. W. MASSEY, Negative Ions. Cambridge 1950.
28. J. B. HASTED, Proc. Roy. Soc. A *222*, 74, 1954.
29. H. D. HAGSTRUM, J. Chem. Phys. *16*, 848, 1948.
30. H. S. W. MASSEY and E. H. S. BURHOP, Electronic and Ionic Impact Phenomena. Oxford 1952.
31. C. A. MCDOWELL and J. W. WARREN, Disc. Farad. Soc. *10*, 53, 1951.
32. W. A. CHUPKA and M. G. INGHRAM, J. Chem. Phys. *21*, 1313, 1953.
33. R. E. HONIG, J. Chem. Phys. *22*, 126, 1954.
34. C. A. MCDOWELL, Institute of Petroleum, Conference on Applied Mass Spectrometry, London 1954, in print.

Tryckt den 1 oktober 1954

Uppsala 1954. Almqvist & Wiksells Boktryckeri AB

ARKIV FÖR FYSIK Band 8 nr 43

Communicated 14 April 1954 by MANNE SIEGBAHN and ERIK HULTHÉN

On the determination of the relative intensities of conversion lines recorded photographically in a semicircular beta-ray spectrograph

By HILDING SLÄTIS

With 4 figures in the text

Contents

Introduction 441
1. Earlier investigations 441
2. Relation between photographic density and exposure 443
3. Photographic density as a function of the electron energy 444
4. Conversion line intensity as a function of the position of the line 445
5. A simple method of measuring relative conversion line intensities 446
6. Experimental results 448
Summary 450

Introduction

The semicircular beta-ray spectrograph with photographic recording of the conversion lines provides an accurate and convenient method for the determination of the energy of the conversion lines. The method is especially useful for beta-ray spectra with a large number of lines. For measuring the intensities, however, the photographic method is generally considered not to be very suitable, partly because of the laborious photometric work in connection with the evaluation of the line intensities, and partly because of uncertainty believed to be connected with measurements of this kind. In this paper it will be shown that quite reliable relative intensities are obtained, when the areas under the conversion lines (corrected for the density-exposure relation) are replaced by rectangles, the heights of which agree with the corrected line heights and the widths of which are equal to the true half width of the lines.

1. Earlier investigations

The problem of the determination of the relative intensities of photographically recorded conversion lines has been treated already by ELLIS and WOOSTER[1] in 1927. They point out the importance of studying

---

[1] C. D. ELLIS and W. A. WOOSTER, Proc. Roy. Soc. *A 114*, 266, 729, 1927.

1) the relation between photographic density and exposure,

2) the photographic density as a function of the energy of the electrons,

3) the intensity of the conversion lines as a function of the position of the line (the distance 2ϱ of the line from the source or the distance x of the line from the baffle in the semicircular spectrometer).

ELLIS and WOOSTER tested the SILBERSTEIN[2] formula

$$D = C\,{}^{10}\mathrm{Log}\,(\alpha E + 1) \tag{1}$$

for the photographic density D, defined by

$$D = {}^{10}\mathrm{Log}\,\frac{I_0}{I} \tag{2}$$

where I_0/I is the ratio of the incident to transmitted light passing through the darkened patch. In formula (1) α and C are constants and E the exposure, expressed for instance in millicuries times the number of hours exposure. ELLIS and WOOSTER proved the validity of the equation (1) for a wide range of exposures, corresponding to densities between about 0.2 to 1.5 and for three different $B\varrho$-values of the electrons, viz. 1450, 3055, and 5830. However, as the relative numbers of electrons emerging from the emanation tube were unknown, the problem 2), the photographic density as a function of the energy of the electrons, was not solved.

The relative photographic sensitivity of an emulsion for electrons of different energy was earlier studied by ARNOULT.[3] ARNOULT used Ilford plates for X-rays (the same plate was used by ELLIS and WOOSTER) and found a maximum sensitivity at about 1100 gauss cm (97 keV).

v. BORRIES[1] made density measurements for electron energies of 12.8–220 keV as a function of the number of electrons—or, more correctly, as a function of the electron charge per cm^2. A large number of emulsions were investigated. It may be mentioned that for 16×10^{-12} coul./cm^2 he found for Perutz Peromnia, Perutz Persenso, Agfa Isopan SS, Agfa Normal and Agfa Mikro at 95 keV densities of 0.18–0.28.

Also BAKER, RAMBERG, and HILLIER[5] have similar results on the investigated emulsions. For Eastman Lantern Slide, Medium, the maximum sensitivity was at about 95 keV. From Fig. 5 in the quoted work we find that the density $D = 0.49$ was obtained for the charge of about 1.3×10^{-12} coul/cm^2.

A beam of monoenergetic electrons emitted from a sample cause a higher density for small ϱ-values (strong field) than for large ones (weak field), because the beam for the higher ϱ-value is spread over a larger area of the focal plane. In order to measure the relative intensities of the conversion lines it is necessary to know the ratio $F(\varrho)$ of these monoenergetic electrons hitting a strip of the width l of the film. l is parallel to the magnetic lines of force in the semicircular beta-ray spectrograph and equal to the length of the slit of the photometer, by means of which the photographic density of the line is recorded (see Fig. 4). Now the formulas (1) and (2) are used in order to construct the true line shape, that is the electron density as a function of the location on the film. If the area under this line be A, the relative intensity I of the line is given by

---

[2] L. SILBERSTEIN, Phil. Mag. *44*, 257, 956, 1922; *45*, 1062, 1923.

[3] R. ARNOULT, Ann. de Phys. *12*, 241, 1939.

[4] B. v. BORRIES, Phys. Z. *43*, 190, 1942.

[5] R. F. BAKER, E. G. RAMBERG, and J. HILLIER, J. Appl. Phys. *13*, 450, 1942.

$$I = \frac{A}{\varepsilon_0 \cdot F(\varrho)} \tag{3}$$

where ε_0 is the photographic sensitivity of the electrons considered.

The calculation of the electron density from the photographic density and the integrating process for the areas A are, however, a very laborious work. In addition the integrating process for the weak lines is almost impossible because of the difficulty to distinguish the background on the low energy tail of the line. In order to overcome this difficulty ELLIS and WOOSTER[1] made a curve from the results for the stronger lines, showing the variation with $B\varrho$ of the particles of the ratio of the total area of the line to the density at the peak. From this curve the appropriate ratio was read off for each of the weaker lines, and this when multiplied by the measured density at the peak gave a value of the area, which was considered to be more accurate than that obtained by measuring the area directly. WOOSTER[6] calculated theoretically the ratio of area to peak density, so it vas only necessary to measure the latter in each case. Calculations of the line shape were also made by LI[7]. RUTLEDGE, CORK, and BURSON[8] investigated experimentally the variation of the intensity of an electron line with the corresponding radius of curvature. This variation was dependent upon the choice of using the peak density or the density integrated over a complete line distribution. They found also that the intensity of a section of a beta-spectrum was attenuated at various radii of curvature by the same amounts as that of a peak of an electron line.

2. Relation between photographic density and exposure

The experiments described below belong to the semicircular permanent magnet beta-ray spectrograph described earlier.[9] Ilford Selochrome 120 film was used. Hence it was desirable to get a density calibration for this film and to test the formula (1). Electrons from a ThB (192 μC)-sample passed through a channel of 7 mm width

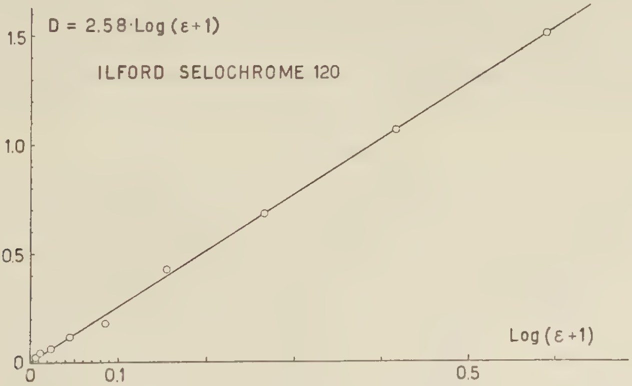

Fig. 1. Relation between photographic density D and electron density ε for Ilford Selochrome 120.

---

[6] W. A. WOOSTER, Proc. Roy. Soc. *A 114*, 729, 1927.
[7] K. T. LI, Proc. Camb. Phil. Soc. *33*, 164, 1937.
[8] W. C. RUTLEDGE, J. M. CORK, and S. B. BURSON, Phys. Rev. *86*, 775, 1952.
[9] H. SLÄTIS, Rev. Sci. Instr. *24*, 464, 1953; Arkiv f. Fysik *6*, 415, 1953.

between lead blocks of 5 cm thickness and hit the film (6 cm away from the sample), which was moved in steps of 19 mm length between each exposure. Fig. 1 shows the experimental points and the theoretical curve

$$D = 2.58\,{}^{10}\mathrm{Log}\,(\varepsilon + 1), \tag{4}$$

where $\varepsilon = \alpha E$. For ε we shall use hereafter the denomination "electron density". Fig. 1 shows that the validity of the formula (4) is very good, in any case for higher densities. The deviations for lower values depend upon the difficulty in determining the height of the photometer peaks because of the background "noise" originating in the grains in the emulsion. The photometer records were taken with the same narrow slit as used for the conversion lines. Of course a separate investigation with a wider slit can be made, but photometer records of conversion lines with lower density than about 0.1 were usually not made.

3. Photographic density as a function of the electron energy

In order to study the photographic density as a function of the energy of the electrons a special device was made. In the circular focus of a lens spectrometer a baffle with a circular hole of 6 mm diameter was placed. Behind this a Geiger-Müller-counter was situated, and alternatively a film could be inserted between the baffle and the GM-counter. The film could be moved from the outside of the spectrometer and eight different places of the film could be exposed for electrons of different energies. For this calibration ThB was used. The intensities of the electron beams, measured by means of the GM-counter, were corrected for the resolving time of the circuits and for the thickness of the GM-counter window. Table 1 and Fig. 2 show the result (mean of two different runs). The maximum sensitivity at about 80 keV or 1000 gauss cm corresponds to a range of the electrons equal to the thickness of the emulsion or a little more. It should be mentioned that the angle between the beam of incident electrons and the normal to the emulsion surface was 30° in these calibration experiments. The thickness of the emulsion was about 18 μ, hence the length of a straight electron path 30° to the normal should be 20.8 μ. This range corresponds to about 60 keV energy.[10] Considering the increase of the path length due to scattering, the

Table 1

Position on the film	Momentum of the electrons gauss cm	Energy of the electrons keV	ε_0 for 10^7 electrons per cm^2	D for 10^7 electrons per cm^2
1	400	14	0.036	0.041
2	600	31	0.225	0.23
3	800	53	0.477	0.44
4	1200	114	0.508	0.463
5	1600	190	0.421	0.395
6	2400	372	0.372	0.356
7	4000	793	0,303	0.300
8	6000	1 359	0.269	0.269

---

[10] B. GAUTHÉ anf J. M. BLUM, C. R. *234*, 2189, 1952.

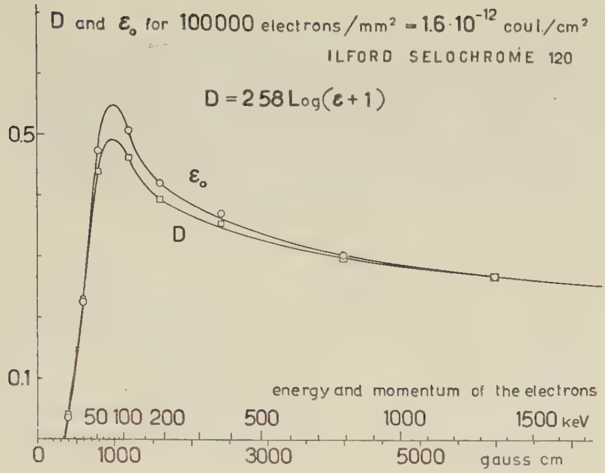

Fig. 2. Photographic density as a function of electron energy and electron momentum.

mean range of the electrons just stopping in the emulsion is of course larger than 20.8 μ—hence the sensitivity maximum does not appear at 60 keV but a little higher, viz. 80 keV according to our experiments.

The curve obtained by ARNOULT (loc. cit.) is similar to those in Fig. 2. The Ilford Selochrome films are coated with a thin protecting cellulose layer. Therefore the curves in Fig. 2 do not go through origo.

A comparison of the sensitivity of the Ilford Selochrome film with those of the emulsions used by v. BORRIES (loc. cit.) and BAKER *et al.* (loc. cit.) shows that the Ilford Selochrome 120 film is about twice as sensitive as the films used by v. BORRIES and that it has about the same sensitivity as the emulsions of BAKER *et al.*

4. Conversion line intensity as a function of the position of the line

The ratio $F(\varrho)$ of monoenergetic electrons hitting a strip of the width l of the film (Formula (3)) will simply be inversely proportional to ϱ if the defining edges of the

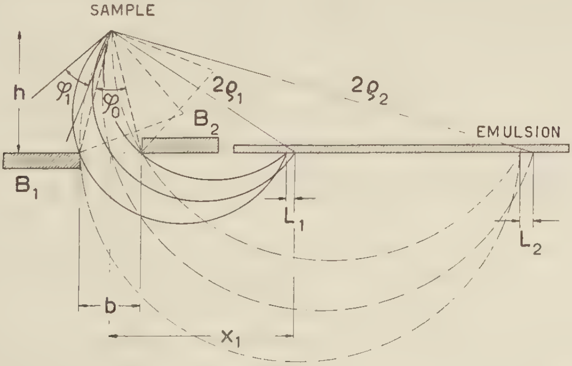

Fig. 3. Arrangement of baffle B_1B_2 and emulsion in order to get a constant angle $\varphi_1 - \varphi_2 = \varphi_0$ of effective electrons.

baffle $B_1 B_2$ (Fig. 3) are in the same plane as the emulsion. The electron paths for two different magnetic fields are illustrated and give rise to lines of the total extension L_1 and L_2. It is easily seen that the angle φ_1, which describes the width of the beam in the first case ($\varrho = \varrho_1$), is equal to the angle φ_0 under which the baffle $B_1 B_2$ is seen from the wire. Hence the angle φ is independent of ϱ and the number of electrons hitting the emulsion surface areas A_1 and A_2 will be the same, if the widths of the areas are L_1 and L_2, respectively, and the heights l_1 and l_2 are proportional to ϱ_1 and ϱ_2 (the heights l_1 and l_2 are normal to the figure plane used in Fig. 3).

For practical reasons we have to use equal heights l for the areas A_1 and A_2. When the field strength varies, the number of monoenergetic electrons hitting the rectangle lL (l = constant, L is a function of φ and ϱ) is proportional to l/ϱ.

In order to measure the relative intensities of conversion lines from photometer records of photographic films we have first to change the densities for the different points on the photometer curves to the corresponding electron densities according to formula (4) and then to integrate the areas under the ε-curves. If these areas be A, then the relative intensities I of the conversion lines are given by

$$I = A \cdot \varrho \cdot \frac{1}{\varepsilon_0} \qquad (5)$$

where ε_0 is obtained from the energy-sensitivity calibration curve in Fig. 2.

5. A simple method of measuring relative conversion line intensities

We have already pointed out in 1 the difficulties connected with the integrating process for the areas A. The usefulness of an exact method will be illusory if the quantities needed are experimentally not sharp, as in this case the extension of the low energy part ("tail") of the conversion line. In addition, the ELLIS-WOOSTER method of using the ratio of area to peak density for weak lines does not take into account the existence of an inherent half-width of the conversion lines [9, 11], different for the K- and the L-lines. In order to overcome these difficulties the following method was introduced.

The line shape, different for different sources, does not vary very much for different values of ϱ. Instead of the area under the intensity-distribution curve for a line, a rectangle is taken, the height of which is equal to the top of the intensity distribution line and the width of which is equal to the true half-width of the line. By comparing this rectangular area with the integrated values of line shapes computed by LI (loc. cit.) it is found that the rectangle is 18 % smaller than the integrated value for a circular wire source and 10 % larger than that for a flat plate. It is, however, to be expected that the *change* for different $B\varrho$-values (different ϱ-values) but the same source is much smaller and probably smaller than the experimental errors in the photometer work.

Fig. 4 shows a part of a film obtained with the semicircular permanent magnet beta-ray spectrograph. In order to get an expression for the intensity of a line G we take photometer records of the areas a and b indicated in the figure. The orientation of the light slit of the photometer and the direction of moving the slit are also illustrated. At the beginning and at the end of each record the light through the photo-

---

[11] H. SLÄTIS and G. LINDSTRÖM, Phys. Rev. *88*, 1929, 1952.

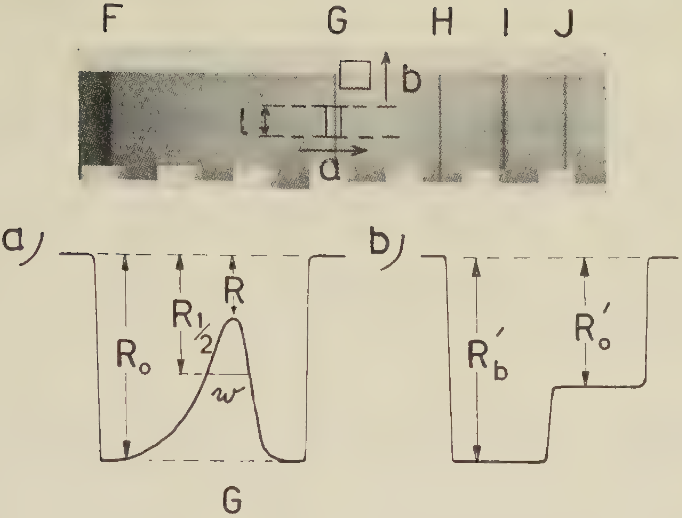

Fig. 4. Photometer records of (*a*) a conversion line *G* and (*b*) the continuous background near the line.* Quantities to be measured in order to get the true half-width *w* and the electron density difference between the top and the background of the conversion line.

meter slit is interrupted by inserting a thin steel sheet in the beam (this gives the upper levels in the records *a* and *b*, Fig. 4). The galvanometer deviations R, R_0 and R_b correspond to light through the top of the line, the continuous spectrum near the line, and the unexposed border of the film, respectively (the strength of light used in *a* is preferably higher than that in *b*). Obviously

$$R_b : R_0 = R_b' : R_0'. \tag{6}$$

From (1), (2), (4) and (6) we get

$$\left.\begin{aligned} \operatorname{Log}\frac{R_b}{R_0} &= \operatorname{Log}\frac{R_b'}{R_0'} = C \operatorname{Log}(E_0+1) \\ \operatorname{Log}\frac{R_b}{R} &= C \operatorname{Log}(E+1) \end{aligned}\right\} \tag{7}$$

and hence

$$\operatorname{Log}\frac{R_0}{R} = C \operatorname{Log}\left(\frac{E-E_0}{E_0+1}+1\right) \tag{8}$$

if E_0 and E are the electron densities near the line, and at the top of the line, respectively. If for brevity we put

$$\varepsilon' = \frac{E-E_0}{E_0+1} \tag{9}$$

the galvanometer reading $R_{1/2}$, which corresponds to the true half-width w of the line, is found from the formula

---

* The arrow near *b* should have the opposite direction.

$$\text{Log}\,\frac{R_0}{R_{1/2}} = C\,\text{Log}\left(\frac{\varepsilon'}{2}+1\right). \tag{10}$$

The expression for the relative intensity of a conversion line will now be, instead of (5), the following

$$I = w(E-E_0)\frac{\varrho}{\varepsilon_0} = w\varepsilon'(E_0+1)\frac{\varrho}{\varepsilon_0}. \tag{11}$$

The quantities ε' and E_0 are conveniently found in the following manner.

Curves are constructed for E as a function of R_b/R. These curves are the same for E_0 as a function of R_b/R_0, for ε' as a function of R_0/R and for $\varepsilon'/2$ as a function of $R_0/R_{1/2}$.

For a given R_0/R (Fig. 4 a) the curves give the corresponding value ε'. This quantity is divided by 2 and the curves again used for the determination of $R_0/R_{1/2}$. When R_0 is divided by this ratio, $R_{1/2}$ is obtained and then w is found diagrammatically (Fig. 4 a). E_0 is obtained from the ratio $R_b/R_0 = R_b'/R_0'$ (Fig. 4 b) when the curves mentioned above are used again.

ϱ is easily obtained from the position of the line (see also ref. (9)) on the film and ε_0 from Fig. 2.

6. Experimental results

The validity of the above considerations was tested in different ways, using ThB as a source. The F-line was recorded by two different magnetic fields, $B_1 = 96.8$ gauss and $B_2 = 252$ gauss, corresponding to ϱ-values of 143 and 55 mm, respectively. Six films were exposed, three films for each field strength. The theoretical intensities I were computed according to (11) and compared with the rate of exposure, calculated from the formula

Table 2

Number of film	ϱ cm	50 w mm	ε'	E_0+1	Y	$I\cdot$ const.	$Q\cdot$ const.	I/Q	Mean value minus I/Q	Diff. in %
188	14.3	18.3	0.97	1.089	1.034	19.29	6.14	3.14	0	0
189	14.3	14.0	0.568	1.028	1.034	8.16	2.61	3.13	0.01	0
190	14.3	12.3	0.288	1.006	1.034	3.57	1.13	3.14	0	0
Mean value								3.14		
193	5.5	16.4	0.936	1.119	1.112	6.13	1.97	3.11	0.01	0
194	5.5	8.9	0.435	1.046	1.112	1.44	0.43	3.34	−0.22	−7
195	5.5	19.6	1.119	1.200	1.112	9.4	3.24	2.90	+0.22	+7
Mean value								3.12		

Table 3

mber film	Line	R_0/R	ε'	50 w mm	R_b/R_0	E_0+1	ϱ cm	ε_0	Y	Intensity $\frac{\varepsilon' w (E_0+1)\varrho}{\varepsilon_0 Y}$	F/I	Mean value F/I	Diff. in %
91	F	4.39	0.783	10.6	1.35	1.123	9.3	0.45	1.046	184.2	7.67	−0.88	−13
	I	1.847	0.269	2.8	1.30	1.107	11.7	0.406	1.000	24.0			
100	F	3.52	0.628	10.7	1.21	1.076	9.3	0.45	1.046	143	6.71	0.08	1
	I	1.515	0.174	3.95	1.21	1.076	11.7	0.406	1.000	21.3			
101	F	3.59	0.641	9.8	1.28	1.100	9.3	0.45	1.046	136.6	7.38	−0.59	− 9
	I	1.676	0.222	2.6	1.33	1.117	11.7	0.406	1.000	18.5			
193	F	0.936	16.4	1.119	5.5	1.112	5.5	0.45	1.112	189	6.04	0.75	11
	I	0.285	6.5	1.062	7.0	1.085	7.0	0.406	1.085	31.3			
194	F	0.435	8.9	1.046	5.5	1.112	5.5	0.45	1.112	44.4	6.46	0.33	5
	I	0.068	6.2	1.02	7.0	1.085	7.0	0.406	1.085	6.87			
195	F	1.119	19.6	1.200	5.5	1.112	5.5	0.45	1.112	289	6.25	0.54	8
	I	0.406	6.5	1.103	7.0	1.085	7.0	0.406	1.085	46.2			
196	F	2.474	25.0	1.77	5.5	1.112	7.5	0.45	1.112	1 202	6.08	0.71	10
	I	0.856	11.1	1.31	7.0	1.085	7.0	0.406	1.085	198			
197	F	2.208	30.0	3.39	5.5	1.112	5.5	0.45	1.112	2 470	7.72	−0.93	−14
	I	1.02	13.2	1.50	7.0	1.085	7.0	0.406	1.085	320			
										Mean value	6.79		

$$Q = B\left[1 - \frac{1}{e^{0.693 \cdot \frac{t}{T}}}\right], \tag{12}$$

where B is the strength of the sample at the beginning of the exposure, T the half-life of the activity and t the time of exposure. If (11) is correct, then I/Q should be a constant.

Table 2 shows the result for the 6 films mentioned above. Y is a correction for a small error arising from the fact that the edges of the baffle $B_1 B_2$ (Fig. 3) were not exactly in the same plane as the emulsion. The expression (11) was divided by Y. The agreement between the I/Q-values for the two quite different positions of the F-line shows that the l/ϱ-expression for $F(\varrho)$ is correct. The same was found for another series of 22 films, 11 films for each field. The mean I/Q-ratio was found to be 3.43 and 3.44, respectively. In this case, however, the vacuum was not controlled, and therefore a larger spread in the different I/Q-values was observed.

The formula (11) was then tested for the intensity ratio of the conversion lines F and I in the beta-spectrum of ThB. Table 3 shows the result.

The mean error in one measurement of the intensity ratio is consequently about 11 %. For very strongly exposed films the intensity ratio determination is of course more difficult and the error may be 20 % in a single determination. The results for

Table 4. Relative intensity of some RaB conversion lines.

Line	Number of film			Weighted mean (author)	ELLIS	Diff. in %
	204	207	214			
F	425	425	425	425	425	–
G	462	422	510	476	480	+1
H	479	448	550	507	530	+4
I	81	81	94	87	85	−2
Weight	1	1	2	4		

the series in Table 3 give the mean value $F/I = 6.8 \pm 0.3$. The probable error in the experimental value 6.8 is $\pm 2.5\,\%$. ELLIS[12] found the intensity ratio $F:I = 7.1$.

In order to study the agreement between other intensity determinations made by ELLIS[13] and by the author the *F*, *G*, *H* and *I* lines in the spectrum of RaB were measured on three films. These lines were of particular interest because they were situated in widely different parts of the films. Table 4 shows the results obtained.

It may be seen that the agreement is very good. Again, in single measurements there may appear differences of $\sim 12\,\%$, but the mean values are very reliable.

The present method was used for the intensity determination of a large number of conversion lines in the beta spectrum of RaB and RaC.[14]

The author is indebted to Dr. MILORAD MLADJENOVIĆ for his stimulating discussions and suggestions on the question of intensity determination of photographically recorded conversion lines.

Summary

1. In order to compare the relative intensities of photographically recorded conversion lines the density-exposure relation, the density-energy relation and the density-radius relation were studied.

2. It is shown that reliable results are obtained when instead of the integrated areas of the conversion lines (photometrically recorded and changed to electron density curves) the product is taken of the true half-width and the electron density difference between the top and the background of the line.

3. The method developed is tested on conversion lines in the beta spectra of ThB and RaB.

Nobel Institute of Physics, Stockholm 50, Sweden.

---

[12] C. D. ELLIS, Proc. Roy. Soc. *A 138*, 318, 1932.
[13] C. D. ELLIS, Proc. Roy. Soc. A. *143*, 350, 1934.
[14] M. MLADJENOVIĆ and H. SLÄTIS, Arkiv f. Fysik *8*, 65, 1954.

Tryckt den 3 november 1954

Uppsala 1954. Almqvist & Wiksells Boktryckeri AB

ARKIV FÖR FYSIK Band 8 nr 44

Communicated 2 June 1954 by G. Borelius and H. Alfvén

Experiments with an ion source having magnetic analysis of the ion beam

By Lars Beckman

With 2 figures in the text

Introduction

The ion sources most often used for production of proton or deuteron beams in high voltage accelerators are the high frequency source, the low voltage arc source, and the magnetic source. In the high frequency source[1-2] the output of atomic ions is 80–90 % of the total output. In the low voltage arc source[3] the corresponding figure is only 15–20 %. The magnetic source uses extraction of the ions either in the direction of the magnetic field[4 6], or transverse to the field[7-8]. The maximum obtainable atomic ion percentage is about 80 %.

Another arc source with a very high atomic ion percentage (98 %) has been developed[9], but because it needs cooling of the cathode and a rather high pressure (0.3–0.4 mm Hg) it is not suitable for use in accelerators.

In order to increase further the relative output of atomic ions a magnetic analyser may be introduced. To place this analyser before the accelerating tube is advantageous with regard to the load on both the high voltage generator and the tube.

The ion beam from the source is accompanied by a beam of neutral atoms and molecules.[10 11] These will produce secondary electrons in the tube when they impinge on the electrode surfaces. By passing the beam through a magnetic analyser the number of neutral particles in the beam will decrease and so the production of secondary electrons in the tube is reduced.

A magnetic ion source is described here in which the ions are extracted at right angles to the magnetic field which is also used for analysis of the beam.

---

[1] Thonemann, P. C., Moffatt, J., Roaf, D. and Sanders, J. H., Proc. Phys. Soc. *61* (1948) 483.

[2] Swann, C. P. and Swingle, J. F., Rev. Sci. Instr. *23* (1952) 636.

[3] Zinn, W. H., Phys. Rev. *52* (1937) 655.

[4] Finkelstein, A. T., Rev. Sci. Instr. *11* (1940) 94.

[5] Bailey, C., Drukey, D. L. and Oppenheimer, F., Rev. Sci. Instr. *20* (1949) 189.

[6] Kistemaker, J., Dekker, H. L. D., Physica *16* (1950) 198.

[7] Heil, H., Z. Phys. *120* (1943) 212.

[8] Kistemaker, J. and Zilverschoon, C. J., Physica *17* (1951) 43.

[9] Lamar, E. S. and Luhr, O., Phys. Rev. *46* (1934) 87.

[10] Inall, E. K., Proc. Phys. Soc. *63* (1950) 1068.

[11] Amdur, I. and Pearlman, H., J. Chem. Phys. *8* (1940) 7.

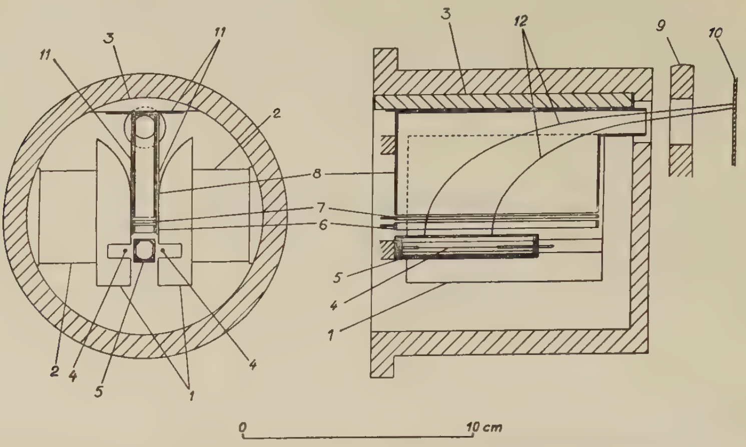

Fig. 1. Arrangement of the ion source. 1, Pole-pieces. 2, Permanent magnets. 3, Iron segment. 4, Cathodes (0.2 mm tungsten wires). 5, Anode (copper). 6, Extraction electrode. 7, Focusing electrode. 8, Accelerating electrode. 9, Diaphragm. 10, Collector. 11, 0.5 mm mica sheets. 12, Ion trajectories in the symmetry plane.

Focusing properties of analysing fields

The ion source is shown in Fig. 1. A magnetic field is obtained in the gap by means of permanent magnets, 2. The cathodes, 4, the pole-pieces, 1, and the iron enclosure are at ground potential. The anode, 5, is at positive potential and the extracting and accelerating electrodes, 6–8, are negative with respect to the anode.

The electrons emitted from the cathode will oscillate in the direction of the magnetic field and ionize the gas inside the anode. Ions are extracted by the electric field of the extracting electrode and are deflected by the magnetic field. Those ions which have a suitable charge-to-mass ratio e/m will reach the exit hole, while ions with smaller e/m will not be deflected enough and those with larger e/m will travel in approximately cycloidal paths.

A rectangular coordinate system is fixed in such a way that the electric and magnetic fields have no gradients in the z-direction except in the region of the outlet. In the symmetry plane $y=0$ the electric field is parallel to the x-axis and the magnetic field is parallel to the y-axis.

The equations of motion for an ion leaving the discharge at $z=z_0$, $x=0$ in the symmetry plane are

$$\frac{m}{2}(\dot{x}^2+\dot{z}^2) = -e(V_0+V_x) \tag{1}$$

$$m\dot{z}+eA_0 = mv_z \tag{2}$$

as the energy and the generalised momentum in the z-direction are constants of the motion. V_0 is the electric potential in the symmetry plane and A_0 is the z-component of the magnetic vector potential in the symmetry plane, the other components being zero. ($V_0 = A_0 = 0$ for $x = 0$.) The initial velocity in the z-direction is denoted by v_z and the initial x-directed kinetic energy by $-e\,V_x$. Combinations of the equations will give, in the case $v_z = V_x = 0$,

$$z - z_0 = \int_0^x \left(-\frac{2\,m\,V_0}{e\,A_0^2} - 1\right)^{-\frac{1}{2}} d\,x. \tag{3}$$

This trajectory will be an asymptote to the line $x = h$ provided

$$\frac{d}{d\,x}\left(\frac{V_0}{A_0^2}\right) = 0; \quad -\frac{2\,m\,V_0}{e\,A_0^2} = 1 \tag{4}$$

when $x = h$. The first condition is satisfied by making V_0 constant in the neighbourhood of $x = h$ and by letting the magnetic field tend to zero as $x \to h$.

Thus it is seen that ions emitted with zero velocity from a narrow slit with length L in the z-direction are focused into a ribbon-shaped beam with the width $L\frac{d\,x}{d\,z}$ in the x-direction. It is then possible to use a large aperture, which is profitable with regard to the intensity of the ion beam.

To get an estimate of the focusing properties, the potential functions are approximated in the following way. V_0 is simplified to a step-function which at $x = 0$ increases from zero to its final value, and A_0 is assumed to be

$$A_0 = -\sqrt{-\frac{2\,m\,V_0}{e}}\sin k\,x, \quad \left(k = \frac{\pi}{2\,h}\right).$$

When the initial velocity is small compared to the final velocity the equation for the trajectory is

$$k\,(z - z_0) = -\log\cos k\,x + \frac{z_0'}{2}\left[\frac{\sin k\,x}{\cos^2 k\,x} + \log\operatorname{tg}\left(\frac{\pi}{4} + \frac{k\,x}{2}\right)\right] \tag{5}$$

where small terms of higher order than the first are omitted. z_0' is the initial inclination towards the plane $z = z_0$.

The y-directed motion of an ion in the neighbourhood of the symmetry plane is governed by the equation

$$m\,\ddot{y} - e\,\dot{z}\frac{\partial A}{\partial y} = 0,$$

where A is the magnetic vector potential outside the symmetry plane. Equation (5) is still valid for the x- and z-coordinates of the path, as for small y

$$A = A_0 - \frac{y^2}{2}\frac{d^2 A_0}{d\,x^2}.$$

Introducing z as independent variable instead of the time by means of (2) with $v_z = 0$, and making use of (5), the equation is transformed to

$$\frac{d^2 y}{d z^2} + k \frac{e^{-2kz}}{1 - e^{-2kz}} \frac{dy}{dz} + k^2 y = 0. \tag{6}$$

For small values of z the solution is

$$k y = \sqrt[4]{k z}\,[1.52\, y_0' \, J_{\frac{1}{4}}(kz) + 1.03\, k y_0 \, J_{-\frac{1}{4}}(kz)] \tag{7}$$

which may be taken as an approximate solution of (6) in the whole region considered. y_0 is the initial y-value and y_0' the initial inclination of the trajectory towards the symmetry plane.

Because of the strong focusing action of the electric field between the anode and the extracting electrode the beam has a cross-over near $x = 0$ and so the first term in (7) will describe the motion. This term has its first maximum for $kz = 1.06$ ($k y_{\max} = 1.14\ y_0'$), which is inside the source, and its first zero for $kz = 2.78$, which is outside the source.

The beam leaving the source is thus convergent in the y-direction but may in part be divergent in the x-direction, depending on the value of z_0', that is to say on the relation between the ionic temperature in the discharge and the final energy of the beam.

Experimental results

The ion source was connected to a vacuum system and hydrogen was admitted by a fine control needle valve. The output current was collected by an electrode, 10, as shown in Fig. 1, and between the collector and the source was inserted a diaphragm, 9, which was 150 volts negative relative to the collector and the accelerating electrode, 8. This diaphragm prevented secondary electrons from leaving the collector and also stopped secondary electrons from the source from reaching the collector.

The collector current as a function of the accelerating voltage measured relative to the anode is shown in Fig. 2. In this case the arc voltage was 85 volts and the arc current 0.4 amp. The focusing electrode, 7, was connected to the accelerating electrode, 8.

Fig. 2 shows current peaks at 1370 and 2600 volts. To identify the ions responsible for the peaks equation (4) is used. The value of A_0 for $x = h$ is equal to the magnetic flux per unit length in the z-direction passing between $x = 0$ and $x = h$ in the symmetry plane. This flux was measured to 7500 gauss · cm (the maximum value of the magnetic field was 2000 gauss). Inserting this value in equation (4) gives $V_0 = 1340$ volts for H_2^+ and 2680 volts for H_1^+. The current peaks then consist of H_2^+ and H_1^+ respectively. There is also a slight indication of H_3^+ at 900 volts and a small peak at 180 volts probably due to N_2^+.

The ratio between the half-value widths of the peaks on a voltage scale and the accelerating voltages at peak current is 0.29, for both H_1^+ and H_2^+. If the initial energy spread were negligible this figure should be 0.10, according to theory, and if the initial energy were responsible for the broadening of the peaks then the relative width of the H_1^+ peak should be half of that for H_2^+. This indicates that the large peak-widths are mainly due to disturbances in the analyzing fields and not to energy spread.

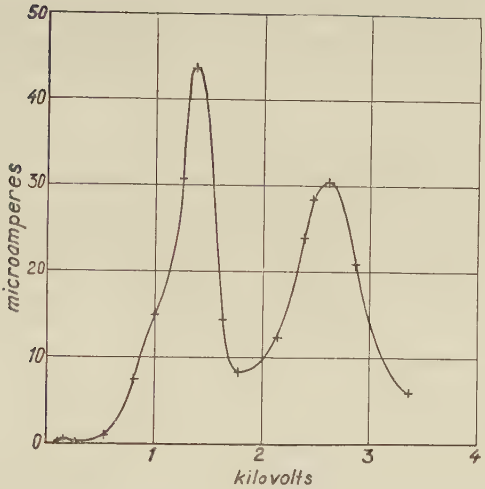

Fig. 2. Output current as a function of accelerating voltage.

The beam has a rectangular cross-section when impinging on the collector. The width in the y-direction is 2–3 mm and in the x-direction about 12 mm. This agrees with the theoretical results obtained above for the y-directed focusing.

During the measurements shown in Fig. 2 the pressure was about $5 \cdot 10^{-3}$ mm Hg. The current to the accelerating electrode was 3.25 ma at the H_2^+ peak and 4.1 ma at the H_1^+ peak. The voltage of the extracting electrode, 6, was 100 volts and 500 volts negative with regard to the anode, respectively. The output current and the current to the accelerating electrode both increase with decreasing pressure until the limit for stable arc operation is reached, at about $5 \cdot 10^{-3}$ mm Hg. The current to the extracting electrode decreases with decreasing pressure. This is probably due to improved y-directed focusing caused by a deeper penetration of the extracting field through the anode slit when the pressure is lowered.

When the pressure is reduced so much that the arc goes out the arc current drops to a very low value. The output current of H_1^+ is in this case reduced to about one fifth of the H_2^+ current, which was found to be 6.5 μa at an arc current of 2.4 ma, arc voltage 400 volts.

The current to the accelerating electrode was 4.1 ma at the H_1^+ peak. This current includes secondary electrons and it is resonable to say that the ion current was 2 ma. About one-third of this is protons and about 80 % of the protons are lost due to inelastic scattering. (The mean free path for H_1^+ is 7 cm at $5 \cdot 10^{-3}$ mm Hg and the length of the path about 12 cm.) There remains 130 μa compared to the output current of 30 μa. In order to reduce this current loss the focusing electrode, 7, was inserted, but it had a negligible effect. This electrode will give an improved y-directed focusing if it is held at either several kilovolts negative potential with regard to the accelerating electrode or at a positive potential relative to the anode. In the latter case the trajectories shown in Fig. 1 (12) will be pushed towards the exit hole and so an increasing amount of ions will be captured by the edge of the exit hole. The other possibility, to hold the focusing electrode at a high negative voltage, could not be realized because of insulation breakdown. The source is being developed further.

ACKNOWLEDGEMENT

This work has been carried out at *Försvarets forskningsanstalt,* Stockholm. The permission of the Director of the Institute to publish this paper is gratefully acknowledged.

Tryckt den 3 november 1954

Uppsala 1954. Almqvist & Wiksells Boktryckeri AB

ARKIV FÖR FYSIK Band 8 nr 45

Communicated 14 April 1954 by ERIK HULTHÉN and G. BORELIUS

The group velocity of light in glass and calcite

By ERIK BERGSTRAND

With 1 figure in the text

Introductory survey

Regarding the propagation of light in media, in contrast to a vacuum, one has to consider the wavelength. At normal dispersion, the velocity increases with the wavelength and one has never to handle a single sine wave. There is no fully monochromatic source of light. The start of an oscillation or the damping of it destroys the sine form. Further, the Doppler effect will always be present in some degree and split the wavelength into several adjacent components. These will interfere and thus there arises the resulting wave as a sum of the components. In the following expression, which may be found in any textbook, there is the resultant y of two slightly different waves with equal amplitudes A:

$$y = A \cdot \sin \frac{2\pi}{\lambda_m}(v \cdot t - x) + A \cdot \sin \frac{2\pi}{\lambda_m + d\lambda_m}[(v + d\,v) \cdot t - x] \tag{1}$$

λ_m and $\lambda_m + d\lambda_m$ are the wavelengths in the medium, v and $v + dv$ are the corresponding wave velocities. The propagation proceeds along the x-axis and x is the distance from the source. Time is denoted t.

After summation in Eq. (1) we can consider $d\lambda_m$ small enough compared to λ_m to write $\lambda_m \cdot (\lambda_m + d\lambda_m) = \lambda_m^2$ and get

$$y = 2A \cdot \cos \frac{2\pi \cdot d\lambda_m}{2\lambda_m^2}\left(\frac{v \cdot d\lambda_m - \lambda_m \cdot dv}{d\lambda_m} \cdot t - x\right) \cdot \sin \frac{2\pi}{\lambda_m}(v \cdot t - x). \tag{2}$$

In Eq. (2) everything left of the sin is the amplitude of the light. The amplitude varies with a beat frequency, the wavelength or the "group" of which is $\frac{2\lambda_m^2}{d\lambda_m}$. The speed of the group is

$$\frac{v \cdot d\lambda_m - \lambda_m \cdot dv}{d\lambda_m} = v - \frac{dv}{d\lambda_m} \cdot \lambda_m = u. \tag{3}$$

Since u is the velocity of the amplitude *it is the velocity of the energy.* Of u and v, in a number of fundamental experiments, only one is available to observation and it is desirable to get hold of the other. Hence, the validity of Eq. (3) is of great importance. RAYLEIGH [1] was the first to derive this equation.

Introducing in Eq. (3) the refractive index $n = \frac{c}{v}$ and the vacuum wave length $\lambda = n \cdot \lambda_m$ we get

$$\frac{c}{u} = n - \frac{dn}{d\lambda} \cdot \lambda = n_g. \qquad (4)$$

If $n < 1$, or the phase velocity $> c$, the negative quantity $\frac{dn}{d\lambda}$ will be numerically large enough to keep $\frac{c}{u} > 1$ according to the theory of relativity. In the very limit of anomal dispersion the light energy is rapidly absorbed. Therefore, Eq. (4) is not valid for this special case and does not express the speed of the energy transport. In a vacuum $\frac{dn}{d\lambda} = 0$ and $u = v = c$.

With one exception, all direct terrestrial determinations of the velocity of light are carried out in air. Then we get the value u, which is corrected according to Eq. (4) for vacuum. The validity of Eq. (4) is verified by MICHELSON [3] for carbon disulfide and by HOUSTOUN [4] for water. As far as I know there are no determinations for gases or solids. On account of c the group correction for air is of great interest and is intended to be the subject of a special investigation later on. Among the solids the crystals attract particular attention because of Huygens' wave velocity surfaces.[1]

The following is a description of some determinations of the group velocity in glass and in different directions of a calcite crystal. The method is based on Fizeau's principle for the determination of the velocity of light. The light modulator is formed of the standing supersonic wave grating, erected in a piezo-quartz crystal vibrating on a high harmonic. This type of modulator for the determination of the velocity of light was first mentioned by BERGMANN [5] and was later used by HOUSTOUN [6]. The 0-positions of the reflecting mirror were obtained by visual observation of the minimum of light intensity. In the present apparatus the 0-position is determined by observation of a zero-passage of the high frequency light intensity amplitudes. This minimum is much more sharply defined than that of the mean light intensity. The following schematic figure shows the disposition of the different parts.

Figures in mm denote the rough dimensions. By the condenser L_1 an image of the glowing spiral of the light source LS is thrown through the semi-transparent mirror SM into a 0.7 mm aperture D_1 in the sooted metal screen S_1. The lens system L_2 parallels the light through the swing quartz crystal K, the optic axis of which is parallel with the beam of light. The objective L_3 again astringes the light to a spot on the sooted screen S_2. By its 150 Mc the short wave radio transmitter RT_1 keeps the crystal K swinging on the 209th harmonic. The erected standing supersonic wave forms and deletes, 3×10^8 times per second, an optic space grating, the compressive and dilative plane layers of which create an intermittent image of the light source. This image, a spectrum of first order, is situated 1.5 mm above the central spot from LS. The spectral image falls into a 0.7 mm aperture D_2. Hence, beyond the screen S_2 we get a beam, mod-

---

[1] JENKINS and WHITE, Fund. of Optics, 2nd ed. 1950, p. 524.

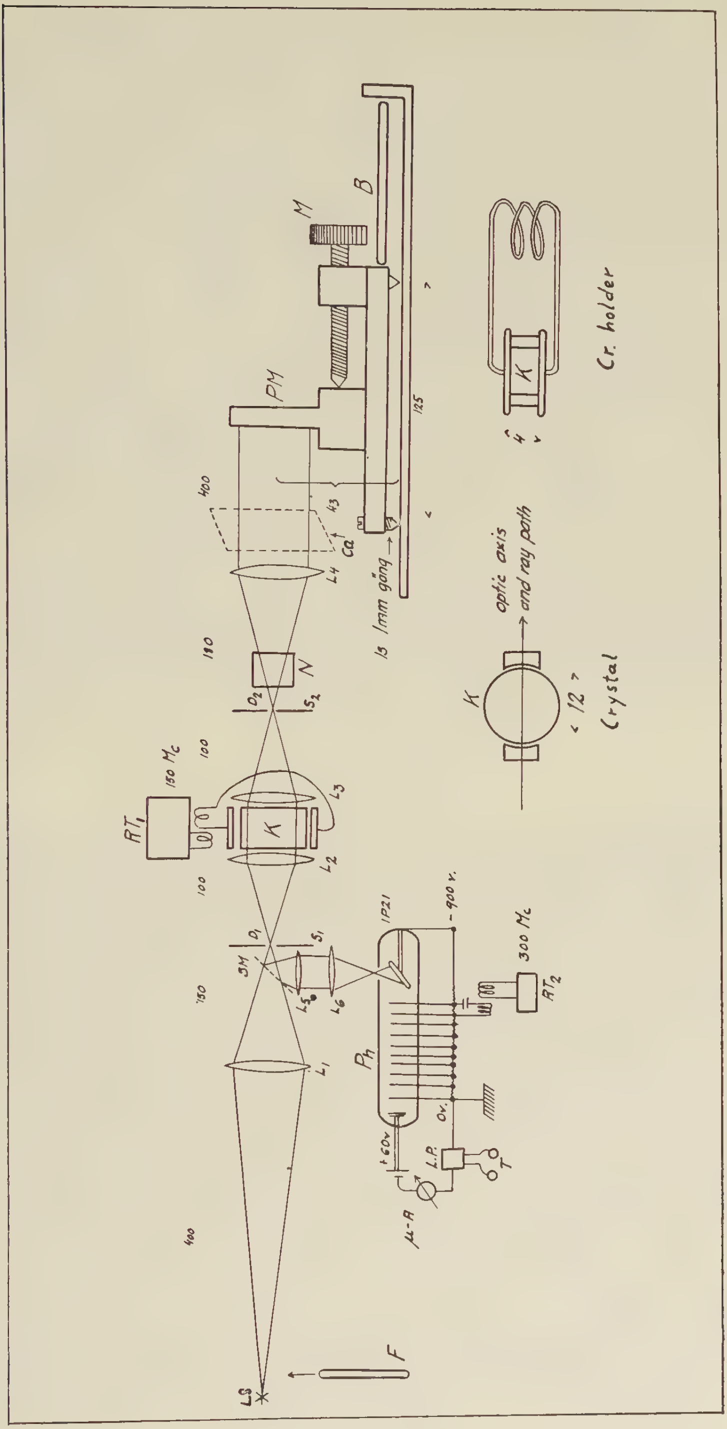
LS
F
400
L1
150
SM
D1
S1
L5
L6
1P21
- 900 v.
300 Mc
RT2
Ph
0v.
+60v
L.P.
T
μ-A
100
L2
K
RT1
150 Mc
L3
100
D2
S2
N
190
L4
Ca
43
400
PM
125
M
B
13 1mm gång
optic axis and ray path
K
12
Crystal
4
K
Cr. holder

Fig. 1.

ulated 100 % with 300 Mc. For certain purposes a Nicol prism N can be inserted here.

By the lens L_4 the beam is paralleled towards the plane mirror PM. The object for investigation can be placed between L_4 and PM. By the graduated micrometer M the mirror can be displaced in the direction of the beam. Further, the complete micrometer can be moved certain fixed distances, the magnitudes of which are determined by a series of iron bars. The position of the bars is denoted B in the figure. By PM the light is thrown back as an image in the aperture D_2, passes the crystal for the second time and will again be reproduced, now on the back of the screen S_1 where the aperture D_1 is just in place of the first order spectrum of the returning beam.

If the mirror PM is situated at such a distance from the crystal K that the returning light and K have a difference in phase of $N \cdot \pi$ ($N =$ integer) in their swinging states, the component 300 Mc will be totally cancelled after this second passage of the aperture D_1. Here the semi-transparent mirror SM directs the beam to the cathode of the photomultiplicator Ph. The tranmitter TM_2 produces an alternating voltage between two of the dynodes of Ph. The frequency is slightly different from the 300 Mc of the light variation. Since the current amplification in Ph is dependent on the dynode voltage, the net result in the presence of any 300 Mc at all of light variation is an audible beat frequency in the telephone T. The harmonics of MT_2, and the light also, give the corresponding acoustic harmonics. They will be stopped by the low-pass filter LP. Thus, a zero-position of the mirror PM occurs at the observed sound minimum in the telephone T. The total photo-current is checked by aid of a μA-meter.

Description in detail

Miscellaneous

The lamp LS uses 4 volts 5 ampere and the dimensions of the wolfram spiral are 1.2×1.2 mm. The lenses $L_1 = L_2 = L_3$ are simple 3-lens photographic antireflex-coated objectives. Their focal distance is 105 mm. To avoid a disturbing reflex the first lens of L_2 has its plane surface turned outwards and slightly inclined. The semi-transparent mirror SM is of the interference type. To avoid reflexes the screens $S_1 S_2$ are sooted and inclined backwards. The apertures D_1 and D_2 are circular and the diameter is 0.7 mm. In L_1 is a diaphragm to limit the beam to a central rectangle on the crystal K. The transmitters TM_1 and TM_2 are crystal-controlled and emit 5 watts of end effect. The frequency of TM_1 is adjusted to fit the 209th harmonic of the modulation crystal K at $+16°$ C of room temperature. One degree of increased temperature decreases the frequency by some 5000 c/s. The frequency of TM_2 is adjustable within certain limits. The alternating voltage from TM_2 is transferred via coil and feeder (interrupted by a condenser stopping the direct voltage) across one of the resistors in the supply potentiometer for the photocell Ph. Ph is an I P21.

The crystal modulator

The crystal K was supplied by Steeg et Reuter. Earlier some trials had been made with a rectangular crystal from the same firm. It was swung easily on its different harmonics. The created grating, however, was irregular and instable. Consequently the zero position of the mirror had the same characteristics. A circular crystal was assumed to be more suitable for a homogenous swinging. The form is now a cylinder, 4 mm in height and 12 mm in diameter. The plane-parallelism of the circular surfaces is of the order of 0.05 μ (according to S. et R.). The optic axis and the passage of light coincide with a diameter. Two addition pieces (detail of the large figure) allow the light to pass the crystal without refraction. The electrodes of the crystal are circular, with a diameter of 15 mm. Crystal and top electrode lie loose on each other on the bottom electrode. Between the addition pieces and the crystal there is a thin layer of apiezon fat, giving better optic contact than air. When the crystal is active and warm, the fat gets flowing and damps the oscillations very slightly on the cylindrical surface. During the very first hours of run the fat flows out on the plane crystal sufaces. On these planes it acts hardly damping and must be removed by ether and a fine brush. After the superfluous fat is removed the rest stays through the surface tension.

The grating in the crystal, swinging on its 209th supersonic, consists of 104.5 compressed and 104.5 dilated planes parallel with the plane ends of the crystal cylinder. The thickness of K being 4 mm, the grating constant will be $d=\frac{4}{104.5}$ mm. The crystal is slightly inclined towards the incident light, which is reflected by the compressed planes analogous to röntgen light in the atom planes of a crystal. Light from the different planes has an equal phase and yield maximum of reflected intensity. The reflecting angle θ is given by Bragg's law:

$$N\cdot\lambda=2\,d\cdot\sin\theta \tag{5}$$

where N is an integer, λ the wavelength of the light, d the grating constant or the distance between two adjacent reflecting layers. In the present case $N=1$, $\lambda=0.00055$ mm, $d=\frac{4}{104.5}$ mm, $\sin\theta=\theta$. If we take the total deflective angle $\varphi=2\theta$, Eq. (5) gives $\varphi=0.014$. The objective focal distance of 105 mm then raises the spectral image 1.5 mm above the central spot. The adjustment of the inclination of the crystal is thus rather critical and is carried out by aid of a special adjusting screw. About $^1/_3$ of the light is reflected.

The crystal system is turned some degree aside, to avoid a back reflection through D_1 from the entrance and departure surfaces. In swinging state the temperature of the crystal at resonance is some 50° C above that of the surroundings. Since the resonance frequency decreases by, say, 5000 c/s per degree of increase in temperature, the crystal must be heated before the start. The working frequency is kept slightly above the resonance of K. The state is stable. If the crystal temperature increases, the resonance frequency declines, and the heating ceases. The distance to the resonance frequency at temperature balance was controlled by variation of the room temperature. An improved proceeding would include a temperature-regulated air current on to the crystal. A trial in this direction yielded a good result. The hum of the fan motor, however, prevented a satisfactory determination of the sound minimum.

The colour of the light used

A wedge-formed interference filter (*F* in the figure) from Aga, Bausch et Lomb was used for the determination of the effective colour. The transmitted colour varied from violet to red in a filter length of 6 cm. The relative intensity decreased to the half 60 Å aside the wavelength for maximum. In maximum the transmission was 40 %. The red part of the filter also transmitted a great amount of blue light. In the parts of the filter used the transmission was fairly pure. The filter was not used during the actual measurement because of insufficient intensity. The following procedure was employed: The filter *F* was moved several times to and fro across the beam of light close to the lamp. The maximum intensity was observed by aid of the λ A-meter. Also, some attention was paid to the colour distribution outside the maximum. In this way the effective colour was determined within ± 50 Å.

By means of a spectrometer the filter was graduated in wavelengths corresponding to the distance in mm from the violet filter glass edge. The following values were observed:

mm	λ Å	mm	λ Å
15	4366	40	5616
20	4607	45	5844
25	4864	50	6112
30	5135	55	6407
35	5384	65	6701

The filter is thus fairly straight. The small bend, however, is real and not dependent on accidental errors. The spectrometer was checked against 5 helium lines.

The measurements

Procedure

The temperature balance of the complete apparatus was reached about one hour after the start. Then the micrometer was placed against the shortest iron bar *B*. The mirror was moved to sound minimum. The inclination of the crystal was checked. In correct situation the ground tone has to be completely out. If the coupling between the transmitter TM_2 and the photocell is considerably loosened, there must be a silent *T* aside the minimum position of the mirror *PM* as well. If not, the light is already tone-modulated from the transmitter TM_1. In this case TM_1 is not sufficiently screened off from TM_2 or it is coupled too loose to its control quartz. Scattered light, of course, is not permitted to cause any audible sound. Such a source is comparatively easy to detect by a systematic screening off of different parts of the optics or by visual inspection of the light incident to the photo cathode. All images of *LS* must be exactly in the focal planes of L_2 and L_3.

The minimum position of the mirror is read off on the micrometer. Then the object for investigation, e.g. a plane parallel glass prism, is placed in the parallel beam between the lens L_1 and the mirror *PM*. Now the light runs the known distance Δ through the glass prism more slowly than earlier in the air. To get an unchanged phase coincidence at sound minimum, the mirror *PM* must be moved nearer. The main displacement is done beforehand by the insertion of a longer iron bar B. The fine adjustment, again, is done by means of the micrometer.

If the object is a crystal (Ca in the figure) instead of glass, a Nicol prism N must be inserted to keep the ordinary (O) and the extra ordinary (EO) rays apart. The best position of N is between L_4 and Ca. Here the beam is comparatively wide (6×12 mm), and a sufficiently large prism was not at hand. The small Glan-Thomson prism (with right-angled ends) was placed in the narrow beam close outside the screen S_2. If N is placed between the modulating crystal K and the lamp, the optical activity of K (chromatic turning of the polarization plane) will upset the whole course. In fact, the rest polarization by the mirror SM gives rise to a slight colouring in the present arrangement also. The effect is observed at the colour determination described above, and the displacement of the maximum may be 100 Å.

Group index

If V_g is the group velocity in glass and the corresponding group index $= n_g$ we get

$$n_g = \frac{c}{V_g}. \tag{6}$$

In the present case we can use the same c for vacuum and air. To obtain sound minimum with and without the Δ mm thick body for investigation, the time for the light en route must be equal in both cases. In air the Δ mm are passed in the time

$$t_1 = \frac{\Delta}{c} \tag{7}$$

If the body is there, the time is

$$t_2 = \frac{\Delta}{V_g}. \tag{8}$$

The difference $t_2 - t_1$ must be compensated for by the displacement δ of the mirror PM. The time for the passing of δ is

$$t_3 = \frac{\delta}{c}. \tag{9}$$

To obtain sound minimum in both cases, the following equation must be valid:

$$t_3 = t_2 - t_1. \tag{10}$$

Using Eq. (6)–(10) we get

$$n_g = 1 + \frac{\delta}{\Delta}. \tag{11}$$

Measurement in glass

A plane parallel square glass prism with an edge length of 45.0 mm was obtained on loan from AGA. The glass was BK7 from Zeiss. The manufacturer gives the following refractive indices:

Line	λ Å	n
C	6563	1.5139
d	5876	1.5163
e	5461	1.5183
F	4861	1.5220
g	4358	1.5262

At the measurements the bar for air had a length of 5.3 mm in series 1–3, and 6.07 in series 4. With glass the bar length was 29.10 mm. On the micrometer the following values were read off:

Series	Air	Glass	Air	Filter
1	18.55	17.7	–	33.0
2	19.5	18.6	–	32.3
3	19.6	18.5	–	30.0
4	21.75	20.00	22.25	36.0
	22.25	20.45	22.80	
	22.80	20.95	22.60	

All figures are in mm (filter: from edge). Using Eq. (11) we get

		n_g	
Series	λ Å	meas.	comp.
1	5285	1.548	1.548
2	5250	1.549	1.549
3	5135	1.554	1.551
4	5430	1.555	1.547

The last column contains n_g as computed from n in the above table.

Measurement in calcite

Even Huygens supposed the wave surfaces from a point light source within a calcite crystal to be a sphere for the ordinary ray and an ellipsoid of revolution for the extra ordinary ray. A real measurement of the velocity gives the group velocity. The group surface will lie just inside the wave surface. First, some values may be given on the wave index for calcite:

λ Å	n_o	n_{eo}
6563	1.65438	1.48461
5893	1.65836	1.48641
5791	1.65906	1.48674
5461	1.66168	1.48792
5270	1.66342	1.48874
4861	1.66785	1.49076
4340	1.67552	1.49428
4307	1.67608	1.49455

Using Eq. (4) we get the corresponding values n_{g_o} and $n_{g_{eo}}$. Presupposing the group surface of the e.o. ray to be an ellipsoid of revolution too, we get for different angles φ with the optic axis

$$n_{g_\varphi} = n_{g_o} \cdot \sqrt{\cos^2 \varphi + \left(\frac{n_{g_{eo}}}{n_{g_o}}\right)^2 \cdot \sin^2 \varphi}.$$

By courtesy of Professor MANNE SIEGBAHN, a very transparent crystal of calcite was furnished from the Nobel Institute for Physics. After plane parallel grinding, the length for the light passage in different directions of the crystal was of the order 40–50 mm.

The very measurements were carried out in essentially the same way as for glass. The only difference was the adding of the prism *N* to separate the ordinary and extra ordinary rays. At the measurements for air *N* must be in the same position as for the corresponding ray through the crystal. At the directions 57° and 45° of the light, the two rays separated totally before the departure. In these cases there was also a determination without Nicol. The rays were alternatively screened off just in front of the mirror *PM*.

90° with the optic axis: The surfaces were fairly well grinded and polished and the distance between them was 53.75 mm where the light passed. Unfortunately the surfaces were not fully parallel. The angle was 20′ to 30′. The consequence was a small refraction of light when the calcite crystal was there. The refraction was compensated for by a slight inclination of the plane mirror *PM*. The necessary turning (in degrees) of the inclination screw *Is* was noted. The inclination of the mirror was equivalent to a correction, which had to be added to the displacement δ of the mirror.

57°: In this case the crystal lay horizontally on a natural surface parallel with the incident light. The light went in and out from the crystal through two natural surfaces. Their angle with the unrefracted beam was 74.5°, i.e. the angle between two natural planes. The ordinary ray was refracted upwards 6.3°. Because of the inclination of the pass out surface, the light way was shortend by $46.35 \times \sin 6.3° \times \sin (90° - 74.5°) = 1.34$ mm. The number 46.35 is the unrefracted length through the crystal. The e.o. ray was only refracted 2 mm aside. The surfaces used were of no good quality and therefore they were covered with 1.05 mm BK7 plane glasses. A thin layer of fat made an improved optic contact. The influence of the glass is introduced as a correction to the distance δ of the mirror displacement.

45°: Here too were there natural surfaces. The distance between them was 39.95 mm. The light was incident normally to the surface. Thus the angle for the ordinary ray was 44.6° and for the e.o. ray 51.°7 with the optic axis. The plane glasses were used to facilitate the light passage.

0°: The surfaces were not good. In spite of the plane glasses only 25 % of the light returned. No Nicol was used (its direction is undeterminable). The distance for passage was 34.97 mm.

The iron bars *B* used in the measurements had the following lengths:

I	5.3
II	29.1
III	20.00
IV	48.86
V	57.68
VI	37.07
VII	9.63
VIII	6.07

Tabl

(Reading

Light path	Series	Method	Air		Ordin.		E.O.		Ordin.
			Bar	Micr.	Bar	Micr.	Bar	Micr.	Micr.
Glass	1		I	18.55	II	17.7			
	2			19.5		18.6			
	3			19.6		18.5			
	4		VIII	21.75		20.00			
				22.25		20.45			
				22.80		20.95			
Ca 90°	1	Nicol	III	16.75	V		IV	18.22	15.93
	2			16.78				18.82	15.93
	3			18.05				20.05	16.20
				18.00				19.35	15.85
				18.15				19.65	17.00
				18.10				19.65	17.35
				20.10				22.50	19.50
	4			17.70		16.45		20.00	
				18.55				19.40	17.00
				17.40		17.25		19.75	
				19.00				20.25	17.00
	5			19.00		17.15		20.40	
				19.80				21.35	17.00
				18.00		17.25		20.55	
				18.70				20.30	17.00
Ca 57°	1	Nicol	III	18.50	IV		IV	19.55	14.65
				18.80				19.70	14.60
				18.70		13.10			
	2	Screen		26.65		22.70		16.10	
				26.40		22.40		16.40	
				26.45		22.00		16.35	
				26.50		22.75		16.90	
				26.70		22.90		16.30	
				26.90		22.55		16.45	
Ca 45°	1	Nicol	III	17.75	IV	16.25	IV	19.80	
				17.05				20.65	14.20
				17.50		16.20		20.85	
				17.75				20.65	15.75
	2			18.00		18.20		22.75	
				18.00				21.70	17.35
				18.80		17.35		22.10	
				18.70				22.00	17.00
				18.05		16.95		21.20	
				18.50				20.50	
	3	Screen		23.40				27.25	23.60
				23.30				29.00	24.60
				23.95				19.10	24.55
				24.15				28.80	23.80
Ca 0°	1	—	VII	15.90	IV	17.65	—	—	—
		—		16.60		17.40	—	—	—
		—		16.25		17.90	—	—	—

/.

n mm)

Air	For δ-corr.					Δ		
	Incl. screw		Filter mm		Pl. glass Corr.	Measured	Corr.	
Micr.	Ord.	E.O.	Ord.	E.O.		Ord. E.O.	Ord.	E.O.
	0	—	33.0	—	—	45.0	0	—
	0	—	32.3	—	—	45.0	0	—
	0	—	30.0	—	—	45.0	0	—
22.25	0	—	36.0	—	—	45.0	0	—
22.80								
22.60								
16.45	+ 135°	+ 120°	35.0	35.0	—	53.75	0	0
18.45								
18.75								
18.05								
18.45								
19.85								
18.35								
17.40								
19.00								
18.40								
19.80								
19.00								
19.00								
19.15								
19.90	+ 170°	+ 170°	36.0	37.0	− 1.15	46.35	− 1.35	+ 0.05
19.05								
26.20	+ 170°	+ 170°	36.0	33.0	− 1.15	46.35	− 1.36	+ 0.05
25.80								
26.45								
26.95								
26.35								
26.70								
16.70	+ 90°	+ 90°	35.0	36.0	− 1.15	39.95	0	+ 0.31
17.95								
17.75								
16.80								
19.15								
18.65								
19.15								
18.65								
18.05								
23.95								
24.25								
24.15								
23.80								
15.00	− 30°	—	36.0	—	− 1.15	34.97	0	0
16.25								
15.80								

All measurements, including those for glass, are put together in Table 1. Each reading is a single measurement. The readings in a horisontal line belongs to one determination. The different series are separated by time or some change or adjustment of the apparatus. A turning of the inclination screw (1 mm thread) of 120° is equivalent to a correction of $\frac{120}{360}\times\frac{43}{125}$ mm for δ according to the mm dimensions in the figure. The colour is expressed in mm according to the table on page 462. The plane glass correction has been made according to Eq. (11), where Δ is 2.10 mm and $n_g = 1.55$.

In the following table all the means are reduced to 5384 Å and put together with values as computed from the indices n_o and in n_{eo} in the table on page 464.

Table 2. Final values for n_g

Light path	Series	Method	$n_g = 1 + \frac{\delta}{\Delta}$		Error limits	Wgt.	Ordinary		Extra Ord.	
			Ordin.	E.O.			Mean, meas.	Comp. fr. n	Mean, meas.	Comp. fr. n
Glass	1	—	1.546	—	0.003	3	1.550	1.547	—	—
	2	—	1.547							
	3	—	1.548							
	4	—	1.556							
Ca 90°	1–5	Nicol	1.718	1.508	0.005	2	1.718	1.712	1.508	1.511
Ca 57°	1	Nicol	1.727	1.573	0.009	2	1.719	1.712	1.568	1.573
	2	Screen	1.702	1.554	0.006	1				
Ca 45°	1–2	Nicol	1.726	1.608	0.003	2	1.714	1.712	1.595[1]	1.591
	3	Screen	1.689	1.568	0.004	1				
Ca 0°	1	—	1.705	—	0.006	1	1.705	1.712	—	—

[1] 51.7° for the e.o. ray.

Discussion

Notable is the good agreement for glass and the obvious systematic difference between the nicoled and the screened-off measurements. The latter are those deviating most. Surely this is a matter of difference in light intensity and, possibly, also of optic reproduction. At all the measurements the sound minimum is not quite pure. Scattered light from the crystal K and up to and including the lens L_4 can no doubt cause a noticeable displacement of the minimum without causing any audible sound in T. This disturbance has a greater effect if the light is damped between L_4 and PM. Thus, a *difference* in damping will cause an error.

I the case of glass, the difference mentioned was 20 % and of no influence. The calcite increased the part to 50 % at Nicol and 75 % at screen off. For this reason, the weights of the measurements are estimated to be, respectively, 3, 2, 1 as in the table. Trials to put in an artifical damping yielded some result.

However, improved optic surfaces, possibly antireflex-coated, would increase the accuracy to parity with the determination for glass.

A further source of error is that all parts of the crystal have not exactly the same resonance frequency. Hence, the effective centre point of the erected grating is somewhat depending on the temperature.

The errors mentioned should be cancelled if the light always passed the modulation crystal in *the same direction*, from the light source as well as from the mirror *PM*. According to trials the somewhat more complicated lightway can be realized by means of two fixed auxiliary mirrors. For the present, lack of time and resources are obstacles to an extended investigation. It is hoped that some complementary measurements will be performed at a later date.

To sum up, one may state that, for glass, the investigation has shown the validity of Rayleigh's formula for group velocity, and, for calcite, has yielded a qualitative proof of the reality of Huygens' velocity surfaces.

The work has been performed at the Royal Institute of Technology, Department for Electronics, and was supported by grants from the Swedish Natural Science Research Council.

REFERENCES

1. Lord Rayleigh, Theory of sound.
2. ——, Proc. Lond. Math. Soc. 9, 21.
3. Michelson, Rep. Brit. Assoc. Montreal 1884, p. 56.
4. Houstoun, R. A., Proc. Roy. Edinb. A 62, 1, 1944.
5. Bergmann, Supersonics, New York 1938, p. 190.
6. Houstoun, Proc. Roy. Soc. Edinb. A 63, 95.

Tryckt den 3 november 1954

Uppsala 1954. Almqvist & Wiksells Boktryckeri AB

ARKIV FÖR FYSIK Band 8 nr 46

Communicated 2 June 1954 by MANNE SIEGBAHN and BENGT EDLÉN

Equipment for excitation of spectra by high frequency pulses

By L. MINNHAGEN and L. STIGMARK

With 6 figures in the text

Introduction

The electrodeless high frequency discharge possesses certain qualities, which makes it convenient to use in spectroscopic research as a means of excitation of spectra. The lack of electrodes in the light source contributes to the purity of the spectrum and the low possible pressure contributes to the emission of sharp lines. The low pressure also makes this type of discharge advantageous to use in combination with vacuum spectrographs. Owing to the flexibility of the high frequency excitation method, spectra belonging to different ionization stages can be excited and distinguished from each other. Occasionally, the relative intensities of the spectrum lines will be different from those obtained by other modes of excitation, implying the enhancement of otherwise very weak lines.

Generally speaking, the excitation by means of continuous periodic electromagnetic oscillations with a frequency ranging from a few kilocycles per sec to a few hundreds of megacycles per sec, and generated by an oscillator of moderate power (between some tens and hundreds of watts) produces the spectra of neutral and singly ionized atoms. The nature of the atoms contained in the discharge tube, and also the experimental conditions, decide whether both spectra or only the first will be excited. In order to enhance the spectrum of the singly ionized atom in relation to the arc spectrum, and to excite higher ionization stages, it is necessary to increase the momentary high frequency power transferred to the discharge tube. This can be done by operating an oscillator of moderate average power intermittently with pulses of high momentary power. During pulse working it is possible to increase the anode voltage of the transmitting tubes to values much above normal. The anode voltage is limited by the high-voltage insulation of the electrodes and by the anode dissipation. Generally, the insulation permits voltages much higher than those recommended for continuous working, and, moreover, if the average power during pulse working does not exceed the normal power of the tubes, then the average anode dissipation will be kept on a permissible level in spite of the high momentary values. Provided that the anode voltage is not raised so much that the anode current attains its saturation value, the momentary high-frequency power will be proportional to the square of the anode voltage. In the high-frequency tech-

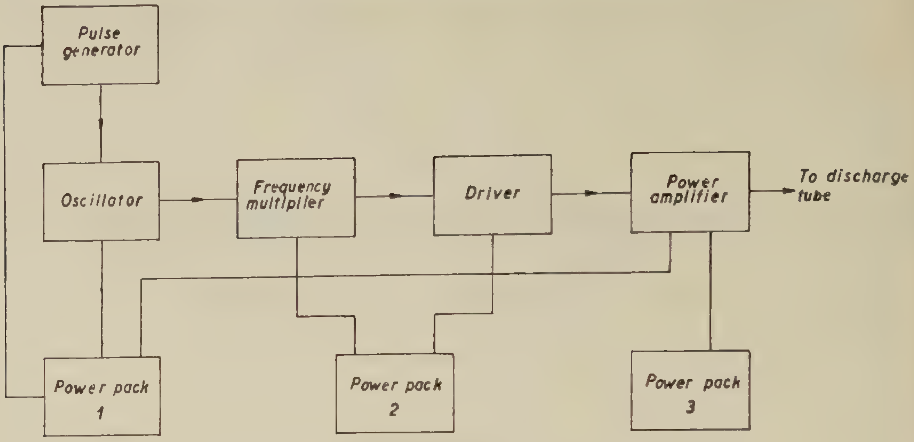

Fig. 1. Block diagram of the high frequency generator.

nique, the pulsing procedure has attained a high stage of development. The attempts to apply it to the special field of excitation of spectra, however, seem to be sparse and rather less elaborate.

Goudet, Herreng and Nief (1), as well as Roig and Buret (2), use self-oscillating devices, the frequency being 150 and 20 megacycles per second respectively. In the first case the pulsing was produced by means of periodic anode voltage peaks and in the latter case by means of a 500 cycles per second grid modulation.

The experimental arrangements in the present work are more advanced both with regard to the oscillator and to the mode of transferring high frequency energy to the discharge tube.

The high-frequency generator

The different parts of the source which generates high-frequency pulses are seen in Fig. 1. From the pulse generator, the pulses—adjustable with respect to frequency and duration within certain limits—are fed to an oscillator which starts at the beginning of each pulse and stops at the end. The frequency of the oscillator is multiplied in a frequency multiplier. The multiplier is followed by a driver which gives sufficient power for the final tube, the power amplifier. The high-frequency power is transferred from the power amplifier to a tuning circuit in close connection to the discharge tube via a coupling link. Three different power supplies, indicated in Fig. 1, yield all necessary voltages to the different parts of the equipment. Power pack 1 serves the pulse generator and the oscillator and also provides the final tube with negative bias voltage and with screen grid voltage. Power pack 2 is connected to the frequency multiplier and to the driver sections. The final tube is supplied from a separate high voltage mercury rectifier, continuously variable, indicated as power pack 3 in Fig. 1.

The circuit diagram of the pulse generator and the oscillator is shown in Fig. 2. The first tube, V_1, of the pulse generator determines the pulse frequency, whereas the double triode V_2 controls the length of the pulse. V_1 is a thyra-

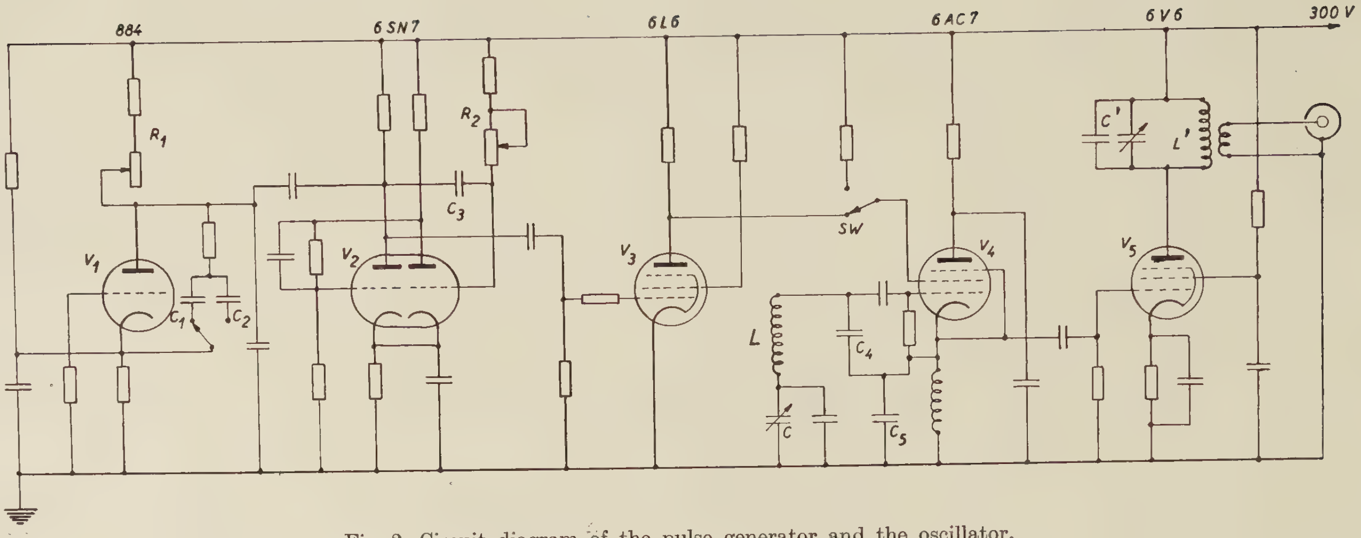

Fig. 2. Circuit diagram of the pulse generator and the oscillator.

tron tube acting as a relaxation oscillator with a frequency mainly depending on the charging condenser (C_1 or C_2) and on the value of the anode resistor, R_1. A coarse control is carried out by using either C_1 or C_2 and the fine control by means of R_1, part of which is continuously variable. The double triode, V_2, acts as a univibrator with one stable state (the right tube conducting, the left one cut off) and one bistable state where the working conditions of the tubes are reversed. The univibrator can be switched into the bistable state by means of negative pulses — formed at the anode of V_1 when this tube fires — which actuate the grid of the conducting tube of the univibrator. The duration of the bistable state is determined by the time constant of the coupling condenser C_3 and the grid resistor R_2. Part of R_2 is variable and permits a continuous variation of the pulse length between 80 and 800 μsec. During the bistable state the anode potential of the left half of V_2 lies about 200 volts below the anode supply voltage. This voltage shift is applied to the grid of the tube V_3 via an *RC* coupling with suitable time constant; as a result, V_3 is cut off during the pulse. Consequently, the anode potential of V_3 is high during a pulse but low between pulses, i.e., a large positive pulse of constant amplitude appears at the anode of V_3. This pulse is used to control the oscillator.

A suitable type of oscillator, which can be controlled by pulses without giving frequency shifts, is the Clapp oscillator (3). In Fig. 2, the tube V_4 represents the oscillator, which is controlled by means of its screen grid being connected to the anode of V_3 (lower position of the switch *SW*). When the switch *SW* is in its upper position the oscillator is running continuously. The frequency of the oscillator, which is about 3 megacycles per sec, is determined by L and C; C_4 and C_5 are large in comparison with C. The oscillations are transferred from the cathode of V_4 to the grid of the tube V_5. From the tuned circuit $L'C'$ of V_5, the amplified 3 Mc per sec oscillations are brought to the frequency multiplier via a coupling link.

The circuit diagram of the frequency multiplier, the driver and the final power amplifier is shown in Fig. 3. The circuit in the anode of the tube V_6 is tuned to the third harmonic (about 9 Mc per sec) of the fundamental frequency (about 3 Mc per sec). In reality, it is possible to operate the equipment at frequencies between 7.8 and 9.6 Mc per sec. The 9 Mc per sec frequency is amplified in the driver tube V_7 in order to obtain sufficient driving power to the final amplifier tube V_8, a Philips *PB* 3/800 tube with a normal anode voltage of 3 kV and an anode dissipation of 450 watts. To avoid self-oscillation in the driver tube it was necessary to introduce neutralisation of the grid-anode capacitance of the tube. It was also found necessary to use small high-frequency chokes shunted with damping resistors in the grid and the anode leads of the frequency multiplier and of the driver in order to prevent parasitic oscillations. The grid circuit of the power amplifier is link-coupled to the driver. The final circuit in the anode of the power amplifier consists of a coil made of copper tubing and a heavy-duty condenser immersed in paraffin-oil to avoid flash-over when the circuit is not properly loaded.

The tuning-up procedure of the equipment is easily performed when the oscillator is running continuously. The meter *M* can be connected to three different parts of the circuit by means of a double-pole three-way switch. In the left position (Fig. 3), the grid current of the frequency multiplier is measured, which allows a correct tuning of the oscillator output circuit and of the input

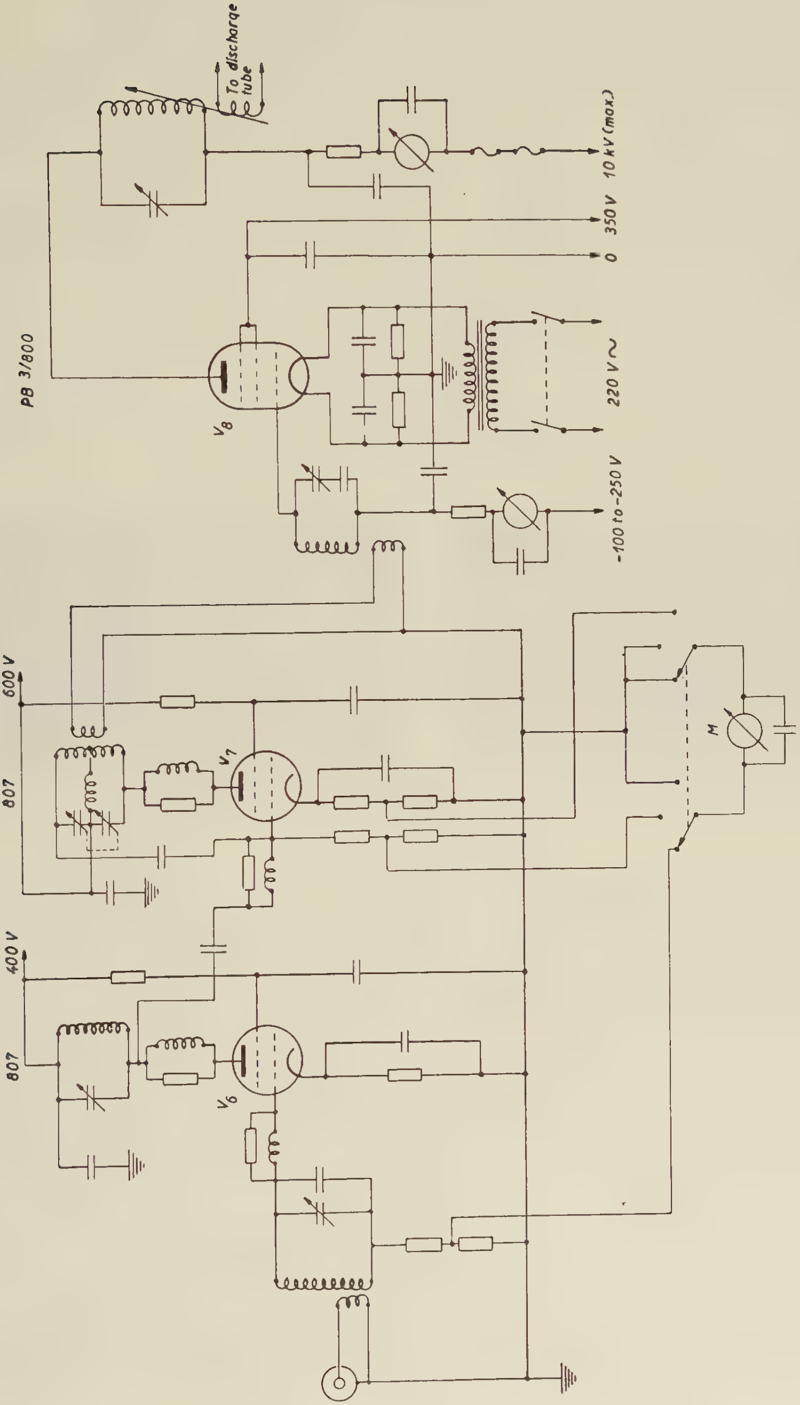

Fig. 3. Circuit diagram of the frequency multiplier, the driver and the power amplifier.

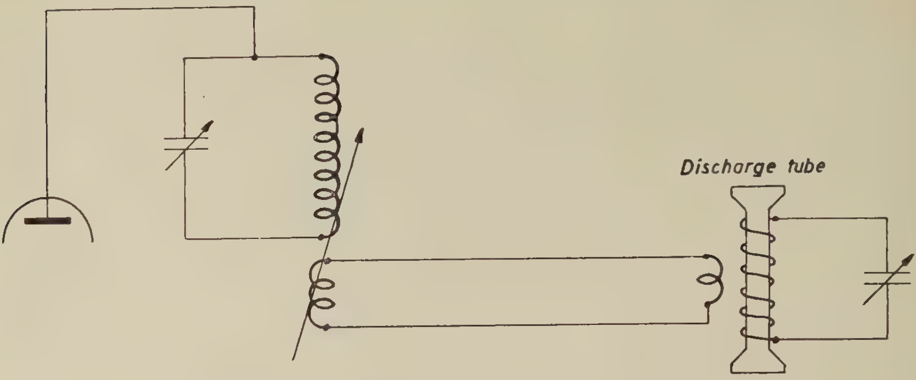

Fig. 4. The separate discharge tube tuning circuit.

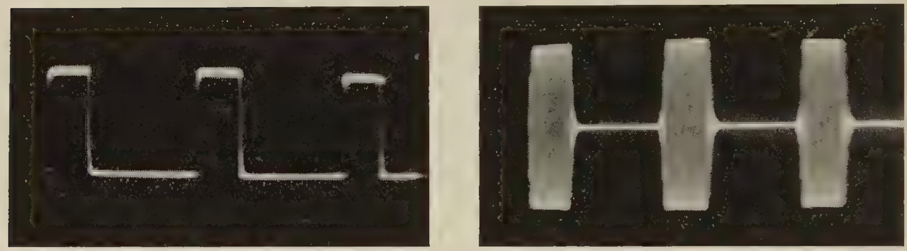

Fig. 5. Oscillogram of (*a*) the pulses generated by the pulse generator, (*b*) the high frequency pulses from the oscillator. (Pulse frequency 1000 cycles per sec, pulse duration about 300 μsec.)

circuit of the multiplier tube. In the middle position the grid current of the driver tube is measured in order to facilitate the tuning of the anode circuit of the frequency multiplier. In the right position, the cathode current of the driver tube is measured and used to indicate the proper tuning of the circuit in its anode. The final tube is provided with separate instruments for checking the grid excitation and the anode current; they indicate, consequently, the correct tuning of the grid and anode circuits and the loading conditions of the tube. The separate, tuned circuit close to the discharge tube is link-coupled to the power amplifier via a coaxial cable (Fig. 4). The coupling degree is controlled by means of a variable link coupled to the power amplifier, thus providing means to obtain optimum loading conditions and maximum power transfer to the discharge tube.

This equipment gives extremely well-defined pulses; the peak power is approximately 3 kilowatts at a mean power of about 500 watts. The shape of the pulses generated by the pulse generator and the associated high-frequency pulses from the oscillator are illustrated in the oscillograms of Fig. 5, corresponding to a pulse frequency and a pulse duration of about 1000 cycles per sec and 300 μsec, respectively.

The discharge tube

The discharge tube is made of fused quartz, the middle part having a cylindric shape with a diameter of 20 mm. Vitreosil windows, 40 mm in diameter, are fused to the widened ends of the tube, the total length of which is 19 cm. The tube is connected to a conventional gas-circulating system containing a mercury diffusion pump, gas-cleaning traps, manometers, etc. The connection is made by means of two long side-tubes fused to the discharge tube near its ends. The sparsely wound free-bearing coil surrounding the discharge tube is made of 2.5 mm silver-coated copper wire and is separated from the walls of the tube by a few millimetres of air. The coil is connected to an oil-insulated variable condenser. The arrangement with the separate discharge tube circuit is appropriate for bringing about optimum loading, which implies the possibility of transferring large amounts of high frequency power to the gas contained in the discharge tube. The separate circuit was preliminarily tuned to the frequency of the oscillator by means of a wave-meter. After the start of the oscillator, the anode voltage of the final tube was raised, first to the stage where the "electrostatic" discharge starts and then up to the onset of the "bright glow". As the anode voltage was further increased, the excitation of the filling-gas changed and thus also the impedance of the separate circuit. The variable condenser of this circuit, therefore, had to be adjusted and the final tank circuit accurately tuned. The setting of the variable condenser was different for different filling-gases and was also influenced by the operation mode used — either continuous with "normal" anode voltage or pulsed with raised voltage. The average high-frequency power transferred to the discharge tube was determined approximately by measuring the input power of the power-amplifier, whose efficiency was roughly known.

The light-source and the final tube were cooled by forced air.

Observations on argon

The equipment was used for an investigation of argon spectra. The pressure of the argon gas in the discharge tube was kept at values between 0.02 and 0.10 mm of mercury. During continuous working the anode voltage of the power amplifier tube amounted to 3.0 to 3.5 kilovolts, the high frequency power transferred to the discharge tube was about 450 watts. During pulse working the anode voltage could be increased to 9 kilovolts, the frequency of the pulses was about 500 per sec and the length of a pulse about 400 microseconds. The average power was about 550 watts and the estimated momentary power 3 kilowatts. The average power used appeared to be appropriate considering the cooling conditions.

Both modes of excitation produced a very intense emission of light, but the relative intensities of the ionization stages were quite different. This is illustrated in Fig. 6, where in each pair of spectrograms the left corresponds to pulse working and the right to continuous working. No changes in the contents of the discharge tube were made between the two exposures. All recordings were made with a Jarrell-Ash 21′ grating spectrograph (JA 71-15). Fig. 6 *a* represents 1st order spectrograms (dispersion 4.7 A/mm), and Figs 6 *b* and *c* 2nd order spectrograms (dispersion 2.4 A/mm). The spectrogram to the left in Fig. 6 *a* was exposed twice as long as that to the right; the exposure times of the recordings reproduced in

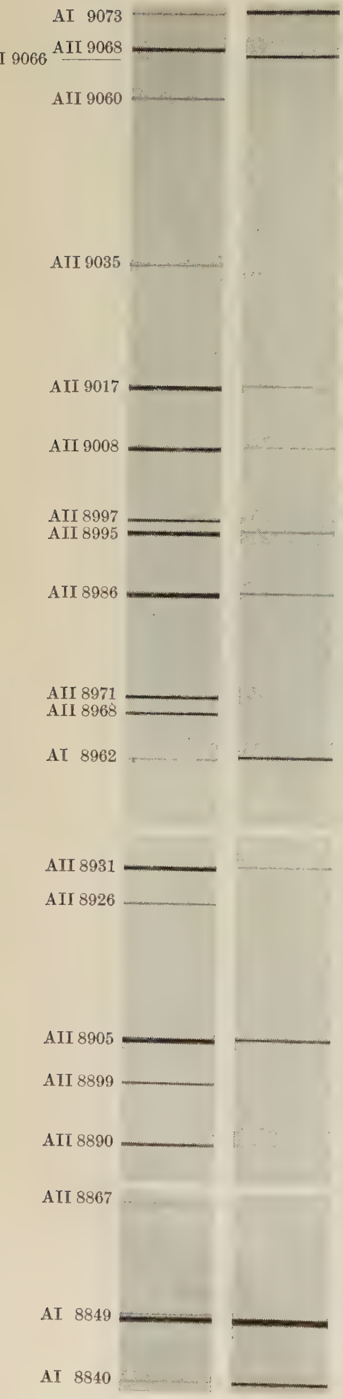

Fig. 6 a.

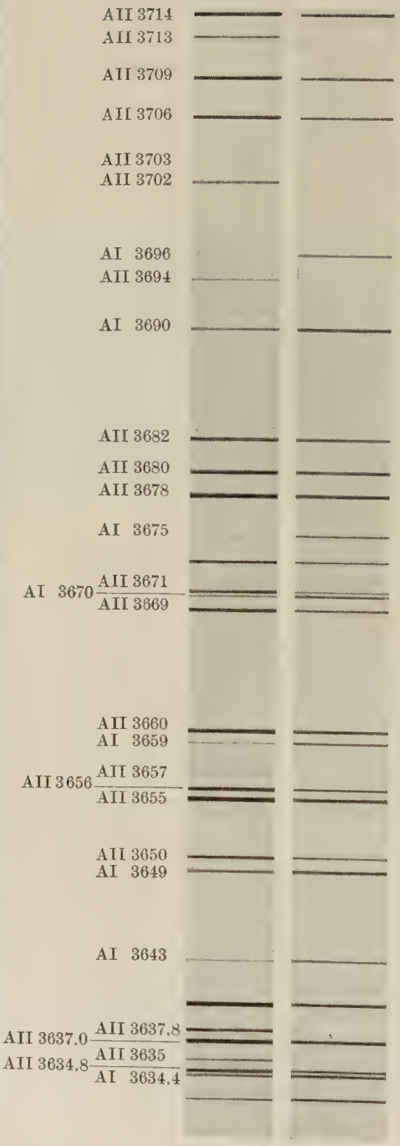

Fig. 6 b.

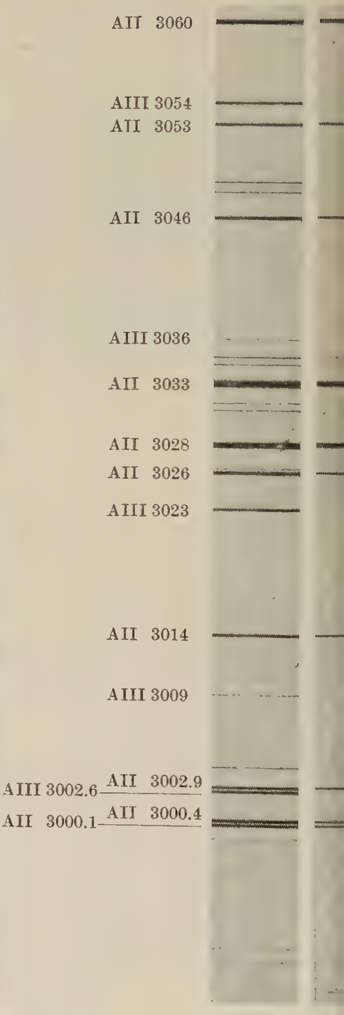

Fig. 6 c.

. 6. Argon spectra obtained by continuous and pulsed excitations; in each pair of spectrograms the lef
ponds to pulsed excitation. (4.2-fold enlargement.)

Fig. 6 *b* were equal; in Fig. 6 *c* the exposure time of the left spectrogram was one third of that of the right exposure.

The continuous excitation gives the argon I spectrum and also spectrum lines of argon II, whereas the pulsed excitation produces argon I, II and III. In the spectral region λ 8840 to 9075 A (reproduced in Fig. 6 *a*) argon I dominates during continuous working and argon II during pulsed working. The strongly enhanced A II lines λ 9068, 9035, 8986, 8968, 8899, 8850 belong to the transitions $4d\,^4D$—$4f\,^4F, ^4D$; λ 9017 represents $4s\,(^1D)\,^2D$—$4p\,(^3P)\,^2P$ and λ 8926 $3d\,^4P$—$4p\,^4D$; some lines are not yet identified. Among the A I lines which grow weaker during pulse working are λ 9075, $2p_2$—$4d_6$, and λ 8962, $2p_2$—$4d_5$, whereas λ 9073, 9066, 8849 and 8840 belong to $3d$—$5f, 6f$. Fig. 6 *b* shows a similar picture of a different region, viz. λ 3634—3714 A. The A I lines, representing $1s$—$4f$ and $1s$—$4p$ transitions, have about the same intensity as the A II lines, when the excitation is continuous, but during pulsed excitation the A II spectrum is strongly dominating. Some spark lines, so far ascribed to the singly ionized atom, are enhanced so strongly that they may be suspected to belong to the A III spectrum. This will be dealt with more thoroughly in a forthcoming paper.

Between λ 3000 and 3060 no A I lines appeared. Continuous excitation produces the A II spectrum, which becomes very much enhanced in the pulsed excitation. This is shown in Fig. 6 *c*, which also illustrates the flaming up of the A III spectrum.

Thus, the pulsed excitation gives the argon II spectrum with very high intensity as well as parts of the argon I and III spectra. These spectra have been recorded between 1900 and 9900 A, and the results of the wavelength measurements will be given in a later paper.

Summary

The present equipment for excitation of spectra by high-frequency pulses consists of a pulse generator, which controls a Clapp oscillator followed by a frequency multiplier and amplifiers. The output frequency is about 9 Mc per second; the frequency and the duration of the pulses are adjustable within certain limits. With appropriate arrangements for bringing about optimum loading the average high-frequency power transferred to the discharge tube amounts to about 500 watts and the peak power to approximately 3 kilowatts. It is also possible to run the generator continuously.

With argon as the filling-gas the continuous excitation gives the argon I spectrum and also spectrum lines of argon II, whereas the pulsed excitation produces argon I, II and III. In the latter case argon II is strongly enhanced and argon I weakened.

Acknowledgement

One of us (L. M.) wishes to thank Mr K. B. Eriksson for his participation in the preliminaries to this work.

Physics Laboratory, University of Lund.

REFERENCES

1. Goudet, G., Herreng, P. and Nief G., C. R. Acad. Sci., Paris, *214*, 62 (1942).
2. Roig, J. and Buret, A., C. R. Acad. Sci., Paris, *230*, 1394 (1950).
3. Clapp, J. K., Proc. I.R.E. *36*, 356 (1948).

Tryckt den 23 november 1954

Uppsala 1954. Almqvist & Wiksells Boktryckeri AB

ARKIV FÖR FYSIK Band 8 nr 47

Mitgeteilt am 2. Juni 1954 durch MANNE SIEGBAHN und ERIK HULTHÉN

Das ultraviolette Bandensystem des Strontiumoxydes

Von ALBIN LAGERQVIST UND GUNNAR ALMKVIST

Mit 3 Figuren im Text

Zusammenfassung

Das ultraviolette Bandensystem von SrO, zwischen 3200 und 3700 Å belegen, ist hier rotationsanalysiert. Das System ist ein ${}^1\Sigma - {}^1\Sigma$ Übergang mit $C\,{}^1\Sigma - X'\,{}^1\Sigma$ bezeichnet. Der untere Zustand ist derselbe wie derjenige der schon analysierten blauen und ultraroten Systeme. Die folgenden Banden sind analysiert: 4,0, 3,0, 2,0, 1,0, 0,0 und 0,1. Für den oberen $C\,{}^1\Sigma$ Zustand sind nachstehende Konstanten berechnet worden:

$$\begin{aligned} B_v &= 0{,}2742 - 0{,}0021\ (v + \tfrac{1}{2})\ \mathrm{K}^* \\ D &= 3{,}5 \cdot 10^{-7} \\ r_e &= 2{,}132 \cdot 10^{-8}\ \mathrm{cm} \\ \omega_e &= 480{,}2 \\ x_e\,\omega_e &\sim 2{,}6 \\ \sigma_{0,0} &= 28546{,}4 \end{aligned}$$

Der obere $C\,{}^1\Sigma$ Zustand wird von mehreren Zuständen gestört. Für einen von diesen sind die Molekülkonstanten approximativ berechnet worden.

§ 1. Einleitung

Das Bandenspektrum des Strontiumoxydes enthält mehrere Systeme, die sich vom ultravioletten Gebiet bis in das photographische ultrarote erstrecken. Kernschwingungsanalysen der ultravioletten und der blauen Banden sind von MAHANTI[1] ausgeführt worden. Er gab folgende Kantengleichungen an:

für das blaue System:

$$\sigma_{v',v''} = 24\,702{,}81 + 519{,}09\ (v' + \tfrac{1}{2}) - 3{,}50\ (v' + \tfrac{1}{2})^2 - 653{,}47\ (v'' + \tfrac{1}{2}) + 4{,}02\ (v'' + \tfrac{1}{2})^2, \quad (1)$$

für das ultraviolette System:

$$\sigma_{v',v''} = 28\,662{,}18 + 497{,}81\ (v' + \tfrac{1}{2}) - 5{,}97\ (v' + \tfrac{1}{2})^2 - 679{,}13\ (v'' + \tfrac{1}{2}) + 9{,}13\ (v'' + \tfrac{1}{2})^2 \quad (2)$$

Im gelben und orangefarbigen Spektralgebiet liegen intensive Banden, die wegen ihrer verwickelten Struktur noch nicht analysiert sind. Das ultrarote Bandensystem war das erste, dessen Rotation analysiert wurde.[1] Es entspricht einem $^1\Sigma$–$^1\Sigma$ Übergang, hier $A\,^1\Sigma$–$X'\,^1\Sigma$ bezeichnet, wo der obere Zustand stark gestört ist[2], während der untere Zustand ungestört ist. Die Nullinien der ultraroten Banden können durch die folgende Gleichung ausgedrückt werden:

---

* 1 K (Kayser) = 1 cm^{-1}

[1] MAHANTI, P. C. Phys. Rev. *42*, 609, 1932.

$$\sigma_{v',v''} = 10\,868{,}8_2 + 624{,}0\,(v'+\tfrac{1}{2}) - 2{,}1\,(v'+\tfrac{1}{2})^2 - 653{,}4_9\,(v''+\tfrac{1}{2}) + 4{,}0_0\,(v''+\tfrac{1}{2})^2. \qquad (3)$$

Die Kernschwingungskonstanten der unteren Zustände des blauen Systems und des ultraroten Systems stimmen ausserordentlich gut überein, obwohl die Konstanten der blauen Banden aus den Kanten berechnet worden sind. Eine Rotationsanalyse der blauen Banden ist von Kovács und Budó[3] ausgeführt, und diese Analyse ist später von Deézsi, Koczskás und Mátrai[4] erweitert worden. Die blauen Banden stellen einen $^1\Pi$–$^1\Sigma$ Übergang dar, der einen gemeinsamen unteren Zustand mit den ultraroten Banden hat, was auch deutlich aus den Kernschwingungskonstanten hervorgeht. Das System wird $B\,^1\Pi$–$X'\,^1\Sigma$ genannt.

In dieser Arbeit und in einer kurzen vorläufigen Mitteilung[5] ist eine Rotationsanalyse der ultravioletten Banden vorgenommen worden. Die Analyse zeigt, dass diese Banden einen $^1\Sigma$–$^1\Sigma$ Übergang darstellen, und dass der untere Zustand auch hier $X'\,^1\Sigma$ ist. Das System wird $C\,^1\Sigma$–$X'\,^1\Sigma$ bezeichnet. Die Kernschwingungskonstanten für $X'\,^1\Sigma$ nach (1) unterscheiden sich von den Konstanten nach (3), welche von den Nullinien berechnet sind. Dieses beruht darauf, dass der Zustand $C\,^1\Sigma$ stark gestört ist, und dass Gleichung (1) aus den stark gestörten Kanten berechnet wurde.

Das niedrigste gefundene Niveau $^1\Sigma$, welches gemeinsam für die ultraroten, blauen und ultravioletten Banden ist, ist mit X' bezeichnet, weil eine Arbeit von Huldt und einem von uns[6] darauf hinweist, dass dieses Niveau nicht der Grundzustand des Moleküles ist.

§ 2. Experimentelles

Die Spektrogramme wurden in der ersten Ordnung mit einem Woods 21 Fuss Konkavgitter aufgenommen. Die Dispersion im aktuellen Spektralgebiet ist ungefähr 1,28 Å/mm. Als Lichtquelle diente ein Bogen zwischen Kohlenelektroden, von welchen die obere negativ, die untere positiv war. Die Stromstärke war 5–10 A, von 440 V Gleichspannung entnommen. Die positive Elektrode war mit geschmolzenem $SrCl_2$ gefüllt. Für Komparierung wurden Eisenlinien benutzt, deren Wellenlängen aus M.I.T. Tabellen[7] entnommen sind.

§ 3. Analyse

Das ultraviolette Bandensystem des Strontiumoxydes befindet sich im Gebiet 3200–3700 Å. Die Banden haben einfache R- und P-Zweige und bilden einen

---

[1] Almkvist, G. u. Lagerqvist, A., Arkiv f. Fysik *1*, 477, 1949.
[2] Almkvist, G. u. Lagerqvist, A., Arkiv f. Fysik *2*, 233, 1950.
[3] Kovács, I. u. Budó, A., Annalen d. Physik *12*, 17, 1953.
[4] Deézsi, I., Kocskás, E. u. Mátrai, T., Acta Phys. Hung. *3*, 95, 1953.
[5] Almkvist, G. u. Lagerqvist, A., Nature *170*, 885, 1952.
[6] Lagerqvist, A. u. Huldt, L., Arkiv f. Fysik *8*, 527, 1954.
[7] M.I.T. Wavelength Tables, 1939 (London: Chapman & Hall).

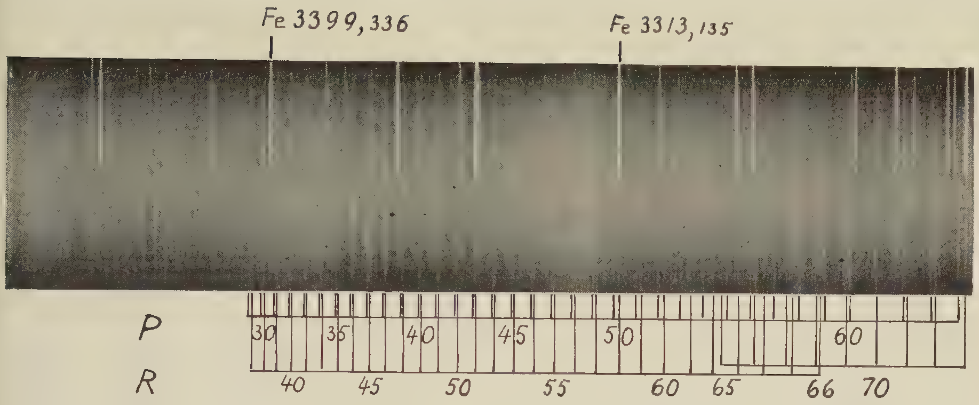

Fig. 1. Eine Reproduktion der 2,0 Bande. Die Störung bei $J \sim 69$ ist im R-Zweig ersichtlich. Die Banden sind von kontinuierlichem Licht des Bogens überlagert, wodurch die Reproduktion etwas unklar ist.

$^1\Sigma$–$^1\Sigma$ Übergang, dessen untere Zustand — wie oben genannt — schon bekannt ist. Die 0,0 Bande wird in Fig. 1 gezeigt. Die Analyse war wegen der starken Störungen schwierig auszuführen, trotzdem die Kombinationen des unteren Zustandes bekannt waren. Die Nullinien der analysierten Banden sind in Tabelle 1 angegeben. Die Wellenlängen der Linien sind in den Tabellen 2 und 3 enthalten. Um die Störungen unterscheiden zu können, werden hier zwei verschiedene Druckarten benutzt.

Die Bandenkonstanten des oberen Niveaus wurden mit Hilfe von GERÖS Methode[1] für die Entdeckung von Störungen im oberen Niveau berechnet. Der folgende Ausdruck wird gebildet

$$\frac{\Delta\, RP}{4\,J} = \frac{R\,(J-2) - R\,(J-1) + P\,(J) - P\,(J+1)}{4\,J} = B'' - B' + 6\,D' - 2\,J^2\,(D'' - D'). \qquad (4)$$

$\Delta\, RP/4\,J$ ist als Ordinate gegen J als Abszisse abgesetzt und die Differenz

Tabelle 1. Die Nullinien der analysierten Banden.

4	$30\,414{,}5_5$		
	$459{,}0_5$		
3	$29\,955{,}0_5$		
	$464{,}0_1$		
2	$29\,491{,}0_4$		
	$469{,}2_7$		
1	$29\,021{,}7_7$		
	$475{,}3_4$		
0	$28\,546{,}4_3$	$645{,}6_3$	$27\,900{,}8_0$
v' / v''	0		1

---

[1] GERÖ, L., Z. Physik *93*, 669, 1935.

Tabelle 2. Wellenzahlen der 0,1, 0,0, 1,0 und 2,0 Banden des System CX.

J	0,1		0,0		1,0		2,0	
	$R(J)$	$P(J)$	$R(J)$	$P(J)$	$R(J)$	$P(J)$	$R(J)$	$P(J)$
24							29 464,64	
25							61,53	
26							58,39	29 430,31
27							55,15	25,86
28					28 989,51		51,78	21,35
29					85,65		48,18	16,76
30					81,64	29 949,88	44,69	12,07
31					77,25	44,40	40,80	07,09
32	27 851,36		28 594,72		73,02	39,28	37,01	02,23
33	47,06		90,19		68,70	33,67	33,14	392,23
34	42,49	27 806,10	85,57	28 449,67	64,14	27,97	28,97	92,07
35	38,29	00,96	80,89	43,71	59,78	22,26	24,77	86,81
36	33,83	795,20	476,17	37,62	55,24	16,64	20,38	81,29
37	29,54	89,74	71,51	31,80	50,43	10,79	15,85	75,77
38	24,73	83,73	66,88	26,07	45,44	04,89	11,12	70,04
39	20,13	77,92	62,08	19,97	*41,86*	898,67	06,48	64,05
40	15,18	72,21	57,30	14,01	*36,61*	92,35	01,63	52,84
41	10,37	66,06	52,05	07,75	*31,35*	*87,52*	396,66	52,07
42	05,32	59,91	46,88	01,51	*26,03*	*80,82*	91,52	45,92
43	00,08	53,66	41,10	395,05	*20,50*	*74,26*	86,10	39,63
44	794,34	47,11	35,63	88,36	*14,45*	*67,65*	80,75	33,09
45	88,88	40,60	29,53	81,59	11,46	*60,77*	75,13	26,47
46	82,64	33,56	23,23	74,51	05,54	*53,42*	69,41	19,67
47	76,06	26,68	16,58	67,15	899,43	49,32	63,58	12,79
48	*87,16*	19,39	09,53 *27,36*	59,58	93,52	41,64	57,70	05,71
49	*80,50*	11,39	*20,84*	51,48	87,52	34,48	51,51	298,60
50	*74,19*	*21,20*	*414,01*	43,11 *61,07*	81,44	27,25	45,30	91,34
51	*67,89*	*13,28*	*07,51*	*53,11*	75,24	19,85	38,93	83,88
52	*61,56*	*05,65*	*00,75*	*45,00*	69,01	12,55	32,37	76,19
53	*54,95*	*697,92*	*394,20*	*37,13*	62,65	04,90	25,71	68,51
54	*48,54*	*90,22*	*87,32*	*29,07*	56,27	297,37	18,82	60,75
55	*42,01*	*82,47*	*80,66*	*21,22*	49,32	89,46	11,85	52,57
56	*35,21*	*74,72*	*73,54*	*13,14*	42,52	81,61	04,76	44,54
57	*28,00* 33,56	*66,69*	*66,23*	*04,97*	33,57	73,58	297,23	36,27
58	*20,40* 24,92	*58,76*	*58,13* 62,71	*296,64*	28,37	65,41	89,76	27,67
59	*11,39* 16,90	*50,26* 55,85	*48,72* 54,79	*87,92*	21,21	57,16	82,07	19,01
60	*00,89* 09,70	*41,08* 45,61	47,12	*78,98* 83,17	13,56	48,86	74,27	10,42
61	02,53	*31,05* 36,71	39,76	*67,72* 73,85	06,26	40,34	66,29	01,37
62	659,30	*19,65* 28,07	32,24	65,06	798,69	31,53	57,51	192,10
63	87,94	19,65	24,58	56,24	90,85	22,77	48,83	88,49
64	80,79	11,10	17,05	47,42	82,96	13,91	39,87	72,80
65	73,24	02,32	09,33	38,48	75,05	04,78	30,25 *54,37*	62,86

J	0,1		0,0		1,0		2,0	
	$R(J)$	$P(J)$	$R(J)$	$P(J)$	$R(J)$	$P(J)$	$R(J)$	$P)J)$
66	27 665,62	27 593,85	28 301,37	28 229,47	28 766,65	29 695,58	29 220,44 *43,41*	29 152,50
67	57,95	85,02	293,40	20,54	58,32	86,18	*32,49*	41,38 *65,57*
68	50,26	76,19	85,19	11,29	49,65	76,59	*22,09*	30,22 *53,37*
69	42,27	67,14	77,04	02,01	40,84	68,83	*11,57*	*41,38*
70	34,12	58,19	68,57	192,60	31,76	56,95	*01,37*	*29,40*
71	25,91	Atomlinie	60,16	83,02	22,77	46,84	*191,04*	*17,45*
72	17,62	39,49	51,52	73,34	12,78	36,51	*80,92*	*06,25*
73	09,24	30,14	42,69	63,54	02,88	25,91	*70,46*	*094,64*
74	00,52	20,45	33,77	53,60		14,94	*59,88*	*83,06*
75	591,67	10,79	24,53	43,48			*48,99*	*71,49*
76	82,57	00,78	15,11				*37,85*	*59,45*
77	73,59	490,58	05,68				*25,91*	*47,26*
78	63,99	80,47	195,90				*13,21*	*34,67*
79	54,48	69,84					25,04	*21,57*
80	44,44	59,09					12,02	*06,18*
81	34,42	48,17					099,80	018,06
82		36,80					88,22	04,14
83		25,08					77,01	28 990,21
84							65,76	77,25
85							54,54	64,79
86							43,28	52,27
87							31,76	39,74
88							20,28	27,06
89							08,65	14,45
90							28 996,94	01,71
91							85,07	888,89
92							73,02	75,84
93							60,81	62,65
94							48,19	49,32
95							34,55	35,98
96							19,80	22,03
97								07,10
98								790,85

$B'' - B'$ kann in den ungestörten Teilen der Kurve abgelesen werden. Eigentlich sollte man $\Delta RP/4J$ gegen J^2 setzen und $B'' - B'$ als Ordinate im Origo erhalten, aber in diesem Fall haben die Kurven keine merkbaren Neigungen in der ungestörten Teilen, was darauf zurückzuführen ist, dass D' und D'' ungefähr gleich gross sind. Fig. 2 zeigt die Kurven.

Um die so erhaltenen B-Werte prüfen und gleichzeitig die σ_0-Werte bestimmen zu können, haben wir den folgenden Ausdruck benutzt

$$R(J-1) + P(J) - 2(B' - B'')J^2 = 2\sigma_0 + 2\Delta B'J^2. \qquad (5)$$

Der linksseitige Ausdruck wird gegen J^2 für die ungestörten Teile der Banden abgesetzt, wodurch $2\sigma_0$ als die Ordinate im Origo abgelesen und die Korrektion $\Delta B'$ aus der Neigung erhalten werden kann.

Tabelle 3. Wellenzahlen der 3,0 und 4,0 Banden des Systems $C\,X$.

J	3,0		4,0	
	$R(J)$	$P(J)$	$R(J)$	$P(J)$
13	29 949,70		30 408,65	
14	48,43		07,37	
15	46,86	29 930,39	05,68	30 389,21
16	45,23	27,61	04,03	86,44
17	43,34	24,64	02,03	83,45
18	41,32	21,60	00,03	80,38
19	38,99	18,42	397,68	77,34
20	36,77	15,08	95,46	73,63
21	34,34	11,63	93,10	69,96
22	32,01	07,97	90,40	66,28
23	29,26	04,28	87,37	62,62
24	26,51	00,25	84,49	58,72
25	23,52	896,32	81,59	54,54
26	20,34	92,18	78,08	49,97
27	16,98	87,92	74,75	45,68
28	13,79	83,53	71,14	41,35
29	10,03	78,72	67,59	36,48
30	06,62	74,08	63,53	31,38
31	02,87	69,25	59,76	26,63
32	899,05	64,25	55,41	21,07
33	94,87	59,08	50,99	15,69
34	90,62	53,80	46,55	10,21
35	86,42	48,48	41,35	04,49
36	81,85	42,85	36,48	289,69
37	77,12	Atomlinie	31,38	92,49
38	72,45	»	25,61	85,93
39	67,53	»	19,83	Atomlinie
40	62,42	»	13,46	72,57
41	57,28	13,04	{ 06,90 *21,07*	65,68
42	51,68	06,65	*14 40*	57,73
43	46,30	00,22	*08,02*	{ 50,04 *64,07*
44	Atomlinie	793,50	*01,49*	*56,22*
45	»	86,60	*295,30*	*48,45*
46	»	79,48	*88,72*	*40,49*
47	»	72,36	*82,50*	*32,78*
48	15,85	65,01	Atomlinie	Atomlinie
49	09,38	57,65	*68,83*	*17,38*
50	02,51	49,55	*61,84*	*09,20*
51	795,47	41,74	*55,16*	*01,20*
52	29 788,13	29 733,59	*30 247,70*	*30 192,9*
53	80,40	25,17	*40,49*	*84,6*
54	{ 72,36 *91,53*	16,43	*32,78*	*76,4*
55	{ 63,72 *82,63*	07,29	Atomlinie	*67,5*
56	*73,79*	{ Atomlinie *17,36*	*17,38*	*58,5*
57	*65,61*	{ 687,95 *07,17*	*09,20*	*49,4*
58	*56,35*	Atomlinie	*01,20*	*40,4*
59	*47,76*	*86,78*	*192,78*	*31,1*
60	*39,26*	*76,76*	*83,78*	*21,6*
61	*30,72*	*66,89*	*75,03*	*11,7*
62	*21,84*	*57,00*	{ *65,55* 99,96	*01,6*
63	*12,92*	*46,98*	{ *56,10* 89,28	Atomlini
64	*04,10*	*36,94*	{ *46,21* 78,46	{ *080,8* 115,1
65	Atomlinie	*26,90*	{ *35,60* 67,50	{ *70,1* 03,2
66	*685,52*	*16,67*	{ *24,89* 56,86	{ *58,7* Atomlini
67	*75,92*	*06,11*	46,21	{ *49,1* 078,8
68	*66,07*	*595,37*	35,60	{ *34,6* 66,7
69	*56,06*	*84,47*	24,89	54,7
70		*73,30*	14,28	42,7
71			03,70	30,8
72			Atomlinie	Atomlini
73			082,47	07,1
74			71,79	29 995,3
75			61,07	83,4
76			50,38	71,3
77			39,70	59,3
78			29,78	47,4
79				35,5
80				24,2

Die bestimmten Rotationskonstanten sind:

$$B'_4 = 0{,}2647\ \mathrm{K} \qquad B'_1 = 0{,}2710$$
$$B'_3 = 0{,}2670 \qquad B'_0 = 0{,}2732$$
$$B'_2 = 0{,}2689 \qquad D' = 3{,}5 \cdot 10^{-7}$$

Die B-Werte können durch die folgende Formel ausgedrückt werden

$$B'_v = 0{,}2742 - 0{,}0021\ (v + \tfrac{1}{2}).$$

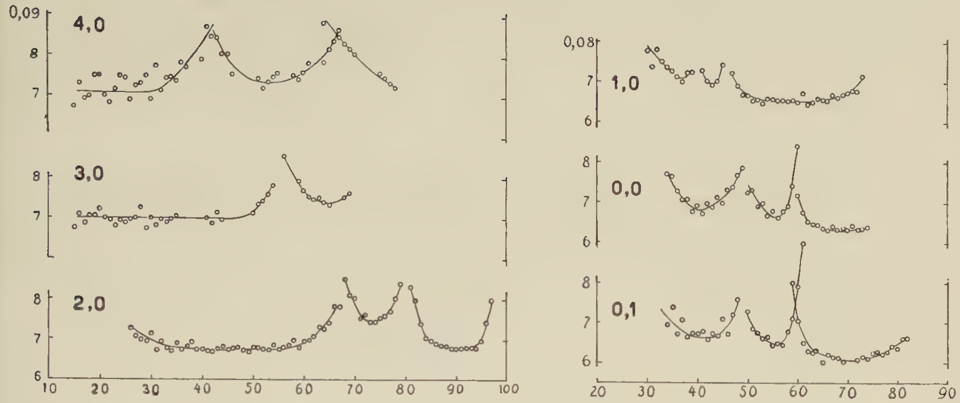

Fig. 2. $\Delta RP/4J = [R(J-2) - R(J-1) + P(J) - P(J+1)]/4J$ gegen J gesetzt. Die Störungen in den Banden sind deutlich ersichtlich.

Der Kernabstand wird

$$r_e' = 2{,}132 \cdot 10^{-8} \text{ cm}.$$

Die Kernschwingungskonstanten sind:

$$\omega_e' = 480{,}2$$

$$x_e' \omega_e' \sim 2{,}6.$$

§ 4. Störungen

Der obere Zustand enthält mehrere Störungen, welche durch die Gleichung (4) entdeckt sind (siehe Fig. 2). Bei einigen Störungen sind überzählige Linien gefunden, wodurch es möglich war, die B-Werte der störenden Termen zu berechnen (siehe z. B. Kovács).[1] In Fig. 3 sind die oberen Kernschwingungszustände als Funktion von $J(J+1)$ gezeichnet. Alle Störungen sind vermerkt. Wir haben wahrscheinlich vier störende Zustände, welche in Fig. 3 mit a, b, c und d markiert sind; durch die Störungsstellen sind Gerade gezogen. Die Zustände b und c haben B-Werte von rund 0,24 und ω-Werte von rund 400 K. Zieht man Gerade mit den Neigungen 0,235, 0,236, 0,237, 0,238 und 0,239 durch die c-Punkte, erhält man die folgenden Ordinaten im Origo: 33122, 32726, 32335, 31943 und 31539. Diese Werte geben die nachstehenden Abstände zwischen den Kernschwingungsniveaus für den störenden Zustand: 396, 391, 392 und 404 K. Alle Störungen sind in Tabelle 4 gegeben.

§ 5. Vergleich zwischen SrO und CaO

Die Bandenspektren SrO und CaO weisen grosse Ähnlichkeiten auf. So haben sie beide vier bekannte Zustände $X'\,^1\Sigma$, $A\,^1\Sigma$, $B\,^1\Pi$ und $C\,^1\Sigma$ mit denselben Übergängen. Eine Tabelle mit den Bandenkonstanten beider Oxyde ist schon kürzlich in dieser Zeitschrift publiziert worden.[2]

---

[1] Kovács, I., Acta Phys. Hung. *2*, 141, 1952.

[2] Lagerqvist, A., Arkiv f. Fysik *8*, 83, 1954.

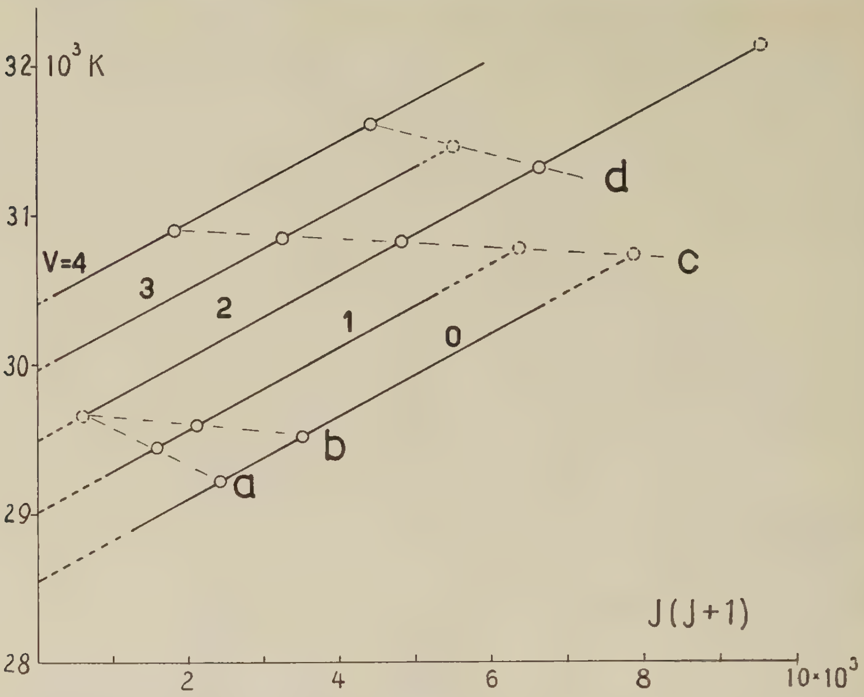

Fig. 3. Kernschwingungsterme mit $v = 0, 1, 2, 3$ und 4 des oberen Zustandes $C\,^1\Sigma$ gegen $J\,(J+1)$ gezeichnet. Die analysierten Teile sind mit dicken, die nicht analysierten Teile mit gestrichelten Linien gezeichnet. Vollständig analysierte Störungen sind durch Zirkel, die übrigen durch gestrichelte Zirkel markiert. Man kann die Linien *a*, *b*, *c* und *d* durch die Störungsstellen ziehen, wodurch gezeigt wird, dass mindestens vier Zustände stören.

Tabelle 4. Störungen im Zustande *C*.

v	J_0	B_s	v	J_0	B_s
4	66	$0{,}23_8$	2	~25	
4	42	$0{,}23_5$	1	~80	
3	~74		1	44,5	
3	56,5	$0{,}23_6$	1	39,5	
2	~97		0	~89	
2	80		0	59	$0{,}24_5$
2	67,5	$0{,}23_7$	0	48,5	

Die gelben und orangefarbigen Bandensysteme sind noch nicht analysiert, aber wir hoffen späterhin auf diese Systeme zurückkommen zu können.

Stockholm, Physikalisches Institut der Universität, Juni 1954.

Tryckt den 23 november 1954

Uppsala 1954. Almqvist & Wiksells Boktryckeri AB

ARKIV FÖR FYSIK Band 8 nr 48

Communicated 2 June 1954 by MANNE SIEGBAHN and ERIK HULTHÉN

The reaction energies of $O^{17}(d,p)\,O^{18}$ and $C^{13}(d,p)\,C^{14}$

By KATARINA AHNLUND, SIGVARD THULIN and ROLF PAULI

With 3 figures in the text

Introduction

The reaction $O^{17}(d,p)\,O^{18}$ has not been reported before. In order to get ufficiently strong thin targets of O^{17} to study this reaction, a method for elec-romagnetic isotope separation of enriched O^{17} gas was developed. The reaction nergy of $O^{17}(d,p)\,O^{18}$ has been measured with the Cockcroft-Walton accelerator nd heavy particle spectrometer [1, 2] of the Nobel Institute. The ground state ransition of $C^{13}(d,p)\,C^{14}$ was measured at the same time.

Preparation of O^{17} targets

The abundance of O^{17} in natural oxygen is only 0.037% and the preparation f useful O^{17} targets from normal oxygen by means of electromagnetic isotope eparation is therefore difficult. However, by using oxygen gas enriched in O^{17} s charge material for the ion source the difficulties are partly overcome. Such sample was supplied to us by Professor CLUSIUS of Zürich. It was prepared y thermal diffusion and was thought to contain mostly $O^{18}O^{18}$, some per cent $)^{17}O^{18}$, and roughly 15% N_2.

By direct oxidation of target plates in this enriched oxygen sample thin oxide ayers were obtained [3]. The O^{17} content of this oxide, of course, amounted o only some per cent of the total oxygen content. Increasing the total amount f oxide was no advantage in the present case, since the total thickness of the ayer must not exceed ~5 keV. It was therefore considered necessary to produce $)^{17}$ targets of higher intensity by means of electromagnetic isotope separation.

Feeding oxygen gas to the ion source of the separator [4] it seems natural o prepare O^{17} targets by collecting the $(O^{17})^+$ ions. However, hydrogen is always resent in the ion source, and it combines very easily with oxygen to form $OH)^+$, $(OH_2)^+$ and $(OH_3)^+$.[1] As O^{16} was present in the sample in large amounts cf. below), the $(O^{17})^+$ ions were mixed up with $(O^{16}H)^+$, and correspondingly he hydride ions of O^{17} were heavily contaminated with O^{16} and O^{18}.

Another possible way of collecting O^{17} is as $(O^{17}O^{17})^+$ at mass number 34.)ue to the low concentration of O^{17} it would however be more convenient to

---

[1] The easy formation of $(OH_2)^+$ ions has in fact been used in earlier separations of O^{18}, which vas then collected as $(O^{18}H_2)^+$.

Table 1.

Mass number	Relative intensity		Occurring ions
	Enriched oxygen + N_2	Normal oxygen	
28	467	20	$N^{14}N^{14}$, $C^{12}O^{16}$
29	5.6	0.3	$N^{14}N^{15}$, $C^{12}O^{17}$, $C^{13}O^{16}$
30	182	5	$N^{14}N^{16}$, $N^{15}N^{15}$, $C^{12}O^{18}$, $C^{13}O^{17}$
31	7.5	—	$N^{14}O^{17}$, $N^{15}O^{16}$, $C^{13}O^{18}$
32	100	100	$O^{16}O^{16}$, $N^{14}O^{18}$, $N^{15}O^{17}$
33	3.1	0.2	$O^{16}O^{17}$, $N^{15}O^{18}$
34	25	0.6[1]	$O^{17}O^{17}$, $O^{16}O^{18}$
35	1.4	—	$O^{17}O^{18}$
36	9.0	—	$O^{18}O^{18}$

[1] This value is higher than expected but may be explained by assuming the presence of $(H_2O^{16}O^{16})^+$ ions.

collect $(O^{17}O^{16})^+$ or $(O^{17}O^{18})^+$. The contamination by O^{16} or O^{18} respectively would not affect the actual measurements.

In order to get an idea of the collection conditions for the O^{17} isotope the ion currents at mass numbers 28–36 were measured. In column 2 of Table 1 are given relative intensities of the ion currents when the enriched oxygen sample was admitted to the ion source. For comparison, the corresponding values for normal oxygen gas are given in column 3. In the last column are listed the ions occurring at each mass number.

From rows 7, 8 and 9 of Table 1 we estimate the relative abundances of the oxygen isotopes in the enriched sample to be

$$O^{16} = 70\% \qquad O^{17} = 4\% \qquad O^{18} = 26\%.$$

As shown in Table 1 the ion current at mass 31 consists of $(N^{14}O^{17})^+$, $(N^{15}O^{16})^+$, and $(C^{13}O^{18})^+$. The relative intensities of these ions are of importance for the separation of useful O^{17} targets. An analysis of the relative intensity values of Table 1 confirms the reasonable assumption that N^{15} is of very low abundance compared to N^{14}. The N^{15}/N^{14} ratio may also be estimated by comparing the O^{18} content in targets prepared by simultaneous collection of masses 32 and 33. The α-particle intensities from the $O^{18}(p,\alpha)N^{15}$ reaction in such targets showed an $N^{15}O^{18} : N^{14}O^{18}$ ratio of less than 0.01. Assuming N^{15} to be 0.4% of the total nitrogen content we compute the following rough values for the composition of the ion current at mass 31:

$$N^{14}O^{17} \approx 90\% \qquad N^{15}O^{16} \approx 7\% \qquad C^{13}O^{18} \lesssim 3\%$$

The O^{17} target preparations were performed by bombarding water-cooled stainless steel plates with ions of mass 31. Three O^{17} samples were prepared. The strongest one was prepared in an 18-hour run and received about 7 μAh ions of mass 31. From the gas consumption (0.5 cm^3 NTP per hr.) and ion current

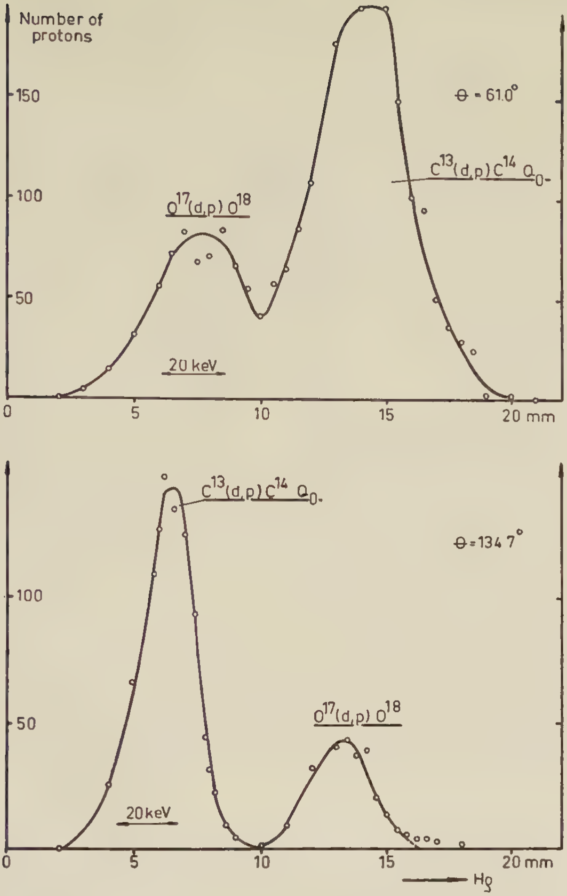

Fig. 1. Spectra of protons from a separated $O^{17} - C^{13}$-target on steel bombarded with 0.855 MeV deuterons showing the relative positions of long-range protons from $O^{17}(d, p)\,O^{18}$ and $C^{13}(d, p)\,C^{14}$ at the observation angles $\theta = 61.0°$ and 134.7° to the incident deuteron beam. The angular width $2\,\Delta\,\theta = 3.4°$. The deuteron bombardment was 2400 μC for each angle.

measurement we estimate the total efficiency ε^1 for the O^{17} separation to be about 1%, assuming a nitrogen content of 15% in the enriched sample and a collection efficiency of 100%.

Measurement of reaction energies

C^{13} and O^{17} are thus collected on the same Fe disk in the separator. By bombardment with 0.855 MeV deuterons they give rise to proton groups of which

---

[1] The efficiency ε is here defined as:

$$\varepsilon = \frac{\text{Amount of } O^{17} \text{ fed to the ion source}}{\text{Amount of } O^{17} \text{ collected}}\,.$$

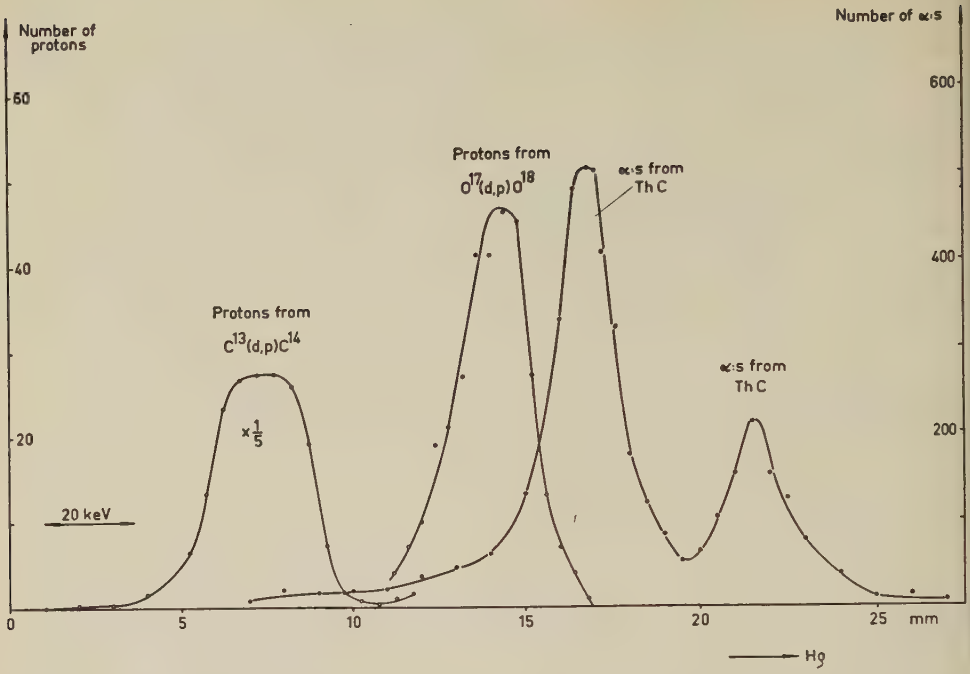

Fig. 2. Proton spectra from $O^{17}(d,p)O^{18}$ and $C^{13}(d,p)C^{14}$ at $E_D = 0.855$ MeV, $\theta = 134.7,°$ compared to the α-lines from ThC which were used to calibrate the energy scale of the nuclear spectrometer. The deuteron bombardment on the $O^{17} - C^{13}$-target was 2400 μ C.

the two of longest range lie very close together in energy at about 6 MeV. By using our strongest O^{17} target we obtained in photographic plates placed after the nuclear spectrometer the distributions shown in Fig 1. The figure shows the spectra of long-range protons studied at the angles 61.0° and 134.7° to the incident deuteron beam. The mutual displacement of the groups helps us to identify them and also gives a numerical value of the reaction energy of $O^{17}(d,p)O^{18}$ in terms of that of $C^{13}(d,p)C^{14}$.

However, a more accurate determination of the reaction energies is possible as one can choose an angle of observation in which the $H\varrho$ value of the protons lies very near to that of the 6082 keV and 6042 keV α-particles from ThC [5–6]. Fig. 2 shows the result of such a comparison. The proton distributions are obtained at 134.7° to the bombarding deuterons and the α-distributions are for an activated 5/100 mm wire as Th source. Elastic scattering of deuterons on clean Ag and on Th-activated Ag showed that no measurable external layer — e.g. from electrostatically collected dust — had been formed on the α-source during the experiment. The external layer on the $C^{13}O^{17}$ plate was measured in the same way. In order to find whether any considerable number of C^{13} atoms appeared in the external layer formed during the deuteron bombardment, we made a similar exposure on a clean Fe disk and got only a few proton tracks. A control is also given by the fact that the distance in the photographic plates between

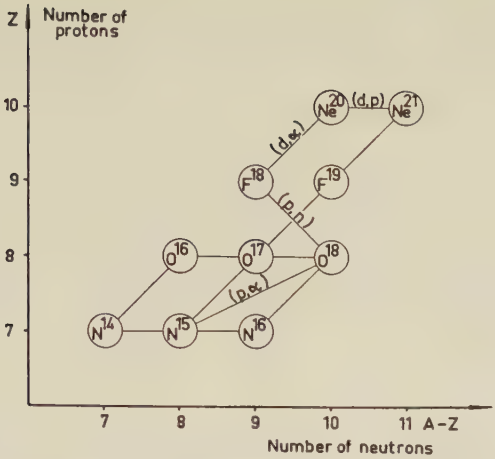

Fig. 3. Schematic diagram of isotopes and nuclear reactions around oxygen. By measuring the Q-value of $O^{17}(d, p)O^{18}$ we have closed a nuclear reaction cycle with the reactions $O^{18}(p, \alpha)N^{15}$ and $O^{17}(d, \alpha)N^{15}$ which have earlier been measured in our laboratory. Each of the three links of this cycle is further closed by one external cycle as shown in the figure.

Table 2.

Source of error	Error	Contribution to Q, keV
Energy of α's leaving ThC source	3 keV	3.2
Displacement between Th source and target spot	0.2 mm	1.6
Reading of distributions	0.8 mm	6.5
Dispersion in plate	3 keV	3.2
Reading of p distributions	0.6 mm	4.9
Spectrometer currents	1 keV	1.1
Target layer	1.5 keV	1.6
Angle measurement	0.3 °	1.5
Deuteron bombarding energy	2.5 keV	1.8
Total probable error		±10 keV

the C^{13} and O^{17} high energy edges was unchanged after long bombardment on the same target spot. This distance was the same in four independent runs on three different targets. The curves were read at the high energy edges. The energy scales of α-particles and protons have been related by $E_p = 0.99078\ E_\alpha$ obtained from the ratio of the relativistic masses of the particles. We get the Q-values

$$O^{17}(d,p)O^{18} : 5821 \pm 10\ \text{keV}$$

$$C^{13}(d,p)C^{14} : 5953 \pm 10\ \text{keV}.$$

Table 2 shows the contributions to the error in Q.

We also get a Q-value for $O^{17}(d,p)O^{18}$ from Fig. 1. If we use the value $Q = 5953 \pm 10$ keV just obtained for $C^{13}(d,p)C^{14}$ we get from the curve at $\theta = 61.0^\circ$ the Q-value of $O^{17}(d,p)O^{18} = 5822 \pm 12$ keV, consistent with the results at $\theta = 134.7^\circ$.

By this measurement we have closed the nuclear reaction cycle $O^{18}(p,\alpha)N^{15}$ $O^{17}(d,\alpha)N^{15}$, $O^{17}(d,p)O^{18}$. See Fig. 3. Our final values for the reaction energies are

$$O^{18}(p,\alpha)N^{15} \quad Q_A = 3967 \pm 9 \text{ keV} \qquad [7$$

$$O^{17}(d,\alpha)N^{15} \quad Q_B = 9807 \pm 12 \text{ keV} \qquad [3$$

$$O^{17}(d,p)O^{18} \quad Q_C = 5821 \pm 10 \text{ keV}.$$

We get $Q_B - Q_A - Q_C = 19 \pm 18$ keV. The components of the cycle are also each checked by one external reaction cycle as indicated in Fig. 3. We thus judge it to be very likely that we have found the ground state transitions of all the three reactions above.

Earlier values for the reaction energy of $C^{13}(d,p)C^{14}$ are 5948 ± 8 keV [8] and 5940 ± 4 keV [9].

A systematic survey of the (d, p)-spectrum from O^{17}, for lower proton energies, which will yield information on the level scheme of O^{18}, is now in progress.

ACKNOWLEDGEMENTS

We are very grateful to Professor KLAUS CLUSIUS, Zürich, for presenting the enriched oxygen gas, and to Professor MANNE SIEGBAHN for continuous interest in our work.

REFERENCES

1. MILEIKOWSKY, C., and PAULI, R. T., Ark. f. Fys. *4*, nr 12, 287 (1952).
2. MILEIKOWSKY, C., Ark. f. Fys. *4*, nr 16, 337 (1952).
3. PAULI, R., AHNLUND, K., and MILEIKOWSKY, C., Ark. f. Fys. (in press).
4. BERGSTRÖM, I., THULIN, S., SVARTHOLM, N., and SIEGBAHN, K., Ark. f. Fys. *1*, 11, 281 (1949).
5. LEWIS, W. B., and BOWDEN, B. U., Proc. Roy. Soc. *A 145*, 235 (1934).
6. BRIGGS, G. H., Proc. Roy. Soc. *A 157*, 183 (1936).
7. MILEIKOWSKY, C., Ark. f. Fys. *7* nr 8, 89 (1953).
8. STRAIT, E. N., VAN PATTER, D. M., SPERDUTO, A., and BUECHNER, W. W., Phys. Rev. *80*, 769 (1950).
9. LI, C. W., and WHALING, W., Phys. Rev. *82*, 122 (1951).

Tryckt den 24 november 1954.

Uppsala 1954. Almqvist & Wiksells Boktryckeri AB

ARKIV FÖR FYSIK Band 8 nr 49

Communicated 2 June 1954 by G. Borelius and H. Alfvén

The solubility of nitrogen in α-iron

By H. U. Åström

With 2 figures in the text

1. Introduction

The preliminary results of measurements on the solubility of nitrogen in α-iron have recently been published in a short paper by Borelius and the author [1]. Here the final results of the investigation will be given and discussed. The investigation was made in search of the sources of discrepancy between the earlier determinations by Dijkstra [2] using the mechanical relaxation effect, and determinations by Borelius, Berglund and Avsan [3] by means of an isothermal calorimetric method. In this re-determination both methods have been used, and the results show good agreement.

2. Relaxation measurements

In the last few years the very small solubilities of nitrogen and carbon in α-iron have been determined from the relaxation phenomenon by measurements of the mechanical elastic after-effect, which can be observed in materials containing small amounts of these elements in solid solution. The essential role that the solute atoms of this kind play in the after-effect was made clear by Snoek [4], who explained the effect by the internal migration of solute atoms between different groups of interstitial positions when the strain of the material is changing.

The equilibrium values of dissolved nitrogen were determined by Dijkstra by means of damping measurements in an apparatus similar to that described by Kê [5]. The specimens were thin wires used as suspension elements in a torsional pendulum system with a period of vibration of about one second. For small vibrational amplitudes the value of the logarithmic decrement Δ was determined as a function of the temperature in the measuring equipment. With the period mentioned, the maximum value $\Delta_{\max}$ will occur at about 20 °C. $\Delta_{\max}$ is a function of the concentration p of the solute, and was assumed by Dijkstra to be proportional to p. The ratio between p and $\Delta_{\max}$ was determined by measurements of $\Delta_{\max}$ versus resistivity in the range up to 0.015 weight % nitrogen, and by use of the relation between resistivity and concentration of nitrogen obtained by Köster [6].

To determine the equilibrium solubility as a function of temperature, $\Delta_{\max}$ was measured after aging the specimens at different temperatures. At 250° and 275 °C a metastable equilibrium appeared, before the stable one could be clearly observed This equilibrium occurs up to about 300 °C. In Fig. 2, showing the atomic ratio o N to Fe in a logarithmic scale versus the reciprocals of the absolute temperatures the values obtained directly from the graphs of DIJKSTRA have been plotted a circles.

The relaxation method used in this investigation is quite different from that o DIJKSTRA. Instead of observing the oscillations of a thin wire, we studied the direc relaxation process of a spiral. This spiral had such dimensions, about 200 grams i weight, that the content of nitrogen put into it by heat treatment could be deter mined by the increase in weight of the sample. The method has been developed i this laboratory by E. LINDSTRAND, whose work on carbon in iron is in progress The spirals used were of technically pure iron from Sandvikens Jernverks A.B with small amounts of Si, Mn, P, S, C, and N as impurities. They were purifie from C and N by heating in wet hydrogen and were charged with various amount of nitrogen by heat treatment in a mixture of H_2 and NH_3. Before weighing, th spirals were cooled down inside the furnace in an inert atmosphere to prevent oxidizing the surface, which would have spoilt the results of weighing. When the tota amount of nitrogen had been determined, the specimens were given a final hea treatment, in order to give them a well-defined state of solution.

The measurements of the elastic after-effect were made at −18 °C, where th time constant of the exponential process is 25 seconds. The spiral was fixed at it upper end. The lower end was turned an angle ε_1 of about 50 degrees, which wa chosen so small as not to give any plastic deformation, only elastic. The spiral wa kept in this position for a sufficiently long time and then released. The after-effec was recorded and always found to be exponential, and its starting value ε_2, just afte the release, was determined by extrapolation. $\frac{\varepsilon_2}{\varepsilon_1}$ is then a measure of the relativ elastic after-effect. It is connected to the logarithmic decrement $\Delta_{\max}$ by means o the simple theory of relaxation, which gives for small after-effects

$$\frac{\varepsilon_2}{\varepsilon_1} = \frac{2}{\pi} \cdot \Delta_{\max} \qquad (1$$

The dependence of $\frac{\varepsilon_2}{\varepsilon_1}$ on the concentration of nitrogen in solution was determine in the following way. The spirals, with known amounts of nitrogen, were quenche from a temperature where all nitrogen was in solution, and special care was take to prevent precipitation during quenching. It was usual to quench in cold water the spirals being dropped directly from the furnace into the water. In order to chec whether this quenching was insufficient we have made comparative quenchings fo some concentrations in other and more effective cooling liquids, such as a 10 % solution of caustic soda in water, but in all these cases the same elastic after-effects within the measuring errors, were observed as after quenching in cold water. W do not think, therefore, that quenching in water involves any error (except possibl for the very highest concentrations). The experimental values of $\frac{\varepsilon_2}{\varepsilon_1}$ versus the concentration of nitrogen in solution are shown in Fig. 1. In the same figure, the lin corresponding to the constant ratio used in the work of DIJKSTRA has been drawn

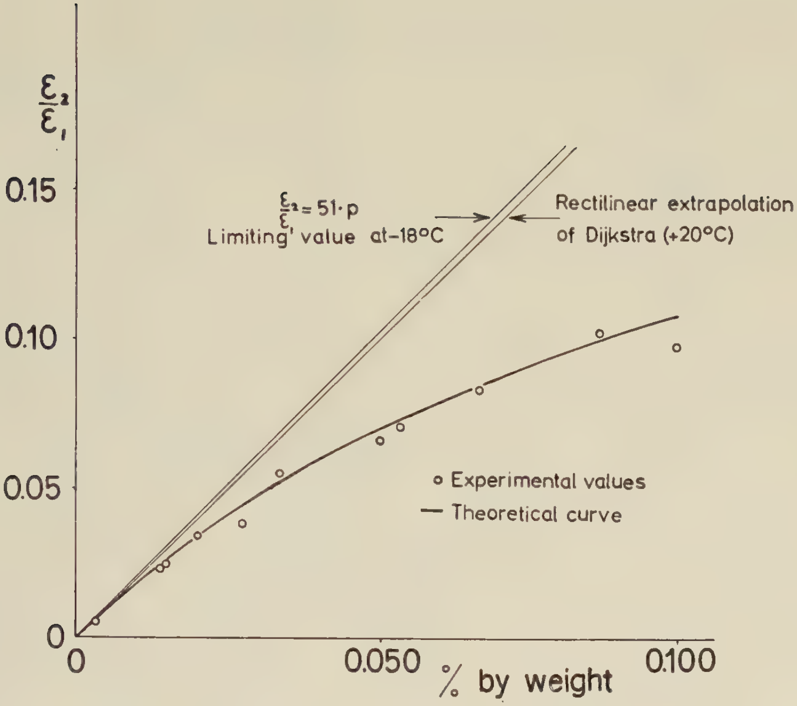

Fig. 1. Elastic after-effect versus concentration of solute nitrogen.

Table 1. Relaxation measurements. Stable phase.

Equilibrium temp. °C	$\frac{\varepsilon_2}{\varepsilon_1}$	Weight % N	Atomic ratio N/Fe
310	0.0268	0.018	0.00067
343	0.0313	0.021	0.00084
445	0.0647	0.048	0.00191

At low concentrations there are only small differences between the curves, but at higher concentrations, not examined in this respect by DIJSKTRA, there appear large discrepancies, the nature of which will be discussed in Section 4.

Using the diagram of Fig. 1, a few determinations of the solubility limit of the stable phase have been made. The results, which have an accuracy of measurement of about 10 %, are given in Table 1 and are included in Fig. 2 as filled circles.

3. Calorimetric measurements

In the investigation of BORELIUS, BERGLUND and AVSAN, the evolution of heat due to the precipitation of nitride was studied in a sample taken from an equilibrium

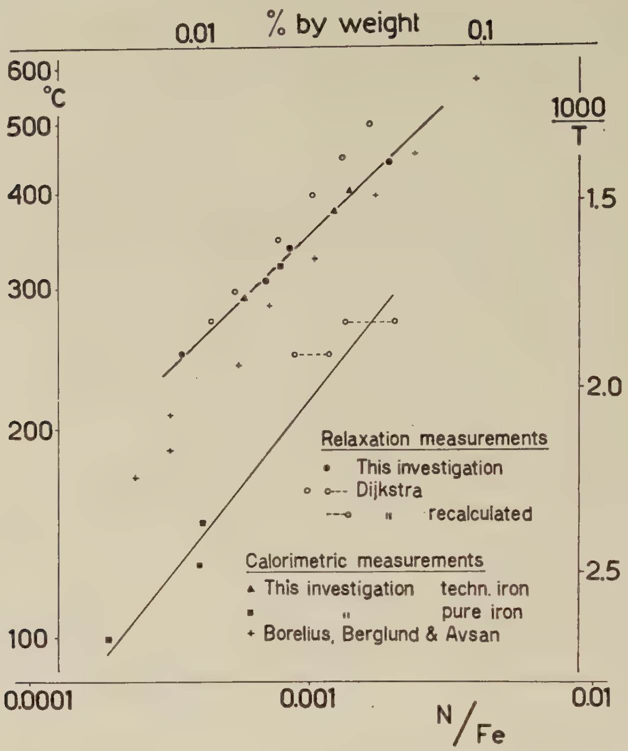

Fig. 2. Solubilities of nitrogen in α-Fe in a logarithmic scale versus the reciprocals of the absolut temperatures.

temperature T directly to the measuring temperature, where most of the nitroge in solution was precipitated. The measuring equipment consisted of a vapour thermostat with very constant temperature, and a series of thermocouples arranged between the sample and the wall of the thermostat. The evolution of heat during th precipitation of nitrogen gave a rise of temperature in the sample which was studied To obtain absolute values of the heat evolved, the arrangement was calibrate with a known amount of Peltier heat, evolved in the junction of a thermocoupl placed in a central boring in the sample.

In order to check the earlier results on the solubility of nitrogen, we have mad some determinations with the same isothermal calorimetric method. It had, however, been observed that the way in which the thermocouple was arranged in th measurements of BORELIUS *et al.* was not quite satisfactory, since part of the Peltie heat could be lost on account of a chimney effect in the boring. Using an improve arrangement of the junction, we have obtained absolute values of the heat evolved which are smaller than those obtained earlier.

The specimens, about 100 grams in weight, were prepared from two bars of iron one of the same technically pure iron as used in the earlier work, and the other a very pure iron from the laboratories of Philips at Eindhoven, Netherlands, kindl placed at our disposal by Mr. J. D. FAST. The technical iron had an initial conten

Table 2. Calorimetric measurements. Stable phase.

Equilibrium temp. °C	Measuring temp. °C	Q_{obs} cal/mole	Q cal/mole	p N/Fe	Weight % N
295	71.0	3.6	3.7	0.00060	0.015
324	72.3	4.3	4.6	0.00076	0.019
381	70.0	7.2	7.4	0.00119	0.030
405	70.5	8.0	8.3	0.00135	0.034

in weight % of 0.01 Si, 0.07 Mn, 0.002 P, 0.007 S, 0.017 C, and less than 0.003 N. This iron was purified from carbon and nitrogen by heat treatment in wet hydrogen gas. The samples were then nitrated in the same way as previously in a mixture of H_2 and NH_3. The amount of nitrogen absorbed was determined from the increase of weight of the samples. The technical iron was given a concentration of nitrogen of 0.07 weight %, and the pure iron 0.03 %.

For measurements of the precipitation of the stable nitride, above 300 °C, the specimens were kept at the equilibrium temperature for a sufficient time, about 20 hours, and then rapidly cooled down to the measuring temperature, 70 °C, where the precipitation took place within a few hours. The stable equilibrium was investigated in the range 295° to 405 °C by three measurements on the technical iron, and one at 324 °C on the very pure iron. Since the solubility of nitrogen at the measuring temperature cannot be neglected, the values of the heat evolved, Q_{obs}, must be corrected by a quantity Q_0 to correspond to complete precipitation. The following relations are valid between the total heat Q, Q_0 and the solubility p (atomic ratio of N to Fe):

$$Q = Q_{\text{obs}} + Q_0 = L \cdot p$$

$$\ln Q = \text{const.} - \frac{L}{RT}. \tag{2}$$

L is the heat of formation of iron nitride in α-Fe and is assumed to be constant for the temperature range considered. Q and p have been calculated by successive approximations, using a $\log Q - 1/T$ diagram, and starting with the approximation $Q_0 = 0$. The results are given in Table 2 and are plotted in Fig. 2.

From Fig. 2 it is found that most of the values from the investigation of BORELIUS, BERGLUND and AVSAN are higher than the present ones. This is due partly to the experimental error mentioned and partly, for temperatures below 300 °C, probably to precipitation of not only the stable phase but also the metastable one.

The precipitation of the metastable phase existing below 300 °C was proceeding much faster than that of the stable phase, the time constant being only a few minutes. On account of the heat inertia of the apparatus, only the later part of the precipitation could be studied and most of the heat evolved was thus lost. We have, however, obtained some data for the solubility limit of the metastable equilibrium by means of a second heat evolution, which it was possible to observe at certain measuring temperatures, when the metastable precipitation was almost or entirely ended. The heat is due to the transformation at the measuring temperature of the metastable equilibrium with the higher solubility into the stable one with the lower solubility of nitrogen.

Table 3. Calorimetric measurements. Metastable phase.

Equilibrium temp. °C	ΔQ $Q_{\text{metast.}}-Q_{\text{stab.}}$ cal/mole	$\Delta Q/L$ N/Fe	$p_{\text{stab.}}$ N/Fe	$p_{\text{metast.}}$ N/Fe	Weight % N
102	0.9	0.00018	0.00002	0.00020	0.005
130	1.9	0.00039	0.00005	0.00044	0.011
150	1.9	0.00039	0.00006	0.00045	0.011

Three determinations have been made on the metastable equilibrium at 102°, 130°, and 150°. The corresponding values of the stable equilibrium have been obtained by extrapolating the solubility limit, which is a straight line in the logarithmic diagram of Fig. 2. These values, as well as the final results on the solubility of the metastable equilibrium, are given in Table 3 and shown in Fig. 2. On account of the small amounts of heat evolved, the values of the solubility are not as accurate as in the stable case. Using the values of DIJKSTRA at 250° and 275 °C, which have been recalculated by means of our experimental $\frac{\varepsilon_2}{\varepsilon_1}$ curve, a probable solubility limit has been drawn. The reason for this recalculation will be stated in Section 4.

The values of the solubility concentration of nitrogen in equilibrium with Fe_4N given by the calorimetric measurements agree well with the results from the relaxation method. A straight line representing the phase boundary has been laid in through the measuring points in Fig. 2. Extrapolation to the eutectoid temperature 590 °C gives a maximum solubility of about 0.1 % by weight of nitrogen in accordance with the value of PARANJPE *et al.* [7] obtained by a nitrogenizing method. For the small solubilities considered here, the present results on the stable equilibrium can be written in exponential form as

$$p = 0.141 \cdot e^{-\frac{6200}{RT}}$$

where 6200 is the heat of formation of Fe_4N in α-iron in calories per mole.

4. Discussion of the dependence of relaxation on concentration

The source of the non-linear dependence of relaxation on concentration shown in Fig. 1 is probably to be found in a mutual interaction between adjacent solute nitrogen atoms, a possibility which has already been discussed to some extent by POLDER [8].

Nitrogen forms an interstitial solid solution in the body-centered cubic lattice of α-iron, and the positions occupied are probably those at the centres of the cube faces and at the centres of the cube edges, which are crystallographically equivalent. The number of these positions is three times the number of Fe-atoms. If the ratio of N-atoms to Fe-atoms is p, the probability of finding an N-atom in a certain interstitial "hole" is thus $p/3$. The distance between two N-atoms in adjacent holes is 1.43 Å, whereas the distance between atoms in the N_2-molecule is about 1.10 Å. It is now assumed that there is also a tendency for adjacent solute atoms to form pairs, though the forces between the atoms are of course weaker than in the case of a gas. If we denote the ratio of free N-atoms, that is N-atoms with no neighbour in any of the (four) adjacent holes, to the number of Fe-atoms, by p_{N}, and the corresponding number of N-atoms coupled together by $2\,p_{\mathrm{N}_2}$, we obtain

$$p_{\mathrm{N}} + 2\,p_{\mathrm{N}_2} = p. \tag{3}$$

We have neglected the probability for groups of three or more N-atoms, and this can be considered permissible because of the very low concentrations of solute atoms. The probability of a random N-atom being free is

$$(1 - p/3)^4 \tag{4}$$

and the probability that it is not free

$$1 - (1 - p/3)^4. \tag{5}$$

According to Boltzmann statistics the ratio of paired to free N-atoms can then be written as

$$\frac{2\,p_{\mathrm{N}_2}}{p_{\mathrm{N}}} = \frac{1-(1-p/3)^4}{(1-p/3)^4} \cdot e^{-\frac{E}{RT}} \tag{6}$$

where E is comparable with a dissociation energy, R the gas constant and T the absolute temperature.

Combining eqs. (6) and (3) and taking into account that p is very small compared with unity, we get

$$p_{\mathrm{N}} = \frac{p}{1 + \frac{4}{3} p \cdot e^{-\frac{E}{RT}}}. \tag{7}$$

Since the relaxation phenomenon is explained by the migration of the N-atoms, after a change in the strain of the material, to the holes which are widened and have become energetically more favourable, we now make the assumption, close at hand, that only the unpaired atoms are free to move, which gives

$$\frac{\varepsilon_2}{\varepsilon_1} = k(T) \cdot p_{\mathrm{N}} \tag{8}$$

where $k(T)$ is independent of the concentration but depends on the temperature. Combining eqs. (8) and (7), we obtain

$$\frac{\varepsilon_2}{\varepsilon_1} = k(T) \cdot \frac{p}{1 + \frac{4}{3} p \cdot e^{-\frac{E}{RT}}}. \tag{9}$$

With $k(T) = 51$ for our measuring temperature of -18°C and $E = -2600$ cal/mole, eq. (9) gives good agreement with the experimental results. The values thus calculated are laid in as a curve in Fig. 1. In this figure we also have drawn the line corresponding to $\frac{\varepsilon_2}{\varepsilon_1} = 51 \cdot p$, which gives the limiting value of our $\frac{\varepsilon_2}{\varepsilon_1}$ curve for low concentrations, and the line corresponding to $\frac{\varepsilon_2}{\varepsilon_1} = 50 \cdot p$, which was the relationship used by DIJKSTRA for his calculation of the solubility from the damping measurements at +20 °C. The small difference between the slopes of the lines makes it possible to calculate, with a certain degree of probability, solubility values from the data of DIJKSTRA corrected with respect to the found dependence on concentration. In this way we have obtained the two points in Fig. 2 for the solubility limit of the metastable phase.

Though of course nothing definite can be concluded from the experimental material of Fig. 1, much can be said for the hypothesis that the non-linear relationship between elastic after-effect and concentration of nitrogen depends on mutual interaction between the solute atoms in the described way. The forces are, however, weak, which is illustrated by the low E-value of the effect (2600 cal/mole). ZENER (9), for the case of strain energy coupling between the carbon atoms in martensite, obtained a value of 2000 cal/mole using a treatment not quite comparable with that of this work. A weak point in the present case is the restriction of the interaction to only four adjacent solute atoms, and the assumption that the pairs formed are absolutely passive in the relaxation process. Nevertheless, it can be concluded that the principal cause of the discrepancy between relaxation and calorimetric determinations of the solubility of nitrogen in α-iron given in the literature is the assumed linear relation between elastic after-effect and concentration used in evaluation of the relaxation measurements.

5. Summary

The solubility of nitrogen in α-iron has been determined by isothermal calorimetric measurements and by studying the elastic after-effect of samples in the shape of iron spirals. The values of the solubility obtained show good agreement. The dependence of the elastic after-effect on the concentration of the solute nitrogen in the spirals was measured in the whole solubility range available, the content of nitrogen being determined by weighing. The dependence was found to be non-linear, in contradiction to results given in the literature. The source of this non-linear relation is thought to be the interaction between the solute nitrogen atoms, and a formula for the elastic after-effect accounting for this phenomenon is derived from statistical considerations. The calculated curve of the after-effect is in good agreement with the experimental values.

Acknowledgement

The present investigation has been carried out at the Royal Institute of Technology, Department of Physics. To the Director of the Department, Professor G. BORELIUS, who suggested the work, I beg to express my gratitude for valuable discussions and advice, and the constant interest he has shown in my work.

I also wish to thank Dr. J. O. LINDE and Mr. E. LINDSTRAND for discussions, and Mr. H. AM ENDE, who assisted me in some measurements.

The work has been supported by a grant from the Swedish Council for Technical Research.

REFERENCES

1. H. U. Åström and G. Borelius, Acta Metallurgica 2 (1954) 547.
2. L. J. Dijkstra, J. Metals *1* (1949) 252.
3. G. Borelius, S. Berglund, and O. Avsan, Arkiv för Fysik *2* (1951) 551.
4. J. L. Snoek, Physica *8* (1941) 711.
5. T. S. Kê, AIME Metals Tech. June 1948, TP 2370.
6. W. Köster, Arch. Eisenhüttenw. *3* (1929/30) 637.
7. V. G. Paranjpe, M. Cohen, M. B. Bever, and C. F. Floe, J. Metals *2* (1950) 261.
8. D. Polder, Philips Res. Rep. *1* (1945) 5.
9. C. Zener, Phys. Rev. *74* (1948) 639.

Tryckt den 23 november 1954

Uppsala 1954. Almqvist & Wiksells Boktryckeri AB

ARKIV FÖR FYSIK Band 8 nr 50

Communicated 12 May 1954 by ERIK HULTHÉN

The band spectrum of the Au_2-molecule

By BENGT KLEMAN, STIG LINDKVIST and LARS-ERIK SELIN

With 2 figures in the text

General procedure

In a recent paper by two of us (1), on the band spectrum of the Cu_2-molecule, it was reported that under experimental conditions similar to those under which the Cu_2-spectrum appears there also appear spectra which are probably due to the Ag_2- and Au_2-molecules.

A King's furnace was loaded with gold, and the emission spectrum at a temperature of about 2100° C was studied. As filling-gas, argon at a pressure of 500 torr was used.

An extended system of bands, commencing in the green region and extending to the red far beyond the Na-lines, was found. The bands, which have sharp heads, are degraded to the red.

The region 4500–6500 Å was photographed on Ilford Thin Film Panchromatic plates in the first order of a plane grating with a dispersion of about 5 Å/mm. The exposure-time was 30–60 min.

Analysis of the bands

We assume, considering the low temperature of the thermic light-source, that the lower state is the ground-state, and designate the band system *A–X* of Au_2. This identification of the carrier of the band system will be discussed later (below).

Some 150 bands, all belonging to the same system, were measured.

The vibrational analysis gives the following equation for the heads of the bands:

$$\begin{aligned}\sigma_{v'v''} = 19643.8 &+ (141.8_3\, v' - 0.447_4\, v'^2 - 0.0014_8\, v'\, 3)\\ &- (190.4_7\, v'' - 0.419_6\, v''^2 - 0.0000_5\, v'')^3.\end{aligned}$$

The constants have been determined graphically. The large difference between the ω-values in the upper and lower states indicates a similarly large difference also in the B-values, and we may consequently expect that the head of a band will not be very far from the origin. Thus the vibrational constants determined from the measurements of the heads will probably differ only very little from those which would be obtained from the origins. The measured band-heads are

Table 1. Wave-numbers of the band-heads A–X

Δv	$v' v''$	σ cm^{-1}
+ 7	10.3	20448.1
	11.4	20392.5
	12.5	20337.6
+ 6	8.2	20370.6
	9.3	20315.4
+ 5	6.1	20288.5
	7.2	20235.3
	8.3	20182.1
+ 4	4.0	20204.8
	5.1	20151.8
+ 3	3.0	20065.3
	4.1	20014.2
+ 2	2.0	19925.8
+ 1	1.0	19785.5
	2.1	–
	3.2	19686.5
0	0.0	19643.7
	1.1	19595.0
	2.2	19546.8
− 1	0.1	19453.9
	1.2	–
	2.3	19357.7
	3.4	19310.1
− 2	0.2	19264.3
	1.3	19217.4
	2.4	–
	3.5	19123.9
− 3	0.3	19075.8
	1.4	19029.7
− 4	0.4	18887.8
	1.5	18843.4
	2.6	18798.0
− 5	0.5	18701.1
	1.6	18656.9
	2.7	18612.6
	3.8	18567.9
	4.9	18523.4
− 6	1.7	18472.8
	2.8	18428.8
	3.9	18385.2
	4.10	18341.1
	5.11	18297.4
	6.12	18253.0
− 7	2.9	18245.6
	3.10	18202.7
− 7	4.11	18159.4
	5.12	18116.5
	6.13	18073.3
− 8	3.11	18021.0
	4.12	17978.8
	5.13	17936.4
	6.14	17894.6
	7.15	17852.0
	8.16	17809.3
	9.17	17766.9
− 9	4.13	17799.2
	5.14	17757.3
	6.15	17716.3
	7.16	17674.1
	8.17	17632.6
	9.18	17590.3
	10.19	–
	11.20	17506.4
−10	5.15	17578.4
	6.16	17538.5
	7.17	17497.8
	8.18	17456.7
	9.19	17416.0
	10.20	17374.7
	11.21	17333.8
	12.22	17293.5
	13.23	17250.5
−11	6.17	17362.0
	7.18	17322.3
	8.19	17282.0
	9.20	17241.7
	10.21	17201.4
	11.22	17160.9
	12,23	17120.1
	13.24	17079.5
	14.25	17038.7
	15.26	16998.7
−12	8.20	17107.7
	9.21	17068.3
	10.22	17029.0
	11.23	16989.5
	12.24	16949.6
	13.25	16909.7
	14.26	16869.7
	15.27	16829.6
	16.28	16789.3
−13	10.23	16858.0
	11.24	16818.7
	12.25	16779.8
	13.26	16741.0
	14.27	16701.7
−13	15.28	16662.3
	16.29	16622.9
	17.30	16582.8
	18.31	16543.0
−14	12.26	16610.5
	13.27	16572.9
	14.28	16534.3
	15.29	16495.7
	16.30	16457.1
	17.31	16418.2
	18.32	16378.9
	19.33	16340.3
	20.34	16300.8
	21.35	16260.8
−15	13.28	16405.2
	14.29	16368.2
	15.30	16330.3
	16.31	16292.2
	17.32	16254.4
	18.33	16216.1
	19.34	16177.8
	20.35	16139.2
	21.36	16100.4
	22.37	16060.9
−16	15.31	16165.5
	16.32	16128.3
	17.33	16091.3
	18.34	16053.8
	19.35	16016.3
	20.36	15978.6
	21.37	15940.5
	22.38	15902.2
	23.39	15864.1
	24.40	15825.4
	25.41	15786.1
−17	17.34	15929.4
	18.35	15892.7
	19.36	15856.2
	20.37	15819.9
	21.38	15782.2
	22.39	15744.5
	23.40	15707.1
	24.41	15669.2
	25.42	15631.0
−18	19.37	15696.8
	20.38	15660.4
	21.39	15624.0
	22.40	15587.8
	23.41	15550.6
	24.42	15513.9
	25.43	15476.4
	26.44	15438.7

given in Table 1. The most intense of the bands are in order the 0,3; 1,4; 1,5; 2,6; 0,2 and 0,1 bands (Fig. 1).

The Franck-Condon distribution of the bands is shown in Fig. 2. The intensities of the heads have been roughly estimated from the plates, and are represented in the v'/v'' scheme by figures varying from 5–1. Since each exposure only covers about 500 Å of the spectrum, there may be some jumps in the intensity-scale for different parts of the spectrum.

Comparison with the Cu_2-bands

For Cu_2 two band systems were found, an extended green system (A–X) and a short blue system (B–X). The carrier of these systems was indentified with the help of the isotope effect.

When copper is used in a King's furnace there appear, at high temperatures, except for the bands mentioned above, only the bands due to CuH. Using silver or gold instead of copper under similar experimental conditions, we obtain some earlier unknown band systems and also the hydride bands in the violet part of the spectrum. We naturally expect that the unknown systems, as in the case of copper, will be emitted by the diatomic metal molecules.

In the present investigation of gold we cannot, in the absence of any isotope effect, adduce rigorous proof that the carrier of the green system is Au_2. This assumption is, however, strengthened by a comparison with the green system of the Cu_2-molecule. The appearance of the systems is very similar, with sharp heads degraded to the red and with long sequences for negative Δv-values. In Table 2 are shown the ω-values for the two molecules.

The ratio between the ω-values of the ground-states for the two molecules Au_2 and Cu_2 is 0.72, and the corresponding ratio for the A-states 0.74. The constancy of this reduction factor is an indication of the relationship between the two molecules. The order of magnitude of the factor seems also compatible with the assumption of the Au_2-molecule as the emitter of the observed band system.

Table 2. ω_0-values in Kayser

$X\ Cu_2$	$X\ Au_2$	$A\ Cu_2$	$A\ Au_2$
265.1	190.5	191.5	141.8

Energy of dissociation

We estimate the energy of dissociation of the ground-state with the help of the formula

$$D_0 = \frac{\omega_0^2}{4\,\omega_0\,x_0}.$$

For D_0^0, the value 2.7 eV is obtained.

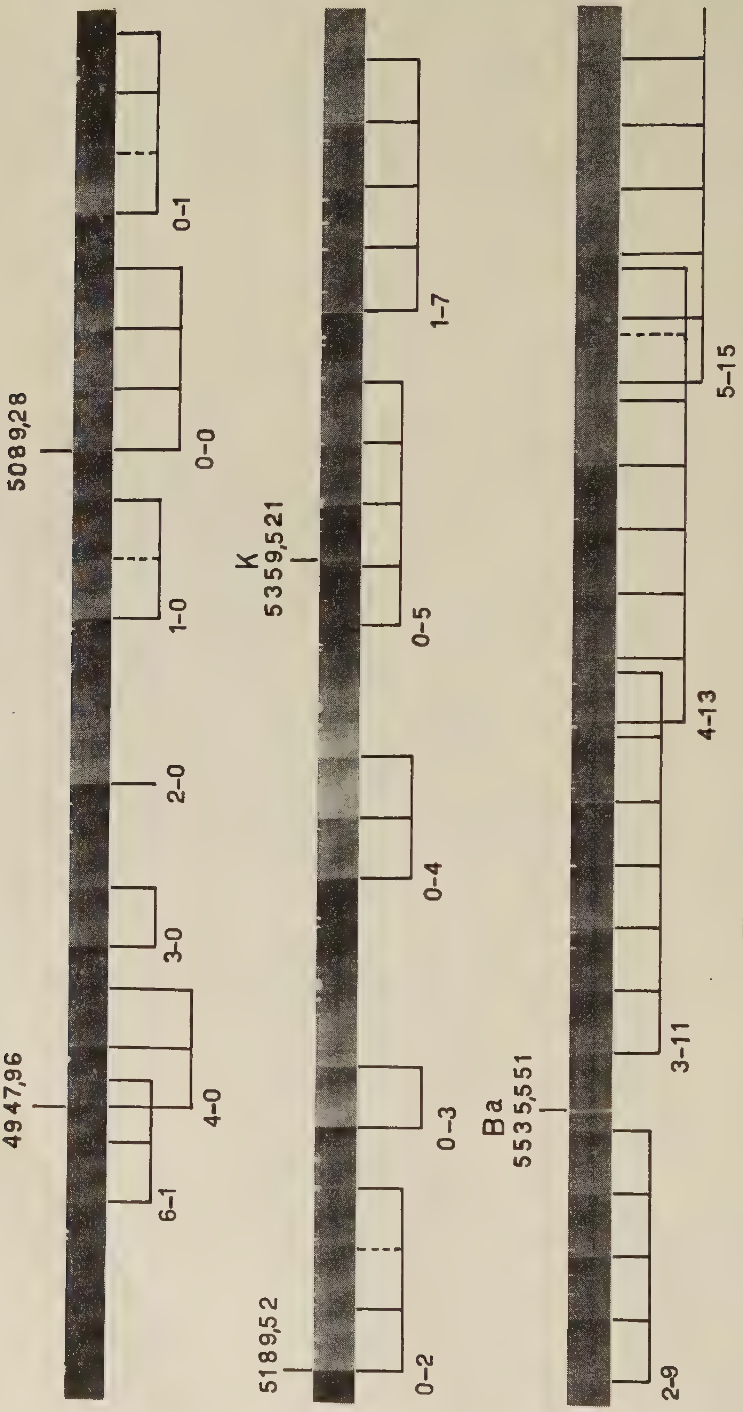

Fig. 1. The green band system of Au_2 (A–X).

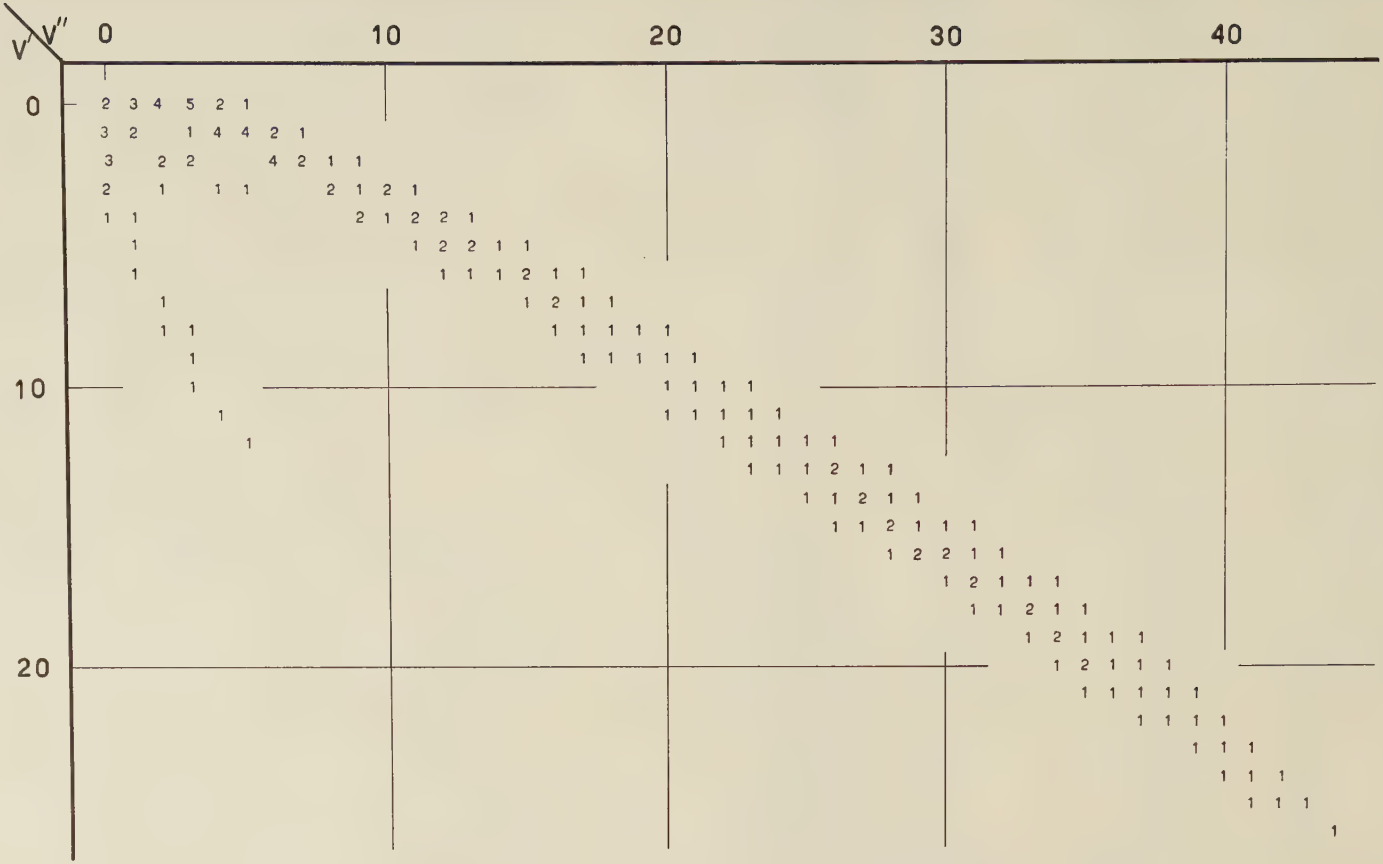

Fig. 2. The Franck-Condon distribution of the observed bands in the A–X system of Au_2.

Constants of the A–X system in Au_2

The following constants (in Kayser) have been obtained from the vibrational analysis

State	T_e	σ_{00}	ω_e	ω_0	$\omega_e x_e$	$\omega_0 x_0$	$\omega_e y_e = \omega_0 y_0$
A . . .	19668.1	19643.8	142.3	141.8	0.445	0.447	−0.0015
X . . .	0		190,9	190.5	0.420	0.420	−0.0001

Summary

With gold in a King's furnace an emission spectrum of bands is obtained. The band system, which has its 0,0 band-head at 5089.28 Å, shows long sequences in the yellow and orange regions. A vibrational analysis of the band system has been carried out

From the experimental conditions under which the spectrum appears and from the relations of the derived band constants to those of the green system of Cu_2, it is concluded that the emitting molecule is Au_2,

Physics Departement, University of Stockholm, May 1954.

REFERENCE

1. KLEMAN, BENGT, and LINDKVIST, STIG, Arkiv för Fysik, *8* nr 32, 1954.

Tryckt den 23 november 1954

Uppsala 1954. Almqvist & Wiksells Boktryckeri AB

ARKIV FÖR FYSIK Band 8 nr 51

Communicated 2 June 1954 by G. Borelius and H. Alfvén

Investigation of the critical shear stress for single crystals of metallic solid solutions. II

By J. O. Linde and Sture Edwardson

With 15 figures in the text

Introduction

In a paper by Linde, Lindell and Stade [1] some preliminary results of measurements of the critical shear stress for pure copper and some dilute copper alloys have been given. Here the results of additional measurements on the same subject follow. This report also includes results of some older measurements by one of the present authors (J. O. L) and Lindell and Stade. Because of the need to answer some questions regarding the accuracy of these older results, the present publication has been considerably delayed.

1. Experimental technique

The methods adopted at the first stage of the investigation, the results of which are included in this paper, differ in some respects from those in [1]. Thus the strain gauge used was of commercial type, consisting of a resistance wire embedded in a plastic material which was fastened directly onto the crystal. For the application of the load during the stress-strain measurements a commercial type of tensile machine was used, allowing a maximum load of 50 kg to be measured. The arrangements for measuring the orientation of the crystal axes in the rods were in all cases those described in [1].

The earliest measurements were performed using alloys with relatively high values of the critical shear stress (Cu-Sn, Cu-In and Cu-Sb alloys). During the course of the preliminary measurements some doubts arose as to the reliability of the strain-gauge equipment used for the measurements. It was feared that the fastening of the plastic material onto the crystal rods would lead to too high values of the critical shear stress. The arrangement was therefore replaced by the one described in [1]. Later experiments have, however, shown that the source of error mentioned can probably be neglected (at all events when measurements on the most soft samples are excluded). In fact, when evaluating the critical shear stress from the stress-strain curves obtained with the one or the other method, fairly good agreement between the results of the different series is obtained.

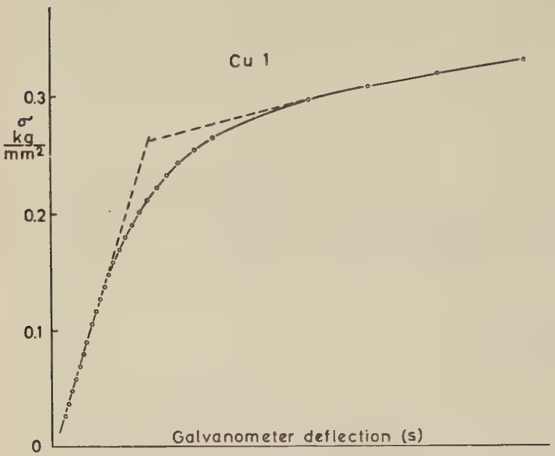

Fig. 1 a.

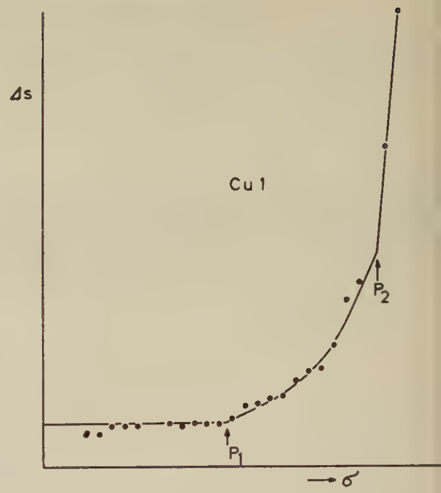

Fig. 1 b.

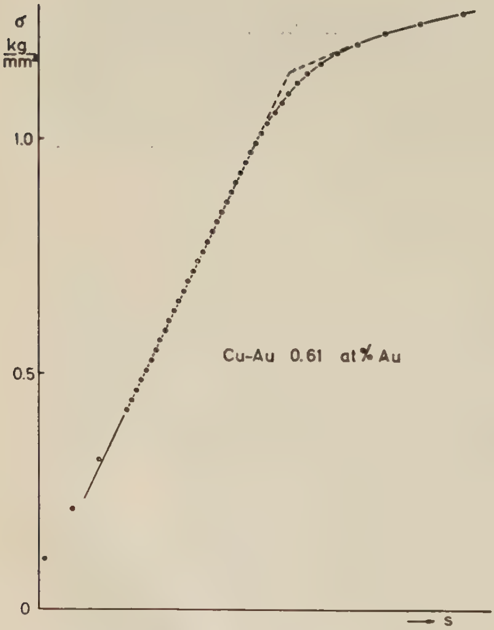

Fig. 2 a.

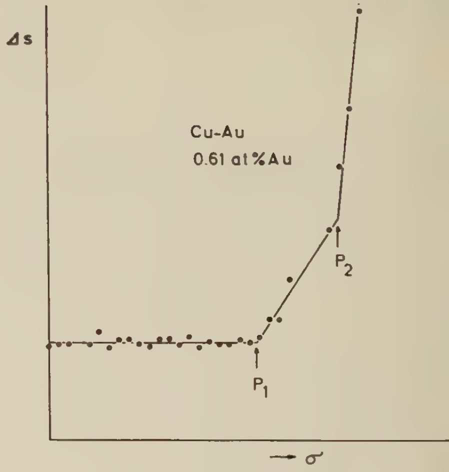

Fig. 2 b.

2. Results

In Figures 1–10 a series of stress-strain curves is shown. The curves give the absolute values of the stress as a function of the galvanometer deflection, absolute values of the strain not being measured. The rate of loading was 2–10 kg per hour. The lower limit is valid for the most soft crystals.

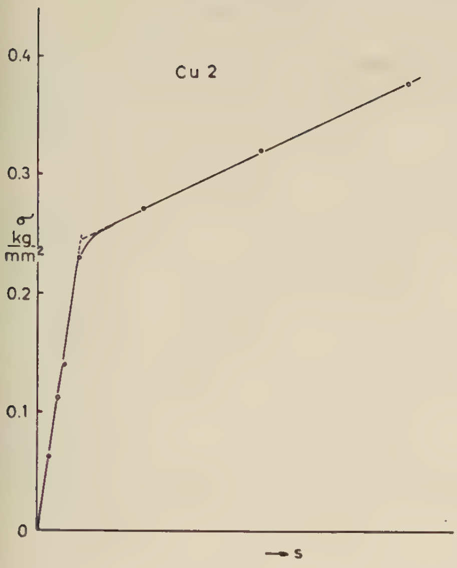

Fig. 3.

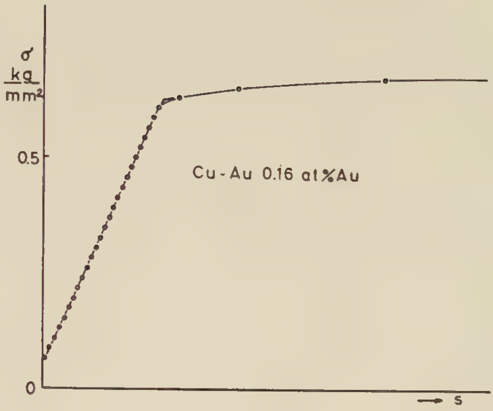

Fig. 4.

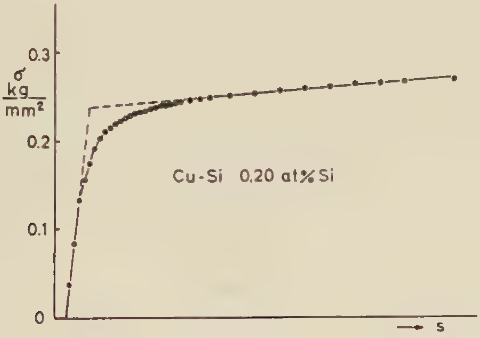

Fig. 5.

In [1] the yield point for a given sample was judged as the point where a noticeable, even if very small, deviation of a given curve from a straight line appears. For curves of the type here exemplified by Figures 4, 6 and 10 this method undoubtedly leads to correct results. More questionable is the method for curves exemplified by Figures 1 a, 2 a, 5, and 8, which are characterized by a very slowly increasing deviation from the straight line at the beginning of the plastic deformation. When in the latter case the increase in strain Δs is plotted as a function of the stress σ at a given rate of loading, curves of the type given in Figures 1 b and 2 b are obtained. In these one observes two different points of discontinuity, P_1 and P_2. A possible explanation of the two discontinuities is that the point P_1 is caused by a small plastic bending of the crystals, while P_2 is the yield point for plastic glide. It is mainly in the case of the most soft crystals that this ambiguity regarding the yield point appears. The dashed lines traced on some of the diagrams show the method of evalution

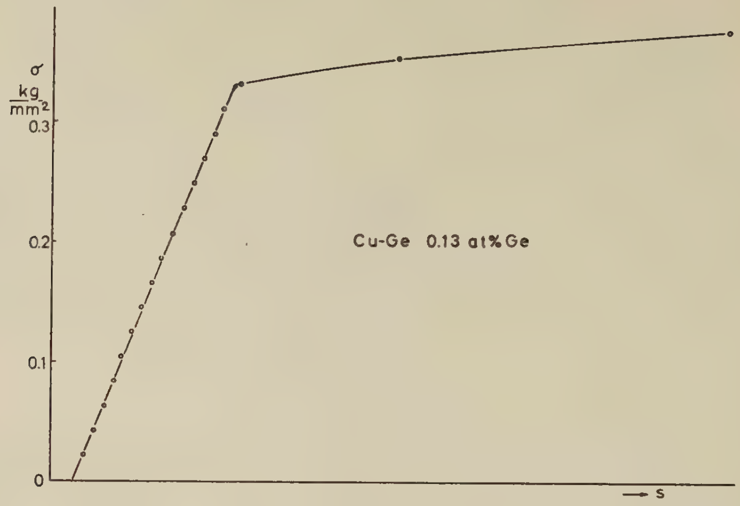

Fig. 6.

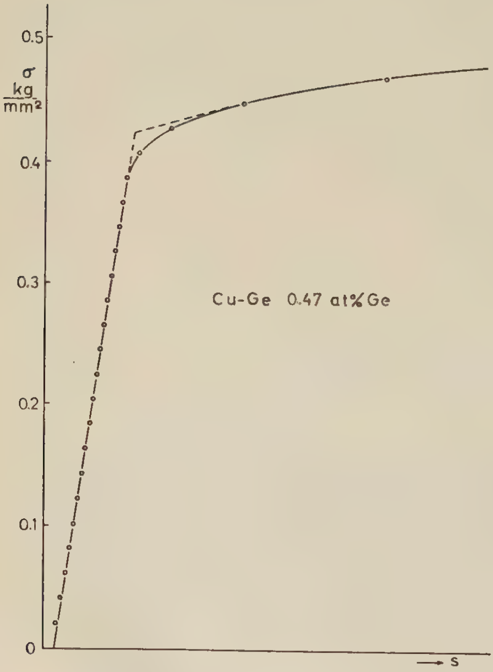

Fig. 7.

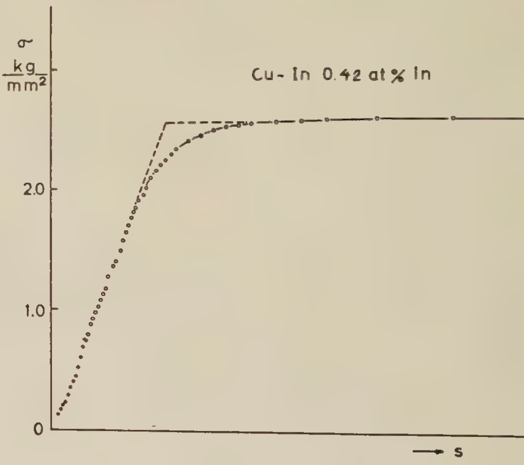

Fig. 8.

of P_2 directly from the stress-strain curves. Accepting this interpretation as a working hypothesis, we have generally in this paper used P_2 when evaluating the critical shear stress for the different samples. As a consequence thereof the values of the critical shear stress for pure copper and for the Cu-Mn and Cu-Sn

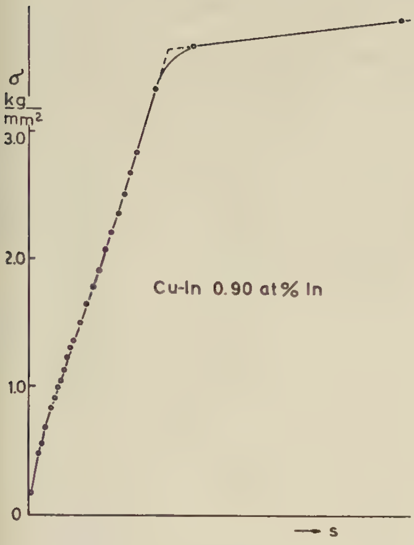

Fig. 9.

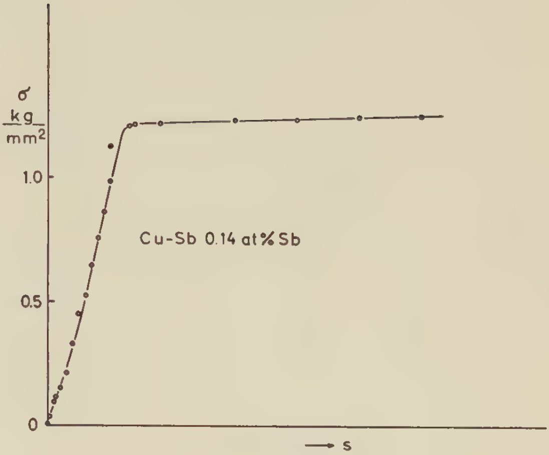

Fig. 10.

alloys now reported are higher than those given in [1]. It may be remarked that the method just mentioned has at times also been used by other workers in this field [2].

In Table 1, the values obtained for the yield stress σ_0 and the critical shear stress τ_0 for copper alloys are collected. The quantity c denotes the concentration of the solute in at %. The table also contains values of the angle ϕ between the direction of σ and the normal to the glide plane and of λ which is the angle between σ and the glide direction in the actual glide plane. The following expression has been used for the calculation of τ_0 from the observed data

$$\tau_0 = \frac{\sigma_0}{\sqrt{6}} (a+c)(c+b-a),$$

where a, b, and c are the direction cosines of the rod axis related to the cubic axis system of the crystal. a, b and c are chosen so that $a<b<c$ and, of course, $a^2+b^2+c^2=1$. For further details see [1].

In Figures 11–14 the values of τ_0 for the different alloy systems are plotted as a function of the concentration c of the solute. The relationship between c and τ_0 is apparently linear for all the alloy systems investigated (dilute alloys), but the scattering of the points is in some cases rather large. The main sources of error are inhomogeneities and deviations from perfectness of the crystals which may vary for the different samples. Furthermore the occasional small bending of the crystals, mentioned already, influences the critical shear stress towards too low values. From the scattering of the points in the figures, an error of ± 10 % seems reasonable. It is probable that the accuracy could be improved considerably by incorporation of some changes in the experimental arrangement. For this purpose, however, crystals of larger dimensions than those used here are needed, or rather the use of larger crystals would appreciably facilitate the introduction of extra arrangements in the apparatus for this purpose.

Table 1

Alloy	c at %	σ_0 kg/mm²	φ	λ	$\cos\varphi\cos\lambda$	τ_0 kg/mm²
Cu 1		0.264	62°7	39°7	0.356	0.094
Cu 2		0.249	59°5	38°5	.397	0.098
Cu-Si	0.20	0.239	41°7	48°0	0.498	0.119
	.60	.379	46°9	46°0	.475	.180
	1.50	.589	50°7	42°3	.471	.277
	3.00	1.04	62°3	32°3	.395	.410
	4.70	1.58	54°3	46°5	.405	.639
Cu-Mn	0.25	0.547	58°5	31°5	0.452	0.247
	.49	.879	49°2	42°0	.485	.426
	.61	.872	67°1	33°2	.326	.264
	.93	1.251	49°2	46°3	.451	.562
Cu-Ni	1.1	0.573	52°0	38°5	0.483	0.276
Cu-Ge		0.325	59°4	31°0	0.436	0.142
		.423	53°5	37°3	0.474	0.200
Cu-In	0.19	0.790	59°0	38°5	0.402	0.318
	.31	1.117	41°5	49°5	0.498	0.558
	.42	2.46	47°0	47°5	0.461	1.12
	.87	3.63	52°3	43°5	0.443	1.61
Cu-Sn	0.09	0.694	44°9	47°4	0.479	0.332
	.26	1.49	60°0	37°0	.400	.549
	.42	2.17	47°3	42°7	.498	1.08
	1.30	5.78	49°9	46°1	.447	2.58
Cu-Sb	0.14	1.17	49°3	40°9	0.492	0.59
	.41	2.11	41°0	51°7	.468	.99
Cu-Au	0.16	0.626	42°3	51°7	0.451	0.286
	.61	1.13	53°0	42°3	.445	.503
	.614	.962	49°5	42°0	.493	.474

Table 2

Alloy system	$\frac{1}{a}\frac{da}{dc}\times 10^3$	$\frac{d\tau_0}{dc}$	Alloy system	$\frac{1}{a}\frac{da}{dc}\times 10^3$	$\frac{d\tau_0}{dc}$
Cu-Si	0.18	0.11	Cu-In	2.60	1.84
Cu-Mn	1.0	0.47	Cu-Sn	2.80	1.99
Cu-Ni	0.26	0.16	Cu-Sb	3.01	2.55
Cu-Ge	0.96	0.28	Cu-Au	1.53	0.72

The fact that the slope of the lines in Figures 11–14 varies considerably from one alloy system to another implies that the increase of τ_0 per atomic percent of the solute has different values in the different alloy systems. The predominating factor that governs the quantity $d\tau_0/dc$ (i.e. the change of τ_0 for 1 at % of the solute), seems to be the difference in atomic volume of the solute and that of the solvent for a given alloy system. Very striking is the small increase of τ_0 in the case of Cu-Si. This may be correlated with the fact that the change in lattice parameter (a) when Si is alloyed with Cu is extremely small. (Table 2.

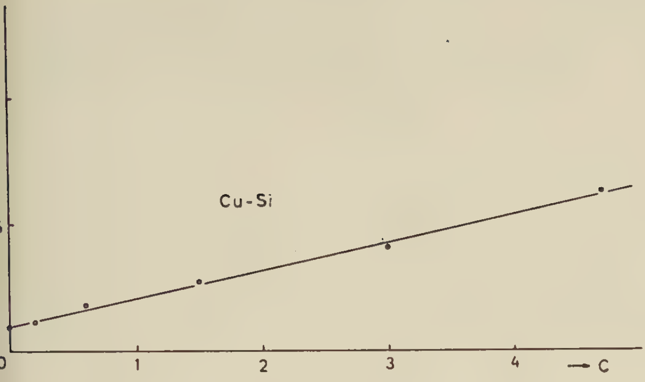

Fig. 11.

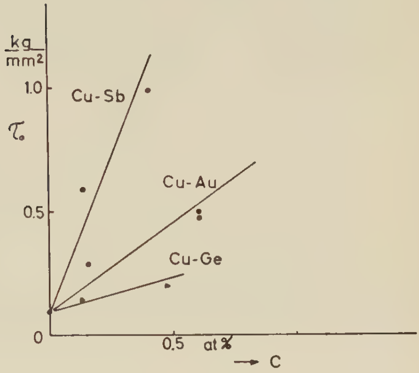

Fig. 12.

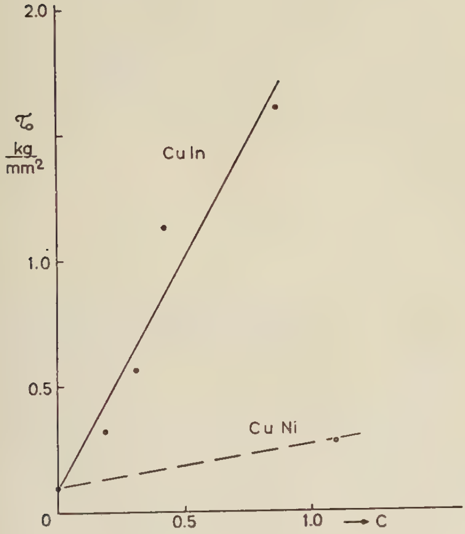

Fig. 13.

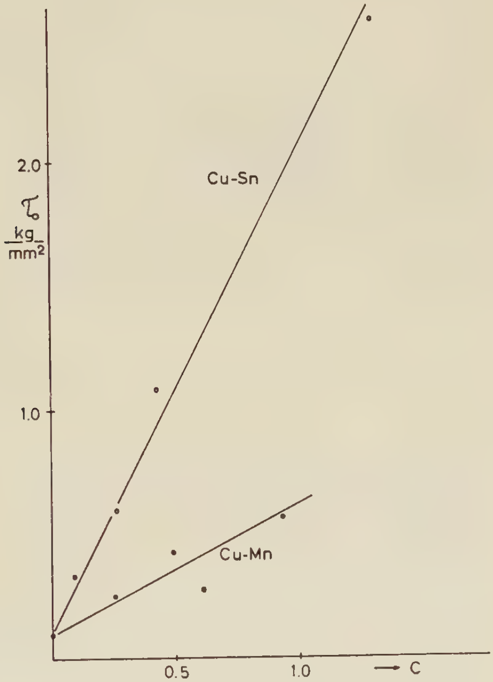

Fig. 14.

In Fig. 15 the quantity $d\tau_0/dc$ obtained from the curves of Figures 11–14 is plotted as a function of $\frac{1}{a}\frac{da}{dc}$, a being the lattice parameter of a given alloy. The curve obtained apparently corresponds to a relation of the type

$$d\tau_0/dc = k\,\varepsilon^n \tag{1}$$

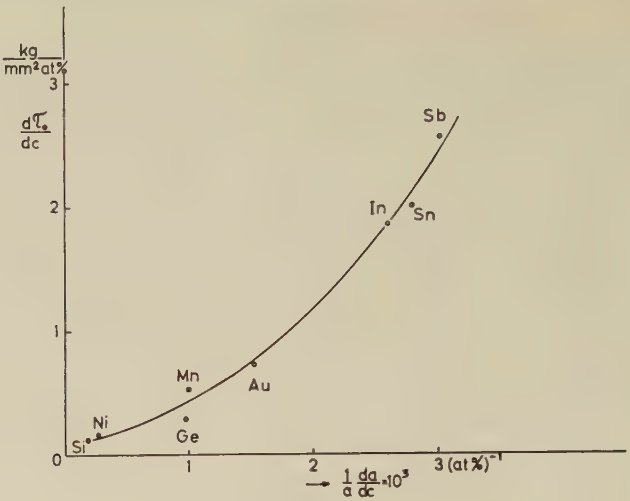

Fig. 15.

where ε stands for $\frac{1}{a}\frac{da}{dc}$ and k is constant. According to the experiments n has a value of about 2.

In theoretical works based on the theories of dislocations, MOTT and NABARRO [3–4] found the following two alternative expressions for the quantity τ_0 as a function of ε $\left(=\frac{1}{a}\frac{da}{dc}\right)$, c and μ in solid solutions

$$\tau_0 = 2.5\,\mu\,c\,\varepsilon^{4/3} \tag{I}$$

$$\tau_0 = \mu\,c\,\varepsilon^2 \tag{II}$$

where μ is the shearing modulus of the material in question and c the concentration of the solute. For the power (n) of ε the experimental results give, as already mentioned, 2 as the most probable value. Thus the functional dependence of τ_0 on ε is in agreement with Formula II. The absolute values, computed from Formula II, however, are too small by a factor of about 10^2. The value of μ used in this calculation is 4×10^3 kg/mm². Formula I gives fortuitously a rather good agreement with the absolute values in certain alloy series (e.g. values too large by a factor only about 2 in the cases of In, Sn, or Sb as solutes), but the power 4/3 for ε is not in accordance with the experimental results.

Summary

The resolved critical shear stress has been measured at room temperature for single crystals of a number of copper-base alloys belonging to the following alloy systems: Cu-Si, Cu-Mn, Cu-Ni, Cu-Ge, Cu-In, Cu-Sn, Cu-Sb, and Cu-Au. For the dilute solid solutions of these systems the critical shear stress is found to increase linearly with the concentration c of the solute. According to the meas-

urements, the increase of the critical shear stress per atomic percent of the solute varies as the square of the corresponding change in lattice parameter occurring in the alloy systems studied.

Acknowledgments

The investigation has been supported by a grant from the Swedish Council for Technical Research.

The authors are indebted to Messrs. Bo LINDELL and C. H. STADE for their active interest in the problem studied and for their permission to publish the results of their earliest measurements. Thanks are also due to Messrs. L. LARSSON and BENGT HEYMAN, who for some time took active part in the measurements here reported. We are obliged to Professor G. BORELIUS for stimulating interest in the investigation.

Physics Department, Kungl. Tekniska Högskolan Stockholm, June 1954.

REFERENCES

1. LINDE, J. O., LINDELL, Bo and STADE, C. H., Arkiv f. Fysik *2*, No. 11 (1950) 89.
2. ROSI, F. D. and MATHEWSON, C. H., Trans. AIME *188* (1950) 1159. (Journal of Metals Sept. 1950)
3. MOTT, N. F., Imperfections in Nearly Perfect Crystals, ed. W. Shockley, New York 1952.
4. MOTT, N. F and NABARRO, F. R. N., Proc. Phys. Soc. *52* (1940) 86. Report on strength of solids, London Phys. Soc. *1*, 1948.

Tryckt den 20 november 1954

Uppsala 1954. Almqvist & Wiksells Boktryckeri AB

ARKIV FÖR FYSIK Band 8 nr 52

Communicated 2 June 1954 by IVAR WALLER

Polarization of nucleons by scattering with spin-orbit coupling

By ALF SJÖLANDER and SIGURD KÖHLER

A polarization of high energy protons which have undergone a double scattering has recently been observed. In the following we will present some general formulas concerning such polarization effects.[†]

The interaction between the incident particles and the nuclei is assumed to be represented by a potential function containing a spin independent central potential and a spin-orbit interaction of the kind assumed in the nuclear shell model.

We have the Schrödinger equation

$$\Delta \Psi + (k^2 - v) \Psi = 0 \tag{1}$$

where k is the wave number in the center of mass system and v is given by

$$v = \frac{2\mu}{\hbar^2} [V_0(r) + V_1(r)\, \boldsymbol{s} \cdot \boldsymbol{l}].$$

Here $\boldsymbol{s}$ and $\boldsymbol{l}$ are the spin and orbital angular momenta in units of $\hbar$, and μ is the reduced mass. The two potentials V_0 and V_1 may be complex, the imaginary part representing the absorption.

If Ψ shall be an appropriate solution of the scattering problem it must have the asymptotic form

$$e^{ikz}\chi + \frac{g(\theta, \varphi)}{r} e^{ikr}. \tag{2}$$

Here χ is either of the two spin functions χ_+ or χ_- representing spin states parallel and antiparallel to the z-axis. We can consider these two spin states of the incident particle separately. θ is the scattering angle and φ is the azimuthal angle.

To solve Schrödinger's equation we expand Ψ in the eigenfunctions of $\boldsymbol{l}^2$, $\boldsymbol{J}^2 = (\boldsymbol{l} + \boldsymbol{s})^2$ and J_z, denoted by $y^{J_z}_{j,\, l,\, 1/2}$.[††] For a definite l[§] we have only eigenfunctions corresponding to $j = l + \frac{1}{2}$ and $j = l - \frac{1}{2}$. Thus

---

[†] This study was carried out in connection with an investigation of the polarization problem, including numerical applications, by W. J. SWIATECKI and T. ERIKSSON, published in Arkiv för Fysik, vol. 0 nr 3101.

[††] See for instance Blatt and Weisskopf: Theoretical Nuclear Physics, p. 789.

[§] l and j are quantum numbers of $\boldsymbol{l}^2$ and $\boldsymbol{J}^2$.

$$\Psi = \sum_{l=0}^{\infty} \left(\frac{u_{l+1/2}(r)}{r} \mathcal{Y}^{J_z}_{l+1/2,\, l,\, 1/2} + \frac{u_{l-1/2}(r)}{r} \mathcal{Y}^{J_z}_{l-1/2,\, l,\, 1/2} \right), \tag{3}$$

where $J_z = \frac{1}{2}$ or $J_z = -\frac{1}{2}$.

Putting (3) into Equation (1) we have

$$u_j'' + \left(k^2 - \frac{l(l+1)}{r^2} - v_j \right) u_j = 0, \tag{4}$$

where

$$v_j = \begin{cases} \dfrac{2\mu}{\hbar^2} \left(V_0 + \dfrac{l}{2} V_1 \right) & \text{for } j = l + \frac{1}{2} \\ \dfrac{2\mu}{\hbar^2} \left(V_0 - \dfrac{l+1}{2} V_1 \right) & \text{for } j = l - \frac{1}{2}. \end{cases} \tag{5}$$

Let us first consider neutron scattering. Later we will extend the formulas to the case of proton scattering.

For the neutron case the asymptotic form of u_j is

$$u_j \sim A_j \left[\eta_j e^{i(kr - l\pi/2)} - e^{-i(kr - l\pi/2)} \right]. \tag{6}$$

The phase factor η_j is determined from the condition

$$u_j(0) = 0$$

and A_j is chosen to give Ψ the correct asymptotic form. The relations (2) and (6) give the following expression for the scattering amplitude

$$g(\theta\varphi) = \frac{1}{2ik} (A \chi_{\pm} \pm B e^{\pm\varphi} \chi_{\mp}). \tag{7}$$

The upper and lower signs correspond to $\chi = \chi_+$ and $\chi = \chi_-$ in (2) respectively. The notations A and B are defined as follows.[†]

$$A = \sum_{l=0}^{\infty} a_l P_l(\cos\theta), \quad B = \sum_{l=0}^{\infty} b_l P_l^1(\cos\theta) \tag{8}$$

where a_l and b_l are expressed in terms of η_l by

$$\begin{cases} a_l = (l+1)\,\eta_{l+1/2} + l\,\eta_{l-1/2} - (2l+1) \\ b_l = \eta_{l+1/2} - \eta_{l-1/2}. \end{cases} \tag{9}$$

According to (7) an unpolarized incoming wave will, after the scattering, have its spin direction preferentially perpendicular to the scattering plane. For the polarization P[†] we get

---

[†] P_l and P_l^1 are the Legendre polynomials of order zero and one. See SCHIFF, Quantum Mechanics, p. 71.

$$P = \frac{2\, Im\,(A^* B)}{|A|^2 + |B|^2},$$

where $Im\,(A^* B)$ denotes the imaginary part of $(A^* B)$.

We note that $P^2 = 1$ only when $A = \pm i B$.

By using the above formulas in a second scattering we get the differential cross section for double scattering. The spin state of the incident particle is now given by (7). To be able to repeat exactly the discussion above, we must express the spin states as a superposition of the states parallel and antiparallel to the new incident direction. Finally we average over all spin directions of the particles, incident in the first scattering. The scattering cross section depends on the azimuthal angle in the second scattering in the following way:

$$\sigma\,(\varphi_2) \sim 1 + P_1\,(\theta_1)\, P_2\,(\theta_2) \cos \varphi_2. \tag{11}$$

Here index 1 refers to the first and index 2 to the second scattering. Hence

$$\frac{\sigma\,(0) - \sigma\,(\pi)}{\sigma\,(0) + \sigma\,(\pi)} = P_1\,(\theta_1)\, P_2\,(\theta_2). \tag{12}$$

If we now include the Coulomb scattering, the derivation of the scattering cross section is analogous to the above, and the formulas (7)–(12) are applicable if we only make the following replacements.

$$\begin{aligned} a_l &\rightarrow e^{2 i \sigma_l}\, a_l \\ b_l &\rightarrow e^{2 i \sigma}\; b_l \\ A &\rightarrow A + 2 i k f_c \\ B &\rightarrow B. \end{aligned} \tag{13}$$

Here σ_l is the Coulomb phase shift defined by

$$\sigma_l = \arg \Gamma\,(l + 1 + i\gamma)$$

and f_c is the Coulomb scattering amplitude

$$f_c = \frac{\gamma}{2\,k\,(\sin \theta/2)^2}\, e^{-i\gamma \ln (\sin \theta/2)^2 + i\pi + 2 i \sigma_0}$$

with

$$\gamma = Z\, e^2/\hbar\, v,$$

P is defined as an average of the expectation values of the spin operator σ

$$P^2 = \bar{\sigma} \cdot \bar{\sigma}.$$

Here $\bar{\sigma}$ denotes both the statistical and quantum mechanical average of σ. Thus $P = 0$ for an unpolarized wave and $P^2 = 1$ for a completely polarized wave. Cf. WOLFENSTEIN, Phys. Rev. *75*, 1664 (1949).

where Z is the proton number of the nucleus and v the velocity of the scattered particle.

To get an idea how the polarization depends on the strength of the spin-orbit interaction we will specialize to weak spin-orbit coupling. Then the phase factor η_j can be written in the form

$$\eta_j = \eta_l^0\, e^{2i\delta_j} \quad j = \begin{cases} l+\frac{1}{2} \\ l-\frac{1}{2} \end{cases}$$

where η_l^0 is the phase factor which refers to the spin independent potential and δ_j is a small phase shift, caused by the spin-orbit interaction.

We determine δ_j by BORN's approximation. Consider Equation (4) with $V_1=0$ as the unperturbed equation and V_1 as a small perturbation. In this approximation δ_j is given by

$$\left.\begin{aligned} \delta_{l+{}^1\!/_2} &= \frac{l}{2}\alpha_l \\ \delta_{l-{}^1\!/_2} &= -\frac{l+1}{2}\alpha_l \end{aligned}\right\} \alpha_l = -\frac{2\mu}{\hbar^2 k}\int\limits_0^\infty V_1\,\{u_l^0\}^2\,dr. \tag{14}$$

Here u_l^0 denotes the undisturbed radial function.

As a first approximation we get the following expression for the polarization.

$$P = \frac{2\,Im\,(A_0^* B_1)}{|A_0|^2 + |B_1|^2 + 2\,Re\,(A_0^* A_2)} \tag{15}$$

where[†]

$$A_0 = \sum_{l=0}^{\infty} (2l+1)\,(\eta_l^0 - 1)\,P_l(\cos\theta)$$

$$A_2 = -\tfrac{1}{2}\sum_{l=0}^{\infty} (2l+1)\,l\,(l+1)\,\eta_l^0\,\alpha_l^2\,P_l(\cos\theta)$$

$$B_1 = i\sum_{l=0}^{\infty} (2l+1)\,\eta_l^0\,\alpha_l\,P_l^1(\cos\theta).$$

Formula (15) may be especially useful to get a crude approximation of the polarization when the form of V_1 is specified but its strength is varied. A_0, A_2 and B_1 may be calculated for a definite potential $V_1(r)$ and then the polarization for a potential $\varepsilon V_1(r)$ is determined by

$$P(\theta) = P_0(\theta)\frac{|A_0|^2 + h(\theta)}{|A_0|^2 + \varepsilon^2 h(\theta)}\,\varepsilon, \tag{16}$$

where $P_0(\theta)$ denotes the polarization for the potential $V_1(r)$ and $h(\theta)$ is defined by

$$h(\theta) = |B_1|^2 + 2\,Re\,(A_0^* A_2).$$

[†] A and B have been expanded in powers of δ_j and the indices denote the order in δ_j.

In the same case the differential scattering cross section is given by

$$\sigma(\theta) = \frac{1}{4k^2}(|A_0|^2 + \varepsilon^2 h(\theta)).$$

We note that for $|A_0| \gg |h(\theta)|$ the polarization increases linearly with ε. On the other hand the polarization may even decrease with increasing spin-orbit coupling for angles, where $A_0 \approx iB_1$, i.e. where $P^2 \approx 1$ and $\sigma(\theta)$ is small.

The authors wish to express their gratitude to Professor IVAR WALLER for suggesting this investigation and to Dr. W. J. SWIATECKI for many valuable discussions.

Institute for Mechanics and Mathematical Physics, University of Uppsala, Uppsala.

Tryckt den 20 november 1954

Uppsala 1954. Almqvist & Wiksells Boktryckeri AB

ARKIV FÖR FYSIK Band 8 nr 53

Communicated 26 May 1954 by Erik Hulthén and Oskar Klein

A quantum mechanical study of the fluorine molecule[1]

By Hans Dinger

With 4 figures in the text

Summary

The dissociation energy and the atomic distance of the fluorine molecule have been computed assuming two valency electrons according to (i) the method of Heitler–London–Slater–Pauling (HLSP) and (ii) the molecular orbit (MO) method. The potential curves have been constructed and the values obtained have been compared with the experimental data. It is shown that the agreement is fairly good.

By use of all $2p$-electrons in both atoms the energy parameters for the electron configurations $\sigma_g^2 \pi_u^4 \pi_g^4$ and $\sigma_g^2 \sigma_u^2 \pi_u^4 \pi_g^2$ have been calculated by the MO method at varying atomic distances. The potential curves have been constructed and the energy of the molecule has been compared with the energy for the unperturbed atom.

In all calculations the effective nuclear charge has been varied. It is shown that this charge depends upon the number of electrons considered and that the effective nuclear charge in all cases here dealt with is substantially smaller than charges calculated from Slater's rules.

Introduction

Fluorine is the simplest of the halogens, the fluorine atom containing only nine electrons. As the fluorine molecule (F_2) has a rather low dissociation energy and large internuclear distance compared with the other halogens, it is of some interest to study this molecule quantum-mechanically.

Mueller [1] has used the method of semi-localized orbits, and has calculated the different states of the fluorine molecule which appear when two fluorine atoms in the ground state influence each other. He has carried out these calculations both considering only two electrons, and considering all the eighteen electrons, and has in both cases calculated the energies for the ${}^1\sum_g^+$ and ${}^3\sum_u^+$ states of F_2. In the two-electron case Mueller [1] got for the unperturbed atom the energy 0.57706 a.u., while in the eighteen-electron case he found 98.85887 a.u. All calculations have been carried out at only one internuclear distance (the experimental value). Mueller [1] has also computed the dissociation energy, but found this energy to be about four times greater than the experimental. In his calculations he used Slater's atomic orbits, using $2p$-orbits in the two-electron case, and the effective nuclear charge $Z^* = 5.2$, found by the help of SLATER's rules [2]. The atomic orbits proposed by DUNCANSON and COULSON [3] have also been used.

---

[1] A preliminary report has been published in J. Chem. Phys. *22*, 346 (1954).

A quite different method of treating the fluorine molecule has been used by SCHLÖGL [4]. Instead of a wave function for the electrons he has constructed a wave function for the "electron holes", following a method given by HEISENBERG [5]. To fill the electron shells we need one more electron in the 2 p-shell, and then we get Ne-configuration $1s^2 2s^2 2p^6$. In these calculations SCHLÖGL [4] used Slater's rules to estimate the Z^*-value, and has taken the value $Z^* = 5.18$.

After my calculations were finished it has come to my knowledge that WATARI [6] has published a study in which he uses the HLSP method, with all the ten $2p$-electrons and a Z^*-value of 5.0, and has shown that the lowest state for the molecule is a ${}^1\sum_g^+$ state. WATARI [6] then examined this state in more detail by considering Z^* as a function of the internuclear distance R, and by the variation principle calculated the dissociation energy and the equilibrium distance. In this way he found the equilibrium distance $R_0 = 1.59$ a.u. and the dissociation energy $D_0 = 0.960$ a.u. At this internuclear distance he found Z^* to be 3.62. WATARI [6] has also discussed the consequences of neglecting the $2s$-electrons, and thinks that this approximation is the reason for the big value of D_0 and the too small value of R_0.

In the calculations given below another method has however been used. The dissociation energy and the atomic distance of the fluorine molecule have been computed assuming two valence electrons according to both (i) the method of Heitler–London–Slater–Pauling (HLSP) and (ii) the molecular orbit (MO) method. Furthermore, by use of all $2p$-electrons in both atoms the energy parameters for the electron configurations $\sigma_g^2 \pi_u^4 \pi_g^4$ and $\sigma_g^2 \sigma_u^2 \pi_u^4 \pi_g^2$ have been calculated by the MO method at varying atomic distances. In the expression for the energy of the molecule the internuclear distance R has at first been kept constant and equal to the distance found by experiment. By varying the Z^*-value until we reach the minimum energy we find a Z^*-value which later has been used to construct the potential curve, that is to say the energy as a function of the internuclear distance R.

The electron configuration of the fluorine atom is, in the ground state, ${}^2P$, $1s^2 2s^2 2p^5$. In all calculations below the influence of the $1s$-shell has been neglected. This is not a serious approximation, because the $1s$-shell is rather firmly bound to the nucleus because of the high nuclear charge ($Z = 9$), and in any case it only plays a very small part in the formation of the molecule. A much more serious approximation is to suppose that the $2s$-shell also takes no part in the formation of the molecule. Taking the $2s$-shell into consideration would however lead to unmanageable calculations, as the effective nuclear charge

$$Z^* = \begin{cases} 2\nu & \text{for a } 2p\text{-orbit} \\ 2\mu & \text{for a } 2s\text{-orbit} \end{cases}$$

cannot be assumed to have the same value in a $2p$-orbit as in a $2s$-orbit (cf. BROWN [7]).

In the calculations where only two electrons have been assumed to take part in the formation of the molecule, the remaining four $2p$-electrons from each atom have been assumed to be unperturbed.

The atomic orbits which have been used in the calculations are of the usual Slater type

$$\begin{aligned}
\psi_{2p_z} &= z = \sqrt{\frac{\nu^5}{\pi}}\, r e^{-\nu r} \cos\vartheta \\
\psi_{2p_x} &= x = \sqrt{\frac{\nu^5}{\pi}}\, r e^{-\nu r} \sin\vartheta \cos\varphi \\
\psi_{2p_y} &= y = \sqrt{\frac{\nu^5}{\pi}}\, r e^{-\nu r} \sin\vartheta \sin\varphi .
\end{aligned} \tag{1}$$

The z-axis has been taken as the molecular axis.

Atomic units have been used, in which the unit of energy is 1 a.u. = 27.205 eV.

Experimental data for the equilibrium distance and dissociation energy

Brockway [8] has by electron diffraction experiments determined the internuclear equilibrium distance R_0 in F_2, and he has found $R_0 = 1.45 \pm 0.05$ Å. Rogers, Shomaker and Stevenson [9] have repeated Brockway's [8] determination and have found $R_0 = 1.435 \pm 0.010$ Å. From Raman spectra of gaseous F_2 at 1 atm. pressure, Andrychuk [10] has got $R_0 = 1.418 \pm 0.001$ Å $= 2.680$ a.u., and the fundamental frequency $\tilde{\nu}_e = 892$ cm^{-1}. This last value of R_0 (2.680 a.u.) has been used throughout in the calculations given below, and will be called R_e in the following.

Great difficulties seem to be involved in the experimental determination of the dissociation energy D_0 of the fluorine molecule. Several experiments give values between 30 and 50 kcal/mole (corresponding to 0.05—0.08 a.u.), e.g. Wicke [11], Wicke and Friz [12] and Gilles and Margrave [13].

Calculations

Calculation by the HLSP method (two electrons)

If the atoms are assumed to be joined with a purely covalent bond, F–F, we get for this type of bond the antisymmetrized, normalized wave function

$$\Psi = \frac{1}{2\sqrt{1+S_{AB}^2}} \left\{ \begin{vmatrix} A(1)\alpha(1) & B(1)\beta(1) \\ A(2)\alpha(2) & B(2)\beta(2) \end{vmatrix} - \begin{vmatrix} A(1)\beta(1) & B(1)\alpha(1) \\ A(2)\beta(2) & B(2)\alpha(2) \end{vmatrix} \right\}. \tag{2}$$

Here $A(1)$ means the z-orbit for electron 1 in the field from atom A, etc. α and β are orthonormalized spin functions.

S_{AB} is the overlap integral, which is defined by

$$S_{AB} = \int A^*(1)\, B(1)\, d\tau_1 .$$

The energy for the system can now be written

$$E = \int \Psi^* H \Psi\, d\tau \tag{3}$$

where H is the Hamiltonian

$$H = T_1 + T_2 + \frac{1}{r_{12}} + \frac{Z^2}{R} - Z\left(\frac{1}{r_{A1}} + \frac{1}{r_{A2}} + \frac{1}{r_{B1}} + \frac{1}{r_{B2}}\right). \tag{4}$$

T_1 and T_2 are the kinetic energy operators of the electrons 1 and 2 respectively,
T_i $= -\frac{1}{2}\nabla_i^2$,
r_{12} is the distance of electron 1 from electron 2,
R is the internuclear distance,
r_{A1} is the distance of electron 1 from the nucleus A, etc.,
Z is the nuclear charge. This charge has been put equal to 1 in the two-electron problems. The remaining eight electrons are thus assumed to screen the atomic nucleus by eight units.

If (2) and (4) are substituted into (3) and we integrate over the spin functions, we get

$$E = \frac{1}{1+S_{AB}^2}\{(zz'|H|zz') + (zz'|H|z'z)\} \tag{5}$$

Table 1. E-values for varying ν-values, when $R = R_e = 2.680$ a.u.

α	ν	E a.u.
1.6	0.599	−0.2350
1.7	0.637	−0.2446
1.8	0.674	−0.2495
1.9	0.712	−0.2495
2.0	0.749	−0.2451
2.1	0.787	−0.2354
2.2	0.824	−0.2214

$E_{\min}$ occurs for $\nu = 0.693$.

Table 2. E-values for varying R-values, when $\nu = \text{const.} = 0.693$. $E_{\text{at}} = -0.1250$ a.u., $R_e = 2.680$ a.u., $D_e = 0.05 - 0.08$ a.u., $\tilde{\nu}_e = 892$ cm^{-1}

α	R a.u.	E a.u.
1.0	1.443	+0.0435
1.5	2.165	−0.1812
2.0	2.886	−0.2656
2.5	3.608	−0.2806
3.0	4.329	−0.2660
3.5	5.051	−0.2494
4.0	5.772	−0.2360
4.5	6.494	−0.2267
5.0	7.215	−0.2207

$E_{\min} = -0.284$ a.u. for $R = 3.45$ a.u.; $\tilde{\nu} = 500$ cm^{-1}.

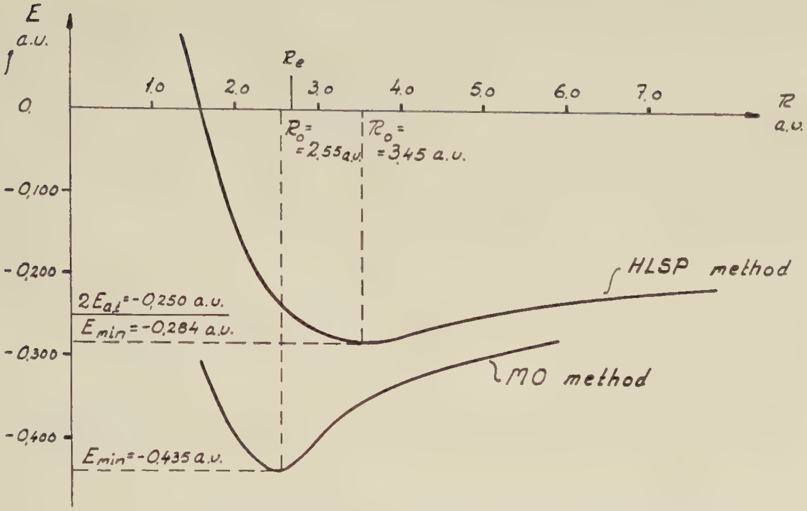

Fig. 1. Potential curves constructed from values of the tables 2 and 4 (2 electrons).

where

$$(z z' | H | z z') = \iint A^*(1) B^*(2) H A(1) B(2) \, d\tau_1 \, d\tau_2$$

and

$$(z z' | H | z' z) = \iint A^*(1) B^*(2) H B(1) A(2) \, d\tau_1 \, d\tau_2 .$$

The energy for the unperturbed atom, E_0, can be calculated from

$$E_0 = \int A^*(1) \left(T_1 - \frac{Z}{r_{A1}} \right) A(1) \, d\tau_1 = U(zz) - Q(zz). \tag{6}$$

The integrals U and Q are defined in the Appendix.

$$\frac{\partial E_0}{\partial \nu} = 0 \text{ gives } (E_0)_{\min} = E_{\text{at}} = -0.1250 \text{ a.u. for } \nu_{\text{at}} = 0.500.$$

Because most of the integrals occurring here are functions of $R \cdot \nu$ we introduce $R \cdot \nu = \alpha$. In order to find the ν-value, we keep the internuclear distance fixed, so that $R = R_e = 2.680$ a.u. We vary ν and try to find that ν-value which makes E minimum. The result is shown in Table 1.

If ν is kept const. $= 0.693$ and the internuclear distance R is varied, we get the potential curve. This result is shown in Table 2 and in Fig. 1.

The equilibrium distance is here 3.45 a.u. and the dissociation energy 0.034 a.u. The value of the dissociation energy is in fairly good agreement with the experimental data, while the equilibrium distance is about 20 per cent too high.

Calculation according to the MO method (two electrons)

The total antisymmetrized normalized wave function is in this case

$$\Psi = \frac{1}{\sqrt{2}} \begin{vmatrix} \varphi_m(1) \alpha(1) & \varphi_m(1) \beta(1) \\ \varphi_m(2) \alpha(2) & \varphi_m(2) \beta(2) \end{vmatrix} \tag{7}$$

φ_m is a molecular orbit formed by the linear combination of atomic orbitals.

$$\varphi_m(1) = N\{A(1) + B(1)\} \text{ etc.} \tag{8}$$

The normalization constant N is obtained from

$$\int \varphi_m^*(1)\varphi_m(1)\,d\tau_1 = 1 \tag{9}$$

$$N = \frac{1}{\sqrt{2 + 2S_{AB}}}. \tag{10}$$

Correspondingly to the HLSP method we get, when we take the z-orbits for the atomic orbits $A(1)$ etc.:

Table 3. E-values for varying ν-values, when $R = R_e = 2.680$ a.u.

α	ν	E a.u.
1.0	0.373	−0.3741
1.5	0.560	−0.4292
2.0	0.749	−0.2562
2.5	0.933	−0.0765
3.0	1.119	+0.1408

E_{min} occurs for $\nu = 0.550$.

Table 4. E-values for varying R-values, when $\nu = \text{const.} = 0.550$. $E_{\text{at}} = -0.1250$ a.u., $R_e = 2.680$ a.u., $D_e = 0.05 - 0.08$ a.u., $\tilde{\nu}_e = 892$ cm^{-1}.

α	R a.u.	E a.u.
1.0	1.818	−0.3638
1.5	2.727	−0.4297
2.0	3.636	−0.3472
2.5	4.546	−0.3172
3.0	5.455	−0.2924

$E_{\text{min}} = -0.435$ a.u. for $R = 2.55$ a.u.; $\tilde{\nu} = 1700$ cm^{-1}.

$$E = \frac{1}{(2 + 2S_{AB})^2}\{2(zz|H|zz) + 8(zz|H|zz') + 2(zz'|H|zz') + 4(zz'|H|z'z)\}. \tag{11}$$

The MO method can in contrast to the HLSP method only be expected to give good results just in the equilibrium position. Proceeding in the same way as in the previous calculations, and with $R = R_e$ determining that ν-value for which E is a minimum, we get the results shown in Table 3.

If ν is kept const. $= 0.550$ and R is varied we get the results in Table 4 and Fig. 1.

The equilibrium distance is here in good agreement with the experimental distance. However, the equilibrium distance and the bond energy calculated by the MO method are rather sensitive to variations in the ν-value. In this case we get the dissociation energy 0.185 a.u., which is about three times greater than the experimental value.

If (2) and (7) are written out and we disregard the normalization constants, we get

for the HLSP method

$$\Psi = \{A(1)B(2) + B(1)A(2)\} \cdot \{\text{spin function}\}, \tag{12}$$

for the MO method

$$\Psi = \{A(1)B(2) + B(1)A(2) + A(1)A(2) + B(1)B(2)\} \cdot \{\text{spin function}\}. \tag{13}$$

In the MO method the ionic bond $F^- F^+$ and $F^+ F^-$ have been given as much importance as the covalent bond F—F. This is not correct, because F_2 has a predominantly covalent character. (13) ought to be written

$$\Psi = \{c_1[A(1)B(2) + B(1)A(2)] + c_2[A(1)A(2) + B(1)B(2)]\} \cdot \{\text{spin function}\} \tag{14}$$

where the constants c_1 and c_2 are to be determined by the variational method.

Calculation by the MO method (ten electrons)

This calculation has been carried out by the MO method, where the molecular orbits have been approximated by linear combination of atomic orbits. For this reason the method is called the LCAO method (linear combination of atomic orbits). This method has been described clearly and concisely by ROOTHAAN [14], whose notation will be used in the following.

A molecular orbit formed by linear combination of atomic orbits can be written

$$\varphi_i = \sum_p \chi_p C_{pi} \tag{15}$$

where χ_p are normalized atomic orbits and C_{pi} are coefficients. A molecular orbit can also be written as a combination of symmetry orbits. In this case the calculations will be much simplified, because the symmetry orbits are in some cases themselves molecular orbits, viz. σ_g and σ_u. In the other cases orbits with the same symmetry have the same value of the energy parameter.

From the energy diagram of homonuclear molecules (cf. EYRING, WALTER, KIMBALL [15]) we can see that at the equilibrium distance the energy levels for the $2p$-orbits ought to be of the succession $\sigma_u > \pi_g > \pi_u > \sigma_g$ or possibly $\sigma_u > \pi_g > \sigma_g > \pi_u$.

The electron configuration $\sigma_g^2 \pi_u^4 \pi_g^4$

Supposing that the σ_u-orbit has the highest energy, we first investigate the configuration $\sigma_g^2 \pi_u^4 \pi_g^4$ using the method of molecular orbits:

$$\begin{array}{llll}
\sigma_1 = z + z'; & \sigma_g & \varphi_1 = N_1 \sigma_1; & \sigma_g \\
\sigma_2 = x + x'; & \pi_u & \varphi_2 = N_2 \sigma_2 + N_3 \sigma_3; & \pi_u \\
\sigma_3 = y + y'; & \pi_u & \varphi_3 = N_4 \sigma_2 + N_5 \sigma_3; & \pi_u \\
\sigma_4 = x - x'; & \pi_g & \varphi_4 = N_6 \sigma_4 + N_7 \sigma_5; & \pi_g \\
\sigma_5 = y - y'; & \pi_g & \varphi_5 = N_8 \sigma_4 + N_9 \sigma_5; & \pi_g
\end{array} \tag{16}$$

Here z means the $2p_z$-orbit in atom A, z' the same orbit in atom B, etc. The N's are orthonormalization constants.

The orbits are orthonormalized by the condition

$$\int \varphi_i^* \varphi_j \, d\tau = \delta_{ij}. \tag{17}$$

Assuming every MO to be filled we get the eigen-parameters ε from the secular equation

$$\mathrm{Det}\,(\boldsymbol{F} - \boldsymbol{\varepsilon}\,\boldsymbol{S}) = 0 \tag{18}$$

where $\boldsymbol{F}$ is the Hartree-Fock matrix, whose elements are

$$F_{kl} = G_{kl} + H_{kl}, \tag{19}$$

$$G_{kl} = \int \sigma_k^* G \sigma_l \, d\tau = \sum n_{pq} G(pq), \tag{20}$$

$$H_{kl} = \int \sigma_k^* H \sigma_l \, d\tau = \sum m_{pq} H(pq). \tag{21}$$

$\boldsymbol{S}$ is the overlap matrix, with the elements

$$S_{kl} = \int \sigma_k^* \sigma_l \, d\tau = \sum r_{pq} S(pq), \tag{22}$$

$$G(pq) = \sum_{i=1}^{5} \left\{ 2 \int\!\!\int p^*(1) \varphi_i^*(2) \frac{1}{r_{12}} q(1) \varphi_i(2) \, d\tau_1 \, d\tau_2 - \right.$$

$$\left. - \int\!\!\int p^*(1) \varphi_i^*(2) \frac{1}{r_{12}} \varphi_i(1) q(2) \, d\tau_1 \, d\tau_2 \right\}, \tag{23}$$

$$\begin{aligned} H(pq) &= \int p^* H q \, d\tau, \\ S(pq) &= \int p^* q \, d\tau, \end{aligned} \tag{24}$$

$$H = T - \frac{Z}{r_A} - \frac{Z}{r_B}. \tag{25}$$

p and q are the atomic orbits z, x, y.

The nuclear charge Z has in this case been put equal to 5, and the $1s$- and $2s$-shells are assumed to screen the nucleus by for units.

$$G_{ii} = \int \varphi_i^* G \varphi_i \, d\tau$$
$$H_{ii} = \int \varphi_i^* H \varphi_i \, d\tau. \tag{26}$$

We now get the eigen-values ε_i from the equations

$$\varepsilon_i = H_{ii} + G_{ii} \quad (i = 1, \ldots, 5). \tag{27}$$

The only $G(pq)$ differing from zero are

$$G(zz); \quad G(zz') = G(z'z); \quad G(xx) = G(yy);$$
$$G(xx') = G(x'x) = G(yy') = G(y'y).$$

The different $G(pq)$ expressed in the integrals S, M, L, C and A are given in the Appendix, where the integrals also are defined.

From (26) we now easily get the different G_{ii}.

$$G_{11} = \frac{1}{1+S(zz)} [G(zz) + G(zz')]$$
$$G_{22} = G_{33} = \frac{1}{1+S(xx)} [G(xx) + G(xx')] \tag{28}$$
$$G_{44} = G_{55} = \frac{1}{1-S(xx)} [G(xx) - G(xx')].$$

The only $H(pq)$ differing from zero are

$$H(zz); \quad H(zz') = H(z'z); \quad H(xx) = H(yy);$$
$$H(xx') = H(x'x) = H(yy') = H(y'y).$$

These are expressed in the integrals T, Q, U, K and J in the Appendix.

From (26) we now get the different H_{ii}. These are

$$H_{11} = \frac{1}{1+S(zz)} [H(zz) + H(zz')]$$
$$H_{22} = H_{33} = \frac{1}{1+S(xx)} [H(xx) + H(xx')] \tag{29}$$
$$H_{44} = H_{55} = \frac{1}{1-S(xx)} [H(xx) - H(xx')].$$

When we calculate the different G_{ii} and H_{ii} at varying ν-values but with the internuclear distance $= R_e = 2.680$ a.u., we get the total energy of the electrons from the expression $2 \sum_i H_{ii} + \sum_i G_{ii}$. The values of G_{ii} and H_{ii} are given in Tables A 1 and A 2 in the Appendix. The values for the expression $2 \sum_i H_{ii} + \sum_i G_{ii}$ for different ν-values are collected in Table 5.

Table 5. The total energy of the electrons for varying ν-values, when $R = R_e = 2.680$ a.u.

α	ν	$2\sum_i H_{ii} + \sum_i G_{ii}$ a.u.
1.0	0.373	+ 9.585
1.5	0.560	− 7.501
2.0	0.749	−14.635
2.5	0.933	−18.563
3.0	1.119	−20.980
3.5	1.306	−22.334
4.0	1.493	−22.989
4.5	1.679	−23.125
5.0	1.866	−22.858

$(2\sum_i H_{ii} + \sum_i G_{ii})_{\min}$ is obtained for $\nu = 1.638$.

Table 6. E-values for varying R-values, when $\nu = \text{const.} = 1.638$. $E_{\text{at}} = -8.1140$ a.u., $R_e = 2.680$ a.u., $D_e = 0.05$–0.08. a.u.

α	R a.u.	E a.u.
1.0	0.611	+154.623
1.5	0.916	+ 32.744
2.0	1.221	+ 0.853
2.5	1.526	− 8.846
3.0	1.832	− 12.330
3.5	2.137	− 13.462
4.0	2.442	− 13.757
4.5	2.747	− 13.756
5.0	3.053	− 13.681

$E_{\min} = -13.824$ a.u. for $R = 2.59$ a.u.

By use of this ν-value we calculate again all G_{ii} and H_{ii}, but now for varying internuclear distance R. The result is shown in Tables A 3 and A 4 in the Appendix.

We can now find the total energy E of the molecule from the expression

$$E = 2\sum_i H_{ii} + \sum_i G_{ii} + \frac{Z^2}{R}. \tag{30}$$

E is tabulated for different R-values in Table 6.

The potential curve constructed from Table 6 is shown in Fig. 2.

To get an idea of the dissociation energy we must calculate the energy for the unperturbed atom. For the electron configuration $2p^n$ the energy for the unperturbed atom is easily calculated by the method of VAN VLECK [16]. This energy is

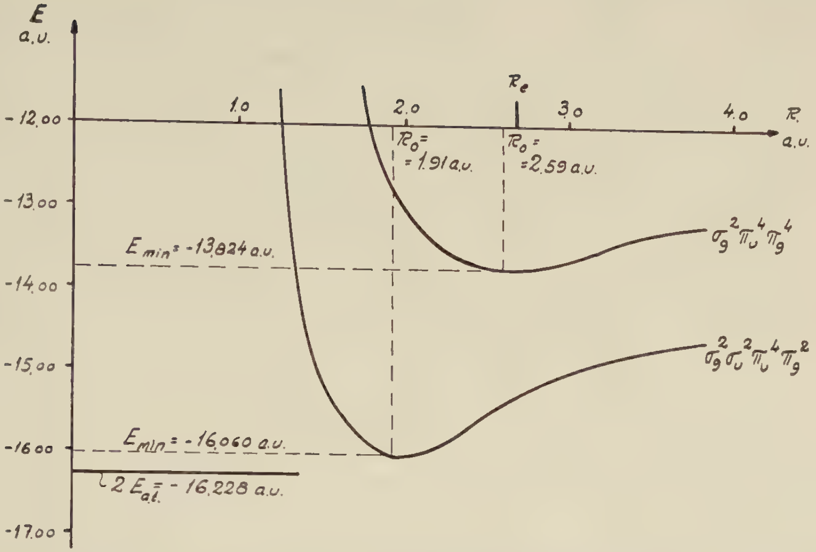

Fig. 2. Potential curves constructed from values of the Tables 6 and 8 (10 electrons).

$$E(2p^n) = n\,I(2p) + \frac{n(n-1)}{2} F^\circ +$$

$$+ \tfrac{1}{2}\{-5n^2 + 20n - 3\,L(L+1) - 12\,S(S+1)\} F^2. \qquad (31)$$

Here $I(2p)$ means the energy for a p-electron in the nuclear field. n = the number of electrons = 5 for fluorine. For the ground state, ^2P, $L = 1$ and $S = \frac{1}{2}$. F^0 and F^2 are integrals defined by

$$F^0 = \iint A_{2p}^*(1)\,A_{2p}^*(2)\,\frac{1}{r_>}\,A_{2p}(1)\,A_{2p}(2)\,d\tau_1\,d\tau_2 = 0.36328 \cdot \nu$$

$$F^2 = \iint A_{2p}^*(1)\,A_{2p}^*(2)\,\frac{r_<^2}{r_>^3}\,A_{2p}(1)\,A_{2p}(2)\,d\tau_1\,d\tau_2 = 0.00703 \cdot \nu.$$

From $\dfrac{\partial\{E(2p^n)\}}{\partial \nu} = 0$ we get $\{E(2p^n)\}_{\min} = E_{\text{at}} = -8.1140$ a.u. for $\nu_{\text{at}} = 1.802$.

This gives for the fluorine molecule the dissociation energy $2E_{\text{at}} - E_{\min} = -2.386$ a.u., which value is negative and in any case far too large. The equilibrium distance is 2.59 a.u., in good agreement with the experimental value.

From the equations (27) we can calculate the energy parameters for the orbits σ_g, π_u and π_g. These are collected in Table A5 in the Appendix and are found in Fig. 3. From this figure we find that the orbits at the equilibrium distance are in the order $\pi_g > \pi_u > \sigma_g$.

The electron configuration $\sigma_g^2\,\sigma_u^2\,\pi_u^4\,\pi_g^2$

The calculations below show that when the $2s$-electrons are neglected we have to take the σ_u-orbit into consideration.

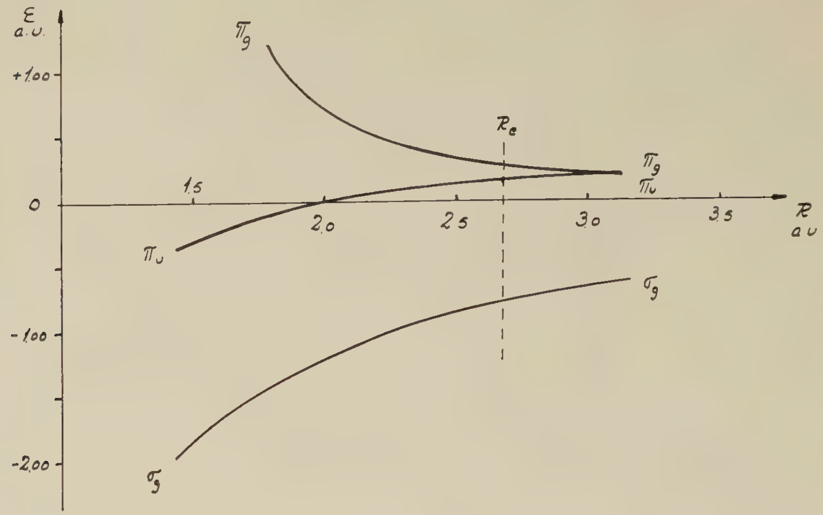

Fig. 3. The energy parameters for the electron configuration $\sigma_g^2 \pi_u^4 \pi_g^4$. Table A 5.

By linear combinations of the atomic orbits x, y and z we choose for this configuration of the molecular orbits:

$$\begin{array}{llll}
\sigma_1 = z + z'; & \sigma_g & \varphi_1 = N_1 \sigma_1; & \sigma_g \\
\sigma_2 = x + x'; & \pi_u & \varphi_2 = N_2 \sigma_2 + N_3 \sigma_3; & \pi_u \\
\sigma_3 = y + y'; & \pi_u & \varphi_3 = N_4 \sigma_2 + N_5 \sigma_3; & \pi_u \\
\sigma_4 = x - x'; & \pi_g & \varphi_4 = N_6 \sigma_4 + N_7 \sigma_5; & \pi_g \\
\sigma_5 = y - y'; & \pi_g & \varphi_5 = N_8 \sigma_6; & \sigma_u \\
\sigma_6 = z - z'; & \sigma_u & &
\end{array} \tag{32}$$

Because the configuration $\varphi_1 \varphi_2 \varphi_3 \varphi_5$ is invariant for a rotation about the z-axis, N_6 and N_7 can be chosen arbitrarily. We have taken $N_6 = N_7$.

The only $G(pq)$ diferent from zero are in this case:

$$G(zz); \quad G(zz') = G(z'z); \quad G(xx) = G(yy);$$

$$G(xx') = G(x'x) = G(yy') = G(y'y); \quad G(xy) = G(yx);$$

$$G(xy') = G(x'y) = G(y'x) = G(yx').$$

The various $G(pq)$ expressed in terms of the integrals S, M, L, C and A are given in the Appendix.

$$G_{11} = \frac{1}{1 + S(zz)} [G(zz) + G(zz')]$$

Table 7. The total energy of the electrons for varying ν-values, when $R = R_e = 2.680$ a.u.

α	ν	$2\sum_i H_{ii} + \sum_i G_{ii}$ a.u.
1.0	0.373	-7.978
1.5	0.560	-14.988
2.0	0.749	-19.105
2.5	0.933	-21.735
3.0	1.119	-23.372
3.5	1.306	-24.276
4.0	1.493	-24.634
4.5	1.679	-24.587
5.0	1.866	-24.232

We get $(2\sum_i H_{ii} + \sum_i G_{ii})_{\min}$ for $\nu = 1.565$.

Table 8. E-values for varying R-values, when $\nu = \text{const.} = 1.565$. $E_{\text{at}} = -8.1140$ a.u., $R_e = 2.680$ a.u., $D_e = 0.05 - 0.08$ a.u.

α	R a.u.	E a.u.
1.0	0.639	$+41.973$
1.5	0.958	-0.402
2.0	1.278	-12.235
2.5	1.597	-15.440
3.0	1.917	-16.052
3.5	2.236	-15.827
4.0	2.556	-15.426
4.5	2.875	-15.095
5.0	3.195	-14.886

$E_{\min} = -16.060$ for $R = 1.91$ a.u.

$$G_{22} = G_{33} = \frac{1}{1 + S(xx)} [G(xx) + G(xx') + G(xy) + G(xy')]$$

$$G_{44} = \frac{1}{1 - S(xx)} [G(xx) - G(xx') + G(xy) - G(xy')] \qquad (33)$$

$$G_{55} = \frac{1}{1 - S(zz)} [G(zz) - G(zz')].$$

The different H_{ii} are

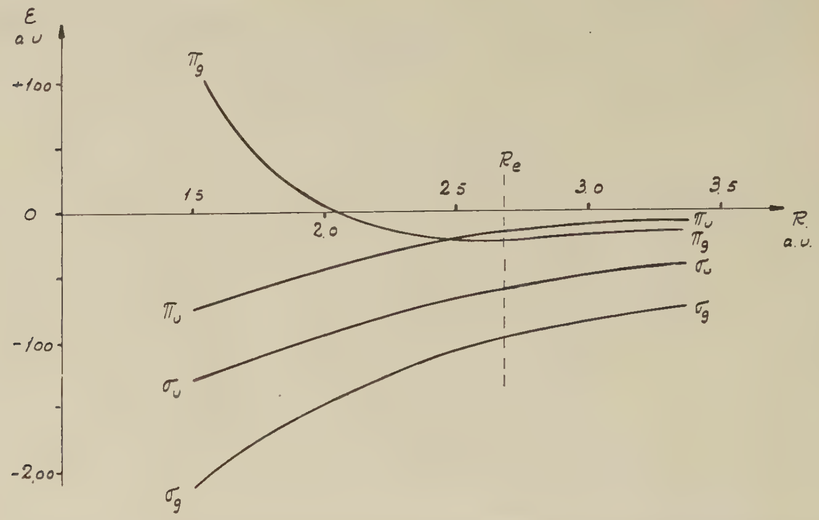

Fig. 4. The energy parameters for the electron configuration $\sigma_g^2\,\sigma_u^2\,\pi_u^4\,\pi_g^2$. Table A 10.

$$\begin{aligned}
H_{11} &= \frac{1}{1+S(zz)}\,[H(zz)+H(zz')]\\
H_{22} = H_{33} &= \frac{1}{1+S(xx)}\,[H(xx)+H(xx')]\\
H_{44} &= \frac{1}{1-S(xx)}\,[H(xx)-H(xx')]\\
H_{55} &= \frac{1}{1-S(zz)}\,[H(zz)-H(zz')].
\end{aligned} \tag{34}$$

In the same way as above we now can calculate all G_{ii} and H_{ii} for varying ν-values at the equilibrium distance 2.68 a.u. The results are given in Tables A 6 and A 7 in the Appendix. From these tables we get the total energy of the electrons shown in Table 7.

If we now calculate all G_{ii} and H_{ii} at varying internuclear distance, with $\nu = 1.565$, we get Tables A 8 and A 9 in the Appendix. From these tables we finally get the total energy of the molecule according to (30). The result is shown in Table 8 and in Fig. 2.

Because $E_{\min}$ is now lower than in the preceding case, the electron configuration $\sigma_g^2\,\sigma_u^2\,\pi_u^4\,\pi_g^2$ is obviously a better approximation than the configuration $\sigma_g^2\,\pi_u^4\,\pi_g^4$. The potential curve, constructed from Table 8, is reproduced in Fig. 2. The dissociation energy is in this case $2\,E_{\mathrm{at}} - E_{\min} = -0.168$ a.u. This value is negative too, but it is numerically much smaller than in the preceding case.

If we now calculate the energy parameters for the orbits $\sigma_g, \sigma_u, \pi_u$ and π_g, we get Table A 10 in the Appendix. They are shown graphically in Fig. 4. From this figure we see that the orbits at the equilibrium distance are now in order $\pi_u > \pi_g > \sigma_u > \sigma_g$.

Table 9. The results of the calculations.

	ν_{at}	E_{at} a.u.	ν	$E_{\min}$ a.u.	D_0 a.u.	R_0 a.u.	$\tilde{\nu}$ cm^{-1}
HLSP method (2 el.) .	0.500	−0.1250	0.693	− 0.284	0.034	3.45	500
MO ,, (2 ,,) .	0.500	−0.1250	0.550	− 0.435	0.185	2.55	1700
MO ,, (10 ,,) .							
$\sigma_g^2\pi_u^4\pi_g^4$ . . .	1.802	−8.1140	1.638	−13.824	−2.386	2.59	—
$\sigma_g^2\sigma_u^2\pi_u^4\pi_g^2$.	1.802	−8.1140	1.565	−16.060	−0.168	1.91	—
Exptl.	—	—	—	—	0.05–0.08	2.68	892

Discussion

The results of the calculations are shown graphically in Figures 1–4; and the table below contains all the values of $\nu_{\text{at}}, E_{\text{at}}, \nu, E_{\min}, R_0, D_0$ and $\tilde{\nu}$ which have been obtained in the different calculations described above.

The calculation of the potential curve for F_2 by the HLSP method gave a value of D_0 which is slightly too low, and too high a value for R_0. The MO method, on the other hand, gave too great a value for D_0, while R_0 is in good agreement with the experimental value. The value of ν_{at} is in complete agreement with the assumption that we have one electron in the field from a nucleus with the charge 1. In this case we have of course $Z = Z_{\text{at}}^* = 2\,\nu_{\text{at}} = 1$.

The treatment of F_2 as a ten-electron problem by the MO method showed that the configuration $\sigma_g^2\sigma_u^2\pi_u^4\pi_g^2$ is a better approximation than the configuration $\sigma_g^2\pi_u^4\pi_g^4$. For both the configurations, D_0 was indeed negative, but for the configuration $\sigma_g^2\sigma_u^2\pi_u^4\pi_g^2$ the difference between $E_{\min}$ and $2\,E_{\text{at}}$ is only about 1 per cent.

In all the calculations presented above the value of the effective nuclear charge (2ν) is smaller than if it were calculated using Slater's rules [2]. According to these rules this charge should be about 5.2. The result is however in good agreement with the results obtained by KOPINECK [17] in his calculation of N_2 as six-electron problem. From the curve $Z^* = f(R)$ obtained by KOPINECK [17] we get for $R = 2.7$ a.u. a Z^*-value of about 2.4. Even the value $Z^* = 3.62$ obtained by WATARI [6] in his calculation of F_2 shows that the generally used effective nuclear charges are not applicable when the electrons, which do not take part in the formation of the molecule, are considered as point charges coinciding with the nucleus.

Because the $1\,s$- and $2\,s$-shells are not in fact point charges coinciding with the nucleus, but in some degree responsible for the formation of the molecule, it also follows that the energy of for instance a $2\,p$-electron cannot be expressed by terms in which the nuclear charge Z in Hamiltonian is a constant. The z-value is dependent upon how much the atomic nucleus is screened by the $1\,s$- and $2\,s$-shells. A method of estimating Z in such cases has been proposed by MUELLER and EYRING [18]. In a complete treatment using all the electrons in the molecule Z is of course equal to the charge of the nucleus.

The calculation of the energy parameters for the electron configuration $\sigma_g^2\pi_u^4\pi_g^4$ shows (Fig 3) that the sequence of the orbits at the equilibrium distance is $\pi_g > \pi_u > \sigma_g$. The corresponding sequence for the configuration $\sigma_g^2 \sigma_u^2 \pi_u^4 \pi_g^2$ is (Fig. 4) $\pi_u > \pi_g > \sigma_u > \sigma_g$. The difference between the π_g- and the π_u-orbit is however in both cases rather small at the equilibrium distance. It is however remarkable that the σ_u-orbit has the next lowest energy, a behaviour which contradicts the usual assumption, namely that the π_u-orbit should have the next lowest energy. This can however be explained if we take into account the results obtained by ARAKI and WATARI [19] in their quantum-mechanical treatment of the C_2-molecule. Their calculations show that when the $2s$-electrons are taken into account we get much higher values of the energy parameters for the σ-orbits in the neighbourhood of the equilibrium distance, while the corresponding parameters for the π-orbits get lower when we take the influence of the $2s$-electrons into account. The $2s$-shell repels σ-electrons and attracts π-electrons; the influence of the $2s$-shell is however greater on the σ-electrons than on the π-electrons. In his treatment of the F_2-molecule WATARI [6] has also discussed the influence of the $2s$- (and $1s$-)electrons on the energy parameters, and how the binding energy depends on the s-shells. In this case he has however not made any quantitative calculations.

Referring to these papers of ARAKI and WATARI [19] and WATARI [6], it seems probable that when we take the $2s$-shell into account the energy parameters for the σ- and the π-orbits will also in the case of the fluorine molecule be displaced in such a way that the sequence of the orbits may be $\sigma_u > \pi_g > \pi_u > \sigma_g$, so that the σ_u-orbit has the highest energy.

A comparison between the HLSP method used by WATARI [6] in his calculation of the fluorine molecule, and the MO method used in the present study, shows that the agreement is fairly good, but it should be remembered that WATARI [6] used a different effective nuclear charge for every internuclear distance.

ACKNOWLEDGMENTS

I am much indebted to Professor O. KLEIN for his kind interest in this study. I should also like to express my gratitude to Dr. INGA FISCHER-HJALMARS, who suggested the present investigation, for many valuable suggestions, and stimulating discussions during the course of the work.

Appendix

Integrals occurring in the calculations

The following integrals have been tabulated by KOPINECK [20, 21], who also gives them explicitly;

$$\zeta, \eta, \lambda, \varrho = x, y, z$$

Overlap integrals

$$S(\zeta, \eta) = \int A_\zeta^*(1)\, B_\eta(1)\, d\tau_1 = f(\alpha)$$

Transfer integrals

$$J(\zeta, \eta) = \int \frac{A_\zeta^*(1)\, B_\eta(1)}{r_{A1}}\, d\tau_1 = \nu \cdot f(\alpha)$$

$$K(\zeta, \eta) = \int \frac{A_\zeta^*(1)\, A_\eta(1)}{r_{B1}}\, d\tau_1 = \nu \cdot f(\alpha)$$

Coulomb integrals

$$C(\zeta, \eta, \lambda, \varrho) = \iint A_\zeta^*(1)\, B_\eta^*(2)\, \frac{1}{r_{12}}\, A_\lambda(1)\, B_\varrho(2)\, d\tau_1\, d\tau_2 = \nu \cdot f(\alpha)$$

Exchange integrals

$$A(\zeta, \eta, \lambda, \varrho) = \iint A_\zeta^*(1)\, B_\eta^*(2)\, \frac{1}{r_{12}}\, B_\lambda(1)\, A_\varrho(2)\, d\tau_1\, d\tau_2 = \nu \cdot f(\alpha)$$

Ionic integrals

$$L(\zeta, \eta, \lambda, \varrho) = \iint A_\zeta^*(1)\, A_\eta^*(2)\, \frac{1}{r_{12}}\, A_\lambda(1)\, B_\varrho(2)\, d\tau_1 d\tau_2 = \nu \cdot f(\alpha)$$

KOPINECK's [20, 21] tabulated values are for the α-values 1.0, 1.5, 2.0, . . ., 7.0. In some cases it has been necessary to use his explicit expressions to calculate the integrals for intermediate values of α. The tables of KOTANI, AMEMIYA and SIMOSE [22] were a help in these cases. Interpolation in KOPINECK's tables [20, 21] has however been used in evaluating the integrals $A(zzzz)$ and $L(zzzz)$.

The kinetic energy integrals

$$T(\zeta, \eta) = -\frac{1}{2} \int A_\zeta^*(1)\, \nabla^2 B_\eta(1)\, d\tau_1 = \nu^2 \cdot f(\alpha)$$

$$U(\zeta, \eta) = -\frac{1}{2} \int A_\zeta^*(1)\, \nabla^2 A_\eta(1)\, d\tau_1 = \nu^2 \cdot \text{const.} = \frac{\nu^2}{2}$$

and the *Coulomb integrals*

$$Q(\zeta,\eta) = \int \frac{A_\zeta^*(1)\,A_\eta(1)}{r_{A1}}\,d\tau_1 = \nu \cdot \text{const.} = \frac{\nu}{2}$$

are easily calculated directly.

Two-electron integrals with one force centre

$$M(\zeta,\eta,\lambda,\varrho) = \int\!\!\int A_\zeta^*(1)\,A_\eta^*(2)\,\frac{1}{r_{12}}\,A_\lambda(1)\,A_\varrho(2)\,d\tau_1\,d\tau_2 = \nu \cdot \text{const.}$$

have been tabulated by BEARDSLEY [23].

$G(p\,q)$ and $H(p\,q)$ expressed in the integrals S, M, L, C and A

The electron configuration $\sigma_g^2\pi_u^4\pi_g^4$

$$\begin{aligned} G(zz) = {} & \frac{1}{2+2S(zz)}\left[M(zzzz)+2L(zzzz)+2C(zzzz)-A(zzzz)\right]+ \\ & + \frac{1}{1+S(xx)}\left[2M(xzxz)+4L(zxzx)+2C(xzxz)-M(xxzz)-\right. \\ & \left.\qquad -2L(zzxx)-A(xzzx)\right]+ \\ & + \frac{1}{1-S(xx)}\left[2M(xzxz)-4L(zxzx)+2C(xzxz)-M(xxzz)+\right. \\ & \left.\qquad +2L(zzxx)-A(xzzx)\right] \end{aligned}$$

$$\begin{aligned} G(zz') = {} & \frac{1}{2+2S(zz)}\left[2L(zzzz)+3A(zzzz)-C(zzzz)\right]+ \\ & + \frac{1}{1+S(xx)}\left[4L(xzxz)+4A(xzxz)-2L(xxzz)-A(xxzz)-\right. \\ & \left.\qquad -C(xxzz)\right]+ \\ & + \frac{1}{1-S(xx)}\left[4L(xzxz)-4A(xzxz)-2L(xxzz)+A(xxzz)+\right. \\ & \left.\qquad +C(xxzz)\right] \end{aligned}$$

$$\begin{aligned} G(xx) = {} & \frac{1}{2+2S(zz)}\left[2M(xzxz)+4L(xzxz)+2C(xzxz)-M(xxzz)-\right. \\ & \left.\qquad -2L(xxzz)-A(xzzx)\right]+ \\ & + \frac{1}{2+2S(xx)}\left[M(xxxx)+2L(xxxx)+2C(xxxx)+2M(xyxy)+\right. \end{aligned}$$

$$\begin{aligned}
&+4\,L(xyxy)+2\,C(xyxy)-A\,(xxxx)-M\,(xxyy)-\\
&-2\,L(xxyy)-A\,(xxyy)]+\\
+\frac{1}{2-2\,S(xx)}&[M\,(xxxx)-2\,L\,(xxxx)+2\,C\,(xxxx)+2\,M\,(xyxy)-\\
&-4\,L(xyxy)+2\,C(xyxy)-A\,(xxxx)-M\,(xxyy)+\\
&+2\,L\,(xxyy)-A\,(xxyy)]
\end{aligned}$$

$$\begin{aligned}
G\,(xx')=\frac{1}{2+2\,S(zz)}&[4\,L\,(zxzx)+4\,A\,(xzxz)-2\,L\,(zzxx)-A\,(xxzz)-\\
&-C\,(xxzz)]+\\
+\frac{1}{2+2\,S(xx)}&[2\,L\,(xxxx)+3\,A\,(xxxx)+4\,L(xyxy)+4\,A\,(xyxy)-\\
&-2\,C\,(xxxx)-2\,L\,(xxyy)-A\,(xxyy)-C\,(xxyy)]+\\
+\frac{1}{2-2\,S(xx)}&[2\,L\,(xxxx)-3\,A\,(xxxx)+4\,L\,(xyxy)-4\,A\,(xyxy)+\\
&+C\,(xxxx)-2\,L\,(xxyy)+A\,(xxyy)+C\,(xxyy)]
\end{aligned}$$

$$\begin{aligned}
H\,(zz)\ &=U\,(zz)-Z\,[Q\,(zz)+K\,(zz)]\\
H\,(zz')\ &=T\,(zz)-2\cdot Z\cdot J\,(zz)\\
H\,(xx)\ &=U(xx)-Z\,[Q\,(xx)+K\,(xx)]\\
H\,(xx')&=T\,(xx)-2\cdot Z\cdot J\,(xx)
\end{aligned}$$

The electron configuration $\sigma_g^2\,\sigma_u^2\,\pi_u^4\,\pi_g^2$

$$\begin{aligned}
G\,(zz)=\frac{1}{2+2\,S(zz)}&[M\,(zzzz)+2\,L\,(zzzz)+2\,C\,(zzzz)-A\,(zzzz)]+\\
+\frac{1}{1+S\,(xx)}&[2\,M\,(xzxz)+4\,L\,(zxzx)+2\,C\,(xzxz)-M\,(xxzz)\\
&-2\,L\,(zzxx)-A\,(xzzx)]+\\
+\frac{1}{2-2\,S\,(xx)}&[2\,M\,(xzxz)-4\,L\,(zxzx)+2\,C\,(xzxz)-M\,(xxzz)+\\
&+2\,L\,(zzxx)-A\,(xzzx)]+\\
+\frac{1}{2-2\,S\,(zz)}&[M\,(zzzz)-2\,L\,(zzzz)+2\,C\,(zzzz)-A\,(zzzz)]
\end{aligned}$$

$$
\begin{aligned}
G(zz') = {} & \frac{1}{2+2S(zz)}[2L(zzzz)+3A(zzzz)-C(zzzz)]+ \\
& + \frac{1}{1+S(xx)}[4L(xzxz)+4A(xzxz)-2L(xxzz)-A(xxzz)- \\
& \qquad -C(xxzz)]+ \\
& + \frac{1}{2-2S(xx)}[3L(xzxz)-4A(xzxz)-2L(xxzz)+A(xxzz)+ \\
& \qquad +C(xxzz)]+ \\
& + \frac{1}{2-2S(zz)}[2L(zzzz)-3A(zzzz)+C(zzzz)]
\end{aligned}
$$

$$
\begin{aligned}
G(xx) = {} & \frac{2}{2+2S(xx)}[2M(xzxz]+4L(xzxz)+2C(xzxz)-M(xxzz)- \\
& \qquad -2L(xxzz)-A(xzzx)]+ \\
& + \frac{1}{2+2S(xx)}[M(xxxx)+2L(xxxx)+2C(xxxx)+2M(xyxy)+ \\
& \qquad +4L(xyxy)+2C(xyxy)-A(xxxx)-M(xxyy)- \\
& \qquad -2L(xxyy)-A(xxyy)]+ \\
& + \frac{1}{4-4S(xx)}[M(xxxx)-2L(xxxx)+2C(xxxx)+2M(xyxy)- \\
& \qquad -4L(xyxy)+2C(xyxy)-A(xxxx)-M(xxyy)+ \\
& \qquad +2L(xxyy)-A(xxyy)]+ \\
& + \frac{1}{2-2S(zz)}[2M(xzxz)-4L(xzxz)+2C(xzxz)-M(xxzz)+ \\
& \qquad +2L(xxzz)-A(xzzx)]
\end{aligned}
$$

$$
\begin{aligned}
G(xx') = {} & \frac{1}{2+2S(zz)}[4L(zxzx)+4A(zxzx)-2L(zzxx)-A(xxzz)- \\
& \qquad -C(xxzz)]+ \\
& + \frac{1}{2+2S(xx)}[2L(xxxx)+3A(xxxx)+4L(xyxy)+4A(xyxy)- \\
& \qquad -C(xxxx)-2L(xxyy)-A(xxyy)-C(xxyy)]+ \\
& + \frac{1}{4-4S(xx)}[2L(xxxx)-3A(xxxx)+4L(xyxy)-4A(xyxy)+
\end{aligned}
$$

$$+C(xxxx)-2L(xxyy)+A(xxyy)+C(xxyy)]+$$

$$+\frac{1}{2-2S(zz)}[4L(zxzx)-4A(xzxz)-2L(zzxx)+A(xxzz)+$$

$$+C(xxzz)]$$

$$G(xy)=\frac{1}{4-4S(xx)}[3M(xxyy)-6L(xxyy)+4C(xxyy)-A(xxyy)-$$

$$-M(xyxy)+2L(xyxy)-A(xyxy)]$$

$$G(xy')=\frac{1}{4-4S(xx)}[6L(xxyy)-7A(xxyy)+C(xxyy)-$$

$$-2L(xyxy)+A(xyxy)+C(xyxy)]$$

$$H(zz)=U(zz)-Z[Q(zz)+K(zz)]$$

$$H(zz')=T(zz)-2\cdot Z\cdot J(zz)$$

$$H(xx)=U(xx)-Z[Q(xx)+K(xx)]$$

$$H(xx')=T(xx)-2\cdot Z\cdot J(xx).$$

Tables of values of G_{ii}, H_{ii} and ε_{ii}

The electron configuration $\sigma_g^2\pi_u^4\pi_g^4$

Table A 1.

G_{ii}-values for varying ν-values, when $R=R_e=2.680$ a.u.

α ν	1.0 0.373	1.5 0.560	2.0 0.749	2.5 0.933	3.0 1.119	3.5 1.306	4.0 1.493	4.5 1.679	5.0 1.866
G_{11}	1.221	1.939	2.514	3.055	3.442	3.823	4.159	4.463	4.742
$G_{22}=G_{33}$	1.623	2.075	2.549	3.007	3.446	3.862	4.258	4.642	5.016
$G_{44}=G_{55}$	10.361	5.132	4.116	3.997	4.154	4.409	4.701	5.010	5.325
ΣG_{ii}	25.187	16.353	15.845	17.063	18.643	20.363	22.077	23.767	25.424

Table A 2.

H_{ii}-values for varying ν-values, when $R=R_e=2.680$ a.u.

α ν	1.0 0.373	1.5 0.560	2.0 0.749	2.5 0.933	3.0 1.119	3.5 1.306	4.0 1.493	4.5 1.679	5.0 1.866
H_{11}	−2.953	−3.695	−4.168	−4.496	−4.735	−4.920	−5.069	−5.190	−5.286
$H_{22}=H_{33}$	−1.754	−2.451	−3.001	−3.425	−3.750	−4.005	−4.217	−4.400	−4.562
$H_{44}=H_{55}$	−0.670	−1.665	−2.535	−3.233	−3.789	−4.209	−4.515	−4.727	−4.866
$2\Sigma H_{ii}$	−15.602	−23.854	−30.480	−35.627	−39.623	−42.698	−45.066	−46.891	−48.282

Table A 3.

G_{ii}-values for varying R-values, when $\nu = \text{const.} = 1.638$.

α	1.0	1.5	2.0	2.5	3.0	3.5	4.0	4.5	5.0
R	0.611	0.916	1.221	1.526	1.832	2.137	2.440	2.747	3.053
G_{11}	5.340	5.653	5.498	5.344	5.018	4.777	4.547	4.338	4.148
$G_{22} = G_{33}$	7.097	6.049	5.574	5.261	5.024	4.825	4.656	4.512	4.388
$G_{44} = G_{55}$	45.315	14.963	9.000	6.992	6.056	5.509	5.139	4.869	4.658
ΣG_{ii}	110.165	47.678	34.647	29.851	27.178	25.444	24.137	23.100	22.239

Table A 4.

H_{ii}-values for varying R-values, when $\nu = \text{const.} = 1.638$.

α	1.0	1.5	2.0	2.5	3.0	3.5	4.0	4.5	5.0
R	0.611	0.916	1.221	1.526	1.832	2.137	2.440	2.747	3.053
H_{11}	−10.922	−9.527	−8.054	−7.124	−6.416	−5.866	−5.431	−5.080	−4.792
$H_{22} = H_{33}$	− 7.395	−6.790	−6.078	−5.524	−5.082	−4.745	−4.497	−4.316	−4.182
$H_{44} = H_{55}$	+13.733	+0.996	−3.463	−4.683	−5.000	−4.973	−4.821	−4.633	−4.449
$2\Sigma H_{ii}$	+ 3.508	−42.232	−54.269	−55.077	−53.158	−50.607	−48.132	−45.956	−44.110

Table A 5.

Values of the energy parameters ε_{ii} for the orbits $\sigma_g \pi_u$ and π_g, for varying R-values, when $\nu = \text{const.} = 1.638$.

α	1.0	1.5	2.0	2.5	3.0	3.5	4.0	4.5	5.0
R	0.611	0.916	1.221	1.526	1.832	2.137	2.440	2.747	3.053
σ_g	− 5.582	− 3,874	−2.556	−1.779	−1.398	−1.090	−0.884	−0.742	−0.645
π_u	− 0.298	− 0.741	−0.504	−0.263	−0.058	+0.080	+0.159	+0.196	+0.206
π_g	+59.048	+15.959	+5.538	+2.309	+1.057	+0.536	+0.319	+0.236	+0.209

The electron configuration $\sigma_g^2 \sigma_u^2 \pi_u^4 \pi_g^2$

Table A 6.

G_{ii}-values for varying ν-values, when $R = R_e = 2.680$ a.u.

α	1.0	1.5	2.0	2.5	3.0	3.5	4.0	4.5	5.0
ν	0.373	0.560	0.749	0.933	1.119	1.306	1.493	1.679	1.866
G_{11}	1.291	1.942	2.480	2.938	3.336	3.690	4.016	4.321	4.607
$G_{22} = G_{33}$	1.341	1.849	2.332	2.778	3.194	3.588	3.972	4.349	4.721
G_{44}	4.629	3.096	3.033	3.267	3.579	3.914	4.257	4.600	4.940
G_{55}	1.148	1.648	2.079	2.450	2.792	3.132	3.495	3.873	4.255
ΣG_{ii}	9.750	10.385	12.256	14.211	16.094	17.914	19.711	21.492	23.243

Table A 7.

H_{ii}-values for varying ν-values, when $R = R_e = 2.680$.

α ν	1.0 0.373	1.5 0.560	2.0 0.749	2.5 0.933	3.0 1.119	3.5 1.306	4.0 1.493	4.5 1.679	5.0 1.866
H_{11}	−2.953	−3.695	−4.168	−4.496	−4.735	−4.920	−5.069	−5.190	−5.286
$H_{22} = H_{33}$	−1.754	−2.451	−3.001	−3.425	−3.750	−4.005	−4.217	−4.400	−4.562
H_{44}	−0.670	−1.665	−2.535	−3.233	−3.789	−4.209	−4.515	−4.727	−4.866
H_{55}	−1.733	−2.424	−2.976	−3.393	−3.720	−3.955	−4.154	−4.322	−4.461
$2\Sigma H_{ii}$	−17.728	−25.373	−31.361	−35.947	−39.466	−42.190	−44.345	−46.080	−47.474

Table A 8.

G_{ii}-values for varying R-values, when $\nu = \text{const.} = 1.565$.

α R	1.0 0.639	1.5 0.958	2.0 1.278	2.5 1.597	3.0 1.917	3.5 2.236	4.0 2.556	4.5 2.875	5.0 3.195
G_{11}	5.395	5.410	5.181	4.911	4.646	4.406	4.195	4.013	3.850
$G_{22} = G_{33}$	5.603	5.152	4.872	4.644	4.449	4.284	4.149	4.039	3.945
G_{44}	19.342	8.624	6.336	5.460	4.984	4.673	4.447	4.272	4.128
G_{55}	4.798	4.591	4.342	4.096	3.889	3.740	3.650	3.597	3.556
ΣG_{ii}	40.742	28.928	25.605	23.754	22.417	21.386	20.589	19.958	19.425

Table A 9.

H_{ii}-values for varying R-values, when $\nu = \text{const.} = 1.565$.

α R	1.0 0.639	1.5 0.958	2.0 1.278	2.5 1.597	3.0 1.917	3.5 2.236	4.0 2.556	4.5 2.875	5.0 3.195
H_{11}	−10.545	−9.189	−7.779	−6.880	−6.196	−5.665	−5.244	−4.906	−4.630
$H_{22} = H_{33}$	− 7.081	−6.512	−5.845	−5.325	−4.907	−4.589	−4.353	−4.181	−4.053
H_{44}	+12.201	+0.586	−3.470	−4.571	−4.848	−4.813	−4.664	−4.484	−4.308
H_{55}	− 6.441	−6.080	−5.762	−5.322	−4.896	−4.540	−4.284	−4.123	−4.025
$2\Sigma H_{ii}$	−37.894	−55.413	−57.402	−54.844	−51.510	−48.391	−45.797	−43.748	−42.136

Table A 10.

Values of the energy parameters ε_{ii} for the orbits $\sigma_g, \sigma_u, \pi_u$ and π_g for varying R-values, when $\nu = \text{const.} = 1.565$.

α R	1.0 0.639	1.5 0.958	2.0 1.278	2.5 1.597	3.0 1.917	3.5 2.236	4.0 2.556	4.5 2.875	5.0 3.195
σ_g	− 5.150	−3.779	−2.598	−1.969	−1.549	−1.259	−1.049	−0.893	−0.780
π_u	− 1.477	−1.360	−0.973	−0.681	−0.459	−0.305	−0.204	−0.142	−0.107
π_g	+31.543	+9.210	+2.866	+0.889	+0.136	−0.149	−0.217	−0.212	−0.180
σ_u	− 1.643	−1.489	−1.420	−1.266	−1.008	−0.800	−0.634	−0.526	−0.469

REFERENCES

1. C. R. Mueller, J. Chem. Phys. *21*, 1013 (1953).
2. H. Eyring, J. Walter, and G. E. Kimball, Quantum Chemistry, New York & London 1944, 163.
3. W. E. Duncanson and C. A. Coulson, Proc. Roy. Soc. Edin. *A 62*, 37—39 (1943—49).
4. F. Schlögl, Z. f. Phys. *131*, 505 (1952).
5. W. Heisenberg, Ann. Phys. V. F. *10*, 888 (1931).
6. W. Watari, Progr. Theor. Phys. *8*, 524 (1952).
7. F. R. Brown, Phys. Rev. *44*, 214 (1933).
8. L. O. Brockway, J. Am. Chem. Soc. *60*, 1348 (1938).
9. M. T. Rogers, V. Schomaker, and D. P. Stevenson, J. Am. Chem. Soc. *63*, 2610 (1941).
10. D. Andrychuk, Canad. J. Phys. *29*, 151 (1951).
11. E. Wicke, J. Phys. Chem. *56*, 358 (1952).
12. E. Wicke and H. Friz, Z. Elektrochem. *57*, 9 (1953).
13. P. W. Gilles and J. L. Margrave, J. Chem. Phys. *21*, 381 (1953).
14. C. C. J. Roothaan, Rev. Mod. Phys. *23*, 69 (1951).
15. H. Eyring, J. Walter, and G. E. Kimball, Quantum Chemistry, New York & London 1944, 207.
16. J. H. van Vleck, Phys. Rev. *45*, 405 (1934).
17. H.-J. Kopineck, Z. f. Naturforsch. *7 a*, 22 (1952).
18. C. R. Mueller and H. Eyring, J. Chem. Phys. *19*, 934 (1951).
19. G. Araki and W. Watari, Progr. Theor. Phys. *6*, 945 (1951).
20. H.-J. Kopineck, Z. f. Naturforsch. *5 a*, 420 (1950).
21. —— Ibidem *6 a*, 177 (1951).
22. M. Kotani, A. Amemiya, and T. Simose, Proc. Phys.-Math. Soc. Japan *20*, extr. no. 1 (1938); ibidem *22*, extr. no. 1 (1940).
23. N. F. Beardsley, Phys. Rev *39*, 913 (1932).

Institute of Theoretical Physics, University of Stockholm, May 1954.

Tryckt den 24 november 1954.

Uppsala 1954. Almqvist & Wiksells Boktryckeri AB

ARKIV FÖR FYSIK Band 8 nr 54

Communicated 26 May 1954 by AXEL E. LINDH and IVAR WALLER

Measurements of electron diffraction intensities by means of Geiger counters

Experimental determination of relative values of the atomic factor for gold, silver, and aluminium

By SVEN LENNANDER

With 28 figures in the text

Contents

Acknowledgements 552
Chapter I. Theory and earlier investigations 552
1. Theoretical survey 552
2. Experimental determination of the atomic factor 555
3. The aim of the present investigation 558
Chapter II. Experimental arrangements 559
1. The diffraction apparatus 559
2. The Geiger counters 567
3. The d.c. amplifier 570
4. Pumps and vacuum gauges 572
5. The high-voltage unit 572
6. The recording procedure 573
Chapter III. Comparison with the photographic method 575
1. The recording time 575
2. Accuracy of the results 575
3. Bombardment of the foil 575
Chapter IV. Preparation of the metal foils 576
1. Method for reducing the degree of preferred crystal orientation in the evaporated films 576
2. Method of preparing very thin self-supporting foils 579
3. Determination of the foil thickness 580
Chapter V. Investigation of the metal foils for preferred crystal orientation 581
Chapter VI. The use of films with partial preferred orientation for determination of the atomic factor 583
1. Determination of the degree of preferred orientation 583
2. Correction when the electron beam is normal to the foil 584
Chapter VII. Intensity measurements and the determination of the atomic factor 586
1. Measurements with Au 586
2. Measurements with Ag 592
3. Measurements with Al 593
4. Discussion of the results 597
Chapter VIII. Widths of the rings and crystal size 604
Chapter IX. Measurement of the background 607
Summary 612
References 612

Acknowledgements

This investigation has been carried out at the Physical Laboratory of Uppsala University. The first plans of the diffraction apparatus were drawn in 1947. The apparatus was practically ready in 1951. Considerable time was devoted to preliminary research on the preparation of the metal foils. Most of the measurements reported in the present paper were carried out in 1953 and 1954.

It is a particular pleasure for me to thank the former head of the Physical Laboratory, Professor AXEL E. LINDH, for the most generous manner in which he has aided this investigation in every way.

During the years 1943–45 I had the privilege of being introduced to the problems of electron diffraction by STEN VON FRIESEN, now Professor in Lund. The present work is a continuation of that I carried out under his guidance. For the many things I have learnt from him, and for the great interest he has always shown for my work, I should like to express my warmest thanks.

I should also like to express my gratitude to Professor PER OHLIN for many discussions and much good advice, which has been of great value for the present work.

Discussions with my colleagues at the Laboratory have also meant a great deal for my work, and I would like to take this opportunity of acknowledging my indebtedness to them.

My thanks are further due to Fil. kand. REGINALD STEDMAN, B. A., for his painstaking work in translating this paper into English.

Last, but not least, I owe a debt of gratitude to my wife, Fil. mag. GERD LENNANDER, who has been of invaluable assistance to me in preparing the material for this thesis, as well as contributing in many other ways to its completion.

Uppsala, October, 1954.

CHAPTER I

Theory and earlier experimental investigations

§ 1. Theoretical survey

a. Atomic scattering of electrons

The basic phenomenon in the present investigation is the scattering of fast electrons by atoms. The theory of elastic scattering was first formulated by BORN [1926]. He started from the Schrödinger wave equation:

$$\Delta \Psi + \frac{8\pi^2 m}{h^2}\{E - V(r)\}\Psi = 0. \tag{1}$$

This equation is satisfied by the wave function for the electron, Ψ. $V(r)$ is the potential energy of the electron in the field of force due to the scattering atom. This field is assumed to be spherically symmetrical. Another assumption is that the electron's velocity is small compared with the velocity of light. The approximate solution of eq. (1) given by BORN is such that the wave function Ψ at a large distance (r) from the atom may be expressed as the sum of the incident and scattered waves:

$$\Psi = e^{ikz} + \frac{1}{r} F_e(\vartheta)\, e^{ikr} \tag{2}$$

vhere $\frac{1}{r} F_e(\vartheta)\, e^{ikr}$ represents the scattered wave.

The most useful solution from the practical point of view is that given by MOTT 1930]. By neglecting, among other things, the reaction of the electrons on the harges in the atom, MOTT arrived at the following expression for the amplitude $F_e(\vartheta)$:

$$F_e(\vartheta) = \frac{e^2}{2\,m\,v^2}\,(Z - F_r)\,\frac{1}{\sin^2 \vartheta/2}\,. \tag{3}$$

In this formula,

e, m and v are the charge, mass, and velocity of the incident electron,
Z the atomic number of the scattering atom,
F_r the atomic amplitude for X-rays, i.e. the ratio of the amplitude elastically scattered by the whole atom to the corresponding amplitude due to a single electron.

The introduction of the de Broglie wavelength

$$\lambda = \frac{h}{m\,v}$$

nto eq. (3) gives

$$|F_e(\vartheta)|^2 = \frac{e^4\,m^2}{4\,h^4}\,(Z - F_r)^2\,\frac{\lambda^4}{\sin^4 \vartheta/2}\,. \tag{4}$$

$|F_e(\vartheta)|^2$ is the *atomic factor for electrons*. If a beam containing N electrons per cm² s incident on an atom, $N \cdot |F_e(\vartheta)|^2$ electrons per unit solid angle are scattered through an angle ϑ.

If the charge distribution of the atom is known, F_r (and hence $|F_e(\vartheta)|^2$ as well) can be calculated. The distribution of charge may be determined for light atoms by means of a theory put forward by HARTREE [1928], and for heavier atoms with the aid of a theory of THOMAS [1927] and FERMI [1928]. F_r has been calculated and tabuated as a function of $\frac{\sin \vartheta/2}{\lambda}$ for all atoms by JAMES and BRINDLEY [1931].

Table 1 gives the values for Au, Ag, and Al, taken from JAMES and BRINDLEY, these being the metals considered in the present investigation.

Table 1

$\frac{\sin \vartheta/2}{\lambda} \cdot 10^{-8}$ cm⁻¹	F_r		
	Al; $Z = 13$	Ag; $Z = 47$	Au; $Z = 79$
0.1	11.0	43.0	74.0
0.2	8.95	36.9	65.0
0.3	7.75	31.3	57.0
0.4	6.6	26.8	49.7
0.5	5.5	23.7	43.9
0.6	4.5	21.3	39.8
0.7	3.7	19.0	36.3
0.8	3.1	17.0	33.0

Eq. (4) and Table 1 have been used to calculate the theoretical values of $|F_e(\vartheta)|^2$ which will be considered later.

Figures somewhat different from those of Table 1 are obtained if the distribution of the atom's charge is computed after PAULING and SHERMAN [1932], who used certain empirical screening constants in their calculations. For Au PAULING and SHERMAN's values give a steeper $|F_e(\vartheta)|^2$ curve than do those of JAMES and BRINDLEY.

b. Scattering by crystals

Equation (4) applies to the scattering of electrons by a single atom. Such scattering may be observed experimentally in diffraction by a gas. But in most cases of electron diffraction the media are crystalline. However, according to the *kinematic theory* of MOTT [1930] eq. (4) can also be employed to express the intensities of reflection from crystals. The necessary condition for this is that in calculating the scattering from one atom of the crystal lattice it is permissible to neglect the effect of the other atoms.

BETHE [1928] worked out a *dynamic theory* for the scattering of electrons by crystals. He considered the case where the scattering is due to a large single crystal, and found the intensity of the scattered electrons to be proportional to $F_e(\vartheta)$ and not to $|F_e(\vartheta)|^2$ as in the kinematic theory. It is not yet clear when the kinematic theory is valid in practice and when the dynamic.

THOMSON and COCHRANE [1939, p. 92] considered that the kinematic theory is a good approximation for small crystals, and that the dynamic theory should be applied to large crystals. But they did not take up the question of the boundary between small and large crystals.

c. The temperature effect

The kinematic theory previously considered does not take into account the thermal motion of the atoms in the crystal lattice. This motion renders the lattice planes somewhat diffuse, which leads to an attenuation of the scattered intensity.

The effect of the temperature of a crystal on its X-ray diffraction has been dealt with theoretically by DEBYE [1914], FAXÉN [1918], and WALLER [1923, 1925], among others. For the coherent radiation at a crystal temperature of $T°$ K, WALLER gave the following expression:

$$I = I_0 \, e^{-2M(T,\vartheta)} \tag{5}$$

where I_0 is the calculated intensity for reflection from a crystal without thermal motion.

For a cubic lattice the function M is as follows:

$$M(T,\vartheta) = \frac{6h^2}{\mu k \Theta} \cdot \frac{\sin^2 \vartheta/2}{\lambda^2} \left\{ \frac{\Phi(\chi)}{\chi} + \frac{1}{4} \right\} \tag{6}$$

where μ is the mass of the atom

Θ the characteristic temperature of the matter

h Planck's constant

k Boltzmann's constant

$\chi = \Theta/T$

(χ) is known as the Debye function. When T is large compared with Θ, $\Phi(\chi) \simeq 1$, nd

$$M(T, \vartheta) \simeq \frac{6\,h^2}{\mu\,k\,\Theta^2} \cdot \frac{\sin^2 \vartheta/2}{\lambda^2} \cdot T. \tag{7}$$

his approximation is permissible for reflections from a Au crystal at room tempera- ure, for instance, since Θ for Au is about 170° K.

As mentioned, the above applies to X-ray reflection. That the same equations are lso valid for electron diffraction has been established by Pisarenko [1935].

An example of the effect of temperature on the intensity is given in Fig. 1, which ncludes curves for both the theoretical atomic factor $C \cdot |F_e(\vartheta)|^2$ (from eq. (4)) and he temperature-corrected function $C \cdot |F_e(\vartheta)|^2 \cdot e^{-2M(T,\vartheta)}$ (for $T = 293°$ K—the dashed urve). As will be seen, the temperature effect is fairly small, the curve being only lightly steeper. Therefore, the theoretical curve later used for comparison with he experimental results is the $|F_e(\vartheta)|^2$ curve without temperature correction.

§ 2. Experimental determination of the atomic factor

a. Theory

Experience from the X-ray field has frequently been utilised for problems of lectron diffraction, both in theory and practice. This applies, for instance, to exper- mental tests of the theories considered in § 1—in particular, the experimental deter- ination of the atomic factor $|F_e(\vartheta)|^2$. The principal method used for fast electrons s closely analogous to the well-known Debye-Scherrer method. Thomson and Reid 1927; Reid, 1928] were the first to employ this method for electron diffraction. he sole difference was that they replaced the crystalline powder customary in -ray diffraction by a very thin foil.

Such a foil is often of a microcrystalline nature. If the orientation of the crystallites s assumed to be completely random, it is possible to derive an expression for the tensities of the Debye-Scherrer rings due to diffraction of the electrons by the foil. he following formula gives the intensity of a ring due to a lattice plane for which he glancing angle satisfying the Bragg condition is $\vartheta/2$:

$$I = \text{const.} \times |F_e(\vartheta)|^2 \cdot p/\sin \vartheta/2. \tag{8}$$

$F_e(\vartheta)|^2$ is the atomic factor and p the number of equivalent planes giving the reflexion. ince the present investigation is concerned only with relative measurements of the tomic factor, the size of the constant is of no interest.

For fast electrons ϑ is small, and the intensity *per unit length* of the ring can be ritten:

$$I = \text{const.} \times |F_e(\vartheta)|^2 \cdot p/\sin^2 \vartheta/2. \tag{9}$$

easuring the relative intensities of the rings allows the atomic factor to be deter- ined from the relation

$$|F_e(\vartheta)|^2 = \text{const.} \times \frac{I \cdot g^2}{p} \tag{10}$$

in which $g^2 = h^2 + k^2 + l^2$, where h, k, and l are the Miller indices of the various lattice planes. The substitution $\sin^2 \vartheta/2 \rightarrow \text{const.}\ g^2$ is derived from Bragg's law $2d \sin \vartheta/2 = n \cdot \lambda$, where $d = \frac{a}{\sqrt{h^2 + k^2 + l^2}}$ for cubic crystals. a is the elementary lattice constant.

Table 2 gives some values of g^2 and p for a face-centred cubic lattice, which will be used later.

Table 2

Ring	111	200	220	311	331	420	422	511 333
g^2	3	4	8	11	19	20	24	27
p	8	6	12	24	24	24	24	32

In comparing the experimental and theoretical (relative) values of the atomic factor it is usual to choose a particular ring as a normal reference. Here, the intensity of the (220) ring has been taken as 100, the intensities of the other rings being assigned proportional values. Thus for the (220) ring it is always true that

$$C \cdot |F_e(\vartheta)|^2 = \frac{I \cdot g^2}{p} = \frac{100 \cdot 8}{12} = 66.7.$$

b. Survey of earlier investigations

G. P. Thomson [1929] was the first to investigate the atomic factor for fast electrons (30–50 kV). He used Au foils of various thickness, prepared by cathode-sputtering on to a celluloid substrate which was afterwards dissolved in acetone. The resolution achieved was not very high, and several closely adjacent peaks could not be separated. However, the results, on application of eq. (10), were in fair agreement with the temperature-corrected kinematic theory.

Mark and Wierl [1930] also obtained results in agreement with the theory when they investigated the atomic factors for Au, Ag, and Al. They made their foils by evaporation on to a polished crystal of rock-salt which was subsequently dissolved in water. The thickness of the foils is not stated, and the results are given in the form of a mean for each element, with margins of error of up to ± 8 %. Their results for Au are given in Fig. 1.

Somewhat different results were obtained by Yearian and Howe [1935] in their intensity measurements with Au and Ag foils. They found that the experimental value of the atomic factor depended on the energy of the incident electrons. There was a satisfactory agreement with the theoretical curve for an accelerating voltage of about 80 kV. At lower voltage (less than 20 kV) the divergence was pronounced. Their paper gives no information about the thickness of the foils used or the method of preparation.

Results even less in agreement with the theory were obtained by Ornstein, Brinkman, Hauer, and Tol [1938], and later by Tol [1940, Tol and Ornstein, 1940]. The former carried out experiments on Ag and Cu (30 kV), and Tol on Au,

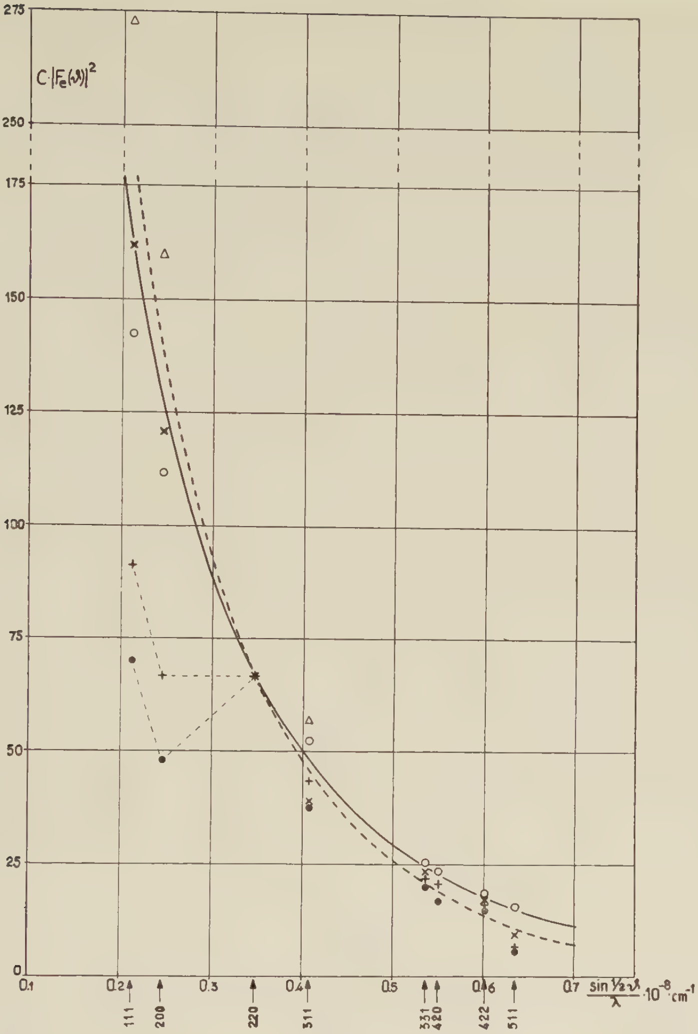

Fig. 1. Experimental values from earlier determinations of the atomic factor for Au.

× Mark and Wierl (mean area values)
+ Tol (260 Å, 30.5 kV, peak-height values)
● Tol (380 Å, 30.5 kV, peak-height values)
△ Sjenitzer (100 Å, area values)
○ Yamzin and Pinsker (mean peak-height values)

The solid curve is the theoretical $|F_e(\vartheta)|^2$ curve as given by eq. (4), the dashed one is the corresponding curve with a temperature correction included: $|F_e(\vartheta)|^2 \cdot e^{-2M(T,\,\vartheta)}$ ($T = 293°$ K; cf. eq. (7)).

Ag, and Cu (24–40 kV). In all cases they found that the experimental curve for $|F_e(\vartheta)|^2$ was less steep than the theoretical. TOL's results for Au (200–420 Å) are noteworthy in some respects. In the first place, there is a large difference between measurements for different foils. And secondly, the $|F_e(\vartheta)|^2$ curve is markedly irregular, especially at the value for the (220) ring. TOL was unable to explain these discrepancies, but he pointed out that the disparity between theory and experiment appears to increase as the thickness and age of the foils increases. TOL prepared his foils by evaporation on to a cellulose acetate substrate, which was subsequently dissolved in acetone. Fig. 1 includes two of TOL's determinations for Au. One of them is the most irregular of his curves for the atomic factor (380 Å, 30.5 kV). The other is from a determination (260 Å, 30.5 kV) that is a rough average of TOL's measurements for Au.

VON FRIESEN and LENNANDER [1946] determined the $|F_e(\vartheta)|^2$ curve for Al, and obtained a less steep curve than did MARK and WIERL, whose curve agreed with the theory.

The influence of the foil's thickness observed by TOL was examined by SJENITZER [1948]. Most of his foils were very thin, even as little as a few Å. He found it impossible to prepare self-supporting foils less than 200 Å thick, and therefore supported them on a base of nitrocellulose, 1000 Å thick. The results show that the thickness of the foil had a very marked effect. SJENITZER's curves for Au and Ag films 100 Å thick, for instance, are steeper than the theoretical curves, and the discrepancy increases as the thickness of the film decreases. His values for a Au foil 100 Å thick are reproduced in Fig. 1.

YAMZIN and PINSKER [1949] determined the atomic factor for Au, Ag, Cu, and Al, as well as for Sn, Mg, and Zn, but their account of the investigation is very brief. In the first paper there is only a single curve (for Ag). But in a later publication by PINSKER [1953, p. 162] curves for the other elements are given. The results differ entirely from those already mentioned for recent years. The agreement with the theoretical $|F_e(\vartheta)|^2$ curve (without the temperature correction) is exceptionally good. Only in the case of Au is there a tendency to deviation. The foils used were prepared by high vacuum condensation on to various kinds of substrates, which in most cases were afterwards dissolved. With Zn, it was found necessary to carry out the condensation inside the diffraction apparatus, in order to avoid oxidation; in this case the substrate remained throughout the experiment. The thickness of the films in this case is stated to have varied between 90 and 300 Å. Foil thickness for the other elements were up to 600 Å. Unlike TOL and SJENITZER, YAMZIN and PINSKER could detect no effect of foil thickness on the results. Nor did they find any variation with the accelerating voltage (15–80 kV). Their values for Au as inserted in Fig. 1 here are the mean of the results published by PINSKER.

§ 3. The aim of the present investigation

Clarification of the intensity relations in electron diffraction is of particular importance for the structural analyses which are performed by this means. Another problem where it is of interest is the calculation of the fine structure of X-ray absorption spectra [see, for instance, KURYLENKO, 1939]. As pointed out in § 1, the theories are not altogether in conformity (see also Chap. VII, § 4). The uncertainty is heightened by the exceptional divergence of the various experimental results, which have been recounted in the preceding paragraph.

All previous determinations of the atomic factor for fast electrons have relied on a photographic method for the intensity measurements. But most of the authors have pointed out that a more direct method of measurement is desirable.

The aim of the present investigation was to work out such a method, and to apply it to the measurement of the atomic factor for Au, Ag, and Al. The method chosen involved the use of Geiger counters. An account of the diffraction apparatus and its Geiger counters will be given in Chap. II.

Several authors [cf. VON FRIESEN and LENNANDER, 1946] have suggested that a possible explanation of the irregularity of the atomic factor curve as determined by TOL may be that the crystallites of the foils used were not randomly oriented. It is customary to examine foils for such orientation by means of photographs taken with the foil tilted at an acute angle to the electron beam. It has earlier been pointed out [VON FRIESEN and LENNANDER, 1946] that *ocular* examination of such photographs is insufficient to determine the usability of the foil, and that even a slight preferred orientation can have a definite influence on the results of intensity measurements.

Accordingly, special care has been devoted to the detection of any orientation trend in the foils used, and to the preparation of foils free from preferred orientation. The technique employed is described in Chap. IV.

It proved to be very difficult to obtain Al foils free from such orientation. Determinations of the atomic factor for Al were therefore carried out with foils for which the crystal orientation was not random, to a degree that was determined by special measurements. The results of the intensity measurements have been corrected by a method described in Chap. VI.

Another aim was to check whether or not the thickness of the foil has any effect on the $|F_e(\vartheta)|^2$ curve. For this purpose very thin *self-supporting* films (< 100 Å) were prepared, by the same method as used for the thicker foils. In this way it has been possible to achieve a direct comparison between different foils over a wide range of thickness, and at the same time to avoid the disturbing effect of a retained substrate. Chap. IV contains an account of the method used for preparation of self-supporting foils of down to 75 Å mean thickness.

CHAPTER II

Experimental arrangements

§ 1. The diffraction apparatus[1]

a. Principle of the apparatus

The most essential requirement for a diffraction apparatus employing Geiger counters is that it should maintain a high constancy in various respects over an adequate period of time. In the photographic method the times of exposure have generally been a few seconds, sometimes less than one second. A recording with a Geiger counter often takes about four hours. During all this time the diffraction pattern has to remain in exactly the same position. Furthermore, the accelerating voltage must be constant, and, preferably, the intensity as well.

---

[1] A preliminary account of the apparatus is given in Arkiv f. Fysik *5*, No. 18 (1952).

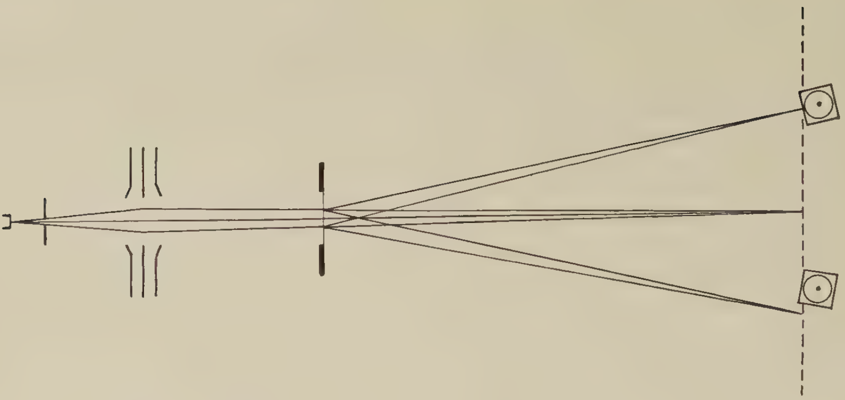

Fig. 2. Schematic diagram of the diffraction apparatus.

The first condition—a constant position of the diffraction pattern—can be fulfilled if the apparatus is of a stable construction, and if there are no disturbing magnetic or electrostatic fields. The electron beam is focused by an electrostatic lens in stable connection with the wall of the apparatus. A schematic diagram of the apparatus as used for the transmission method with a thin foil is given in Fig. 2.

To avoid any kind of distortion of the diffraction rings, there must be no deflection of the electrons by magnetic fields; the apparatus is therefore constructed from non-magnetic material—chiefly brass—and placed in the centre of a large Helmholtz coil that compensates the Earth's magnetic field.

The constant accelerating voltage is obtained from a smoothing circuit, which will be described later on.

The last condition—constant intensity while recording—can be achieved by electronic devices. But it was decided to avoid the problems associated with that method, and the monitor method was adopted instead. A second Geiger counter is employed as an integrating recorder of the primary intensity. This counter is situated in a fixed position in the diffraction pattern. The first counter is moved along a radius of the ring system, recording the number of impulses at a certain point during the time that is needed for the second counter to record a fixed number of impulses. Both counters are switched on and off simultaneously with a double switch. In this way it was possible to eliminate the effect of any variations of the primary intensity.

Fig. 3 is a drawing of the diffraction apparatus from above, showing the main parts. Most of them will be described in detail in the following paragraphs.

A is the electron source, and *B* the anode. In the centre of the anode there is a hole, 0.05 × 0.05 mm square. It is made of two molybdenum slits placed crosswise. This hole is focused by the electrostatic lens *D* in a plane through the slits of the Geiger counters *H* and *H'*.

*D*1 is a simple deflector coil of copper wire. It is placed under the electron beam. When there is no current in the coil, it does not affect the direction of the electron beam. A current of about 250 mA in the coil will (at an accelerating voltage of 30 kV) deflect the beam into the Faraday cylinder *D*2. The Faraday cylinder is connected to a d.c. amplifier (see § 3). This enables a check to be made on the primary intensity, when photographic plates were exposed, for instance. The switch of the coil is then

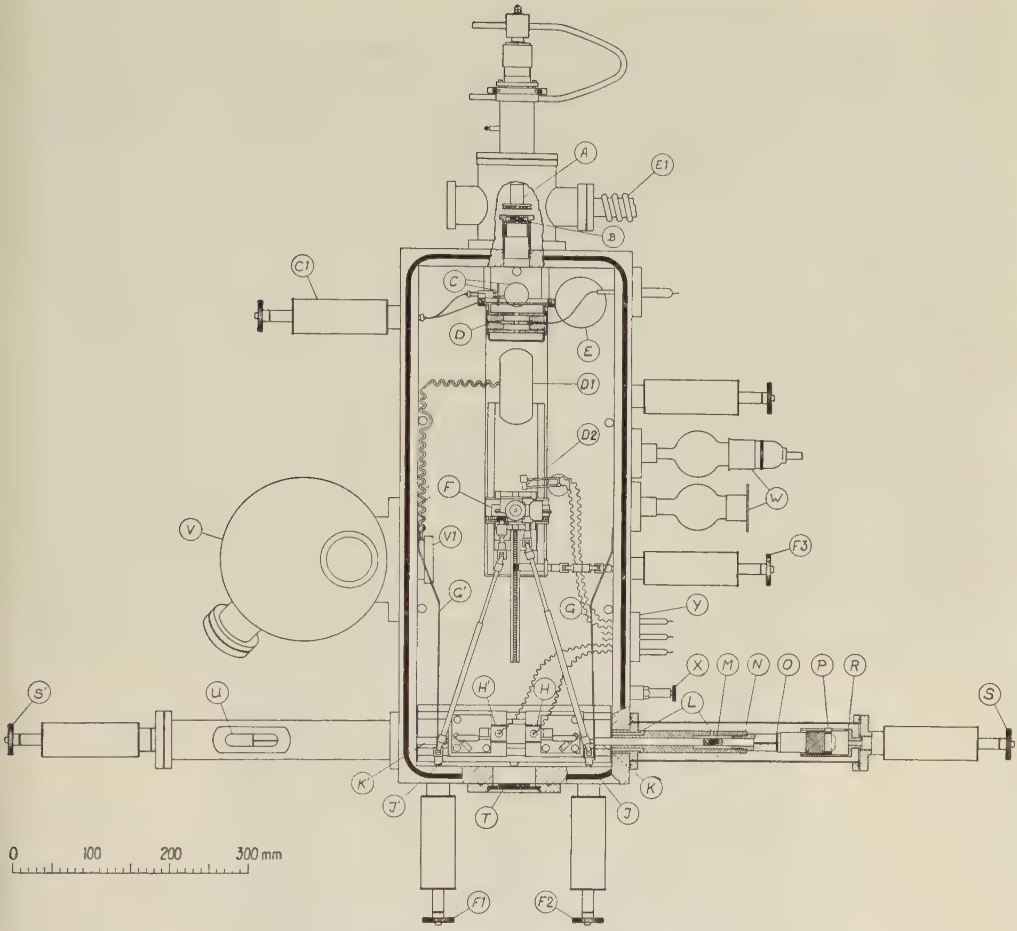

Fig. 3. The diffraction apparatus from above.

used for controlling the exposure time for the photographic plates needed in investigating the degree of crystal orientation in the foils.

F is the foil-holder described in § 1, d. *T* is a window, on the inner side of which there is a fluorescent screen to render direct observation of the diffraction pattern possible.

Most of the main parts of the apparatus are enclosed in a vacuum tank of brass with inner dimensions 650 × 250 × 125 mm. The thickness of the walls is 25 mm. The apparatus is vacuum-sealed by means of rubber rings. It is evacuated through the connection *E*, and the discharge tube through a separate connection *E*1. *W* indicates two manometer tubes—an ionisation gauge and a Pirani manometer. *X* is a needle valve, and *Y* a plate with six insulated electric inlets.

In direct connection with the apparatus there is an evaporation chamber *V* for making metal foils. In most cases, however, a separate evaporation chamber, described in Chap. IV, has been used. *V*1 is a light-trap, which must be used when photographic exposures are made.

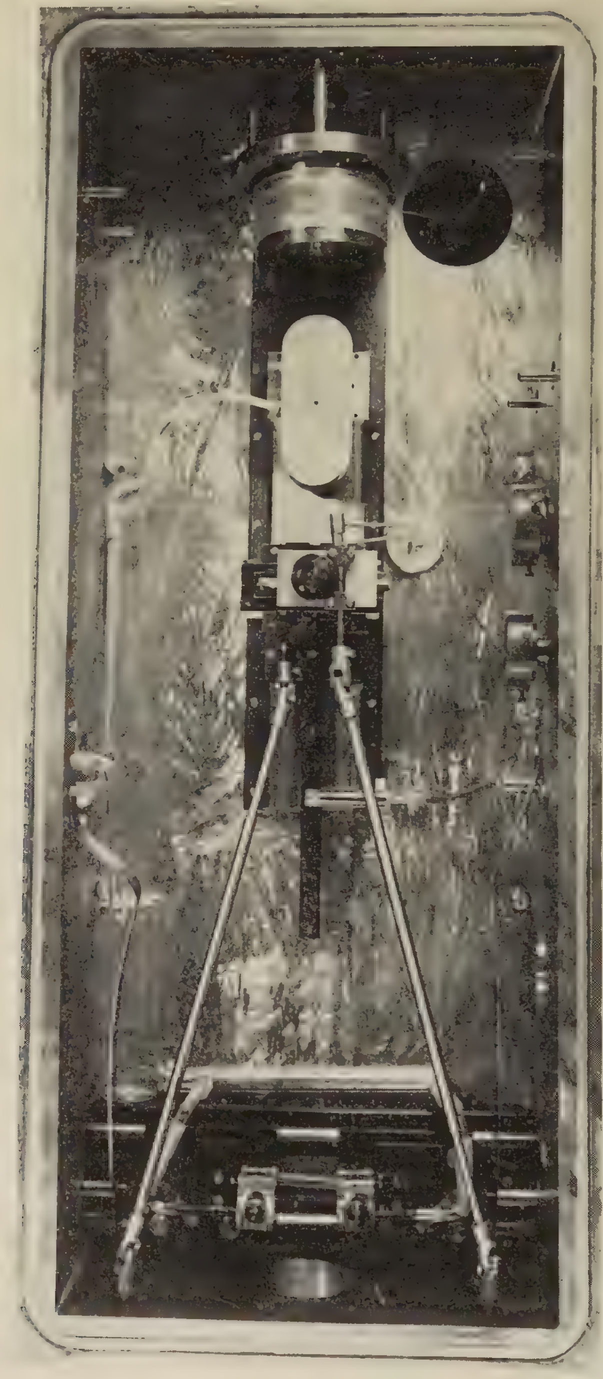

Fig. 4. View of the interior of the apparatus.

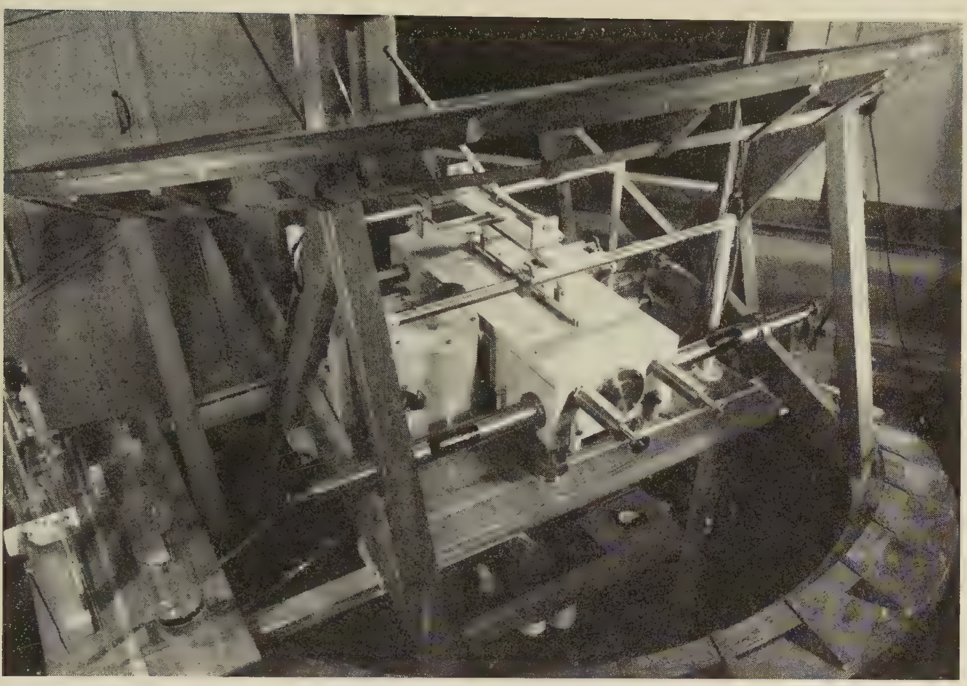

Fig. 5. View of the diffraction apparatus.

b. The electron source

The electron source was a low temperature cathode, which can be seen in Fig. 6. It has an oxide-coated platinum emitter, *B*. The filament has a diameter of 0.5 mm except for the upper emitting part, which has been flattened out into a disc 0.1 mm thick. This disc is partly covered by a thin layer of a special kind of white sealing-wax, which after its formation has good emission properties. However, investigation showed that the emission from such an oxide cathode is from a number of points in the emitting layer. The emission from such a point is frequently not stable for any length of time. To obtain emission from a single well-defined point there is an insulated metal disc, *A*, 1.5 mm in front of the filament. In the centre of this disc there is a hole of diameter 0.1 mm. About 100 V, taken from an earth-insulated battery, is applied (through inlet *G*) between the filament and disc *A*. During the recordings the current from the filament to the disc was about 1 μA.

The stability of the emission was good, and the cathode was in use for more than one year without any renewal of the emitting layer. Contact with air when the apparatus was opened merely enhanced the emission a little.

The filament and the disc-holder are fixed in the upper part of the water-cooled copper tube *E*. The copper tube is soldered to the sylphon bellows *L* via the ring *N*. By means of the ring *M* it was possible to alter the distance between the cathode disc *A* and the fixed anode. This distance was 8 mm.

The cathode is adjusted so that the electron beam strikes the anode hole and then follows the central axis of the apparatus (in the absence of focusing). This adjust-

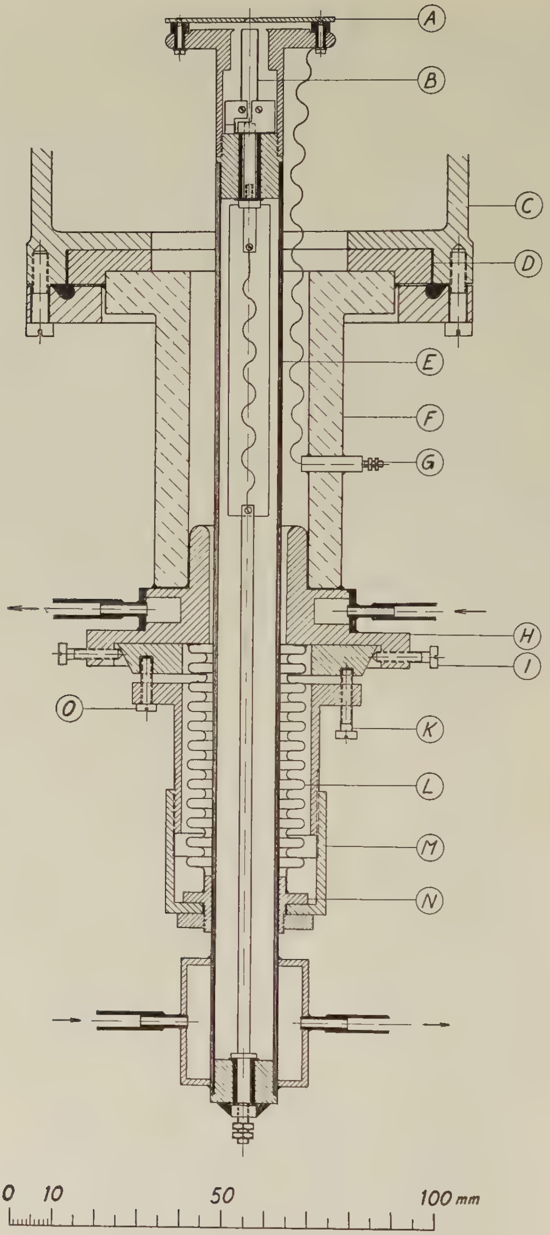

Fig. 6. The electron source.

ment can be performed by two sets of adjusting screws. Three screws similar to K enable the copper tube to be tilted to any desired position (usually parallel to the central axis of the apparatus), and then locked in this position by three screws similar to O. The vertical position of the cathode is adjustable by means of four screws similar to I. These screws are threaded into the water-cooled metal block H, which is fixed to the porcelain insulator F. H and the metal ring D are fastened to the porcelain insulator with picein.

As the filament had a long lifetime, it was seldom necessary to remove the electron source. When replaced the position was about the same as before, and a slight adjustment of a screw I was generally sufficient.

c. The electrostatic lens

The lens (D, Fig. 3) is made of brass, insulated with perspex. It is of much the same form as that described by JOHANNSON and SCHERZER [1933], though the dimensions have been modified somewhat. The position of the lens is adjusted from the outside by means of two rotatable vacuum connections. Only one of them, $C1$, can be seen in Fig. 2. These two controls are connected with two rotating discs, C, which can move the lens in perpendicular directions in the vertical plane. The adjustment of the lens proved to be very stable: after the first adjustment no others were needed.

The lens requires 39.8 % of the accelerating voltage, and the focusing is then good even when the accelerating voltage varies over a very wide range. The lens voltage is taken from a voltage divider. This is connected between the cathode and the anode, and consists of 100 two-watt resistors of 1 MΩ each. To obtain the exact voltage for good focusing, there is a second divider, consisting of 10 resistors of 5 MΩ each, which can be applied across any one of the 1 MΩ resistors.

d. The foil-holder

The details of the foil-holder can be seen in Fig. 7. It can hold four different foils. This can be seen from Fig. 7a, which is a front view of the holder, showing two different types of foil support. The net support was mostly used. The support is attached by two springs to a mounting which can be rotated about its axis. Each foil can be moved to a suitable diffraction position by the pinion arrangement D, which is connected to the external control $F1$ in Fig. 3. When a foil is in a diffraction position, the upper part of the mounting fits into a groove in the boss C (see Fig. 7b). C is the end of the shaft rotated by the worm-gear A. This worm-gear can be rotated from the external control $F2$ of Fig. 3, which is connected to the worm-shaft B. In this way each foil in the diffraction position can be rotated from the outside around a vertical axis through the foil and through the electron beam. This is of importance when investigating the degree of preferred orientation of the crystallites in the foil.

Lastly, the distance between the entire foil-holder and the Geiger counters can be adjusted externally, which makes it possible to vary the diameter of the diffraction rings for a fixed value of the accelerating voltage. This adjustment is made by pinion E, connected to control $F3$ in Fig. 3. The shafts from the external controls $F1$ and $F2$ are of a special telescopic construction, which accommodates the necessary variation of their length.

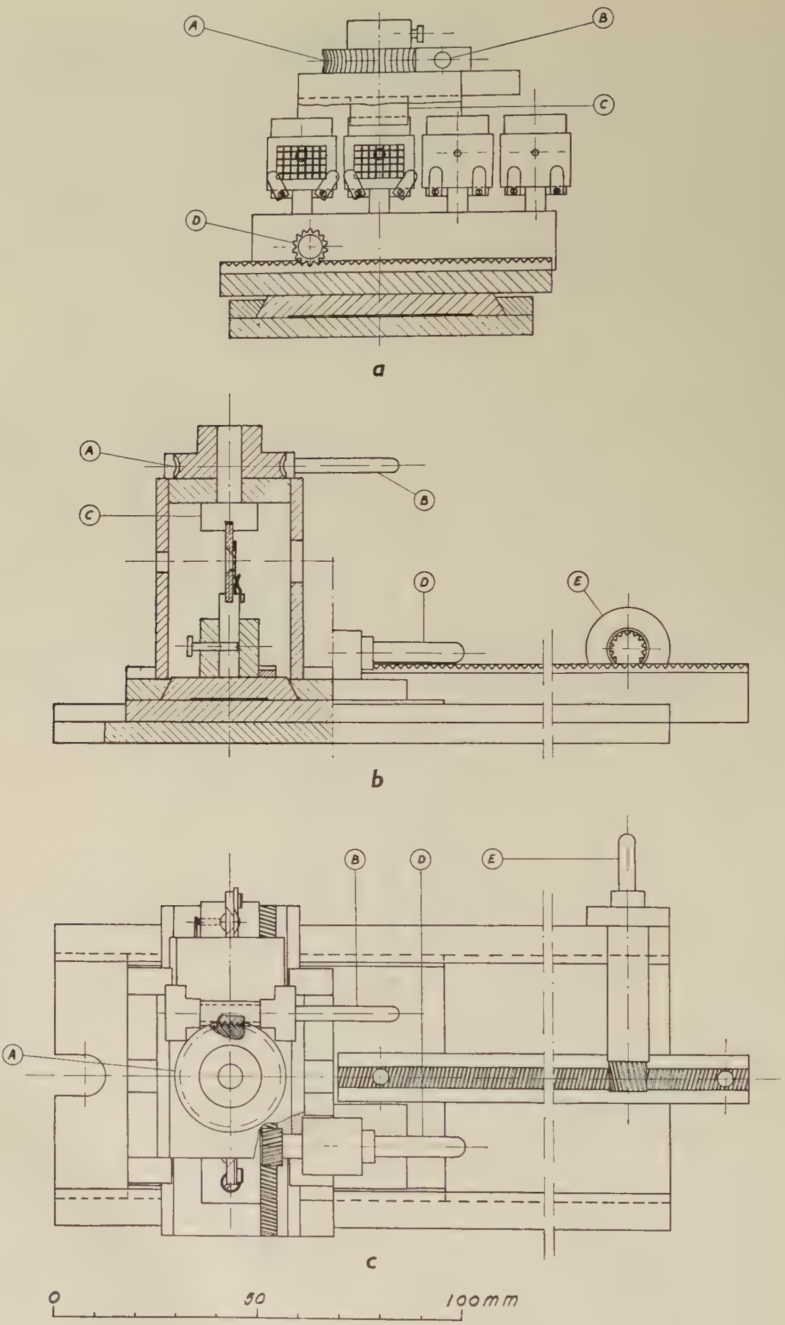

Fig. 7. The foil-holder: *a*, front view; *b*, side view; *c*, from above.

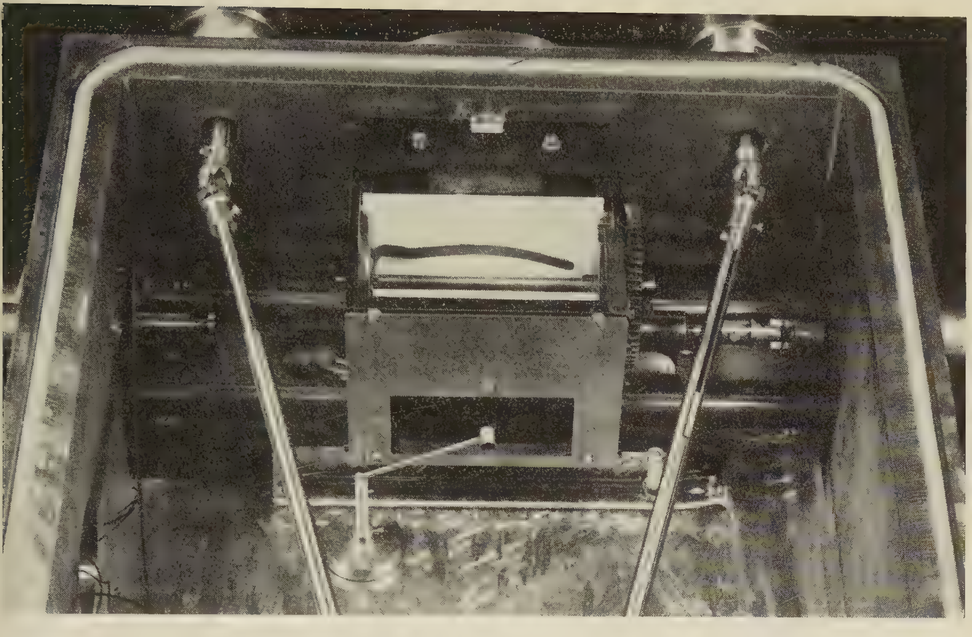

Fig. 8. The plate-holder mounted in the apparatus.

e. The plate-holder

Photographic plates were used to examine the foils as regards the degree of preferred orientation of the crystallites. For this purpose the apparatus is provided with a plate-holder, which can replace the Geiger counters. Fig. 8 is a photograph of the plate-holder mounted in the apparatus. It can hold four plates of the size 4.1 × 8.2 cm. When the plate-holder is placed in position, the Geiger counters and the micrometer screw of the left counter are removed. The control S' (Fig. 3) is connected to the plate-holder, and by means of it the plates can be brought into the exposure position.

§ 2. The Geiger counters

a. Construction

It has been necessary to make the dimensions of the counters comparatively small. The counters are to be seen in Fig. 9. Each was made from a square brass bar 40 × 20 × 20 mm, bored through with a hole 18.5 mm in diameter. The anode is a molybdenum wire 0.12 mm in diameter. It runs through the narrow channel of the metal rod A (Fig. 9b), which is melted into the glass body B of a commercial glass-metal seal. The wire is soldered to the outer end of the metal rod. The metal flange C of the seal is soldered to the end-plate D. Each end-plate is fastened to the body by means of four screws, and the edge vacuum-sealed with Glyptal lacquer, dried at 100° C. In the centre of the front of the counter is a hole 0.5 mm in diameter (G,

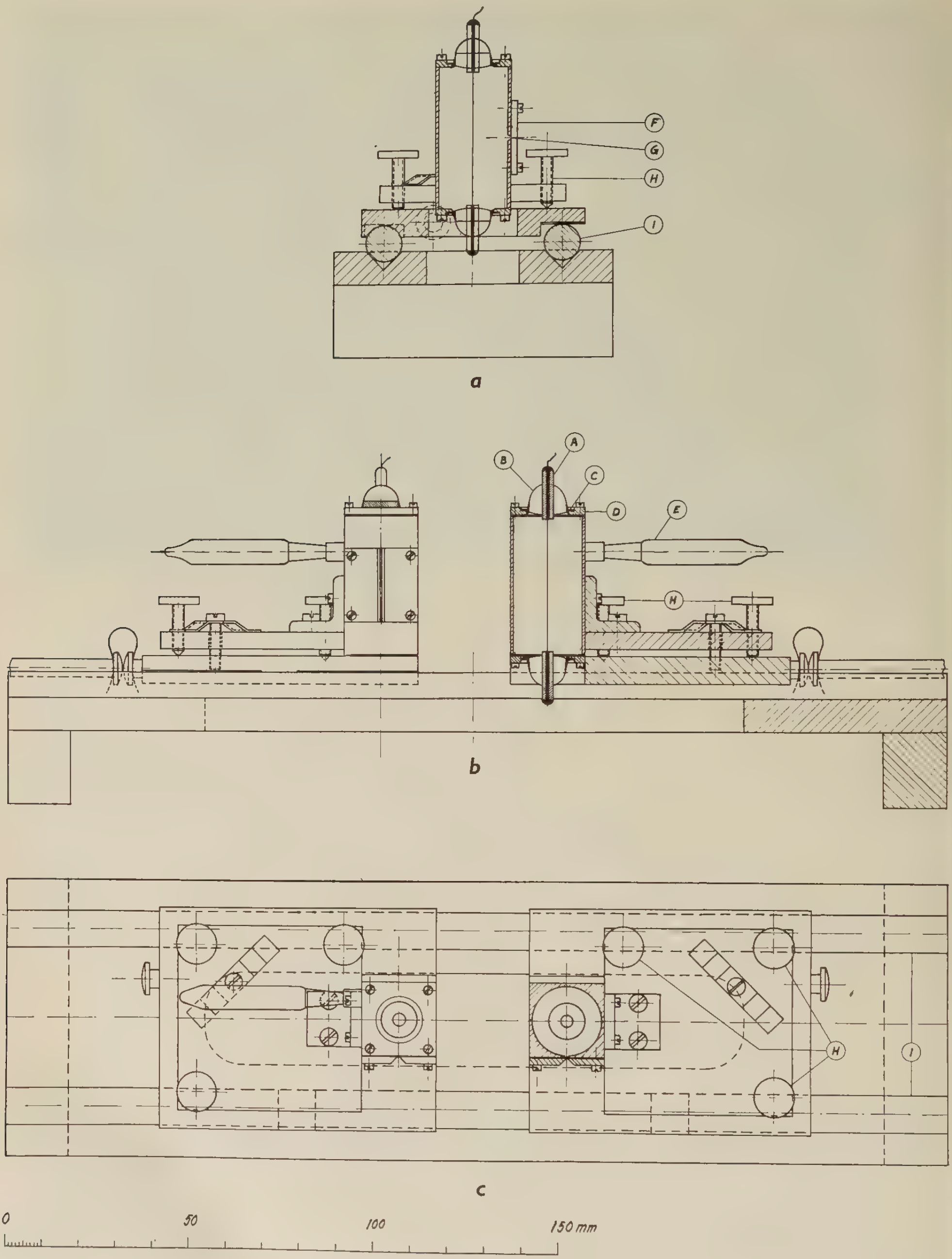

Fig. 9. The Geiger counters mounted on the slides: *a*, side view; *b*, front view; *c*, from above.

Fig. 9a). The hole is bevelled from the inside. This tiny counter window is partly covered with a Zapon film, 0.25 μ thick. To reinforce this film and reduce the diffusion through it, it is first stuck over a 0.5 × 0.2 mm slit in a piece of cellulose tape, this tape then being stuck over the window hole. The tape makes a vacuum-tight seal. This window permits the passage of electrons with energies down to 5 keV and less. For 30 keV electrons the transmission is about 100% [cf. LANE and ZAFFARANO, 1954]. The window also tolerates atmospheric pressure. The counters can thus be filled outside the apparatus, if desired.

From the details mentioned above it is clear that the maximum height of the counter slit is no more than 0.5 mm. This is necessary, as the arcs of all the rings ought to be practically straight in comparison with the slit. With a slit height of 0.5 mm this condition is well fulfilled, as the diameter of the smallest diffraction ring investigated was about 17 mm.

As can be seen from Fig. 9, the jaws of the slit, F, are attached directly to the body of the counter by means of four screws. During the measurements the recording counter had a slit-width of 0.04 mm, and the reference counter one of about 0.12 mm. In other respects the counters are identical and interchangeable.

b. Filling

The Geiger counters were filled through the copper-glass tube E (Fig. 9b), usually with 15 mm ethyl alcohol and 85 mm argon. The plateau was then at about 300 V, with a very slight slope. The dead-times of the two counters were somewhat different, despite the exactly similar construction. For the recording counter the dead-time was $0.25 \cdot 10^{-3}$ sec., and for the monitor counter $0.35 \cdot 10^{-3}$ sec. The background was the same for both counters, 16 impulses/min.

As already mentioned, the windows were not too thin for the counters to be filled outside the apparatus and sealed off in the usual manner. However, the lifetime of the counters was quite short (3 to 4 weeks)—mainly on account of diffusion. It was therefore advantageous to fill the counters inside the apparatus. For this purpose the counters have a common connection to a filling apparatus, which is visible to the left in Fig. 5. The vacuum connection passes through the evaporation chamber V in Fig. 3. The connection is joined to the Geiger counters by glass tubes, which have flexible joints of latex rubber in two places, to allow for the movement of the counters. A connection from the filling apparatus to the fore-vacuum pump of the diffraction apparatus enabled the Geiger counters and the diffraction apparatus to be evacuated simultaneously.

Besides enabling the counters to be rapidly refilled, the arrangement described above has the advantage that the filling gas is the same for both the recording counter and the monitor. Thus the variation of the two counters is parallel—assuming the variation to be entirely due to the gas.

c. Mounting

The Geiger counters are mounted on two slides, the construction of which is shown in Fig. 9. The vertical position and height of each counter is adjustable by the screws H. The scattered electrons are not in general normally incident on the window of the counter. In order to minimise the deviation, the recording counter is mounted at right angles to the direction of the middle ring among those investigated (ring (311)). The maximum deviation from normal incidence was thus not greater than 2°.

The slides move on two horizontal rods (I, Figs. 9a and c) of phosphor-bronze. The movement is controlled by two micrometer screws, one of which, O, is visible in the section on the right of Fig. 3. Each screw has a graduation of 50 mm (in 1/100 mm). The position can be read off through a window U, visible on the left of the figure. Each slide is connected to a rod K, which the spring G presses against the micrometer screw at a point M, where the contact surfaces are made of hard metal. L indicates evacuation channels. The sleeve of the micrometer is fixed to the wall of the apparatus by the tube N. The projection P from the screw follows the slot in the concentric cylinder R, which is fixed to the end of the shaft from the external control knob S. In order to avoid any play between the slide and the micrometer screw, the latter was always moved *against* the spring G when measurements were being made.

The micrometer screws were of steel, and were the only parts of the apparatus that might possibly give rise to disturbing magnetic fields. It is for that reason that they were placed so far away from the Geiger counters.

d. The electrical equipment

The voltage for the Geiger counters was taken from two stabilised high-voltage units of the type described by EVANS [1934]. They give a very well stabilised voltage in the range 600–2000 V.

The quenching circuits were of the Neher-Pickering type [NEHER and PICKERING, 1938]. A scale-of-64 unit coupled to a Cenco high-impedance counter was used with the recording tube, while the impulses from the monitor tube were counted by a scale-of-128 unit and a telephone counter. Both scalers were built in accordance with a circuit described by AMBROSEN, NIELSEN and SIGURGEIRSSON [1942].

§ 3. The d.c. amplifier

For the photographic exposures the intensity was measured with the aid of a d.c. amplifier, constructed as shown in Fig. 10.[1] The amplifier has seven measuring ranges. The full deflection in the most sensitive range corresponds to 10^{-12} A. Two Faraday cylinders, both of 6 mm diameter, were connected to the amplifier. One of them ($D2$ in Fig. 3) was used to measure the primary intensity immediately before and after exposure of a plate, while the other, which may be seen in front of the plate-holder in Fig. 8, was used to check the intensity during exposure of the plate—the cylinder being used to collect the central beam.

The latter Faraday cylinder could also be utilised in adjusting the foils into the desired diffraction position. In this way it was easy to expose plates for three different foils without admitting light or air into the apparatus. In this case the fourth plate was used to receive the diffracted beam during the adjustment of the various foils.

The first Faraday cylinder ($D2$) is provided with a screen against secondary

---

[1] The d.c. amplifier was designed by Fil. lic. C. REUTERSWÄRD, and I should like to express my gratitude to him for making this excellent instrument available to me.

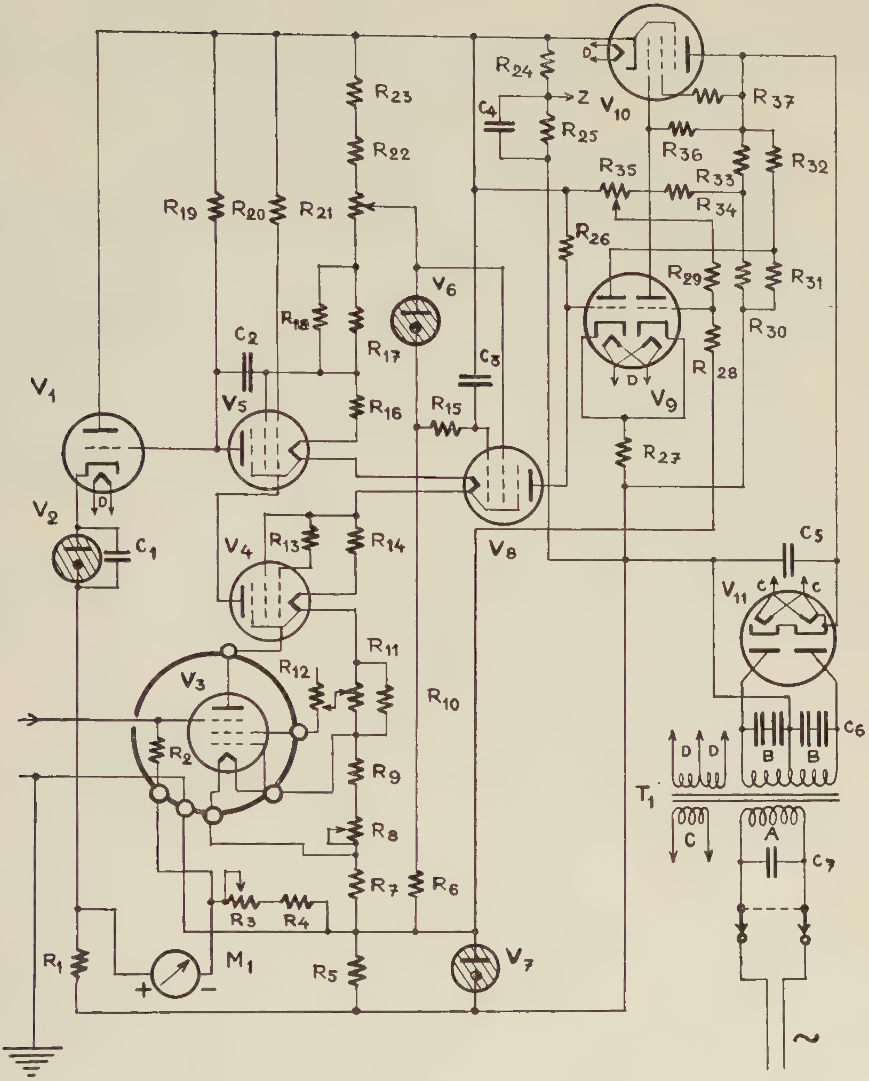

Fig. 10. The d.c. amplifier.

*V*1 —6SN7-GT (RCA)
*V*2 —LS 75/5 (Luma)
*V*3 —959 (RCA)
*V*4 —1S5 (RCA)
*V*5 —1S5 (RCA)
*V*6 —85A-1 (Philips)
*V*7 —VR-75 (RCA)
*V*8 —1S5 (RCA)
*V*9 —6SL7-GT (RCA)
*V*10—6Y6-G (RCA)
*V*11—83V (RCA)
*C*1 —10000 pF
*C*2 —10000 pF
*C*3 —0.1 μF
*C*4 —30000 pF

*C*5 —30 μF
*C*6 —20000 pF (×4)
*C*7 —10000 pF
*R*1 —15 kΩ
*R*2 —100 kMΩ
*R*3 —9900 Ω
*R*4 —100 Ω
*R*5 —3 kΩ
*R*6 —5 kΩ
*R*7 —55 Ω
*R*8 —8×10 Ω
*R*9 —75 Ω
*R*10—100 Ω
*R*11—10 kΩ
*R*12—50 kΩ

*R*13—500 kΩ
*R*14—400 Ω
*R*15—50 kΩ
*R*16—500 Ω
*R*17—1500 Ω
*R*18—5 kΩ
*R*19—3 MΩ
*R*20—5 MΩ
*R*21—10×10 Ω
*R*22—1000 Ω
*R*23—200 Ω
*R*24—30 kΩ
*R*25—50 kΩ
*R*26—500 kΩ
*R*27—200 Ω

*R*28—2 MΩ
*R*29—5 MΩ
*R*30—150 kΩ
*R*31—200 kΩ
*R*32—100 kΩ
*R*33—100 kΩ
*R*34—2 MΩ
*R*35—100 kΩ
*R*36—500 kΩ
*R*37—100 Ω
*M*1—0–1 mA
T1—NT-551 (Sundberg)
A : 220 V
B : 2×350 V 60 mA
C : 5 V 2 A
D : 2×3.15 V 3 A

radiation. When the screen voltage was varied from 0 to about –40 V the recorded intensity rose by almost 15 %, but varying the voltage beyond –40 V had no further effect.

§ 4. Pumps and vacuum gauges

The apparatus was evacuated by three pumps in series—two oil diffusion pumps and a mechanical pump. The high-vacuum pump was a two-stage diffusion pump generating a final vacuum of *c.* 10^{-6} mm Hg.

The both diffusion pumps could be shut off by valves, which enabled them to be kept continually under vacuum. Before opening these valves the apparatus was evacuated to about 10^{-2} mm Hg through a direct connection to the mechanical pump.

The tube between the apparatus and the high-vacuum pump was short and wide to ensure a high rate of pumping. To avoid contamination of the foils it was necessary to prevent flowback of oil vapour into the apparatus. A large metal cooling trap situated on top of the high-vacuum pump and filled with liquid air accomplished this. The previously mentioned direct connection from the apparatus to the mechanical pump was water-cooled.

The rubber rings used to seal the apparatus were another possible source of foil contamination. Certain types of ring (especially a black type and a light-red) were found to have an appreciable effect on copper and silver foils in particular. Such contamination disappears completely if the rings are made of latex rubber, cleaned in warm potassium hydroxide solution [cf. YARWOOD 1946].

As a rule it took about 45 minutes to reach a pressure of 10^{-5} mm Hg from atmospheric pressure. The vacuum was usually about $5 \cdot 10^{-6}$ mm Hg during measurements.

The vacuum was measured by a Pirani gauge (for pressures down to 10^{-3} mm) and an ionisation gauge, type *Standard* 3S31. The manometer circuit was of the type described by VON FRIESEN [1940].

§ 5. The high-voltage unit

Fig. 11 is a diagram of the high-voltage circuit and the stabiliser circuit. The latter follows a circuit given by VON FRIESEN [1935, 1948]. The output from a high-voltage transformer is first full-wave rectified and then smoothed by a resistance-capacity filter which includes two 1 μF condensers. The positive side of the d.c. output from the filter is connected to earth via the valve V (Marconi MT-4). Rapid fluctuations of the high voltage are compensated by means of the grid condenser $C3$. In order to maintain the desired potential across $C3$ an arrangement with two photocells is used, which respond to the beam from a mirror galvanometer. The galvanometer measures the current in a potentiometer circuit that is used to compare the output voltage with the voltage of a Nife cell, $E4$. The exact e.m.f. of this cell was measured by comparison with a certified Weston cell. The resistance $R7$ was about 20 MΩ, and consisted of a Kanthal wire-wound resistor of 10 MΩ [see VON FRIESEN, 1948] in series with an approximately equal resistor of chrome-nickel wire immersed in transformer oil. The resistor $R8$, which was used to regulate the voltage to the desired constant value, was provided by a Wolff precision resistance box. $R7$ was determined on several occasions with a high-precision Wheatstone bridge

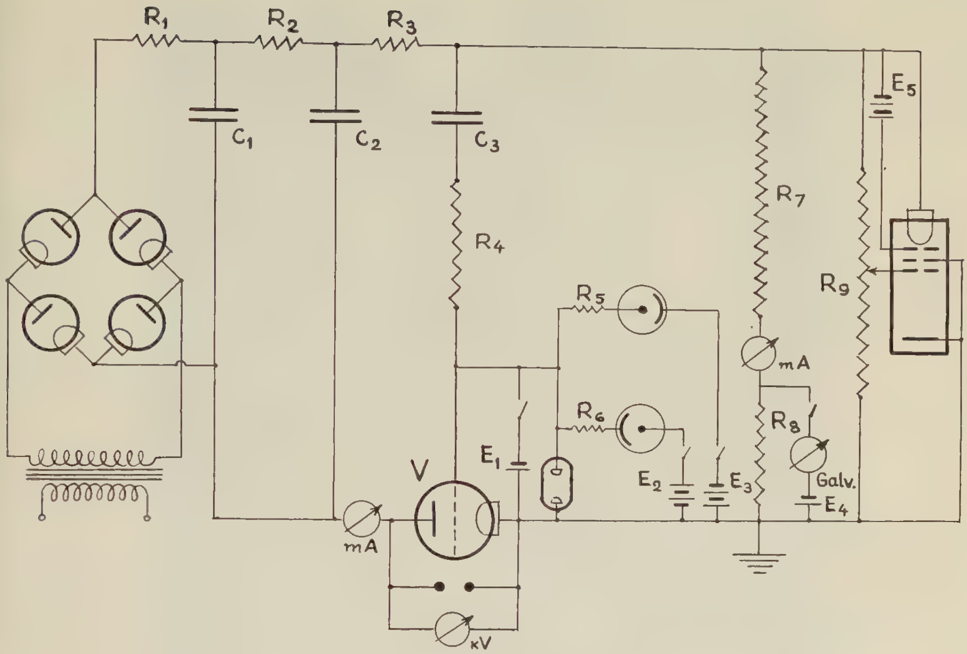

Fig. 11. The high voltage circuit.

V – MT4 (Marconi)
*C*1 – 1 μF (40 kV)
*C*2 – 1 μF (40 kV)
*C*3 – 0.1 μF
*R*1 – 50 kΩ
*R*2 – 40 kΩ
*R*3 – 50 kΩ
*R*4 – 1 MΩ
*R*5 – 1 MΩ
*R*6 – 1 MΩ
*R*7 – 20 MΩ
*R*8 – 0–2000 Ω
*R*9 – 100 MΩ
*E*1 – 4.5 V
*E*2 – 90 V
*E*3 – 90 V
*E*4 – Nife cell
*E*5 – 100 V

by Wolff, the resistance being divided up into several parts for this purpose. *R*8 was also measured with the same bridge. The accuracy with which the accelerating voltage could be determined was about ± 0.05 %.

The stabilisation circuit was very reliable. Even when the recording time was more than 4 hours the light spot from the galvanometer remained practically immovable in the zero position between the two photocells. It was impossible, however, to prevent a certain rise in the temperature of the potentiometer resistors and the Nife cell over a period as long as 4 hours, though this leads to but an insignificant change of the voltage. The temperature rise was seldom more than 1°. With temperature coefficients of $6\cdot 10^{-5}$ deg.$^{-1}$ for *R*7, $2\cdot 10^{-5}$ deg.$^{-1}$ for *R*8, and $-2\cdot 10^{-4}$ deg.$^{-1}$ for the Nife cell, a temperature rise of 1° implies a voltage change of less than 0.02 %. A voltage change manifests itself mainly as a change in the diameter of the diffraction rings. For such a change of diameter to be detectable, the corresponding voltage change must be *c.* 0.2 %, for which the outer rings would shift 0.02 mm.

§ 6. The recording procedure

Prior to each run the functioning of the Geiger counters was checked by determining their plateaus. The foil was then adjusted into the diffraction position. This was done visually, by means of the fluorescent screen placed at the window of the apparatus.

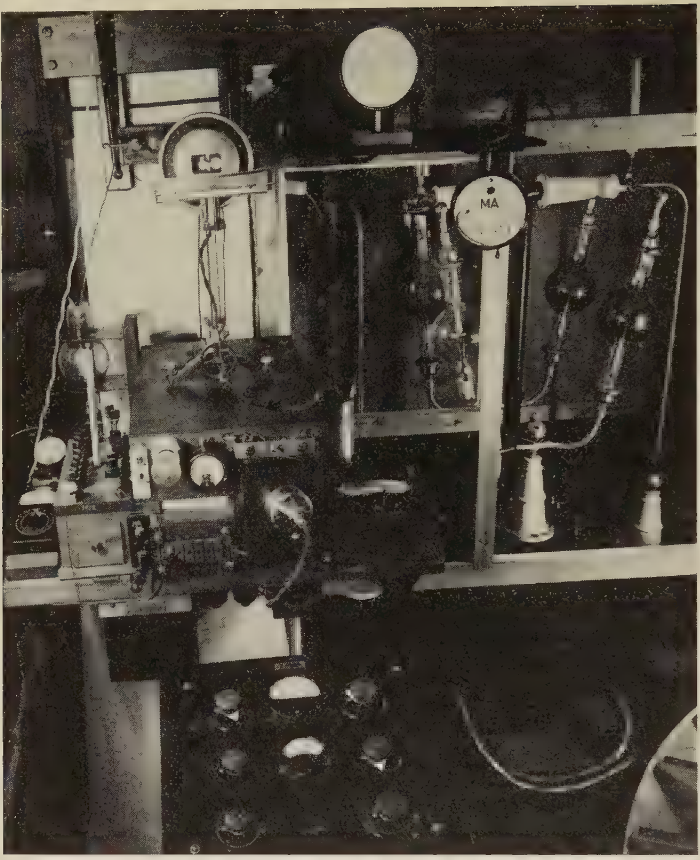

Fig. 12. View of the high voltage source. To the left the smoothing circuit arrangements with the stabilising valve.

The monitor counter was adjusted to a suitable position in the diffraction pattern each time a new foil was set up. This position was generally chosen so that the counting rates of the two Geiger counters were about the same when the recording counter was situated at the peak of the ring (220), the position adopted for the monitor counter also being on a relatively flat part of the intensity curve.

As a rule, the number of impulses counted by the monitor counter for each point was 30 × 128, and the duration of the counting of each point about 45 sec. In order to avoid unnecessarily high counting rates for the highest intensities, the recording time for such points was extended by lowering the primary intensity. Furthermore, in recording the highest parts of the peaks the accuracy was increased by raising the monitor count to 60 × 128 impulses. The same applies to certain points of special significance for the background curve.

In general, the intensity curve for each foil was plotted from the (111) ring to the (511) ring (inclusive). But where there was a poor contrast between rings and background only six rings were included.

CHAPTER III

Comparison with the photographic method

§ 1. The recording time

It has already been pointed out that the time required for recording an intensity curve (for 8 rings) with Geiger counters was 4 hours, whereas the exposure of a photographic plate took only a few seconds. With the photographic method, however, the final intensity curve is achieved only after further time-consuming operations—microphotometer measurements, construction of blackening curves, and so on. The method with Geiger counters has thus proved to be much more rapid than the photographic method.

§ 2. Accuracy of the results

In the photographic method, a point on the intensity curve is the final result of several measurements of varying accuracy. With the method employing Geiger counters, a point on the intensity curve can be determined by a single measurement, the accuracy of which depends to a large extent on the number of impulses counted. If one wishes to investigate a particular section of the intensity curve more precisely, the accuracy of the measurements can be raised at will—a possibility not available with the photographic method.

It may be seen from the results set out in Chap. VII that the maximum error in measuring the height of peaks in the intensity curve is on an average between ± 2 and $\pm 3\,\%$—an accuracy which is, according to our experience, more than twice as good as the accuracy obtainable with the photographic method. The maximum error of the area determinations is somewhat higher, about $\pm 4\,\%$, chiefly on account of possible errors introduced when drawing the background curve, and of the difficulty in achieving a correct separation of superimposed peaks.

§ 3. Bombardment of the foil

During measurements with Geiger counters the foil is bombarded for a relatively long period. There is a certain risk that this long bombardment may produce changes in the foil while the measurements are in progress. The occurrence of such changes has been investigated by TOL [1940, pp. 58 ff.] and SJENITZER [1948, pp. 87 ff.], among others. This risk has also been adduced as an argument against direct methods of measurement.

In order to reduce the bombardment time during recordings with the Geiger counters, the switch to the deflecting coil (*D*1, Fig. 3) was placed close to the switch common to the two counters. It was thus possible to deflect the electron beam from the foil immediately after the recording of a point. In this way the foil was under bombardment only while the counters were in operation.

The use of electron-optical focusing is even with respect to bombardment risks much to be preferred to the direct limitation of the beam by means of apertures, as done by Tol and Sjenitzer. In their apparatus the area bombarded was about 0.01 mm². In the present apparatus the area of foil bombarded was in the form of a square 0.4 × 0.4 mm.

Moreover, the incident intensity for recordings with Geiger counters is much lower than for photographic exposures. For exposures with Gevaert Diapositive Contrast plates the beam current was *c.* 2×10^{-10} A for a 30 sec. exposure. For recordings with Geiger counters the beam current was as a rule about 6×10^{-12} A.

Tol took a series of 15 photographic exposures for each of his intensity measurements. The bombardment to which the foil was subjected for such a series can be estimated as about 10^{-5} amp. sec./mm². For the determination of one point with the present apparatus the bombardment of the foil was *c.* 2×10^{-9} amp. sec./mm². So one of Tol's photographic series corresponds to about 5000 points with the Geiger counter apparatus, that is to say, to many more points than were normally recorded with a single foil. Thus the bombardment of the foil during intensity measurements with the Geiger counters was considerably less than that necessary for the photographic determinations mentioned above. In no case was any change in the foil on account of the electron bombardment observed.

Chapter IV

Preparation of the metal foils

§ 1. Method for reducing the degree of preferred crystal orientation in the evaporated films

As already mentioned in Chap. I (§ 3), the main consideration in the preparation of the metal foils was the avoidance of preferred orientation of the microcrystals.

The three principal methods of preparation that have been used to produce thin metal films for diffraction purposes are: (1) rolling or beating, followed by etching with some acid to reduce the thickness, (2) cathode sputtering, and (3) evaporation. Sputtering and evaporation are on to a substrate, which is usually dissolved afterwards.

Method (1) generally produces a pronounced preferred orientation of the microcrystals; it is therefore out of the question here.

Cathode sputtering takes place in the presence of a gas—usually nitrogen—which probably leads to an undesirable occlusion of gas. Furthermore, it has been found difficult to prepare self-supporting sputtered films of about 100 Å thickness.

Evaporation in a high vacuum, on the other hand, is a convenient method that produces very even and pure films. All the foils used in the present investigation were prepared by evaporation.

However, if no precautions are taken, the evaporated film usually evidences a marked degree of preferred orientation. This is probably due principally to a rise in the temperature of the substrate and film owing to heat radiation from the evaporation heater. In order to prevent this as far as possible one may (1) screen off all superfluous heat radiation from the evaporation heater, (2) make the distance between the evaporation heater and the substrate large, and (3) cool the substrate during the process of evaporation.

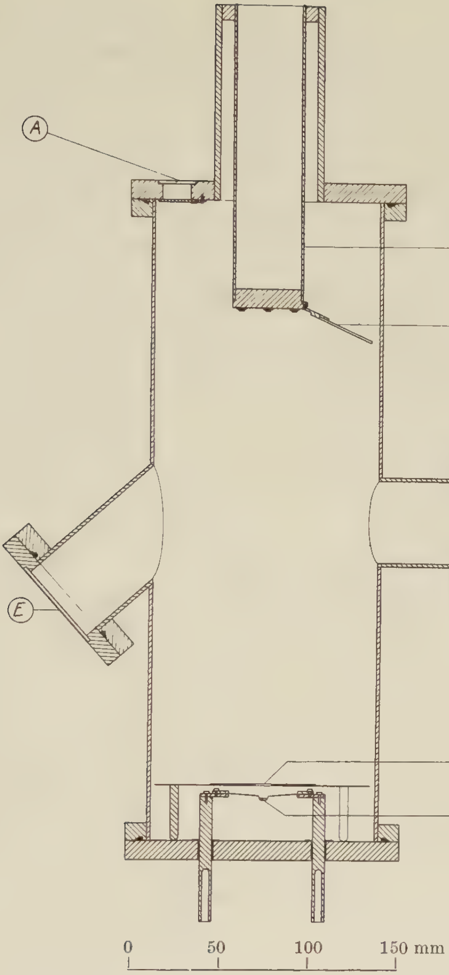

Fig. 13. The evaporation apparatus.

The construction of the apparatus used for evaporation is illustrated in Fig. 13. The evaporation heater was in most cases a piece of tungsten strip 6 mm wide and 0.04 mm thick, with a depression (*G*) in the middle, in which the metal to be evaporated was placed. The tungsten strip was fastened to two insulated steel holders. Each strip was cleaned before using for evaporation by heating with a current of about 50 A. The maximum evaporation current was 45 A (for Au).

F is a steel screen against heat radiation from the tungsten strip, with an aperture opposite the depression containing the metal under evaporation.

Four pieces of 0.35 mm tungsten wire twisted together were also used as a heater for the evaporation of Al. In that case only the outer parts of the wires were screened. The temperature of this heater was not particularly high, as the relatively low evaporation temperature of Al and its good contact with the tungsten surface made this unnecessary.

The substrate is situated above the evaporation heater, on the bottom of the metal cooler *B*. The distance between the substrate and the heater was usually 28.5 cm. *C* is a mirror by means of which the evaporated film and the evaporation heater could be observed through the window *E*. Only the heater can be seen through the smaller window *A*.

The vacuum is sealed by rubber rings. A two-stage mercury diffusion pump is connected to the apparatus at *D*. A large metal cooling-trap filled with liquid air prevents mercury vapour from the pump from entering the evaporation apparatus. The vacuum immediately prior to evaporation was about 10^{-6} mm Hg.

Various types of substrate were tried: polished crystals of rocksalt and alum, and thin membranes of Zapon lacquer and collodion. No distinction could be made between these different substrates as regards the degree of preferred orientation in the foils. It proved to be difficult to prepare very thin ($\ll 200$ Å) self-supporting metallic films when crystal substrates were used, and the substrate most used was Zapon lacquer. These membranes were easier to handle than the other substrates.

The crystals of rocksalt and alum were made into plates 2 mm thick to obtain so efficient cooling as possible. These plates were pressed against the bottom of the cooling-trap, *B*, by small springs. The substrates of Zapon lacquer were placed on a polished copper plate (20 × 15 × 1.5 mm). Three such plates could be attached to the bottom of the cooling-trap simultaneously. Liquid air was used as cooling fluid, and cooling commenced as a rule 10 to 15 min. before evaporation.

In order to reduce the risk of contamination of the foils during the process of evaporation, as well as the risk of heating, the evaporation process was of short duration, *c*. 5–10 sec.

The metals used were of the highest degree of purity, delivered with certificate from Johnson, Matthey & Co. Ltd., London.

After evaporation the substrates and foils were allowed to warm up slowly (for about 1 hr.) *under vacuum* to room temperature. The substrate was then dissolved. Zapon lacquer was dissolved in acetone (see § 2). Rocksalt and alum were placed just above the surface of distilled water in a bowl, at an angle of about 30° with the surface. As the water surface was slowly raised the metal foil was lifted from the crystal and floated on the water, where it could be taken up on a supporter.

The above method of preparation gave satisfactory results with Au and Ag. But the Al foils so prepared all had an appreciable degree of preferred orientation.

It has already been mentioned that the main causes for the reduction of the degree of preferred orientation of the microcrystals in the foils prepared by the above method is the screening of heat radiation from the evaporation heater and the cooling of the substrate. The reduction of the temperature thus achieved diminishes the motion of the atoms on arrival at the substrate, which tends to make the microcrystals small, thereby increasing the likelihood of random orientation. However, it is probable that some recrystallisation occurs as the temperature rises to that of the room, leading to an increase in the degree of preferred orientation. It was observed that the effect of this temperature rise was smallest when the foils remained in vacuo. It is not clear why this should be so, but the observation accords with that of PRESTON and BIRCUMSHAW [1936], who found that while a Au foil will recrystallise at about 450° when heated in air, it will not do so in hydrogen or in vacuo up to 700°. They were unable to detect any signs of oxidation, and neither were there any rings that could be attributed to a foreign structure. Much the same experience is reported by FINCH and FORDHAM [1937], who found that evaporated foils of pure gold did not undergo recrystallisation when they were heated in a vacuum to 550° (at which temperature they collapsed).

The reason that the Al foils cannot be prepared free of preferred orientation to the same extent as the Au and Ag foils is most probably connected with Al's greater tendency to form large microcrystals. That the crystals of the Al foils were considerably larger than those of Au and Ag foils, can be seen in Tables 19–21 (p. 606). An investigation carried out by LEVINSTEIN [1949] is of interest in this connection: he found that the tendency of metals to form large microcrystals on evaporation varies in inverse proportion to their melting-points.

The significance of microcrystal size for the degree of preferred orientation is evidenced by the fact that all the foils with a *high* degree of orientation that were examined were found to consist of exceptionally large microcrystals. Such foils produce very sharp rings against a weak background.

As regards the investigation of the degree of preferred orientation among the microcrystals of a foil, see Chap. V.

§ 2. Method of preparing very thin self-supporting foils

In the preceding paragraph it was stated that the purest and most even foils for diffraction purposes are obtained by evaporation. The best substrates in several respects have been found to be those made from some cellulose substance. TOL [1940] and SJENITZER [1948], however, considered it impossible to produce self-supporting foils thinner than 200 Å even using this kind of substrate. They found that thinner foils are dissolved together with the substrate when immersed in amyl acetate or acetone. We have found that this is the case only when the cellulose membranes are comparatively thick and unsupported. The method adopted for the preparation of very thin self-supporting films was the following.

A drop of Zapon lacquer is allowed to spread out on a dust-free shielded water-surface. The Zapon lacquer should be of such dilution that after the solvent has evaporated a membrane 0.2 μ is formed. This film is taken up on a polished copper plate (cf. the preceding paragraph), where it is allowed to dry. When the metal film has been formed by evaporation, the copper plate is placed on a small stand, which is slowly lowered into a bowl containing acetone. The metal film then remains intact when the membrane of Zapon lacquer dissolves, and it is thereby freed from the copper plate. Care must be taken to see that the membrane of Zapon laquer initially covers the *entire* copper plate, for otherwise it may be difficult to get the foil completely free of the plate. Even if only a very small part of the foil is attached to the plate there is a great risk that the whole foil will be spoilt.

When the film is free from substrate and plate it can be made to float free by causing very slight currents in the solvent. The foil will then remain suspended in the liquid. Au foils of a mean thickness of only 20–30 Å was successfully prepared in this way. But it was not possible to take up such thin foils out of suspension and dry them. They always disintegrated.

The foils were taken up from the acetone bath on a net of brass wire, set in a frame of solder. The net was first rolled and polished until the surface was completely flat. For very thin foils the net used had holes 1.3 × 1.3 mm. A coarser mesh (holes 1.8 × 1.8 mm) was used for foils that were somewhat thicker, as well as frames with a single circular opening 2 mm in diameter (see Fig. 7a).

The acetone solvent dries very rapidly, and it was at this stage that the weaker foils collapsed. If a foil withstood the drying process it was found to be relatively durable. The stability of the film during drying depends to a great extent on the purity of the Zapon lacquer membrane used as substrate during the evaporation process. Even the smallest speck or impurity in the membrane can weaken the film.

The drying process is slower if amyl acetate is used instead of acetone. But it was not observed that the use of amyl acetate led to more stable films. It was found, however, that with this solvent it was more difficult to dislodge the foil from the copper plate, so acetone was used in general.

As already mentioned, the method described above enabled foils some few tens of Å thick to be obtained in suspension in the solvent. The least mean thickness successfully removed from the solvent and dried was 75 Å.

§ 3. Determination of the foil thickness

A calibration of the evaporation apparatus was performed in order to determine the thickness of the foils [cf. GERMER, 1939]. For this purpose it was assumed that the thickness Δ is inversely proportional to the square of the distance from the evaporation heater, i.e. that

$$\Delta = k \cdot \frac{M}{L^2 \cdot \varrho} \tag{11}$$

where k = an apparatus constant
M = the weight of metal evaporated
L = the distance between the substrate and the evaporation source
ϱ = the density of the metal.

The calibration was thus a question of the constant k, which may also be written

$$k = \frac{m L^2}{M A} \tag{12}$$

where m is the weight of metal deposited on the surface A. M and L have the same significance as in eq. (11).

The experimental determination of k was carried out for different values of M and L, as recorded in Table 3. The metals evaporated were Au and Ag. The evaporation heater was the tungsten strip with a central depression described in § 1. The vacuum immediately prior to evaporation was better than 5 × 10^{-6} mm Hg.

Table 3

M, gram	L, cm	A, cm²	m, gram	$k = \frac{m L^2}{M A}$
$233.1 \cdot 10^{-3}$	18.1	9.05	$2.40 \cdot 10^{-3}$	0.373
221.0	20.0	9.05	1.95	0.390
335.0	22.0	9.05	2.50	0.399
358.2	24.0	9.05	2.25	0.400
304.9	28.4	9.05	1.35	0.395
				Mean: 0.391

The weight evaporated each time was *c.* 115 mg, the above values of M being achieved by two or three repetitions of the process. This was done so that evaporation should occur under conditions resembling those of the actual foil preparations, where only small amounts of metal were used.

The value obtained from Table 3 is

$$k = 0.39 \pm 0.01.$$

With this margin of error for k, and with an uncertainty of 0.5 % in the determination of L and M, the accuracy attained in the estimation of the foil thickness by means of eq. (11) is ± 3 %.

A further check on the thickness of the foils was made by measuring the absorption of white light by means of a microphotometer. Foils of known thickness were used for calibration. In order to perform this check rapidly a glass plate was in most cases placed close beside the substrate when evaporation took place. The absorption measurement could then be carried out immediately the evaporation apparatus was opened. By way of example it can be mentioned that the absorption was 57.5 % for a Ag foil of a mean thickness of 75 Å. The results of the two methods agreed in general very well.

When Al was evaporated from a heater made of tungsten wire, eq. (11) could not be applied, and the sole determinations were then from absorption measurements.

CHAPTER V

Investigation of the metal foils for preferred crystal orientation

In examining the foils for the degree of preferred crystal orientation the method used was the usual photographic one, with the foil inclined at a certain angle to the electron beam [cf. KIRCHNER, 1932]. If the orientation of the microcrystals is entirely random there will be an even intensity distribution along all the diffraction rings. Whereas if there is some preferred orientation of the microcrystals, it will manifest itself as an intensification of the rings in certain directions. With a marked degree of preferred orientation there are no complete rings, but only a pattern of arcs. This enables both the degree and type of orientation to be determined. To perform such determinations accurately it was found to be necessary to make photometric measurements along different radii of the diffraction pattern on the photographic plate [cf. VON FRIESEN and LENNANDER, 1946].

The simplest and most usual type of preferred orientation is when the microcrystals tend to orient themselves with a particular lattice plane parallel to the plane of the foil. The directions in which the intensity is then highest may be calculated for a cubic lattice from the following formula:

$$\cos \Phi \cdot \sin \delta = \frac{hu + kv + lw}{\sqrt{h^2+k^2+l^2}\,\sqrt{u^2+v^2+w^2}} \tag{13}$$

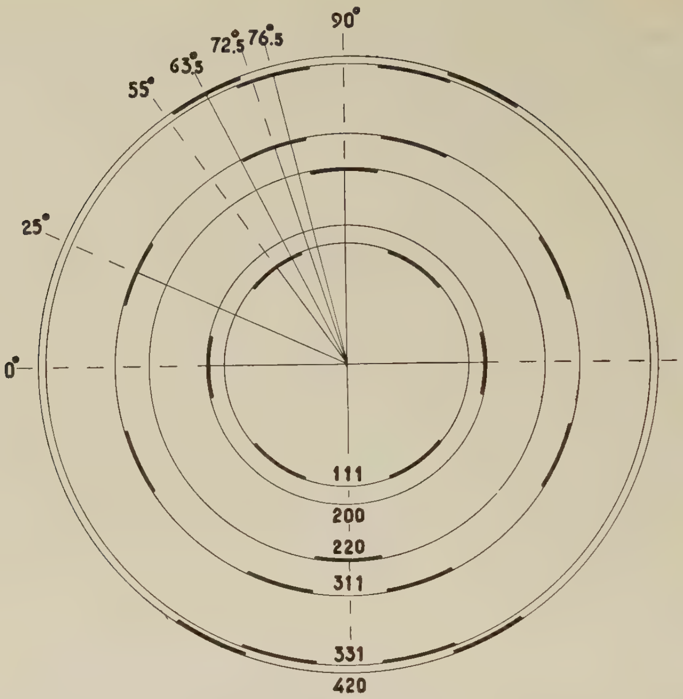

Fig. 14. Schematic diagram of a diffraction pattern from a foil where the microcrystals (cubic face-centred lattice) are oriented with the (111) plane parallel to the plane of the foil. The foil is inclined to the electron beam with $\delta = 35°$ (cf. eq. (13)). The axis of inclination is parallel to the 90° direction.

where h, k, l = the Miller indices for the ring in question
u, v, w correspond to the type of orientation, i.e. to the lattice plane that is parallel to the plane of the foil
Φ = the angle between the radius to the centroid of the intensified arc of the ring and the projection of the normal to the (u, v, w) plane
δ = the angle between the electron beam and the normal to the foil.

Fig. 14 is a diagrammatic representation of the intensity reinforcements for the inner six rings (cubic face-centred lattice) for the case where the microcrystals are oriented with the (111) plane parallel to the plane of the foil (referred to below as (111) orientation). Also, δ is taken to be 35°. The projection of the normal to the (111) plane is in the direction 0°. Suitable radii for photometric measurements on such a plate are in the directions 0°, 55°, and 90°. When the degree of preferred orientation is slight it is often difficult to detect all the regions of intensification. (111) orientation is most easily detected by comparing the intensity differences between the (200) and (220) rings in the directions 0° and 90°.

In the present investigation δ was first chosen as 35°, whereupon photometer measurements were made in the directions mentioned. If the result of this test gave any reason to suspect preferred orientation of some other type than (111) orientation, another plate was exposed with $\delta = 45°$. In this case photometer measurements were made in the directions 0°, 45°, and 90°. The foils were examined in this way both before and after the measurements with the Geiger counters. As a rule there was no detectable difference.

With Au foils prepared as described in Chap. IV, the most common type of preferred orientation was (111) orientation. (110) orientation occurred in about 20 % of the foils examined. The findings were much the same for the Ag foils, except that (110) orientation was somewhat more frequent—occurring in 30–40 % of the foils. (111) and (110) orientation were the only types of orientation detected in the Au and Ag foils. (111) orientation was the only type found in the Al foils.

The *degree* of preferred orientation often varied somewhat, even though the method of preparation was the same. However, the degree of preferred orientation in the Au and Ag foils was invariably very low when the foils were prepared by the method of Chap. IV. The foils with the lowest degree were chosen for intensity measurements. Absolute freedom from preferred orientation proved to be difficult to attain, and only two or three foils showed no detectable orientation. However, the tendency to preferred orientation in the other foils used was so slight that there was no appreciable effect on the relative intensities of the different rings. An illustration of this is that two foils gave approximately the same value of the atomic factor, even though only one of them had no detectable tendency to preferred orientation. By way of example it may be mentioned that in intensity measurements on Au (see Chap. VII) foil Au 5 (170 Å) exhibited a tendency to (111) orientation, and Au 7 (225 Å) to (110) orientation. But in the foil Au 6 (200 Å) it was not possible to detect any tendency to preferred orientation.

Chapter VI

The use of films with partial preferred orientation for determination of the atomic factor

§ 1. Determination of the degree of preferred orientation

As mentioned in Chap. IV, Al films could not be successfully prepared without a certain degree of preferred crystal orientation. Consequently, it was necessary to use partially oriented films for determination of the atomic factor in the case of Al. Before the final calculation of the atomic factor for Al the measured values of the relative intensity were first corrected with regard to the foil's degree of preferred orientation. The latter was determined by special measurements.

As the correction was applied solely to Al films with a partial (111) orientation, only this type of orientation and the face-centred cubic lattice are considered.

The method used to estimate the degree of preferred orientation was that mentioned in the previous chapter, where the foil is inclined to the electron beam at an acute angle—in the present case 55°. If all the microcrystals were oriented the pattern would consist entirely of arc fragments. In the films under consideration here, in which there were crystals with a definite orientation and crystals oriented at random, the diffraction pattern has complete rings, with the intensity enhanced in certain directions. The intensity in the sections of the rings that are *not* intensified must therefore correspond to the microcrystals that are oriented at random. The degree of preferred orientation may be determined by measuring the extra intensity in the regions where the intensity is higher, due to the combined effects of both the crystals with a definite orientation and those oriented at random.

The (220) ring was found to be suitable for such measurements. The intensity of this ring is not subject to superposition of other rings. Moreover, it is the (220) ring that manifests the greatest increase of intensity (among the inner rings) when the electron beam is normal to the foil. The result may be checked by similar measurements on the (200) ring. In one respect the latter ring is more advantageous than the (220) ring: when the foil is inclined to the electron beam the partial intensification of the (200) ring is double as great as that for the (220) ring. This may be seen from eq. (13): all the 6 (200) planes give $\Phi = 0°$ (180°) (when $\delta = 35°$), i.e. all these planes contribute to an intensification in this direction. For the (220) ring $\Phi = 90°$ for 6 of the 12 (220) planes, the others giving $|\cos\Phi| > 1$, i.e. only half the number of (220) planes contribute to the intensification.

For the measurements indicated above it is preferable to choose rings with as few arcs of intensification as possible, in order to obtain sections of the ring that are not affected by the arcs of intensification. There are only two such arcs in the (200) ring when $\delta = 35°$. The same applies to the (220) ring. But in this case conditions are even more favourable, since both the number and positions of the arcs of intensification are independent of δ within certain limits.

The absolute degree of preferred orientation, i.e. the percentage of microcrystals with a preferred orientation, cannot be obtained directly from such measurements of local intensification. However, as will be shown in the next paragraph, it is not necessary to know the absolute degree of orientation in order to apply the correction in question here.

§ 2. Correction when the electron beam is normal to the foil

It has already been mentioned that half the number of the (220) planes contribute to the partial intensification when the foil is inclined to the electron beam. It is easily shown that the same planes contribute to the intensification of the (220) ring even in the case of normal incidence. For, if we use the equation

$$\cos\Theta = \frac{hu + kv + lw}{\sqrt{h^2+k^2+l^2}\,\sqrt{u^2+v^2+w^2}} \tag{14}$$

for calculation of the angle Θ between the planes (h, k, l) and (u, v, w), we find that the (220) planes in question are at right angles to the (111) planes. These (220) planes are thus parallel to the incident electron beam in an *exactly* (111) oriented crystal. Actually, the glancing angle may be regarded as very small, and the planes as in a reflection position.[1]

In the case of normal incidence we desire to determine the intensity of the (220) ring that corresponds only to the random oriented crystals. The measured intensity has thus to be reduced. According to what has been said above the reduction percentage can be directly obtained by comparing the intensity of the (220) ring in an intensified section with that of another section not intensified, when the foil is in the inclined position.

---

[1] A similar assumption is implicit in eq. (13).

The above applies to the (220) planes. For other lattice planes in an *exactly* oriented crystal the least angle of inclination to the electron beam is often not equal to zero. (We will in the following denote this least angle by α.) However, since the crystals are spread around the exact position of orientation there may be an intensification of the ring even when $\alpha \neq 0$. The question is, how large α must be if there is to be no such intensification.

A limiting value of α has been estimated from measurements with a highly (111) oriented foil inclined to the electron beam ($\delta = 35^\circ$). The intensity of the (111) ring was measured in the direction 0° (hence not intensified, cf. Fig. 14) and compared with the intensity of the (220) ring in the direction 90°. After this the intensity of the (111) ring was measured and compared with that of the (220) ring when the foil was normal to the beam. The comparison gave in both cases the same result. This means that there was no detectable intensification of the (111) ring in the case of normal incidence (in spite of a strong intensification of the (220) ring).

As the angle α for the (111) planes is 19.5°, the intensification—in accordance with the above results—was taken to be negligible for the foils used in the main series of intensity measurements when $\alpha = 19.5^\circ$ or more.

The correction for the (220) ring has already been dealt with. Let us assume that it has been found to be a %. Then:

For *the (111) ring* $\alpha = 19.5^\circ$. According to what has been said above, the intensification $\simeq 0$, i.e. the entire intensity of the (111) ring is due to random oriented crystals. The correction to be applied is therefore 0 %.

For *the (200) ring* $\alpha = 35.3^\circ$, from which it follows that the correction is 0 %.

For *the (311) ring* $\alpha = 10^\circ$, and the glancing angle = 1.9° (at an accelerating voltage of 27 kV). Hence there may be a slight intensification. But only 6 of the 24 (311) planes contribute to this intensification, so that it cannot be more than half as great as that of the (220) ring. A precise estimate of the intensification requires complete information about the distribution of crystal orientation. The correction is here taken to be approximately $\frac{1}{2}\,a$ %.

For *the (331) ring* $\alpha = 7.6^\circ$, and the glancing angle = 2.3°. The number of planes contributing to the intensification is 12 out of 24. We assume that the intensification is the maximum possible in this case too, and take the correction to be a %.

For *the (420) ring* $\alpha = 15.0^\circ$, and the glancing angle 2.4°. Thus reflection occurs only for crystals at angles of 12.6° or 17.4° to the exact direction of orientation. Half the number of the (420) planes contribute to the intensification. The contribution from the 17.4° crystals is probably very small. A comparison of rings (331) and (420) has actually shown that the intensification of the latter is approximately half that of the former. The correction for the (420) ring has therefore been taken as approximately $\frac{1}{2}\,a$ %

For *the (422) ring* $\alpha = 0^\circ$. Six of the 24 (422) planes contribute to the intensification. The correction is therefore $\frac{1}{2}\,a$ %.

For *the (511) ring* $\alpha = 19.5^\circ$, so the correction may be taken to be 0 %.

Summarising these conclusions, we may say that for an Al foil with (111) orientation relatively reliable values of the necessary corrections may be obtained for rings (111), (200), (220), (422), and (511)—i.e. for five points on the atomic factor curve. Only approximate values of the corrections (probably somewhat too high) have been obtained for rings (311), (331), and (420). A more exact value of these latter corrections could be obtained from measurements with inclined foils. However, since an alteration of the size of the correction would have no more than an insignificant effect on the calculated value of the atomic factor, the approximate corrections may be regarded as satisfactory.

Once the correction for the (220) ring (a %) has been determined in the manner already described, the various corrections are as follows:

Intensity corrections

Ring	111	200	220	311	331	420	422	511 333
Correction in %	0	0	a	$\frac{1}{2}a$	a	$\frac{1}{2}a$	$\frac{1}{2}a$	0

CHAPTER VII

Intensity measurements and the determination of the atomic factor

§ 1. Measurements with Au

The intensity measurements for Au were carried out with seven foils, of thicknesses between 90 and 225 Å. They were all without substrates, and prepared by the method described in Chap. IV. The age of the foils varied between 2 and 40 days at the time of the first measurements. Between preparation and use they were kept under vacuum. The accelerating voltage was 30.0 kV. For one foil—Au 3 (110 Å)—the intensity curve was also recorded for an accelerating voltage of 18.0 kV.

The intensity curve was in general recorded four times for each foil. Fig. 15 shows one of the curves for Au 3 (110 Å) at an accelerating voltage of 30.0 kV, and Fig. 16 a curve for the same foil at 18.0 kV.

The scale of the figures used for the graphical part of the computations was 6 times as large as that of Fig. 15. The intensity curve and the background curve were first drawn, and after that superimposed peaks separated. It was very difficult to achieve a correct separation of certain pairs of peaks—(331) and (420), for instance, and (111) and (200) as well. In the latter case the separation is of considerable importance for the subsequent calculation of the atomic factor. The method used to separate the (111) and (200) peaks involved reflection of the undisturbed half of the (111) peak. The axis of reflection was the ordinate through the peak maximum. When the (111) peak had been constructed, the (200) peak was obtained by subtraction from the original intensity curve. One objection that may be advanced against this method is that theoretically the peak should not be symmetrical. For it is the number of scattered electrons that ought to be the same on either side of the direction that is determined by the Bragg angle. This number of electrons is distributed over a region of smaller radius on one side than on the other, which should lead to a certain asymmetry. SJENITZER [1948, pp. 36 ff.] performed some calculations on this asymmetry, and found that the difference between the (111) and (200) peaks theoretically separated and those constructed by direct reflection may be quite large. That the latter method has nonetheless been applied here is mainly due to two considerations. Firstly, a theoretical construction of the (111) peak would result in a (200) peak of improbable breadth. Secondly, the theoretical shape was not observed for any foil in the case of the relatively undisturbed (220) peak.

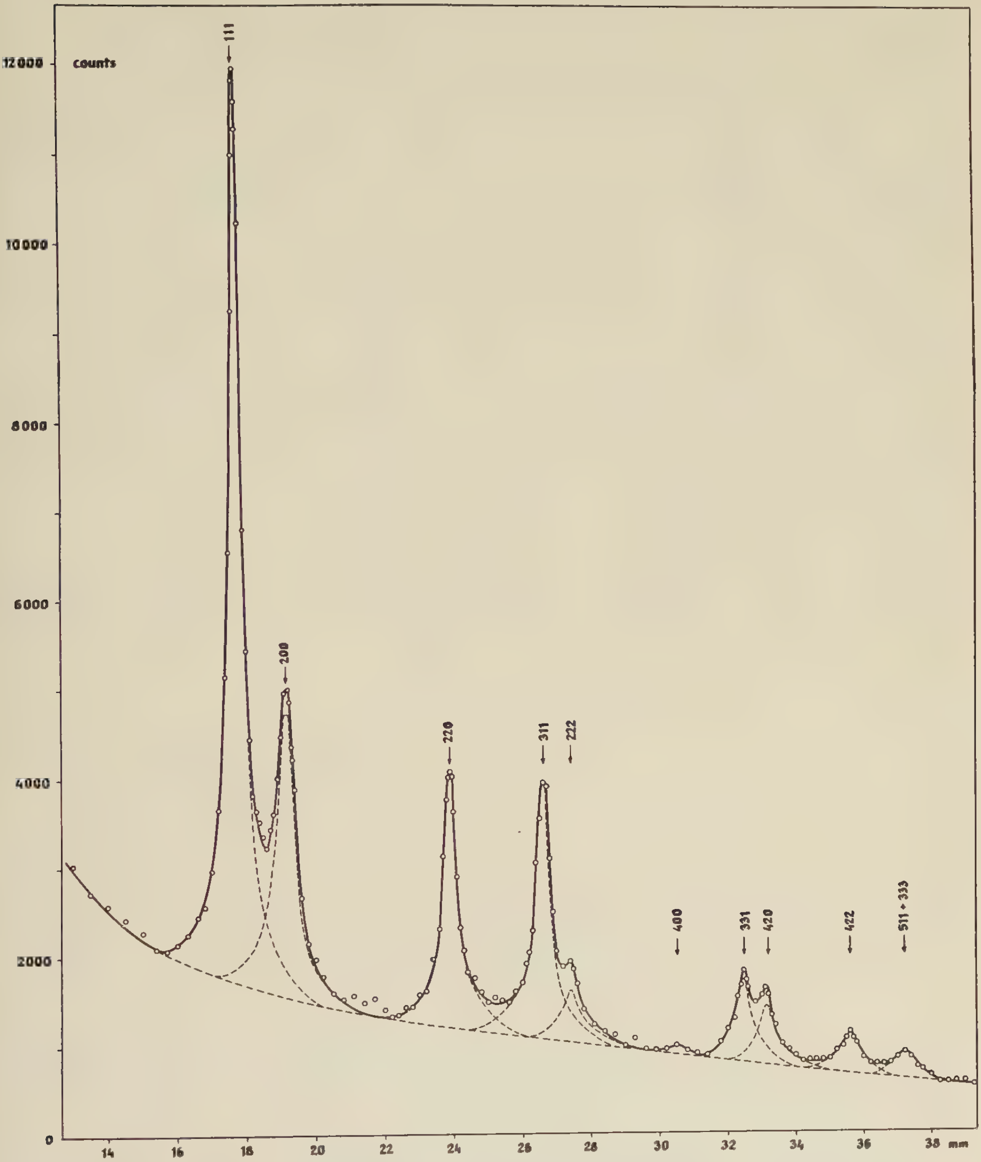

Fig. 15. A recording of the intensity distribution in the diffraction pattern from a Au foil at 30.0 kV (Foil Au 3, 110 Å).[1]

---

[1] The statistical accuracy is often greater than that indicated by the number of counts, since double the given number of impulses was counted for some points, e.g. at the tops of the peaks. Furthermore, the number of points determined was in some places greater than the number that could be conveniently plotted on the graph, so that several points are actually the means of two or three determinations. The same applies to the curves in Figs. 16, 20, and 23.

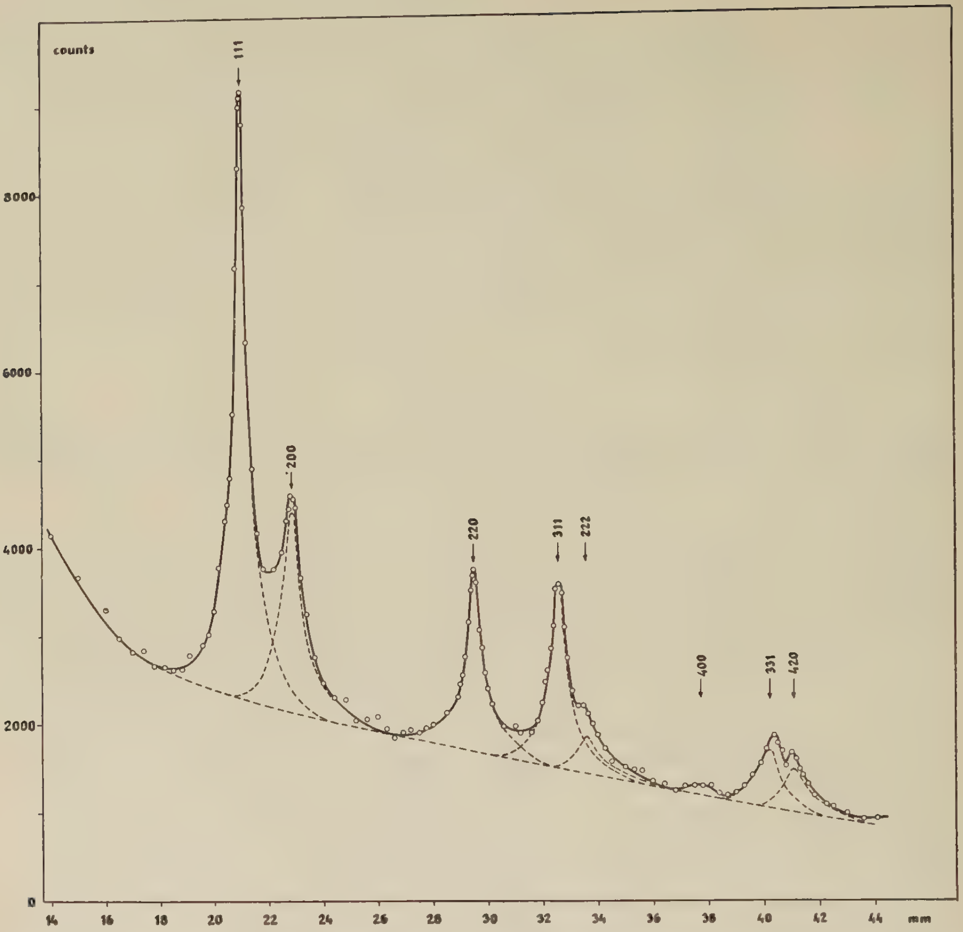

Fig. 16. A recording of the intensity distribution in the diffraction pattern from a Au foil at 18.0 kV (Foil Au 3, 110 Å).

For the separation of the (331) and (420) peaks a preliminary reflection of the left side of the (331) peak was first carried out, after which the peaks were constructed with due regard to the original joint contour.

In previous investigations the measure of a ring's intensity has either been the height of the corresponding peak [Tol, 1940; Yamzin and Pinsker, 1949] or the area under it [Mark and Wierl, 1930; Sjenitzer, 1948]. The former method is more rapid and convenient, but it assumes that all the peaks have the same form and the same half-width—an assumption which is certainly not justified (cf. Chap. VIII). Measurements of the area should therefore give a more accurate result. In order to facilitate comparison with earlier results calculations have been made according to both methods. The areas under the peaks were measured with a precision planimeter (C. Coradi, Zürich). Three to four measurements were performed on each peak, and the maximum deviation from the mean was usually no more than 0.5 %.

Table 4. Measured intensities for foil Au 3 (110 Å).

Ring		Recording No.				Mean
		1	2	3	4	
111	Peak height	362	359	361	368	364
	Area	325	328	347	338	335
200	P. h.	107	112	106	105	108
	A.	138	131	141	138	137
220	P. h.	100	100	100	100	100
	A.	100	100	100	100	100
311	P. h.	98.5	100	99	99	99
	A.	106	104	111	115	109
331	P. h.	29.8	32.1	32.1	30.0	31
	A.	33.8	34.8	39.0	37.0	36
420	P. h.	22.2	22.3	22.7	23.0	22.5
	A.	23.8	24.4	29.0	28.7	26.5
422	P. h.	16.9	16.5	16.1	16.3	16.5
	A.	21.6	18.7	20.2	19.7	20
511	P. h.	10.5	10.6	10.8	10.3	10.5
333	A.	14.3	14.1	13.5	13.3	14

Table 5. The relative intensities of the Au rings.

Foil No.		Ring							
		111	200	220	311	331	420	422	511 333
Au 1	Peak height	369	107	100	101	32.5	22.5	17	12
(90 Å)	Area	353	132	100	107	37.5	28.5	23	16
Au 2	P. h.	361	105	100	97	33	23.5	17	11
(105 Å)	A.	341	140	100	109	40.5	26.5	24	16
Au 3	P. h.	364	108	100	99	31	22.5	16.5	10.5
(110 Å)	A.	335	137	100	109	36	26.5	20	14
Au 4	P. h.	360	113	100	105	34.5	24	18.5	13.5
(140 Å)	A.	352	139	100	111	37	25	22	15
Au 5	P. h.	339	108	100	107	36	24.5	20	15.5
(170 Å)	A.	355	138	100	113	43.5	32.5	24.5	18
Au 6	P. h.	327	115	100	107	37	25.5		
(200 Å)	A.	339	131	100	115	41.5	29		
Au 7	P. h.	324	106	100	107	36.5	26		
(225 Å)	A.	330	129	100	113	37.5	30		

Table 6. The atomic factor for Au.

Foil No.		Ring							
		111	200	220	311	331	420	422	511 333
Au 1	Peak height	138	71.5	66.7	46.5	25.5	19	17	10
(90 Å)	Area	132	88	66.7	49	29.5	24	23	13.5
Au 2	P. h.	135	70	66.7	44.5	26	19.5	17	9.5
(105 Å)	A.	128	93.5	66.7	50	32	22	24	13.5
Au 3	P. h.	136	72	66.7	45.5	24.5	19	16.5	9
(110 Å)	A.	126	91.5	66.7	50	28.5	22	20	12
Au 4	P. h.	135	75.5	66.7	48	27.5	20	18.5	11.5
(140 Å)	A.	132	92.5	66.7	51	29.5	21	22	12.5
Au 5	P. h.	127	72	66.7	49	28.5	20.5	20	13
(170 Å)	A.	133	92	66.7	52	34.5	27	24.5	15
Au 6	P. h.	123	76.5	66.7	49	29.5	21		
(200 Å)	A.	127	87.5	66.7	52.5	33	24		
Au 7	P. h.	122	70.5	66.7	49	29	21.5		
(225 Å)	A.	124	86	66.7	52	29.5	25		
Theoretical values		165	128	66.7	48	24.5	22.5	17.5	14.5

Table 7. Measured intensities for foil Au 3 (110 Å) at 18.0 and 30.0 kV.

Voltage		Ring					
		111	200	220	311	331	420
18.0 kV	Peak height	337	106	100	98	31.5	23.5
	Area	320	138	100	105	38	31
30.0 kV	Peak height	364	108	100	99	31	22.5
	Area	335	137	100	109	36	26.5

Table 8. The atomic factor for Au at 18.0 and 30.0 kV.

Voltage		Ring					
		111	200	220	311	331	420
18.0 kV	Peak height	126	70.5	66.7	45	25	19.5
	Area	120	92	66.7	48	30	26
30.0 kV	Peak height	136	72	66.7	45.5	24.5	19
	Area	126	91.5	66.7	50	28.5	22
Theoretical values		165	128	66.7	48	24.5	22.5

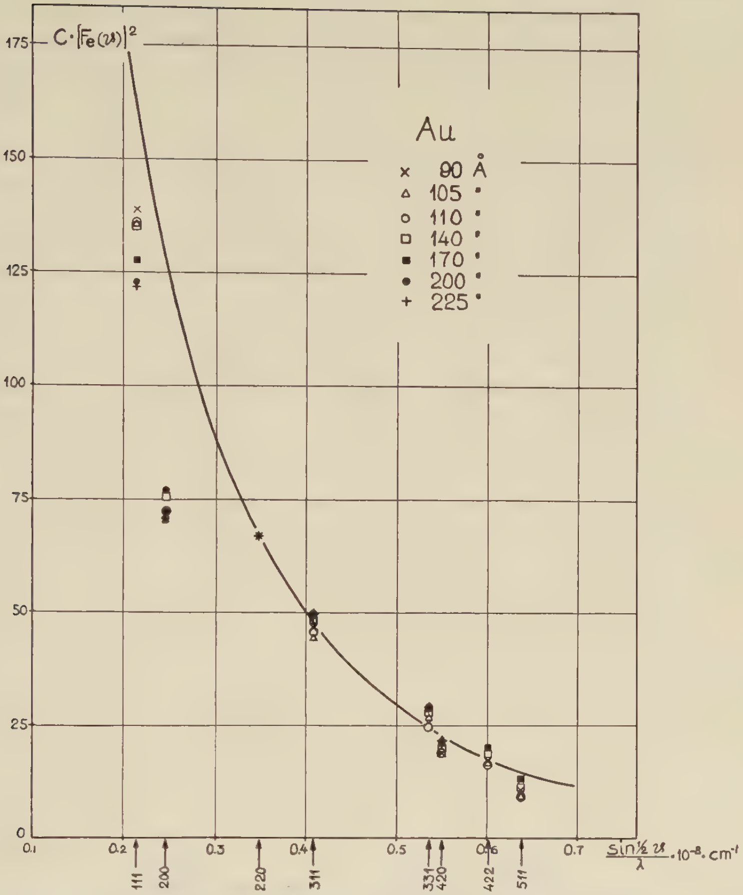

Fig. 17. Experimental values of the atomic factor for Au (peak-height values, 30.0 kV). The solid curve is theoretical, in accordance with eq. (4).

The values obtained from the four intensity curves recorded for foil Au 3 (110 Å) are given in Table 4. The two series of relative intensities are derived from the heights of peaks and from the areas under them.

Table 5 gives the mean values of the relative intensities as determined for the seven Au foils. Table 6 gives the corresponding values of the atomic factor as calculated by eq. (10) from the peak-height intensities and from the area-under-peak intensities. The theoretical values are derived from eq. (4) (with F_r values interpolated from Table 1).

Values of the atomic factor calculated from the peak-height intensities have been inserted in Fig. 17, and those calculated from the area intensities in Fig. 18. The solid curve represents in each case the atomic factor according to the kinematic theory. In calculating the abscissae the lattice constant for Au has been taken to be 4.07 Å.

The results of the measurements on foil Au 3 (110 Å) at 18.0 kV are reproduced in

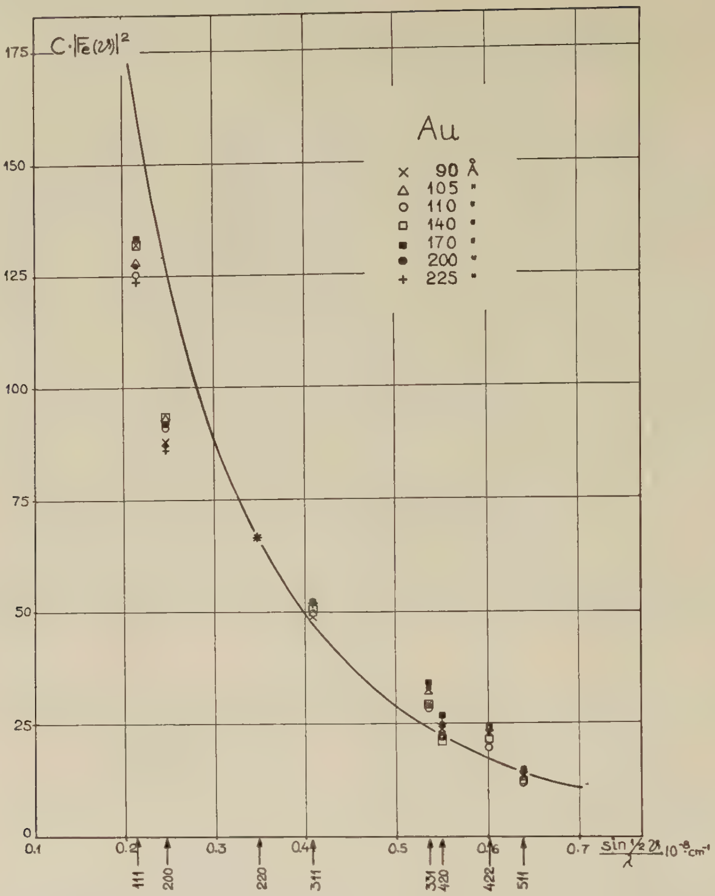

Fig. 18. Experimental values of the atomic factor for Au (area values, 30.0 kV).

Table 7 and the corresponding values of the atomic factor in Table 8. The figures for the same foil at 30.0 kV are included for comparison. The area values of the atomic factor are given graphically in Fig. 19.

§ 2. Measurements with Ag

Intensity measurements were carried out on six Ag foils, of which the thinnest had an average thickness of 75 Å and the thickest 250 Å. The mode of preparation, approximate age, and method of storage were the same as for the Au foils. The accelerating voltage was 29.5 kV. As for Au, four series of recordings were performed for each Ag foil. Fig. 20 shows one of the curves for foil Ag 3 (100 Å). The separation of superimposed peaks and the other stages of the computations were analogous to those for Au. The results are presented in Tables 9–11 and in Figs. 21 and 22. The value adopted for the lattice constant for Ag was 4.08 Å.

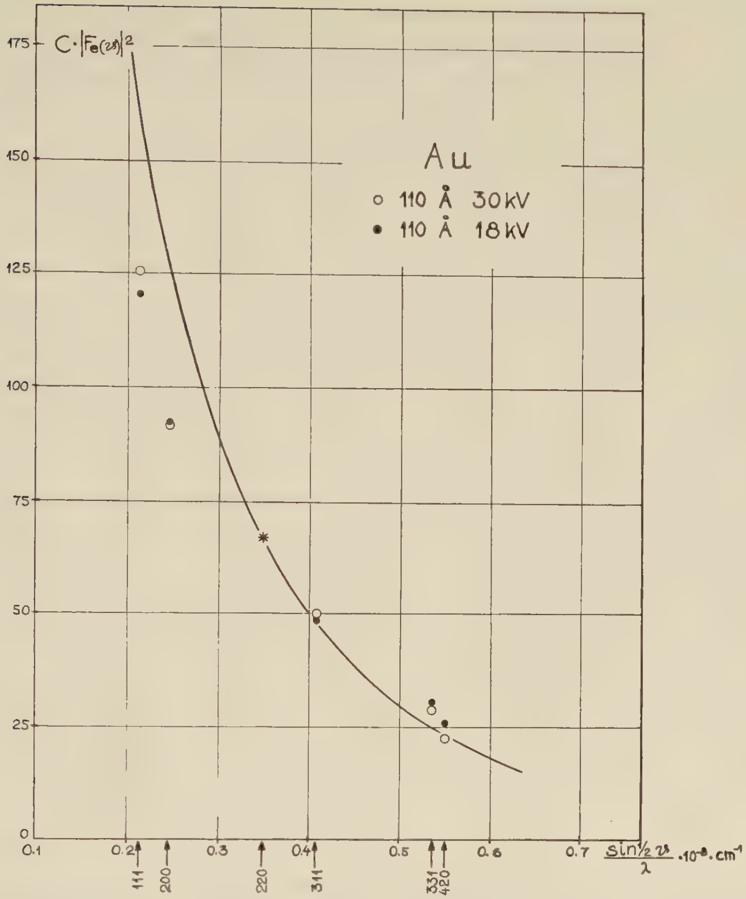

Fig. 19. Experimental values of the atomic factor for Au at 18.0 kV, and 30.0 kV (area values).

§ 3. Measurements with Al

Intensity measurements were made with four Al foils, of thicknesses 140 Å, 290 Å, 325 Å, and 410 Å. Prior to the measurements with the Geiger counters the degree of preferred crystal orientation in the foils was investigated by the method explained in Chap. VI. Since it was necessary to carry out intensity measurements along different diameters of the diffraction pattern, the Geiger counters were not convenient[1], so the photographic method was employed instead. Series of four plates each were taken with different exposure times (in the ratio 1:2:4:8) but with approximately the same primary intensity. The latter was accurately determined by means of the Faraday cylinder and d.c. amplifier. The exposed plates of each series were placed in a common holder, and thus developed and fixed under identical conditions. Photo-

---

[1] A foil-holder constructed so that the foil could be rotated about an axis along the electron beam would permit the Geiger counters to be used also for this purpose.

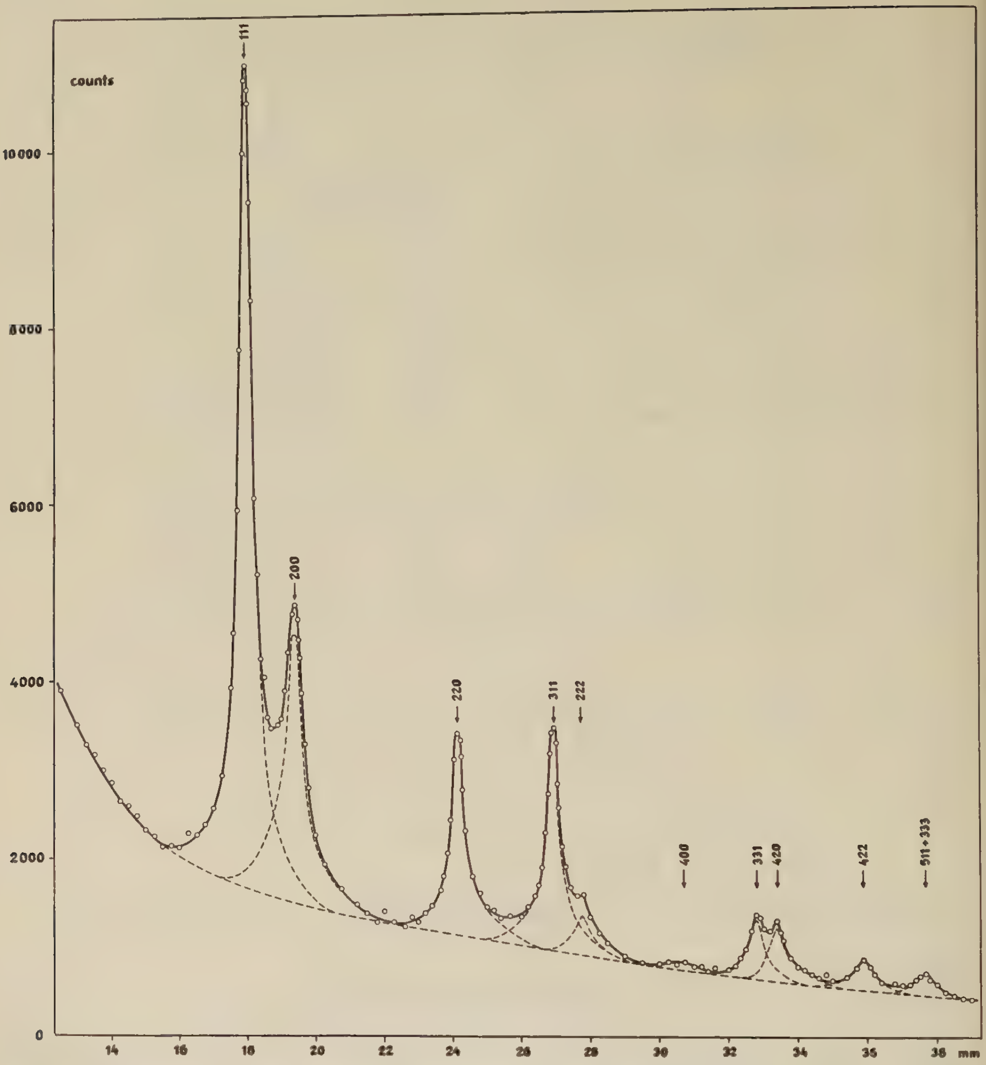

Fig. 20. A recording of the intensity distribution in the diffraction pattern from a Ag foil at 29.5 kV (Foil Ag 3, 100 Å).

metric analysis of the plates was performed with a Moll recording microphotometer (Kipp and Zonen, Type A, No. K 15) in the directions 0° and 90° (cf. Fig. 14). The blackening curve for each series was constructed by a method described in an earlier paper [von Friesen and Lennander, 1946; cf. also Mark and Wierl, 1930, Skinner and Johnston, 1937]. The degree of exposure has been taken to be proportional to the intensity × the exposure time. This presupposes that Schwarzschild's factor may be taken as unity—a justified assumption in the present case according to investigations by, among others, Ellis [1929], and von Borries and Knoll [1934].

Table 9. Measured intensities for foil Ag 3 (100 Å).

Ring		Recording No.				Mean
		1	2	3	4	
111	Peak height	414	413	406	410	411
	Area	401	410	404	396	403
200	P. h.	132	131	133	136	133
	A.	174	171	178	182	176
220	P. h.	100	100	100	100	100
	A.	100	100	100	100	100
311	P. h.	105	106	109	105	106
	A.	106	113	111	109	110
331	P. h.	30.0	28.8	28.2	29.1	29
	A.	28.7	30.0	27.8	27.4	28.5
420	P. h.	25.6	24.3	25.7	26.0	25.5
	A.	23.5	28.3	27.4	23.6	25.5
422	P. h.	14.2	15.3	14.7	15.0	15
	A.	16.3	19.0	18.2	16.9	17.5
511	P. h.	10.4	10.8	10.7	11.4	11
333	A.	11.7	13.2	12.1	11.8	12

Table 10. The relative intensities of the Ag rings.

Foil No.		Ring							
		111	200	220	311	331	420	422	511 333
Ag 1	Peak height	433	138	100	105	23.5	22	13	8.5
(75 Å)	Area	410	171	100	106	25.5	22.5	15	11
Ag 2	P. h.	406	127	100	103	28	25	13	10
(95 Å)	A.	404	172	100	106	28	25	17.5	12
Ag 3	P. h.	411	133	100	106	29	25.5	15	11
(100 Å)	A.	403	176	100	110	28.5	25.5	17.5	12
Ag 4	P. h.	381	133	100	110	30	27.5	18	12.5
(150 Å)	A.	407	172	100	114	30	28	20	14.5
Ag 5	P. h.	362	124	100	106	33	29	16	12
(195 Å)	A.	384	164	100	111	33	28.5	18.5	14.5
Ag 6	P. h.	358	122	100	109	33	29.5	18.5	12.5
(250 Å)	A.	377	161	100	113	33.5	30	21.5	14

Table 11. The atomic factor for Ag.

Foil No.		Ring							
		111	200	220	311	331	420	422	511 333
Ag 1	Peak height	162	92	66.7	48	18.5	18.5	13	7
(75 Å)	Area	154	114	66.7	48.5	20	18.5	15	9.5
Ag 2	P. h.	152	84.5	66.7	47	22	21	13	8.5
(95 Å)	A.	152	115	66.7	48.5	22	21	17.5	10
Ag 3	P. h.	154	88.5	66.7	48.5	23	21.5	15	9.5
(100 Å)	A.	151	117	66.7	50.5	22.5	21.5	17.5	10
Ag 4	P. h.	143	88.5	66.7	50.5	24	23	18	10.5
(150 Å)	A.	153	115	66.7	52.5	24	23.5	20	12
Ag 5	P. h.	136	82.5	66.7	48.5	26	24	16	10
(195 Å)	A.	144	109	66.7	51	26	24	18.5	12
Ag 6	P. h.	134	81.5	66.7	50	26	24.5	18.5	10.5
(250 Å)	A.	141	107	66.7	52	26.5	25	21.5	12
Theoretical values		174	134	66.7	46	21.5	20	15.5	13

The intensities of both the (200) and (220) rings were measured in the directions 0° and 90°. The heights of the respective peaks were taken as the measure of the intensity. Such a procedure is here satisfactory, since the comparison is between different parts of the same ring. The results of the measurements (the mean of 3–4 determinations) are given in Table 12. The measurements on the (200) ring were undertaken solely as a control. According to the discussion in Chap. VI, the intensification of the (200) ring should be double as great as that of the (220) ring, and the experimental results agree quite well with that conclusion. Table 13 gives the percentage correction for the Al foils, calculated from the figures of Table 12 and the correction scheme of Chap. VI (p. 586). This correction is derived from the difference between two intensity measurements, and its uncertainty is therefore relatively large, being *c.* 8–10 % of the given values.

The recordings with the Geiger counters and the treatment of the intensity curves was the same as for the Au and Ag foils. The accelerating voltage was 27.0 kV. Fig. 23 is one of the curves recorded with the foil Al 2 (290 Å). The separation of superimposed peaks was somewhat easier than for the Au and Ag curves, due to the fact that the width of the rings, and thus the extent of the superposition, was much smaller in the Al curves.

The values of the relative intensities of the rings obtained from the four intensity curves recorded for foil Al 2 (290 Å) are reproduced in Table 14. Table 15 gives the mean relative ring intensities computed from all the measurements of the areas under the various peaks. Table 16 shows the intensity values corrected according to Table 13, and the corresponding values of the atomic factor are given in Table 17. Fig. 24 is of the atomic factor (of Table 17). The value adopted for the lattice constant of Al in the calculations was 4.04 Å.

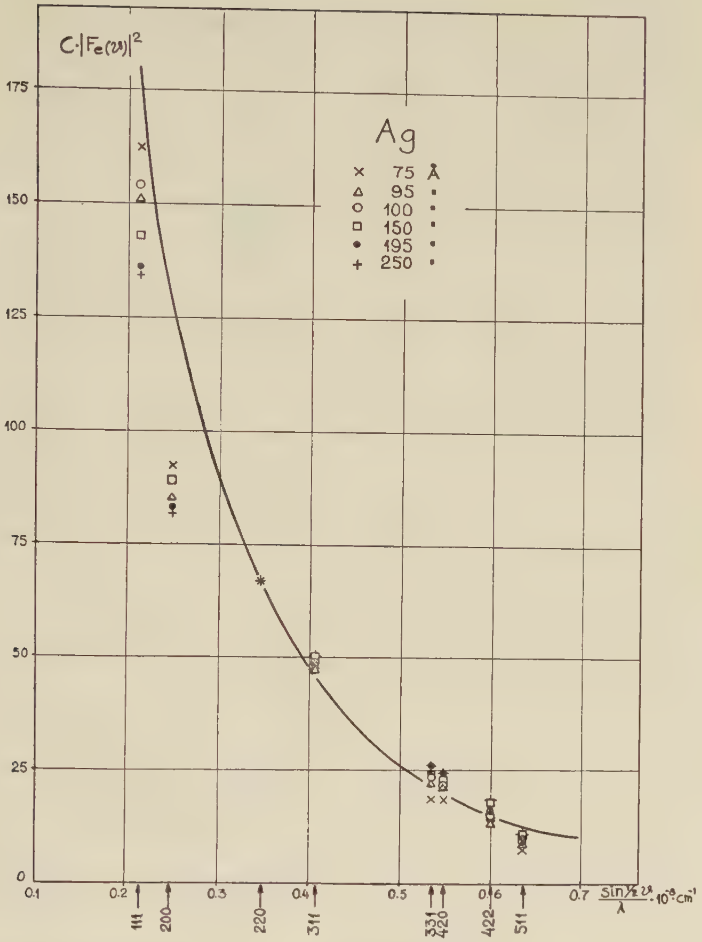

Fig. 21. Experimental values of the atomic factor for Ag (peak-height values, 29.5 kV).

§ 4. Discussion of the results

a. Comparison with theory

The $|F_e(\vartheta)|^2$ curves reproduced in preceding paragraphs provide a direct comparison between the kinematic theory and the present experimental results. In every case the experimental points lie on a less steep curve than the theoretical one. The discrepancy is most marked for Au. If the temperature correction is also taken into account, the discrepancy becomes even greater (cf. Fig. 1, p. 557). The difference may arise from (1) the foils used, (2) the intensity measurements, (3) the theory.

As regards the foils, it has already been mentioned that they were thoroughly examined for signs of preferred crystal orientation, and that the metal used for their preparation was of the highest grade of purity. However, there is a certain risk that

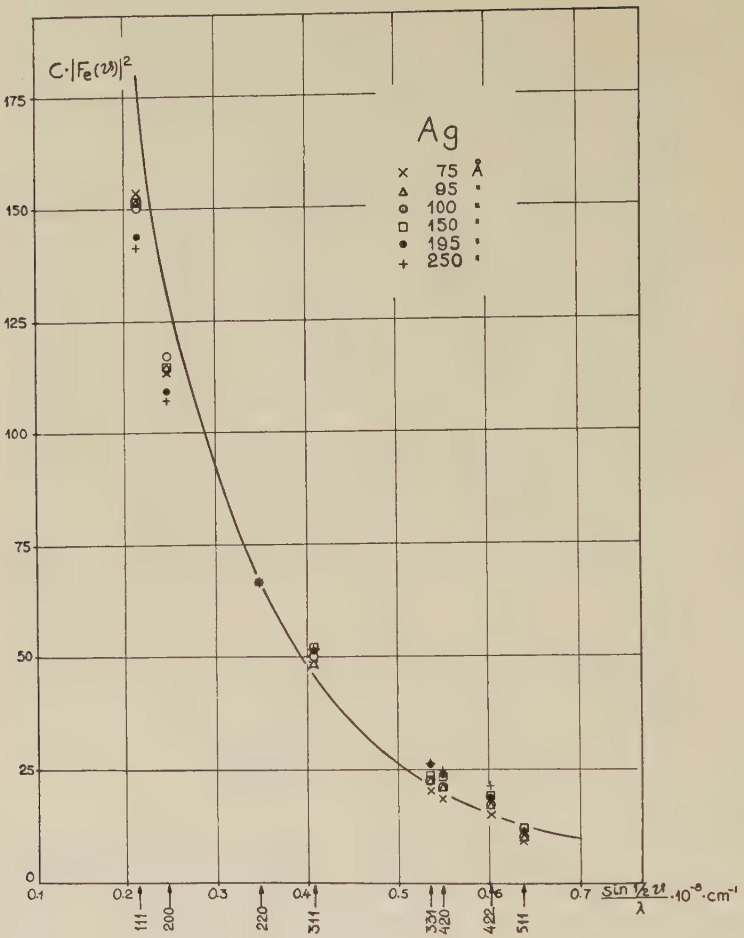

Fig. 22. Experimental values of the atomic factor for Ag (area values, 29.5 kV).

oxidation may have occurred, despite the fact that they were kept under vacuum. In order to investigate the effect of oxidation, tests were carried out on an Al foil that had been exposed to the air for 11 months. The diffraction rings were still sharp and no traces of oxidation could be detected. Nevertheless, oxidation may have been present, since BELWE [1936] observed that an amorphous or highly dispersed oxide is formed on Al during atmospheric oxidation. Such oxidation would merely strengthen the background, and would therefore not affect the relative intensities of the rings.

The accuracy of the intensity measurements has been considered earlier (Chap. III, § 2). The maximum error is considerably less than the deviation from the theoretical values.

Lastly, as regards the theory, the Born approximation on which the kinematic theory is based has been critically examined by several investigators. Some of them —e.g. DISTEL [1932] and MØLLER [1930]—consider that the Born approximation is

Table 12. Measured intensities with the foils inclined ($\delta = 35°$).

Foil No.	Ring	Directions		Intensification %
		0°	90°	
Al 1	200	298	224	33
(140 Å)	220	100	118	18
Al 2	200	311	232	34
(290 Å)	220	100	119	19
Al 3	200	327	210	56
(325 Å)	220	100	128	28
Al 4	200	288	201	43
(410 Å)	220	100	125	25

Table 13. Intensity corrections in per cent.

Foil No.	Ring							
	111	200	220	311	331	420	422	511 333
Al 1 (140 Å) . . .	0	0	15	7.5	15	7.5	7.5	0
Al 2 (290 Å) . . .	0	0	16	8	16	8	8	0
Al 3 (325 Å) . . .	0	0	22	11	22	11	11	0
Al 4 (410 Å) . . .	0	0	20	10	20	10	10	0

Table 14. Measured intensities for foil Al 2 (290 Å).

Ring		Recording No.				Mean
		1	2	3	4	
111	Peak height	510	497	520	512	510
	Area	494	471	467	489	480
200	P. h.	181	171	177	180	177
	A.	191	182	183	192	187
220	P. h.	100	100	100	100	100
	A.	100	100	100	100	100
311	P. h.	83	83.5	85	82	83.5
	A.	92	89	95.5	90	91.5
331	P. h.	21.4	22.8	19.7	20.0	21
	A.	16.7	17.0	15.3	14.9	16
420	P. h.	16.3	18.1	18.0	16.4	17
	A.	14.3	15.1	13.8	13.0	14

Table 15. The relative intensities of the Al rings (uncorrected area values).

Foil No.	Ring							
	111	200	220	311	331	420	422	511 333
Al 1 (140 Å) . . .	472	174	100	83.5	19	15.5		
Al 2 (290 Å) . . .	480	187	100	91.5	16	14		
Al 3 (325 Å) . . .	439	163	100	75	16	13.5	8.5	
Al 4 (410 Å) . . .	420	170	100	97	20	18.5	9	8

Table 16. The relative intensities of the Al rings (corrected area values).

Foil No.	Ring							
	111	200	220	311	331	420	422	511 333
Al 1 (140 Å) . . .	555	204	100	91	19	17		
Al 2 (290 Å) . . .	571	223	100	100	16	15.5		
Al 3 (325 Å) . . .	563	209	100	85.5	16	15.5	9.5	
Al 4 (410 Å) . . .	525	213	100	109	20	20.5	10	10

Table 17. The atomic factor for Al.

Foil No.	Ring							
	111	200	220	311	331	420	422	511 333
Al 1 (140 Å) . . .	208	136	66.7	41.5	15	14		
Al 2 (290 Å) . . .	214	149	66.7	46	12.5	13		
Al 3 (325 Å) . . .	211	139	66.7	39	12.5	13	9.5	
Al 4 (410 Å) . . .	197	142	66.7	50	16	17	10	8.5
Theoretical values	250	166	66.7	44	22	20	16	13.5

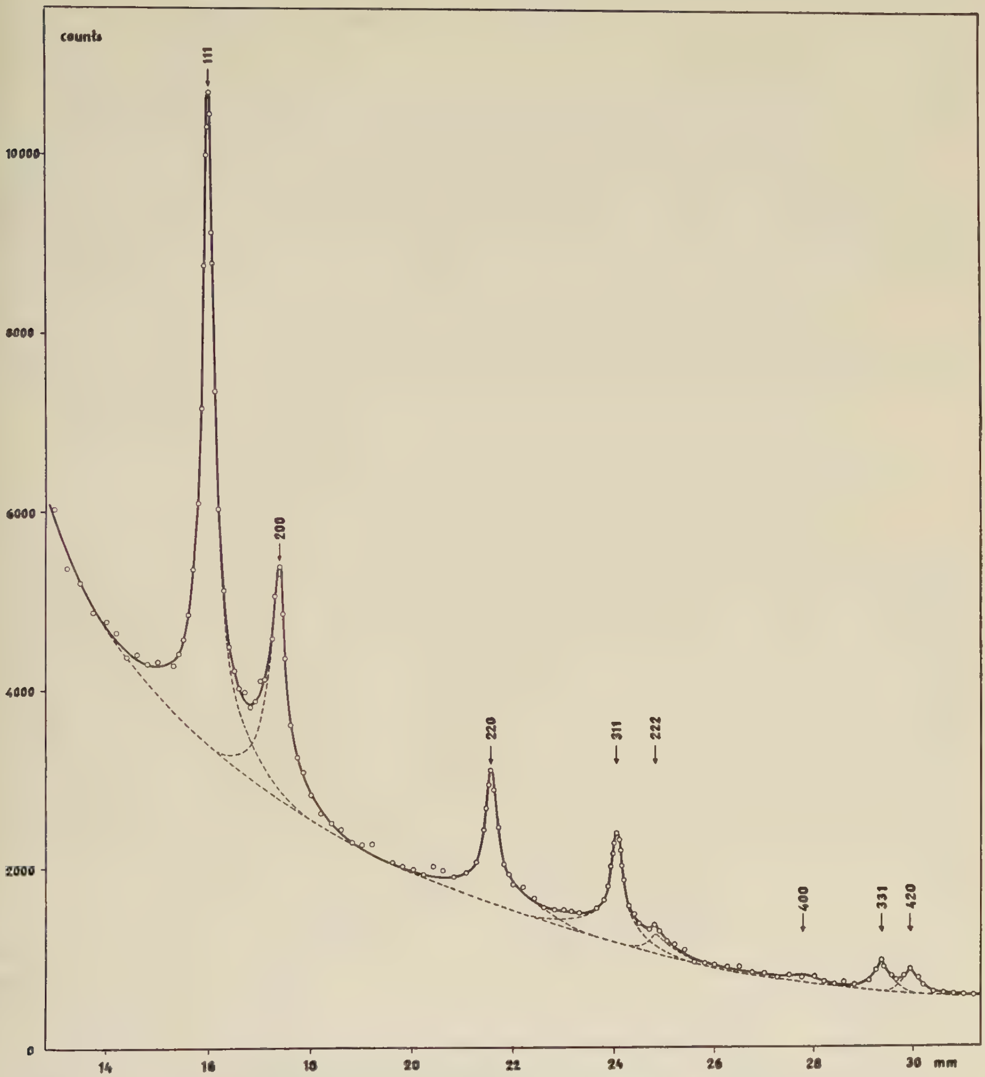

Fig. 23. A recording of the intensity distribution in the diffraction pattern from an Al foil at 27.0 kV (Foil Al 2, 290 Å).

often unsatisfactory for accelerating voltages such as are often used in electron diffraction experiments (e.g. about 30 kV). Hengstenberg and Wolf [1935] made use of Møller's calculations to determine a lower limit for the accelerating voltage in this respect. They found this limiting value to be 50 Z^2 volts. For Au ($Z = 79$) this means 312 kV, for Ag ($Z = 47$) 110 kV, and for Al ($Z = 13$) 8.5 kV.

This offers an explanation of the discrepancy in the case of Au and Ag, but not for Al, where the accelerating voltage (27 kV) was according to the above calculations sufficiently high.

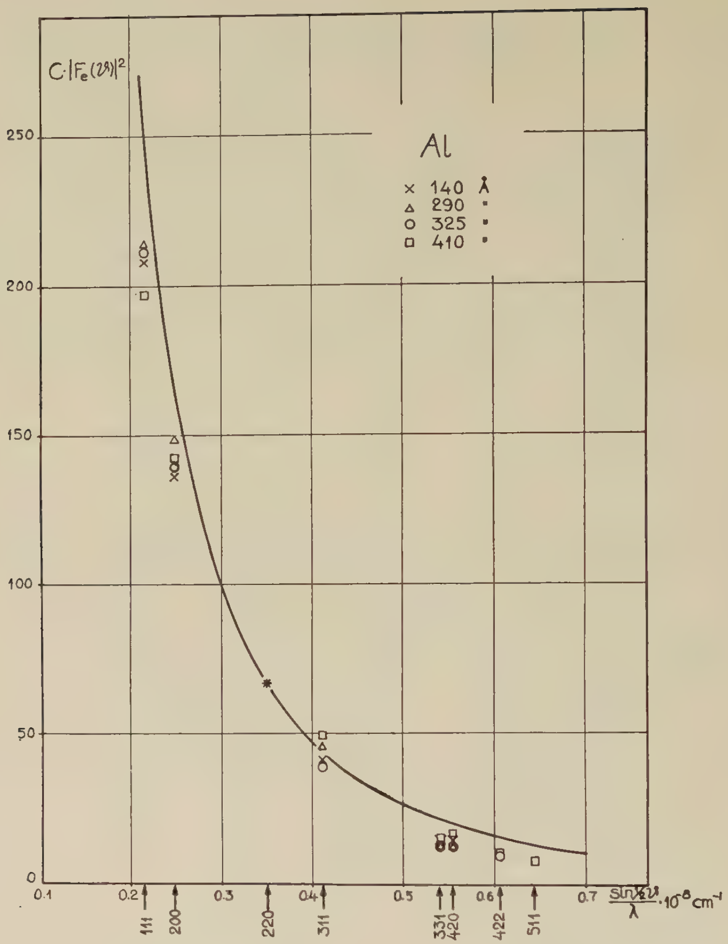

Fig. 24. Experimental values of the atomic factor for Al (area values, 27.0 kV).

It should also be mentioned that HENNEBERG [1933] treated the atomic scattering of electrons by means of an approximation which is mathematically more exact than that employed by BORN. HENNEBERG's calculations give an atomic factor curve which falls less steeply than that obtained from eq. (4) (p. 553). However, the difference diminishes as the electron energy increases and as Z decreases. For Au and an acceleration voltage of 30 kV the discrepancy is quite pronounced, whereas for Ag it is relatively small.

As already mentioned in Chap. I, there is some uncertainty about the range of application of the kinematic theory. PINSKER [1953, p. 167], for instance, considers that the theory is quite applicable for crystal dimensions of up to 100 Å. On the other hand, BLACKMAN [1939] investigated the matter and came to the conclusion that the kinematic theory is unusable for crystals with more than just a few lattice planes. This agrees with previous results obtained by KIRCHNER [1932 a], who found that the conditions of the kinematic theory can only be fulfilled for crystals of dimensions up to about 10 Å.

In the present results, however, the departure from the kinematic theory for Al is small compared with that for Au, although the crystal size was as much as 120 Å for the Al foils and as little as 45 Å for the Au (cf. Chap. VIII).

It is not impossible that the discrepancy in the case of Al may be accounted for by the crystal size, while in the case of Au and Ag it may be due to the accelerating voltage being less than the minimum value prescribed by HENGSTENBERG and WOLF for the application of the Born approximation. As can be seen from Fig. 19, the points for foil Au 3 at 18.0 kV lie on a curve slightly less steep than the corresponding points at 30.0 kV.

The discrepancy with regard to the *dynamic theory's* prediction of proportionality between the intensity and $F_e(\vartheta)$ is much greater than the discrepancy with regard to the kinematic theory (except for the higher Au values).

b. Comparison with earlier experimental results

As pointed out in Chap. I, earlier experimental investigations have given very variable results. There is nowhere complete agreement with the present results.

However, one or two general features may be said to agree with TOL's [1940, TOL and ORNSTEIN, 1940] findings for Au and Ag. The comparison should be made with the peak-height intensities (Figs. 17 and 21), as that was the method used by TOL. The spread of TOL's figures for the different foils is quite large, but the mean of them, like the present results, gives a $|F_e(\vartheta)|^2$ curve that is less steep than the theoretical curve. Another feature in common is that the values for the (200) ring are everywhere too low to give a smooth $|F_e(\vartheta)|^2$ curve. Use of area-under-peak values reduces this unevenness to a mere tendency in our case, since the (200) ring is wider than the neighbouring rings (cf. Chap. VIII). The particularly marked irregularity of TOL's values and the large discrepancies between different foils—which are to some extent discernible in the examples given in Fig. 1 here—was not found to occur, however. It has already been mentioned that the irregularity in TOL's results may have been due to preferred crystal orientation. The most irregular values in Fig. 1 (380 Å, 30.5 kV) should in such case have originated from a foil with considerable preferred orientation. If the foil had a (111) orientation the corrections on p. 586 should be applicable. If such a correction is undertaken, with $a \simeq 40\,\%$, values are obtained that agree relatively well with the present experimental results. The same applies to the other measurements of TOL reproduced in Fig. 1 (260 Å, 30.5 kV) if a here is taken to be c. 18 % (see Table 18).

There is also agreement with VON FRIESEN and LENNANDER's [1946] measurements on Al as regards the kind of deviation from the kinematic theory. The magnitude of the deviation is greater for the former values, however.

There is no agreement whatsoever with the results of SJENITZER [1948] (cf. Fig. 1). The very pronounced effect of different foil thicknesses (under 200 Å) observed by SJENITZER was not discernible, despite the fact that the mean foil thickness ranged down to 75 Å (Ag). But the method of preparation of the foils differed a great deal in the two cases. As previously indicated, the present foils were all prepared in the same way and mounted without substrate—even the thinnest—in order to obtain reliable information about the effect of foil thickness. It has already been mentioned

Table 18. The atomic factor for Au (peak-height values).

	Ring					
	111	200	220	311	331	420
Tol 380 Å; 30.5 kV; uncorrected . . .	70	48	66.7	37.5	20	16.5
Tol 260 Å; 30.5 kV; uncorrected . . .	92	66	66.7	43.5	22	20
Lennander 200 Å; 30.0 kV	123	76.5	66.7	49	29.5	21
Tol 380 Å; 30.5 kV; corrected: $a = 40\,\%$	117	80	66.7	50	20	22
Tol 260 Å; 30.5 kV; corrected: $a = 18\,\%$	112	80.5	66.7	48.5	22	22

in Chap. I that Sjenitzer retained a substrate of nitrocellulose (1000 Å) with his foils. Furthermore, the evaporation process was in his case very slow (40 min. for a foil 125 Å thick; in our case 5–10 sec.; cf. Chap. IV). Sjenitzer [1948, p. 88] has published results which seem to indicate that this slow evaporation can produce foils that are more or less amorphous: a Ag foil (160 Å) was found to be practically amorphous, and did not acquire a crystalline form until it had been subject to heavy electron bombardment. We have examined some hundreds of metal foils without finding any that was amorphous, despite the fact that the bombardment was as a rule much weaker than that employed by Sjenitzer (cf. Chap. III, § 3).

Nor is there any agreement with the results of Yearian and Howe [1935], who found that variation of the accelerating voltage had a pronounced effect on the slope of the $|F_e(\vartheta)|^2$ curve, with a distinct difference between 23 and 17 kV for Au. As already mentioned, only a very slight change was detected in the present $|F_e(\vartheta)|^2$ values when the accelerating voltage was altered from 30.0 kV to 18.0 kV for the same Au foil (Fig. 19).

The atomic factor curve for Au, obtained by Yamzin and Pinsker [1949] is somewhat less steep than the theoretical curve (see Fig. 1), i.e. there is a discrepancy in the same direction as that observed here, though less marked. The same applies to the results for Ag and Al to some extent, if the temperature correction is applied to the theoretical values.

Chapter VIII

Widths of the rings and crystal size

The width of a diffraction ring is usually ascribed to three main factors: (1) variation of the accelerating voltage, (2) the width of the primary beam, and (3) the dimensions of the microcrystals.

The variation of the accelerating voltage is very small in the present case, and can be entirely neglected. The width of the primary beam may be directly determined by spreading out the focal point to a line by means of alternating magnetic field. The half-width of the primary beam (b) was in this way found to be 0.11 mm.

The relation between ring width and crystal size makes it possible to determine the latter approximately. A formula derived by BRILL [1934] may be used for this purpose. The main assumptions involved are that the microcrystals are all of about the same size, and that they are approximately cubic in shape. Then, according to BRILL,

$$B = 0.94 \frac{\lambda}{\cos \vartheta/2 \cdot \Lambda} - b \tag{15}$$

where B = the half-width of the ring (in radians)
b = the width due to the finite width of the primary beam
Λ = the mean edge of each cube
$\vartheta/2$ = the Bragg angle
λ = the wavelength of the electrons.

In the present case $\cos \vartheta/2$ may be taken as unity. Introduction of L, the distance between the foil and the focal plane gives (B and b now lengths)

$$\Lambda = 0.94 \frac{L \cdot \lambda}{B - b}. \tag{16}$$

The half-widths B of the rings were determined in connection with the intensity measurements for Au, Ag, and Al. The results are shown in Tables 19–21. The values there are the means of four determinations, i.e. are derived from all the intensity curves for a single foil. The maximum variation from the mean was in most cases less than ± 4 to ± 5 %.

The tables also include the mean crystal size, calculated with the help of eq. (16) from the half-width of the (220) ring. The value of b employed was 0.11 mm, from the determination previously mentioned. For the measurements with Au and Ag foils, $L = 325$ mm, and the accelerating voltage was 30.0 and 29.5 kV respectively. In both these cases the value of $L\lambda$ has been taken as $22.7 \cdot 10^{-7}$ mm². For the measurements with Al, $L = 280$ mm, and the accelerating voltage was 27.0 kV. In this case, $L\lambda = 20.5 \cdot 10^{-7}$ mm².

As mentioned, one of the assumptions for eq. (15) is that the microcrystals are approximately cubic in shape. In other cases eq. (16) gives the dimension of the crystals only in the direction normal to the primary beam [cf. KIRCHNER, 1932]. However, as there was no discernible alteration of the half-width when the foil was inclined, we may assume that the crystals had approximately the same dimensions in all directions.

The measurements indicate that the crystal size in the Ag foils was in general somewhat greater than in the Au foils, and the crystal size in the Al foils about double as great as in the Au foils. This is in agreement with the results obtained by LEVINSTEIN [1949], already mentioned in Chap. IV (p. 579), and with an investigation by YAMZIN [published by PINSKER, 1953, p. 206] of the relation between crystal size and melting-point.

Measurements of half-widths reveal that (1) the half-width increases with increasing scattering angle, and (2) the half-width of the (200) ring is much greater than the two neighbouring rings.

Table 19. Au: The half-widths of the rings (in mm) and the mean crystal size (in Å).

Foil No.	Ring								Mean crystal size in Å
	111	200	220	311	331	420	422	511 333	
Au 1 (90 Å)	0.42	0.58	0.48	0.47	0.66	0.64	0.84	0.85	60
Au 2 (105 Å)	0.43	0.61	0.47	0.48	0.62	0.58	0.84	0.85	60
Au 3 (110 Å)	0.42	0.60	0.48	0.50	0.63	0.60	0.81	0.87	60
Au 4 (140 Å)	0.49	0.67	0.51	0.53	0.70	0.66	0.80	0.80	55
Au 5 (170 Å)	0.47	0.61	0.47	0.50	0.71	0.70	0.81	0.80	60
Au 6 (200 Å)	0.56	0.68	0.57	0.61	0.79	0.76			45
Au 7 (225 Å)	0.48	0.59	0.49	0.52	0.70	0.70			55

Table 20. Ag: The half-widths of the rings (in mm) and the mean crystal size (in Å).

Foil No.	Ring								Mean crystal size in Å
	111	200	220	311	331	420	422	511 333	
Ag 1 (75 Å)	0.48	0.66	0.49	0.51	0.66	0.62	0.72	0.78	55
Ag 2 (95 Å)	0.44	0.63	0.44	0.45	0.53	0.52	0.72	0.74	65
Ag 3 (100 Å)	0.48	0.68	0.49	0.49	0.59	0.57	0.72	0.72	55
Ag 4 (150 Å)	0.49	0.66	0.47	0.49	0.55	0.52	0.68	0.76	60
Ag 5 (195 Å)	0.41	0.54	0.40	0.40	0.50	0.47	0.65	0.68	75
Ag 6 (250 Å)	0.46	0.66	0.46	0.48	0.53	0.55	0.72	0.70	60

Table 21. Al: The half-widths of the rings (in mm) and the mean crystal size (in Å).

Foil No.	Ring								Mean crystal size in Å
	111	200	220	311	331	420	422	511 333	
Al 1 (140 Å)	0.27	0.32	0.29	0.32	0.35	0.35			105
Al 2 (290 Å)	0.30	0.34	0.30	0.34	0.35	0.37			100
Al 3 (325 Å)	0.25	0.30	0.27	0.29	0.32	0.32	0.40		120
Al 4 (410 Å)	0.24	0.29	0.27	0.29	0.31	0.31	0.36	0.40	120

At first sight it seems likely that the cause of the first effect is increasing defocusing as the distance from the centre increases. However, closer examination shows that this is not so. For, with a foil of larger crystals, narrow rings are obtained farther out in the diffraction pattern. The half-width of the (422) ring ($B = 0.16$ mm) was about the same as that of the (220) ring ($B = 0.15$ mm). Moreover, if the cause of the widening, e.g. in the case of Au, is defocusing, this must be so pronounced that the half-width due to the primary beam is almost 5 times as broad at the (422) ring as at the (220) ring. Such defocusing is highly improbable.

The large half-width of the (200) ring seems difficult to explain. It is hardly likely that it is due to an incorrect separation of the (111) and (200) peaks. This separation has already been discussed in Chap. VII § 1.

Tol [1940, p. 62] has published figures for the half-widths of the (111) and (220) rings for a Au foil and a Ag foil. He found that the (111) ring was 25 % wider. It will be seen from Tables 19–21 that the present results differ entirely from Tol's. The difference between the (111) and (220) rings was in most cases small, and in conformity with the general tendency of the half-width to increase with increasing scattering angle.

CHAPTER IX

Measurement of the background

The continuous background of the diffraction pattern is often quite strong relative to the interference maxima. It is usually stated that the background becomes stronger as the thickness of the foil increases, and as the accelerating voltage decreases. However, our experience is that the size of the crystals is also of great importance in this respect. The background for a foil with small crystals may be higher than that for another foil twice as thick but with larger crystals. This circumstance is the source of some difficulty in the experimental determination of the atomic factor, since the films without preferred orientation of the crystals that are required for these determinations can only be prepared with relatively small crystals. From this point of view very thin films are to be preferred. The thickest Au and Ag films used here were respectively 225 and 250 Å thick, because thicker films were found to give too high a background.

The cause of the continuous background is not yet known with certainty. It is generally considered that the background is mainly due to inelastic scattering [cf. Thomson and Cochrane, 1939, p. 103]. Von Friesen [1948] measured the loss of energy of background electrons due to diffraction in an Al foil *c.* 500 Å thick, and found that the mean loss of energy was less than 0.17 % at an electron energy of 30 keV.

Tol [1940] suggests that the background may be due to crystal imperfections. Experiments showing that the background rises when the foil is bombarded for long periods are advanced as evidence for this view. Tol attributes this to additional crystal imperfections caused by the electron bombardment. It seems, however, that Tol used an oil diffusion pump without a cooling trap. With such an arrangement it is easy for a layer of carbon to be formed on the foil during bombardment, and this layer heightens the background. The phenomenon is well known from investigations with the electron microscope [cf. König, 1948].

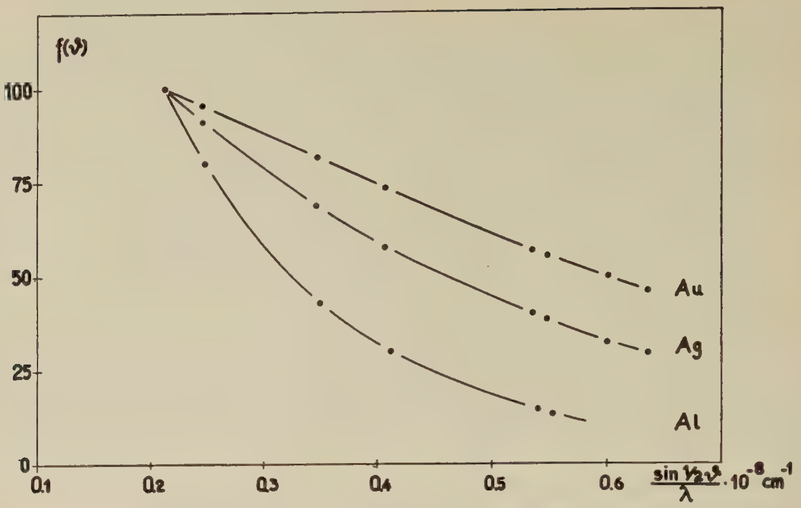

Fig. 25. The intensity distribution of the background in diffraction patterns from foils of Au (140 Å), Ag (150 Å), and Al (140 Å).

THOMSON [1929] was the first to put forward the view that the background is due to electrons that are reflected more than once during their passage through the foil. SJENITZER [1948] is of the same opinion. In support of this view he puts forward certain calculations, e.g. concerning the shape of the background curve.

In connection with the intensity measurements described in Chap. VII, the intensity of the background was also measured in the region of the diffraction pattern between rings (111) and (511). The intensity of the background relative to that of the rings was described by the contrast factor

$$C'_{hkl} = \frac{I_{hkl}}{B_{hkl}}$$

where I_{hkl} is the height of a particular peak (h, k, l), and B_{hkl} the height of the background exactly under the (h, k, l) peak.

The results are given in Tables 22–24, where B_{111} is taken to be 100. Measurements were made on all the intensity curves, so the stated values are as a rule the means of four determinations. The spread of these determinations is small, only about $\pm 1\,\%$ for the higher values. Tables 25–27 give the contrast C_{hkl} for the Au, Ag, and Al foils. The crystal sizes included for purposes of comparison are taken from the measurements of Chap. VIII.

To illustrate the dependence of the background on the material of the foil, Fig. 25 gives the background intensity ($f(\vartheta)$) plotted against $\frac{\sin \vartheta/2}{\lambda}$ for Au, Ag, and Al foils of about the same thickness (140 to 150 Å).

The angular distribution of the background electrons is obtained by multiplying $f(\vartheta)$ by $\sin \vartheta/2$. The resulting curve is shown in Figs. 26–28, where $f(\vartheta) \cdot \sin \vartheta/2$ is plotted against $\frac{\sin \vartheta/2}{\lambda}$ for various thicknesses of Au, Ag, and Al foils.

Table 22. Au: The intensity distribution of the background.

Foil No.	B_{111}	B_{200}	B_{220}	B_{311}	B_{331}	B_{420}	B_{422}	B_{511}
Au 1 (90 Å) . . .	100	93	76	65.5	48.5	47.5	43	40
Au 2 (105 Å) . . .	100	92	72	61.5	44	42.5	37.5	34.5
Au 3 (110 Å) . . .	100	92	72.5	64	46.5	45	39	36.5
Au 4 (140 Å) . . .	100	95.5	81.5	73.5	56.5	55	49.5	45.5
Au 5 (170 Å) . . .	100	95.5	81	73	57	55.5	50	46.5
Au 6 (200 Å) . . .	100	96	85	78	65	63.5		
Au 7 (225 Å) . . .	100	96.5	84.5	78	63.5	62	56.5	53

Table 23. Ag: The intensity distribution of the background.

Foil No.	B_{111}	B_{200}	B_{220}	B_{311}	B_{331}	B_{420}	B_{422}	B_{511}
Ag 1 (75 Å) . . .	100	89.5	64	51	35	34	28	25.5
Ag 2 (95 Å) . . .	100	92	71.5	60.5	43	42	35.5	31.5
Ag 3 (100 Å) . . .	100	91	68	57	38.5	37.5	32	28.5
Ag 4 (150 Å) . . .	100	91	68.5	57.5	40	38.5	32	29
Ag 5 (195 Å) . . .	100	94	76.5	67.5	51.5	50.5	44.5	39.5
Ag 6 (250 Å) . . .	100	94	77.5	68	50.5	49	45	42

Table 24. Al: The intensity distribution of the background.

Foil No.	B_{111}	B_{200}	B_{220}	B_{311}	B_{331}	B_{420}	B_{422}	B_{511}
Al 1 (140 Å) . . .	100	80	43	30	14.5	13.5		
Al 2 (290 Å) . . .	100	80.5	47	34.5	18.5	18		
Al 3 (325 Å) . . .	100	80	45	32	16	15	11.5	
Al 4 (410 Å) . . .	100	81	47.5	35.5	19.5	18.5	14.5	12.5

Table 25. Au: The contrast $C_{\mathrm{hkl}} = \dfrac{I_{\mathrm{hkl}}}{B_{\mathrm{hkl}}}$.

	Au 1 (90 Å)	Au 2 (105 Å)	Au 3 (110 Å)	Au 4 (140 Å)	Au 5 (170 Å)	Au 6 (200 Å)	Au 7 (225 Å)
C_{111}	7.50	6.70	6.05	4.35	3.60	2.15	2.95
C_{220}	2.70	2.60	2.30	1.50	1.30	0.80	1.05
Mean crystal size in Å	60	60	60	55	60	45	55

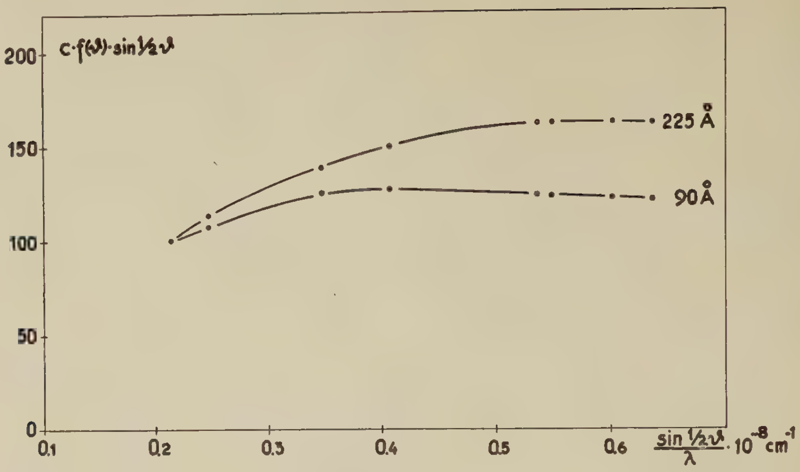

Fig. 26. Au.

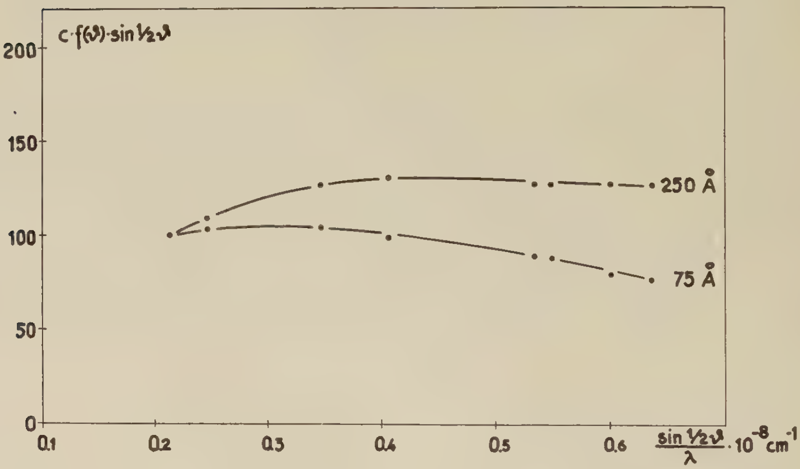

Fig. 27. Ag.

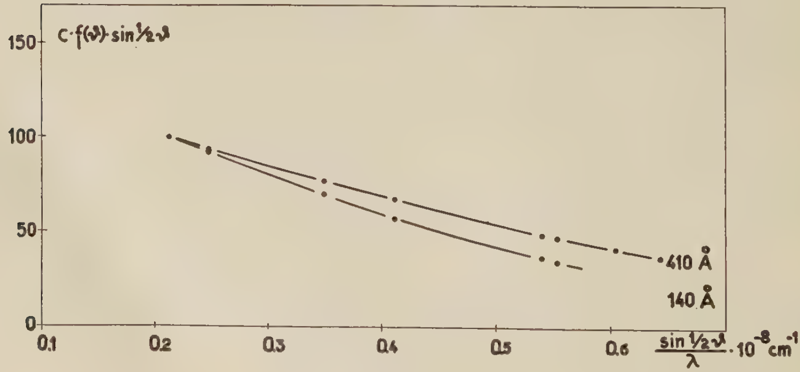

Fig. 28. Al.

Figs. 26–28. The angular distribution of the background electrons in diffraction patterns from Au, Ag, and Al foils of different thickness.

Table 26. Ag: The contrast $C_{\mathrm{hkl}} = \frac{I_{\mathrm{hkl}}}{B_{\mathrm{hkl}}}$.

	Ag 1 (75 Å)	Ag 2 (95 Å)	Ag 3 (100 Å)	Ag 4 (150 Å)	Ag 5 (200 Å)	Ag 6 (250 Å)
C_{111}	6.45	8.05	5.45	3.25	4.35	2.90
C_{220}	2.35	2.80	1.95	1.30	1.70	1.05
Mean crystal size in Å	55	65	55	60	75	60

Table 27. Al: The contrast $C_{\mathrm{hkl}} = \frac{I_{\mathrm{hkl}}}{B_{\mathrm{hkl}}}$.

	Al 1 (140 Å)	Al 2 (290 Å)	Al 3 (325 Å)	Al 4 (410 Å)
C_{111}	2.60	2.20	2.70	2.85
C_{220}	0.95	0.85	1.05	1.20
Mean crystal size in Å	105	100	120	120

Table 28. The intensity distribution of the background. The contrast C_{hkl}.
Foil Au 3, 18.0 and 30.0 kV.

	B_{111}	B_{200}	B_{220}	B_{311}	B_{331}	B_{420}	C_{111}	C_{220}
18.0 kV	100	92.5	73.5	64.5	45	43	3.00	1.20
30.0 kV	100	92	72.5	64	46.5	45	6.05	2.30

The measurements on foil Au 3 at accelerating voltages of 30.0 and 18.0 kV are a clear illustration of the decrease in the contrast for a lower accelerating voltage. As may be seen from Table 28, the contrast is approximately twice as great at 30.0 kV as at 18.0 kV. But the *shape* of the background curve is not affected by a change in the accelerating voltage, as may be seen from a comparison of the B_{hkl} values.

Measurements of the contrast C_{hkl} for Au at 30.0 kV (Table 25) show that it decreases fairly evenly as the foil thickness increases. Foil Au 6 (200 Å) is exceptional, as the contrast is there a minimum. However, comparison of the crystal size shows that for this foil it is 20–25 % less than for the other Au foils. The deviations from the rule that the contrast decreases as the thickness of the foil increases, which are discernible in Tables 26 and 27 may also be explained by variations in crystal size.

As regards the *shape* of the background curve, it is interesting to compare the foil Au 6 (200 Å) just mentioned with Au 7 (225 Å), the foil next in thickness. It is found that the difference in crystal size that had such a marked effect on the contrast does not influence the shape of the background curve.

Summary

1. An electron diffraction apparatus has been constructed for intensity measurements with Geiger counters. This method of registration provides more accurate intensity curves than the photographic method hitherto in use, while at the same time considerable time is gained.

2. A method of preparing self-supporting metal foils of down to 75 Å mean thickness has been developed.

3. The method of preparation is also designed to ensure that the microcrystals in the foils have no tendency to preferred orientation—or only a negligible one. Satisfactory results were obtained with Au and Ag, but the Al foils all exhibited a certain tendency to such preferred orientation.

4. An approximate scheme of corrections has been worked out for Al foils with partial (111) orientation, for use in the experimental determination of the atomic factor.

5. Relative diffraction pattern intensities have been measured for Au (30.0 kV, 90–225 Å; 18.0 kV, 110 Å), Ag (29.5 kV, 75–250 Å), and Al (27.0 kV, 140–410 Å), and from these the atomic factors determined. The atomic factor curve obtained is in each case less steep than that predicted by the kinematic theory. The deviation from the theory is greatest for Au. Foil thickness has not been found to have any distinct effect on these results.

6. The half-widths of the diffraction rings have been determined. That of the (200) ring was found to be larger than those of the neighbouring rings. There is a general increase of the half-width with the scattering angle.

7. The mean size of the microcrystals in the foils has been determined. On an average, the crystal dimensions were: 55 Å for the Au foils, 60 Å for Ag, and 110 Å for Al.

8. The intensity distribution of the background has been investigated for all foils, over a range extending in most cases from the (111) to the (511) ring. The results appear from Figs. 25–28.

9. The contrast between the diffraction rings and the background has been determined for the different foils, and is compared with the foil thickness and the crystal size. The results are given in Tables 25–27.

REFERENCES

Ambrosen, J., Nielsen, F., and Sigurgeirsson, T., Fys. Tidskr. *40*, 101 (1942).
Belwe, E., Zs. f. Phys. *100*, 192 (1936).
Bethe, H., Ann. d. Phys. *87*, 55 (1928).
Blackman, M., Proc. Roy. Soc. *A 173*, 68 (1939).
Born, M., Zs. f. Phys. *38*, 803 (1926).
von Borries, B., and Knoll, M., Phys. Zs. *35*, 279 (1934).
Brill, R., Zs. f. Krist. *87*, 275 (1934).
Debye, P., Ann. d. Phys. *43*, 49 (1914).
Distel, F., Zs. f. Phys. *74*, 785 (1932).
Ellis, C. D., Proc. Roy. Soc. *A 119*, 645 (1928).
Evans, R. D., Rev. Sci. Inst. *5*, 371 (1934).
Faxén, H., Ann. d. Phys. *54*, 615 (1918).
Fermi, E., Zs. f. Phys. *48*, 73 (1928).

FINCH, G. I., and FORDHAM, S., Soc. Chem. Ind., London, *56*, 632 (1937).
VON FRIESEN, S., Uppsala Univ. Årsskrift No. 14 (1935).
—— Arkiv f. Mat.. Astr. o. Fysik *27 B*, No. 11 (1940).
—— Arkiv f. Mat., Astr. o. Fysik *35 A*, No. 18 (1948).
VON FRIESEN, S., and LENNANDER, S., Arkiv f. Mat., Astr. o. Fysik *33 A*, No. 20 (1946).
GERMER, L. H., Phys. Rev. *56*, 58 (1939).
HARTREE, D. R., Proc. Cambr. Phil. Soc. *24*, 89, 426 (1928).
HENNEBERG, W., Zs. f. Phys. *83*, 555 (1933).
HENGSTENBERG, J., and WOLF, K., Hand- und Jahrbuch der chem. Phys. *6*, 1, Leipzig 1935.
JAMES, R. W., and BRINDLEY, G. W., Zs. f. Krist. *78*, 470 (1931).
JOHANNSON, H., and SCHERZER, O., Zs. f. Phys. *80*, 183 (1933).
KIRCHNER, F., Zs. f. Phys. *76*, 576 (1932).
—— Ann. d. Phys. *13*, 38 (1932 a).
KÖNIG, H., Naturwiss. *35*, 261 (1948).
KURYLENKO, C., Thèse. Paris 1939.
LANE, R. O., and ZAFFARANO, D. J., Phys. Rev. *94*, 960 (1954).
LENNANDER, S., Arkiv f. Fysik *5*, No. 18 (1952).
LEVINSTEIN, H., J. Appl. Phys. *20*, 306 (1949).
MARK, H., and WIERL, R., Zs. f. Phys. *60*, 741 (1930).
MØLLER, C., Zs. f. Phys. *66*, 513 (1930).
MOTT, N. F., Proc. Roy. Soc. *A 127*, 658 (1930).
NEHER, H. V., and PICKERING, W. H., Phys. Rev. *53*, 316 (1938).
ORNSTEIN, L. S., BRINKMAN, H., HAUER, A., and TOL, T., Physica *5*, 693 (1938).
PAULING, L., and SHERMAN, J., Zs. f. Krist. *81*, 1 (1932).
PINSKER, Z. G., Electron Diffraction. London 1953.
PISARENKO, N. L., Phys. Zs. Sowjet. *7*, 26 (1935).
PRESTON, G. D., and BIRCUMSHAW, L. L., Phil. Mag. *21*, 713 (1936).
REID, A., Proc. Roy. Soc. *A 119*, 665 (1928).
SJENITZER, F., Diss. Utrecht 1948.
SKINNER, H. W. B., and JOHNSTON, J. E., Proc. Roy. Soc. *A 161*, 420 (1937).
THOMAS, L. H., Proc. Cambr. Phil. Soc. *23*, 542 (1927).
THOMSON, G. P., Proc. Roy. Soc. *A 125*, 352 (1929).
THOMSON, G. P., and COCHRANE, W., Theory and Practice of Electron Diffraction. London 1939.
THOMSON, G. P., and REID, A., Nature *119*, 890 (1927).
TOL, T., Diss. Utrecht 1940.
TOL, T., and ORNSTEIN, L. S., Physica *7*, 685 (1940).
WALLER, I., Zs. f. Phys. *17*, 398 (1923).
—— Diss. Uppsala 1925.
YAMZIN, I. I., and PINSKER, Z. G., Doklady Akad. Nauk SSSR *65*, 645 (1949).
YARWOOD, J., High Vacuum Technique. New York 1946.
YEARIAN, H. J., and HOWE, J. D., Phys. Rev. *48*, 381 (1935).

Tryckt den 26 oktober 1954

Uppsala 1954. Almqvist & Wiksells Boktryckeri AB

DATE DUE

OVERNIGHT NOV 21 '73

OVERNIGHT JAN 7 '75

OVERNIGHT FEB 22 '75

REC'D DEC 15 2014

1/5/15

UTQ Rec'd DEC 22 2014

GAYLORD PRINTED IN U.S.A.

3 8198 314 370 071